

STING agonists for cancer  
immunotherapy pp. 921, 935, & 993

Rethinking the lead–acid  
battery p. 923

A 21st-century atlas of  
the human brain p. 988

# Science

\$15  
21 AUGUST 2020  
[sciencemag.org](http://sciencemag.org)

AAAS

## A WORLD OF MUD

SPECIAL ISSUE





# CONTENTS

21 AUGUST 2020 • VOLUME 369 ISSUE 6506

## SPECIAL SECTION

# MUD

### 894 INTRODUCTION

By D. Malakoff

### 896 MUD ON THE MOVE

By D. Malakoff, N. Desai, and X. Liu

### 898 A MUDDY LEGACY

A dozen years after two scientists showed how centuries-old mud has smothered many U.S. streams, their ideas are guiding restoration efforts *By P. Voosen*

### 902 THE MUD IS ELECTRIC

Bacteria that conduct electricity are transforming how we see sediments *By E. Pennisi*

### 904 Next up: a phone powered by microbial wires?

*By E. Pennisi*

PODCAST

### 906 A DAM BIG PROBLEM

A string of catastrophic failures has raised alarm about dams meant to contain muddy mine wastes *By W. Cornwall*

### 910 RED ALERT

Researchers are working to find new uses for red mud, the caustic byproduct of aluminum production *By R. F. Service*

## ON THE COVER



The muddy Markarfljót River in Iceland carries a heavy load of sediment to the sea. Throughout the world, mud—a mix of fine sediment and water—is one

of the most common and consequential substances. For better and worse, humans are now heavily influencing how mud forms and where it piles up. See page 894. *Photo: Arctic-Images/Getty Images*

## INSIGHTS

### POLICY FORUM

#### 912 Knowledge transfer for large-scale vaccine manufacturing

Massive, rapid production will require firms to share know-how not just about what to make but how to make it *By W. Nicholson Price II et al.*

### PERSPECTIVES

#### 915 The foundation of efficient robot learning

Innate structure reduces data requirements and improves robustness *By L. P. Kaelbling*

#### 917 A glycoprotein in urine binds bacteria and blocks infections

Direct imaging of a human fluid illuminates the molecular basis of urinary tract protection from disease *By W. Kukulski*  
REPORT p. 1005

#### 918 When the smallest details count

The type of liquid crystals formed by smooth colloidal rods depends on their degree of curvature *By M. H. Godinho*  
RESEARCH ARTICLE p. 950

#### 919 Remodeling vasculature to avoid blindness

Pathological vasculature marks itself for repair by deploying neutrophil extracellular traps *By E. A. Podrez and T. V. Byzova*  
RESEARCH ARTICLE p. 934

#### 921 Immunotherapy with a sting

New agonists of an innate immune pathway induce antitumor immunity in mice *By T. F. Gajewski and E. F. Higgs*  
RESEARCH ARTICLE p. 935; REPORT p. 993

#### 923 Past, present, and future of lead-acid batteries

Improvements could increase energy density and enable power-grid storage applications *By P. P. Lopes and V. R. Stamenkovic*

#### 925 James G. Townsel (1935–2020)

Neuroscientist and devoted mentor of diverse scientists *By R. Nishi et al.*

### BOOKS ET AL.

#### 926 One step forward, two steps back

Interest groups and state-level political inertia have stalled many of America's clean energy initiatives *By S. H. Ali*

#### 927 Ray Bradbury, luminary of the space age, at 100

A new biography chronicles the golden years of Earth's first martian *By I. Ockert*

## NEWS

### IN BRIEF

#### 886 News at a glance

### IN DEPTH

#### 888 Critics question whether novel reactor is 'walk-away safe'

Design approval nears for NuScale Power's small modular reactors, but deployment plans slip 3 years *By A. Cho*

#### 889 Paradox puts objectivity on shaky footing

Quantum test of venerable thought experiment suggests facts are relative *By G. Musser*

#### 890 Coronavirus creates a flu season guessing game

SARS-CoV-2's interactions with other pathogens remain unknown as winter looms *By K. Servick*

#### 892 Pandemic's fallout on malaria control appears limited so far

Countries avert disaster by resuming bed net campaigns *By L. Roberts*

#### 893 Pandemic lockdown stirs up ecological research

Biologists launch studies of how wildlife around the world responded to the "anthropause" *By E. Stokstad*

PODCAST



## LETTERS

### 928 Baer's pochard duck at risk of extinction

By X. Tong

### 928 Waterbirds' coastal habitat in danger

By Y. Wu et al.

### 929 Protect the giant ibis through the pandemic

By H. Yang et al.

## 929 Errata

# RESEARCH

## IN BRIEF

**930** From *Science* and other journals

## REVIEW

### 933 Photosynthesis

Light harvesting in oxygenic photosynthesis:

Structural biology meets spectroscopy

R. Croce and H. van Amerongen

REVIEW SUMMARY; FOR FULL TEXT:

DX.DOI.ORG/10.1126/SCIENCE.AAY2058

## RESEARCH ARTICLES

### 934 Biomedicine

Neutrophil extracellular traps target senescent vasculature for tissue remodeling in retinopathy F. Binet et al.

RESEARCH ARTICLE SUMMARY; FOR FULL TEXT:

DX.DOI.ORG/10.1126/SCIENCE.AAY5356

PERSPECTIVE p. 919

### 935 Drug development

An orally available non-nucleotide STING agonist with antitumor activity B.-S. Pan et al.

RESEARCH ARTICLE SUMMARY; FOR FULL TEXT:

DX.DOI.ORG/10.1126/SCIENCE.ABA6098

PERSPECTIVE p. 921; REPORT p. 993

### 936 Cancer immunology

Cross-reactivity between tumor MHC class I-restricted antigens and an enterococcal bacteriophage A. Fluckiger et al.

### 942 Cancer immunology

BTN3A1 governs antitumor responses by coordinating  $\alpha\beta$  and  $\gamma\delta$  T cells K. K. Payne et al.

### 950 Liquid crystals

Shaping colloidal bananas to reveal biaxial, splay-bend nematic, and smectic phases C. Fernández-Rico et al.

PERSPECTIVE p. 918



Ice core drilled at Concordia Station in Antarctica suggests fast, pulse-like jumps in atmospheric CO<sub>2</sub> of the distant past.

### 956 Coronavirus

Isolation of potent SARS-CoV-2 neutralizing antibodies and protection from disease in a small animal model T. F. Rogers et al.

### 963 Global climate change

Synchronous timing of abrupt climate changes during the last glacial period E. C. Corrick et al.

## REPORTS

### 970 Organic chemistry

Asymmetric remote C–H borylation of aliphatic amides and esters with a modular iridium catalyst R. L. Reyes et al.

### 974 Chemical physics

Attosecond spectroscopy of liquid water I. Jordan et al.

### 979 Surface chemistry

Covalent surface modifications and superconductivity of two-dimensional metal carbide MXenes V. Kamysbayev et al.

### 984 Immunology

SOSTDC1-producing follicular helper T cells promote regulatory follicular T cell differentiation X. Wu et al.

### 988 Neuroscience

Julich-Brain: A 3D probabilistic atlas of the human brain's cytoarchitecture K. Amunts et al.

### 993 Drug development

Antitumor activity of a systemic STING-activating non-nucleotide cGAMP mimetic E. N. Chin et al.

PERSPECTIVE p. 921; RESEARCH ARTICLE p. 935

### 1000 Global carbon cycle

Abrupt CO<sub>2</sub> release to the atmosphere under glacial and early interglacial climate conditions C. Nehrbass-Ahles et al.

### 1005 Microbiology

Architecture and function of human uromodulin filaments in urinary tract infections G. L. Weiss et al.

PERSPECTIVE p. 917

## Coronavirus

**1010** Studies in humanized mice and convalescent humans yield a SARS-CoV-2 antibody cocktail J. Hansen et al.

**1014** Antibody cocktail to SARS-CoV-2 spike protein prevents rapid mutational escape seen with individual antibodies A. Baum et al.

## DEPARTMENTS

### 884 Editorial

Black scientists matter  
By Malegapuru William Makgoba

### 885 Editorial

A dangerous rush for vaccines  
By H. Holden Thorp

### 1026 Working Life

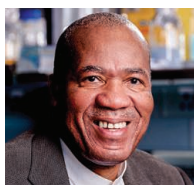
Choose your adviser wisely  
By Akshata Naik

Science Careers ..... 1019

SCIENCE (ISSN 0036-8075) is published weekly on Friday, except last week in December, by the American Association for the Advancement of Science, 1200 New York Avenue, NW, Washington, DC 20005. Periodicals mail postage (publication No. 484460) paid at Washington, DC, and additional mailing offices. Copyright © 2020 by the American Association for the Advancement of Science. The title SCIENCE is a registered trademark of the AAAS. Domestic individual membership, including subscription (12 months): \$165 (\$74 allocated to subscription). Domestic institutional subscription (51 issues): \$2148; Foreign postage extra: \$98. First class, airmail, student, and emeritus rates on request. Canadian rates with GST available upon request. GST #R125488122. Publications Mail Agreement Number 1069624. Printed in the U.S.A.  
Change of address: Allow 4 weeks, giving old and new addresses and 8-digit account number. Postmaster: Send change of address to AAAS, P.O. Box 96178, Washington, DC 20090-6178. Single-copy sales: \$15 each plus shipping and handling available from backissues.sciencemag.org; bulk rate on request. Authorization to reproduce material for internal or personal use under circumstances not falling within the fair use provisions of the Copyright Act can be obtained through the Copyright Clearance Center (CCC), www.copyright.com. The identification code for Science is 0036-8075. Science is indexed in the Reader's Guide to Periodical Literature and in several specialized indexes.



# Black scientists matter



**Malegapuru William Makgoba**

is the Health Ombud of the Republic of South Africa, Pretoria, South Africa. mmakgoba@ohsc.org.za

**T**he recent murder of George Floyd by police in the United States, the Black Lives Matter protests around the world, and racial inequalities everywhere that have been exposed by the coronavirus disease 2019 (COVID-19) pandemic—such as the disproportionately high vulnerability and mortality in African-American, Afro-Caribbean, and Afro-Latin communities—are a wake-up call for humankind to recalibrate, restructure, and reimagine its beliefs and behaviors. It's important to recognize that beneath overt racism are subtle forms of structural and institutionalized racism that have existed for a very long time, unabated, across communities—in homes, hospitals, churches, schools, governments, and so many other institutions—throughout the Western world. Now, societies are being provoked to ponder fundamental questions about racism. What about the scientific world? Do Black scientists matter?

My perspective is based on my experiences as a Black and African scientist in South Africa, the United Kingdom, and the United States, as well as in African nations through the African AIDS Vaccine Program. I've had the opportunity to interact with a range of Black African colleagues, from young African scientists to African scientific leaders in their fields or in their institutions. We often discussed our dreams, aspirations, and passions as well as work environments in the Western world where Black scientists (African or otherwise) are not well-represented or valued—where Black scientists have felt like aliens of the scientific enterprise.

One problem in the Western world is that the scientific enterprise is in denial about its inherent racism. Black scientists encounter discrimination when they embark on a science career in Western countries. The overwhelming message from their experiences is that the culture of academic science where Black scientists are underrepresented is riddled with deeply entrenched racism of various forms and subtleties. For example, although science is supposed to be objective, many white scientists who are part of the enterprise refuse to believe and acknowledge the racism and alienation that is articulated by Black scientists regarding their work and career. I have experienced, and have heard of, some white scientific leaders who feel that the problem is not the system, but how Black

scientists fail to adapt to and cope with the discipline, standards, and work ethic demands of the science establishment. White scientists may think that they know what racism is and that they can better explain to Black scientists the experiences that those Black individuals have endured. This dismissive attitude ignores the reality of discrimination and alienation experienced by Black scientists. These realities include differences in the way young people are encouraged (or discouraged) to pursue scientific careers, the lack of role models, not having access to meaningful career guidance and mentorship, and not being plugged into influential career networks. Consequently, even the best and brightest can fail to be recognized and admitted into top scientific programs.

Research and academic institutions, scholarly academies, and scientific publications in the Western world all show a paucity of Black scientists in leadership positions, on editorial boards, and as authors. And although the Western scientific establishment has several recognition systems for meritorious scientific discoveries, rarely are Black scientists represented among the awardees. In fact, some young Black African scientists have told me that their research was credited to their superiors and even patented and sold without their involvement. Sadly, Black scientists who do not assimilate or conform, or who abandon their African or Caribbean

or Latin American identity altogether in exchange for the so-called superior white Western identity, can become intellectually and socially isolated. Identity changes and health crises can cause some Black scientists to suffer alienation even within Black communities in these Western nations.

Racism in science has a long history throughout the world and manifests largely through systems of evaluation, recognition, funding, and promotion. The scientific community can postpone confronting this pernicious reality, but it cannot stop the train of change—it has left the station. For equality in the global scientific enterprise to be addressed, meaningful change should start in the Western world's scientific system, where a new environment must be created in which not only Black scientists but all scientists can thrive—one that values human dignity, equity, and social justice.

—Malegapuru William Makgoba

**“...Black scientists have felt like aliens of the scientific enterprise.”**



# A dangerous rush for vaccines

**T**he chasm between science and politics continues to grow, with Russian President Putin announcing this week that a fast-tracked vaccine for coronavirus disease 2019 (COVID-19) is ready for use, and President Trump indicating days earlier that a vaccine could be ready in the United States before the 3 November presidential election. There's been a dangerous rush to get to the vaccine finish line first. In a race of "Sputnik" proportions (as Putin puts it), quick approval by regulatory agencies is needed to "win." This is dangerous thinking, driven by political goals and instant gratification: Shortcuts in testing for vaccine safety and efficacy endanger millions of lives in the short term and will damage public confidence in vaccines and in science for a long time to come.

The Russian vaccine remains shrouded in mystery—there is no published information about it, and what has been touted comes from the mouths of politicians. In the United States, the pressure applied to government scientists by the administration on any aspect of the pandemic is becoming increasingly palpable, as they have been criticized or quieted in plain sight by the administration and Trump. Anthony Fauci, the nation's foremost leader on infectious diseases and a member of the White House Coronavirus Task Force, has been the most willing to state things clearly, but he has had to deal with muzzling and outright abuse from Trump and White House adviser Peter Navarro (not to mention shameful threats of violence against him and his family).

The majority of epidemiologists worldwide who work on infectious diseases are firmly committed to randomized controlled trials ("phase 3") for all interventions, but especially for vaccines to be given to healthy people. This method allows comparison to a control group that receives a placebo. The phase 3 studies now under way on promising COVID-19 vaccine candidates involve approximately 30,000 patients. A randomized controlled trial is particularly important for determining the effectiveness of the vaccine, and the trial must continue until individuals in the control group become infected. It is impossible to predict how long that will take. Physicians who seek to advise healthy patients on taking the vaccine will rightfully require these data.

The U.S. Food and Drug Administration (FDA) has

a Vaccines and Related Biological Products Advisory Committee to consult on the approval of vaccines and any associated emergency use authorizations. There are calls for assurances that there will not be any such authorization for COVID-19; the only emergency use authorization ever granted for a vaccine was for one against anthrax because of the purported threat of biological warfare involving this agent. In any event, the scientific community in the United States must insist that approvals of an emergency use authorization or for a COVID-19 vaccine itself should be made in consultation with the FDA's Committee—and actions around the world should involve similar scientific oversight.

Premature approval of a vaccine in the United States (or anywhere) could be a disastrous replay of the hydroxychloroquine fiasco but with much higher stakes. Approval of a vaccine that is harmful or isn't effective could be leveraged by political forces that already propagate vaccine fears.

So far, U.S. government scientists are holding strong. Francis Collins, director of the National Institutes of Health, emphatically called for phase 3 trials of vaccines, and FDA director Stephen Hahn also has stated that he will follow the science. There's a lot riding on Hahn, and as long as he holds firm with the science, the scientific community should

support him. He made a mistake in granting an emergency use authorization for hydroxychloroquine but withdrew it once he saw the data—randomized clinical trials showing that the drug was useless against COVID-19. Now the other faces of the U.S. government's science apparatus—Robert Redfield (director of the Centers for Disease Control and Prevention), Deborah Birx (response coordinator of the White House Coronavirus Task Force), and Brett Giroir (assistant secretary for Health)—need to push all their chips onto the table in favor of a phase 3 randomized controlled trial on any COVID-19 vaccine. Despite their periodic squirming and equivocation, these leaders all deserve and need the nation's support as long as they continue to respect the science on this issue.

Countless lives are at stake—no compromises on the vaccine.

—H. Holden Thorp



**H. Holden Thorp**  
Editor-in-Chief,  
*Science* journals.  
hthorp@aaas.org;  
@holdenthorp

**"...Shortcuts  
in testing  
for vaccine safety  
and efficacy  
endanger millions  
of lives..."**



“We have tried to make this work, but it is not working.”

**Barbara Rimer**, dean of public health at the University of North Carolina, Chapel Hill, as it moved to online-only instruction, just 1 week after in-person classes resumed, because campus COVID-19 cases surged.

## IN BRIEF

Edited by **Jeffrey Brainard**



Arecibo's dish lost 250 of its 40,000 panels when a cable broke—less damage than this view suggests.

## ASTRONOMY

### Arecibo telescope damage assessed

**T**he iconic Arecibo radio telescope in Puerto Rico was damaged on 10 August when a snapped steel cable smashed into a receiver and tore a 30-meter gash in its 307-meter-wide dish. No one was injured during the early morning incident. The damage to the dish is not critical, but the broken cable has destabilized a platform holding receiver antennas high above the dish. Managers have halted observations for at least 2 weeks while investigations are carried out, and no cost estimate or restart schedule will be available before then, says Ramon Lugo of the University of Central Florida, which manages the observatory for the National Science Foundation. Engineers are examining what went wrong with the 23-year-old cable, whether a temporary replacement can be rigged up, and what damage was done to the antennas. Set in a depression in the hills, Arecibo was the world's largest single dish for 5 decades until a Chinese telescope surpassed it in 2016 and is still widely used for astronomy, planetary science, and atmospheric research.

## Africa halts wild poliovirus

**INFECTIOUS DISEASES** | After a long fight, Africa has wiped out the wild poliovirus. The last case occurred 4 years ago, and on 25 August, the independent Africa Regional Certification Commission, acting on behalf of the World Health Organization, is expected to officially declare the continent free of the wild virus. Africa came close before, going 2 years without a case until 2016, when the wild virus appeared seemingly out of the blue in Borno state in northeastern Nigeria, where the militant group Boko Haram reigns, and paralyzed four children. Polioviruses derived from the oral polio vaccine continue to circulate and cause paralysis across Africa; wiping them out has proved extremely difficult. Pakistan and Afghanistan are now the last bastions of the wild virus.

## U.K. replaces health agency

**COVID-19** | Facing criticism over its response to the COVID-19 pandemic, the U.K. government announced on 18 August that it will replace England's disease-control agency with a United Kingdom-wide one focused on infectious diseases. The move merges Public Health England (PHE) with England's contact tracing program, NHS Test and Trace, and the U.K. Joint Biosecurity Centre, to create the new agency, the National Institute for Health Protection. Its interim leader will be businesswoman and Conservative parliamentarian Dido Harding, who had headed NHS Test and Trace. PHE's work on obesity and other noncommunicable health conditions will be shifted to local authorities, but the government has not yet clarified how. Critics said the change was poorly conceived and questioned whether the new agency is set up to succeed, citing a need for close coordination with the National Health Service's hospital-based scientists.

## Redo for radiocarbon dates

**GEOCHRONOLOGY** | The first update of carbon dating in nearly a decade, published last week, allows scientists to probe 5000 years further into the past and revises the timing of big events in human history.

PHOTO: ARECIBO OBSERVATORY



Living things incorporate radioactive carbon-14 from the environment, and the decay of this carbon after death provides a clock for dating specimens from the recent past. The update extends the technique's use to about 55,000 years ago. The recalibrated timeline shows that *Homo sapiens* and Neanderthals overlapped in Europe for centuries longer than once thought. It also shows the volcanic eruption that devastated the island of Thera in Greece may have occurred as recently as 1544 B.C.E., in line with archaeological evidence.

## Mathematician's sentence delayed

**CRIMINAL JUSTICE** | Eva Lee, an applied mathematician at the Georgia Institute of Technology who admitted to making false statements related to a U.S. National Science Foundation (NSF) grant, won't begin to serve her sentence until next spring so she can continue to build models to help control the COVID-19 pandemic. On 12 August, U.S. District Court Judge Steve Jones rejected the government's request for 8 months of immediate home confinement, saying the country "needs her" talents now. Instead, he ordered Lee confined for 2 months starting in April 2021 and said that schedule could be further modified. Lee pleaded guilty in December 2019 to misrepresenting information to NSF in a report related to the \$40,000 grant and then lying to federal agents investigating her actions. She told Jones she didn't understand the reporting requirements and that her university withheld the necessary administrative support for her grant, which it has disputed.

## U.S. academies to study racism

**RACIAL JUSTICE** | The National Academies of Sciences, Engineering, and Medicine (NASEM) is gearing up for an in-depth study of systemic racism in U.S. academic research. Representative Eddie Bernice Johnson (D-TX), who leads the science committee in the U.S. House of Representatives, has asked it to analyze "the extent to which the U.S. scientific enterprise perpetuates systemic inequities to the detriment of society as a whole, as well as how those inequities are manifested." National Academy of Sciences President Marcia McNutt says such a study could set the table for needed changes in the same way that a 2018 NASEM report on sexual harassment catalyzed discussion and action. Structural racism in academia is "hindering our ability to deal with some of our biggest challenges, including the current COVID-19 pandemic," says Freeman Hrabowski, president of the University of Maryland, Baltimore County.

## TRUMP TRACKER

## Trump environmental plans spark new controversies

The White House this month announced it will move ahead with controversial changes to two major environmental policies, but suffered a legal setback on a third.

### Arctic drilling OK'd

The U.S. Interior Department on 17 August announced it will move ahead with plans to sell leases to drill for oil in Alaska's Arctic National Wildlife Refuge. The decision followed an environmental review that concluded drilling on much of the refuge's 6300-square-kilometer coastal plain wouldn't endanger caribou or polar bears, or exacerbate climate change. Scientists have warned the effects of oil drilling could harm the animals, and environmental groups swiftly vowed legal challenges.

### Methane rule relaxed

Several state governments and environmental groups are preparing court challenges to a new Trump administration rule, finalized last week, that gives oil and gas companies greater leeway to allow leaks of methane, a potent climate-warming gas, from their facilities. Critics say the rule has fatal flaws, including how it calculates costs and benefits, and many larger firms opposed the change, saying it would create uncertainty and discourage efficiency improvements. If Democrats win control of the Senate and the White House in January 2021, they could overturn this and other recent regulatory decisions.

### Bird protections upheld

A federal judge on 11 August overturned an administration reinterpretation of the 1918 Migratory Bird Treaty Act that had helped companies avoid fines for inadvertently killing birds. "It is not only a sin to kill a mockingbird," U.S. District Court Judge Valerie Caproni wrote in her decision, quoting *To Kill a Mockingbird*, "it is also a crime" under federal law. Conservationists had objected to the reinterpretation, because it meant businesses could not be fined for failing to protect birds from foreseeable fatal hazards, such as oil spills and uncovered oil waste pits.



A worker aids a pelican covered in oil from the 2010 Deepwater Horizon accident.

PHOTO: GERALD HERBERT/AP PHOTO



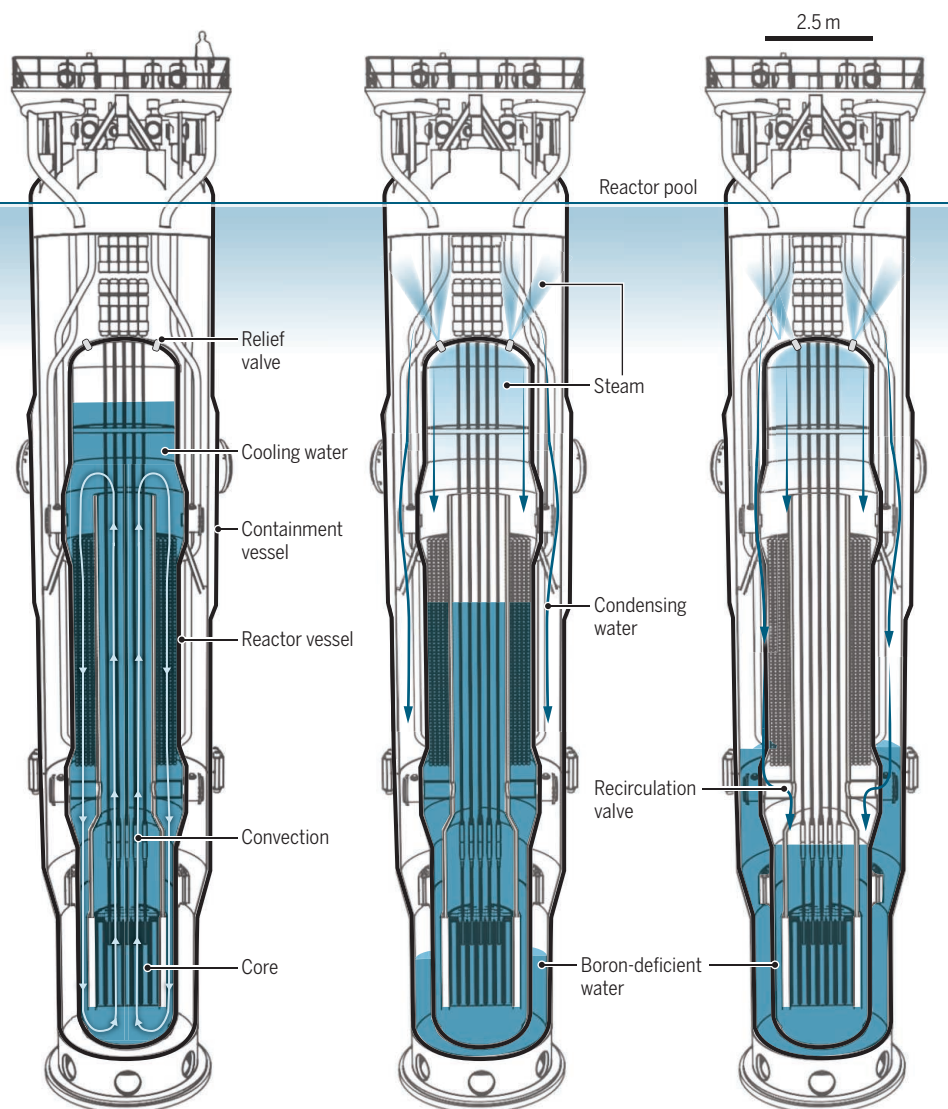
## IN DEPTH

## NUCLEAR POWER

# Critics question whether novel reactor is 'walk-away safe'

Design approval nears for NuScale Power's small modular reactors, but deployment plans slip 3 years

By Adrian Cho



**PASSIVE SAFETY?** Normally, convection circulates water—laced with boron to tune the nuclear reaction—through the core of NuScale's reactor (left). If the reactor overheats, it shuts down and valves release steam into the containment vessel, where it conducts heat to a surrounding pool and condenses (center). The water flows back into the core, keeping it safely submerged (right). But the condensed water can be low in boron, and reviewers worried it could cause the reactor to spring back to life.

Engineers at NuScale Power believe they can revive the moribund U.S. nuclear industry by thinking small. Spun out of Oregon State University in 2007, the company is striving to win approval from the U.S. Nuclear Regulatory Commission (NRC) for the design of a new factory-built, modular fission reactor meant to be smaller, safer, and cheaper than the gigawatt behemoths operating today (*Science*, 22 February 2019, p. 806). But even as that 4-year process culminates, reviewers have unearthed design problems, including one that critics say undermines NuScale's claim that in an emergency, its small modular reactor (SMR) would shut itself down without operator intervention.

The issues are typical of the snags new reactor designs run into on the road to approval, says Michael Corradini, a nuclear engineer at the University of Wisconsin, Madison. "I don't think these things are show-stoppers." However, M. V. Ramana, a physicist who studies public policy at the University of British Columbia, Vancouver, and has been critical of NuScale, says the problems show the company has oversold the claim that its SMRs are "walk-away safe." "They have given you the standard by which to evaluate them and they're failing," Ramana says.

Even critics expect that next month NRC will issue a safety evaluation report approving the NuScale design, which will be a major milestone, says José Reyes, NuScale's co-founder and chief technology officer. "This is the document that says, 'This design is safe,'" says Reyes, who hatched the idea for the reactor in 1999. NuScale will resolve the lingering technical issues before anything gets built, he says.

However, NuScale's likely first customer, Utah Associated Municipal Power Systems (UAMPS), has delayed plans to build a NuScale plant, which would include a dozen of the reactors, at the Department of Energy's (DOE's) Idaho National Laboratory. The \$6.1 billion plant would now be completed by 2030, 3 years later than previously planned, says UAMPS spokesperson LaVarr Webb. "UAMPS is still very committed to the project," Webb says. "Our members really want to decarbonize their electric supply and replace coal." The delay will give UAMPS more time to develop its application for an NRC license to build and operate the plant, Webb says. The deal depends on DOE contributing \$1.4 billion to the cost of the plant, he adds.

A nuclear reactor is essentially a boiler. In its core, uranium atoms split, releasing heat and neutrons, which split other uranium atoms in a chain reaction. Highly pressurized cooling water circulates through the core and carries heat to a steam generator,



where it boils water in a separate circuit to drive turbines and generate electricity. The cooling water also slows the speeding neutrons, increasing the probability that they will split the uranium atoms.

Expense and safety worries have stalled nuclear power despite increasing demand for carbon-free electricity. NuScale's remedy is a radically new design. A conventional reactor relies on huge pumps and pipes to drive the cooling water through its core and ferry it to the steam generator. A NuScale reactor—which would be less than 25 meters high, hold about one-eighth as much fuel as a large power reactor, and generate less than one-tenth as much electric power—would rely on natural convection to circulate the water (see diagram, p. 888).

It is also designed to shut itself down in a pinch. Each reactor fits within a steel containment vessel, which in turn sits in a pool of water holding up to a dozen modules. Ordinarily, the space between the reactor and containment vessel remains evacuated, like the vacuum jacket in a thermos bottle. Should the core overheat or the reactor leak, relief valves would vent steam into the evacuated space, where it would conduct heat to the pool and condense into the bottom of the containment vessel. When enough water had accumulated, it would flow back into the reactor to keep the core safely submerged. NuScale is so confident in the design that it has asked NRC to allow its plants to run without the standard 32-kilometer-wide emergency planning zone.

In March, however, a panel of independent experts found a potential flaw in that scheme. To help control the chain reaction, the reactor's cooling water contains boron, which, unlike water, absorbs neutrons. But the steam leaves the boron behind, so the element will be missing from the water condensing in the reactor and containment vessel, NRC's Advisory Committee on Reactor Safeguards (ACRS) noted. When the boron-poor water re-enters the core, it could conceivably revive the chain reaction and possibly melt the core, ACRS concluded in a report on its 5–6 March meeting.

NuScale modified its design to ensure that more boron would spread to the returning water. The small changes eliminated any potential problem, Reyes says. However, at a 21 July meeting, ACRS concluded that operators could still inadvertently drive deborated water into the core when trying to recover from an accident. "I'm not saying that this [scenario] is going to happen," ACRS member Jose March-Leuba said, ac-

cording to the meeting transcript. "I don't see a calculation that proves it wrong."

Ultimately, whoever applies for a license to build and operate a NuScale plant—presumably UAMPS—must devise an operating procedure that ensures such a scenario never occurs. But NuScale should provide guidance, Vesna Dimitrijević, a nuclear engineer and ACRS member, argued at the meeting. The issue demonstrates how slippery a seemingly black-and-white technical issue can be. "The applicant thinks there isn't a problem here," Corradini says. "The ACRS isn't so sure and want the staff and the applicant to think through the steps to make sure this isn't a problem." The NRC staff, which writes the safety evaluation report, thinks it can be dealt with in the operating license, he adds.

The issue pokes a hole in NuScale's credibility, says Edwin Lyman, a physicist with the Union of Concerned Scientists. "This is a case of the public relations driving the science instead of the other way around," he says. Sarah Fields, program director of the environmental group Uranium Watch, says the safety questions argue against NuScale's request to operate without an emergency planning zone. "That's a crazy thing to do for a reactor design that's totally new and with which you have no operating experience."

Reyes says the company's analysis justifies that request. NuScale's studies show that under any credible scenario, the radiation at the plant periphery will not exceed NRC's limits for the edge of the traditional emergency planning zone, he says. Permission to forgo the buffer zone could help NuScale market its plants where space is tight, he says.

ACRS found a few other problems, including one with NuScale's novel steam generator, which sits within the reactor vessel and could be prone to damaging vibrations. Still, on 29 July, ACRS recommended that NRC issue the safety evaluation report and certify NuScale's design. "If there really was a fatal flaw, ACRS would not have published a positive report," Reyes says.

NRC plans to publish its safety evaluation report next month, and by year's end it is expected to issue draft "rules" that would essentially approve the design. But that won't end the regulatory odyssey. The current design specifies a reactor output of 50 megawatts of electricity, whereas the UAMPS plan calls for 60 megawatts. The change requires a separate NRC approval, Reyes says, during which NuScale will resolve the outstanding technical issues. That additional 2-year review should start in 2022. ■

**"If there really was a fatal flaw, ACRS would not have published a positive report."**

**José Reyes**, NuScale Power

## QUANTUM THEORY

# Paradox puts objectivity on shaky footing

Quantum test of venerable thought experiment suggests facts are relative

By **George Musser**

**N**early 60 years ago, Nobel Prize-winning physicist Eugene Wigner captured one of the many oddities of quantum mechanics in a thought experiment. He imagined a friend of his, sealed in a lab, measuring a particle such as an atom while Wigner stood outside. Quantum mechanics famously allows particles to occupy many locations at once—a so-called superposition—but the friend's observation "collapses" the particle to just one spot. Yet for Wigner, the superposition remains: The collapse occurs only when he makes a measurement sometime later. Worse, Wigner also sees the friend in a superposition. Their experiences directly conflict.

Now, researchers in Australia and Taiwan offer perhaps the sharpest demonstration that Wigner's paradox is real. In a study published this week in *Nature Physics*, they transform the thought experiment into a mathematical theorem that confirms the irreconcilable contradiction at the heart of the scenario. The team also tests the theorem with an experiment, using photons as proxies for the humans. Whereas Wigner believed resolving the paradox requires quantum mechanics to break down for large systems such as human observers, some of the new study's authors believe something just as fundamental is on thin ice: objectivity. The puzzle could mean there is no such thing as an absolute fact, one that is as true for me as it is for you.

"It's a bit disconcerting," says co-author Nora Tischler of Griffith University. "A measurement outcome is what science is based on. If somehow that's not absolute, it's hard to imagine."

Some physicists dismiss thought experiments like Wigner's as interpretive navel gazing. But the study shows that the contradictions emerge in actual experiments, says Dustin Lazarovici, a physicist and philosopher at the University of Lausanne who was not part of the team. "The paper goes to great lengths to speak the language of those



who have tried to merely discuss foundational issues away and may thus compel at least some to face up to them,” he says.

Wigner’s thought experiment has seen renewed attention in recent years. In 2015, Časlav Brukner of the University of Vienna tested the most intuitive way around the paradox: that the friend inside the lab has in fact seen the particle in one place or another, and Wigner just doesn’t know where it is yet. In the jargon of quantum theory, the friend’s result is a hidden variable.

Brukner sought to rule out that conclusion in a thought experiment of his own, using a trick—based on quantum entanglement—to bring the hidden variable out into the open. He imagined setting up two friend-Wigner pairs and giving each a particle, entangled with its partner in such a way that their attributes, upon measurement, are correlated. Each friend measures the particle, each Wigner measures the friend measuring the particle, and the two Wigners compare notes. The process repeats. If the friends saw definite results—as you might suspect—the Wigners’ own findings would show only weak correlations. But instead they find a pattern of strong correlations. “You run into contradictions,” Brukner says.

In 2018, Richard Healey, a philosopher of physics at the University of Arizona, pointed out a loophole in Brukner’s argument, which Tischler and her colleagues have now closed. In their new scenario they make four assumptions. One is that the results the friends obtain are real: They can be combined with other measurements to form a shared body of knowledge. The researchers also assume quantum mechanics is universal, as valid for observers as for particles; that the choices the observers make are free of peculiar biases induced by a godlike superdeterminism; and that physics is local, so that one observer’s choices do not affect another’s results.

Yet the analysis shows the contradictions of Wigner’s paradox persist. The team’s table-

top experiment, in which it made pairs of entangled photons, also backs up the paradox. Optical elements steered each photon onto a path that depended on its polarization: the equivalent of the friends’ observations. The photon then entered a second set of elements and detectors that played the role of the Wigners. The team found, again, a mismatch between the observations of the friends and the Wigners. What is more, when they varied exactly how entangled the photons were, they found that the mismatch occurs for different conditions than in Brukner’s scenario. “That shows that we really have something new here,” Tischler says.

It also indicates that one of the four assumptions has to give. Few physicists believe superdeterminism could be to blame. Locality is already under fire in quantum theory, but a failure in this case would imply an especially potent form of nonlocality. So some are questioning the tenet that observers can pool their measurements empirically. “It could be that there are facts for one observer, and facts for another; they need not mesh,” says study co-author and Griffith physicist Howard Wiseman. It is a radical relativism, still jarring to many. “From a classical perspective, what everyone sees is considered objective, independent of what anyone else sees,” says Olimpia Lombardi, a philosopher of physics at the University of Buenos Aires.

And then there is Wigner’s verdict: that quantum mechanics itself breaks down. Of all the assumptions, it is the most testable, by efforts to probe quantum mechanics on ever larger scales. But the one position that doesn’t survive the analysis is having no position, says Eric Cavalcanti, a co-author at Griffith. “Most physicists, they think: ‘That’s just philosophical mumbo-jumbo.’” Now, he says, “They will have a hard time.” ■

George Musser is a journalist based in New Jersey and author of *Spooky Action at a Distance*.

## COVID-19

# Coronavirus creates a flu season guessing game

SARS-CoV-2’s interactions with other pathogens remain unknown as winter looms

By Kelly Servick

In March, as the Southern Hemisphere braced for winter flu season while fighting COVID-19, epidemiologist Cheryl Cohen and colleagues at South Africa’s National Institute for Communicable Diseases (NICD) set up a plan to learn from the double whammy. They hoped to study interactions between seasonal respiratory viruses and SARS-CoV-2, which causes COVID-19. Does infection with one change a person’s risk of catching the other? How do people fare when they have both?

But the flu season—and the answers—never came. NICD’s Centre for Respiratory Disease and Meningitis, which Cohen leads, has logged only a single flu case since the end of March. In previous years, the country’s surveillance platforms, which capture a sampling of flu cases from doctors’ offices, hospitals, and clinics, have documented, on average, about 700 cases during that period, Cohen says. “We’ve been doing flu surveillance since 1984, and it’s unprecedented.”

Some cases probably got overlooked as clinics temporarily closed and people with mild symptoms avoided medical care, Cohen says. “But I don’t believe it possible that we’ve entirely missed the flu season with all of our [surveillance] programs.” Apparently, travel restrictions, school closures, social distancing, and mask wearing have all but stopped flu from spreading in South Africa. Similar stories have emerged from Australia, New Zealand, and parts of South America.

The Northern Hemisphere hopes to be so lucky. Few cases in the south might mean little infection spreading north, says Pasi Penttinen, head of the influenza and respiratory illness program at the European Centre for Disease Prevention and Control



When observers observe observers, a quantum paradox persists, suggesting measurements are relative.

Science’s COVID-19 reporting is supported by the Pulitzer Center and the Heising-Simons Foundation.

ILLUSTRATION: DAVIDE BONAZZI/SALZMANART





Australia stepped up flu vaccination efforts to reduce strain on hospitals during its winter.

(ECDC). But if lockdowns and social distancing measures aren't in place in October, November, and December, flu will spread much more readily than it has in the south, warns virologist John McCauley, director of the Worldwide Influenza Centre at the Francis Crick Institute.

The prospect of a flu season during the coronavirus pandemic is chilling to health experts. Hospitals and clinics already under strain dread a pileup of new respiratory infections, including influenza and respiratory syncytial virus (RSV), another seasonal pathogen that can cause serious illness in young children and the elderly. In the United States, where some areas already face long waits for COVID-19 test results, the delays could grow as flu symptoms boost demand. "The need to try to rule out SARS-CoV-2 will be intense," says Marc Lipsitch of the Harvard T.H. Chan School of Public Health.

Because flu has largely spared the Southern Hemisphere, researchers have little evidence about how COVID-19 might influence the course of a flu outbreak. One big concern is coinfection—people getting COVID-19 and flu at once, says Ian Barr, deputy director of the World Health Organization Collaborating Centre for Reference and Research on Influenza in Melbourne, Australia. "Two or three viruses infecting you are normally worse than one," he says.

But the consequences of coinfections with SARS-CoV-2 haven't been thoroughly studied. In April, a team at Stanford University found that among 116 people in Northern California who tested positive for the coronavirus in March, 24 also tested positive for at least one other respiratory

pathogen, most often rhinoviruses and enteroviruses that cause cold symptoms, as well as RSV. Only one of the patients had influenza, although there likely wasn't much flu circulating so late in the season, says Stanford pathologist Benjamin Pinsky, a co-author. The study didn't find a difference in outcomes between COVID-19 patients with and without other infections. But it was too small to draw broad conclusions.

To make things more complicated, having one virus can change a person's chance

of getting infected with another. Epidemiologist Sema Nickbakhsh and her team at the University of Glasgow have studied interactions between different pairs of respiratory viruses, adjusting for confounding factors that would cause two viruses to show up concurrently or at separate times, such as tendencies to wax and wane with the seasons.

Coinfections with flu and other respiratory viruses are relatively rare, Nickbakhsh says, and the interactions her group has documented suggest some protective effects. For example, being infected with influenza A seemed to reduce the chance of also having a rhinovirus, the researchers reported in 2019. (The mechanism behind this effect isn't yet clear.)

Nickbakhsh is more concerned about RSV, which her team found to have positive interactions with CoV-OC43, a coronavirus species of the same genus as SARS-CoV-2. It's possible, she says, that having COVID-19 could increase a person's susceptibility to RSV, or vice versa. Pinning down interactions between COVID-19 and other infections requires a large number of patient samples tested for SARS-CoV-2 and other respiratory viruses. Rapid, dual diagnostic

## The flu season that wasn't

COVID-19 control measures dramatically reduced transmission of flu in many Southern Hemisphere countries (documented cases, April through mid-August).

COUNTRY	2018	2019	2020
Argentina	1517	4623	53
Chile	2439	5007	12
Australia	925	9933	33
South Africa	711	1094	6

tests will be important for both research and treatment decisions, says Benjamin Singer, a pulmonary and critical care physician at Northwestern University. The U.S. Food and Drug Administration has issued emergency use authorizations for three flu-COVID-19 combination tests, developed by two companies and the U.S. Centers for Disease Control and Prevention (CDC).

Meanwhile, health authorities preparing for the Northern Hemisphere winter are hoping flu vaccines can help keep hospital admissions down as health systems grapple with the pandemic. Flu vaccine manufacturers including GlaxoSmithKline and AstraZeneca have announced production increases for the 2020–21 season. CDC expects to have a record-setting 194 million to 198 million doses—a 20 million-dose increase from last year. Last month, the United Kingdom's National Health Service announced it would expand the age groups eligible for a free flu shot among both children and adults.

But what if the flu season is minor? Pouring resources into an immunization campaign necessarily subtracts from COVID-19 responses, says Penttinen, whose team provides guidance to European member states on flu vaccination. Still, rates of vaccination have long been "suboptimal" in Europe, he adds. (Rates among older adults—the target population for the flu vaccine in many countries—range from 2% to 72.8%, depending on the country, according to the most recent ECDC data, released in 2018.) "I think the tendency is to say, 'We should err on the side of caution—putting efforts into at least maintaining if not increasing the influenza vaccine coverage,'" Penttinen says.

The dearth of flu in the Southern Hemisphere could complicate efforts to develop its next influenza vaccine. Less circulating influenza virus means fewer clues about which genetic variants are most prevalent and likely to contribute to a new season. The current record-low season creates a genetic bottleneck, McCauley says, and the flu variants that survive "will be presumably the fittest ones." It's not clear what variants will dominate when flu, inevitably, rears its head again.

Barr and McCauley, whose institutions are two of the six that collect and analyze flu samples to decide the composition of the annual vaccine, say they've received fewer patient samples than in previous years. Insufficient data could lead to a less effective vaccine for the Southern Hemisphere in 2021. The contents of that cocktail must be decided by the end of September. "It's a little unsettling," Barr says, "but we'll do the best we can with the viruses that we have." ■





A malaria worker distributes bed nets on 28 April in Cotonou, Benin.

## GLOBAL HEALTH

# Pandemic's fallout on malaria control appears limited so far

Countries avert disaster by resuming bed net campaigns

By **Leslie Roberts**

**B**ack in March when COVID-19 hit, Pedro Alonso became alarmed about a different infectious disease. “I thought I would be witnessing the biggest malaria disaster in 20 years,” says Alonso, a malaria scientist at the World Health Organization (WHO). African countries went on lockdown to curtail COVID-19; worried about mass gatherings, they suspended campaigns to distribute mosquito-fighting bed nets. Fears abounded that with clinics overwhelmed by COVID-19, patients would be unable to get treatment for malaria, which kills an estimated 405,000 per year, mostly African children. In the worst case scenario, models projected, malaria deaths could more than double this year.

“It does not seem to be happening,” Alonso says. Lobbied hard by WHO’s Global Malaria Programme (GMP), which he heads, and its partners, countries resumed bed net campaigns. Rapid diagnostic tests and effective malaria drugs remain available. The situation could still go south as the COVID-19 epidemic accelerates, but for now, Alonso says, “We probably stopped the first big blow.”

In March, WHO recommended that countries halt mass vaccination campaigns for measles and other diseases, fearing they might spread COVID-19 (*Science*, 10 April, p. 116). Like other health agencies, the Africa Centres for Disease Control and Prevention advised people to stay home unless

they were very, very sick, Alonso says. But a broad lockdown would be “a bullet straight to the heart of the malaria program,” he says. “For the past 40 years we have been saying that malaria can kill within hours. If a child has fever ... go straight to the clinic.”

By 25 March, WHO had issued guidance telling countries they should proceed with malaria prevention and treatment—and could do so safely. “WHO was very effective in getting the message out,” says Thomas Churcher of Imperial College London (ICL), who published an alarming model about the effects of scaling back malaria interventions in *Nature Medicine* on 7 August.

The distribution of insecticide-treated bed nets was GMP’s first concern. Malaria deaths plunged from an estimated 839,000 in 2000 to 405,000 in 2018 largely thanks to the massive net rollout across Africa. But bed nets need to be replaced every 3 years, as the insecticide wears off and nets tear. Twenty-six African countries had scheduled mass distribution campaigns this year—but in March, many were wary of proceeding.

Benin was the most urgent priority. It had already completed the first phase of its campaign, distributing vouchers door to door that families could use to pick up their bed nets from a central point 1 month later. But the government had canceled the second phase. The concern was that people, worried about supplies, would rush to distribution centers to pick up their nets, says Marcy Erskine of the International Federation of the Red Cross

and Red Crescent Societies. “Crowds can be very difficult to control,” she says, making physical distancing all but impossible.

“We all knew if Benin did not go ahead, there would be a massive domino effect” on other countries, Erskine says. So GMP and its partners—including the Global Fund to Fight AIDS, Tuberculosis and Malaria; the U.S. President’s Malaria Initiative; and the Alliance for Malaria Prevention (AMP)—started to lobby leaders in Benin and elsewhere, she says, armed with models. AMP advised countries on how to reduce COVID-19 risks—for instance, by distributing nets door to door instead of from a central point.

Benin agreed, distributing 8 million nets in April and setting an example for other governments, says Sussann Nasr of the Global Fund: “In the end, every country said yes.” Still, “We don’t want to get a false sense of security,” Nasr says. “We have to be sure that the 2021 countries do their campaigns, too,” says Hannah Slater, a modeler at PATH, a global health nonprofit in Seattle. The same holds for indoor spraying with insecticides and seasonal chemoprevention, in which children are given antimalaria drugs during the disease’s high season.

Even if preventive interventions continue, malaria deaths could soar if sick children don’t receive effective treatment—for instance, because frightened mothers keep them home. The ICL model projects that if access to treatment drops by 50% for 6 months, 129,000 additional malaria deaths would occur between May 2020 and May 2021.

Getting a fix on how many children are being treated is tough, Alonso says. But there are ominous hints. Antenatal visits are down in some places, and that’s where pregnant women, who are very vulnerable to severe malaria, receive chemoprevention and bed nets along with regular checkups. And routine immunizations for diseases such as measles have fallen off. “What I really worry about is a child who won’t be treated and deaths will go uncounted,” says Regina Rabinovich of the Harvard T.H. Chan School of Public Health—a problem even before the pandemic. Undercounting probably explains the “paradoxical” finding that reported malaria cases are down this year, Alonso says.

Churcher fears some countries may see COVID-19 peak during the high malaria season, leaving fragile health systems dealing with simultaneous epidemics. Even countries that go into strict lockdown must continue malaria services, he says: “It’s not a trade-off. You have to do both.” ■

Leslie Roberts is a journalist in Washington, D.C.



## COVID-19

# Pandemic lockdown stirs up ecological research

Biologists launch studies of how wildlife around the world responded to the “anthropause”

By Erik Stokstad

**A**fter a COVID-19 lockdown earlier this year prevented biologist Eduardo Silva-Rodríguez from visiting his field sites in rural Chile, he moved his research closer to home. He and other Chilean researchers set up automated cameras to monitor wildlife in urban settings, including on his own campus at the Austral University of Chile, Isla Teja. The cameras soon captured surprises: rare animals, including endangered southern river otters and a wild cat called the *güiña*, roaming through pandemic-quieted cities where they'd never been documented before.

The snapshots are just one example of how wildlife is responding to what scientists are calling the “anthropause”—the dramatic slowdown in human activity caused by the pandemic. Some researchers are tracking how animals and ecosystems are reacting to steep declines in tourism. Others are pooling data on animal movements to probe large-scale responses to emptier roads and airports. The unique natural experiment is allowing scientists to compare how animals behaved before, during, and after the pandemic—and perhaps glean insights into how to better protect wildlife once human activity resumes full speed. “The lockdown has given us the capacity to find where we can optimize conservation,” says Amanda Bates, an ecologist at Memorial University.

In one collaboration led by the International Bio-Logging Society, researchers are contributing tracking data collected by satellite tags, radio collars, and other tools from some 180 species of birds, mammals, reptiles, and fish from all continents and oceans. “There is a gold mine of data,” says ecologist Christian Rutz of the University of St. Andrews. Among other things, researchers will be investigating whether animals changed their movements during the anthropause—crossing roads more frequently, for example, or venturing out at unusual times of day.

A separate team of 16 researchers, organized by conservation biologist Nicola Koper at the University of Manitoba, is exploring similar questions for 85 bird species in Canada and the United States. Working with data

from eBird, a citizen science project run by the Cornell Lab of Ornithology, the researchers are examining bird communities in 95 U.S. and Canadian counties. They wonder, for example, whether species that don't like noise, such as yellow-rumped warblers, became more abundant around airports. And they are checking whether low-flying species became more common near roads, suggesting fewer were dying in collisions with cars.

At popular destinations such as national parks, the tourism standstill has created research opportunities. In Ecuador's Galápagos Marine Reserve, the decline in visitors has been “unlike anything that would ever

In the Society Islands of French Polynesia, researchers are probing how coral reefs are faring now that hotels have gone dark. On one hand, local residents appear to be returning to subsistence fishing to make ends meet. That could mean trouble for reefs by removing herbivorous fish, which control algae that can blanket and kill coral. But empty hotels could help reefs if it means less nutrient pollution from wastewater, which stimulates algae growth. It's “a once-in-a-lifetime opportunity to better understand the links between humans and coral reefs,” says ecologist Sally Holbrook of the University of California (UC), Santa Barbara, who works at the Moorea Coral Reef Long Term Ecological Research site.

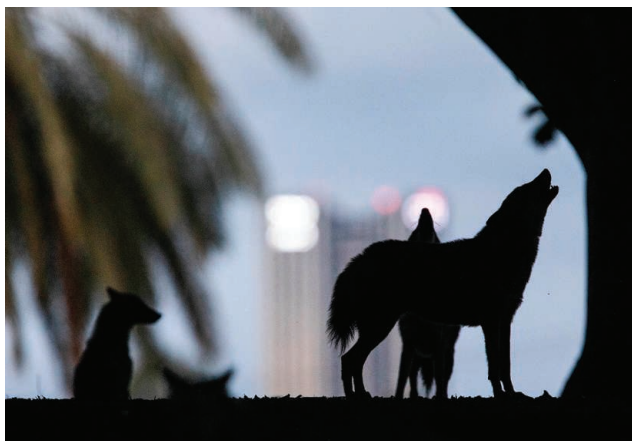
In Italy, ecologist Francesca Cagnacci also got a rare chance to see how the absence of mountain bikers, hunters, and traffic affected wildlife in the forests surrounding Trentino, where she is tracking deer and other animals with radio collars. In March, Cagnacci saw something very unusual in the hushed woods: deer and birds wandering during daylight. “I won't forget this for my entire life,” says Cagnacci, who works at the Edmund Mach Foundation's Research and Innovation Centre.

The anthropause has quieted the oceans, too. In California's Monterey Bay, marine ecologist Ari Friedlaender of UC Santa Cruz took to the water with colleagues in March and early April, when lockdowns reduced boat traffic. Equipped with a crossbow and special arrows, they collected blubber samples from 45 humpback whales.

When they can return to the lab, they'll measure levels of cortisol, a stress hormone. They plan to collect new samples over the next year, when boat traffic is expected to pick up, in an effort to discover just how much additional stress—if any—the vessel noise creates for whales.

Scientists acknowledge that the opportunity to study the anthropause is coming at the expense of much human death and suffering. “It's our sincere hope that no one ever gets a chance to study this again,” Witman says. “But incredible things are happening in natural ecosystems.” ■

With reporting by Rasha Aridi.



Normally timid jackals wandered in Tel Aviv, Israel, during an April lockdown.

happen, short of a world war,” says ecologist Jon Witman of Brown University. He and his colleagues are studying, among other things, whether shy marine fish become bolder now that recreational divers aren't around, a behavioral change that could alter how the ecosystem functions. Witman is heading to the Galápagos this week: “We're chasing a fleeting moment,” he says.

In the Bahamas, researchers are examining how the tourism crash is affecting critically endangered rock iguanas. Visitors routinely feed the iguanas bread, meat, fruit, and vegetables; now the change in diet “could have really profound effects,” says Susannah French, a physiological ecologist at Utah State University. Researchers hope to sail to the Bahamas soon to weigh the animals, take blood samples, and check their gut microbiota. The data could help local officials better manage tourists once they return, says Chuck Knapp, a biologist at the Shedd Aquarium.




FEATURES

# MUD

By David Malakoff





**G**lop. Mire. Ooze. Cohesive sediment. Call it what you want, mud—a mixture of fine sediment and water—is one of the most common and consequential substances on Earth. Not quite a solid, not quite a liquid, mud coats the bottoms of our lakes, rivers, and seas. It helps form massive floodplains, river deltas, and tidal flats that store vast quantities of carbon and nutrients, and support vibrant communities of people, flora, and fauna. But mud is also a killer: Mudslides bury thousands of people each year.

Earth has been a muddy planet for 4 billion years, ever since water became abundant. But how it forms and moves have changed dramatically. About 3 billion years ago, the arrival of land plants boosted the breakdown of rock into fine particles, slowed runoff, and stabilized sediments, enabling thick layers of mud to pile up in river valleys. Tectonic shifts that gave rise to mountains, as well as climate changes that enhanced precipitation, accelerated erosion, and helped blanket sea floors with mud hundreds of meters thick. Over time, many mud deposits hardened into mudrock, the most abundant rock in the geologic record, accounting for roughly half of all sedimentary formations.

Now, humans are a dominant force in the world of mud. Starting about 5000 years ago, erosion rates shot up in many parts of the world as our ancestors began to clear forests and plant crops. Even more sediment filled rivers and valleys, altering landscapes beyond recognition (see p. 898.) In some places dams and dykes trapped that mud, preventing fresh sediment from nourishing floodplains, deltas, and tidal flats and causing them to shrink (see p. 896). And industrial processes began to produce massive quantities of new forms of mud—mine and factory waste—that is laden with toxic compounds and often stored behind dams that can fail, unleashing deadly torrents (see pp. 906, 910).

Despite its ubiquity, mud still harbors mysteries. Biologists, for example, are just beginning to grasp the vast menagerie of organisms that live in mud, and unravel the remarkable adaptations that allow them to cope with special challenges, such as a lack of oxygen (see p. 902). And biogeochemists are still grappling with the immense role mud plays in cycling carbon, and hence influencing global climate. Such issues, as the cliché goes, are still just clear as mud.

Waterlogged sediment can be vital for life, but also poses a threat. Torrents of mud, such as this one unleashed by the failure of a mine tailings dam in Brazil, periodically kill people, bury communities, and pollute rivers.

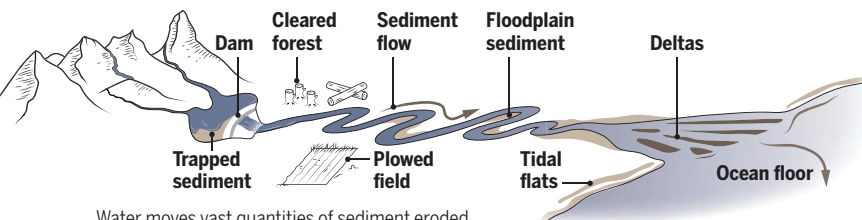
PHOTO: DOUGLAS MAGNO/AFP VIA GETTY IMAGES



# MUD ON THE MOVE

By **David Malakoff**; Graphics by **Nirja Desai** and **Xing Liu**

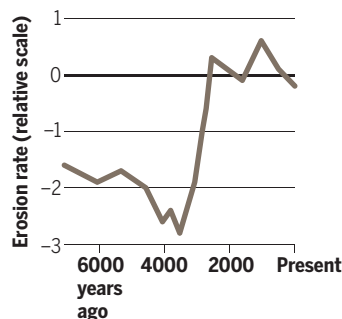
Humans are reshaping the world's mud supply, altering where—and how fast—it piles up. Thousands of years ago, our ancestors caused erosion rates to surge by starting to clear forests and plant crops, muddying lakes and rivers. Today, deforestation and urbanization are causing some rivers to carry more sediment, even as dams and efforts to curb erosion choke off sediment supplies to other waterways. Such changes, together with precipitation shifts driven by climate change, are leading to sometimes dramatic transformations in river deltas, coastal mud flats, and the amount of mud that ultimately collects at the bottom of the sea.



Water moves vast quantities of sediment eroded in highlands to the ocean, but human activities can greatly boost or reduce sediment flows.

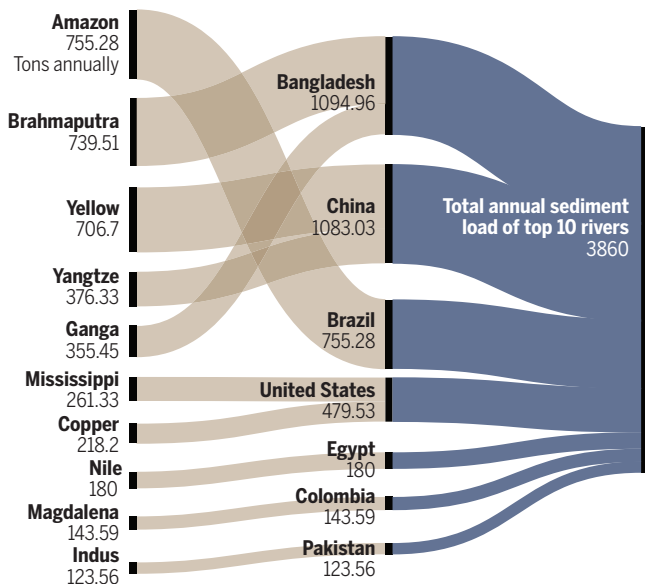
## The human imprint

Around the world, mud cores drilled from lake bottoms show a pattern similar to that found in Lake Dojran in Greece and Macedonia (right): Sedimentation rates rose sharply about 4000 years ago as humans began to clear landscapes. At Lake Dojran, researchers used sediment levels of a lithium isotope as a proxy for erosion.



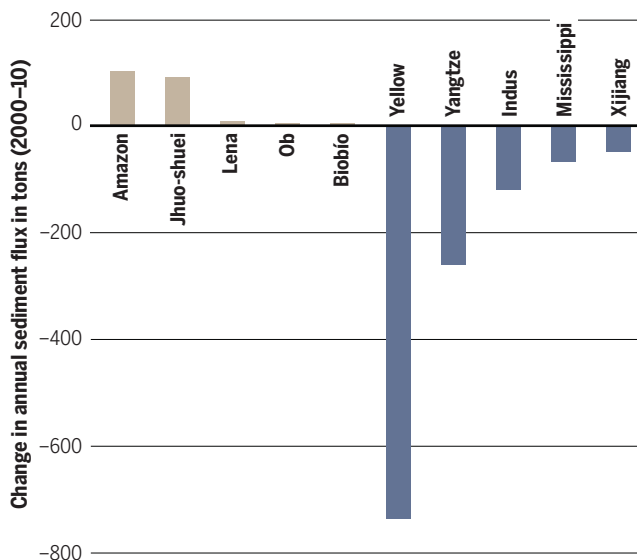
## Roll on, muddy rivers

The Amazon currently tops the list of the world's 10 largest transporters of sediment to the sea. Other large muddy rivers help make Bangladesh and China major suppliers of sediment.



## Clearer waters

Deforestation and farming increased sediment in some large rivers from 2000 to 2010, particularly in South America. But dams have cut loads elsewhere, especially in Asia. A 2019 study of 193 large rivers estimated a 20.8% overall decline in sediment load. Here are the top sediment gainers and losers.



## The (less) muddy Mississippi

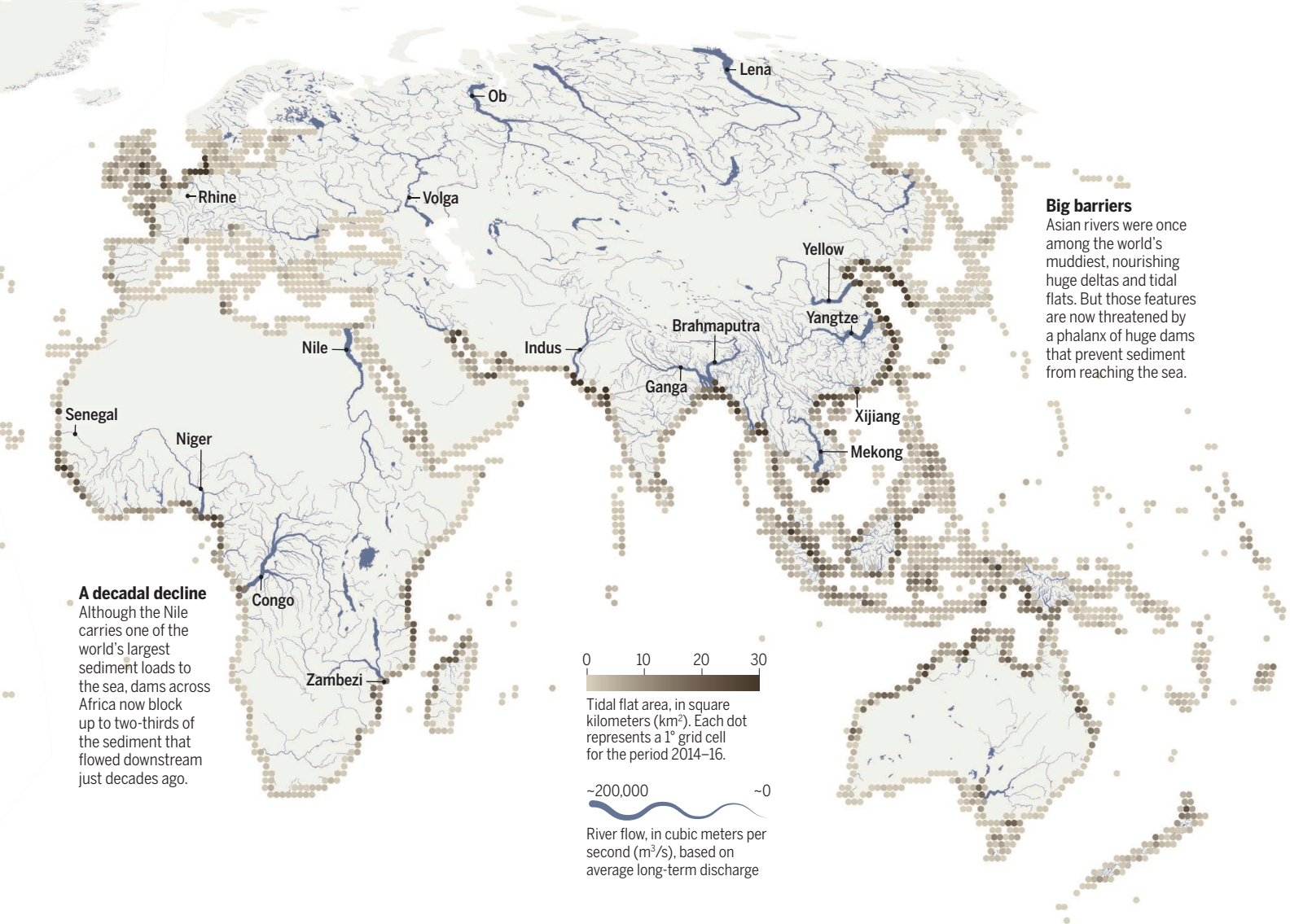
North America's biggest river has seen sediment loads drop, accelerating the loss of its delta in Louisiana.

## Deforestation leads to larger deltas

Deforestation has increased sediment loads in the Amazon and other South American rivers in recent decades, helping expand the continent's river deltas by some 16 kilometers per year.

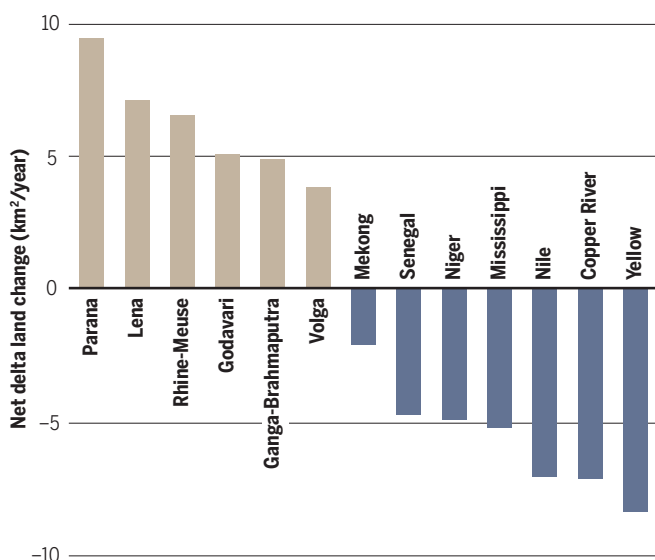
CREDITS: (RIVERS MAP) HYDROSHEDS/NASA SHUTTLE RADAR TOPOGRAPHY MISSION; (TIDAL FLATS MAP) MURRAY ET AL., NATURE, 566, 222 (2019); (EROSION PROXY DATA) ROTHACKER ET AL., SCIENTIFIC REPORTS, 8, 247 (2018); (SEDIMENTS DATA) LI ET AL., SCIENCE BULLETIN, 65, 1, 62 (2020); JINREN NI





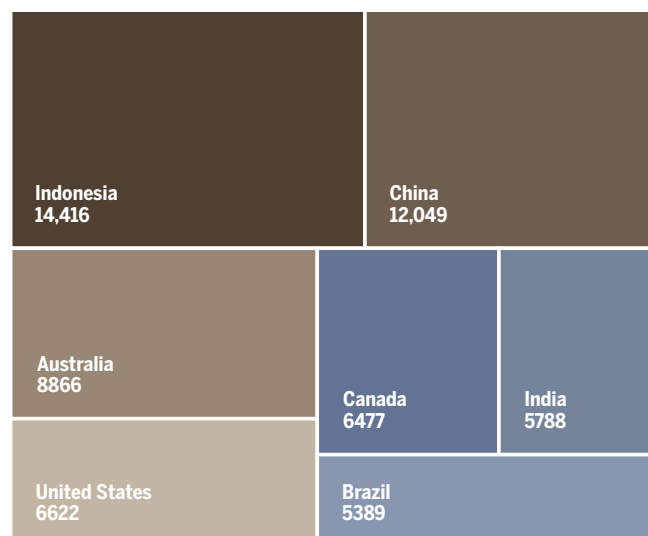
## Deltas of change

Muddy deltas that form where rivers meet the sea support rich farmlands and ecosystems. A 2020 study of 11,000 deltas found that 9% lost land from 1985 to 2015, whereas 14% added area. Globally, deltas grew by 54 square kilometers (km<sup>2</sup>) per year over that period, mostly in South America and Asia. The leading land gainers and losers.



## Shifting tides

Tidal flats, vast banks of mud that flank many coasts, are key habitats for marine organisms and seabirds, as well as important players in the global processing and storage of carbon and nutrients. Asian nations boast the largest total expanses (below), but other regions have extensive flats (above). Reductions in sediment flows imperil some flats; one recent global study estimated flats have shrunk by at least 20,000 km<sup>2</sup> since 1984.





# A MUDDY LEGACY

A dozen years after two scientists showed how centuries-old mud has smothered many U.S. streams, their ideas are guiding restoration efforts

By **Paul Voosen**, on Big Spring Run in Pennsylvania

**C**enturies ago, parts of the eastern United States were drowned in mud. Now, Robert Walter was dancing in it. The geochemist stood calf deep in this small stream 100 kilometers west of Philadelphia, thick curls of chocolate sediment flowing around his legs. Walter did a little jig as his colleague and spouse, geomorphologist Dorothy Merritts, watched. More mud stirred, heading downstream.

Brown water might not hold much interest for many researchers. But a dozen years ago, it catapulted Merritts and Walter to scientific prominence. The pair, professors at Franklin & Marshall College (F&M), showed that Big Spring Run and many other meandering, high-banked streams in the eastern United States look nothing like the low-banked, marshy waterways that existed when European explorers first arrived nearly 500 years ago. The original streams, Merritts and Walter argued in an influential 2008 paper published in *Science*, are now buried beneath millions of tons of “legacy sediment” that was released by colonial-era farming and logging, and then trapped behind countless dams built to power flour, timber, and textile mills. “We realized,” Walter says, “that the [streams] had been completely manufactured and altered.”

The finding challenged decades of conventional scientific wisdom and sparked pushback from researchers who said the pair had overstated its case. It called into question expensive efforts to restore rivers by using heavy equipment to resculpt them into what practitioners believed had been their natural shapes. And the work raised concerns that a massive, multibillion-dollar effort to clean up the nearby Chesapeake Bay would

fail if planners didn’t figure out how to prevent massive slugs of legacy sediment, which also carries harmful nutrients, from sloshing down the bay’s many tributaries. “It was uncomfortable,” Merritts says, “because I knew that my colleagues had other ideas.”

Now, a dozen years later, new research is settling many of the debates that Merritts’s and Walter’s paper touched off. Although dams are not solely to blame for legacy sediment, it’s now clear colonial-era erosion did dramatically alter streams in much of the continent’s tectonically quiet eastern half, says Ellen Wohl, a geomorphologist at Colorado State University, Fort Collins. “There’s been an accelerated recognition of how ubiquitous this sediment is,” she says. And that recognition has been driven by Walter and Merritts, says Noah Snyder, a geomorphologist at Boston College. Their study is “one of the most influential papers I’ve seen.”

Now, the duo is hoping to inspire a new approach to stream restoration by turning back the clock at Big Spring Run. By removing centuries of mud, they have returned the stream to its marshy, precolonial glory, and are now demonstrating the environmental payoff such strategies can deliver.

**MERRITTS AND WALTER** weren’t the first to realize that erosion has clogged many U.S. stream valleys with sediment. In 1917, Grove Karl Gilbert, a storied geologist who studied western North America, revealed that gold mining in the late 1800s had caused sediment to fill and reshape deep river valleys in the California Sierra Nevadas. In the 1940s, Stafford Happ, a soil scientist at the U.S. Department of Agriculture, documented how silt eroded over centuries had buried and transformed Wisconsin waterways. In the following decades, two other researchers—

geomorphologist Jim Knox and hydrologist Stanley Trimble—documented thick beds of legacy sediments beneath waterways in Georgia and the Upper Midwest.

“Agricultural erosion in parts of this country was far more severe” than many geologists realized, says Trimble, who recently retired from the University of California, Los Angeles. “We are talking about buried farms and villages.” Beaver, a small town in Minnesota, had been smothered by nearly 5 meters of eroded silt from uphill farms that reached the second floors of homes. Port Tobacco, Maryland, once a boomtown, faded after its wharfs silted up. But these

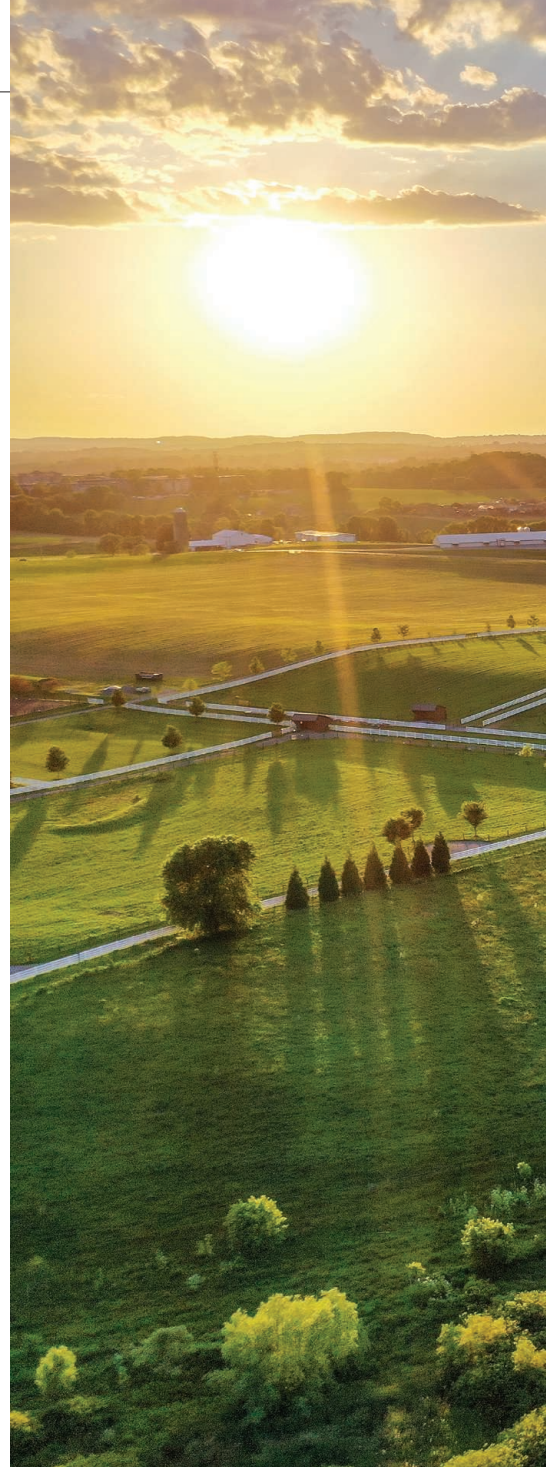


PHOTO: NICHOLAS HERTZLER



As the result of a restoration project that removed 22,000 tons of colonial-era sediment, Big Spring Run in Pennsylvania now snakes through lush wetlands.



pioneering studies never quite persuaded scientists that some waterways had been utterly transformed.

Much of our understanding of how rivers behave and evolve comes from two geomorphologists, Luna Leopold and Gordon “Reds” Wolman. While working together at the U.S. Geological Survey (USGS) in the 1950s, they studied streams in Virginia, Maryland, and Pennsylvania—all easily accessible from USGS headquarters in Reston, Virginia. Using quantitative techniques rare at the time, they developed an influential explanation for how rivers form stable, braided, meandering channels and sculpt

the land around them. As part of their work, they showed the importance of rivers frequently spilling over their banks during floods and depositing sediment on adjacent floodplains; such overbank deposition, they found, was a fundamental part of a natural, healthy waterway.

Merritts, 62, says she grew up wanting to tell her own stories about the landscape. Raised in central Pennsylvania, she spent her childhood outdoors, climbing and hiking with packs of kids. Her grandfather, a conductor on the Pennsylvania Railroad, told her of the wonders he saw in the state’s valleys. “That’s what I wanted to do,” she

recalls. “I wanted to be able to understand everywhere around me.”

After earning a doctorate in geomorphology from the University of Arizona in 1987, Merritts joined the F&M faculty. She became a field junkie, spending much of her career deciphering how plate tectonics had reshaped landscapes around the Pacific Rim by looking at how rivers had shifted over time. The work often took her to hazardous spots, including East Timor, where she needed a bodyguard because of a civil war, and Humboldt county in California, where she was threatened at gunpoint by cannabis growers. Until recently, Merritts carried two life insurance policies.



These hazards prompted her, in 2002, to look for a safer project closer to home. She had heard concerns about silt eroding from the banks of rivers flowing through farms in Pennsylvania, so she and her students began to survey local waterways. They appeared to behave in the ways that Leopold and Wolman had laid out. But the traditional model of river evolution couldn't fully explain a picture that a student showed Merritts one day; it displayed a nearly vertical, 6-meter-high wall of layered sediments along the Little Conestoga River.

As it happened, Walter, who had recently arrived at F&M, was visiting as Merritts and the student discussed the photo. Now 69, Walter was born and raised in Lancaster, Pennsylvania, where F&M is located, and had spent days fishing nearby streams, but

towering bank of finely laminated mud they found the remains of a colonial-era milldam. That's when Walter made a leap. "These are everywhere," he said. "I bet all these streams come from these old dams."

Merritts was doubtful. "I thought it was kind of crazy that you could [make that] leap from one outcrop," she recalls. But subsequent trips to Lancaster's historical society, along with reviews of other records, confirmed the dams had, indeed, been seemingly everywhere. On some rivers, settlers had built one every few kilometers. "It was," Merritts says, "just astonishing."

It was also disconcerting. The ubiquitous dams could mean many of the rivers that Leopold and Wolman had used to draw their conclusions had this unrecognized backstory, and so sat atop far more

midable team, say those who know them. Merritts is meticulous, Wohl says, "just thorough and detailed and comprehensive." Walter is more of a provocateur and discipline jumper. Their qualities are complementary, says Kathy Boomer, a river scientist at the Foundation for Food and Agriculture Research. "They're the most collaborative and open-minded scientists I know."

In January 2008, Merritts and Walter unveiled their ideas in *Science*. "The modern, incised, meandering stream is an artifact of the rise and fall of mid-Atlantic streams in response to human manipulation of stream valleys for water power," they wrote. Ultimately, they concluded, the findings "imply the need to reconsider current procedures for stream restoration" that rest on "the assumption that eroding channel banks are natural and replenishable." The paper quickly became the most influential of their careers, with some 750 citations.

**NOT ALL THE ATTENTION** was positive. "What surprised me was the resistance they met," Wohl says. "People really had a hard time accepting this."

In critiques later published in *Science* and elsewhere, some researchers faulted Walter and Merritts for implying that their findings, based largely on rivers in eastern Pennsylvania, where colonial mill dams were common, could be applied widely throughout the eastern United States. "I thought the conclusions far exceeded the evidence," Trimble recalls. Other research, he and others noted, had found that legacy sediments had piled up even along river reaches that didn't have dams. But until the couple's paper came out, those studies had failed to gain broad traction.

Other scientists were irked by the suggestion that Leopold and Wolman's iconic theoretical framework was flawed. "To say channel morphology is dependent on historic milldams is incorrect," says Martin Doyle, a river ecologist at Duke University. "The classic understanding of how rivers work is still true."

The real-world implications raised the stakes. River restoration specialists risked wasting heaps of cash on projects that might be quickly undone if floods pushed piles of old sediment into newly carved streams. State and federal agencies had to decide how to account for legacy sediments as they set water quality guidelines and environmental cleanup goals. And efforts to curb the supply of silt washing into the Chesapeake Bay might have to contend with far more of it than planners had counted on. "This is the 900-pound gorilla for how we restore our streams," says Gregory Noe, a USGS ecologist who studies mid-Atlantic streams.



Dorothy Merritts and Robert Walter put their research on rivers to a real-world test by helping restore Big Spring Run.

landscape evolution was not his focus. A specialist in the chemistry of volcanic rocks, he began his career dating the terrain surrounding the skeleton known as Lucy, the famed human ancestor discovered in Ethiopia. Still, one look at the student's photo was enough to persuade him that the layers of sediment it showed had been deposited in still—not moving—water. "There has to be a dam there," he said. There's only one way to get that kind of deposit, Merritts adds. "A lake."

**CURIOUS**, the next day the two researchers journeyed to the Little Conestoga. Sure enough, just downstream from the

anthropogenic sediment than realized. It suggested that efforts to restore streams to meandering, high-banked single channels were misguided. And it implied that massive blankets of stored sediment could be a major source of nutrient pollution that would run downriver for decades to come.

The duo spent the next several years building its case, driving to dam sites and documenting and dating sediments. The collaboration also became a courtship, as the two scientists found they made both a scientific and personal match. They were married next to an old mill in 2004.

Together, Merritts and Walter make a for-



**AS THE DEBATE** swirled, Merritts and Walter decided to put their ideas into practice. During their research, they had met Joe Sweeney, a farmer who owned land that encompassed Big Spring Run, and Ward Oberholtzer, an engineer at LandStudies, a river restoration firm. Sweeney had hired Oberholtzer to examine why trees he had planted on Big Spring Run's high banks to prevent erosion were dying. The conclusion: Their roots couldn't reach the groundwater; trenches dug by Merritts, Walter, and their students suggested several meters of legacy sediment caked over the site. To restore such connections, the team proposed re-creating the kind of languid wetland that Walter and Merritts believed had once existed on the spot. But first they would monitor it for several years, to establish a baseline that could be used to evaluate any post-restoration changes.

In 2011, after more than 2 years of planning and assistance from the Pennsylvania Department of Environmental Protection, the National Science Foundation, the Environmental Protection Agency (EPA), USGS, and others, bulldozers began to remove 22,000 tons of legacy sediment along 4 square kilometers of the valley. (The silt was trucked to F&M and used as fill beneath a new building.) A layer of rich, black, precolonial soil emerged from beneath the legacy sediment. In it, researchers found seeds that provided an archive of the wetland plants that had once grown along the stream. Although federal regulations required the restoration team to carve a single new channel, they built low banks and installed stumps and other obstacles that would encourage high waters to jump the banks, transforming the stream into a multithreaded wetland.

Within 1 year, the banks bloomed with sedges like a Chia pet. Today, bog turtles scuttle and geese nest in thick native vegetation that has put down roots that hold sediment in place. There's room for floodwaters to slow down and spread out, instead of sweeping away bankside trees and plants. "The biology does not have to re-establish itself" after every severe storm, Oberholtzer says.

Monitoring shows the restoration has also altered the stream's biogeochemistry. Storage of organic carbon tripled in the restored area and levels of nitrate, a key pollutant, dropped sharply, soaked up by the wetland plants. The load of sediment swept downstream from the

restored area declined drastically, by 85%, according to a USGS report published this year. Polluting phosphorus, which hitches a ride on silt particles, dropped 79%. Ken Forshay, a research ecologist with EPA based in Ada, Oklahoma, says he was skeptical he'd see such improvements. But the data have "turned a nonbeliever into a believer," he says.

Even before all the results were in, the Big Spring Run project prompted similar restorations in Pennsylvania and Maryland, with 20 now completed and 10 more underway. It's simple to see why: Though the project would have cost \$1 million in today's dollars to restore its 800 meters, it was at least 16 times more cost effective at reducing pollution than other techniques, found Patrick Fleming, an agricultural economist at F&M. "This practice blew the other ones away."



Meters of mud had buried the rich, black soil that typified Big Spring Run before Europeans arrived (top). It took heavy machines to remove the legacy sediment.

**TWELVE YEARS AFTER** their *Science* paper appeared, a clearer picture is emerging of how far beyond Big Spring Run the ideas floated by Merritts and Walter can be applied. Evidence that precolonial streams often resembled wetlands has popped up in more places—in Kentucky, for example, says Arthur Parola, a stream scientist at the University of Louisville. "The more we look, the more we're finding," he says. "These wetland systems were maybe the common types of streams in the eastern United States."

In New England, however, Merritts and Walter found a different picture when they surveyed streams with Snyder. Although co-

lonial dams did trap sediment, they found, the glaciated landscapes provided far less grist than those farther south. The thick beds of legacy sediment seen in the mid-Atlantic are "not going to be seen everywhere," Merritts says. And "not every place had that many milldams."

Noe found similar variation in a massive study of 68 river sites in the mid-Atlantic, now nearing publication. "There's more nuance now," Noe says. "Milldams are very important" in understanding sediment in some watersheds, he says, "but they're not necessarily the causative factor everywhere."

Noe's study will also provide the first detailed, large-scale accounting of sediment sources and sinks for the region. The good news is that, at nearly all the rivers his team studied, the floodplains downstream were capturing as much sediment as was eroding upstream, potentially curbing pollution. The floodplains are acting as kidneys, he says, and are "water quality superheroes."

But Noe adds that if those floodplains weren't busy capturing colonial silt, they could instead be a greater sink for the sediment runoff from farms and cities. And the further removal of dams, as many states are pursuing, will only free up new slugs of mud. So legacy sediment problems aren't going away, says Karl Wegmann, a geomorphologist at North Carolina State University. "It's like Chernobyl. We're going to be living with it for centuries."

The question now is what to do about it. The Chesapeake Bay Commission, which leads the cleanup of the bay, is evaluating how to credit legacy sediment restorations for their pollution reductions, based on long-term data from project like Big Spring Run. It's "been tremendously valuable," says David Wood of the Chesapeake Stormwater Network, a nonprofit that coordinates restoration practices. This is "the type of research that is needed elsewhere across the watershed," he says.

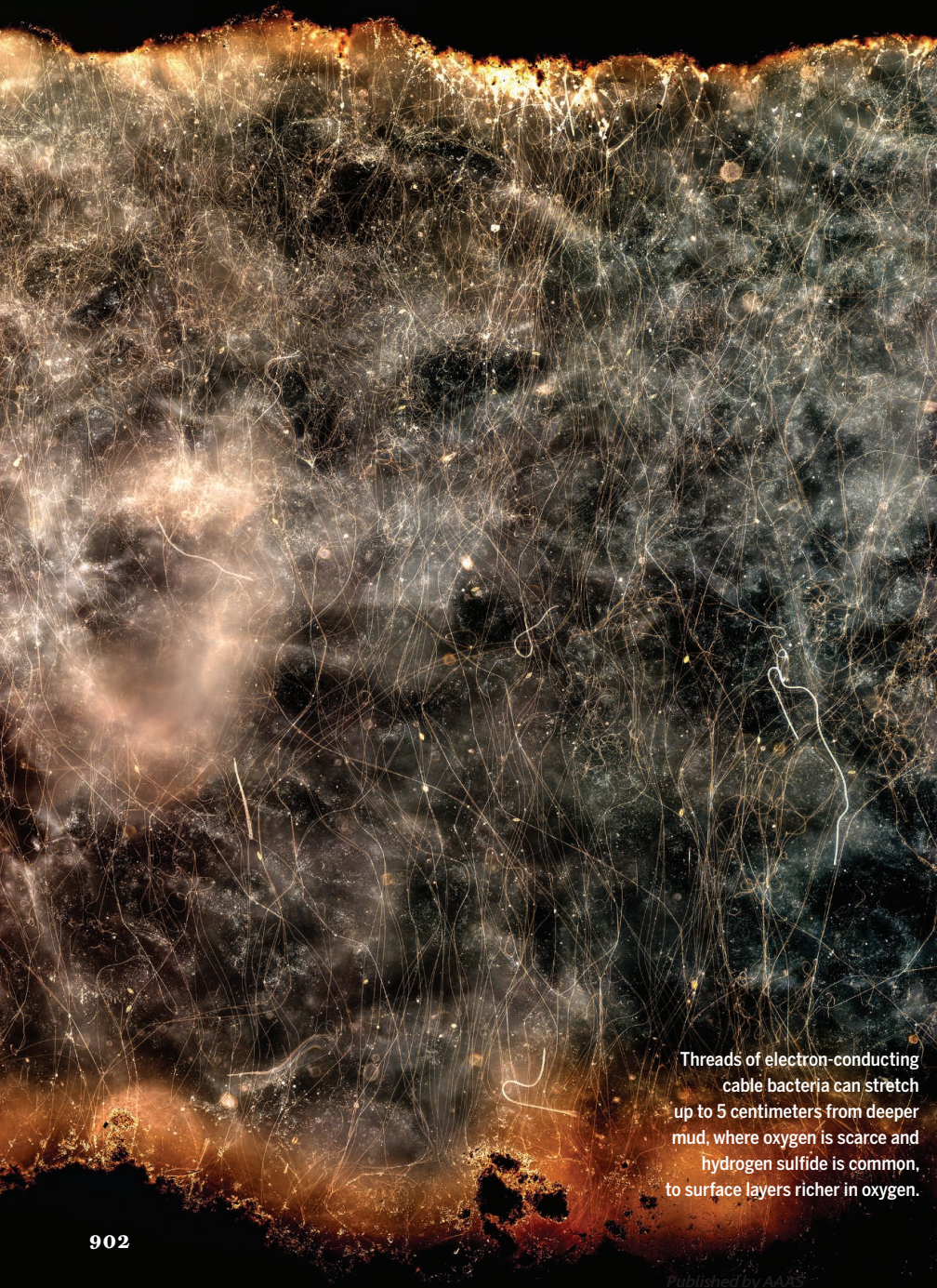
For their part, Merritts and Walter are pragmatic, not environmental romantics. They may have revealed a prehuman baseline for many waterways, but they know change is a constant of geology. Many rivers are so drowned in silt that they cannot be redeemed. The world is not pristine. But only by acknowledging and accounting for the legacy of the past, they say, can we take a first step toward solving the problems of today. ■



# THE MUD IS ELECTRIC

Bacteria that conduct electricity are transforming how we see sediments

By Elizabeth Pennisi



Threads of electron-conducting cable bacteria can stretch up to 5 centimeters from deeper mud, where oxygen is scarce and hydrogen sulfide is common, to surface layers richer in oxygen.

For Lars Peter Nielsen, it all began with the mysterious disappearance of hydrogen sulfide. The microbiologist had collected black, stinky mud from the bottom of Aarhus Harbor in Denmark, dropped it into big glass beakers, and inserted custom microsensors that detected changes in the mud's chemistry. At the start of the experiment, the muck was saturated with hydrogen sulfide—the source of the sediment's stink and color. But 30 days later, one band of mud had become paler, suggesting some hydrogen sulfide had gone missing. Eventually, the microsensors indicated that all of the compound had disappeared. Given what scientists knew about the biogeochemistry of mud, recalls Nielsen, who works at Aarhus University, "This didn't make sense at all."

The first explanation, he says, was that the sensors were wrong. But the cause turned out to be far stranger: bacteria that join cells end to end to build electrical cables able to carry current up to 5 centimeters through mud. The adaptation, never seen before in a microbe, allows these so-called cable bacteria to overcome a major challenge facing many organisms that live in mud: a lack of oxygen. Its absence would normally keep bacteria from metabolizing compounds, such as hydrogen sulfide, as food. But the cables, by linking the microbes to sediments richer in oxygen, allow them to carry out the reaction long distance.

When Nielsen first described the discovery in 2009, colleagues were skeptical. Filip Meysman, a chemical engineer at the University of Antwerp, recalls thinking, "This is complete nonsense." Yes, researchers knew bacteria could conduct electricity, but not over the distances Nielsen was suggesting. It was "as if our own metabolic processes would have an effect 18 kilometers away," says microbiologist Andreas Teske of the University of North Carolina, Chapel Hill.

But the more researchers have looked for "electrified" mud, the more they have found it, in both saltwater and fresh. They have also identified a second kind of mud-loving electric microbe: nanowire bacteria, individual cells that grow protein structures capable of moving electrons over shorter distances (see graphic, p. 903). These nanowire microbes live seemingly everywhere—including in the human mouth.

The discoveries are forcing researchers to rewrite textbooks; rethink the role that mud bacteria play in recycling key elements such as carbon, nitrogen, and phosphorus; and reconsider how they influence aquatic ecosystems and climate change. Scientists are also pursuing practical applications, exploring the potential of cable and nanowire bacteria to

PHOTO: LARS RIS-DAMGAARD AND STEFFEN LARSEN



battle pollution and power electronic devices (see sidebar, p. 904). “We are seeing way more interactions within microbes and between microbes being done by electricity,” Meysman says. “I call it the electrical biosphere.”

**MOST CELLS THRIVE** by robbing electrons from one molecule, a process called oxidation, and donating them to another molecule, usually oxygen—so-called reduction. Energy harvested from these reactions drives the other processes of life. In eukaryotic cells, including our own, such “redox” reactions take place on the inner membrane of the mitochondria, and the distances involved are tiny—just micrometers. That is why so many researchers were skeptical of Nielsen’s claim that cable bacteria were moving electrons across a span of mud equivalent to the width of a golf ball.

The vanishing hydrogen sulfide was key to proving it. Bacteria produce the compound in mud by breaking down plant debris and other organic material; in deeper sediments, hydrogen sulfide builds up because there is little oxygen to help other bacteria break it down. Yet, in Nielsen’s laboratory beakers, the hydrogen sulfide was disappearing anyway. Moreover, a rusty hue appeared on the mud’s surface, indicating that an iron oxide had formed.

One night, waking from his sleep, Nielsen came up with a bizarre explanation: What if bacteria buried in the mud were completing the redox reaction by somehow bypassing the oxygen-poor layers? What if, instead, they used the ample supplies of hydrogen sulfide as an electron donor, then shuttled the electrons upward to the oxygen-rich surface? There, the oxidation process would produce rust if iron was present.

Finding what was carrying these electrons proved complicated. First, Nils Risgaard-Petersen on Nielsen’s team had to rule out a simpler possibility: that metallic particles in the sediment were shuttling electrons to the surface and causing the oxidation. He accomplished that by inserting a layer of glass beads, which don’t conduct electricity, into a column of mud. Despite that obstacle, the researchers still detected an electric current moving through the mud, suggesting metallic particles were not the conductor.

To see whether some kind of cable or wire was ferrying electrons, the researchers next used a tungsten wire to make a horizontal slice through a column of mud. The current flickered out, as if a wire had been snipped. Other work narrowed down the conductor’s size, suggesting it had to be at least 1 micrometer in diameter. “That’s the conventional size for bacteria,” Nielsen says.

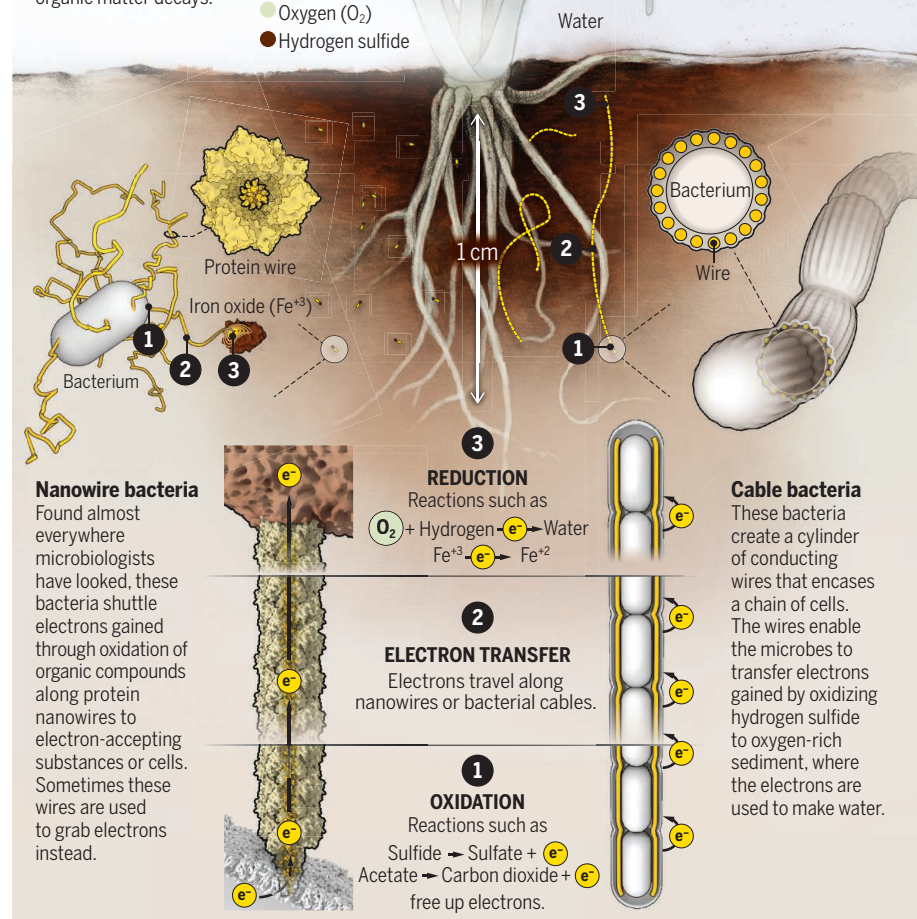
Ultimately, electron micrographs revealed a likely candidate: long, thin, bac-

## Mud’s electric microbes

At least two kinds of bacteria have evolved electric solutions to gaining energy. These microbes, first discovered in mud, separate the reduction and oxidation reactions that release the energy needed to fuel life. To enable these reactions, nanowire bacteria move electrons just micrometers between cells, particles, or other electron acceptors. Cable bacteria move electrons farther: up to 5 centimeters to oxygen-rich sediments.

### A challenging environment

In ocean and freshwater sediments, the oxygen needed for metabolism is typically restricted to surface layers or near plant roots. In deeper layers, toxic hydrogen sulfide accumulates as organic matter decays.



terial filaments that appeared in the layer of glass beads inserted in the beakers filled with the Aarhus Harbor mud. Each filament was composed of a stack of cells—up to 2000—encased in a ridged outer membrane. In the space between that membrane and the stacked cells, many parallel “wires” stretched the length of the filament. The cablelike appearance inspired the microbe’s common name.

Meysman, the one-time skeptic, quickly became a convert. Not long after Nielsen announced his discovery, Meysman decided to examine one of his own marine mud samples. “I noticed the same color changes

in the sediment that he saw,” Meysman recalls. “It was an instruction from Mother Nature to take this more seriously.”

His team began to develop tools and techniques for investigating the microbes, sometimes working collaboratively with Nielsen’s group. It was tough going. The bacterial filaments tended to degrade quickly once isolated, and standard electrodes for measuring currents in small conductors didn’t work. But once the researchers learned how to pick out a single filament and quickly attach a customized electrode, “We saw really high conductivity,” Meysman says. The living cables don’t rival copper wires, he says,



## Next up: a phone powered by microbial wires?

**T**he discoverers of electric microbes have been quick to think about how these bacteria could be put to work. “Now that we have found out that evolution has managed to make electrical wires, it would be a shame if we didn’t use them,” says Lars Peter Nielsen, a microbiologist at the University of Aarhus.

One potential use is to detect and control pollutants. Cable microbes seem to thrive in the presence of organic compounds, such as petroleum, and Nielsen and his team are testing the possibility that an abundance of cable bacteria signals the presence of undetected pollution in aquifers. The bacteria don’t degrade the oil directly, but they may oxidize sulfide produced by other oil-eating bacteria. They might also aid cleanup; sediments recover faster from crude oil contamination when they are colonized by cable bacteria, a different research team reported in January in *Water Research*. In Spain, a third team is exploring whether nanowire bacteria can speed the cleanup of polluted wetlands. And even before nanowire bacteria were shown to be electric, they showed promise for decontaminating nuclear waste sites and aquifers contaminated with aromatic hydrocarbons such as benzene or naphthalene.

Fighting climate change is another target. Lab tests have demonstrated that cable bacteria can reduce the amount of methane—a major contributor to global warming—generated by rice cultivation by 93%, researchers reported on 20 April in *Nature Communications*. They do this by helping break down substances that methane-producing bacteria rely on.

Electric bacteria could also give rise to new technologies. They can be genetically modified to alter their nanowires, which could then be sheared off to form the basis of sensitive, wearable sensors, says Derek Lovley, a microbiologist at the University of Massachusetts (UMass), Amherst. “We can design nanowires and tailor them to specifically bind compounds of interest.” For example, in the 11 May issue of *Nano Research*, Lovley, UMass engineer Jun Yao, and their colleagues described a nanowire sensor that detects ammonia at concentrations relevant for agricultural, industrial, environmental, and biomedical applications.

Fashioned into a film, nanowires can generate electricity from the moisture in the air. The film generates power, researchers believe, when a moisture gradient develops between the film’s upper and lower edges. (The upper edge is more exposed to moisture.) As the water’s hydrogen and oxygen atoms separate because of the gradient, a charge develops and electrons flow. Yao and his team reported on 17 February in *Nature* that such a film can create enough power to light a light-emitting diode, and 17 such devices connected together can power a cellphone. The approach is “a revolutionary technology to get renewable, green, and cheap energy,” says Qu Liangti, a materials scientist at Tsinghua University. (Others are more cautious, noting that past attempts to wring energy from moisture, using graphene or polymers, have not panned out.)

Ultimately, researchers hope to exploit the bacteria’s electrical talents without having to deal with the finicky microbes themselves. Lovley, for example, has coaxed a common lab and industrial bacterium, *Escherichia coli*, to make nanowires. That should make it easier for researchers to mass produce the structures and explore practical applications. —E.P.

but they are on par with conductors used in solar panels and cellphone screens, as well as the best organic semiconductors.

The researchers also dissected the cable bacteria’s anatomy. Using chemical baths, they isolated the cylindrical sheath, finding it holds 17 to 60 parallel fibers, glued along the inside. The sheath is the source of the conductance, Meysman and colleagues reported last year in *Nature Communications*. Its exact composition is still unknown, but could be protein-based.

“It’s a complicated organism,” says Nielsen, who now heads a Center for Electromicrobiology, established in 2017 by

the Danish government. Among the challenges the center is tackling is mass producing the microbes in culture. “If we had a pure culture, it would be a lot easier” to test ideas about cell metabolism and environmental influences on conductance, says the center’s Andreas Schramm. Cultured bacteria would also make it easier to isolate the cable’s wires and test potential applications for bioremediation and biotechnology.

**EVEN AS RESEARCHERS** puzzle over cable bacteria, others have been studying another big player in electric mud: nanowire bacteria, which instead of stacking cells into

cables sprout protein wires spanning 20 to 50 nanometers from each cell.

As with cable bacteria, some puzzling sediment chemistry led to the discovery of nanowire microbes. In 1987, microbiologist Derek Lovley, now at the University of Massachusetts, Amherst, was trying to understand how phosphate from fertilizer runoff—a nutrient that promotes algal blooms—is released from sediments beneath the Potomac River in Washington, D.C. He suspected microbes were at work and began to sieve them from the mud. After growing one, now called *Geobacter metallireducens*, he noticed (under an electron microscope) that the bacteria sprouted connections to nearby iron minerals. He suspected these wires were transporting electrons, and eventually figured out that *Geobacter* orchestrates chemical reactions in mud by oxidizing organic compounds and transferring the electrons to minerals. Those reduced minerals then release their hold on phosphorus and other elements.

Like Nielsen, Lovley faced skepticism when he first described his electrical microbe. Today, however, he and others have documented almost a dozen kinds of nanowire microbes, finding them in a variety of environments besides mud. Many shuttle electrons to and from particles in sediment. But some rely on other microbes to obtain or store electrons. Such biological partnerships allow both microbes to “do new types of chemistry that neither organism can do on their own,” says Victoria Orphan, a geobiologist at the California Institute of Technology. Whereas cable bacteria solve their redox requirements by long-distance transport to oxygenated mud, these microbes depend on each other’s metabolisms to satisfy their redox needs.

Some researchers are still debating how the bacterial nanowires conduct electrons. Lovley and his colleagues are convinced that chains of proteins called pilins, which consist of ring-shaped amino acids, are key. When he and his colleagues reduced the number of ringed amino acids in pilin, the nanowires became poorer conductors. “That was really surprising,” Lovley says, because proteins are generally thought to be insulators. But others think the issue is far from settled. Orphan, for one, says that although “there is some compelling evidence ... I still don’t think [nanowire conductance] is well understood.”

**WHAT IS CLEAR** is that electrical bacteria are everywhere. In 2014, for example, scientists found cable bacteria in three very different habitats in the North Sea: an intertidal salt marsh, a seafloor basin where oxygen levels drop to near zero at some times of the year, and a submerged mud





Derek Lovley (left) discovered mud bacteria that sprout electron-transporting nanowires, while Lars Peter Nielsen (right) described microbes that build conducting cables.

plain just off the coast. (They didn't find them in a sandy area populated by worms that stir up the sediments and disrupt the cables.) Elsewhere, researchers have found DNA evidence of cable bacteria in deep, oxygen-poor ocean basins, hydrothermal vent areas, and cold seeps, as well as mangrove and tidal flats in both temperate and subtropical regions.

Cable bacteria have also shown up in freshwater environments. After reading Nielsen's papers in 2010 and 2012, a team led by microbiologist Rainer Meckenstock re-examined sediment cores drilled during a study of groundwater pollution in Dusseldorf, Germany. "We found [cable bacteria] exactly where we thought we would find them," at depths where oxygen was depleted, recalls Meckenstock, who works at the University of Duisburg-Essen.

Nanowire bacteria are even more broadly distributed. Researchers have found them in soils, rice paddies, the deep subsurface, and even sewage treatment plants, as well as freshwater and marine sediments. They may exist wherever biofilms form, and the ubiquity of biofilms provides further evidence of the big role these bacteria may play in nature.

The broad range of electric mud bacteria also suggest they are a major force in eco-

systems. By preventing the buildup of hydrogen sulfide, for example, cable bacteria are likely making mud more habitable for other life forms. Meckenstock, Nielsen, and others have found them on or near the roots of seagrasses and other aquatic plants, which bubble off oxygen that the bacteria likely exploit to break down hydrogen sulfide. That, in turn, protects the plants from toxic gas. The partnership "seems to be a very generic property of water plants," Meckenstock says.

Robert Aller, a marine biogeochemist at Stony Brook University, thinks the bacteria may also aid many undersea invertebrates, including worms that build burrows that allow oxygenated water to flow into the mud. He has discovered cable bacteria sticking out the sides of worm tubes, likely so they can tap that oxygen for electron storage. In return, those worms are kept safe from the toxic hydrogen sulfide. "The bacteria make [the burrow] more livable," says Aller, who described these connections in a July 2019 paper in *Science Advances*.

The microbes also alter the properties of mud, says Sairah Malkin, an ecologist at the University of Maryland Center for Environmental Science. "They are particularly efficient ... ecosystem engineers." Cable bacteria "grow like wildfire," she says; on inter-

tidal oyster reefs, she has found, a single cubic centimeter of mud can contain 2859 meters of cables, which cements particles in place, possibly making sediment more stable for marine organisms.

The bacteria also alter the mud's chemistry, making layers closer to the surface more alkaline and deeper layers more acidic, Malkin has found. Such pH gradients can affect "numerous geochemical cycles," she says, including those involving arsenic, manganese, and iron, creating opportunities for other microbes.

With vast swaths of the planet covered by mud, cable and nanowire bacteria are likely having an influence on global climate, researchers say. Nanowire bacteria, for example, can strip electrons from organic materials, such as dead diatoms, then shuttle them to other bacteria that produce methane—a potent greenhouse gas. Under different circumstances, cable bacteria can reduce methane production.

In coming years, "We are going to see a broad acceptance of the importance of these microbes to the biosphere," Malkin says. Just over a decade after Nielsen noticed the mysterious disappearance of hydrogen sulfide from the Aarhus mud, he says, "It is dizzying to think about what we're dealing with here." ■







# A DAM BIG PROBLEM

A string of catastrophic failures has raised alarm about dams meant to contain muddy mine wastes

By Warren Cornwall

**T**he dam, a 40-meter wall of rocks and dirt, gave way without warning, unleashing a torrent of mud. Within a day, some 21 million cubic meters of gray goo and water—the tailings waste left behind by 16 years of copper and gold mining at the Mount Polley mine in western Canada—escaped from a holding pond behind the dam, buried a creek, and poured into Quesnel Lake, home to one-third of British Columbia's legendary Fraser River sockeye salmon.

The 2014 Mount Polley disaster shocked mining engineers around the world. Many considered Canada a leader in developing rules aimed at preventing the failure of such tailings dams, and respected the mine's owner, Imperial Metals. "That wasn't supposed to be able to happen," Jim Kuipers, an engineer and former tailings dam manager who now consults for environmental groups, recalls a colleague telling him.

Since then, the sense of crisis has deepened. In 2015, a tailings dam in Brazil collapsed, unleashing a mammoth mud spill that killed 19 people, contaminated 668 kilometers of river, and reached the Atlantic Ocean. In 2018, a dam failed at a major mine in Australia; luckily, a second barrier prevented disaster. Last year, a dam disintegrated at a decommissioned Brazilian iron mine, releasing a torrent that killed 270 people.

Engineers fear more catastrophes await, as the world confronts a swelling volume of muddy mine tailings, contained by more and larger dams. Some rise to nearly the height of the Eiffel Tower and hold back enough waste to fill Australia's Sydney Harbor. "The conse-

quences of a failure are getting much bigger," says Priscilla Nelson, a geotechnical engineer at the Colorado School of Mines.

In response, scientists, governments, environmentalists, and miners are searching for safer ways to handle the tainted mud. Some are trying to simply inventory the world's tailings dams—estimates of the number range from 3500 to 21,000—and identify those most at risk of failure. A few have called for a ban on one common but failure-prone design. Others are working on regulatory and management fixes. "The mining industry," says Joseph Scalia, a geotechnical engineer at Colorado State University, "is realizing they can't just spend as little as possible and the problem is going to go away."

**TAILINGS ARE THE TRASH** of the mining world. To extract most metals, from iron to gold, miners often mix pulverized rock with water, creating a milkshake of silt and gravel. As higher quality mineral deposits run out, miners are turning to lower grade sources that generate more waste. Worldwide, the metal content of copper ore has fallen by nearly half since the mid-20th century. Extracting a single kilogram of copper can now produce 200 kilograms of sludge. The muck is often contaminated with toxic metals or minerals that produce sulfuric acid when exposed to air.

Tailings dams, unlike those built to store water or generate power, don't earn revenue, creating an incentive for mine owners to minimize costs. Many are built piecemeal throughout the life of a mine. And the barriers are often made from a mixture of rock and the tailings themselves, rather than a more uniform and predictable material such as concrete. Those factors contribute to a failure rate that, over the past century, was more than 100 times higher

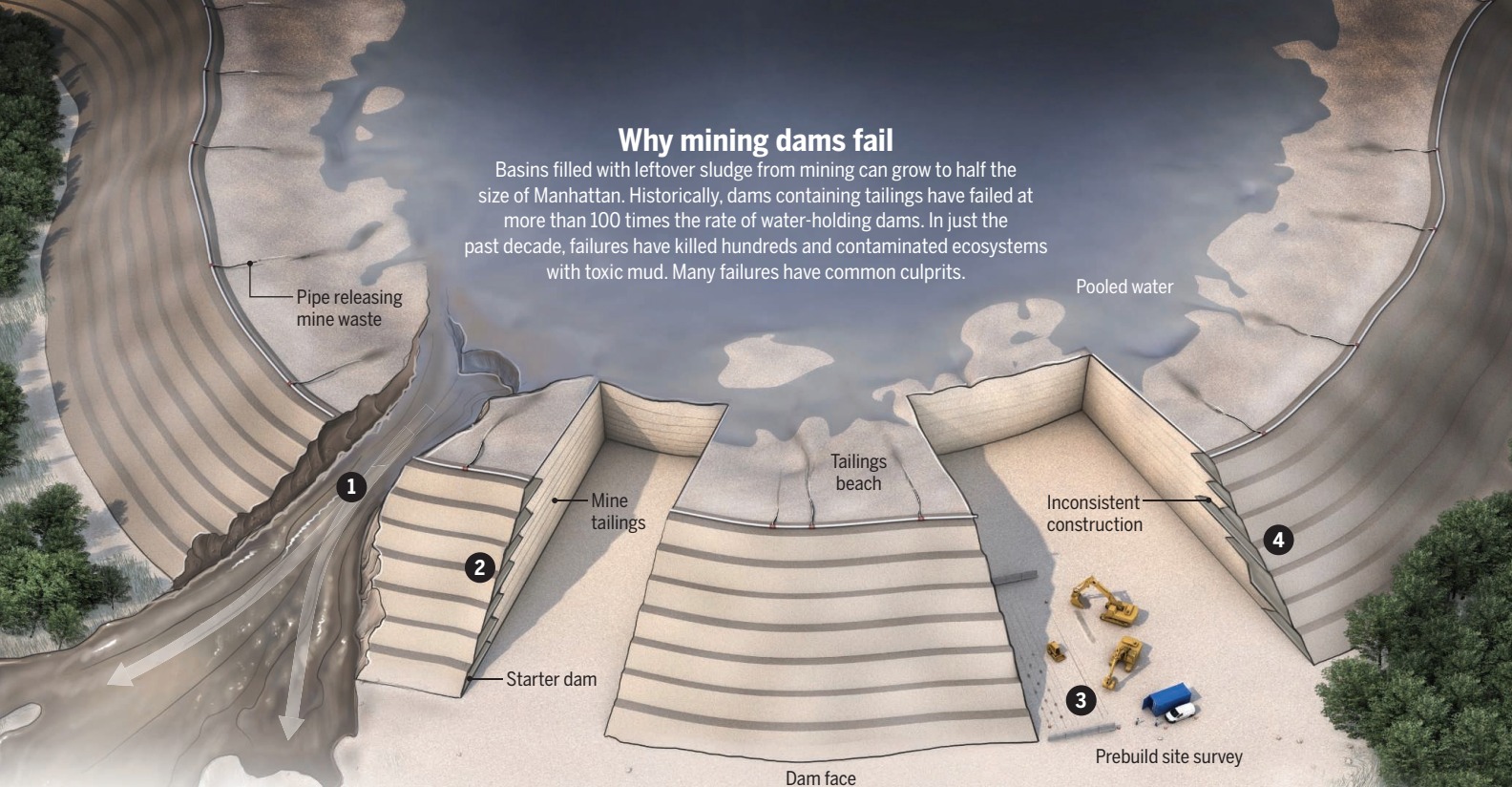
Mud released by a burst tailings dam at an iron mine near Brumadinho, Brazil, killed 270 people in 2019.

PHOTO: WASHINGTON ALVES/REUTERS



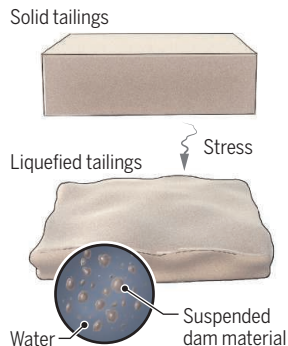
## Why mining dams fail

Basins filled with leftover sludge from mining can grow to half the size of Manhattan. Historically, dams containing tailings have failed at more than 100 times the rate of water-holding dams. In just the past decade, failures have killed hundreds and contaminated ecosystems with toxic mud. Many failures have common culprits.



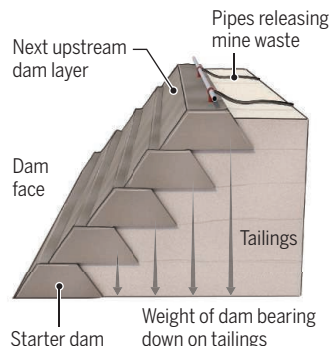
### 1 Liquefaction

Infiltration of water into the dam is a chief source of failures. In extreme cases, water combined with stress such as an earthquake can cause an earthen dam to suddenly turn to liquid.



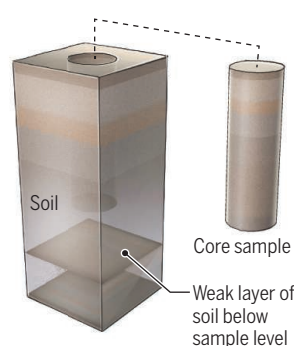
### 2 A risky design

Upstream construction is a common but failure-prone approach. The dam is raised gradually, as tailings accumulate. With each new level, the dam tilts upstream, relying on tailings below to help carry the load.



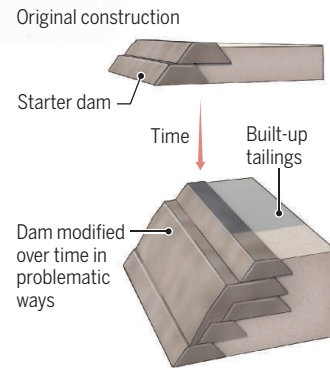
### 3 Shaky ground

Geologic weaknesses in the ground below a dam can leave it vulnerable. In one of the biggest recent failures, dam builders didn't drill deep enough to discover a weak layer left by receding glaciers.



### 4 Piecemeal changes

Unlike water dams, tailings dams evolve. They are built bit by bit over decades as mine waste piles up. This creates more potential for errors.



than that of reservoir and power dams, according to one estimate.

Each disaster has its own constellation of causes, but some arise from seemingly trivial errors. At Mount Polley, investigators led by Norbert Morgenstern, a geotechnical engineer at the University of Alberta concluded that part of the dam was built on a weak patch of silt and clay. Exploratory boreholes drilled prior to construction were too shallow to find the problem. Builders further weakened the dam by making its walls steeper than planned, after the company ran short of rock. One night, the weight of the sludge became more than the dam could bear.

It could have been much worse. No one died. Workers ultimately repaired the dam

and shoveled up much of the mud that had buried the creek. (The company says the spill didn't cause long-term harm to the Quesnel Lake ecosystem, but some ecologists say it's still too early to tell.)

Morgenstern, who also led the investigations into the 2015 Brazilian incident and the 2018 Australia failure, has found that faulty engineering, including inadequate scrutiny of the underlying geology, was at the heart of all but two of 15 major incidents between 1980 and 2015.

One major problem, he says, is the "normalization of deviance." The phrase, coined after the 1986 explosion of the space shuttle Challenger, describes how engineers can be lulled into accepting a se-

ries of seemingly small risks that snowball into a catastrophe.

There is an unwritten covenant that regulators and mine owners can count on engineers to design a safe tailings system, Morgenstern told a gathering of Brazilian geotechnical engineers in 2018. "That covenant," he said, "has been broken."

**THE SEARCH IS ON** for fixes. Some mining watchdogs are calling for replacing one common type of dam, called an upstream dam, and banning future use of the design. Upstream dams are built in stairlike stages, heading upstream over the accumulating tailings (see graphic, above). Part of the weight of each added step is borne by the



tailings below. This approach is often the cheapest, because the tailings serve as construction material.

More than 40% of major tailings dams are the upstream design, according to a global inventory of more than 1700 dams recently launched by pension funds of Sweden and the Church of England, which have pressed the mining industry to strengthen environmental and safety measures. A study of 8000 tailings dams in China found that 95% were upstream dams. And such dams are involved in three-quarters of tailings dam failures, according to one estimate.

The problem is that tailings aren't a predictable building material, and they are often waterlogged. The water can act like a lubricant, reducing the friction that binds an earthen dam together. Engineering flaws such as poor drainage can exacerbate the problem. In extreme cases—such as the 2019 disaster at the Brazilian iron mine—dam sections simply liquefy.

In Chile, where earthquakes make upstream dams even riskier, the government has forbidden the design since 1970. Brazil banned them in the wake of the 2019 accident, and has ordered the mothballing of all upstream dams by 2027. Worldwide, such a policy could mean the demise of thousands of mines and tailings dams (which could be replaced by dams with different designs). Although such a change might be expensive for companies, right now communities near dams are bearing the costs of cheaper construction, says Payal Sampat of Earthworks, a nonprofit group that promotes mining reforms. “That is unacceptable.”

Some experts caution against a one-size-fits-all approach. Upstream dams can perform safely, particularly in places with dry climates and few earthquakes, says David Williams, a geotechnical engineer at the University of Queensland, St. Lucia. “You can construct [an upstream dam] to be perfectly safe. You can also build it in a not so good way.”

One knowledge gap is an understanding of the forces that can suddenly turn an earthen dam into a liquid river of mud. At the Georgia Institute of Technology, geotechnical engineer Jorge Macedo is stress testing tailings in his lab to document the conditions that trigger liquefaction, particularly in silt, a little-studied material that is common in tailings used to build upstream dams.

Other researchers are looking at better ways to spot dams on the verge of failure. Moe Momayez, an engineer and geophysicist at the University of Arizona, is testing sensors on an Arizona dam that track temperature and moisture levels. Some dams

are already equipped with radar or lasers that watch for worrying bulges. Momayez's goal is to integrate streams of data in a computer system that can spot problems that might escape periodic inspections. “We have a pretty good idea how these tailing dams fail,” Momayez says. “The question is, can we predict that, can we get ahead of the curve?”

Some engineers would like to simply eliminate the need for massive dams. “The best tailings dam is no dam at all,” Nelson says. She is studying whether mine waste can be melted into glasslike fibers that could be used for textiles or reinforcing concrete. In June, mining gi-

dams for Klohn Crippen Berger, a private firm. It's also an enormous challenge to process tailings at big mines churning out 100,000 tons of waste per day, particularly in wet climates. “It's easier said than done,” McLeod says.

**MANY GROUPS** are also pushing for regulatory and management reforms. After the 2019 Brazilian disaster, investment funds worth more than \$10 trillion helped bring together officials from industry, government, and the investor group Principles for Responsible Investment to create a set of global guidelines for tailings dam construc-

Firefighters search for survivors in the mud unleashed by a 2019 tailings dam failure in Brazil.



ant BHP said it would spend \$10 million to study such reuse of copper tailings.

A more mature approach is to wring the water from tailings, creating waste the consistency of damp earth, which can be sculpted into mountains. The leftovers can still be toxic, but there's less danger of a devastating flood, says Jan Morrill of Earthworks. “Filtered tailings should be considered the industry standard,” Morrill says.

Although the approach has been around for decades, it's rarely used, representing just 4% of tailings systems in the pension funds' inventory. Filtered tailings systems can cost five to 10 times more than a conventional dam, says Harvey McLeod, a geological engineer who designs tailings

tion. Earlier this month, the coalition issued its plan, calling for stiffer engineering standards for new dams. It also urges top mining executives, rather than lower level staff, to be responsible for tailings safety, and for independent experts to review companies' waste plans. But it doesn't push for a ban on upstream dams.

Morgenstern notes that similar reforms he and others suggested in the late 1990s, after an earlier string of dam disasters, were never fully embraced. He expects it won't become clear until the end of the year whether the new proposals will fare better. Still, he's heartened that, after the recent tragedies, muddy mine waste is again in the spotlight. “The tree,” he says, “has been shaken.” ■



# RED ALERT

Researchers are working to find new uses for red mud, the caustic byproduct of aluminum production

By Robert F. Service



**P**ractical and glamorous, aluminum is prized for making products from kitchen foil and beverage cans to Tesla Roadsters and aircraft. But the silvery metal—abundant, cheap, lightweight, and corrosion resistant—has a dark side: red mud. This brownish red slurry, a caustic mishmash of metal- and silicon-rich oxides, often with a dash of radioactive and rare earth elements, is what's left after aluminum is extracted from ore. And it is piling up. Globally, some 3 billion tons of red mud are now stored in massive waste ponds or dried mounds, making it one of the most abundant industrial wastes on the planet. Aluminum plants generate

an additional 150 million tons each year.

Red mud has become trouble looking for a place to happen. In 2010, an earthen dam at one waste pond in Hungary gave way, unleashing a 2-meter-high wall of red mud that buried the town of Ajka, killing 10 people and giving 150 severe chemical burns. (For more on the dangers posed by waste dams, see p. 907.) Even when red mud remains contained, its extreme alkalinity can leach out, poison groundwater, and contaminate nearby rivers and ecosystems. Such liabilities, as well as growing regulatory pressure on industry to develop sustainable practices, have catalyzed global efforts to find ways to recycle and reuse red mud. Some researchers are developing ways to extract the valuable rare earth

metals, whereas others turn the mud into cement or bricks.

“There is hope here,” says Yiannis Pontikes, a mechanical engineer at the Catholic University of Leuven. But economic and marketing hurdles remain, and “the clock is ticking” as regulators consider new controls, says Efthymios Balomenos, a metallurgical engineer at the National Technical University of Athens. “At some point we will not be able to produce waste. So, there is an urgent need to make changes.”

**ALUMINUM IS ONE** of the most commonly recycled materials, with 75% of all aluminum ever produced still in use. But there is an ever-burgeoning demand. Aluminum





A worker inspects ponds holding 30 million tons of red mud at an aluminum plant in Hungary. A 2010 spill from the ponds killed 10 people.

production starts with mining bauxite, a rock rich in aluminum oxide that also contains a wealth of other elements, including silicon, iron, and titanium. Workers extract the aluminum with a combination of treatments, including caustic chemicals, heat, and electricity. What remains is usually red, because of the iron, but its exact makeup can vary from region to region, depending on the ore, making it still harder to contend with. “The composition of [red mud] varies so much it means one [type of solution] will not work,” says Brajendra Mishra, a materials scientist at the Worcester Polytechnic Institute.

One approach that does seem to be working is tapping red mud as a source of scan-

dium, a rare earth metal used to strengthen metal alloys. Researchers have recently shown that scandium-aluminum alloys are as much as 40% stronger than pure aluminum. That has manufacturers eagerly eyeing the alloy; aircraft manufacturers, for instance, could use it to build planes that have lighter aluminum framing and burn less fuel. But scandium currently costs \$3500 per kilogram, so there's plenty of incentive to find new, cheaper sources.

Scientists have come up with several ways to purify scandium from red mud. Balomenos's group, for example, has shown it can use both sulfuric acid and compounds called ionic liquids to extract the rare earth. Ultimately, red mud could meet 10% of Europe's demand for scandium, Balomenos says. Rusal, one of the largest aluminum producers in the world, is already building a pilot plant that uses related methods to extract scandium from red mud at one of its facilities in the Ural Mountains of Russia. But scandium makes up only about 140 parts per million of red mud, Pontikes notes, so “99.99% of the residue” still remains.

**OTHER APPROACHES** aim to use more of the waste. One idea is to harness red mud, which is typically 40% to 70% iron oxide, to make iron-rich cements. The world uses more than 4 billion tons of cement per year, mostly as the binder in concrete. The most common version is Portland cement, made from calcium silicates that react with water to make create a tough, hard matrix.

But in 2015, researchers in New Zealand reported that by adding a common cement additive called silica fume to red mud, together with a modest amount of iron, they could create a cement with roughly the same hardness as Portland cement. Pontikes and his colleagues are working to extend these findings, by developing recipes that would enable manufacturers to make cement from a wide range of red muds with varying iron concentrations. The team hopes red mud could become a source of both the extra iron added to their cements and the alkaline compounds needed to catalyze the hardening reactions.

In the meantime, Pontikes's lab is already producing about 1000 kilograms of iron-rich cements per day. They've even used their product for demonstration projects, such as a 2-ton staircase made with ultra-high-strength concrete. “This is no longer a lab-scale endeavor,” Pontikes says. He's begun to talk with companies about making the cement on an industrial scale.

Red mud could form the basis for other construction materials. Pontikes and his team have found that if they add about 10% clay and silicate minerals to red mud

and bake the mixture in a furnace, they can make bricks able to withstand 80 megapascals of compressive force, 40 times more than conventional bricks. They're now looking to scale up the technique, which could be used to make everything from roofing tiles to sidewalk pavers.

Because of its chemistry, red mud can also capture and lock away carbon dioxide (CO<sub>2</sub>), the major climate warming gas. In Australia, aluminum producer Alcoa bubbles CO<sub>2</sub> into red mud, creating a mild acid that reacts with the alkaline waste, forming carbonate minerals that turn the red mud into red sand that can be used to level road beds. The company estimates that the red mud from a single aluminum refinery can lock up 70,000 tons of CO<sub>2</sub> per year, equivalent to taking more than 15,000 cars off the road.

**YET THESE GLIMMERS** of progress could fade, Balomenos says, just as earlier hopes have. Since 1964, he notes, researchers have patented some 700 uses for red mud, including tapping it to make decorative ceramics, dyes, and even fertilizer. Yet just 3% of red mud is currently recycled.

One major reason is that many schemes envision using red mud to make commodities that are already cheap and produced with methods that have been optimized over a century or more. In addition, red mud isn't easy to handle. The iron industry has shied away from extracting the metal from it, for example, because the caustic waste destroys key components in their smelters. “The industry has iron ore available with much better quality,” Mishra says.

Balomenos argues that countries could push progress by establishing zero waste mandates for aluminum makers, or other incentives that force companies to recycle red mud instead of letting it pile up. The European Union has considered instituting a tax on waste deposited in landfills, for example. But it hasn't done so, and there appears to be little appetite elsewhere for similar ideas.

Another obstacle, Balomenos says, is international opposition to allowing hazardous materials to cross borders. As a result, it can be cumbersome and costly to move red mud that contains even trace amounts of heavy metals or radioactivity. For now, he says, simply putting the waste in a landfill is both cheaper and far simpler.

Finally, there is the question of consumer acceptance. Even if scientists and engineers manage to come up with a suite of practical uses for red mud, consumers still have the final say in whether they will buy products with such a noxious starting point. “Will you use roofing tiles made with red mud?” Pontikes asks. “It's up to the market to say ‘yes.’” ■



# INSIGHTS

## POLICY FORUM



### VACCINES: COVID-19

## Knowledge transfer for large-scale vaccine manufacturing

Massive, rapid production will require firms to share know-how not just about what to make but how to make it

By **W. Nicholson Price II**<sup>1,2</sup>, **Arti K. Rai**<sup>3</sup>,  
**Timo Minssen**<sup>2</sup>

**A**s the world rushes to identify safe and effective vaccines and therapeutics to counter the coronavirus disease 2019 (COVID-19) pandemic, attention is turning to the next step: manufacturing these products at enormous scale. To speed up the process, firms are even establishing manufacturing capacity “at risk,” before products receive regulatory approval (1). Yet for at least some complex COVID-19 vaccines and biological therapeutics, fast manufacturing, particularly of products originally developed by other firms, will require not only physical capacity but also ac-

cess to knowledge not contained in patents or in other public disclosures; one reason for the expense and delay historically associated with entry of biosimilars into the market has been the cost and time associated with reverse engineering originator firms’ manufacturing processes (2). But a change may be coming. A group of six biopharmaceutical firms researching monoclonal antibody (mAb) candidates recently sought [and the U.S. Department of Justice (DOJ) granted] permission under antitrust law to exchange “technical information” on each other’s manufacturing processes and platforms (but not information on cost or price) (3). A focus on rapid information exchange of the sort recently encouraged by the DOJ will not only

be critical for the current crisis but could also create the foundation for fewer siloes, improved standardization, and less secrecy over manufacturing information in the future.

### METHODS, KNOW-HOW, AND SECRECY

Knowledge transfer can facilitate manufacturing scale-up in multiple contexts. Most straightforwardly, other firms may need to manufacture the “winning” vaccine of an originator firm under some form of license that encompasses transfer of know-how. Knowledge of one firm’s processes can also facilitate the manufacturing efforts of firms with other vaccines, particularly if the vaccines use the same manufacturing platform. And sometimes, a firm may even need knowledge held by others to make its own product in large quantities. For example, Inovio claimed in a June court filing that its own experimental vaccine is being held “hostage” by a contract manufacturer that refuses to share manufacturing details (4).

One might reasonably ask why robust dissemination of manufacturing knowledge for complex biologics is only beginning to emerge, given the longstanding dominance of patenting in biopharmaceutical innovation and the legal requirement that patents



Workers prepare a production line at the Bio Farma Pharmacy in West Java to produce a COVID-19 coronavirus vaccine. Sharing of manufacturing know-how across firms will be critical.

disclose how to make the products they cover. Regrettably, for reasons related to the early timing of when patent applications are filed and failure on the part of patent offices to enforce disclosure obligations, patents on biologic products often fail to disclose necessary manufacturing information (2).

Reliance on manufacturing secrecy (including secrecy that improperly overlaps with patent protection over the manufactured products) is not specific to the pharmaceutical industry. But secrecy in other industries has generally been more time-limited than it has been with complex biologics. In the latter case, the combination of tight regulatory control over biologic products and complex and sometimes idiosyncratic manufacturing methods has slowed both competition and innovation.

To be sure, product lines differ, and crises can be valuable catalysts. As noted, in the case of mAbs and the COVID-19 crisis, large biopharmaceutical firms are now willing to share—and perhaps ultimately standardize on the basis of—information that they might previously have viewed as providing at least some competitive advantage (5). The available evidence suggests, however, that vaccine manufacturing still lacks standardization, even within manufacturing platforms (6). And some new vaccine technology platforms, such as mRNA, have never been manufactured at scale. Given this variation, the persistence of secrecy is unsurprising.

But maintaining pervasive secrecy for manufacturing COVID-19 vaccines during the pandemic could cause dramatic failure. Relevant information for quick and effective scale-up must be readily available. Vaccines are being developed in a massively parallel fashion; the World Health Organization (WHO) reports that as of 31 July 2020, there are 26 candidates in clinical evaluation and 139 candidates in preclinical evaluation. Preparations for manufacturing scale-up of vaccines are taking place before a single effective vaccine has been identified, let alone multiple vaccines (7). Along the way, firms are developing information about manufacturing, both of the specific product at issue and of vaccine manufacture more generally. This information is added to existing firm-

specific stocks of knowledge about how to make products.

Greater sharing of firm-specific manufacturing knowledge—as well as firm-specific and otherwise secret manufacturing precursors, such as cell lines and production software—help the information ecosystem generally. Especially for more established platforms, knowledge transfer could promote standardized best practices across the industry. Newer technologies could also benefit from greater background or case-specific knowledge. For example, even mRNA vaccines, which should be simpler to make than traditional vaccines (7), appear to have involved technology transfer—that is, transfer of both knowledge and material—to other firms (8). And nongovernmental organizations (NGOs) such as the Coalition for Epidemic Preparedness (CEPI) appear to build into their funding contracts provisions for technology transfer to additional parties that may be needed to perform manufacturing (7). Similarly, an 11 August 2020 Securities and Exchange Commission filing by the firm Moderna indicates that at least some U.S. government contracts build in provisions for technology transfer in the event of the firm's decision to terminate production.

Although individual contracts that anticipate technology transfer are important, when the products that will ultimately be made at scale are as-yet unidentified, broader efforts to ensure their eventual scalability should happen as quickly as possible so that all potential manufacturers are prepared once the right candidates are identified. This is particularly true given U.S. government pronouncements that capacity established during the scale-up for potential vaccines will be used regardless of which firm has developed capacity, requiring the ability to retrofit and adapt facilities to products different from their initial design parameters.

As with mAbs, we see signs in the vaccine context that some firms are open to more collaboration and knowledge-sharing than in the ordinary course. Sanofi and GlaxoSmithKline have entered a collaboration for the development of a joint vaccine, which likely requires at least some technology transfer about production of the underlying vaccine elements (9). Robust knowledge-sharing across platforms and products should be commonplace during the pandemic response.

Transferring such knowledge may not be trivial. Aside from the competitive concerns, some knowledge may be tacit—that is, more context-specific, based on experience, and more difficult to codify. The tacit knowledge concern may be less acute for biopharmaceutical products than other goods, however, for the simple reason that regulatory approval

typically requires the extensive codification of tacit manufacturing knowledge.

Where knowledge is already explicit and codified, whether in regulatory filings or elsewhere, that knowledge should be shared, at least as a club good within the universe of major industry players working to develop COVID-19 vaccines or, ideally, even more broadly. If explicit knowledge is codified in patents, pooling of those patent rights or other licenses should also be pursued, although patents surrounding manufacturing processes generally reveal little information and are therefore particularly unhelpful as a vehicle of knowledge transfer for manufacturing (2). And where tacit knowledge has not been codified at all, collaboration should include efforts to explore and share such tacit knowledge.

### INCENTIVES, ACTORS, AND REALPOLITIK

Several entities might facilitate this type of knowledge transfer, at least if they could provide the right incentives and potentially the administrative infrastructure for such sharing to occur. In determining the best facilitators, international aspects are key because knowledge transfer will necessarily occur across borders.

Existing international organizations are one set of candidates. WHO is currently promoting the idea of a COVID-19 intellectual property (IP) pool (10). Although patents seem not to be the key barrier to successful scale-up, the pool as organized does include provisions related to nonpatent knowledge transfer. Under the proposal, any government, pharmaceutical company, or organization developing COVID-19 vaccines or tests could transfer its IP to WHO on a voluntary, uncompensated basis. It is unclear how much uncompensated transfer of know-how this pool will receive, and there appears to be some industry resistance (11).

National governments can and should also address issues of knowledge transfer. Although the rhetoric of war on the virus might suggest all-out government coordination along the lines of the U.S. government's mass production of penicillin during World War II (12), it is unclear how broadly the current federal government will invoke its more coercive powers. At the moment, the U.S. government, operating primarily through Operation Warp Speed, appears focused on using the lure of very substantial funding to secure future supply of various vaccine candidates. Specifically, the United States has committed billions of dollars to multiple vaccine manufacturers (Astra-Zeneca, J&J, Novavax, Moderna, Pfizer, and Sanofi/GSK), with each contract aiming to secure hundreds of millions of doses and manufacturing platforms ranging from viral vectors (AstraZeneca and

<sup>1</sup>University of Michigan Law School, Ann Arbor, MI, USA.

<sup>2</sup>Centre for Advanced Studies in Biomedical Innovation Law, University of Copenhagen, Copenhagen, Denmark. <sup>3</sup>Duke

University Law School and Center for Innovation Policy, Durham, NC, USA. <sup>4</sup>University of Copenhagen Faculty of Law, Copenhagen, Denmark. Email: [rai@law.duke.edu](mailto:rai@law.duke.edu)



J&J) to RNA (Moderna and Pfizer) to protein subunit (Novavax and Sanofi/GSK).

Particularly given the U.S. government's commitment to use all capacity available, regardless of the winner vaccine(s), a government commitment could usefully require transfer of manufacturing know-how across firms with which it has contracted. A contract manufacturing firm to which the U.S. government has given hundreds of millions of dollars, Emergent Biosolutions, is already committed to manufacturing for J&J, Astra-Zeneca, and Novavax and could therefore serve as a natural locus for such knowledge transfer. Of course, like the exchange of mAb manufacturing information recently approved by DOJ, such transfer would be limited to a few firms. And unlike the DOJ process, any process that may be occurring through Warp Speed is not transparent (13), which might be highly problematic from a competition and antitrust law perspective.

Regional organizations could also facilitate knowledge transfer. For example, given the substantial resources that the European Union (EU) has committed to a vaccine and the EU's demonstrated commitment to data sharing and willingness to allow some pharmaceutical sector cooperation under EU competition law, the EU might be well suited to using the lure of funding to nudge firms toward knowledge transfer (14). Ideally, this would be done through a transparent process such as the DOJ review letter.

NGOs could also be an option for facilitating knowledge transfer. NGOs such as CEPI are providing funding for some vaccine candidates; they could condition receipt of funds on the contribution of manufacturing knowledge to a central pool of information. Even if NGOs were not able to bargain for such general sharing, if each agreement includes a requirement to provide knowledge transfer to other manufacturers funded by the NGO, such provisions would widen the base of available knowledge. This approach has worked in the past in the semiconductor industry, where the U.S. government-led partnership SEMATECH increased knowledge transfer across the industry (15).

Whatever the facilitator, the knowledge transfer could take different forms. One model would provide open access to essential information—including patents, know-how, and critical components—to all comers, without need of licensing. This would maximize access but decrease private sector incentives and strikes us as politically challenging. Another would leave all knowledge transfer to purely private mechanisms (if permitted by antitrust authorities). But history suggests that purely private mechanisms are unlikely to transfer enough knowledge quickly. An intermediate position,

which seems more feasible, would leave control with the originator firm but use the lure of funds to require early knowledge transfer and licensing to third parties necessary for adequate scale-up and production—knowledge transfer that occurred even before the product was a clear success.

It is possible, perhaps even likely, that some or all of the ongoing efforts to facilitate product development and manufacturing may already include provisions to foster knowledge transfer, including codification of tacit knowledge and the sharing of otherwise-secret manufacturing process information. Certainly, the recent activity by manufacturers of mAbs suggests a recognition that knowledge transfer is important. However, unlike the business review letter from DOJ, the contracts that have been executed by Warp Speed are not public. Although the NGO Knowledge Ecology International has used Freedom of Information Act requests to secure outlines of a few contracts, almost all key information is redacted as commercially confidential. Ironically, this may include information on knowledge sharing.

## BROADER IMPLICATIONS

Although the issues described here apply most directly to COVID-19 vaccines and therapeutics, a push for information sharing of manufacturing know-how could have broader positive effects across the industry. Where highly complementary skill sets and know-how are brought to the table and more problematic collaborations on costs and prices are excluded, as specified in the recent DOJ letter, this can also have a positive effect on competition in the sector. However, where the know-how of foreign companies is part of the deal, such as in the recent U.S. mAb agreement, the long-term effects on fair global competition and international sensitivities should also be considered very carefully.

In the most transformative scenario, robust sharing of manufacturing information in the current crisis could drive more robust sharing of such information more generally. Rather than relying on secrecy to limit competition in the underlying products, firms could share basic information about manufacturing processes, enabling greater innovation, flexibility, and quality. Outside the COVID-19 context, the current levers for maintaining exclusivity in the underlying products—patents and regulatory market and data exclusivity—could still shape competition rather than manufacturing secrecy, which impedes any transfer of information outside firms. Sharing in the pandemic could catalyze an industry-wide move to a high-information, high-innovation state of manufacturing, overcoming the collective action problem inherent in any one firm disclosing

more on its own and confronting the free-rider dilemma directly.

Of course, transformation is easy to call for and difficult to achieve. Even without transformation—that is, in the scenario in which pharmaceutical companies maintain secrecy over manufacturing information that does not relate to COVID-19 vaccines and therapeutics—one-time sharing of knowledge could still advance the field's collective understanding. Such an outcome would be a missed opportunity for long-term broader change but would still carry substantial benefits, even outside those arising from improved manufacturing during the pandemic.

Whatever the long-term effects on industry innovation, the most important goal is to make high-quality vaccines for COVID-19 available as quickly and broadly as possible. To pursue that goal and to promote global solidarity and reciprocity, the policy-makers and companies jointly engaged in the worldwide race to develop COVID-19 drugs and vaccines should share information about how to actually make them. ■

## REFERENCES AND NOTES

1. N. Lurie, M. Saville, R. Hatchett, J. Halton, *N. Engl. J. Med.* **382**, 1969 (2020).
2. W. N. Price 2nd, A. K. Rai, *Science* **348**, 188 (2015).
3. "U.S. clears way for drugmakers to share COVID antibody capacity," *New York Times*, 23 July 2020.
4. C. Koons, S. Decker, "Inovio tells court supplier is holding covid vaccine 'hostage,'" *Bloomberg*, 3 June 2020; [www.bloomberg.com/news/articles/2020-06-03/inovio-tells-court-supplier-is-holding-covid-vaccine-hostage](http://www.bloomberg.com/news/articles/2020-06-03/inovio-tells-court-supplier-is-holding-covid-vaccine-hostage).
5. B. Kelley, *Nat. Biotechnol.* **38**, 540 (2020).
6. D. Hosangadi et al., *Vaccine* **38**, 4167 (2020).
7. N. A. C. Jackson, K. E. Kester, D. Casimiro, S. Gurunathan, F. DeRosa npj, *Vaccines* **5**, 11 (2020).
8. "Moderna and Lonza announce worldwide strategic collaboration to manufacture Moderna's vaccine (mRNA-1273) against novel coronavirus," press release, 1 May 2020; <https://investors.modernatx.com/news-releases/news-release-details/moderna-and-lonza-announce-worldwide-strategic-collaboration>.
9. D. Roland, "GlaxoSmithKline, Sanofi team up for coronavirus vaccine," *Wall Street Journal* 14 April 2020.
10. E. Silverman WHO embraces plan for Covid-19 intellectual property pool, *Stat* 15 May 2020; [www.statnews.com/pharmalot/2020/05/15/who-covid19-coronavirus-patents-intellectual-property](http://www.statnews.com/pharmalot/2020/05/15/who-covid19-coronavirus-patents-intellectual-property).
11. E. Silverman Pharma leaders shoot down WHO voluntary pool for patent rights on Covid-19 products, *Stat* 28 May 2020; [www.statnews.com/pharmalot/2020/05/28/who-voluntary-pool-patents-pfizer](http://www.statnews.com/pharmalot/2020/05/28/who-voluntary-pool-patents-pfizer).
12. P. Neuschul, *J. Hist. Med.* **48**, 371 (1993).
13. K. Blankenship, "Warp Speed initiative aims for COVID-19 vaccine production within 6 weeks," *Fierce Pharma* 14 July 2020; [www.fiercepharma.com/manufacturing/trump-administration-hopes-for-covid-19-shot-manufacturing-to-start-within-6-weeks](http://www.fiercepharma.com/manufacturing/trump-administration-hopes-for-covid-19-shot-manufacturing-to-start-within-6-weeks).
14. E. U. Commission, "EU vaccines strategy," 31 July 2020; [https://ec.europa.eu/info/live-work-travel-eu/health/coronavirus-response/public-health\\_en#eu-vaccines-strategy](https://ec.europa.eu/info/live-work-travel-eu/health/coronavirus-response/public-health_en#eu-vaccines-strategy).
15. L. D. Browning, J. M. Beyer, J. C. Shetler, *Acad. Manage. J.* **38**, 113 (1995).

## ACKNOWLEDGMENTS

W.N.P. and T.M. were supported by the Novo Nordisk Foundation (NNF17SA0027784). We thank J. Barnes-Weise of the Global Health Innovation Alliances Accelerator for comments on an earlier draft.

Published online 13 August 2020

10.1126/science.abc9588



## PERSPECTIVES

### ARTIFICIAL INTELLIGENCE

# The foundation of efficient robot learning

Innate structure reduces data requirements and improves robustness

By **Leslie Pack Kaelbling**

**T**he past 10 years have seen enormous breakthroughs in machine learning, resulting in game-changing applications in computer vision and language processing. The field of intelligent robotics, which aspires to construct robots that can perform a broad range of tasks in a variety of environments with general human-level intelligence, has not yet been revolutionized by these breakthroughs. A critical difficulty is that the necessary learning depends on data that can only come from acting in a variety of real-world environments. Such data are costly to acquire because there is enormous variability in the situations a general-purpose robot must cope with. It will take a combination of new algorithmic techniques, inspiration from natural systems, and multiple levels of machine learning to revolutionize robotics with general-purpose intelligence.

Most of the successes in deep-learning applications have been in supervised machine learning, a setting in which the learning algorithm is given paired examples of an input and a desired output and it learns to associate them. For robots that execute sequences of actions in the world, a more appropriate framing of the learning problem is reinforcement learning (RL) (1), in which an “agent” learns to select actions to take within its environment in response to a “reward” signal that tells it when it is behaving well or poorly. One essential difference between supervised learning and RL is that the agent’s actions have substantial influence over the data it acquires; the agent’s ability to control its own exploration is critical to its overall success.

Computer Science and Artificial Intelligence Laboratory and Center for Brains, Minds, and Machines, Massachusetts Institute of Technology, Cambridge, MA, USA. Email: lpk@csail.mit.edu



General-purpose robots are being designed to help with domestic tasks. However, developing the learning applications needed to allow robots to undertake even simple tasks is extremely challenging.

The original inspirations for RL were models of animal behavior learning through reward and punishment. If RL is to be applied to interesting real-world problems, it must be extended to handle very large spaces of inputs and actions and to work when the rewards may arrive long after the critical action was chosen. New “deep” RL (DRL) methods, which use complex neural networks with many layers, have met these challenges and have resulted in stunning performance, including solving the games of chess and Go (2) and physically solving Rubik’s Cube with a robot hand (3). They have also seen useful applications, including energy efficiency improvement in computer installations. On the basis of these successes, it is tempting to imagine that RL might completely replace traditional methods of engineering for robots and other systems with complex behavior in the physical world.

There are technical reasons to resist this temptation. Consider a robot that is designed to help in an older person’s household. The robot would have to be shipped with a considerable amount of prior knowledge and ability, but it would also need to be able to learn on the job. This learning would have to be sample efficient (requiring relatively few training examples), generalizable [applicable to many situations other than the one(s) it learned], compositional (represented in a form that allows it to be combined with previous knowledge), and incremental (capable of adding new knowledge and abilities over time). Most current DRL approaches do not have these properties: They can learn surprising new abilities, but generally they require a lot of experience, do not generalize well, and are monolithic during training and execution (i.e., neither incremental nor compositional).

How can sample efficiency, generalizability, compositionality, and incrementality be

enabled in an intelligent system? Modern neural networks have been shown to be effective at interpolating: Given a large number of parameters, they are able to remember the training data and make reliable predictions on similar examples (4). To obtain generalization, it is necessary to provide “inductive bias,” in the form of built-in knowledge or structure, to the learning algorithm. As an example, consider an autonomous car with an inductive bias that its braking strategy need only depend on cars within a bounded distance of it. Such a car’s intelligence could learn from relatively few examples because of the limited set of possible strategies that would fit well with the data it has observed. Inductive bias, in general, increases sample efficiency and generalizability. Compositionality and incrementality can be obtained by building in particular types of structured inductive bias, in which the “knowledge” acquired through learning is decomposed into factors with independent semantics that can be combined to address exponentially more new problems (5).

The idea of building in prior knowledge or structure is somewhat fraught. Richard Sutton, a pioneer of RL, asserted (6) that humans should not try to build any prior knowledge into a learning system because, historically, whenever we try to build something in, it has been wrong. His essay incited strong reactions (7), but it identified the critical question in the design of a system that learns: What kinds of inductive bias can be built into a learning system that will give it the leverage it needs to learn generalizable knowledge from a reasonable amount of data while not incapacitating it through inaccuracy or overconstraint?

There are two intellectually coherent strategies for finding an appropriate bias, with different time scales and trade-offs, that can



be used together to discover powerful and flexible prior structures for learning agents. One strategy is to use the techniques of machine learning at the “meta” level—that is, to use machine learning offline at system design time (in the robot “factory”) to discover the structures, algorithms, and prior knowledge that will enable it to learn efficiently online when it is deployed (in the “wild”).

The basic idea of meta-learning has been present in machine learning and statistics since at least the 1980s (8). The fundamental idea is that in the factory, the meta-learning process has access to many samples of possible tasks or environments that the system might be confronted with in the wild. Rather than trying to learn strategies that are good for an individual environment, or even a single strategy that works well in all the environments, a meta-learner tries to learn a learning algorithm that, when faced with a new task or environment in the wild, will learn as efficiently and effectively as possible. It can do this by inducing the commonalities among the training tasks and using them to form a strong prior or inductive bias that allows the agent in the wild to learn only the aspects that differentiate the new task from the training tasks.

Meta-learning can be very beautifully and generally formalized as a type of hierarchical Bayesian (probabilistic) inference (9) in which the training tasks can be seen as providing evidence about what the task in the wild will be like, and using that evidence to leverage data obtained in the wild. The Bayesian view can be computationally difficult to realize, however, because it requires reasoning over the large ensemble of tasks experienced in the factory that might potentially include the actual task in the wild.

Another approach is to explicitly characterize meta-learning as two nested optimization problems. The inner optimization happens in the wild: The agent tries to find the hypothesis from some set of hypotheses generated in the factory that has the best “score” on the data it has in the wild. This inner optimization is characterized by the hypothesis space, the scoring metric, and the computer algorithm that will be used to search for the best hypothesis. In traditional machine learning, these ingredients are supplied by a human engineer. In meta-learning, at least some aspects are instead supplied by an outer “meta” optimization process that takes place in the factory. Meta-optimization tries to find parameters of the inner learning process itself that will enable the learning to work well in new environments that were drawn from the same distribution as the ones that were used for meta-learning.

Recently, a useful formulation of meta-learning, called “model-agnostic meta-learning” (MAML), has been reported (10). MAML

is a nested optimization framework in which the outer optimization selects initial values of some internal neural network weights that will be further adjusted by a standard gradient-descent optimization method in the wild. The RL2 algorithm (11) uses DRL in the factory to learn a general small program that runs in the wild but does not necessarily have the form of a machine-learning program. Another variation (12) seeks to discover, in the factory, modular building blocks (such as small neural networks) that can be combined to solve problems presented in the wild.

The process of evolution in nature can be considered an extreme version of meta-learning, in which nature searches a highly unconstrained space of possible learning algorithms for an animal. (Of course, in nature, the physiology of the agent can change as well.) The more flexibility there is in the inner optimization problem solved during a robot’s lifetime, the more resources—including example environments in the factory, broken robots in the wild, and computing capacity in both phases—are needed to learn robustly. In some ways, this returns us to the initial problem. Standard RL was rejected because, although it is a general-purpose learning method, it requires an enormous amount of experience in the wild. However, meta-RL requires substantial experience in the factory, which could make development infeasibly slow and costly. Thus, perhaps meta-learning is not a good solution, either.

What is left? There are a variety of good directions to turn, including teaching by humans, collaborative learning with other robots, and changing the robot hardware along with the software. In all these cases, it remains important to design an effective methodology for developing robot software. Applying insights gained from computer science and engineering together with inspiration from cognitive neuroscience can help to find algorithms and structures that can be built into learning agents and provide leverage to learning both in the factory and in the wild.

A paradigmatic example of this approach has been the development of convolutional neural networks (13). The idea is to design a neural network for processing images in such a way that it performs “convolutions”—local processing of patches of the image using the same computational pattern across the whole image. This design simultaneously encodes the prior knowledge that objects have basically the same appearance no matter where they are in an image (translation invariance) and the knowledge that groups of nearby pixels are jointly informative about the content of the image (spatial locality). Designing a neural network in this way means that it

requires a much smaller number of parameters, and hence much less training, than doing so without convolutional structure. The idea of image convolution comes from both engineers and nature. It was a foundational concept in early signal processing and computer vision (14), and it has long been understood that there are cells in the mammalian visual cortex that seem to be performing a similar kind of computation (15).

It is necessary to discover more ideas like convolution—that is, fundamental structural or algorithmic constraints that provide substantial leverage for learning but will not prevent robots from reaching their potential for generally intelligent behavior. Some candidate ideas include the ability to do some form of forward search using a “mental model” of the effects of actions, similar to planning or reasoning; the ability to learn and represent knowledge that is abstracted away from individual objects but can be applied much more generally (e.g., for all A and B, if A is on top of B and I move B, then A will probably move too); and the ability to reason about three-dimensional space, including planning and executing motions through it as well as using it as an organizing principle for memory. There are likely many other such plausible candidate principles. Many other problems will also need to be addressed, including how to develop infrastructure for training both in the factory and in the wild, as well as methodologies for helping humans to specify the rewards and for maintaining safety. It will be through a combination of engineering principles, biological inspiration, learning in the factory, and ultimately learning in the wild that generally intelligent robots can finally be created. ■

## REFERENCES AND NOTES

1. A. Barto, R. S. Sutton, C. W. Anderson, *IEEE Trans. Syst. Man Cybern.* **13**, 834 (1983).
2. D. Silver *et al.*, *Science* **362**, 1140 (2018).
3. OpenAI, *arXiv* 1910.07113 (2019).
4. M. Belkin, D. Hsu, S. Ma, S. Mandal, *Proc. Natl. Acad. Sci. U.S.A.* **116**, 15849 (2019).
5. P. W. Battaglia *et al.*, *arXiv* 1806.01261 (2018).
6. R. Sutton, “The bitter lesson”; [www.incompleteideas.net/IncIdeas/BitterLesson.html](http://www.incompleteideas.net/IncIdeas/BitterLesson.html).
7. R. Brooks, “A better lesson”; <https://rodneymbrooks.com/a-better-lesson/>.
8. J. Schmidhuber, *Evolutionary Principles in Self-Referential Learning* (Technische Universität München, 1987).
9. D. Lindley, A. F. M. Smith, *J. R. Stat. Soc. B* **34**, 1 (1972).
10. C. Finn, P. Abbeel, S. Levine, in *Proceedings of the 34th International Conference on Machine Learning* (2017), pp. 1126–1135.
11. Y. Duan *et al.*, *arXiv* 1611.02779 (2016).
12. F. Alet *et al.*, *Proc. Mach. Learn. Res.* **87**, 856 (2018).
13. Y. Lecun, L. Bottou, Y. Bengio, P. Haffner, *Proc. IEEE* **86**, 2278 (1998).
14. A. Rosenfeld, *ACM Comput. Surv.* **1**, 147 (1969).
15. D. H. Hubel, T. N. Wiesel, *J. Physiol.* **195**, 215 (1968).

## ACKNOWLEDGMENTS

The author is supported by NSF, ONR, AFOSR, Honda Research, and IBM. I thank T. Lozano-Perez and students and colleagues in the CSAI Embodied Intelligence group for insightful discussions.

10.1126/science.aaz7597



# A glycoprotein in urine binds bacteria and blocks infections

Direct imaging of a human fluid illuminates the molecular basis of urinary tract protection from disease

By Wanda Kukulski

**H**uman urinary tracts are highly susceptible to bacterial infections. Pathogenic bacteria initiate infections by attaching to sugar chains (glycans) exposed on the surface of the urinary tract epithelium (1). It has long been suspected that uromodulin (UMOD)—the most abundant protein in human urine—prevents bacteria from binding to urinary tract glycans, thus defending the organism from such infections (2). However, the mechanism underlying this protection has remained elusive. Now, on page 1005 of this issue, Weiss *et al.* reveal, at the molecular level, how UMOD filaments interact with uropathogenic *Escherichia coli* cells in human urine (3). These results provide a structural basis for understanding the protective function of UMOD.

UMOD forms filaments first visualized by electron microscopy more than 60 years ago (4). Despite these early images, the filaments' structural organization is unknown, which is, in part, why the protective role of UMOD has eluded scientists. An important hint regarding UMOD function came from the fact that myriad glycans decorate the filaments, possibly presenting bacteria with binding opportunities that compete with glycan receptors on the urinary tract walls (5).

Weiss *et al.* deciphered a comprehensive map of the glycosylation pattern of UMOD, the structure of UMOD filaments, and the nature of bacteria-filament interaction. Infective *E. coli* cells attach to the urinary tract epithelium through needlelike structures called pili. At their tip, *E. coli* type I pili consist of the protein FimH (type 1 fimbriae D-mannose specific adhesin) (6).

The authors show that the armlike structures extending from UMOD filaments interact with FimH. The interaction between UMOD and FimH is biochemically strong and likely leads to stable binding. Indeed, Weiss *et al.* show that through this binding, UMOD mediates the stable formation of clumps of bacteria.

The suggested mechanism of UMOD-based defense is notably simple and robust: The abundant UMOD filaments outcompete receptors on the urinary tract walls in binding to bacterial pili. Each flexible filament has multiple binding sites, and each

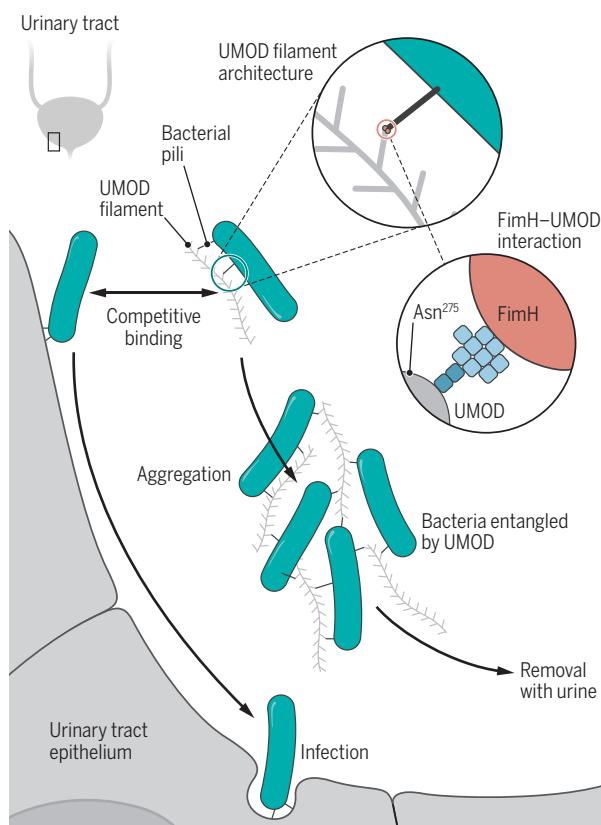
bacterium can have several pili. Therefore, this multitude of interactions causes bacterial aggregation, effectively preventing individual bacterial cells from attaching to and infecting the urinary tract. In case of the *E. coli* strain studied by Weiss *et al.*, the interaction between UMOD and bacterial cells occurs through specific binding of FimH to a glycan at asparagine 275 of the UMOD protein (see the figure).

However, UMOD contains several other complex glycosylation sites whose functions have not yet been dissected. A compelling possibility is that these serve as binding sites for proteins of other uropathogenic bacteria. In line with this idea, when Weiss *et al.* imaged urine from patients infected with different bacteria, namely *Klebsiella*, *Pseudomonas*, and *Streptococcus*, the authors found similarly aggregated bacterial cells embedded in UMOD filaments. Given its implication in various aspects of kidney function (7), UMOD might have other molecular roles that rely on its distinct glycosylation pattern or its adoption of a filamentous structure, besides protection from bacterial infections.

What has enabled this breakthrough in understanding of the association between UMOD and uropathogenic bacteria? The careful and systematic mass spectrometry data for the glycosylation map laid the foundation for resolving this mystery. The key, however, was the integration of these data with cryo-electron tomography (cryo-ET). This electron microscopy (EM)-based method allows one to visualize three-dimensional architectures of near-natively preserved samples at a resolution high enough to see individual macromolecules. Cryo-ET can be applied to samples that are too irregular, large, or heterogeneous for cryo-EM, which allows cryo-ET to span the range from purified samples to complex reconstitutions with diverse components and even undisturbed cellular samples. Similar to cryo-EM data, cryo-ET data can be processed by averaging structures in subvolumes, thereby further increasing the resolution (8). Whereas cryo-EM is currently revolutionizing structural biology by visualizing protein structures at atomic resolution (9), cryo-ET lags behind in terms of resolution, although for certain structures a resolution better than 5 Å can be achieved (10, 11).

## Filaments fight infection

Uromodulin (UMOD) forms filaments that compete with the adhesion of uropathogens to the urinary tract epithelium. By binding to bacterial pili, UMOD filaments corral uropathogens, block bacterial adhesion in the urinary tract, and permit pathogen clearance through urination. FimH, type 1 fimbriae D-mannose specific adhesin.



Institute of Biochemistry and Molecular Medicine,  
University of Bern, Bülhlstrasse 28, 3012 Bern,  
Switzerland. Email: wanda.kukulski@ibmm.unibe.ch

GRAPHIC: JOSHUA BIRD/SCIENCE



A singular asset of cryo-ET, however, is its ability to seamlessly investigate a structure across multiple scales of complexity. The power of this approach is demonstrated impressively in this study. The authors used cryo-ET followed by subtomogram averaging to determine the architecture of purified native UMOD filaments and the interaction region between UMOD filaments and FimH. They also used cryo-ET to image the binding of bacterial cells to UMOD. The visualization of entangled bacteria is particularly notable, as it involved direct imaging of unprocessed urine from patients diagnosed with urinary tract infections.

Although cryo-ET continues to provide unprecedented views of large macromolec-

**“...directly imaging a human fluid...represents a milestone by demonstrating the potential of cryo-electron tomography for biomedical imaging.”**

ular assemblies and cellular architecture (12, 13), its application to primary samples of human origin is thus far scarce (14). The approach taken by Weiss *et al.*—to assess the molecular basis of disease by directly imaging a human fluid—is conceptually simple, yet represents a milestone by demonstrating the potential of cryo-ET for biomedical imaging. Future studies likely will expand the use of cryo-ET to explore fundamental questions on the role of supramolecular architecture in human health and disease. ■

#### REFERENCES AND NOTES

1. G. Zhou *et al.*, *J. Cell Sci.* **114**, 4095 (2001).
2. F. Serafini-Cessi, A. Monti, D. Cavallone, *Glycoconj. J.* **22**, 383 (2005).
3. G. L. Weiss *et al.*, *Science* **369**, 1005 (2020).
4. K. R. Porter, I. Tamm, *J. Biol. Chem.* **212**, 135 (1955).
5. J. Pak, Y. Pu, Z. T. Zhang, D. L. Hasty, X. R. Wu, *J. Biol. Chem.* **276**, 9924 (2001).
6. E. Hahn *et al.*, *J. Mol. Biol.* **323**, 845 (2002).
7. O. Devuyt, E. Olinger, L. Rampoldi, *Nat. Rev. Nephrol.* **13**, 525 (2017).
8. S. Pfeffer, J. Mahamid, *Trends Cell Biol.* **21**, 11 (2018).
9. E. Callaway, *Nature* **582**, 156 (2020).
10. F. K. Schur *et al.*, *Science* **353**, 506 (2016).
11. A. von Kügelgen *et al.*, *Cell* **180**, 348 (2020).
12. J. Mahamid *et al.*, *Science* **351**, 969 (2016).
13. M. A. Jordan, D. R. Diener, L. Stepanek, G. Pigino, *Nat. Cell Biol.* **20**, 1250 (2018).
14. A. Al-Amoudi, D. C. Diez, M. J. Betts, A. S. Frangakis, *Nature* **450**, 832 (2007).

#### ACKNOWLEDGMENTS

W.K. is supported by the National Centre of Competence in Research (NCCR) TransCure and the University of Bern.

10.1126/science.abd7124

#### LIQUID CRYSTALS

# When the smallest details count

The type of liquid crystals formed by smooth colloidal rods depends on their degree of curvature

By Maria Helena Godinho

Natural and synthetic micro- and nanoparticles—in an appropriate solvent and within a given range of concentration, pressure, and temperature—can form colloidal liquid crystalline systems that combine the optical properties of crystals (anisotropy) and the fluidity of liquids. The particles are largely anisotropic, with one or two characteristic dimensions much larger than the third. The particles can also be bent or curved or, if derived from natural materials, can have chiral interactions, all of which can affect how the particles self-assemble and form liquid crystalline phases. On page 950 of this issue, Fernández-Rico *et al.* (1) report on a simple method allowing the production of large quantities of polydisperse colloidal synthetic rods from a viscous photoresin. They imposed a well-controlled curvature on these rods by fine-tuning the cross-link density of the resin and the temperature. They show that curvature has pronounced effects on the liquid crystalline phase behavior.

Bawden *et al.* (2) first reported the formation of colloidal liquid crystals in aqueous solutions of rodlike tobacco mosaic virus. Later, Onsager (3) used entropic arguments to explain the formation of parallel alignment (nematic phase) of long, hard rods from a disorder phase. For ellipsoidal particles, in addition to the nematic phase, helicoidal structures (chiral nematic order), which are characterized by the existence of successive pseudonematic layers that are rotated by a small angle about an axis perpendicular to the plane of the layers, were also reported. Colloidal solutions of cellulose nanorods (4) have a chiral nematic structure that can be frozen-in (see the figure, top), by removing the solvent so that scanning electron microscopy can reveal the layers of the precursor liquid crystalline phase (5). This helicoidal structure is often found in animals and plants and is interpreted by a twisted plywood model proposed by Bouligand (6). Similarly, for spherocylinders (cylinders capped with a hemisphere on both ends), smectic phases with layered structures more ordered than

nematics were also reported. Bent colloidal particles have also been reported to produce liquid crystalline solutions. Yang *et al.* (7) generated suspensions of silica particles that exhibited different smectic structures, including a twisted smectic phase, by controlling the bending angle and aspect ratio of the particles, which were different from the curved systems Fernández-Rico *et al.* produced.

Curved filaments are common in nature and have inspired theoretical investigations and functional applications. A straight filament converted into a curved shape can sometimes coil into a helix even when the filament lacks chirality (8, 9). The intrinsic curvature was attributed to the existence across the filament of materials with different mechanical characteristics that contract asymmetrically. The resulting shapes of the filaments depend on diameter, length, and boundary conditions at extremities. Long filaments tend to generate spirals, if supported by one end, or helical structures, if clamped at both ends. In the latter case, left- and right-handed helices, separated by straight segments, were observed, so the overall system was still achiral (see the figure, bottom left).

The tuning of the curvature can be precisely controlled by varying the asymmetric characteristics of the materials existing along the filament. Similar mechanisms imposed by asymmetric cross-linking should be at work in the formation of the curved spherocylinders that Fernández-Rico *et al.* made by cross-linking and heating photoresin rods. The particles were stiffened by further cross-linking, which fixed their curved shapes before creating colloidal suspensions.

Fernández-Rico *et al.* used confocal microscopy to image a series of different liquid crystalline phases obtained from three types of curved particles. The most interesting finding was the first experimental evidence of the nematic splay-bend phase, in which the less-curved polydisperse particles were organized in a serpentine undulated structure (see the figure, bottom right). Only the less curved particles are at the origin of the splay-bend phase. More curved particles generate liquid crystalline phases described previously for molecular banana-shaped molecules (10) and colloidal rods. Thus, small details had large effects on the packing of the particles, in accord with theoretical predictions (11). Indeed, the smectic phase was

Centro de Investigação de Materiais—I3N (CENIMAT/I3N), Department of Materials Science, Faculty of Science and Technology, University NOVA of Lisbon, Campus da Caparica, 2829-516 Caparica, Portugal. Email: mhg@fct.unl.pt



predicted to be destabilized if polydisperse, smooth curved particles were used to produce the colloidal suspensions. However, in the work of Fernández-Rico *et al.*, there was no evidence for the twist-bend nematic phase (see the figure, bottom right). This phase is characterized by the simultaneous assembly of curved particles into right and left helices to form an achiral system, as has been seen in thermotropic molecular liquid crystals (12).

Through precise control of the curvature of the particles, Fernández-Rico *et al.* could tune the sequence of phases that includes not only the splay-bend phase but also the biaxial nematic and smectic phases. For small curvature, the microparticles self-assemble into nematic and smectic phases as the concentration of the solvent decreases. As the value of the curvature increases, the splay-bend nematic phase disappears. At the highest curvature (almost circular arcs), only the isotropic phase develops.

The study of Fernández-Rico *et al.* makes possible the production of a range of nematic colloidal liquid crystals. Theoretical predictions suggest that tuning the curvature and the interactions with the boundaries could lead to phases not yet observed for colloidal

liquid crystals, including the twist-bend nematic. Chiral particles could further enhance this class of smooth curved colloidal particles and generate new phases. The optical properties and response to external fields of these phases may form the basis for future studies that cannot be carried out for molecular liquid crystalline phases. ■

#### REFERENCES AND NOTES

1. C. Fernández-Rico *et al.*, *Science* **369**, 950 (2020).
2. F. C. Bawden, N. W. Pirie, J. D. Bernal, I. Fankuchen, *Nature* **138**, 1051 (1936).
3. L. Onsager, *Ann. N. Y. Acad. Sci.* **51**, 627 (1949).
4. J. F. Revol *et al.*, *Liq. Cryst.* **16**, 127 (1994).
5. A. P. C. Almeida *et al.*, *Adv. Mater.* **30**, 1703655 (2018).
6. Y. Bouligand, *C. R. Acad. Sci. Hebd. Seances Acad. Sci. D* **261**, 4864 (1965).
7. Y. Yang *et al.*, *J. Am. Chem. Soc.* **138**, 68 (2016).
8. S. J. Gerbode, J. R. Puzey, A. G. McCormick, L. Mahadevan, *Science* **337**, 1087 (2012).
9. P. E. S. Silva, F. Vistulo de Abreu, M. H. Godinho, *Soft Matter* **13**, 6678 (2017).
10. A. Jákli, O. D. Lavrentovich, J. V. Selinger, *Rev. Mod. Phys.* **90**, 045004 (2018).
11. I. Dozov, *Europhys. Lett.* **56**, 247 (2001).
12. D. A. Paterson *et al.*, *Soft Matter* **12**, 6827 (2016).

#### ACKNOWLEDGMENTS

M.H.G. is supported by the Portuguese Foundation for Science and Technology under project nos. UID/CTM/50025/2019 and M-ERA-NET2/0007/2016 (CellColor) and by the European Topology Interdisciplinary Action (EUTOPIA CA17139).

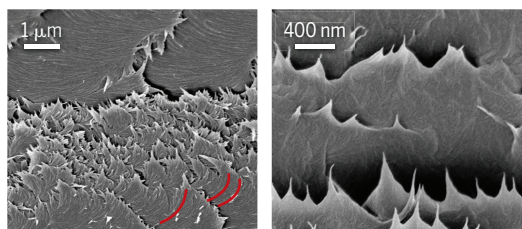
10.1126/science.abd3548

## Liquid crystals from smooth curved colloidal systems

Fernández-Rico *et al.* found that different liquid crystals form from microrods with different degrees of curvature. Natural systems such as cellulose nanorods form liquid crystals but have a chiral nature.

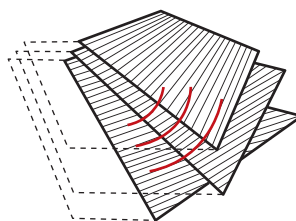
### Cellulose-nanorod chiral nematics

Solutions of cellulose nanorods form a nematic liquid crystalline phase that has a chiral twist.



#### Scanning electron microscopy images

Curved solid lines are equidistant twisted layers and arcs (red, left), and the “peaks” (right) can be attributed to the fracture of the twisted layers.

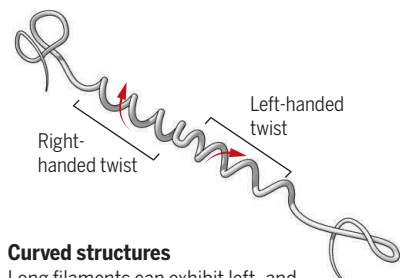


#### Helicoidal structure

The twisted plywood model, proposed by Bouligand (6), accounts for the helicoidal nature of the layers and arcs.

### Long-curved filaments

Similar structures are formed in certain liquid crystal phases.

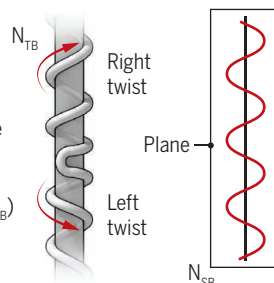


#### Curved structures

Long filaments can exhibit left- and right-handed helices or spirals.

#### Curved phases

Slightly curved rods organize in a nematic splay-bend ( $N_{SB}$ ) phase (right). No microrod studied (1) led to the nematic twist bend ( $N_{TB}$ ) phase that can switch from right- to left-handed helices (left).



## MEDICINE

# Remodeling vasculature to avoid blindness

Pathological vasculature marks itself for repair by deploying neutrophil extracellular traps

By Eugene A. Podrez and Tatiana V. Byzova

Vascular remodeling is essential for building hierarchically structured vascular networks, which in turn support proper organ function (1). The retina is particularly dependent on optimal blood supply, and insufficient or excessive vasculature often leads to blindness. The process of vascular regression reduces blood vessel density, facilitating normalization of vasculature and subsequent tissue repair (2). Regression is either caused by the withdrawal of essential vascular growth factors or by triggering endothelial apoptosis and subsequent pruning of vasculature (3). However, it is unknown how dysfunctional and excessive retinal blood vessels are selected and marked for pruning. On page 934 of this issue, Binet *et al.* (4) reveal that pathological vasculature in the retina of mice and humans orchestrates its own remodeling by promoting the extrusion of neutrophil extracellular traps (NETs). This mechanism might be applied to other pathologies that require vascular remodeling, such as cancer, pulmonary hypertension, and heart disease (3).

Retinal ischemic diseases, such as retinopathy of prematurity and diabetic retinopathy, are triggered by insufficient vasculature, leading to ischemia (lack of oxygen), which is compensated for by excessive production of vascular growth factors, primarily vascular endothelial growth factor (VEGF). This leads to overgrowth of misdirected and leaky vasculature, with signs of vascular deterioration and senescence (in which cells stop dividing and become dysfunctional) stimulated by aging or stress, similar to processes observed in tumors (3). Regression of this excessive and pathological vasculature is a necessary step to avoid

Lerner Research Institute, Cleveland Clinic, Cleveland, OH, USA. Email: byzovat@ccf.org



chronic inflammation and to ensure tissue repair. Thus, a precise understanding of the exact molecular mechanisms governing vascular regression in retinal and other diseases is of the utmost clinical importance.

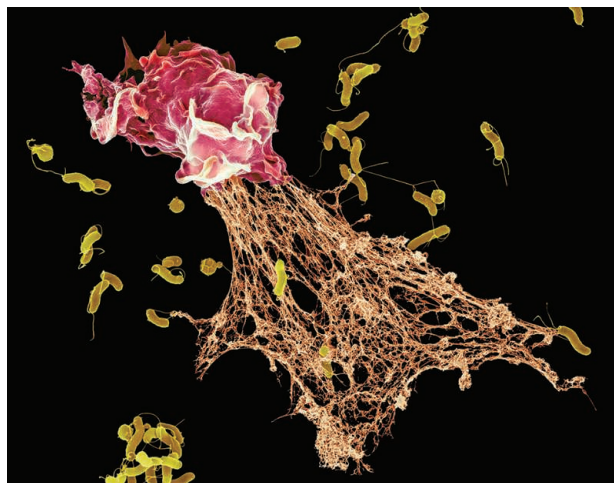
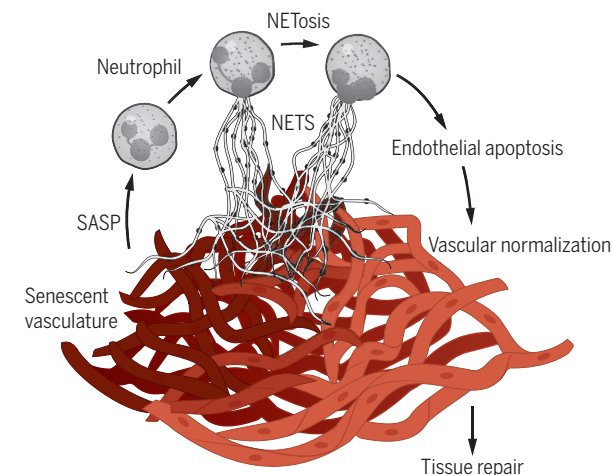
Using high-resolution droplet-based RNA sequencing and sophisticated bioinformatics approaches in animal models of retinopathy, Binet *et al.* were able to effectively tease out the main players of vascular regression at the molecular, cellular, and tissue levels. They showed in mice and humans that the entire process relies on the innate immune system, namely neutrophils, which are deployed during the late phase of retinal disease, which is associated with vascular regression rather than vascular growth.

Neutrophils serve as a first line of innate immunity against pathogens by means of oxidative burst, phagocytosis, and release of web-like DNA and protein structures called NETs. Besides their originally defined role in pathogen defense (5), NETs also mediate severe inflammatory reactions of primarily a destructive nature, such as cancer metastasis and tissue and organ damage within the vascular, pulmonary, and renal systems (6). Most recently, NETs have been implicated in organ damage and other complications of coronavirus disease 2019 (COVID-19) (7). Binet *et al.* show that during the process of retinal vascular repair, NETs perform a very different function of marking senescent vascular branches (see the figure). Under different circumstances, this tagging for destruction might lead to impaired blood supply and eventually to organ failure; however, in ischemic retinopathy, this process serves an essential prerequisite for tissue repair. It remains to be determined whether this role of NETs is restricted only to tissues of primarily postmitotic nature, such as the retina and central nervous system, or whether it also operates in other pathologies, such as neoplasms, or even whether it might underlie developmental vascular restructuring.

Involvement of NETs in other pathologies seems to be likely because NETosis is stimulated by a specific combination of factors, including interleukin-1 $\beta$  (IL-1 $\beta$ ) and C-X-C motif chemokine 1 (CXCL1), which are secreted by senescent cells and found

## Vascular senescence facilitates tissue repair

Dysfunctional senescent retinal vasculature produces senescence-associated secretory phenotype (SASP) components, attracts neutrophils, and stimulates the extrusion of neutrophil extracellular traps (NETosis, see photo below). This causes endothelial cell apoptosis and vascular pruning, which is essential for vascular repair and tissue recovery in ischemic retinopathy.



not only in aging but also during development (8) and in actively growing tissues such as tumors (9). In diseased retinas, this senescence-associated secretory phenotype (SASP) is observed in endothelial cells, pericytes, astrocytes, and Müller glia but not in retinal ganglion cells (which connect photosensitive cells in the retina to the optic nerve), which are also known to undergo senescence. Together, these findings indicate that various types of senescent cells might be able to attract neutrophils and deploy NETs. It will be interesting to explore why only certain types of senescent cells promote NETs.

Acquisition of a SASP signature is believed to be mainly detrimental because of its contribution to inflammation, oxidative stress, thrombosis (blood clotting), and metabolic imbalance (10). In endothelium,

the SASP signature includes pro-angiogenic factors that promote vascularization in tumors (9) and in age-related diseases, including retinopathy (11). In tumors, SASP facilitates drug delivery, thus making tumors vulnerable to chemotherapy (9). In proliferative diabetic retinopathy, however, SASP cytokines such as IL-6, IL-8, and VEGF directly promote pathological vascular growth, delaying tissue repair (11). However, similar to Binet *et al.*, studies found beneficial roles of SASP in tissue growth (8) and wound healing (12) as inducers of stem-like characteristics of keratinocytes, driving epithelial regeneration (13).

It is notable that the retinal vasculature activates a “self-correcting” program by acquiring the SASP. Binet *et al.* demonstrate that the SASP signature is associated with activation of RAS pathways within a population of senescent retinal endothelial cells. In cancer, proangiogenic SASP components are the result of inhibition rather than activation of the KRAS pathway (9). Nevertheless, even in cancer, SASP promotes therapeutically beneficial vascular remodeling. Together, these results support the concept that cellular senescence has substantial value as a therapeutic target in a variety of disorders associated with vascular dysfunction, and that induction of vascular senescence is a prerequisite for vascular remodeling and optimization. Moreover, because most of the vasculature requires active and uninterrupted maintenance, this

senescence-induced regression and remodeling aided by neutrophils might also be applicable to vascular homeostasis. ■

### REFERENCE AND NOTES

1. A. R. Pries, T. W. Secomb, *Physiol.* **29**, 446 (2014).
2. E. C. Watson, Z. L. Grant, L. Coultas, *Cell. Mol. Life Sci.* **74**, 4387 (2017).
3. C. Korn, H. G. Augustin, *Dev. Cell* **34**, 5 (2015).
4. F. Binet *et al.*, *Science* **369**, eaay5356 (2020).
5. V. Brinkmann *et al.*, *Science* **303**, 1532 (2004).
6. V. Papayannopoulos, *Nat. Rev. Immunol.* **18**, 134 (2018).
7. B. J. Barnes *et al.*, *J. Exp. Med.* **217**, e20200652 (2020).
8. D. Muñoz-Espín *et al.*, *Cell* **155**, 1104 (2013).
9. M. Ruscetti *et al.*, *Cell* **181**, 424 (2020).
10. J. Sabbatinelli *et al.*, *Front. Physiol.* **10**, 1523 (2019).
11. M. Oubaha *et al.*, *Sci. Transl. Med.* **8**, 362ra144 (2016).
12. M. Demaria *et al.*, *Dev. Cell* **31**, 722 (2014).
13. B. Ritschka *et al.*, *Genes Dev.* **31**, 172 (2017).

### ACKNOWLEDGMENTS

The authors are supported by National Institutes of Health (HL142772 and HL145536).

10.1126/science.abd7063



# Immunotherapy with a sting

New agonists of an innate immune pathway induce antitumor immunity in mice

By **Thomas F. Gajewski** and **Emily F. Higgs**

**T**umor antigen-specific CD8<sup>+</sup> T cells are a critical component of the anti-tumor immune response. Many cancer patients display evidence of an endogenous T cell response against their tumors, yet fail to eliminate tumors unaided. The failure of spontaneous immune-mediated tumor rejection is thought to be partially due to the action of negative regulatory mechanisms (immune checkpoints) that inhibit key functional properties of tumor-infiltrating T cells (1). Checkpoint blockade immunotherapies have demonstrated notable therapeutic success by overcoming tumor-induced T cell inhibition; however, their efficacy is poor when patients lack evidence of a spontaneous T cell response (2, 3). Innate immune agonists may promote priming and recruitment of tumor-specific CD8<sup>+</sup> T cells and are gaining traction as a cancer immunotherapy approach. On page 935 and 993 of this issue, Pan *et al.* (4) and Chin *et al.* (5), respectively, describe innate immune agonists that show antitumor activity in preclinical cancer models.

Antibodies targeting the immune checkpoint receptor, programmed cell death protein 1 (PD-1), or its major ligand, PD-L1, have been approved by the U.S. Food and Drug Administration for clinical use in ~15 different cancer entities (6). Clinical benefit has been correlated with the presence of an activated T cell gene signature prior to treatment (2), and following anti-PD-1 administration, a marked expansion of tumor-infiltrating CD8<sup>+</sup> T cells has been observed (3). Despite clinical successes, a major subset of cancer patients lack sufficient T cell inflammation, and these patients generally do not respond to checkpoint blockade immunotherapy (7). It is thought that triggering productive T cell-based inflammation within the tumor microenvironment may offer the potential to expand the fraction of patients benefiting from anti-PD-1 treatment and other immunotherapies.

One strategy toward this goal has been to gain an understanding of the fundamental mechanistic steps involved in spontaneous T cell activation and tumor infiltration

when it does occur, with the aim of mimicking or reproducing those steps in the cases when it does not occur. In general, an adaptive immune response (i.e., induction of a T cell or antibody response) first requires activation of the innate immune system, which nonspecifically signals the presence of “danger” or an outside threat. Preclinical tumor models revealed that endogenous CD8<sup>+</sup> T cell priming (activation) by innate antigen-presenting cells (APCs) was markedly reduced in mice deficient for STING (stimulator of interferon genes) (8). Mice lacking STING also showed reduced cytokine production, including interferon- $\beta$  (IFN- $\beta$ ), in response to tumor implantation and failed to reject highly immu-

STING molecule but not human STING (11). The first generation of human STING agonists, including MIW815 (ADU-S100) and MK-1454, have been investigated in early-phase clinical trials alone and in combination with anti-PD-1. So far, some clinical responses to these agonists have been observed, but only in a minority of patients (12, 13). Several biological considerations are being explored to understand mechanisms of response versus resistance. These include deciphering which immune cells in the tumor microenvironment must be present for STING agonists to induce downstream T cell priming, understanding the optimal dose and schedule of STING agonists to avoid overstimulation and negative regulation, and identifying predictive biomarkers for clinical activity.

The metabolic instability of cyclic dinucleotide-based STING agonists requires them to be administered intratumorally. The constraint for intratumoral administration itself has limitations,

because physical issues such as increased intratumoral pressure, restraints on diffusion of the injected agent, and the impossibility of injecting all metastatic lesions in an advanced cancer patient are all potential barriers to therapeutic efficacy. A small number of intravenous STING agonists have begun evaluation in clinical trials (NCT03843359, NCT04420884, and NCT04096638), and the next focus of STING agonist development will likely be on agonists formulated for systemic administration, such as those reported by Pan *et al.* and Chin *et al.* (see the figure).

Clinical development of systemically administered STING agonists needs to account for several important considerations. One is that systemic administration may lead to greater toxicity, because engaging APCs outside the tumor microenvironment may release high amounts of IFN- $\beta$  and other inflammatory cytokines. Chin *et al.* report that efficacious doses of SR-717 led to significantly lower concentrations of serum IFN- $\beta$  than another recently developed systemic STING agonist, diABZI-2. Systemic administration of diABZI-2 also promoted tumor control; however, diABZI-2 stabilizes STING in its open conformation, similar to the bacterial

**“Understanding which innate immune pathway is functionally relevant... will be paramount toward optimization of innate immune agonist combinations with existing immunotherapies.”**

nogenic tumors. These defects were not observed in mice deficient in other innate immune pathways, such as specific Toll-like receptors (TLRs).

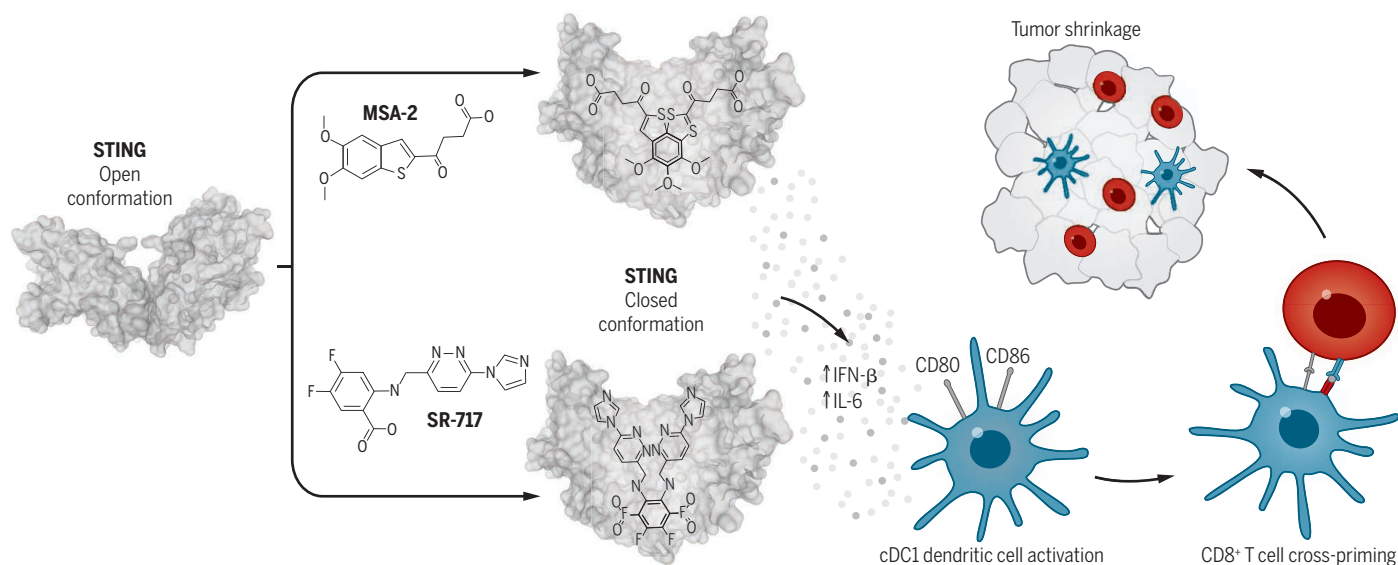
The STING pathway is a cytosolic DNA-sensing pathway, and tumor-derived DNA could be found within the cytosol of tumor-infiltrating APCs. Cytosolic DNA is detected within cells when it binds to cGAS [cyclic guanosine monophosphate (GMP)-adenosine monophosphate (AMP) (cGAMP) synthase], which generates cGAMP, which in turn engages and activates STING (9). Signaling downstream of STING leads to APC activation and inflammatory cytokine production, which subsequently promotes T cell priming and recruitment (10). Together, these observations led to the hypothesis that exogenous agonists of the STING pathway may have the potential to trigger de novo innate immune activation, leading to an adaptive immune response that can control tumor growth alone or in combination with checkpoint blockade immunotherapy.

The first STING agonist investigated for immunotherapy was the molecule DMXAA, which had antitumor activity in preclinical models and was subsequently determined to interact with the mouse



## New innate immune agonists

The non-nucleotide stimulator of interferon genes (STING) agonists MSA-2 and SR-717 reported by Pan *et al.* and Chin *et al.*, respectively, stabilize STING in its closed conformation. STING activation induces downstream signaling events that culminate in the expression of inflammatory cytokines such as interferon- $\beta$  (IFN- $\beta$ ) and interleukin-6 (IL-6). Secretion of these cytokines in the tumor microenvironment promotes the maturation and activation of cDC1 dendritic cells, which then promote antitumor immunity by priming tumor antigen-specific CD8<sup>+</sup> T cells in the tumor-draining lymph node.



product cyclic di-GMP but unlike endogenous cGAMP (14). The agonists presented by Pan *et al.* and Chin *et al.* both stabilize the closed conformation of STING. Further study is necessary to tease apart the biological consequences of stabilizing STING in its open versus closed conformations. The MSA-2 compound described by Pan *et al.* also demonstrated limited toxicity in mice despite systemic administration, owing to its preferential bioactivity within the acidic milieu of the tumor microenvironment.

A second important consideration is the effect of systemic STING agonists on specific immune cell subpopulations. Chin *et al.* noted that SR-717 induced expression of the immunosuppressive molecules PD-L1 and indoleamine 2,3-dioxygenase 1 (IDO1) in primary human peripheral blood mononuclear cells *in vitro*. Additionally, intraperitoneal injection of SR-717 in a melanoma mouse model led to increased PD-L1 expression on CD11c<sup>+</sup>CD8<sup>-</sup> dendritic cells but not on CD8<sup>+</sup> dendritic cells isolated from tumor-draining lymph nodes. Although CD8<sup>+</sup> dendritic cells are thought to be the key APC subset for inducing tumor-specific CD8<sup>+</sup> T cell priming, it is notable that SR-717 affected these dendritic cell subtypes differently. Further characterization of the ways by which STING agonists induce both stimulatory and suppressive

events in relevant cell subpopulations within the tumor microenvironment will be critical. Antitumor efficacy of SR-717 was not improved by either anti-PD-1 or anti-PD-L1 treatment in a mouse model of melanoma, which is in contrast to MSA-2, which did show improved tumor shrinkage when combined with anti-PD-1 therapy. These differences could be due to different molecular properties of these STING agonists, differences in dose and schedule of administration in combination with immune checkpoint blockade, or distinctions between the experimental models used.

A third consideration for clinical development is the dose and schedule of administered drug. These need to be optimized carefully, because systemic administration also may give rise to a bell-shaped efficacy curve. Probing pharmacodynamic endpoints within the tumor microenvironment associated with activity should guide selection of therapeutic dosing. Fourth, the consideration of which tumor types and which patients have the potential to respond to these agents also needs to be addressed, so predictive biomarkers for appropriate patient selection also need to be pursued. A final consideration is that other innate immune agonists are advancing in clinical development, including agents targeting TLR pathways, such as TLR9 (15). Understanding which innate immune pathway is functionally relevant in distinct patient populations will be paramount toward optimization of innate im-

mune agonist combinations with existing immunotherapies.

The compounds reported by Chin *et al.* and Pan *et al.* illustrate how distinctive molecular properties of STING agonists can determine the balance of activity in the tumor versus systemically. Non-nucleotide small-molecule STING agonists that can be administered systemically may represent an attractive approach for targeting this pathway and have the potential to transform the therapeutic landscape once optimized. ■

### REFERENCES AND NOTES

1. G. J. Freeman *et al.*, *J. Exp. Med.* **192**, 1027 (2000).
2. M. Ayers *et al.*, *J. Clin. Invest.* **127**, 2930 (2017).
3. P. C. Tumeh *et al.*, *Nature* **515**, 568 (2014).
4. B.-S. Pan *et al.*, *Science* **369**, aba6098 (2020).
5. E. N. Chin *et al.*, *Science* **369**, 993 (2020).
6. R. K. Vaddepally, P. Kharel, R. Pandey, R. Garje, A. B. Chandra, *Cancers (Basel)* **12**, 738 (2020).
7. J. A. Trujillo, R. F. Sweis, R. Bao, J. J. Luke, *Cancer Immunol. Res.* **6**, 990 (2018).
8. S.-R. Woo *et al.*, *Immunity* **41**, 830 (2014).
9. L. Sun, J. Wu, F. Du, X. Chen, Z. J. Chen, *Science* **339**, 786 (2013).
10. L. Corrales *et al.*, *Cell Rep.* **11**, 1018 (2015).
11. J. Conlon *et al.*, *J. Immunol.* **190**, 5216 (2013).
12. F. Meric-Bernstam *et al.*, *J. Clin. Oncol.* **37** (15\_suppl.), 2507 (2019).
13. K. J. Harrington *et al.*, *Ann. Oncol.* **29**, viii712 (2018).
14. J. M. Ramanjulu *et al.*, *Nature* **564**, 439 (2018).
15. M. Reilly *et al.*, *J. Clin. Oncol.* **37** (15\_suppl.), TPS2669 (2019).

### ACKNOWLEDGMENTS

The authors are funded by the National Institutes of Health (grants F30CA250255 to E.F.H. and R35CA210098 to T.F.G.). T.F.G. reports a licensing agreement and receives research support and consultancy fees from Aduro Biotech.

Department of Pathology, University of Chicago, Chicago, IL, USA. Email: tgajewski@medicine.bsd.uchicago.edu



# Past, present, and future of lead–acid batteries

Improvements could increase energy density and enable power-grid storage applications

By **Pietro P. Lopes** and  
**Vojislav R. Stamenkovic**

**W**hen Gaston Planté invented the lead–acid battery more than 160 years ago, he could not have foreseen it spurring a multibillion-dollar industry. Despite an apparently low energy density—30 to 40% of the theoretical limit versus 90% for lithium-ion batteries (LIBs)—lead–acid batteries are made from abundant low-cost materials and nonflammable water-based electrolyte, while manufacturing practices that operate at 99% recycling rates substantially minimize environmental impact (1). Nevertheless, forecasts of the demise of lead–acid batteries (2) have focused on the health effects of lead and the rise of LIBs (2). A large gap in technological advancements should be seen as an opportunity for scientific engagement to expand the scope of lead–acid batteries into power grid applications, which currently lack a single energy storage technology with optimal technical and economic performance.

In principle, lead–acid rechargeable batteries are relatively simple energy storage devices based on the lead electrodes that operate in aqueous electrolytes with sulfuric acid, while the details of the charging and discharging processes are complex and pose a number of challenges to efforts to improve their performance. This technology accounts for 70% of the global energy storage market, with a revenue of 80 billion USD and about 600 gigawatt-hours (GWh) of total production in 2018 (3). Lead–acid batteries are currently used in uninterrupted power modules, electric grid, and automotive applications (4, 5), including all hybrid and LIB-powered vehicles, as an independent 12-V supply to support starting, lighting, and ignition modules, as well as critical systems, under cold conditions and in the event of a high-voltage battery disconnect (3). Although the principle of operation has not changed, manufacturers have improved this technology by optimizing performance of the

electrodes and active components mainly for application in vehicles. Future performance goals include enhanced material utilization through more effective access of the active materials, achieving faster recharging rates to further extend both the cycle life and calendar life and to reduce their overall life cycle cost with a direct impact on the implementation of grid storage systems.

The constant dissolution and redeposition of the cell's active materials, over each charge–discharge cycle, creates a situation where both positive and negative electrode morphology and microstructure are constantly changing (see first the figure). These structural changes enable the corrosion of electrode grids typically made of pure lead or of lead–calcium or lead–antimony alloys and affect the battery cycle life and mate-

Pb and PbO<sub>2</sub>, which is a thermodynamically and kinetically more demanding process given the poor solubility of the PbSO<sub>4</sub> crystals. The intricate relationship between acid concentration gradients within the electrode pores and lead sulfate dissolution rates underscores the challenge of improving the battery's ability to recharge at fast rates.

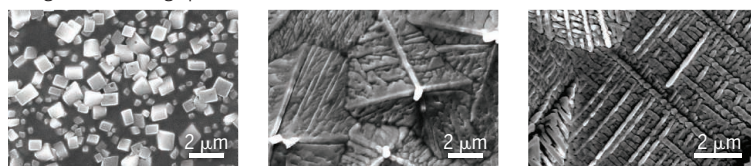
All of these processes occur in competition with the thermodynamically favored but undesired water-splitting reactions that evolve O<sub>2</sub> and H<sub>2</sub> gases. Lead and lead dioxide are poor catalysts for these reactions and have high overpotentials that kinetically limit these processes unless fast charging occurs with high voltages. However, metal and ionic impurities in electrodes and electrolyte facilitate electrolysis of water and its loss (5). The requirement for a small yet constant

charging of idling batteries to ensure full charging (trickle charging) mitigates water losses by promoting the oxygen reduction reaction, a key process present in valve-regulated lead–acid batteries that do not require adding water to the battery, which was a common practice in the past.

Some of the issues facing lead–acid batteries discussed here are being ad-

## Morphological changes

Both electrodes form surface PbSO<sub>4</sub> during discharging. Scanning electron microscopy images of Pb/PbSO<sub>4</sub> electrodes show marked surface morphology changes for distinct charge and discharge protocols.



A charged Pb electrode

First discharge at a slow rate

First discharge at a faster rate

rial utilization efficiency. Because such morphological evolution is integral to lead–acid battery operation, discovering its governing principles at the atomic scale may open exciting new directions in science in the areas of materials design, surface electrochemistry, high-precision synthesis, and dynamic management of energy materials at electrochemical interfaces. This understanding could have a direct impact on battery life, as preserving the overall electrode surface area ensures effective charge–discharge processes.

These efforts must take into account the complex interplay of electrochemical and chemical processes that occur at multiple length scales with particles from 10 nm to 10 μm (see the second figure) (5). The active materials, Pb and PbO<sub>2</sub>, are traditionally packed as a self-structured porous electrode. When discharged, Pb<sup>2+</sup> ions quickly react with the available sulfuric acid in the electrolyte and nucleate insoluble PbSO<sub>4</sub> crystals. During charging, PbSO<sub>4</sub> must be converted back to

addressed by introduction of new component and cell designs (6) and alternative flow chemistries (7), but mainly by using carbon additives and scaffolds at the negative electrode of the battery (4), which enables different complementary modes of charge storage (supercapacitor plus faradaic Pb charge–discharge). These electrodes also offer a rigid, unreactive, and conductive electrode backbone that prolongs cycle life.

At the positive electrode, identification of a material that can withstand the high electrode potentials and harsh acidic environment remains a problem to be solved. Utilization of bipolar electrodes can reduce the amount of lead used for structural components (electrode grid), immediately improving material utilization, but challenges with corrosion and cost-effective manufacturing are still a limiting factor. Implementation of battery management systems, a key component of every LIB system, could improve lead–acid battery operation, efficiency, and cycle life.

Materials Science Division, Argonne National Laboratory, Lemont, IL 60439, USA. Email: vrstamenkovic@anl.gov

PHOTOS: MILENA ZORKO/CENTER FOR NANOSCALE MATERIALS AT ARGONNE



Perhaps the best prospect for the unutilized potential of lead-acid batteries is electric grid storage, for which the future market is estimated to be on the order of trillions of dollars. For that reason, the low cost of production and materials, reduced concerns about battery weight, raw material abundance, recyclability, and ease of manufacturing make it an attractive solution if technical barriers can be addressed. At a current spot price below \$2/kg and an average theoretical capacity of 83 ampere hours (Ah)/kg (which includes  $\text{H}_2\text{SO}_4$  weight and the average contribution from Pb and  $\text{PbO}_2$  active materials) that rivals the theoretical capacity of many LIB cathode materials (8), lead-acid batteries have the baseline economic potential to provide energy storage well within a \$20/kWh value (9).

Despite perceived competition between lead-acid and LIB technologies based on energy density metrics that favor LIB in portable applications where size is an issue (10), lead-acid batteries are often better suited to energy storage applications where cost is the main concern. In reality, LIB technology has been more detrimental to nickel-metal hydride and nickel-cadmium battery markets (3). The increased cost, small production rates, and reliance on scarce materials have limited the penetration of LIBs in many energy storage applications.

The inherent concern surrounding lead-acid batteries is related to the adverse health and environmental effects of lead (11). More effective mitigation is feasible with application of known practices, strict government regulations, and improved training and engineering controls, which would further increase the already impressive recycling rate of 99% (12). Also, many serious safety and health concerns exist as part of LIB manufacturing and operation, including the carcinogenic potential of Ni and Co oxide components of cathode materials, the production of highly toxic organofluorophosphate neurotoxins as a consequence of thermal runaway events (battery fire and explosion) (8, 13) and potential contamination of the environment with toxic organofluorine by-products arising from electrolytes and additives (14).

As with any technology, many of the associated risks can be limited with proper management of materials, good manufacturing practices, and committed waste management. The 99% recycling rate of lead-acid batteries (12) and stringent regulations on Pb environmental emissions greatly minimize the risk of Pb release to the environment. Alternatively, the lack of economically feasible recycling solutions to LIB technology in the short term, combined with the expected increase in the number of battery cells that are approaching their end of life, aggravate the potential for environmental contamination from discarded LIB systems. Accidental inclusion of LIBs in lead battery recycling has proven hazardous, and better safety and recycling protocols are needed.

The range of tools and methods developed over the past 30 years, both experimentally and theoretically, are readily applicable to further develop and elucidate the science of lead-acid batteries. These topics would greatly benefit from further engagement from U.S. National Laboratories and across academia (15). Leveraging our current scientific knowledge and an established manufacturing industry with admirable safety and recycling records would ensure strong economic, technical, and environmental support for lead-acid batteries to continue serving as part of a future portfolio of energy storage technologies. ■

## Multiscale electrochemistry

The technical challenges facing lead-acid batteries are a consequence of the complex interplay of electrochemical and chemical processes that occur at multiple length scales. Atomic-scale insight into the processes that are taking place at electrodes will provide the path toward increased efficiency, lifetime, and capacity of lead-acid batteries.

### Macroscopic components (centimeters)

The Pb anode and  $\text{PbO}_2$  cathode electrodes and separator are illustrated. Charging regenerates these materials.

### Microstructural and fluid flows (10 $\mu\text{m}$ to 1 mm)

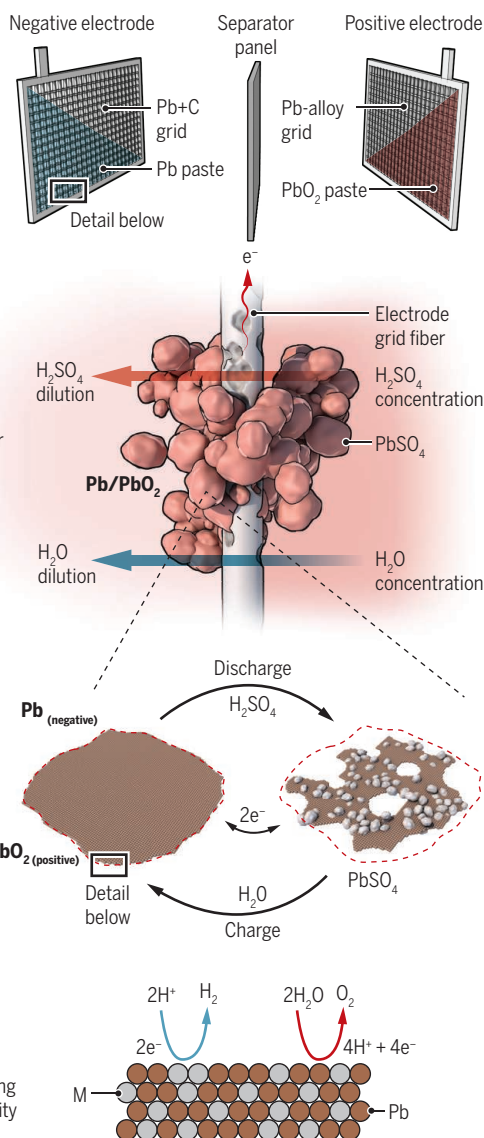
Charge and discharge cycles form complex particle interfaces between Pb and  $\text{PbSO}_4$  or  $\text{PbO}_2$  and  $\text{PbSO}_4$  on the micrometer scale. These self-structured porous networks create acid and water concentration gradients at the electrochemical interfaces.

### Nanostructural crystal formation (~10 nm to ~10 $\mu\text{m}$ )

Continuous dissolution and redeposition of active materials occur at the surface of particles and drive changes in microstructure.

### Water-splitting reactions (0.1 to 1 nm)

Charging can also split water into  $\text{H}_2$  and  $\text{O}_2$  during overcharging or at impurity metal (M) atom.



## REFERENCES AND NOTES

1. I. Feldman et al., *Environ. Law Rep.* **46** (2016).
2. R. Rapier, *Forbes* 27.1; [www.forbes.com/search/?q=lead%20battery#6222d028279f](http://www.forbes.com/search/?q=lead%20battery#6222d028279f) (2020).
3. C. Pillot, in 11th International Advanced Automotive Battery Conference (2020), pp. 1–111; [www.avicenne.com/pdf/Fort\\_Lauderdale\\_Tutorial\\_C\\_Pillot\\_March2015.pdf](http://www.avicenne.com/pdf/Fort_Lauderdale_Tutorial_C_Pillot_March2015.pdf).
4. G. J. May, A. Davidson, B. Monahov, *J. Energy Storage* **15**, 145 (2018).
5. D. Pavlov, *Lead-Acid Batteries: Science and Technology* (Elsevier Science, 2011).
6. D. Rand, *Batter. Int.* (no. 100), pp. 25–27 (2017); [www.batteriesinternational.com/back-issues-3/](http://www.batteriesinternational.com/back-issues-3/).
7. A. Hazza, D. Pletcher, R. Wills, *Phys. Chem. Chem. Phys.* **6**, 1773 (2004).
8. D. Doughty, E. P. Roth, *Electrochem. Soc. Interface* **21**, 37 (2012).
9. M. S. Ziegler et al., *Joule* **3**, 2134 (2019).
10. A. J. Bard, R. Parsons, J. Jordan, *Standard Potentials in Aqueous Solution* (Taylor & Francis, 1985).
11. G. Flora, D. Gupta, A. Tiwari, *Interdiscip. Toxicol.* **5**, 47 (2012).
12. SmithBucklin Statistics Group, "National Recycling Rate Study" (2019).
13. W. Weber et al., *J. Chromatogr. A* **1394**, 128 (2015).
14. K. Liu, Y. Liu, D. Lin, A. Pei, Y. Cui, *Sci. Adv.* **4**, eaas9820 (2018).
15. A. Davidson, Consort. Batter. Innov. (2019); <https://batteryinnovation.org/lead-battery-innovation-and-the-year-ahead/>.

## ACKNOWLEDGMENTS

The approach applied to develop structure-function correlations was funded by the U.S. Department of Energy, Office of Science, Office of Basic Energy Sciences, Materials Sciences and Engineering Division. The research efforts were supported by the Lead Battery Science Research Program through a Cooperative Research and Development Agreement. Use of the Center for Nanoscale Materials, an Office of Science user facility, was supported by the U.S. Department of Energy, Office of Science, Office of Basic Energy Sciences, under contract no. DE-AC02-06CH11357. We thank E. Coleman, D. Strmcnik, M. Zorko, C. Ferels, N. Chaudhari, and in memoriam Stefan Djokic for support in experiments.

10.1126/science.abd3352



# James G. Townsel (1935–2020)

Neuroscientist and devoted mentor of diverse scientists

By **Rae Nishi<sup>1</sup>**, **Byron D. Ford<sup>2</sup>**,  
**John G. Hildebrand<sup>3</sup>**

**J**ames “Jim” Garfield Townsel, a neuroscientist who devoted his life to diversifying the field, died on 22 June. He was 84. Jim made valuable contributions to the field of neurotransmission through his research, but he is best known for his unwavering focus on eliminating racial health disparities by mentoring underrepresented trainees and supporting their scientific advancement.

Born on 9 September 1935 in Albemarle, North Carolina, Jim grew up in the inner city of Harrisburg, Pennsylvania. He graduated in 1958 with high honors from Virginia State University (VSU), where he majored in biology and participated in the Reserve Officers’ Training Corps. After working in the U.S. Army Medical Service Corps, he began graduate school, a transition made possible by Richard Dunn, a botanist at VSU who, as Jim put it, “rolled boulders out of my way and was committed to my success.”

After earning his Ph.D. in physiology at Purdue University in 1968, Jim was recruited immediately to the faculty of VSU. In 1971, he accepted a postdoctoral traineeship at Harvard Medical School in the laboratory of neurobiologist Edward Kravitz. Jim’s experience at Harvard galvanized his passion for neuroscience. In 1973, he accepted an assistant professorship at Meharry Medical College, a historically Black medical school in Nashville, Tennessee. He later moved to the University of Illinois at Chicago to administer its Urban Health Program. In 1984, he returned to Meharry, where he was a professor and chair of the physiology department until his retirement in 2010.

When he arrived at Meharry in 1973, Jim quickly secured research grants from the National Institutes of Health (NIH) and the National Science Foundation, but the lack of research culture at the college hindered his work. He would later recall that the summary statement of his first NIH research project grant application expressed admiration for him as an applicant but considered his chance of success in the school’s environment to be vanishingly small. Nonetheless, Jim persisted

and built a strong research program that made substantial contributions to the fields of neurotransmitter biochemistry and trafficking of proteins involved in neurotransmission. When he returned to Meharry as chair in 1984, he drew upon his early experiences to create a culture of research that benefited students. He hired two active neuroscientists, secured competitive federal funding for research, created a multidisciplinary graduate program that earned an NIH training grant, and developed an NIH-funded collaborative program with Vanderbilt University for predoctoral trainees.

Devoted to training his students to become effective scientists, Jim mentored with tough love. Each day, he would walk through the lab and grill his trainees about



their research. He expected productivity but also emphasized rigor and reproducibility, qualities that were not yet fully appreciated by the scientific community. He always demanded intellectual accountability. As his Ph.D. student, I (B.D.F.) understood that it was acceptable not to know something, but that I had best learn it before I was asked about it again. Jim’s view was that Black scientists had to be better than scientists from more commonly represented backgrounds in order to succeed in academia. He prepared these scientists well and continued to support them throughout their careers.

Jim collaborated with neuroscientists Joseph Martinez and James Jones to lead the Diversity Program in Neuroscience (DPN), a diversity-focused training program funded by the NIH and supported by the American Psychological Association. DPN began in 1988 and, in addition to providing

a training stipend, offered mentorship, annual monitoring, and enrichment activities. For 23 years, DPN supported almost 300 trainees from underrepresented groups. The enrichment program, codirected by Jim and Joseph Martinez, consisted of a monthlong experience encompassing professional development, lectures in neuroscience, mentoring, and networking at the Marine Biological Laboratory in Woods Hole, Massachusetts. Although DPN lost its funding, the enrichment component lives on as the Summer Program in Neuroscience, Excellence, and Success (SPINES).

All three of us worked closely with Jim as he spearheaded these diversity programs and saw firsthand his passion for furthering the careers of underrepresented trainees in neuroscience. He did not believe in giving handouts, and he sought to instill in all trainees the qualities necessary to succeed in science. He was truly frustrated to discover mentors who thought they were supporting their trainees of color by putting them on papers as honorary authors. For Jim, what mattered was an earned first authorship, because that would lead to advancement and research grants.

Jim was deeply disturbed by racial disparities in health. He recognized that diversifying the scientific workforce is essential to mitigating such disparities. It was therefore critically important to him that trainees of color stay in science, get research grants, and advance the field. He knew that to ensure this result, the students he trained would have to carry on in his footsteps, becoming mentors themselves and remaining lifelong supporters of their trainees, and that those trainees would have to become mentors in turn, bringing ever more diverse scientists into academia.

In DPN advisory committee meetings, Jim was always very serious, but when we worked with him at SPINES, he was friendly and supportive, often giving every participant a hug at the end of his teaching session. During a lively discussion with one of us (R.N.) last summer, he emphasized the long-term commitments that true mentorship requires and expressed disappointment that such emotional investment is often overlooked. He concluded, “There are many books about mentoring, but none of them tell you how to have a heart, which is what you need to succeed.”

Jim had that heart. Most of his trainees from the lab as well as hundreds from SPINES remain in research and are now faculty members at research universities. They serve as role models, carrying his legacy forward and continuing to fulfill his vision of a more equitable scientific landscape and world. ■

10.1126/science.abd8380

<sup>1</sup>Falmouth, MA 02540, USA. <sup>2</sup>Biomedical Sciences Division, University of California, Riverside, CA 92521, USA. <sup>3</sup>Department of Neuroscience, University of Arizona, Tucson, AZ 85721, USA. Email: raeko.nishi@gmail.com





## ENERGY POLICY

# One step forward, two steps back

Interest groups and state-level political inertia have stalled many of America's clean energy initiatives

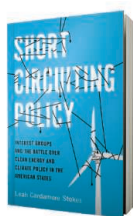
By **Saleem H. Ali**

**W**hy is it that America has not been able to achieve science-based targets for carbon emissions reductions despite the availability of numerous economically and ecologically rational solutions?

This question is often framed in terms of job losses or energy security arguments. In *Short Circuiting Policy*, a timely political ethnography of U.S. energy policy, Leah Cardamore Stokes argues that clean energy programs initially gained traction as potential opportunities to create green jobs and reduce carbon footprints but then waned, even as the economics increasingly favored their success. Focusing on state-level politics, Stokes carefully lays out how Arizona, Kansas, Texas, and Ohio struggled to contain the power of the fossil fuel and electric utilities industries and, in doing so, failed to sustain a clean energy trajectory.

The book's title is a reference to a passage from political scientist E. E. Schattschneider's 1942 book, *Party Government*, which reads: "Pressure politics is a method of short-circuiting the majority." This sentiment is

echoed in economist Mancur Olson's 1965 book, *The Logic of Collective Action*, which laid out a theory of how concentrated benefits can trump diffuse cost factors. Stokes convincingly argues that climate change fits this paradigm perfectly. She reveals how successful green energy policies are eroded through a process she refers to as retrenchment, and how renewable energy infrastructure development has succumbed to a series of negative feedback loops that have kept progress on a treadmill of policy inertia.



**Short Circuiting Policy**  
Leah Cardamore Stokes  
Oxford University Press,  
2020. 338 pp.

Drawing on more than a hundred interviews with key decision-makers and stakeholders, as well as detailed document and media analysis, Stokes explores the consequences of stalled environmental policies at length. She discusses the usual mechanisms of influence, such as political lobbying and advertising campaigns,

but also reveals more pernicious phenomena, including "astroturfing," wherein the entity advancing a particular policy is concealed by an ostensibly grassroots campaign. Such efforts, she argues, create a "fog of enactment"—a gap between interest groups' expectations of a given policy and its actual implementation—comparable to what others have documented in tobacco legislation (1).

The democratic process is fragile, reveals Stokes, and highly vulnerable to powerful interests. What's more, when citizens agree

Wind turbines loom behind an oil pump in Texas, illustrating the enduring tension between clean energy and fossil fuels.

with a politician on a particular issue, they often take cues from them on unrelated issues, including energy policy.

The environment was once a unifying cause in American politics. In 2007, former Speaker of the House Newt Gingrich, an otherwise polarizing Republican, co-wrote a book called *A Contract with the Earth* to remind conservatives of as much, referencing the party's environmental legacy (2). However, Stokes shows that a carefully curated campaign advanced by conservative groups such as the American Legislative Exchange Council, the State Policy Network, and Americans for Prosperity—sensing ambivalence toward green policies from core Republican Party supporters—began targeting the base with messaging against renewable energy in the late 20th century. Such campaigns gained momentum between 2000 and 2010. The impact of this anti-environmentalist miasma continues to this day.

Using the heuristic of what she calls a "narwhal curve," Stokes provides a useful visual primer for how steep a rise in renewable energy transition is needed. She is also more sympathetic to nuclear power in her analysis, noting that the retirement of nuclear plants is making our task of transition even more challenging. On this point, I had hoped that Stokes would have been more willing to critique environmentalist organizations as another sort of special interest group. Many of the pathologies that she identifies in fossil fuel and electric utility interests also apply to the anti-nuclear movement, which derailed any potential for economies of scale being realized from this clean technology. [Extreme risk aversion and a misapplication of the precautionary principle trumped hard data in this regard as well (3).] She could have also engaged with some of the literature that challenges the dominance of the interest group hypothesis in explaining political influence, for example, the work of Gunnar Trumbull (4). Despite these minor misses, Stokes has written a highly readable and compelling book that will be of interest to environmental policy scholars and the general public alike. ■

## REFERENCES AND NOTES

1. N. Oreskes, E. M. Conway, *Merchants of Doubt* (Bloomsbury, 2010).
2. N. Gingrich, T. L. Maple, *A Contract with the Earth* (Johns Hopkins Univ. Press, 2007).
3. S. L. Montgomery, T. Graham Jr., *Seeing the Light* (Cambridge Univ. Press, 2017).
4. G. Trumbull, *Strength in Numbers* (Harvard Univ. Press, 2012).

10.1126/science.abc8702

The reviewer is at the College of Earth, Ocean and Environment, University of Delaware, Newark, DE 19716, USA. Email: saleem@udel.edu



## SCIENCE LIVES

# Ray Bradbury, luminary of the space age, at 100

A new biography chronicles the golden years of Earth's first martian

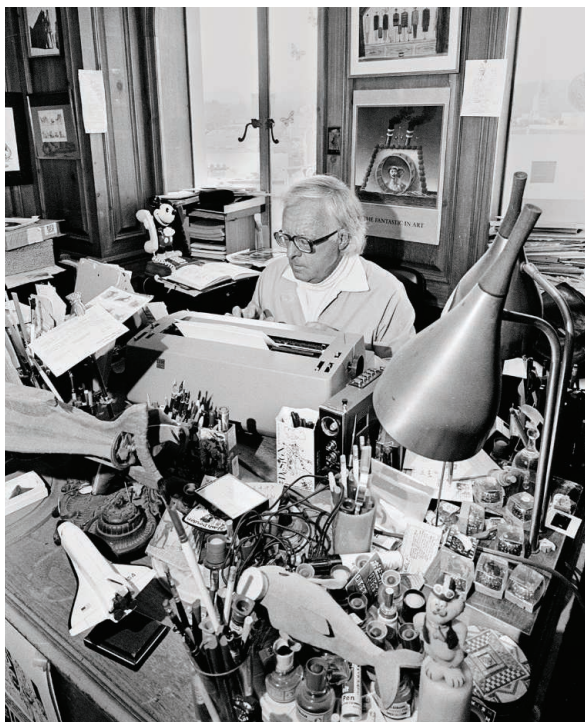
By Ingrid Ockert

One hundred years ago this month, the poet laureate of Mars was born in sleepy Waukegan, Illinois. To a generation of baby boomers, Ray Bradbury was best known for his masterpiece *The Martian Chronicles* (1950), a lyrical collection of stories that wondered how humans might adapt to life on the red planet. His poetic descriptions captured the world's collective imagination, spurring the development of space technologies, including Mars-bound satellites and rovers. As Norman Corwin noted in 1971, "[Bradbury] got to Mars before the scientists...No amount of scientific data, no logs and extrapolations of computer codes, will ever dislodge him from that planet."

To mark the centennial of Bradbury's birth, Jonathan Eller, a professor of English at Indiana University and director of the Center for Ray Bradbury Studies, has written *Bradbury Beyond Apollo*, the final biography in a trilogy that explores Bradbury's life. Eller's thoughtful narrative is meticulous, offering more than 300 pages of analysis and snippets from Bradbury's unpublished letters and manuscripts to document every moment of the writer's golden years, starting with the launch of Apollo 15 in 1971 and ending with his final days in 2012. Along the way, Eller offers readers insights into how Bradbury established his legacy as a luminary of the space age.

Throughout his career, Eller explains, Bradbury looked for opportunities to collaborate, to strengthen his connection with fans, and to grow as a writer. *Bradbury Beyond Apollo* dives deep into the writer's expansive personal and professional network of scientists, filmmakers, writers, and artists. Bradbury, we learn, established friendships early on with key players and looked for projects that would allow them to work together. He met Walt Disney in the 1960s, for example,

and worked with Disney's "imagineers" on several projects before their partnership bore fruit, namely in the form of Epcot's ride Spaceship Earth and Walt Disney Production's film *Something Wicked This Way Comes* (1982) based on Bradbury's novel of the same name. Similarly, Eller reveals how Bradbury helped Bruce Murray and others at the Planetary Society promote space travel and planetary exploration. While not all of the writer's projects came to fruition, he continued to dream up new films, books, exhibits, and other projects and collaborations.

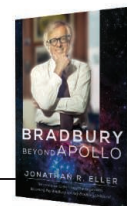


Surrounded by Disney and NASA mementos, Bradbury writes in 1981.

For a historian of science like myself, Eller's careful analysis of Bradbury's professional networks is invaluable. Too often, the files of influential public figures remain closed, reinforcing their enigmatic, two-dimensional public image. The careful detail of this biography paints a rich portrait of Bradbury as a talented conversationalist and gifted collaborator and allows readers to understand the nuances of his professional relationships. The writer's correspondence, meanwhile, offers incredible perspective into the interconnected

## Bradbury Beyond Apollo

Jonathan R. Eller  
University of Illinois Press,  
2020. 376 pp.



world of postwar science communication.

Equally valuable is the full picture of Bradbury's career as a public speaker that Eller provides readers. Bradbury appeared regularly on television and in auditoriums across the United States, strengthening his relationships with fans and helping to establish him as a leading voice for space-

flight. Although some biographers might have omitted discussion of Bradbury's public lectures, Eller's decision to include a detailed recounting of the author's outreach efforts proves vital to understanding his continued influence within the scientific community.

Even as Bradbury established a persona as a martian luminary, he continued to write stories in other genres—strange tales of haunted crypts, hard-boiled noirs, and sweet musings of childhood innocence. Eller documents the continued development of Bradbury's writing prowess, describing how the author experimented with poetry and with more realistic stories.

Bradbury was careful to delineate his expertise as that of a writer, not a scientist, when speaking alongside professionals at NASA symposiums. But his popularity demonstrated that inspiration, not just education, was an important dimension of science communication. Today, many successful scientists recognize that effective communication weaves to-

gether awe and information.

Bradbury's lectures offered audiences opportunities to connect with him, and with each other, over a positive vision of human spaceflight. As he explained in a letter to officials at the Smithsonian in 1981, "[I am] in the business of shaking people up and rousing their blood so they go out of the show half-mad with love and stunned with the beauties of space. If we do that, the rest will follow." ■

The reviewer is a historian of science based in Berkeley, CA, USA. Email: ingrid.ockert@gmail.com

10.1126/science.abc2948





Human activities threaten the dwindling Baer's pochard population.

Edited by Jennifer Sills

## Baer's pochard duck at risk of extinction

The Baer's pochard (*Aythya baeri*), a migratory duck, used to be widespread in northeast China and eastern Russia, where it would breed, and in central and south-east Asia, where it would migrate for the winter (1). However, in recent years, the Baer's pochard population has decreased to between 150 and 700 Critically Endangered individuals (2, 3). China, as the primary residence of Baer's pochard (3), must take more protective measures to alleviate the threats to the species and prevent their extinction.

Anthropogenic activities have exacerbated the rapid decline of the Baer's pochard population. Wetlands are the duck's primary habitats and breeding grounds, but 33% of wetlands in China were lost between 1978 and 2008 (4). Environmental pollution has killed Baer's pochards and further restricted their habitats (5). Human activities such as fishing, illegal hunting, and picking up bird eggs have disrupted Baer's pochard populations and threatened their breeding (5).

The Baer's pochard is an important species in the biosphere and vital for maintaining biodiversity and freshwater ecosystems. Urgent and coordinated action from government and the public is required to protect this species. The Chinese government should update the

National Key-protected Species List, where the Baer's pochard is still listed as a lower-priority class III protected species (6, 7). Local governments must strictly enforce the Wildlife Protection Law of China to stop illegal hunting and trade (8) and increase the investigation and monitoring of the Baer's pochard population, distribution, and habitats (9). China should also promote the protection and restoration of the inland freshwater wetlands that serve as the duck's primary habitats by strengthening the management of wetland nature reserves and improving the infrastructure of wetland parks. The government, scientists, and the public must work together to control China's pollution (10). Finally, the government should work to raise the public's awareness of wildlife protection.

**Xin Tong**

College of Environmental Science and Engineering, Nankai University, Tianjin 300350, China. Email: tongxin@mail.nankai.edu.cn

### REFERENCES AND NOTES

1. X. Wang *et al.*, *Bird Conserv. Int.* **22**, 2 (2012).
2. BirdLife International, Baer's Pochard (*Aythya baeri*) (IUCN Red List Threatened Species, 2019).
3. A. U. Chowdhury *et al.*, *FORKTAIL* **28**, 57 (2012).
4. Z. G. Niu *et al.*, *Nature* **471**, 7338 (2011).
5. X. F. Wang *et al.*, *Chin. J. Wildl.* **40**, 1 (2019) [in Chinese].
6. The Department of Forestry and Grassland, "The National Key-protected Species List" (2018); [www.forestry.gov.cn/main/3954/content-1063883.html](http://www.forestry.gov.cn/main/3954/content-1063883.html) [in Chinese].
7. The Department of Forestry and Grassland, "List of National Protected Terrestrial Wildlife Beneficial to Economic or Scientific Value" (2000); <http://www.forestry.gov.cn/main/3954/content-959027.html> [in Chinese].

8. The National People's Congress of the People's Republic of China, "The Wildlife Protection Law of China" (2018); [www.npc.gov.cn/npc/c12435/201811/f4d2b7a3024b41ee8ea0ce54ac117daa.shtml](http://www.npc.gov.cn/npc/c12435/201811/f4d2b7a3024b41ee8ea0ce54ac117daa.shtml) [in Chinese].
9. The Department of Forestry and Grassland, "International Workshop of the Baer's Pochard Conservation" (2018); [www.forestry.gov.cn/portal/xdly/s/5188/content-1086081.html](http://www.forestry.gov.cn/portal/xdly/s/5188/content-1086081.html) [in Chinese].
10. L. Zhang *et al.*, *Bird Conserv. Int.* **27**, 2 (2017).

10.1126/science.abd2087

## Waterbirds' coastal habitat in danger

Migratory waterbirds, especially shorebirds, depend on China's coastal wetlands (1). China's plans to reclaim the coastal region for industry, aquaculture, and other infrastructure could destroy the last remaining habitat of many vulnerable species (2, 3). From 2000 to 2010, the local governments of China's coastal areas, motivated by rapid urbanization and economic development, have reclaimed more than 320,000 ha of coastal wetlands (4). In 2012, China approved plans to reclaim 246,900 ha of coastal wetlands for construction by 2020 (4). The largest reclamation project—the Oufei Project in Wenzhou Bay—spans an area of 8854 ha (5) and threatens a crucial waterbird habitat. China should halt reclamation plans until environmental needs are addressed.

Wenzhou Bay is an important stopover site for birds migrating along the East Asian-Australasian flyway. More than 100,000



waterbirds rest in the area (6), including the Endangered black-faced spoonbill (*Platalea minor*) and spoon-billed sandpiper (*Calidris pygmaea*) (7, 8). There is no other suitable waterbird habitat that could serve as an alternative resting area (9). To protect rare waterbirds, we must protect their habitats from reclamation.

China's coastal wetland protection contains substantial gaps (10). Of the 110 waterbird priority conservation sites, 67 are located outside the protected area (11). The Chinese government must take biodiversity conservation needs into account before proceeding with reclamation projects. National parks, nature reserves, and other protections should be designated to fill the gaps in the current system. The addition of the Yellow Sea-Bohai Gulf (Phase I) to the World Heritage List in 2019 is a step in the right direction (12). To further strengthen protections, China should fund the investigation and monitoring of migratory birds on coastal wetlands (4) and carry out ecosystem restoration in the reclamation region.

Yi Wu, Wenwen Zhang, Fan Yong, Daqing Zhou, Peng Cui\*

Key Laboratory of Biosafety, State Environmental Protection Scientific Observation and Research Station for Ecology and Environment of Wuyi Mountains, Nanjing Institute of Environmental Sciences, Ministry of Ecology and Environment, Nanjing 210042, China.

\*Corresponding author.

Email: cuipeng1126@163.com

#### REFERENCES AND NOTES

1. Q. Bai *et al.*, *Avian Res.* **6**, 12 (2015).
2. H. Yang *et al.*, *Proc. Natl. Acad. Sci. U.S.A.* **114**, 201706111 (2017).
3. C. E. Studds *et al.*, *Nat. Commun.* **8**, 14895 (2017).
4. G. C. Lei, Z. W. Zhang, X. B. Yu, M. X. Zhang, "Blueprint of coastal wetland conservation and management in China (Higher Education Press, Beijing, 2017), pp. 227–239 [in Chinese].
5. X. P. Bao, Z. Zhang, B. Q. Lv, P. Y. Bao, Y. D. Ma, *Ocean Dev. Manag.* **31**, 65 (2014) [in Chinese].
6. Kuaidianwenzhou team, "Protect the stopover site for global migratory waterbirds in Wenzhou Bay," *Sohu* (2019); [www.sohu.com/a/306942021\\_467914](http://www.sohu.com/a/306942021_467914) [in Chinese].
7. BirdLife International, *Platalea minor* (The IUCN Red List of Threatened Species, 2017).
8. BirdLife International, *Calidris pygmaea* (The IUCN Red List of Threatened Species, 2018).
9. H. R. Jiang, *Chin. Nat.* **3**, 68 (2019) [in Chinese].
10. T. T. Ma, X. W. Li, J. H. Bai, B. S. Cui, *Glob. Ecol. Conserv.* **17**, e00585 (2019).
11. S. Xia *et al.*, *Biol. Conserv.* **210**, 72 (2017).
12. UNESCO, World Heritage List: Migratory Bird Sanctuaries along the Coast of Yellow Sea-Bohai Gulf of China (Phase I) (2019); <http://whc.unesco.org/en/list/1606>.

10.1126/science.abc9000

## Protect the giant ibis through the pandemic

The giant ibis (*Thaumatibis gigantea*), Cambodia's national bird, is edging toward extinction. The ibis's historical range stretched across Southeast Asia, but only 194 Critically Endangered individuals

remain, constrained to the northeastern region of Cambodia (1). The small population suffers from habitat loss and disturbance caused by human activities, and tensions between humans and wildlife have escalated during the coronavirus disease 2019 (COVID-19) pandemic. In April, 3 giant ibises and more than 100 other birds were poached in Cambodia's Chhep Wildlife Sanctuary (2). To save the giant ibis, conservation efforts must continue, even during the pandemic.

Giant ibises nest in forests and frequent nearby wetlands, where they prey on frogs, insects, and larvae (3), all historically plentiful in their habitats. However, extensive clearance of Cambodia's lowland dry forest for agro-industry, coupled with widespread wetland agricultural drainage, has disrupted the ecosystems on which the ibises depend. Under China's Belt and Road Initiative (4), new roads are planned to run through the Siem Pang District in northeast Cambodia, as well as protected forests in the Keo Seima Wildlife Sanctuary in eastern Cambodia, further disrupting the ibis's habitats (5). Hydroelectric dams on the Mekong River and its tributaries will change water levels in riverine wetlands, potentially decreasing habitat quality and affecting ibis prey species (6, 7).

As their habitats diminish, ibises are also vulnerable to climate fluctuations. Prolonged drought in the 2009–2010 dry seasons decreased ibis breeding rates by about 50% (4). Potential increases in drought severity due to climate change could replicate these declines (8).

To conserve the giant ibis population, we must protect key habitats, enforce environmental regulations, and reconcile conservation and agricultural development through trade-offs between land-sparing, wildlife-friendly farming and intensification to increase yields from smaller farmland areas (9). It is also essential to ensure that local people benefit from conservation, especially during uncertain times such as the COVID-19 pandemic. International tourists spent more than US\$100,000 visiting Cambodia to view giant ibises in the past decade (2). With global tourism in decline for an indeterminate period of time, this income will decrease, and pressure on the environment may increase. Planning for the return of tourists should focus on community-based eco-tourism initiatives, such as those developed at some Cambodian wetland protected areas (10). With financial and institutional support from international nongovernmental organizations, local communities can build

the infrastructure they will need to host future domestic and international tourists. By preparing to provide eco-tourism services, these communities can benefit from alternative income sources once tourism resumes, thereby allowing them to continue their support for the conservation of the giant ibis and the region's other endangered species.

Hong Yang<sup>1,2\*</sup>, Mingguo Ma<sup>1</sup>, Julian R. Thompson<sup>3</sup>, Roger J. Flower<sup>3</sup>

<sup>1</sup>Chongqing Engineering Research Center for Remote Sensing Big Data Application, School of Geographical Sciences, Southwest University, Chongqing 400715, China. <sup>2</sup>Department of Geography and Environmental Science, University of Reading, Reading RG6 6AB, UK. <sup>3</sup>Department of Geography, University College London, London, WC1E 6BT, UK.

\*Corresponding author.

Email: hongyanghy@gmail.com

#### REFERENCES AND NOTES

1. BirdLife International, *Thaumatibis gigantea* (The IUCN Red List of Threatened Species, 2018).
2. Wildlife Conservation Society, "COVID-19 fueling an uptick in poaching: Three critically endangered giant ibis—Cambodia's national bird—killed in protected area" (2020).
3. O. Keo, *Birding Asia* **9**, 100 (2008).
4. A. M. Lechner, F. K. S. Chan, A. Campos-Arceiz, *Nat. Ecol. Evol.* **2**, 408 (2018).
5. R. Loveridge, S. Ty, "Ten-year species action plan for the giant ibis (*Thaumatibis gigantea*) in Cambodia 2015–2025" (BirdLife International Cambodia Programme, Cambodia, 2015).
6. J. E. Chastant, D. E. Gawlik, *Waterbirds* **41**, 35 (2018).
7. A. H. Claassen, "Abundance, distribution, and reproductive success of sandbar nesting birds below the Yali Falls hydro-power dam on the Sesan River, Northeastern Cambodia" (World Wildlife Foundation/Danida/Wildlife Conservation Society/BirdLife International, Cambodia, 2004).
8. T. Amnuaylojaroen, P. Chanvichit, *Clim. Change* **155**, 175 (2019).
9. B. Phalan, M. Onial, A. Balmford, R. E. Green, *Science* **333**, 1289 (2011).
10. Wildfowl and Wetlands Trust, "Cambodia: The kingdom of wetlands" (2019); [www.wwt.org.uk/news/2019/09/20/cambodia-the-land-of-wetlands/17652#](http://www.wwt.org.uk/news/2019/09/20/cambodia-the-land-of-wetlands/17652#).

10.1126/science.abd0141

#### ERRATA

**Erratum for the Perspective "Opening the floodgates at Fukushima" by K. O. Buesseler, *Science* 369, eabe3043 (2020).** Published online 21 August 2020; 10.1126/science.abe3043

**Erratum for the Report: "Anti-Markovnikov alcohols via epoxide hydrogenation through cooperative catalysis" by C. Yao *et al.*, *Science* 368, eabc6177 (2020).** Published online 8 May 2020; 10.1126/science.abc6177

**Erratum for the Report: "Widely tunable compact terahertz gas lasers" by P. Chevalier *et al.*, *Science* 368, eabc5418 (2020).** Published online 8 May 2020; 10.1126/science.abc5418

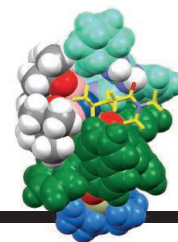
**Erratum for the Review "On the essentials of drought in a changing climate" by T. R. Ault, *Science* 368, eabc4034 (2020).** Published online 24 April 2020; 10.1126/science.abc4034



# RESEARCH

## Remote C–H borylation by a modular iridium catalyst

Reyes et al., p. 970



## IN SCIENCE JOURNALS

Edited by Michael Funk



### GLOBAL CARBON CYCLE

#### Pulses of the past

**B**ursts of carbon dioxide, released into the atmosphere and occurring on centennial time scales, were seen during the cold periods of the last glacial cycle but not in older or warmer conditions. Nehrbass-Ahles *et al.* present a record of atmospheric carbon dioxide concentrations retrieved from the European Project for Ice Coring in Antarctica Dome C ice core showing that these carbon dioxide jumps occurred during both cold and warm periods between 330,000 and 450,000 years ago. They relate these pulses to disruptions of the Atlantic meridional overturning circulation caused by freshwater discharge from ice sheets. Such rapid carbon dioxide increases could occur in the future if global warming also disrupts this ocean circulation pattern. —HJS  
*Science*, this issue p. 1000

Tiny gas bubbles visible in a freshly drilled ice core provide evidence of atmospheric composition 330,000 to 450,000 years ago.

### MICROBIOLOGY

#### How uromodulin helps flush out bacteria

Urinary tract infections (UTIs) are one of the most frequent bacterial infections in humans. The glycoprotein uromodulin is the most abundant urinary protein and can provide some protection from UTIs, but the precise mechanism has been unclear. Weiss *et al.* found that uromodulin forms stacked, fishbone-like filaments that act as a multivalent decoy for bacterial pathogens with adhesive pili that attach to the uromodulin glycans (see the Perspective by Kukulski). The resulting uromodulin-pathogen aggregates prevent bacterial adhesion to glycoproteins of the urinary epithelium and promote pathogen clearance as urine is

excreted. This innate protection against UTIs is likely to be particularly important in infants and children. —SMH

*Science*, this issue p. 1005;  
see also p. 917

### CANCER

#### A deeper look at cancer immunity

A key goal in oncology is diagnosing cancer early, when it is more treatable. Despite decades of progress, early diagnosis of asymptomatic patients remains a major challenge. Most methods involve detecting cancer cells or their DNA, but Beshnova *et al.* suggest a different approach that is focused on the body's immune response. The authors reasoned that the presence of cancer may cause

alterations in the T cell receptor repertoire, which could then be detected. They designed a deep-learning method for distinguishing the T cell repertoires in the blood of patients with and without cancer, which they validated in samples from multiple clinical cohorts. —YN

*Sci. Transl. Med.* **12**, eaaz3738 (2020).

### MOLECULAR BIOLOGY

#### A fork in the road for drug resistance

Inhibitors of the enzyme poly(ADP-ribose) polymerase (PARP) block the repair and restart of stalled replication forks, which eventually kills cancer cells. Kharat *et al.* found that the DNA demethylase TET2 was critical for sensitivity to PARP inhibitors by promoting

repair-mediated degradation of stalled forks. The TET2 product 5-hydroxymethylcytosine at stalled replication forks recruited a base excision repair-associated endonuclease. Without TET2, stalled replication forks were stabilized instead of degraded, thereby reducing PARP inhibitor sensitivity. —LKF

*Sci. Signal.* **13**, eaba8091 (2020).

### CANCER IMMUNOLOGY

#### Phages and cancer immunity

Gut bacteria are involved in the education of T cell immune responses, and the intestinal ecosystem influences anticancer immunity. Fluckiger *et al.* report microbial antigens that might cross-react with antigens



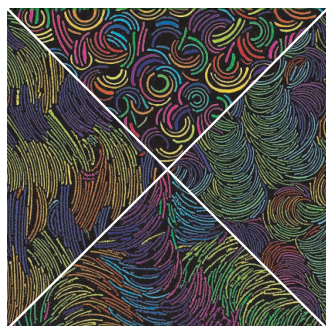
associated with tumor cells. They found that a type of intestinal bacteria called enterococci harbor a bacteriophage that modulates immune responses. In mouse models, administration of enterococci containing the bacteriophage boosted T cell responses after treatment with chemotherapy or programmed cell death protein 1 (PD-1) blockade. In humans, the presence of the bacteriophage was associated with improved survival after PD-1 immunotherapy. A fraction of human T cells specific for naturally processed melanoma epitopes appeared to be able to recognize microbial peptides. This “molecular mimicry” may represent cross-reactivity between tumors and microbial antigens. —PNK

*Science*, this issue p. 936

## LIQUID CRYSTALS

### Controlling the curvature

Molecular chirality is often required to make chiral liquid crystalline phases, but liquid crystallinity has also been obtained using curved elongated rods known as bent-core or banana-shaped molecules. Fernández-Rico *et al.* developed a method to controllably alter the curvature of the rods using ultraviolet light and a photoresponsive polymer (see the Perspective by Godinho). From a single starting batch can come a family of rods with different curvatures but similar overall rod thickness, length, and length distribution. The researchers explored a range of liquid crystalline phases, including the splay-bend nematic



**Curved nanorods, observed by confocal microscopy, adopt different phase behavior depending on their curvature.**

phase that was predicted more than 40 years ago. —MSL

*Science*, this issue p. 950;

see also p. 918

## IMMUNOLOGY

### SOSTDC1 for germinal center regulation

T follicular helper ( $T_{FH}$ ) cells are  $CD4^+$  T cells that facilitate B cell antibody production and B cell memory responses in the germinal centers (GCs) of lymphoid organs. These activities are in turn restrained by T follicular regulatory ( $T_{FR}$ ) cells, a population of T cells with unclear origins. Wu *et al.* now demonstrate that a subpopulation of  $T_{FR}$  cells and fibroblastic reticular cells both produce sclerostin domain-containing protein 1 (SOSTDC1), which drives  $T_{FR}$  cell generation by inhibiting Wnt- $\beta$ -catenin signaling. In mice lacking the gene *Sostdc1*,  $T_{FR}$  cell numbers were substantially decreased and GC responses were enhanced. These insights into  $T_{FR}$  cell biology and GC regulation may have important implications for autoantibody-mediated diseases and the future development of vaccines and therapies for autoimmune disease. —STS

*Science*, this issue p. 984

## CHEMICAL PHYSICS

### Attosecond science in liquid phase

Many physical properties of liquid water remain unresolved due to the very fast dynamics involved in the liquid phase. Using attosecond time-resolved photoelectron spectroscopy, Jordan *et al.* found that photoemission of electrons from water in the liquid phase shows a time delay of about 50 to 70 attoseconds compared with photoemission from the gas phase. This difference was attributed to solvation effects and was validated by analysis of various contributions to the measured delays and by using theoretical simulations in water clusters of different sizes. —YS

*Science*, this issue p. 974

## IN OTHER JOURNALS

Edited by **Caroline Ash**  
and **Jesse Smith**

## PLANT ECOLOGY

### Let the grass grow old

Over the past decade, there has been a reappraisal of the importance of grasslands in the global ecosystem. While they have often been regarded as a successional step en route to forest and woodland, there is increasing recognition of the conservation value of old-growth grasslands. Nerlekar and Veldman synthesized data on species richness in grasslands worldwide, showing that old-growth grasslands display high plant species diversity and that weedy secondary grasslands can take centuries to recover old-growth richness. They conclude that old-growth grasslands should be prioritized for conservation for their value in providing ecosystem services and supporting herbivore populations, analogous to the values perceived in old-growth forest. —AMS

*Proc. Natl. Acad. Sci. U.S.A.* **117**, 18550 (2020).

Old-growth grasslands are highly diverse, support herbivores, and provide important ecosystem services that are vulnerable to damage.



## MUTATION

### Calibrating mtDNA mutations through age

Mitochondrial DNA (mtDNA) is a separate genome found in eukaryotic cells that is maternally inherited. Mutations in mtDNA underlie several human diseases, and the accumulation of these mutations has been associated with aging. Arbeithuber *et al.* used duplex sequencing to trace accumulation of spontaneous mtDNA mutations in oocytes, brain, and muscle cells of mice. Ten-month-old mothers showed a

two- to threefold increased rate of mtDNA mutation compared with their 1-month-old pups. The authors found that the D-loop, a stretch of triple-stranded highly variable DNA in the noncoding region of the circular mtDNA where replication initiates, accumulated the most mutations. These mtDNA mutations occurred in patterns, indicating that they were caused by replication errors. It is possible that inheritance of aged mtDNA from older mothers may have health consequences for their offspring. —LMZ

*PLOS BIOL.* **18**, e3000745 (2020).





## ARCTIC WARMING High heat

**M**arine heat waves, like their more commonly discussed terrestrial counterparts, are occurring with increasing frequency and strength. The Arctic is warming at a higher rate than any other comparably sized region on Earth. How are Arctic marine heat waves changing? Hu *et al.* examined sea surface temperature data and show that these marine heat waves have grown in frequency, duration, and intensity mostly in the places where sea ice coverage no longer lasts through the summer. This finding implies that marine heat waves will be even more common and intense as the multiyear ice cover of the Arctic continues to decrease. —HJS *Geophys. Res. Lett.* **47**, e2020GL089329 (2020).

Arctic sea ice loss causes stronger and more frequent marine heat waves there.

## NEUROSCIENCE

### Basal ganglia, beta oscillations, and insomnia

Insomnia affects up to 60% of Parkinson's disease patients. Beta oscillations are especially prominent in the basal ganglia in idiopathic Parkinson's disease. Mizrahi-Kliger *et al.* hypothesized that basal ganglia pathophysiology may not only play a mediating role in Parkinson's motor symptoms but may also contribute to Parkinson's insomnia. Using the vervet monkey Parkinson's model, which replicates the major biochemical, pathological, and clinical signs of the disease, the authors found that beta activity was consistently more prominent and widespread, including during non-rapid eye movement (non-REM) sleep. The Parkinsonian

state was accompanied by synchronized beta oscillations across the basal ganglia and cortex. Non-REM sleep beta oscillations associated with reduced cortical slow oscillations increased before spontaneous awakening and were correlated with the degree of insomnia. —PRS

*Proc. Natl. Acad. Sci. U.S.A.* **117**, 17359 (2020).

## QUANTUM SENSING

### Trap and isolate to extend quantum lifetime

The coherence time of a quantum system is an important parameter in the development of technologies that exploit the sensitive nature of quantum mechanics. Rubidium atoms have quantum mechanical spin,

each atom behaving like a tiny magnetic compass, which makes them exquisitely sensitive to local fluctuations in the magnetic field. Upadhyay *et al.* trapped single rubidium atoms in an ultracold parahydrogen matrix and then applied a sequence of pulses that further decoupled them from their immediate decoherence-inducing environment. With this trap-and-isolate protocol, the coherence lifetime of the rubidium atoms can be extended to a fraction of a second. The authors suggest that co-trapping a single molecule alongside a single rubidium atom could provide a platform for single-molecule nuclear magnetic resonance studies and the development of other quantum sensing technologies. —ISO

*Phys. Rev. Lett.* **125**, 043601 (2020).

## PHYSICS

### A transient superconductor

Systems of interacting particles occupying a lattice can often be described by the so-called Hubbard model. This model has been studied extensively with cold atoms in optical lattices, where its parameters can be easily tuned. In a complementary approach, Buzzi *et al.* investigated the organic molecular superconductor  $\kappa$ -(BEDT-TTF)<sub>2</sub>Cu[N(CN)<sub>2</sub>]Br, which can be described by the model, and used light to modulate the Hubbard parameters. The frequency of the light was tuned to a vibrational mode of the molecular building block of this material. The photoexcitation caused the sample to (briefly) become superconducting at temperatures much higher than the critical temperature. Calculations indicated that this was a consequence of an unusual long-range state of doubly occupied lattice sites. —JS

*Phys. Rev. Lett.* **X10**, 031028 (2020).

## MEDICINE

### Preventing protein truncation

A rare neurodegenerative disease called CLN3 Batten disease causes fatality by 20 to 30 years of age. The *CLN3* gene encodes a lysosome membrane protein subject to deletions in exons 7 and 8, which introduces a premature termination codon and truncates the resulting protein by 257 amino acids. Centa *et al.* developed an antisense oligonucleotide that restored most of the carboxyl-terminal part of the protein by inducing exon 5 skipping in messenger RNA processing. Injection of these oligonucleotides into the central nervous system of neonatal mice lacking *Cln3* exons 7 and 8 improved motor coordination and survival, indicating that even partial restoration of protein function can be therapeutically beneficial. —GKA

*Nat. Med.* **10.1038/s41591-020-0986-1** (2020).



ALSO IN *SCIENCE* JOURNALS

Edited by Michael Funk

## PHOTOSYNTHESIS

**Architectures for light harvesting**

Conversion of light energy into chemical energy ultimately drives most biochemistry on earth. Photosynthetic organisms use diverse chemical and biological structures to harvest light in different environmental contexts. Croce and van Amerongen synthesized recent structural and spectroscopic work on photosystem complexes from oxygenic photosynthetic organisms. To best capture light, photosystems contain accessory light-harvesting complexes harboring complex networks of pigments that shuttle electronic excitations toward the core complex, which contains the reaction center. The arrangement of pigments and their connectivity, as seen in high-resolution x-ray and cryo-electron microscopy structures, inform our understanding of energy transfer rates derived from spectroscopic measurements and vice versa. The model that emerges is one of many parallel and unconnected pathways for energy transfer into the reaction center from the exterior light-harvesting complexes. —MAF

*Science*, this issue p. 933

## ARTIFICIAL INTELLIGENCE

**Making robots useful**

The goal of creating generally intelligent robots that can carry out diverse tasks is a huge challenge. In particular, programming how robots learn and adapt to their surroundings quickly and nondestructively is proving especially difficult. In a Perspective, Pack Kaelbling discusses advances in machine learning based on ideas from cognitive neuroscience. In particular, the applications of reinforcement learning, where a valued outcome is reinforced, and how robots can be taught general lessons to apply to numerous situations are discussed. —GKA

*Science*, this issue p. 915

## BIOMEDICINE

**Remodeling senescent blood vessels**

The retina is a thin layer of nervous tissue at the back of the eye that transforms light into neuronal signals. The retina is essential for vision and is supported by networks of blood vessels. In diabetic retinopathy, a common cause of vision loss, these microvessels degenerate and regrow in an aberrant manner. Such degeneration and regrowth can compromise the functioning of retinal nerve cells. Binet *et al.* observed that, after rapid proliferation, vascular endothelial cells in diseased blood vessels engaged molecular pathways linked to cellular senescence (see the Perspective by Podrez and Byzova). Senescent vascular units summoned an inflammatory response in which neutrophils extruded neutrophil extracellular traps onto diseased vessels to remodel them. This endogenous repair mechanism promoted the elimination of senescent blood vessels and could lead to beneficial vascular remodeling. —SMH

*Science*, this issue p. 934;  
see also p. 919

## CANCER IMMUNOLOGY

**BTN3A1 governs antitumor responses**

T lymphocytes are immune cells that can be activated through their gamma delta ( $\gamma\delta$ ) or alpha beta ( $\alpha\beta$ ) receptors. Both T cell types are found in human cancers, but current immunotherapies do not harness their coordinated antitumor activity. Payne *et al.* found that BTN3A1 and BTN2A1, two members of the butyrophilin family of proteins, partner to activate the most abundant subset of  $\gamma\delta$  T cells in peripheral blood. Antibodies targeting BTN3A1 redirect  $\gamma\delta$  T cells to attack cancer cells while also increasing the activity of tumor-specific

$\alpha\beta$  T cells. Thus, the killing of established tumors by different T cell subsets can be achieved through BTN3A1 targeting and may provide new strategies for cancer immunotherapy. —PNK  
*Science*, this issue p. 942

## CORONAVIRUS

**Protective neutralizing antibodies**

Antibodies produced by survivors of coronavirus disease 2019 (COVID-19) may be leveraged to develop therapies. A first step is identifying neutralizing antibodies, which confer strong protection against severe acute respiratory syndrome coronavirus 2 (SARS-CoV-2). Rogers *et al.* used a high-throughput pipeline to isolate and characterize monoclonal antibodies from convalescent donors. Antibodies were selected for binding to the viral spike protein, which facilitates entry into host cells by binding to the angiotensin-converting enzyme 2 (ACE2) receptor. Most isolated antibodies bound to regions of the spike outside of the receptor binding domain (RBD); however, a larger proportion of the RBD-binding antibodies were neutralizing, with the most potent binding at a site that overlaps the ACE2 binding site. Two of the neutralizing antibodies were tested in Syrian hamsters and provided protection against SARS-CoV-2 infection. —VV

*Science*, this issue p. 956

## ORGANIC CHEMISTRY

**Targeting a distant C–H bond**

Enzymes often have intricate active sites that bind one portion of a molecule to orient a distant portion for optimal reactivity. This type of orienting effect has proven a much greater challenge for small-molecule catalysts. Reyes *et al.* now report a simple ligand that can simultaneously

bind to an iridium catalyst through a pyridine substituent while positioning an amide or ester reactant through a hydrogen-bonding urea. As a result, the catalyst exclusively borylates the site three carbons away from the carbonyl, with a second chiral ligand inducing high enantioselectivity. —JSY

*Science*, this issue p. 970

## SURFACE CHEMISTRY

**Modifying MXene surfaces**

Unlike graphene and transition-metal dichalcogenides, two-dimensional transition-metal carbides (MXenes) have many surface sites that can be chemically modified. Etching of the aluminum layer of a parent MAX phase  $\text{Ti}_3\text{AlC}_2$  layered material with hydrofluoric acid leads to the MXene  $\text{Ti}_3\text{C}_2$  with various surface terminations. Molten salts can achieve uniform chloride terminations, but these are difficult to further modify. Kamysbayev *et al.* show that etching of MAX phases in molten cadmium bromide leads to bromide-terminated MXenes that can then be substituted with oxygen, sulfur, selenium, tellurium, and NH groups as well as with vacancy sites. The surface groups can alter electronic transport. For example, the  $\text{Nb}_2\text{C}$  MXenes exhibit surface group-dependent superconductivity. —PDS

*Science*, this issue p. 979

## NEUROSCIENCE

**A present-day atlas of the human brain**

Defining brain regions and demarcating their spatial extent are important goals in neuroscience. A modern map of the brain's cellular structure, a cytoarchitectonic atlas, should provide maps of areas in three dimensions, integrate recent knowledge about brain



parcellation, consider variations between individual brains, rely on reproducible workflows, and provide web-based links to other resources and databases. Amunts *et al.* created such an atlas based on serial histological sections of brain. They developed a computational framework and refined the current boundaries of the human brain based on cytoarchitectural patterns. This technique can easily be transferred to build brain atlases for other species or a spatial framework for other organs, other modalities, or multimodal maps for regions of interest at higher spatial scales. This research makes similar future attempts simultaneously reproducible and flexible. —PRS

*Science*, this issue p. 988

## DRUG DEVELOPMENT Targeting STING for cancer therapy

Activation of the STING (stimulator of interferon genes) protein by cyclic dinucleotide metabolites plays a critical role in antitumor immunity. The development of synthetic STING agonists is therefore being pursued as a strategy for cancer therapy, but the inherent instability of dinucleotides has limited current efforts. Pan *et al.* and Chin *et al.* identified stable STING agonists that act in a “closed” conformation similar to the natural STING ligand, cyclic guanosine monophosphate–adenosine monophosphate (see the Perspective by Gajewski and Higgs). The small molecules can be given orally—an advantage over previously developed STING agonists, which required intratumoral administration. After oral or systemic administration in mice, the agonists activated STING and diverse immune cell types to promote antitumor immunity. These studies represent progress toward clinically viable STING agonists for cancer immunotherapy. —PNK

*Science*, this issue p. 935, p. 993; see also p. 921

## CORONAVIRUS An antibody cocktail against SARS-CoV-2

There is an urgent focus on antibodies that target the severe acute respiratory syndrome coronavirus 2 (SARS-CoV-2) viral spike and prevent the virus from entering host cells. Hansen *et al.* generated a large panel of antibodies against the spike protein from humanized mice and recovered patients. From this panel, they identified several neutralizing antibodies, including pairs that do not compete for binding to the receptor binding domain. Baum *et al.* focused in on four of these antibodies. All four are effective against known spike variants. However, by growing a pseudovirus that expresses the spike in the presence of individual antibodies, the authors were able to select for spike mutants resistant to that antibody. In contrast, escape mutants are not selected when pseudovirus is grown in the presence of pairs of antibodies that either do not compete or only partially compete for binding to the RBD. Such a pair might be used in a therapeutic antibody cocktail. —VV

*Science*, this issue p. 1010, p. 1014

## GLOBAL CLIMATE CHANGE All together then

Many geographically dispersed records from across the globe reveal the occurrence of abrupt climate changes, called interstadial events, during the last glacial period. These events appear to have happened at the same time, but the difficulty of determining absolute dates in many of the records have made that proposition difficult to prove. Corrick *et al.* present results from 63 precisely dated speleothems that confirm the synchrony of those interstadial events. Their results also provide a tool with which to validate model simulations of abrupt climate change and calibrate other time series such as ice-core chronologies. —HJS

*Science*, this issue p. 963

## DEVELOPMENTAL BIOLOGY In utero treatment for hypertension

Chronic hypoxia during fetal development increases cardiovascular risk in offspring. In experiments in sheep, Botting *et al.* found that inhibition of hypoxia-induced mitochondrial stress through in utero delivery of mitochondria-targeted ubiquinone (MitoQ) prevented growth restriction and cardiovascular dysfunction. Offspring of the treated sheep were protected from adult-onset hypertension. In chick embryos, MitoQ treatment precluded structural and functional heart defects due to hypoxia. Thus, in utero therapy to mitigate fetal hypoxia exposure may protect against adult-onset cardiovascular dysfunction. —JP

*Sci. Adv.* 10.1126/sciadv.abb1929 (2020).

## CYTOKINES Delivering IL-2 to T<sub>regs</sub>

Interleukin-2 (IL-2) not only promotes activation and expansion of conventional T cells but also plays a crucial role in regulating homeostasis and functions of regulatory T cells (T<sub>regs</sub>). Because expression of the high-affinity IL-2 receptor is largely restricted to T<sub>regs</sub>, engineering IL-2 variants called muteins that selectively bind to the high-affinity IL-2 receptor and potentiate T<sub>reg</sub> functions can be used in the treatment of autoimmune diseases. Khoryati *et al.* engineered a mouse IL-2 mutein that selectively promotes expansion of T<sub>regs</sub>. They demonstrate that administration of this IL-2 mutein resolved ongoing diabetes in nonobese diabetic mice. This proof-of-principle study raises the possibility that engineered human IL-2 muteins could be used in the treatment of autoimmune diseases. —AB

*Sci. Immunol.* 5, eaba5264 (2020).

## MICROROBOTS Robots fuel up

Batteries are a convenient source of energy for untethered

miniature robots. However, the low specific energy of small-scale batteries sets limits on how long such a robot can operate. Yang *et al.* report an insect-scale robot called RoBeetle that is powered by the controlled catalytic combustion of methanol, a fuel with more than 10 times the specific energy of a small-scale battery. RoBeetle, with size and mass comparable to a small insect, can carry payloads of up to 2.6 times its body weight, crawl on rough surfaces, and ascend inclines of 15 degrees. —MML

*Sci. Robot.* 5, eaba0015 (2020).



## REVIEW SUMMARY

## PHOTOSYNTHESIS

## Light harvesting in oxygenic photosynthesis: Structural biology meets spectroscopy

Roberta Croce\* and Herbert van Amerongen

**BACKGROUND:** The harvesting of photons is the first step in photosynthesis, the biological process that transforms solar energy into chemical energy. The photosynthetic membranes of algae and plants are packed with protein complexes binding many chlorophyll and carotenoid pigments, which are combined to form functional units. These units, called the photosystem I and II (PSI and PSII) supercomplexes, are composed of a reaction center (RC) where photochemistry occurs and an antenna comprising hundreds of pigments. Because even direct sunlight is a dilute form of

RCs of PSI and PSII *in vivo* occurs within 20 to 300 ps, and the maximal quantum efficiency is close to 1.0 for PSI and 0.9 for PSII. How is this high efficiency achieved?

**ADVANCES:** In recent years, structures of supercomplexes from various algae and plants have been determined at near-atomic resolution using cryo-electron microscopy. These structures revealed the pigment-binding architecture of many subunits and showed the static interactions between subunits in detail for the first time. The biggest surprise was

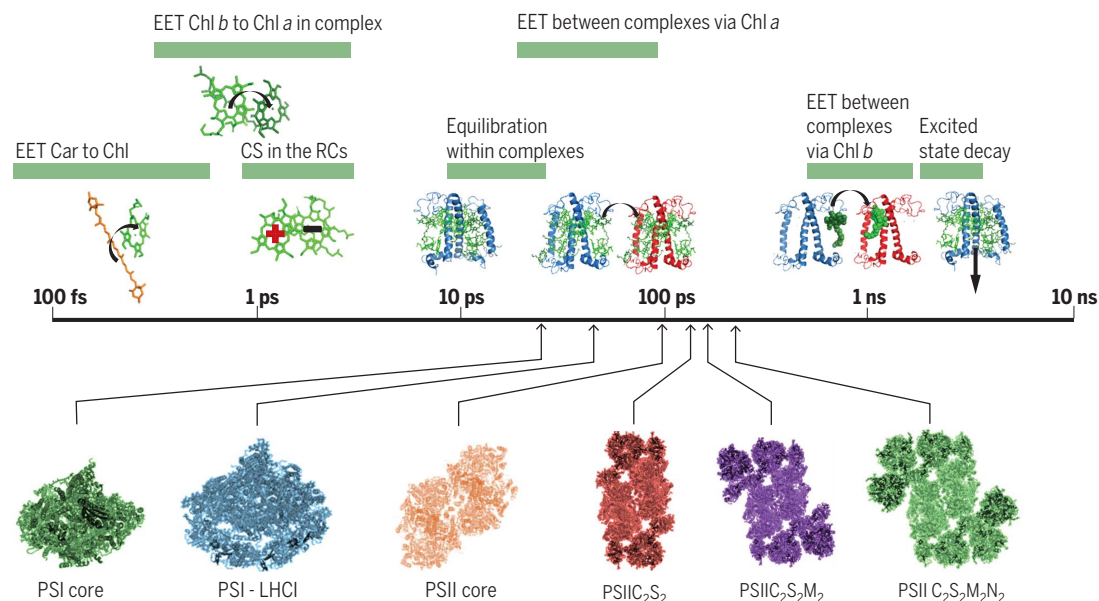
but more modular antenna system to quickly respond to the typical changes in light intensity experienced on land.

The processes of EET and CS in some of these supercomplexes and their subcomplexes have been studied with a variety of time-resolved spectroscopic techniques. The excited-state kinetics of these complexes can now be related to the structures to reveal the preferred EET pathways and possible bottlenecks of the process. This leads to, for example, the surprising conclusion that excitations created in the major light-harvesting complex of plants and green algae are not always transferred to the RCs through the minor antenna complexes, but rather, several parallel transfer pathways exist that may facilitate regulatory processes. It is also becoming clear that the antenna of PSI can become substantially larger than that of PSII while maintaining a high quantum efficiency.

**OUTLOOK:** The high-resolution structures of the supercomplexes of plants and algae represent an excellent starting point for studying

energy flow in detail using advanced modeling. Complexes such as plant PSI have been studied in detail by spectroscopy, but little is known about the functional behavior of most of the algal supercomplexes. Spectroscopic measurements on these complexes are now required to relate structure to functionality. All supercomplexes *in vivo* are embedded in the very crowded environment of the thylakoid membrane, where they can interact with each other, so the next step is to study the complexes in their natural environment. The combination of structural biology, advanced spectroscopy, and modeling will provide a molecular understanding of light harvesting and its regulation in physiologically relevant conditions. These insights will also provide a basis for

rational redesign of the photosynthetic apparatus, which could yield increases in crop productivity. ■



**Timeline of light-harvesting processes.** (Top) Many transfer steps between carotenoid and chlorophyll (Chl) *a* and *b* molecules occurring on different time scales eventually lead to CS and trapping in the RCs. Transfer between complexes occurs mainly through Chl *a* and not Chl *b*. (Bottom) Together, these individual steps determine the average trapping times in the PSI and PSII supercomplexes.

energy, the antenna is crucial to increasing the light-harvesting capacity of the RC. After light is absorbed by a pigment in one of these complexes, excitation energy transfer (EET) to a nearby pigment occurs. EET proceeds until the excitation reaches the RC, where charge separation (CS) takes place. The faster the energy reaches the RC, the higher the photon-to-electron conversion efficiency is because this process needs to beat the natural excited-state decay of the pigments. The trapping in the

probably the large variability between organisms in the design of the organization of the antenna around a highly conserved core. This is particularly striking for PSI, which can accommodate many antenna subunits associated to the core at positions that can change between organisms. These differences mainly reflect adaptation to specific light conditions. For example, whereas organisms living in water or in a low-light environment have developed a large antenna, plants seem to have a smaller

The list of author affiliations is available in the full article online.

\*Corresponding author. Email: r.croce@vu.nl

Cite this article as R. Croce, H. van Amerongen, *Science* 369, eaay2058 (2020). DOI: 10.1126/science.aay2058

**READ THE FULL ARTICLE AT**  
<https://doi.org/10.1126/science.aay2058>



## REVIEW

## PHOTOSYNTHESIS

# Light harvesting in oxygenic photosynthesis: Structural biology meets spectroscopy

Roberta Croce<sup>1\*</sup> and Herbert van Amerongen<sup>2</sup>

Oxygenic photosynthesis is the main process that drives life on earth. It starts with the harvesting of solar photons that, after transformation into electronic excitations, lead to charge separation in the reaction centers of photosystems I and II (PSI and PSII). These photosystems are large, modular pigment-protein complexes that work in series to fuel the formation of carbohydrates, concomitantly producing molecular oxygen. Recent advances in cryo-electron microscopy have enabled the determination of PSI and PSII structures in complex with light-harvesting components called “supercomplexes” from different organisms at near-atomic resolution. Here, we review the structural and spectroscopic aspects of PSI and PSII from plants and algae that directly relate to their light-harvesting properties, with special attention paid to the pathways and efficiency of excitation energy transfer and the regulatory aspects.

**P**rimarily production on our planet is performed by the process of photosynthesis (1). The mechanisms through which living organisms convert light energy into chemical energy are complicated and diverse. Although a number of subprocesses have been studied at considerable depth, there are still many knowledge gaps concerning the overall performance. Understanding oxygenic photosynthesis in particular is essential for improving photosynthetic efficiency to increase crop productivity (2, 3). Recent proofs of principle showed that subprocesses in both the light and dark phase of photosynthesis can be improved, leading to a substantial increase of biomass production (4–7). These advances can only be made by building on a vast amount of fundamental research performed in numerous laboratories around the world.

Photosynthesis research has addressed many detailed aspects of the performance of specific subunits, whereas the interaction between subunits remained underexposed. Progress is now being made on understanding higher-level organizations of components with the publication of the structures of a variety of photosynthetic multiprotein complexes (“supercomplexes”) at near-atomic resolution. With these structures, we can now see in detail how the subcomplexes are physically connected to each other, which will contribute to our understanding of how they functionally interact. Complexes from a variety of organisms are also becoming available, informing on the diversity of mechanisms. The central core of these complexes is common to all organisms, whereas other features show variations related to adaptation

to different environmental conditions. In this review, we discuss a number of recently determined structures of supercomplexes of photosystems I and II (PSI and PSII), the main players in the light phase of oxygenic photosynthesis. Together, they capture sunlight to extract electrons from water (PSII) and reduce NADP<sup>+</sup> to NADPH (PSI), whereas in parallel, they contribute to the creation of a proton gradient used for ATP formation. NADPH and ATP are then used in the dark reactions to synthesize carbohydrates from CO<sub>2</sub> in the Calvin-Benson-Bassham cycle. Here, we analyze how these structures relate to earlier spectroscopic and functional studies and arrive at some unexpected outcomes that should be further addressed in future research.

## The photosystems

The basic working principles of the PSI and PSII supercomplexes are the same: Light is harvested by their associated pigments (chlorophylls and carotenoids; Box 1 and Fig. 1) and the resulting excitation energy is transferred, mainly through closely spaced chlorophyll *a*

(Chl *a*) molecules, to the reaction center (RC) complex, where a stable charge separation (CS) is created (8).

A typical plant photosystem contains ~150 Chls per RC, meaning that it can absorb at most one photon every millisecond (1). After light absorption has occurred, the energy is stored in the excited state of the pigments for a very short amount of time [for chlorophylls in the thylakoid membrane, the excited-state lifetime ( $\tau$ ) is typically 2 ns (9)] as all molecules relax rapidly to the ground state through a number of deexcitation processes. To ensure a high photon-to-electron conversion efficiency (also called quantum efficiency), it is therefore necessary that the harvested energy is transferred to the RC fast enough to beat the other deexcitation processes. The time that it takes for an excitation to reach the RC and induce CS ( $\tau_{CS}$ ) varies considerably, from ~20 ps in the PSI core (10, 11) to ~300 ps in large PSII complexes (12, 13). For the PSI core, this leads to a maximum quantum efficiency of CS of  $\varphi_{CS} = 1 - \tau_{CS}(20 \text{ ps})/\tau(2 \text{ ns}) = 0.99$ , whereas it can be  $\varphi_{CS} = 1 - \tau_{CS}(300 \text{ ps})/\tau(2 \text{ ns}) = 0.85$  for PSII in vivo. However, in most conditions, and especially in high light when photoprotective mechanisms are turned on, the quantum efficiency can decrease substantially (4). It is important to realize that this quantum efficiency is not the same as the photosynthetic efficiency, which compares the energy of the final products (sugars) with the original energy contained in the absorbed photons and depends on many additional processes [see, e.g., (2) and (14)].

Both PSI and PSII can be divided into two parts: (i) a core complex, which contains both the RC and the inner antenna system, coordinating ~100 Chls *a* in PSI and ~35 Chls *a* in PSII, and is highly conserved in cyanobacteria, algae, and plants; and (ii) an outer antenna, the size and composition of which depend on the type of organism and growth conditions (15, 16). The antenna is needed to increase the absorption cross section of the RC because even in the highest possible natural light conditions, one Chl would absorb a photon only ~10 times

### Box 1. Pigments and EET between them (see Fig. 1).

Plants and green algae make exclusive use of Chls *a* and *b*, whereas some algae contain Chl *c* (23) and some cyanobacteria can synthesize Chl *d* and Chl *f* (102, 103). Directly after excitation of a Chl, relaxation (internal conversion) takes place within at most several hundred femtoseconds to the first excited state, from where EET to neighboring Chls takes place. The rate of transfer (*k*) can be approximated by making use of Förster theory (104) [for the equation, see Fig. 1; numbers were taken from (105)]. Even for the short distances present in LHCs, this theory provides reasonable values for amplitudes and rates of transfer (45, 105). After rapid thermal equilibration of an excitation within a Chl *a*–Chl *b* pair as indicated in Fig. 1, the probability of finding the excitation on Chl *a* and *b* at room temperature is 0.90 and 0.10, respectively, using either the principle of detailed balance or applying the Boltzmann equilibrium equation. In addition, carotenoids are present in photosynthetic organisms and are involved in both light harvesting and photoprotection. Carotenoids absorb green and blue light and rapidly (<1 ps) transfer their energy to neighboring Chls (106).

<sup>1</sup>Department of Physics and Astronomy, Faculty of Science, Vrije Universiteit Amsterdam, Amsterdam, Netherlands.

<sup>2</sup>Laboratory of Biophysics, Wageningen University & Research, Wageningen, Netherlands.

\*Corresponding author. Email: r.croce@vu.nl



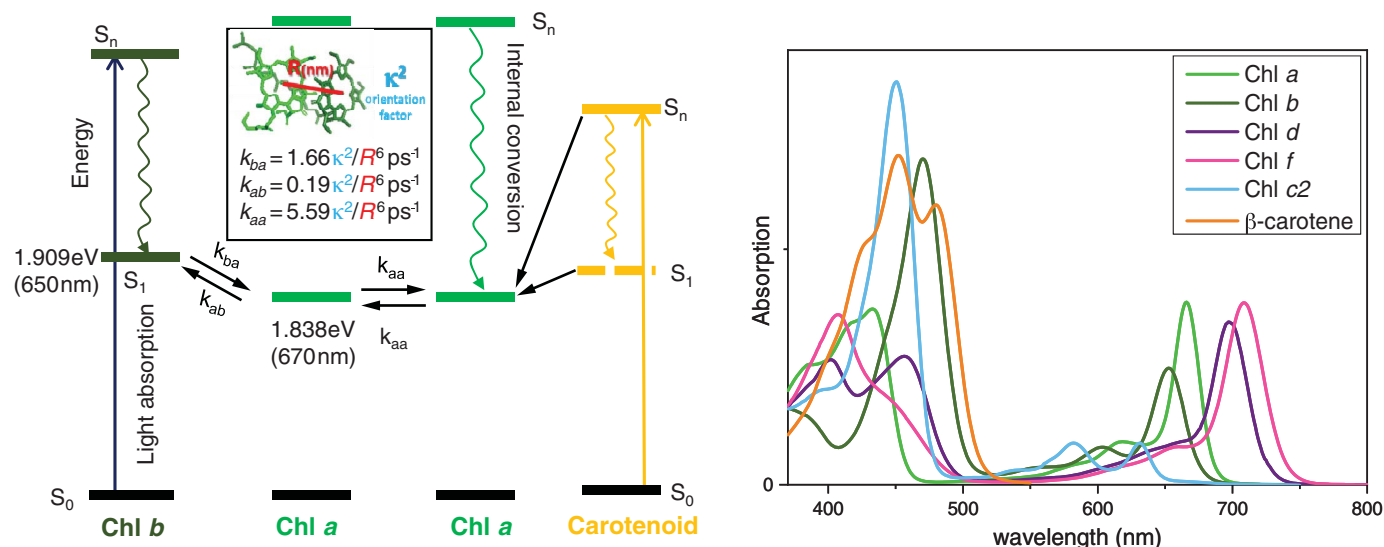


Fig. 1. Properties of photosynthetic pigments. Left, energy diagram. Right, absorption spectra. See Box 1 for details.

per second (1). In cyanobacteria, the outer antenna is composed of phycobilisomes: huge, water-soluble multiprotein complexes anchored to the membrane (17–20) that are also present in red algae. In plants and most algae, the outer antennas are located in the thylakoid membrane and are members of the light-harvesting complex (LHC) multigenic family. Together with the core, they form the PSI and PSII supercomplexes, which will be addressed in this review. The plant LHCs all have an almost identical pigment-protein organization (21), but they can have very different spectroscopic properties (Fig. 2). Each monomer is composed of an apoprotein of ~25 kDa with three transmembrane helices and a number of pigments accounting for another ~15 kDa (11 to 15 Chls and three to four carotenoid molecules) (Fig. 2). Although the core complexes, in addition to carotenoids, only bind Chl *a*, the LHCs of plants and green algae also bind Chl *b*, the lowest energy transition of which is at higher energy than that of Chl *a* (Fig. 1). This makes Chl *b* an excellent excitation energy donor for Chl *a*, but a not so good energy acceptor (Figs. 1 and 3). The Chl *a/b* ratio varies between antenna complexes from 1 to 6 but for most of them it is ~2 (22). The LHCs of diatoms, called fucoxanthin-binding proteins (FCPs) (Fig. 2), do not bind Chl *b*, but rather Chl *c*, and they contain fewer Chls (nine or 10 in total) and more carotenoids (six or seven fucoxanthins) (23). Fucoxanthin and Chl *c* relatively increase the absorption cross section for blue-green light, which is dominant in a water environment. Chl *c* is peculiar because it lacks the phytol chain that is present in all other chlorophylls, and this absence allows the binding of more carotenoids in FCPs (Fig. 2, inset) (24).

The structures of the supercomplexes of PSI (25–27) and PSII (28–30), as well as the number of associated LHCs, differ substantially. In plant PSI (Fig. 4), four LHCs (Lhca1 to Lhca4) are associated with a monomeric core forming the PSI-LHCI supercomplex. The PSII C<sub>2</sub>S<sub>2</sub>M<sub>2</sub> supercomplex (Fig. 5) instead contains a dimeric core (C<sub>2</sub>), and each core is associated with three monomeric LHCs (CP29, CP26, and CP24, also called minor antennas) and two LHCII trimers called S (strongly bound) and M (moderately bound). The M-trimer and CP24 are absent in the smaller version of the plant supercomplex (C<sub>2</sub>S<sub>2</sub>, Fig. 5), which is the dominant form in high-light conditions (31). Slightly different C<sub>2</sub>S<sub>2</sub>M<sub>2</sub> supercomplexes lacking CP24 have been observed in conifers (32), pointing to variation in structure inside the plant kingdom. Very recently, cryo-electron microscopy (cryo-EM) has also provided high-resolution structures of complexes from various algae. Although the basic unit is similar in all species studied, the organization and the dimension of the outer antenna differ depending on the environmental niche where the organisms live (33). For example, PSI and PSII of the model green alga *Chlamydomonas reinhardtii* (Figs. 4 and 5) are far larger than those of plants, containing 10 or 11 antennas per core or even more (34–38). PSII of diatoms (*Chaetoceros gracilis*; Fig. 5), on the other hand, has a similar overall organization as the plant complex but contains more subunits (up to 35) and the outer antennas (FCPs) form tetramers instead of trimers (39, 40).

The supercomplex structures have recently been used as a starting point for molecular dynamics simulations to unveil channels for the oxidized or reduced quinones entering or leaving the RCs, respectively (41), or for protons

that leave PSII after water splitting has occurred (42). Conversely, pathways for excitation energy transfer (EET) to the RC are less specific in the sense that many pigments can transfer their excitation energy to different neighbors, thereby creating a multitude of transfer pathways to the RC. Detailed modeling of EET in the photosystems might be performed using advanced quantum-mechanical methods that were applied to early models of the PSII supercomplexes (43, 44) but not yet to the new structures. Therefore, we will use a simplified and more intuitive approach to discuss EET in the supercomplexes.

#### Chl *b* molecules limit free diffusion of excitation energy

A crucial parameter for the rate of EET between two pigments is their mutual distance. In the LHCs, most nearest neighbors within one complex are ~10 Å from each other and show strong electrostatic (excitonic) interactions, which lead to extremely fast EET. EET in individual complexes has been studied extensively, showing that within a few hundred femtoseconds after Chl *b* excitation, most of the excitations are already localized on Chl *a* molecules (33, 45–47), which are lower in energy (Box 1 and Fig. 1). EET within individual complexes has been modeled with quantum-mechanical methods, and the light-harvesting properties of these complexes are now relatively well understood, particularly those of LHCII (16, 45, 48). On the other hand, EET from a Chl *b* molecule on one complex to a Chl molecule on a neighboring complex, which are in general more than 15 Å apart, is far slower, typically ~10 to 20 ps (Fig. 3). The effective time of transfer from one complex to the other through such a Chl *b*–Chl *a* donor–acceptor

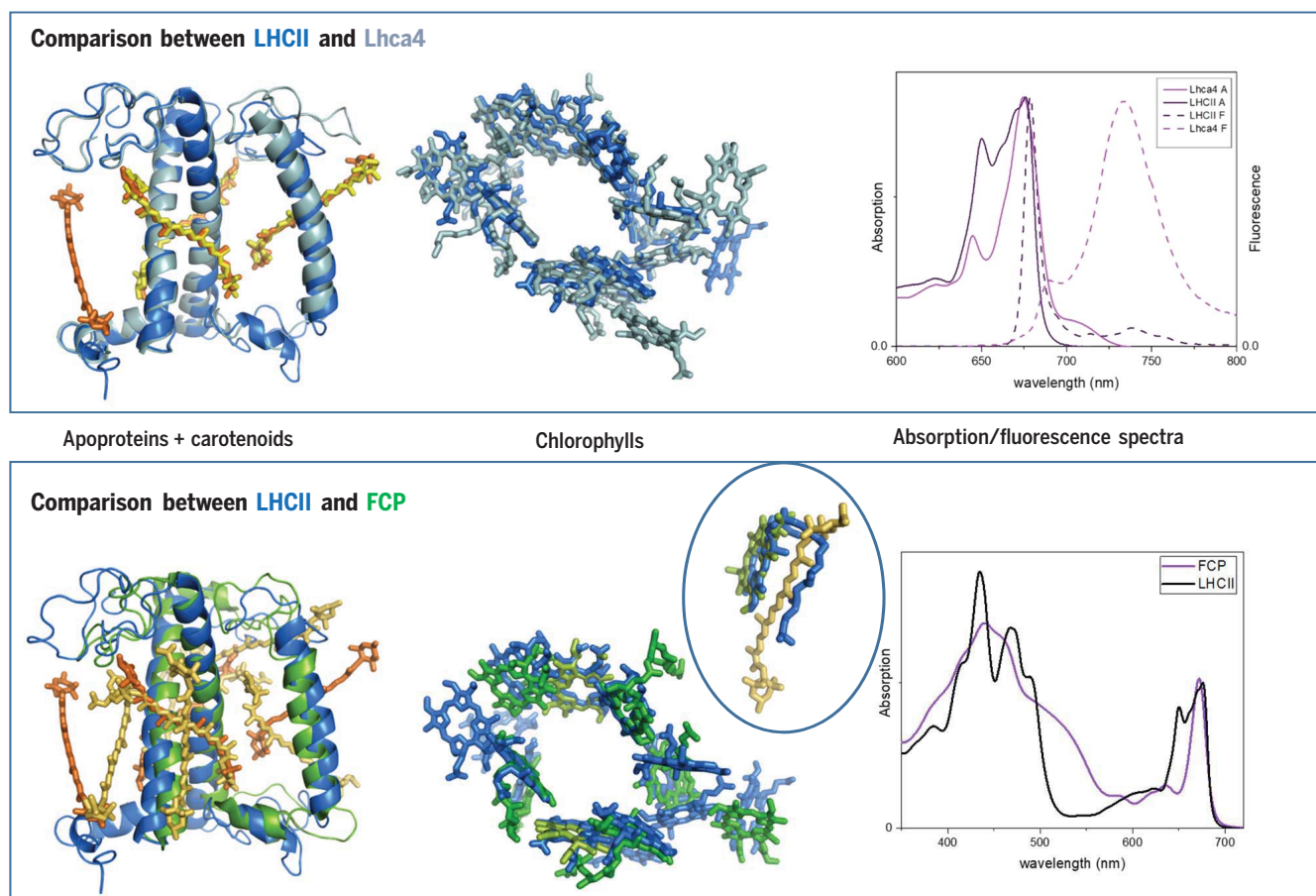


**Fig. 2. Comparison of the structures and the absorption and fluorescence spectra of LHCII, Lhca4 (a PSI subunit), and FCP.** [For original data, please see (107), (25), and (24), respectively.] (Left) Comparison of apoprotein structure and carotenoid organization (LHCII in orange, Lhca4 in yellow, FCP in dark yellow). (Center) Chlorophyll organization; the inset shows the overlay of a Chl *a* of LHCII including its phytol chain and a Chl *c* and fucoxanthin occupying the same position in FCP. (Right) 77K absorption (solid) and fluorescence (dashed) spectra.

### Box 2. Estimating rates of EET between different pigment-protein complexes.

The rate of EET from LHC A to B ( $k_{AB}$ ) can be estimated as follows. When this transfer is dominated by transfer between two pigments  $i$  (in A) and  $j$  (in B) (hopping rate  $k_{ij}$ ), then the overall transfer rate can be approximated by  $k_{AB} = p_i k_{ij}$ , where  $p_i$  is the probability that the excitation resides on donor pigment  $i$  when complex A is excited. Using the numbers provided in Fig. 1, it can be calculated that the average probability  $p_b$  in monomeric LHCII is  $\sim 0.013$  and that one of the six Chl *b* molecules is in the excited state, whereas  $p_a \sim 0.115$  for one of the eight Chl *a* molecules. The total rate of transfer from complex A to B should in general be summed over all pigment pairs  $i$  and  $j$  of both complexes, but only one or a few pigment pairs dominate in most cases. The effective transfer time from complex A to B is thus  $\tau_{hop}/p_i$  ( $\tau_{hop} = k_{ij}^{-1}$ ), and this time has to be augmented with the migration time  $\tau_{mig}$ , which is the average time that it takes for an excitation within the complex to reach the pigment that is transferring to the neighboring complex:  $\tau_{eff} = \tau_{hop}/p_i + \tau_{mig}$  (76). The value of  $\tau_{mig}$  for an LHCII trimer is  $\sim 25$  ps (105), and for the monomeric complexes, we use an approximate value of 10 ps.

pair is even a factor of  $\sim 80$  slower. The reason for this is that an excitation in, e.g., an LHCII monomer spends only 1.3% of its time on one of its Chl *b* molecules (see Box 2), leading to an effective “hopping” time of 1 to 2 ns. Because this is far longer than the average hopping

time between complexes, which was estimated to be  $\sim 25$  ps based on time-resolved fluorescence studies (49), it can safely be concluded that EET between complexes does not proceed through Chls *b*, and transfer pathways that involve interacting Chl *a* molecules are the

most prominent. Only after direct excitation might one or two Chls *b* preferably transfer their excitation energy to a neighboring complex, but even these Chls do not function as efficient bridges for EET between complexes. A timeline of the different EET processes occurring within the complexes and between them is shown in Fig. 3.

### Light harvesting of PSI supercomplexes

PSI is considered to be the most efficient photon-to-electron converter in nature (50). In the PSI core (Fig. 4) of organisms as different as cyanobacteria and plants, it takes only  $\sim 20$  ps after the absorption of a photon by one of the  $\sim 100$  core Chls to extract an electron from the RC. Therefore, the quantum efficiency of CS is close to 1. In cyanobacteria, the core is usually present as a trimer and sometimes as a tetramer (51). In plants, it is instead monomeric, and four antenna complexes are associated with it as Lhca1-4 and Lhca2-3 dimers (PSI-LHCI; Fig. 4), increasing the absorption cross section of the PSI core by  $\sim 60\%$ . The



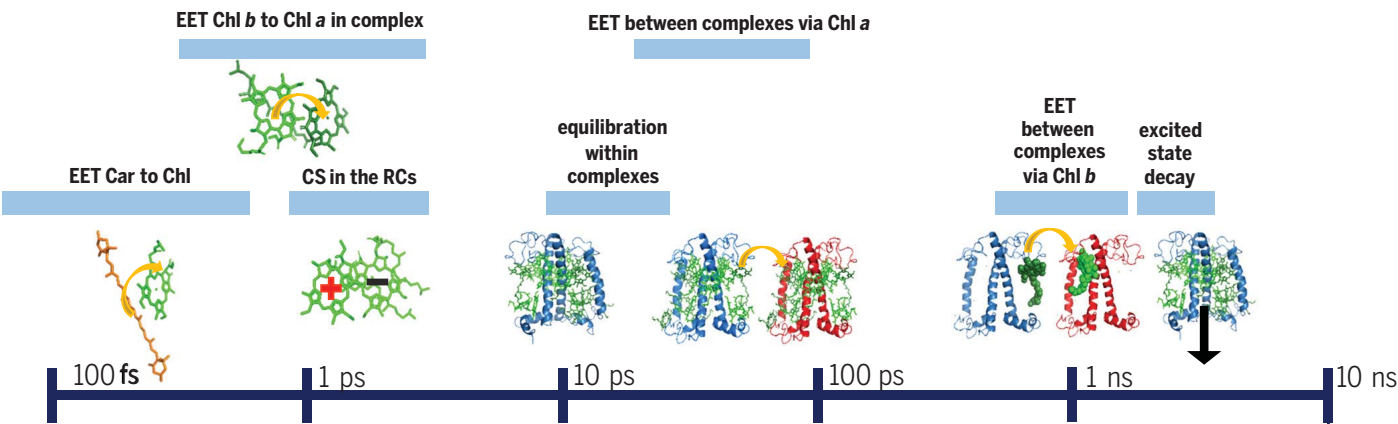


Fig. 3. Timeline of different processes related to light harvesting.

<b>PSI core</b> <i>Thermosynechococcus elongatus</i>	<b>PSI-LHCI</b> <i>Zea mays</i>	<b>PSI-LHCI-LHCII</b> <i>Zea mays</i>
Chls = 96 $\tau$ : 20 ps	Chls = 158 $\tau$ : 50 ps	Chls = 200 $\tau$ : 70 ps
<b>PSI-LHCI</b> <i>Chlamydomonas reinhardtii</i>	<b>PSI-LHCR</b> <i>Cyanidioschyzon merolae</i>	<b>PSI-LHC</b> <i>Physcomitrella patens</i>
Chls = 237-244 $\tau$ : 50 ps	Chls = 158 $\tau$ : 25-55 ps	Chls = 257* $\tau$ : n.d.

Fig. 4. Structures of PSI from various organisms. [For original data, please see (27), (38), (62), (64), and (108)]. For most complexes, the number of Chls and the average time of trapping of excitations in the reaction center are provided (11, 57, 65, 109). In each structure, the new elements compared with the structure before are highlighted in brighter colors and/or their names are given. The subunits that are common to several complexes are shown in the same color; e.g., the individual subunits of the PSI core are shown in different blue colors in the PSI core of cyanobacteria, whereas in the other structures, the core is shown in light blue. Chl a is shown in green, Chl b in blue, and carotenoids in orange. \*The number of Chls is estimated based on the number of LHCs (68).

structures of the Lhcas are highly conserved but their spectroscopic properties differ substantially (52), especially because both Lhca3 and Lhca4 contain Chls that absorb >700 nm (Fig. 2); these are called red Chls. Their excited-state energies are lower than those of most of the Chls of PSI (absorbing in the 670 to 680 nm range; these are called bulk Chls) and thus strongly influence EET by introducing energetically uphill transfer steps (10). The intrasubunit equilibration time in all Lhcas is very fast (<10 ps), whereas the intersubunit time of EET within the Lhca dimers is somewhat slower (53). When they are part of the PSI supercomplex, these Lhcs mainly transfer directly to the core. The transfer is very fast for Lhca1 and Lhca2, whereas from Lhca3 and Lhca4, it appears to be slower, mainly because of their red Chls. Despite several slow EET transfer steps, the overall trapping time in the PSI-LHCI supercomplex is only ~50 ps, with quantum efficiency still close to 1 (54–56). Considering the experimental results mentioned above, the organization of the Chls in the x-ray structures of PSI not showing connections between Lhca2 and the core was puzzling (25, 26). This apparent inconsistency was solved by the most recent cryo-EM structure, which revealed the position of one additional subunit (PsaN, in pink in Fig. 4), which is located between Lhca2 and the core and binds two Chls (27). By applying the calculation method provided in Box 2, we obtain effective times of transfer within the dimers and from individual complexes to the core that are all close to what was determined experimentally (54, 55), demonstrating that the simplified way of estimating transfer times can help us to better understand the origin of the experimental findings. An overview of the various transfer times and pathways in PSI is given in Fig. 6.

For a long time, the structure described above was considered to represent the definitive PSI complex of plants. However, the picture that is now emerging is that in most conditions, at least one LHCII trimer is also present, forming PSI-LHCI-LHCII complexes (57–59) (Fig. 4). This addition results in an increase of the absorption cross section by 25% without substantially influencing the charge separation efficiency. It is important to note here that LHCII does not contain any red Chls (45) (Fig. 3). LHCII is energetically very well connected to PSI, transferring its energy directly to the core while increasing the overall trapping time of the complex by only ~10 to 20 ps (57, 60). In a more recent study, the transfer from LHCII to PSI appeared to be heterogeneous, suggesting the presence of two particles with slightly different LHCII-core connections (61). The structure of the PSI-LHCI-LHCII complex of maize (27) shows that LHCII is directly connected to the core through two

Chls on a newly identified subunit (PsaO, in brown in Fig. 4), and the calculated transfer time is ~75 ps, which is relatively close to the slowest time obtained by spectroscopy (61).

New structural data from organisms that can experience low-light conditions show that the antenna size of PSI can be further increased by the association of additional Lhcas (37, 38, 62–64). In the green algae *C. reinhardtii* (37, 38) and *Bryopsis corticulans* (63), four more Lhcas form a second belt associated with the PSI-LHCI basic structure as present in plants, whereas two more Lhcas are directly connected to the core, which is also the case in PSI from the red alga *Cyanidioschyzon merolae* (Fig. 4). The absorption cross section is increased by >50% compared with that of plant PSI, but the trapping time of the two complexes is very similar (65). This may not seem intuitive because the trapping time usually increases with antenna size [see, e.g., (66)], but the reason is that the Lhcas in *C. reinhardtii* do not contain the same red Chls that are present in plants. Therefore, the energetic uphill step is far less steep, leading to faster EET, which compensates for the larger antenna size (65). Unfortunately, the EET rates cannot be calculated from the available *C. reinhardtii* structures because the resolution does not allow discrimination between Chls *a* and *b*, information that is crucial to permit the identification of the transfer pathways, and only ~50% of the expected Chls *b* (67) were assigned (38). Recently, the structure of an even larger complex from the moss *Physcomitrella patens*, containing 12 LHCs, was determined. Although the current resolution does not allow identification of the pigments, this structure shows new docking sites for the antennas (64, 68), suggesting that the antenna size of PSI can be even larger than that observed in the complexes purified up to now.

### Light harvesting of PSII supercomplexes

The core complex of PSII (69) (Fig. 5) is highly conserved in all organisms performing oxygenic photosynthesis [for a recent review, see (70)]. Its average excited-state lifetime is typically ~60 to 100 ps (66, 71–73), and the observed variation may be due to different stability of the isolated complexes (74). This lifetime is dominated by the relatively slow transfer from the internal antennas CP43 and CP47 to the RC, whereas the process of CS itself is much faster (70). Although the core complex is mainly present as a dimer, calculations based on the available structures indicate that EET between both adjacent monomers is relatively slow.

Compared with PSI, the association of the outer antenna to PSII is weaker, easily leading to disassembly during purification. As a result, the first homogeneous preparation of the PSII supercomplex was not reported until 2009 (75), and the number of spectroscopic studies has been limited. In a study comparing different

supercomplexes of plants, an increase in average lifetimes was reported going from the core to  $C_2S_2$  and  $C_2S_2M_2$  (66), consistent with the expectation that a larger antenna size corresponds to a longer excited-state lifetime (trapping time) (76).

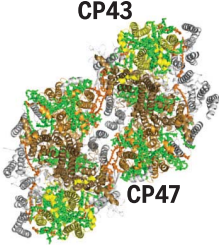
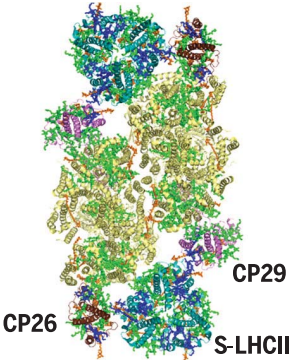
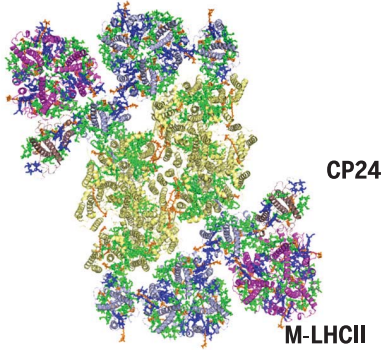
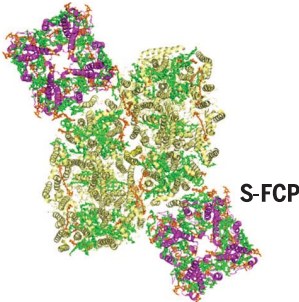
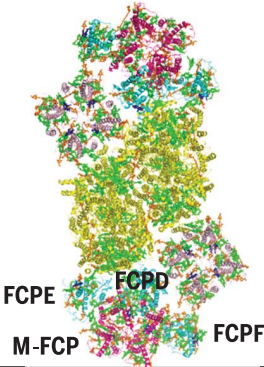
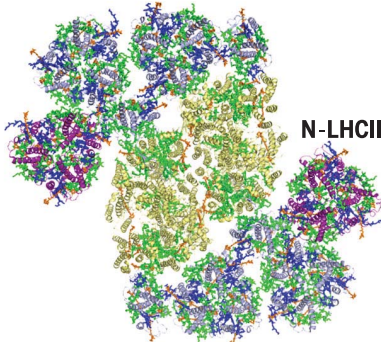
Applying the calculation method presented in Box 2 to the PSII  $C_2S_2$  structure (29) (Fig. 5) shows that the minor complexes CP26 and CP29 are well connected to the core. However, in contrast to what has been reported previously (28, 29), they do not function as bridges between S-LHCII and the core: All LHCII pigments that are close enough for efficient transfer to CP26/CP29 were reported to be Chl *b* molecules (28, 29) and therefore S-LHCII transfers directly to the core.

In the  $C_2S_2M_2$  complex (28, 30) (Fig. 5), the M-LHCII trimer is physically connected to CP24, CP29, and S-LHCII, but it transfers excitations mainly (80%) to CP29 and the connection is excellent. According to the structures, the close connections between the Chls of CP24 and those of CP29 all involve Chl *b* molecules, so EET to the core should proceed through M-LHCII. It cannot be ruled out that the assignment of the Chl *b* and Chl *a* pigments in the structure of CP24 is not entirely correct. It was experimentally determined that in CP24 after exciting Chl *b*, >~85% of the excitation energy arrives on Chl *a* with a time constant of 600 fs (77); however, based on the published structure, this percentage is calculated to be <50%, whereas most EET is substantially slower than 1 ps.

In 2019, several groups published the structure of the PSII supercomplex  $C_2S_2M_2N_2$  of the green alga *C. reinhardtii* (34–36) (Fig. 5). This complex is not only larger, containing an additional N-LHCII trimer (also called an L-trimer) compared with plants, but it also lacks CP24 and shows a different orientation of the M-trimer. This different orientation leads to different excitation energy transfer pathways in plants and algae, as will be discussed below. Its  $C_2S_2$  part is very similar to that of plants and the calculated effective rates of EET from S-LHCII, CP29, and CP26 to the core are nearly identical. Although it was originally believed that excitations from M-LHCII and N-LHCII flow to the core through CP29 (35), closer inspection of the structures shows that all close contacts between CP29 and the S-, M-, and N-trimers involve Chl *b*. Conversely, the N-LHCII trimer has many good connections with M-LHCII, and M-LHCII is also better connected to one of the S-LHCII than to CP29; therefore, S-LHCII functions as the bridge between the N- and M-trimers and the core.

Fig. 6 provides an overview of the EET pathways in the various supercomplexes. It was unexpected that there are mainly parallel pathways to the core. It had always been accepted that the minor complexes functionally



<b>PSII core,C<sub>2</sub></b> <i>Thermosynechococcus vulcanus</i>	<b>C<sub>2</sub>S<sub>2</sub></b> <i>Spinacia oleracea</i>	<b>C<sub>2</sub>S<sub>2</sub>M<sub>2</sub></b> <i>Pisum sativum</i>
		
Chls* = 35*2 τ: 60-100 ps	Chls = 105 τ: 140 ps	Chls = 158 τ: 160 ps
<b>C<sub>2</sub>S<sub>2</sub></b> <i>Chaetoceros gracilis</i>	<b>C<sub>2</sub>S<sub>2</sub>M<sub>2</sub></b> <i>Chaetoceros gracilis</i>	<b>C<sub>2</sub>S<sub>2</sub>M<sub>2</sub>N<sub>2</sub></b> <i>Chlamydomonas reinhardtii</i>
		
Chls = 79 τ: ?	Chls = 144-145 τ: n.d.	Chls = 185-189 τ: 200 ps

**Fig. 5. Structures of PSII from various organisms.** [For original data, please see (28), (29), (35), (39), (40), and (110).] For most complexes, the number of Chls and the average time of trapping of excitations in the reaction center are provided (66, 73, 111). Chl *a* is shown green, Chls *b* in blue, and carotenoids in orange.

connect LHCII to the core, whereas the structural studies now imply that this is only the case for CP29 in C<sub>2</sub>S<sub>2</sub>M<sub>2</sub> of plants, which acts as the main “bridge” between M-LHCII and the core. Analyses of plant mutants lacking individual antenna complexes show that, although the absence of CP26 has a negligible effect on the transfer of energy in PSII, the impact of the absence of CP29, and especially of CP24, is very large, leading to functional disconnection of the antenna from the core (12, 78). Taken together, the structural and functional results suggest that some of the minor antennas perform a structural role in maintaining the organization of the supercomplex. However, they play a limited role in light harvesting in the sense that they contain relatively few pigments and do not connect LHCII to the core, with the exception of CP29 in plants and, to a far lesser extent, in *C. reinhardtii*. The view that the minor complexes have a structural role rather than an important direct role in light har-

vesting is compatible with the situation in *C. reinhardtii*, in which CP24 is absent and CP29 therefore appears to be less strongly anchored in the supercomplex. Indeed, in this green alga, CP29 can migrate to PSI together with LHCII to rebalance the excitations over the two photosystems in the light conditions that are favorable for PSII, a process known as state transitions (79). It is important to note that the organization of EET along parallel (only weakly interconnected) pathways is not favorable for the robustness and speed of transfer toward the RC, for which interconnected pathways are in principle better. The presence of alternative transfer pathways enhances the robustness and, because two-dimensional excitation diffusion is faster than one-dimensional diffusion (76), interacting EET pathways would lead to faster excitation trapping in the RC and thus increased quantum efficiency. Because of the presence of only weakly interconnected path-

ways, it seems more likely that evolution has favored the current design for regulatory reasons, which will still have to be unveiled. In principle, it might also be possible that in the stacked thylakoid membranes of, for example, plant chloroplasts, EET between different membrane layers would occur, thereby invalidating the above reasoning, but a comparison between time-resolved fluorescence measurements on stacked and unstacked grana has shown that almost no intermembrane transfer takes place (80).

**PSI versus PSII**

When we compare the plant supercomplexes of PSI and PSII, it appears that the different trapping kinetics in the two photosystems can to a large extent be traced back to differences in their core complexes. As stated above, for the PSI core, the trapping time is ~20 ps, whereas for the PSII core, average trapping times up to 100 ps and above have been

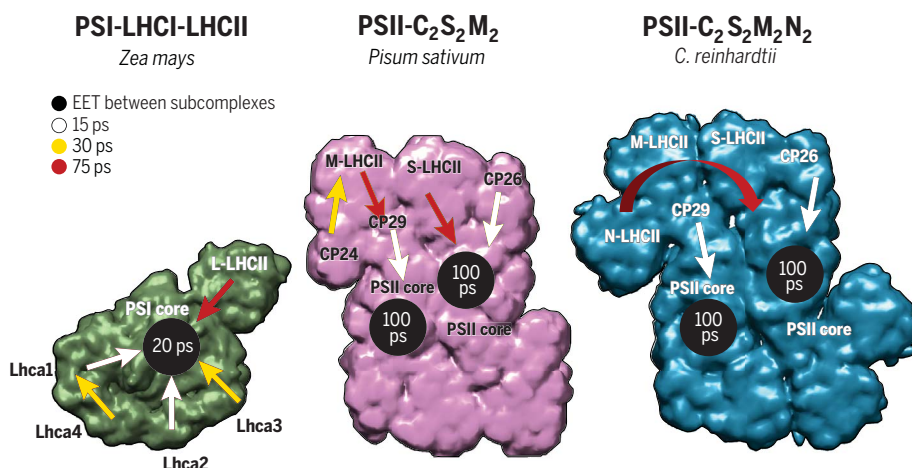


**Fig. 6. Major EET pathways in different supercomplexes.** The colors of the arrows represent approximate effective transfer times from one complex to another, as indicated in the inset. The semicircular red arrow indicates the main pathway for EET from N-LHCII through M-LHCII and S-LHCII to the core in the upper half of the supercomplex and replaces three orange arrows between the individual trimers and from S-LHCII to the core. The most interesting features of these structures is that there are many “parallel” EET pathways from the outer antenna to the core that are relatively weakly connected to each other, and that in most cases, the minor complexes do not play a major role in connecting LHCII to the core.

reported, but the number of pigments is almost a factor of three lower. The reason for this difference seems to be the number of pigments connecting the antenna and the RC, which is lower for PSII. They are also at larger distances with respect to each other, presumably to avoid oxidation of the antenna pigments by the primary donor with its high oxidation potential (81). An immediate consequence of the high efficiency of the PSI core is that it can accommodate substantially more LHCs around it. In the PSI-LHCI supercomplex of *C. reinhardtii*, with its ~240 Chls, the reported trapping time is 50 ps and the quantum efficiency is still higher than that of the PSII core, with its 35 pigments.

The recently observed structures also suggest that there is a far larger variability in size, composition, and organization in PSI than in PSII. In PSI, the antennas can be associated to the core in many different positions and in several layers completely surrounding it.

### Photosystems in the membrane

All of the structures discussed above were obtained for detergent-isolated complexes. Are these complexes representative of the *in vivo* situation, where they may be larger or in a different functional state? It is known that the number of LHCII trimers in the membrane changes with the growth conditions of the plant or alga, increasing in low light and decreasing in high light, and can be far larger than in the purified supercomplexes (82–84). Although in plants, the  $C_2S_2M_2$  complex is the prominent form in low light and  $C_2S_2$  is relatively more abundant in high light, the largest adjustments concern a pool of LHCII

(called L), which are loosely bound to the supercomplexes and are lost during purification (84). At present, only a low-resolution projection map of spinach PSII complexes containing one L-trimer is available (85). Functionally, the L-trimers are well connected to the PSII core, providing excitation energy efficiently, albeit more slowly, than the S- and M-trimers (84). A similar picture is now emerging for PSI, suggesting that in plants, more than one LHCII trimer can be associated with each PSI (59, 86–88).

Experimental data clearly show that the antenna of PSI and PSII can be enlarged with extra L-LHCII. But by how much? Is there a maximal antenna size for the photosystems? When the size of the antenna becomes larger, more photons are absorbed and the light-harvesting capacity goes up, but the trapping time also increases, thereby lowering the quantum yield. These counteracting effects lead to an optimal (maximal) antenna size in low light of 200 to 250 Chl *a* molecules per PSII RC in *A. thaliana* (84). This number is far higher for PSI, as already discussed above, which seems to be largely due to the extremely short trapping time in the PSI core. It can thus be expected that PSI complexes with far larger antenna size can be found in organisms living in shaded environments. Is there also a minimal antenna size? In *A. thaliana*, even in very high light, there are still almost two LHCII trimers present per PSII (84), although this is not needed to have sufficient light-harvesting capacity. However, mutants without outer antennas are more sensitive to photodamage (89), suggesting that a minimal antenna is needed for photoprotec-

tion. At first sight, this may seem counterintuitive, but it should be realized that the functional antenna size can also be regulated by changing the excited-state lifetime (33). This is particularly important for sudden changes in light intensity for which protein synthesis and degradation is not an option. As a short-term response, the antenna switches between a light-harvesting state, characterized by a long excited-state lifetime, and a quenched state, in which the excited-state lifetime is strongly reduced and the functional antenna size is decreased (90). In plants, this mechanism, called non-photochemical quenching, requires the presence of the protein PsbS (91), the location and action mechanism of which are still enigmatic. It has been proposed that PsbS binds in the cleft between CP24 and the core in the  $C_2S_2M_2$  supercomplex (28), but this proposal still needs validation. In green algae, the main protein responsible for nonphotochemical quenching is instead LHCSR3 (92), which in *C. reinhardtii* was suggested to be located at the periphery of the  $C_2S_2$  complex in direct contact with the outer antenna (93).

### Outlook

The high-resolution structures of the supercomplexes revealed recently represent an excellent starting point for studying energy flow in detail through advanced modeling. This will contribute to the basic understanding of light harvesting in oxygenic photosynthesis, but will also furnish the basis for a rational redesign of the photosynthetic apparatus that should lead to an increase in crop productivity [e.g., regulated reduction of the antenna size and extension of the photosynthetic-active-radiation regime (3)]. However, it is important to realize that the correct assignment of the Chl identities species is crucial to identifying EET pathways from the structures. Moreover, whereas complexes such as plant PSI have been studied in detail using spectroscopy, little is known about the functional behavior of most of the algal supercomplexes. Therefore, spectroscopic measurements on these complexes are now required to relate structure to functionality.

It is expected that cryo-EM will continue to provide new structures, e.g., of the much wanted PSII-PsbS complex, and will also permit exploration of the flexibility of photosynthesis by studying complexes of different organisms, especially the ones living in extreme environments. The structures of PSI from cyanobacteria adapted to far-red light (94, 95) or to iron deficiency (96) are good examples of this.

The most important next step, however, is a molecular understanding of light harvesting and regulation in physiologically relevant conditions. This requires studying the complexes in their natural environment: the thylakoids. How are the complexes assembled in the membrane? How are they organized? How do



the functional changes observed in different conditions relate to changes in their organization? Recent developments in cryo-electron tomography hold the promise to provide detailed maps of the complexes in the membrane (97, 98). These results, combined with functional in vivo data and advanced calculations and modeling, should enable us to understand the various processes in physiological conditions. Highly sophisticated x-ray free electron laser experiments on PSI and PSII crystals will permit observation of the photosystems in action, providing new insights for, e.g., electron transfer and water splitting (99–101)

## REFERENCES AND NOTES

1. R. E. Blankenship, *Molecular Mechanisms of Photosynthesis* (Blackwell Science, 2014).
2. X. G. Zhu, S. P. Long, D. R. Ort, Improving photosynthetic efficiency for greater yield. *Annu. Rev. Plant Biol.* **61**, 235–261 (2010). doi: [10.1146/annurev-arplant-042809-112206](https://doi.org/10.1146/annurev-arplant-042809-112206); pmid: [20192734](https://pubmed.ncbi.nlm.nih.gov/20192734/)
3. D. R. Ort et al., Redesigning photosynthesis to sustainably meet global food and bioenergy demand. *Proc. Natl. Acad. Sci. U.S.A.* **112**, 8529–8536 (2015). doi: [10.1073/pnas.1424031112](https://doi.org/10.1073/pnas.1424031112); pmid: [26124102](https://pubmed.ncbi.nlm.nih.gov/26124102/)
4. J. Kromdijk et al., Improving photosynthesis and crop productivity by accelerating recovery from photoprotection. *Science* **354**, 857–861 (2016). doi: [10.1126/science.aai8878](https://doi.org/10.1126/science.aai8878); pmid: [27856901](https://pubmed.ncbi.nlm.nih.gov/27856901/)
5. P. F. South, A. P. Cavanagh, H. W. Liu, D. R. Ort, Synthetic glycolate metabolism pathways stimulate crop growth and productivity in the field. *Science* **363**, eaat9077 (2019). doi: [10.1126/science.aat9077](https://doi.org/10.1126/science.aat9077); pmid: [30606819](https://pubmed.ncbi.nlm.nih.gov/30606819/)
6. M. Ermakova, P. E. Lopez-Calcano, C. A. Raines, R. T. Furbank, S. von Caemmerer, Overexpression of the Rieske FeS protein of the Cytochrome *b<sub>6</sub>f* complex increases *C<sub>4</sub>* photosynthesis in *Setaria viridis*. *Commun. Biol.* **2**, 314 (2019). doi: [10.1038/s42003-019-0561-9](https://doi.org/10.1038/s42003-019-0561-9); pmid: [31453378](https://pubmed.ncbi.nlm.nih.gov/31453378/)
7. A. J. Simkin, P. E. López-Calcano, C. A. Raines, Feeding the world: Improving photosynthetic efficiency for sustainable crop production. *J. Exp. Bot.* **70**, 1119–1140 (2019). doi: [10.1093/jxb/ery445](https://doi.org/10.1093/jxb/ery445); pmid: [30772919](https://pubmed.ncbi.nlm.nih.gov/30772919/)
8. R. Croce, R. van Grondelle, H. van Amerongen, I. H. van Stokkum, *Light Harvesting in Photosynthesis* (Foundations of Biochemistry and Biophysics Series, CRC, ed. 1, 2018).
9. E. Belgio, M. P. Johnson, S. Juric, A. V. Ruban, Higher plant photosystem II light-harvesting antenna, not the reaction center, determines the excited-state lifetime-both the maximum and the nonphotochemically quenched. *Biophys. J.* **102**, 2761–2771 (2012). doi: [10.1016/j.bpj.2012.05.004](https://doi.org/10.1016/j.bpj.2012.05.004); pmid: [22735526](https://pubmed.ncbi.nlm.nih.gov/22735526/)
10. R. Croce, H. van Amerongen, Light-harvesting in photosystem I. *Photosynth. Res.* **116**, 153–166 (2013). doi: [10.1007/s1120-013-9838-x](https://doi.org/10.1007/s1120-013-9838-x); pmid: [23645376](https://pubmed.ncbi.nlm.nih.gov/23645376/)
11. B. Gobets, R. van Grondelle, Energy transfer and trapping in photosystem I. *Biochim. Biophys. Acta* **1507**, 80–99 (2001). doi: [10.1016/S0005-2728\(01\)00203-1](https://doi.org/10.1016/S0005-2728(01)00203-1); pmid: [11687209](https://pubmed.ncbi.nlm.nih.gov/11687209/)
12. B. van Oort et al., Effect of antenna-depletion in Photosystem II on excitation energy transfer in *Arabidopsis thaliana*. *Biophys. J.* **98**, 922–931 (2010). doi: [10.1016/j.bpj.2009.11.012](https://doi.org/10.1016/j.bpj.2009.11.012); pmid: [20197046](https://pubmed.ncbi.nlm.nih.gov/20197046/)
13. P. H. Lambrev, Y. Miloslavina, P. Jahns, A. R. Holzwarth, On the relationship between non-photochemical quenching and photoprotection of Photosystem II. *Biochim. Biophys. Acta* **1817**, 760–769 (2012). doi: [10.1016/j.bbabi.2012.02.002](https://doi.org/10.1016/j.bbabi.2012.02.002); pmid: [22342615](https://pubmed.ncbi.nlm.nih.gov/22342615/)
14. R. E. Blankenship et al., Comparing photosynthetic and photovoltaic efficiencies and recognizing the potential for improvement. *Science* **332**, 805–809 (2011). doi: [10.1126/science.1200165](https://doi.org/10.1126/science.1200165); pmid: [21566184](https://pubmed.ncbi.nlm.nih.gov/21566184/)
15. N. Nelson, W. Junge, Structure and energy transfer in photosystems of oxygenic photosynthesis. *Annu. Rev. Biochem.* **84**, 659–683 (2015). doi: [10.1146/annurev-biochem-092914-041942](https://doi.org/10.1146/annurev-biochem-092914-041942); pmid: [25747397](https://pubmed.ncbi.nlm.nih.gov/25747397/)
16. T. Mirkovic et al., Light absorption and energy transfer in the antenna complexes of photosynthetic organisms. *Chem. Rev.* **117**, 249–293 (2017). doi: [10.1021/acs.chemrev.6b00002](https://doi.org/10.1021/acs.chemrev.6b00002); pmid: [27428615](https://pubmed.ncbi.nlm.nih.gov/27428615/)
17. N. Adir, S. Bar-Zvi, D. Harris, The amazing phycobilisome. *Biochim. Biophys. Acta Bioenerg.* **1861**, 148047 (2020). doi: [10.1016/j.bbabi.2019.07.002](https://doi.org/10.1016/j.bbabi.2019.07.002); pmid: [31306623](https://pubmed.ncbi.nlm.nih.gov/31306623/)
18. J. Zhang et al., Structure of phycobilisome from the red alga *Griffithsia pacifica*. *Nature* **551**, 57–63 (2017). doi: [10.1038/nature24278](https://doi.org/10.1038/nature24278); pmid: [29045394](https://pubmed.ncbi.nlm.nih.gov/29045394/)
19. H. Liu et al., Phycobilisomes supply excitations to both photosystems in a megacomplex in cyanobacteria. *Science* **342**, 1104–1107 (2013). doi: [10.1126/science.1242321](https://doi.org/10.1126/science.1242321); pmid: [24288334](https://pubmed.ncbi.nlm.nih.gov/24288334/)
20. J. Ma et al., Structural basis of energy transfer in Porphyridium purpureum phycobilisome. *Nature* **579**, 146–151 (2020). doi: [10.1038/s41586-020-2020-7](https://doi.org/10.1038/s41586-020-2020-7); pmid: [32076272](https://pubmed.ncbi.nlm.nih.gov/32076272/)
21. X. Pan, P. Cao, X. Su, Z. Liu, M. Li, Structural analysis and comparison of light-harvesting complexes I and II. *Biochim. Biophys. Acta Bioenerg.* **1861**, 148038 (2020). doi: [10.1016/j.bbabi.2019.06.010](https://doi.org/10.1016/j.bbabi.2019.06.010); pmid: [31229568](https://pubmed.ncbi.nlm.nih.gov/31229568/)
22. L. Nicol, R. Croce, “Light harvesting in higher plants and green algae,” in *Light Harvesting in Photosynthesis*, R. Croce, R. van Grondelle, H. van Amerongen, I. H. van Stokkum, Eds. (Foundations of Biochemistry and Biophysics Series, CRC, ed. 1, 2018), pp. 59–76.
23. C. Büchel, Light harvesting complexes in chlorophyll c-containing algae. *Biochim. Biophys. Acta Bioenerg.* **1861**, 148027 (2020). pmid: [31153887](https://pubmed.ncbi.nlm.nih.gov/31153887/)
24. W. Wang et al., Structural basis for blue-green light harvesting and energy dissipation in diatoms. *Science* **363**, eaav0365 (2019). doi: [10.1126/science.aav0365](https://doi.org/10.1126/science.aav0365); pmid: [30733387](https://pubmed.ncbi.nlm.nih.gov/30733387/)
25. X. Qin, M. Suga, T. Kuang, J. R. Shen, Structural basis for energy transfer pathways in the plant PSI-LHCI supercomplex. *Science* **348**, 989–995 (2015). doi: [10.1126/science.aab0214](https://doi.org/10.1126/science.aab0214); pmid: [26023133](https://pubmed.ncbi.nlm.nih.gov/26023133/)
26. Y. Mazar, A. Borovikova, I. Caspy, N. Nelson, Structure of the plant photosystem I supercomplex at 2.6 Å resolution. *Nat. Plants* **3**, 17014 (2017). doi: [10.1038/nplants.2017.14](https://doi.org/10.1038/nplants.2017.14); pmid: [28248295](https://pubmed.ncbi.nlm.nih.gov/28248295/)
27. X. Pan et al., Structure of the maize photosystem I supercomplex with light-harvesting complexes I and II. *Science* **360**, 1109–1113 (2018). doi: [10.1126/science.aat1156](https://doi.org/10.1126/science.aat1156); pmid: [29880686](https://pubmed.ncbi.nlm.nih.gov/29880686/)
28. X. Su et al., Structure and assembly mechanism of plant *C<sub>2</sub>S<sub>2</sub>M<sub>2</sub>*-type PSII-LHCII supercomplex. *Science* **357**, 815–820 (2017). doi: [10.1126/science.aan0327](https://doi.org/10.1126/science.aan0327); pmid: [28839073](https://pubmed.ncbi.nlm.nih.gov/28839073/)
29. X. Wei et al., Structure of spinach photosystem II-LHCII supercomplex at 3.2 Å resolution. *Nature* **534**, 69–74 (2016). doi: [10.1038/nature18020](https://doi.org/10.1038/nature18020); pmid: [27251276](https://pubmed.ncbi.nlm.nih.gov/27251276/)
30. L. S. van Bezouwen et al., Subunit and chlorophyll organization of the plant photosystem II supercomplex. *Nat. Plants* **3**, 17080 (2017). doi: [10.1038/nplants.2017.80](https://doi.org/10.1038/nplants.2017.80); pmid: [28604725](https://pubmed.ncbi.nlm.nih.gov/28604725/)
31. R. Kouril, J. P. Dekker, E. J. Boekema, Supramolecular organization of photosystem II in green plants. *Biochim. Biophys. Acta* **1817**, 2–12 (2012). doi: [10.1016/j.bbabi.2011.05.024](https://doi.org/10.1016/j.bbabi.2011.05.024); pmid: [21723248](https://pubmed.ncbi.nlm.nih.gov/21723248/)
32. R. Kouril, L. Nosek, J. Bartoš, E. J. Boekema, P. Illik, Evolutionary loss of light-harvesting proteins Lhcb6 and Lhcb3 in major land plant groups—Break-up of current dogma. *New Phytol.* **210**, 808–814 (2016). doi: [10.1111/nph.13947](https://doi.org/10.1111/nph.13947); pmid: [27001142](https://pubmed.ncbi.nlm.nih.gov/27001142/)
33. R. Croce, H. van Amerongen, Natural strategies for photosynthetic light harvesting. *Nat. Chem. Biol.* **10**, 492–501 (2014). doi: [10.1038/nchembio.1555](https://doi.org/10.1038/nchembio.1555); pmid: [24937067](https://pubmed.ncbi.nlm.nih.gov/24937067/)
34. L. Shen et al., Structure of a *C<sub>2</sub>S<sub>2</sub>M<sub>2</sub>N<sub>2</sub>*-type PSII-LHCII supercomplex from the green alga *Chlamydomonas reinhardtii*. *Proc. Natl. Acad. Sci. U.S.A.* **116**, 21246–21255 (2019). doi: [10.1073/pnas.1912462116](https://doi.org/10.1073/pnas.1912462116); pmid: [31570614](https://pubmed.ncbi.nlm.nih.gov/31570614/)
35. X. Sheng et al., Structural insight into light harvesting for photosystem II in green algae. *Nat. Plants* **5**, 1320–1330 (2019). doi: [10.1038/s41477-019-0543-4](https://doi.org/10.1038/s41477-019-0543-4); pmid: [31768031](https://pubmed.ncbi.nlm.nih.gov/31768031/)
36. R. N. Burton-Smith et al., Structural determination of the large photosystem II-light-harvesting complex II supercomplex of *Chlamydomonas reinhardtii* using nonionic amphipol. *J. Biol. Chem.* **294**, 15003–15013 (2019). doi: [10.1074/jbc.RA119.009341](https://doi.org/10.1074/jbc.RA119.009341); pmid: [31420447](https://pubmed.ncbi.nlm.nih.gov/31420447/)
37. X. Su et al., Antenna arrangement and energy transfer pathways of a green algal photosystem-I-LHCI supercomplex. *Nat. Plants* **5**, 273–281 (2019). doi: [10.1038/s41477-019-0380-5](https://doi.org/10.1038/s41477-019-0380-5); pmid: [30850819](https://pubmed.ncbi.nlm.nih.gov/30850819/)
38. M. Suga et al., Structure of the green algal photosystem I supercomplex with a dimeric light-harvesting complex I. *Nat. Plants* **5**, 626–636 (2019). doi: [10.1038/s41477-019-0438-4](https://doi.org/10.1038/s41477-019-0438-4); pmid: [31182847](https://pubmed.ncbi.nlm.nih.gov/31182847/)
39. X. Pi et al., The pigment-protein network of a diatom photosystem II-light-harvesting antenna supercomplex. *Science* **365**, eaax4406 (2019). doi: [10.1126/science.aax4406](https://doi.org/10.1126/science.aax4406); pmid: [31371578](https://pubmed.ncbi.nlm.nih.gov/31371578/)
40. R. Nagao et al., Structural basis for energy harvesting and dissipation in a diatom PSII-FCPII supercomplex. *Nat. Plants* **5**, 890–901 (2019). doi: [10.1038/s41477-019-0477-x](https://doi.org/10.1038/s41477-019-0477-x); pmid: [31358960](https://pubmed.ncbi.nlm.nih.gov/31358960/)
41. F. J. Van Eerden, M. N. Melo, P. W. J. M. Frederix, X. Periole, S. J. Marrink, Exchange pathways of plastoquinone and plastoquinol in the photosystem II complex. *Nat. Commun.* **8**, 15214 (2017). doi: [10.1038/ncomms15214](https://doi.org/10.1038/ncomms15214); pmid: [28489071](https://pubmed.ncbi.nlm.nih.gov/28489071/)
42. N. Sakashita, H. C. Watanabe, T. Ikeda, H. Ishikita, Structurally conserved channels in cyanobacterial and plant photosystem II. *Photosynth. Res.* **133**, 75–85 (2017). doi: [10.1007/s11210-017-0347-1](https://doi.org/10.1007/s11210-017-0347-1); pmid: [28188547](https://pubmed.ncbi.nlm.nih.gov/28188547/)
43. D. I. G. Bennett, K. Amarnath, G. R. Fleming, A structure-based model of energy transfer reveals the principles of light harvesting in photosystem II supercomplexes. *J. Am. Chem. Soc.* **135**, 9164–9173 (2013). doi: [10.1021/ja403685a](https://doi.org/10.1021/ja403685a); pmid: [23679235](https://pubmed.ncbi.nlm.nih.gov/23679235/)
44. C. Kreisbeck, A. Aspuru-Guzik, Efficiency of energy funneling in the photosystem II supercomplex of higher plants. *Chem. Sci.* **7**, 4174–4183 (2016). doi: [10.1039/C5SC04296H](https://doi.org/10.1039/C5SC04296H); pmid: [30155062](https://pubmed.ncbi.nlm.nih.gov/30155062/)
45. V. Novoderezhkin, A. Marin, R. van Grondelle, Intra- and inter-monomeric transfers in the light harvesting LHClI complex: The Redfield-Förster picture. *Phys. Chem. Chem. Phys.* **13**, 17093–17103 (2011). doi: [10.1039/c1cp21079c](https://doi.org/10.1039/c1cp21079c); pmid: [21866281](https://pubmed.ncbi.nlm.nih.gov/21866281/)
46. G. S. Schlau-Cohen et al., Pathways of energy flow in LHClI from two-dimensional electronic spectroscopy. *J. Phys. Chem. B* **113**, 15352–15363 (2009). doi: [10.1021/jp9066586](https://doi.org/10.1021/jp9066586); pmid: [19856954](https://pubmed.ncbi.nlm.nih.gov/19856954/)
47. P. H. Lambrev, P. Akhtar, H. S. Tan, Insights into the mechanisms and dynamics of energy transfer in plant light-harvesting complexes from two-dimensional electronic spectroscopy. *Biochim. Biophys. Acta Bioenerg.* **1861**, 148050 (2019). doi: [10.1016/j.bbabi.2019.07.005](https://doi.org/10.1016/j.bbabi.2019.07.005); pmid: [31326408](https://pubmed.ncbi.nlm.nih.gov/31326408/)
48. V. Mascoli, V. Novoderezhkin, N. Liguori, P. Xu, R. Croce, Design principles of solar light harvesting in plants: Functional architecture of the monomeric antenna CP29. *Biochim. Biophys. Acta Bioenerg.* **1861**, 148156 (2020). doi: [10.1016/j.bbabi.2020.148156](https://doi.org/10.1016/j.bbabi.2020.148156); pmid: [31987813](https://pubmed.ncbi.nlm.nih.gov/31987813/)
49. J. Chmeliov, G. Trinkunas, H. van Amerongen, L. Valkunas, Light harvesting in a fluctuating antenna. *J. Am. Chem. Soc.* **136**, 8963–8972 (2014). doi: [10.1021/ja5027858](https://doi.org/10.1021/ja5027858); pmid: [24870124](https://pubmed.ncbi.nlm.nih.gov/24870124/)
50. N. Nelson, Plant photosystem I: The most efficient nano-photochemical machine. *J. Nanosci. Nanotechnol.* **9**, 1709–1713 (2009). doi: [10.1166/jnn.2009.S101](https://doi.org/10.1166/jnn.2009.S101); pmid: [19435029](https://pubmed.ncbi.nlm.nih.gov/19435029/)
51. M. Suga, J. R. Shen, Structural variations of photosystem I-antenna supercomplex in response to adaptations to different light environments. *Curr. Opin. Struct. Biol.* **63**, 10–17 (2020). doi: [10.1016/j.sbi.2020.02.005](https://doi.org/10.1016/j.sbi.2020.02.005); pmid: [32294569](https://pubmed.ncbi.nlm.nih.gov/32294569/)
52. R. Croce, A close view of photosystem I. *Science* **348**, 970–971 (2015). doi: [10.1126/science.aab3387](https://doi.org/10.1126/science.aab3387); pmid: [26023121](https://pubmed.ncbi.nlm.nih.gov/26023121/)
53. E. Wientjes, I. H. van Stokkum, H. van Amerongen, R. Croce, Excitation-energy transfer dynamics of higher plant photosystem I light-harvesting complexes. *Biophys. J.* **100**, 1372–1380 (2011). doi: [10.1016/j.bpj.2011.01.030](https://doi.org/10.1016/j.bpj.2011.01.030); pmid: [21354411](https://pubmed.ncbi.nlm.nih.gov/21354411/)
54. C. Slavov, M. Ballottari, T. Morosinotto, R. Bassi, A. R. Holzwarth, Trap-limited charge separation kinetics in higher plant photosystem I complexes. *Biophys. J.* **94**, 3601–3612 (2008). doi: [10.1529/biophysj.107.117101](https://doi.org/10.1529/biophysj.107.117101); pmid: [18222996](https://pubmed.ncbi.nlm.nih.gov/18222996/)
55. E. Wientjes, I. H. van Stokkum, H. van Amerongen, R. Croce, The role of the individual Lhcas in photosystem I excitation energy trapping. *Biophys. J.* **101**, 745–754 (2011). doi: [10.1016/j.bpj.2011.06.045](https://doi.org/10.1016/j.bpj.2011.06.045); pmid: [21806943](https://pubmed.ncbi.nlm.nih.gov/21806943/)
56. E. Engelmann et al., Influence of the photosystem I-light harvesting complex I antenna domains on fluorescence decay. *Biochemistry* **45**, 6947–6955 (2006). doi: [10.1021/bi060243p](https://doi.org/10.1021/bi060243p); pmid: [16734430](https://pubmed.ncbi.nlm.nih.gov/16734430/)
57. E. Wientjes, H. van Amerongen, R. Croce, LHClI is an antenna of both photosystems after long-term acclimation. *Biochim. Biophys. Acta* **1827**, 420–426 (2013). doi: [10.1016/j.bbabi.2012.12.009](https://doi.org/10.1016/j.bbabi.2012.12.009); pmid: [23298812](https://pubmed.ncbi.nlm.nih.gov/23298812/)
58. M. Grieco, M. Suorsa, A. Jajoo, M. Tikkanen, E. M. Aro, Light-harvesting II antenna trimers connect energetically the entire photosynthetic machinery - including both photosystems II and I. *Biochim. Biophys. Acta* **1847**, 607–619 (2015). doi: [10.1016/j.bbabi.2015.03.004](https://doi.org/10.1016/j.bbabi.2015.03.004); pmid: [25843550](https://pubmed.ncbi.nlm.nih.gov/25843550/)
59. V. U. Chukhutsina, X. Liu, P. Xu, R. Croce, Light-harvesting complex II is an antenna of photosystem I in dark-adapted plants. *Nat. Plants* **6**, 860–868 (2020). doi: [10.1038/s41477-020-0693-4](https://doi.org/10.1038/s41477-020-0693-4); pmid: [32572215](https://pubmed.ncbi.nlm.nih.gov/32572215/)

60. P. Galka *et al.*, Functional analyses of the plant photosystem I-light-harvesting complex II supercomplex reveal that light-harvesting complex II loosely bound to photosystem II is a very efficient antenna for photosystem I in state II. *Plant Cell* **24**, 2963–2978 (2012). doi: [10.1105/tpc.112.100339](https://doi.org/10.1105/tpc.112.100339); pmid: [22822202](https://pubmed.ncbi.nlm.nih.gov/22822202/)
61. S. Santabarbara, T. Tibiletti, W. Remelli, S. Caffarri, Kinetics and heterogeneity of energy transfer from light harvesting complex II to photosystem I in the supercomplex isolated from *Arabidopsis*. *Phys. Chem. Chem. Phys.* **19**, 9210–9222 (2017). doi: [10.1039/C7CP00554G](https://doi.org/10.1039/C7CP00554G); pmid: [28319223](https://pubmed.ncbi.nlm.nih.gov/28319223/)
62. X. Pi *et al.*, Unique organization of photosystem I-light-harvesting supercomplex revealed by cryo-EM from a red alga. *Proc. Natl. Acad. Sci. U.S.A.* **115**, 4423–4428 (2018). doi: [10.1073/pnas.1722482115](https://doi.org/10.1073/pnas.1722482115); pmid: [29632169](https://pubmed.ncbi.nlm.nih.gov/29632169/)
63. X. Qin *et al.*, Structure of a green algal photosystem I in complex with a large number of light-harvesting complex I subunits. *Nat. Plants* **5**, 263–272 (2019). doi: [10.1038/s41477-019-0379-y](https://doi.org/10.1038/s41477-019-0379-y); pmid: [30850820](https://pubmed.ncbi.nlm.nih.gov/30850820/)
64. M. Iwai, P. Grob, A. T. Iavarone, E. Nogales, K. K. Niyogi, A unique supramolecular organization of photosystem I in the moss *Physcomitrella patens*. *Nat. Plants* **4**, 904–909 (2018). doi: [10.1038/s41477-018-0271-1](https://doi.org/10.1038/s41477-018-0271-1); pmid: [30374090](https://pubmed.ncbi.nlm.nih.gov/30374090/)
65. C. Le Quiniou *et al.*, PSI-LHCI of *Chlamydomonas reinhardtii*: Increasing the absorption cross section without losing efficiency. *Biochim. Biophys. Acta* **1847**, 458–467 (2015). doi: [10.1016/j.bbabi.2015.02.001](https://doi.org/10.1016/j.bbabi.2015.02.001); pmid: [25681242](https://pubmed.ncbi.nlm.nih.gov/25681242/)
66. S. Caffarri, K. Broess, R. Croce, H. van Amerongen, Excitation energy transfer and trapping in higher plant Photosystem II complexes with different antenna sizes. *Biophys. J.* **100**, 2094–2103 (2011). doi: [10.1016/j.bpj.2011.03.049](https://doi.org/10.1016/j.bpj.2011.03.049); pmid: [21539776](https://pubmed.ncbi.nlm.nih.gov/21539776/)
67. Y. Takahashi, T. A. Yasui, E. J. Stauber, M. Hippler, Comparison of the subunit compositions of the PSI-LHCI supercomplex and the LHCI in the green alga *Chlamydomonas reinhardtii*. *Biochemistry* **43**, 7816–7823 (2004). doi: [10.1021/bi035988z](https://doi.org/10.1021/bi035988z); pmid: [15196024](https://pubmed.ncbi.nlm.nih.gov/15196024/)
68. A. Pinnola *et al.*, A LHCb9-dependent photosystem I megacomplex induced under low light in *Physcomitrella patens*. *Nat. Plants* **4**, 910–919 (2018). doi: [10.1038/s41477-018-0270-2](https://doi.org/10.1038/s41477-018-0270-2); pmid: [30374091](https://pubmed.ncbi.nlm.nih.gov/30374091/)
69. Y. Umena, K. Kawakami, J. R. Shen, N. Kamiya, Crystal structure of oxygen-evolving photosystem II at a resolution of 1.9 Å. *Nature* **473**, 55–60 (2011). doi: [10.1038/nature09913](https://doi.org/10.1038/nature09913); pmid: [21499260](https://pubmed.ncbi.nlm.nih.gov/21499260/)
70. F. Müh, A. Zouni, Structural basis of light-harvesting in the photosystem II core complex. *Protein Sci.* **29**, 1090–1119 (2020). doi: [10.1002/pro.3841](https://doi.org/10.1002/pro.3841); pmid: [32067287](https://pubmed.ncbi.nlm.nih.gov/32067287/)
71. Y. Miloslavina *et al.*, Charge separation kinetics in intact photosystem II core particles is trap-limited. A picosecond fluorescence study. *Biochemistry* **45**, 2436–2442 (2006). doi: [10.1021/bi052248c](https://doi.org/10.1021/bi052248c); pmid: [16475833](https://pubmed.ncbi.nlm.nih.gov/16475833/)
72. C. D. van der Weij-de Wit, J. P. Dekker, R. van Grondelle, I. H. van Stokkum, Charge separation is virtually irreversible in photosystem II core complexes with oxidized primary quinone acceptor. *J. Phys. Chem. A* **115**, 3947–3956 (2011). doi: [10.1021/jp1083746](https://doi.org/10.1021/jp1083746); pmid: [21341818](https://pubmed.ncbi.nlm.nih.gov/21341818/)
73. S. Vassiliev, C. I. Lee, G. W. Brudvig, D. Bruce, Structure-based kinetic modeling of excited-state transfer and trapping in histidine-tagged photosystem II core complexes from *Synechocystis*. *Biochemistry* **41**, 12236–12243 (2002). doi: [10.1021/bi0262597](https://doi.org/10.1021/bi0262597); pmid: [12356326](https://pubmed.ncbi.nlm.nih.gov/12356326/)
74. R. Croce, H. van Amerongen, Light-harvesting and structural organization of Photosystem II: From individual complexes to thylakoid membrane. *J. Photochem. Photobiol. B* **104**, 142–153 (2011). doi: [10.1016/j.jphotobiol.2011.02.015](https://doi.org/10.1016/j.jphotobiol.2011.02.015); pmid: [21402480](https://pubmed.ncbi.nlm.nih.gov/21402480/)
75. S. Caffarri, R. Kouril, S. Kereiche, E. J. Boekema, R. Croce, Functional architecture of higher plant photosystem II supercomplexes. *EMBO J.* **28**, 3052–3063 (2009). doi: [10.1038/emboj.2009.232](https://doi.org/10.1038/emboj.2009.232); pmid: [19696744](https://pubmed.ncbi.nlm.nih.gov/19696744/)
76. H. Van Amerongen, L. Valkunas, R. van Grondelle, *Photosynthetic Excitons* (World Scientific, 2000).
77. A. Marin, F. Passarini, R. Croce, R. van Grondelle, Energy transfer pathways in the CP24 and CP26 antenna complexes of higher plant photosystem II: A comparative study. *Biophys. J.* **99**, 4056–4065 (2010). doi: [10.1016/j.bpj.2010.10.034](https://doi.org/10.1016/j.bpj.2010.10.034); pmid: [21156149](https://pubmed.ncbi.nlm.nih.gov/21156149/)
78. L. Dall'Osto, S. Cazzaniga, D. Zappone, R. Bassi, Monomeric light harvesting complexes enhance excitation energy transfer from LHClI to PSII and control their lateral spacing in thylakoids. *Biochim. Biophys. Acta Bioenerg.* **1861**, 148035 (2020). doi: [10.1016/j.bbabi.2019.06.007](https://doi.org/10.1016/j.bbabi.2019.06.007); pmid: [31226317](https://pubmed.ncbi.nlm.nih.gov/31226317/)
79. R. Tokutsu, M. Iwai, J. Minagawa, CP29, a monomeric light-harvesting complex II protein, is essential for state transitions in *Chlamydomonas reinhardtii*. *J. Biol. Chem.* **284**, 7777–7782 (2009). doi: [10.1074/jbc.M809360200](https://doi.org/10.1074/jbc.M809360200); pmid: [19144643](https://pubmed.ncbi.nlm.nih.gov/19144643/)
80. S. Farooq, J. Chmeliov, G. Trinkunas, L. Valkunas, H. van Amerongen, Is there excitation energy transfer between different layers of stacked photosystem-II-containing thylakoid membranes? *J. Phys. Chem. Lett.* **7**, 1406–1410 (2016). doi: [10.1021/acs.jpclett.6b00474](https://doi.org/10.1021/acs.jpclett.6b00474); pmid: [27014831](https://pubmed.ncbi.nlm.nih.gov/27014831/)
81. E. G. Andrihievskaya, D. Frolov, R. van Grondelle, J. P. Dekker, On the role of the CP47 core antenna in the energy transfer and trapping dynamics of Photosystem II. *Phys. Chem. Chem. Phys.* **6**, 4810–4819 (2004). doi: [10.1039/b411977k](https://doi.org/10.1039/b411977k)
82. M. Ballottari, L. Dall'Osto, T. Morosinotto, R. Bassi, Contrasting behavior of higher plant photosystem I and II antenna systems during acclimation. *J. Biol. Chem.* **282**, 8947–8958 (2007). doi: [10.1074/jbc.M606417200](https://doi.org/10.1074/jbc.M606417200); pmid: [17229724](https://pubmed.ncbi.nlm.nih.gov/17229724/)
83. J. M. Anderson, W. S. Chow, J. De Las Rivas, Dynamic flexibility in the structure and function of photosystem II in higher plant thylakoid membranes: The grana enigma. *Photosynth. Res.* **98**, 575–587 (2008). doi: [10.1007/s11120-008-9381-3](https://doi.org/10.1007/s11120-008-9381-3); pmid: [18998237](https://pubmed.ncbi.nlm.nih.gov/18998237/)
84. E. Wientjes, H. van Amerongen, R. Croce, Quantum yield of charge separation in photosystem II: Functional effect of changes in the antenna size upon light acclimation. *J. Phys. Chem. B* **117**, 11200–11208 (2013). doi: [10.1021/jp401663w](https://doi.org/10.1021/jp401663w); pmid: [23534376](https://pubmed.ncbi.nlm.nih.gov/23534376/)
85. E. J. Boekema, H. van Roon, F. Calkoen, R. Bassi, J. P. Dekker, Multiple types of association of photosystem II and its light-harvesting antenna in partially solubilized photosystem II membranes. *Biochemistry* **38**, 2233–2239 (1999). doi: [10.1021/bi9827161](https://doi.org/10.1021/bi9827161); pmid: [10029515](https://pubmed.ncbi.nlm.nih.gov/10029515/)
86. A. J. Bell, L. K. Frankel, T. M. Bricker, High yield non-detergent isolation of photosystem I-light-harvesting chlorophyll II membranes from spinach thylakoids: Implications for the organization of the PS I antennae in higher plants. *J. Biol. Chem.* **290**, 18429–18437 (2015). doi: [10.1074/jbc.M115.663872](https://doi.org/10.1074/jbc.M115.663872); pmid: [26055710](https://pubmed.ncbi.nlm.nih.gov/26055710/)
87. K. N. Yadav *et al.*, Supercomplexes of plant photosystem I with cytochrome b6f, light-harvesting complex II and NDH. *Biochim. Biophys. Acta Bioenerg.* **1858**, 12–20 (2017). doi: [10.1016/j.bbabi.2016.10.006](https://doi.org/10.1016/j.bbabi.2016.10.006); pmid: [27755973](https://pubmed.ncbi.nlm.nih.gov/27755973/)
88. S. L. Benson *et al.*, An intact light harvesting complex I antenna system is required for complete state transitions in *Arabidopsis*. *Nat. Plants* **1**, 15176 (2015). doi: [10.1038/nplants.2015.176](https://doi.org/10.1038/nplants.2015.176); pmid: [27251716](https://pubmed.ncbi.nlm.nih.gov/27251716/)
89. L. Dall'Osto, S. Cazzaniga, M. Havaux, R. Bassi, Enhanced photoprotection by protein-bound vs free xanthophyll pools: A comparative analysis of chlorophyll b and xanthophyll biosynthesis mutants. *Mol. Plant* **3**, 576–593 (2010). doi: [10.1093/mp/ssp117](https://doi.org/10.1093/mp/ssp117); pmid: [20100799](https://pubmed.ncbi.nlm.nih.gov/20100799/)
90. A. V. Ruban, Nonphotochemical Chlorophyll Fluorescence Quenching: Mechanism and Effectiveness in Protecting Plants from Photodamage. *Plant Physiol.* **170**, 1903–1916 (2016). doi: [10.1104/pp.15.01935](https://doi.org/10.1104/pp.15.01935); pmid: [26864015](https://pubmed.ncbi.nlm.nih.gov/26864015/)
91. X. P. Li *et al.*, A pigment-binding protein essential for regulation of photosynthetic light harvesting. *Nature* **403**, 391–395 (2000). doi: [10.1038/35000131](https://doi.org/10.1038/35000131); pmid: [10667783](https://pubmed.ncbi.nlm.nih.gov/10667783/)
92. G. Peers *et al.*, An ancient light-harvesting protein is critical for the regulation of algal photosynthesis. *Nature* **462**, 518–521 (2009). doi: [10.1038/nature08587](https://doi.org/10.1038/nature08587); pmid: [19940928](https://pubmed.ncbi.nlm.nih.gov/19940928/)
93. D. A. Semchonok *et al.*, Interaction between the photoprotective protein LHCSR3 and C<sub>2</sub>S<sub>2</sub> Photosystem II supercomplex in *Chlamydomonas reinhardtii*. *Biochim. Biophys. Acta Bioenerg.* **1858**, 379–385 (2017). doi: [10.1016/j.bbabi.2017.02.015](https://doi.org/10.1016/j.bbabi.2017.02.015); pmid: [28257778](https://pubmed.ncbi.nlm.nih.gov/28257778/)
94. K. Kato *et al.*, Structural basis for the adaptation and function of chlorophyll f in photosystem I. *Nat. Commun.* **11**, 238 (2020). doi: [10.1038/s41467-019-13898-5](https://doi.org/10.1038/s41467-019-13898-5); pmid: [31932639](https://pubmed.ncbi.nlm.nih.gov/31932639/)
95. C. Gisriel *et al.*, The structure of Photosystem I acclimated to far-red light illuminates an ecologically important acclimation process in photosynthesis. *Sci. Adv.* **6**, eaay6415 (2020). doi: [10.1126/sciadv.aay6415](https://doi.org/10.1126/sciadv.aay6415); pmid: [32076649](https://pubmed.ncbi.nlm.nih.gov/32076649/)
96. H. Toporik, J. Li, D. Williams, P. L. Chiu, Y. Mazor, The structure of the stress-induced photosystem I-LsIIa antenna supercomplex. *Nat. Struct. Mol. Biol.* **26**, 443–449 (2019). doi: [10.1038/s41594-019-0228-8](https://doi.org/10.1038/s41594-019-0228-8); pmid: [31133699](https://pubmed.ncbi.nlm.nih.gov/31133699/)
97. M. Schaffer *et al.*, A cryo-FIB lift-out technique enables molecular-resolution cryo-ET within native *Caenorhabditis elegans* tissue. *Nat. Methods* **16**, 757–762 (2019). doi: [10.1038/s41592-019-0497-5](https://doi.org/10.1038/s41592-019-0497-5); pmid: [31363205](https://pubmed.ncbi.nlm.nih.gov/31363205/)
98. W. Wietrzynski *et al.*, Charting the native architecture of *Chlamydomonas* thylakoid membranes with single-molecule precision. *eLife* **9**, e53740 (2020). doi: [10.7554/eLife.53740](https://doi.org/10.7554/eLife.53740); pmid: [32297859](https://pubmed.ncbi.nlm.nih.gov/32297859/)
99. J. Kern *et al.*, Structures of the intermediates of Kok's photosynthetic water oxidation clock. *Nature* **563**, 421–425 (2018). doi: [10.1038/s41586-018-0681-2](https://doi.org/10.1038/s41586-018-0681-2); pmid: [30405241](https://pubmed.ncbi.nlm.nih.gov/30405241/)
100. M. Suga *et al.*, An oxyl/oxo mechanism for oxygen-oxygen coupling in PSII revealed by an x-ray free-electron laser. *Science* **366**, 334–338 (2019). doi: [10.1126/science.aax6998](https://doi.org/10.1126/science.aax6998); pmid: [31624207](https://pubmed.ncbi.nlm.nih.gov/31624207/)
101. C. Gisriel *et al.*, Membrane protein megahertz crystallography at the European XFEL. *Nat. Commun.* **10**, 5021 (2019). doi: [10.1038/s41467-019-12955-3](https://doi.org/10.1038/s41467-019-12955-3); pmid: [31685819](https://pubmed.ncbi.nlm.nih.gov/31685819/)
102. F. Gan *et al.*, Extensive remodeling of a cyanobacterial photosynthetic apparatus in far-red light. *Science* **345**, 1312–1317 (2014). doi: [10.1126/science.1256963](https://doi.org/10.1126/science.1256963); pmid: [25214622](https://pubmed.ncbi.nlm.nih.gov/25214622/)
103. M. Chen, Chlorophyll modifications and their spectral extension in oxygenic photosynthesis. *Annu. Rev. Biochem.* **83**, 317–340 (2014). doi: [10.1146/annurev-biochem-072711-162943](https://doi.org/10.1146/annurev-biochem-072711-162943); pmid: [24635479](https://pubmed.ncbi.nlm.nih.gov/24635479/)
104. T. Forster, "Delocalized excitation and excitation transfer," in *Modern Quantum Chemistry, Part III Action of Light and Organic Crystals*, O. Sinanoglu, Ed. (Academic, 1965), vol. 3, pp. 93–137.
105. H. van Amerongen, R. van Grondelle, Understanding the energy transfer function of LHClI, the major light-harvesting complex of green plants. *J. Phys. Chem. B* **105**, 604–617 (2001). doi: [10.1021/jp0028406](https://doi.org/10.1021/jp0028406)
106. T. Polívka, H. A. Frank, Molecular factors controlling photosynthetic light harvesting by carotenoids. *Acc. Chem. Res.* **43**, 1125–1134 (2010). doi: [10.1021/ar100030m](https://doi.org/10.1021/ar100030m); pmid: [20446691](https://pubmed.ncbi.nlm.nih.gov/20446691/)
107. Z. Liu *et al.*, Crystal structure of spinach major light-harvesting complex at 2.72 Å resolution. *Nature* **428**, 287–292 (2004). doi: [10.1038/nature02373](https://doi.org/10.1038/nature02373); pmid: [15029188](https://pubmed.ncbi.nlm.nih.gov/15029188/)
108. P. Jordan *et al.*, Three-dimensional structure of cyanobacterial photosystem I at 2.5 Å resolution. *Nature* **411**, 909–917 (2001). doi: [10.1038/35082000](https://doi.org/10.1038/35082000); pmid: [11418848](https://pubmed.ncbi.nlm.nih.gov/11418848/)
109. M. Abram *et al.*, Remodeling of excitation energy transfer in extremophilic red algal PSI-LHCI complex during light adaptation. *Biochim. Biophys. Acta Bioenerg.* **1861**, 148093 (2020). doi: [10.1016/j.bbabi.2019.148093](https://doi.org/10.1016/j.bbabi.2019.148093); pmid: [31669460](https://pubmed.ncbi.nlm.nih.gov/31669460/)
110. M. Suga *et al.*, Native structure of photosystem II at 1.95 Å resolution viewed by femtosecond X-ray pulses. *Nature* **517**, 99–103 (2015). doi: [10.1038/nature13991](https://doi.org/10.1038/nature13991); pmid: [25470056](https://pubmed.ncbi.nlm.nih.gov/25470056/)
111. E. Kim, S. Akimoto, R. Tokutsu, M. Yokono, J. Minagawa, Fluorescence lifetime analyses reveal how the high light-responsive protein LHCSR3 transforms PSII light-harvesting complexes into an energy-dissipative state. *J. Biol. Chem.* **292**, 18951–18960 (2017). doi: [10.1074/jbc.M117.805192](https://doi.org/10.1074/jbc.M117.805192); pmid: [28972177](https://pubmed.ncbi.nlm.nih.gov/28972177/)

# ACKNOWLEDGMENTS

We thank V. Mascoli for help in setting up the program for the analysis of the structures. **Competing interests:** The authors declare no competing interests.

10.1126/science.aay2058



## RESEARCH ARTICLE SUMMARY

## BIOMEDICINE

## Neutrophil extracellular traps target senescent vasculature for tissue remodeling in retinopathy

François Binet, Gael Cagnone, Sergio Crespo-Garcia, Masayuki Hata, Mathieu Neault, Agnieszka Dejda, Ariel M. Wilson, Manuel Buscarlet, Gaelle Tagne Mawambo, Joel P. Howard, Roberto Diaz-Marin, Celia Parinot, Vera Guber, Frédérique Pilon, Rachel Juneau, Rémi Laflamme, Christina Sawchyn, Karine Boulay, Severine Leclerc, Afnan Abu-Thuraia, Jean-François Côté, Gregor Andelfinger, Flavio A. Rezende, Florian Sennlaub, Jean-Sébastien Joyal\*, Frédéric A. Mallette\*, Przemyslaw Sapielha\*

**INTRODUCTION:** Vision provides a critical survival advantage but requires a tight coupling between neuronal energy demands and their vascular supply. The degeneration and consequent aberrant regrowth of retinal vasculature is the hallmark of diseases such as diabetic retinopathy, retinopathy of prematurity, and age-related macular degeneration, which collectively are the most common causes of loss of sight in industrialized countries. Although considerable effort has been devoted to under-

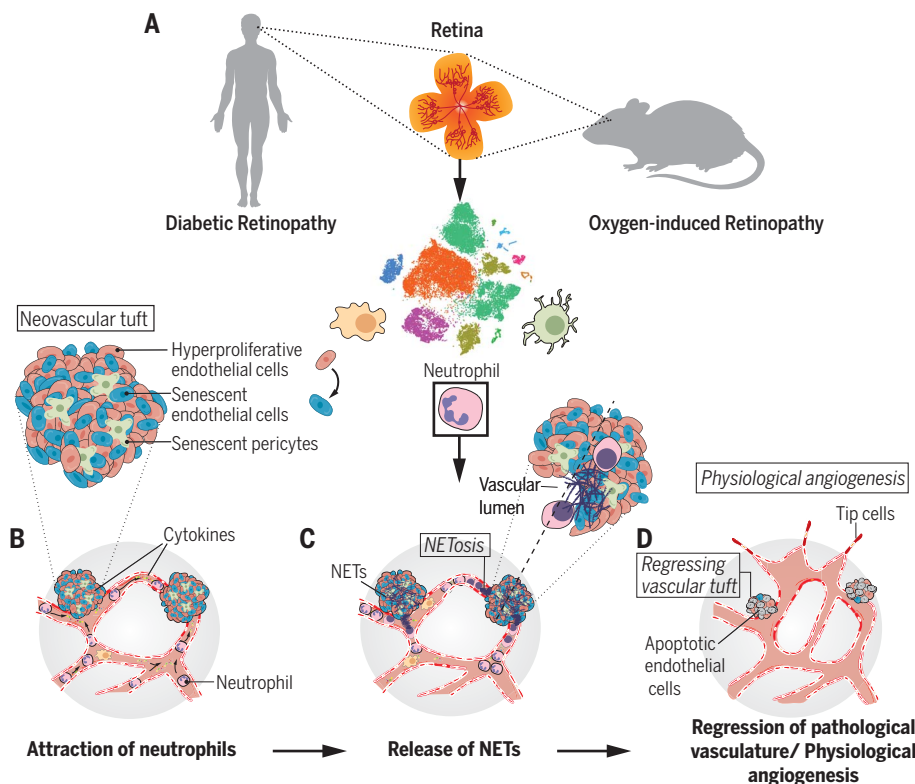
standing how diseased blood vessels form, relatively little is known of the processes at play during late stages of pathological angiogenesis when blood vessels remodel and subsets of diseased vasculature regress.

**RATIONALE:** The retina is part of the central nervous system and thus has limited regenerative capacity. A relative exception to this rule are retinal blood vessels, which have a greater propensity to remodel depending on metabo-

lic demand. We investigated the cellular mechanisms activated during the remodeling and regression of pathological blood vessels in retinopathy. We focused on a mouse model of oxygen-induced retinopathy, which has distinct and timed phases of vascular degeneration, neovascularization, and vascular regression. Our findings were verified in human patients with proliferative diabetic retinopathy. Understanding how diseased blood vessels remodel and yield functional networks has the potential to lead to strategies that enhance vascular normalization and helps to explain why retinas in certain patients have the propensity to repair themselves more readily than others.

**RESULTS:** We found that vascular remodeling in retinopathy is associated with bouts of sterile inflammation and tardy recruitment of neutrophils, an immune population typically associated with a first wave of invading leukocytes. We observed that, after rapid proliferation, vascular endothelial cells in diseased blood vessels engaged molecular pathways shared with aging and cellular damage that lead to cellular senescence. Senescent vascular units then released a secretome of cytokines and factors that attracted neutrophils and triggered the production of neutrophil extracellular traps (NETs). Through extrusion of NETs, neutrophils eliminated diseased senescent vasculature by promoting its apoptosis. By crippling the ability of neutrophils to produce NETs by genetically removing the peptidyl arginine deiminase type IV (PAD4) enzyme, clearance of senescent cells was impaired and regression of pathological angiogenesis compromised. Similar effects were observed with the neutrophil-depleting antibody anti-Ly6G or by pharmacological inhibition of the neutrophil receptor CXCR2.

**CONCLUSION:** We conclude that neutrophils, through the release of NETs, targeted pathological senescent vasculature for clearance and thus prepare the ischemic retina for reparative vascular regeneration. These findings imply that elimination of senescent blood vessels leads to beneficial vascular remodeling. Although cellular senescence is not necessarily synonymous with aging, our study may provide insight into a general mechanism in which senescent endothelial cells trigger NETosis and predispose to thrombotic events such as myocardial infarction, atherosclerosis, and stroke, which are typically seen in older populations. ■



**Senescent blood vessels trigger neutrophil extracellular traps in retinopathy.** (A) Human samples and a mouse model were used to elucidate mechanisms of vascular remodeling in retinopathy. (B) Upon rapid proliferation, vascular cells in pathological tufts triggered pathways of cellular senescence, leading to cytokine secretion and the recruitment of neutrophils. (C) Factors secreted by senescent cells triggered NETosis. (D) NETs promoted the removal of senescent endothelial cells, ultimately leading to regression of pathological angiogenesis and promoting the regeneration of functional vessels.

The list of author affiliations is available in the full article online.

\*Corresponding author. Email: mike.sapielha@umontreal.ca (P.S.); fa.mallette@umontreal.ca (F.A.M.); js.joyal@umontreal.ca (J.-S.J.)  
Cite this article as F. Binet *et al.*, *Science* 369, eaay5356 (2020).  
DOI: 10.1126/science.aay5356

**S READ THE FULL ARTICLE AT**  
<https://doi.org/10.1126/science.aay5356>

## RESEARCH ARTICLE

## BIOMEDICINE

## Neutrophil extracellular traps target senescent vasculature for tissue remodeling in retinopathy

François Binet<sup>1,2</sup>, Gael Cagnone<sup>3,4</sup>, Sergio Crespo-Garcia<sup>1,2</sup>, Masayuki Hata<sup>1,2</sup>, Mathieu Neault<sup>2</sup>, Agnieszka Dejda<sup>1,2</sup>, Ariel M. Wilson<sup>1</sup>, Manuel Buscarlet<sup>2</sup>, Gaëlle Tagne Mawambo<sup>2</sup>, Joel P. Howard<sup>3</sup>, Roberto Diaz-Marin<sup>2</sup>, Celia Parinot<sup>1</sup>, Vera Guber<sup>1</sup>, Frédérique Pilon<sup>1</sup>, Rachel Juneau<sup>1</sup>, Rémi Laflamme<sup>1</sup>, Christina Sawchyn<sup>2</sup>, Karine Boulay<sup>2</sup>, Severine Leclerc<sup>3</sup>, Afnan Abu-Thuraia<sup>5</sup>, Jean-François Côté<sup>5</sup>, Gregor Andelfinger<sup>3</sup>, Flavio A. Rezende<sup>1</sup>, Florian Sennlaub<sup>6</sup>, Jean-Sébastien Joyal<sup>1,3,4,7\*</sup>, Frédéric A. Mallette<sup>2,8\*</sup>, Przemyslaw Sapieha<sup>1,2,9\*</sup>

In developed countries, the leading causes of blindness such as diabetic retinopathy are characterized by disorganized vasculature that can become fibrotic. Although many such pathological vessels often naturally regress and spare sight-threatening complications, the underlying mechanisms remain unknown. Here, we used orthogonal approaches in human patients with proliferative diabetic retinopathy and a mouse model of ischemic retinopathies to identify an unconventional role for neutrophils in vascular remodeling during late-stage sterile inflammation. Senescent vasculature released a secretome that attracted neutrophils and triggered the production of neutrophil extracellular traps (NETs). NETs ultimately cleared diseased endothelial cells and remodeled unhealthy vessels. Genetic or pharmacological inhibition of NETosis prevented the regression of senescent vessels and prolonged disease. Thus, clearance of senescent retinal blood vessels leads to reparative vascular remodeling.

The propensity of a tissue to rapidly repair and remodel after injury or in pathology dictates fitness and functional recovery. An example occurs in ischemic retinopathies such as retinopathy of prematurity (ROP) and diabetic retinopathy (DR). Collectively, these diseases are the primary causes of blindness in pediatric and working-age populations in developed countries, and for DR, affect >100 million people worldwide (1–6). Both diseases are characterized by an initial loss of retinal vascular supply and compromised nutrient and oxygen delivery (7–9). The ensuing tissue hypoxia-ischemia triggers the release of angiogenic and inflammatory factors that potentiate vascular growth (10). However, these neovessels fail to regenerate into the ischemic retina and are instead misdirected toward the vitreous part of the eye; they are leaky, senescent, and in severe instances, be-

come fibrotic and lead to blinding retinal detachment (3, 5, 11).

In ROP, the pathological vessels driving disease often regress and sight is spared (5, 6, 12). This is in part illustrated by the fact that patients with ROP often spontaneously recover and of the estimated 14,000 to 16,000 infants that are initially affected by ROP each year in the United States, ~90% do not necessitate treatment. Of the ~1500 infants that do require treatment, ~1/3 will become legally blind (12). In DR, spontaneous regression of neovascularization (NV) has been reported (13, 14), albeit less frequently given that upon diagnosis, standard of care calls for immediate pan-retinal photocoagulation (15), anti-vascular endothelial growth factor (anti-VEGF) therapy (16), or other treatments such that physiological regression is not readily monitored. The mechanisms mediating spontaneous regression and normalization of pathological retinal vessels in these conditions are poorly understood.

Physiological regression and remodeling of vascular networks occur during the transition from fetal to neonatal life in various tissues such as the hyaloid vasculature in the eye (17–19) and ductus arteriosus (20), as well as in the female reproductive system during endometrial maturation (21). Failure of proper vascular regression leads to diseases such as persistent fetal vasculature and familial exudative vitreoretinopathy (22), patent ductus arteriosus (23), and suboptimal reproductive performance (24). In pathology, less is known about the endogenous mechanisms that drive vascular remodeling. Anti-VEGF therapies in tumors either

induce apoptosis of endothelial cells (ECs) [reviewed in (25)] or normalize blood vessels by pruning tortuous, leaky vessels not covered by pericytes (26), allowing enhanced delivery of cytotoxic factors in combination therapies (27). Vascular remodeling is therefore an evolutionarily adaptive mechanism critical to development and regeneration after tissue injury. Here, we sought to understand how diseased retinal blood vessels remodel in retinopathies and consequently influence prognosis.

## Results

*Vascular remodeling in retinopathy is associated with sterile inflammation*

To investigate the mechanisms involved in pruning of pathological vasculature in retinopathies, we first used a mouse model of oxygen-induced retinopathy (OIR) (28) that yields ischemic avascular zones followed by preretinal NV similar to that observed in proliferative DR (PDR) and ROP (28). Mouse pups were exposed to 75% oxygen from postnatal day 7 (P7) to P12 to induce vaso-obliteration and returned to ambient air, where maximal preretinal NV occurs at P17, followed by a phase of vascular regression (Fig. 1A). To gain insight into the physiological processes occurring during NV (P12 to P17 of OIR), vascular remodeling and regression (from P17 of OIR), we first performed transcriptome analyses using bulk-RNA sequencing. Enrichment analysis using gene sets from the Gene Ontology (GO) Consortium at P14 of OIR revealed the highest expression of transcripts linked to endoplasmic reticulum homeostasis (Fig. 1B, left), which is consistent with previous findings (11, 29). At the tipping point from maximal pathological angiogenesis to normalization of vasculature at P17 of OIR, we observed transcript enrichment primarily in processes related to inflammation and, more precisely, activation of the innate immune system (P17 of OIR) (Fig. 1B, right).

To tease out the primary contributors of the sterile inflammatory response associated with vascular remodeling in the late stages of retinopathy, we heightened resolution by performing droplet-based single-cell RNA sequencing (Drop-seq) (30) of retinas during OIR. Principal components analysis and a t-distributed stochastic neighbor embedding (t-SNE) plot of different clustered retinal cell types with similar transcriptional profiles revealed the typical cell populations present in the retina, including neurons, glial cells, and vascular cells (Fig. 1C, left inset, and fig. S1A). Among the populations defined as immune cells, we identified five independent subclusters (Fig. 1C, middle inset). One subpopulation (cluster 3) was found to be especially enriched at P17 of OIR (Fig. 1C, right inset) and corresponded to disease-associated leukocytes defined using the SingleR tool (31) (fig. S1B). Gene-set variation analysis (GSVA) revealed that this group of

<sup>1</sup>Departments of Ophthalmology and <sup>2</sup>Biochemistry and Molecular Medicine, Maisonneuve-Rosemont Hospital Research Centre, University of Montreal, Montreal, Quebec HIT 2M4, Canada. <sup>3</sup>Departments of Pediatrics and <sup>4</sup>Pharmacology, Centre Hospitalier Universitaire Ste-Justine, University of Montreal, Montréal, Quebec H3T 1C5, Canada. <sup>5</sup>Institut de Recherches Cliniques de Montréal, University of Montreal, Montreal, Quebec H2W 1R7, Canada. <sup>6</sup>Institut National de la Santé et de la Recherche Médicale, U 968 Paris F-75012, France. <sup>7</sup>Department of Pharmacology and Therapeutics, McGill University, Montreal, Quebec H3A 2B4, Canada. <sup>8</sup>Department of Medicine, Maisonneuve-Rosemont Hospital Research Centre, University of Montreal, Montreal, Quebec HIT 2M4, Canada. <sup>9</sup>Department of Neurology-Neurosurgery, McGill University, Montreal, Quebec H3A 2B4, Canada.

\*Corresponding author. Email: mike.sapieha@umontreal.ca (P.S.); fa.mallette@umontreal.ca (F.A.M.); js.joyal@umontreal.ca (J.-S.J.)



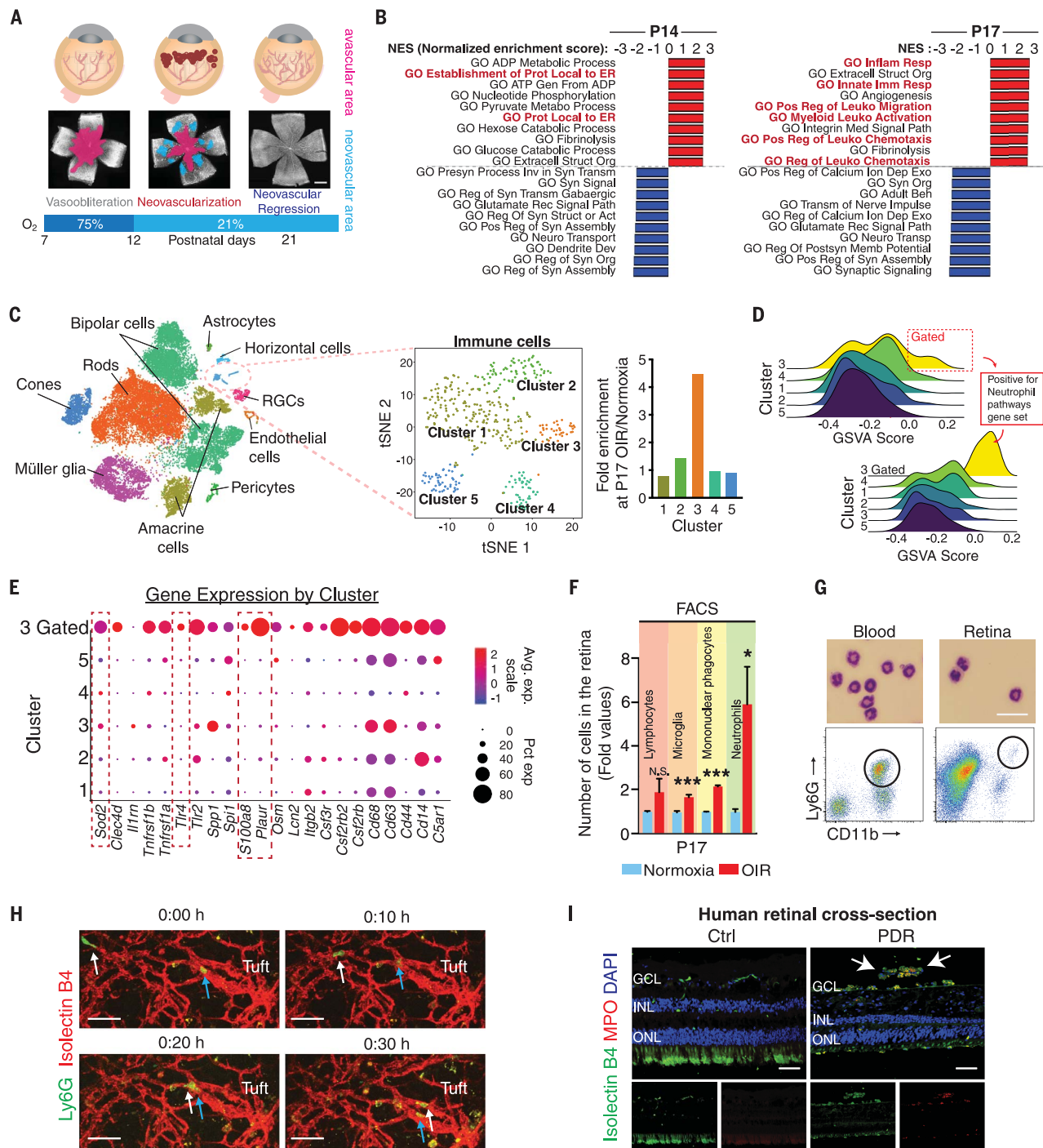


**Fig. 1. Vascular remodeling in retinopathy is associated with sterile inflammation and the presence of neutrophils.** (A) Schematic of the mouse OIR model. Exposure to hyperoxic conditions (75% O<sub>2</sub>) in mice from P7 to P12 induces an initial phase of vascular dropout (pink). Upon return to room air at P12, ischemia triggers pathological preretinal NV that peaks at P17 (blue). From P17 to P21, preretinal NV regresses. (B) Hierarchical clustering of GO gene sets for RNA-seq from OIR and normoxic mouse retinas at P14 or P17 ( $n = 2$  to 3 mice per condition). [(C), left inset] t-SNE for single-cell RNA-seq of retinal cells from normoxic and OIR retinas at P14 and P17 (from two normoxic and three OIR sets of data) and subclustering of immune cells reveal five distinct cell populations. Each dot represents one cell. [(C), right inset] Cluster 3 displays a 4.5-fold enrichment in cells in OIR compared with normoxic controls, with positive GSEA score enrichment for genes classically found in neutrophils (D). (E) Dot plot representing expression level and frequency

among cell clusters for neutrophil-related genes in each of the five populations identified in (C) as well as the neutrophil-enriched population gated from cluster 3 as performed in (D). (F) Accretion in OIR of lymphocytes, microglia, mononuclear phagocytes, or neutrophils assessed at P17 by FACS (see gating strategy in fig. S4) ( $n = 3, 6$  to 9 mice/group). (G) The presence of neutrophils was evaluated by sorting Ly6G<sup>+</sup>/CD11b<sup>+</sup>/F4/80<sup>+</sup> cells from OIR retinas and staining with Giemsa ( $n = 5$  mice). (H) Live-cell tracking by confocal microscopy identifies neutrophils (see arrows) migrating toward a preretinal tuft in P17 OIR retinas representative of three separate experiments. (I) Retinal cross sections from human patients with PDR showing invasion of MPO<sup>+</sup> neutrophils [(I), right inset], which are absent from control patients [(I), left inset]. Scale bars: (A), 500  $\mu$ m; (G), 20  $\mu$ m; (H), 50  $\mu$ m; (I), 100  $\mu$ m. ONL, outer nuclear layer; INL, inner nuclear layer; GCL, ganglion cell layer. For (F), \* $P < 0.05$ , \*\*\*  $P < 0.001$ , Student's  $t$  test. Data are shown as means  $\pm$  SEM.

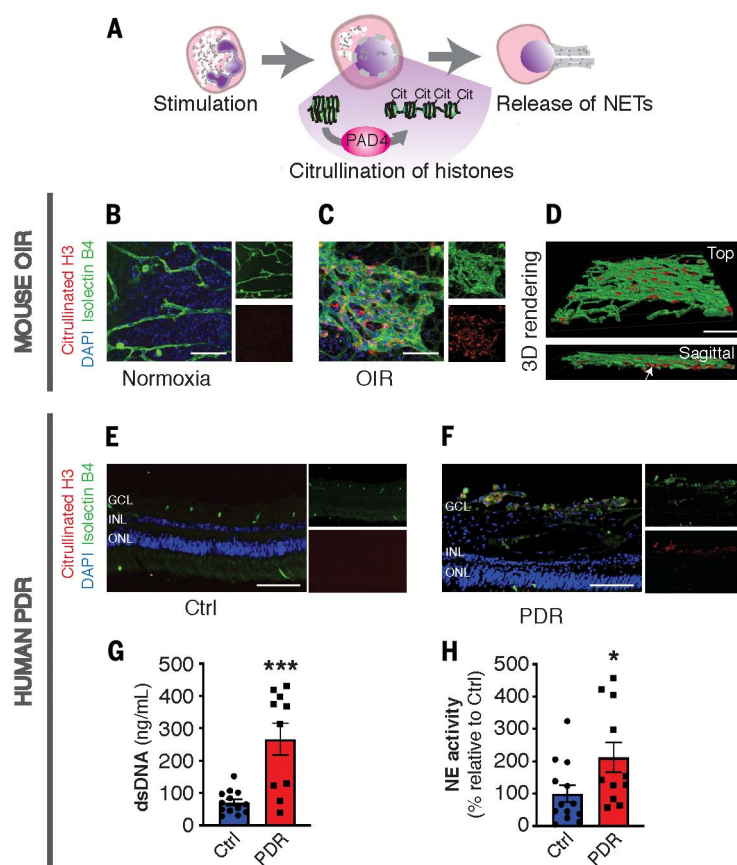


**Fig. 2. NETs are found on vascular tufts.** (A) Production of NETs is mediated by the enzymatic activity of PAD4, which citrullinates histones to allow relaxation and extracellular release of nuclear DNA. (B and C) Representative confocal micrographs of retinal flat mounts at P17 with immunofluorescence for citrullinated histone H3. NETs are absent from normoxic retinas (B) and present in retinas after OIR (C) (results are representative of three separate experiments). (D) Three-dimensional rendering of NETs in retinas at P17 of OIR. Immunofluorescence for citrullinated histone H3 in human retinal cross sections reveals selective staining in retinal vessels (isolectinB4-stained) of a patient with PDR compared with a patient with no known vascular pathology (E and F). dsDNA was ~3.7-fold higher (G) and neutrophil elastase (NE) activity was ~2.1-fold higher (H) in the vitreous of patients with PDR compared with controls with nonvascular pathology ( $n = 13$  controls and 11 PDR patients; see Table 1 for patient details). \* $P < 0.05$ . \*\*\* $P < 0.001$ , Student's  $t$  test. Scale bars: (B) to (D), 50  $\mu\text{m}$ ; (E) and (F), 100  $\mu\text{m}$ . Data are shown as means  $\pm$  SEM.

activated leukocytes contained a fraction of cells with enhanced expression of the biological pathways traditionally found in neutrophils (Fig. 1, D and E, and fig. S1C) and expressed inflammatory neutrophil-associated genes such as *Sod2*, *S100a8*, *Tlr4*, and *Plaur* (Fig. 1E).

To verify these findings, we designed specific gene sets to investigate the main effectors of the innate CNS immune response, microglia, macrophages, and neutrophils, with bulk RNA sequencing, and used curated GO gene sets specific for leukocyte functions such as migration or activation (figs. S2 and S3, respectively). Gene-set enrichment analysis (GSEA) revealed a strong positive correlation at P17 of OIR in gene clusters associated with microglia [normalized enrichment score (NES) = 2.018; false discovery rate (FDRq) = 0.000], mono-

nuclear phagocytes (NES = 2.067; FDRq = 0.000), as well as neutrophils (NES = 2.257; FDRq = 0.000) (fig. S2), consistent with the potential presence of neutrophils at a time when regression of pathological vasculature occurs.

#### Neutrophils invade sites of pathological vasculature in humans and mice

Although microglia, monocytes, and mononuclear phagocytes have been well studied in retinal sterile inflammation during retinopathy (32–34), the contribution of neutrophils is ill-defined. Unlike macrophages and microglia, neutrophils are typically associated with the initial phases of inflammation. However, we observed neutrophil-related transcripts in the late stages of disease when pathological vasculature resolves. Neutrophils have relatively low transcriptional activity, so we sought to

determine their presence in the retina using complementary approaches. First, fluorescence-activated cell sorting (FACS) analysis showed that neutrophils ( $\text{CD45}^+/\text{CD11b}^+/\text{Ly6C}^{\text{int}}/\text{Ly6G}^{\text{high}}$ ) were robustly increased in the retina at P17 of OIR (~6-fold; Fig. 1F and fig. S5A; also see fig. S4 for the gating strategy). Other myeloid populations were also increased in OIR, such as mononuclear phagocytes (~2.2-fold) and microglia (~1.7-fold), but not lymphocytes (Fig. 1F). Moreover, a time-course assessment by FACS over the duration of OIR revealed that neutrophils specifically arrived at P17 when vascular regression was initiated (fig. S5B).

This population of cells was sorted and stained with Giemsa, and displayed polymorphonuclear structures characteristic of neutrophils (Fig. 1G). We then performed a myeloperoxidase (MPO) assay to detect the enzymatic activity of neutrophils. MPO is a heme-based peroxidase enzyme found at high levels in the primary granules of neutrophils (35). Consistent with our data, a robust increase in MPO enzymatic activity was observed at P17 of OIR compared with normoxic controls (fig. S5C). In addition, immunostaining for MPO revealed a preferential localization of neutrophils to neovascular tufts but was almost absent outside of tufts or in healthy normoxic retinas (fig. S5D). We also used ex vivo live confocal-imaging microscopy to track intraretinal neutrophils after intravenous infusion of a  $\text{Ly6G}^+$  antibody. Neutrophils were found to be migrating toward neovascular tufts in retinas from pups at P17 of OIR (Fig. 1H and movie S1). Finally, immunostaining of cross sections of eyes from human patients with PDR using an antibody raised against MPO detected neutrophils in the proximity of neovascular tufts, confirming their presence in human pathology (Fig. 1I).

#### NETs are released on pathological retinal vasculature in humans and mice

Given the potential role of neutrophils in sterile inflammation (36), as well as their presence at the onset of vascular remodeling (Fig. 1), we investigated how these cells influence vascular remodeling. One of the potential features of neutrophils is their ability to exude extracellular traps. Neutrophil extracellular traps (NETs) are primarily described as being deployed to sequester against invading bacteria and fungi through a mesh of DNA decorated with granular proteins (MPO, elastase, and cathelicidin) (37). The extrusion of NETs is dependent on the citrullination of histones by the peptidyl arginine deiminase type IV (PAD4) enzyme and decondensation of the chromatin (38) (Fig. 2A). In addition to their bactericidal properties, NETs have also been documented in sterile inflammation in cases of atherosclerosis (39) or ischemia-reperfusion injury (40). We therefore sought



Table 1. Clinical characteristics of patients who underwent vitreous biopsy.

Pathology	Sex	Age*	Diabetes	
			Type	Duration (y)
Control patients				
MH	M	71	-	-
MH	F	76	-	-
MH	F	74	-	-
ERM	F	46	-	-
ERM	F	84	-	-
ERM	F	77	-	-
ERM	M	57	-	-
MH	M	82	-	-
MH	M	65	-	-
ERM	F	69	-	-
ERM	M	69	-	-
ERM	M	81	-	-
MH	F	65	-	-
Diabetic patients				
PDR	F	56	NA	NA
PDR	M	80	NA	28
PDR	M	74	II	NA
PDR	F	72	NA	NA
PDR	M	35	NA	NA
PDR	M	36	II	NA
PDR	F	70	II	40
PDR	F	74	NA	35
PDR	F	67	II	30
PDR	M	69	II	4
PDR	M	45	II	NA

MH, macular hole; ERM, epiretinal membrane; NA, not available

\*Mean age for control patients, 70.5 ± 2.9 years; mean age for diabetic patients, 61.6 ± 4.8 years.

to determine whether NETs were found in retinas during the phases of vascular remodeling when neutrophil levels are elevated. We performed immunofluorescence against citrullinated histone H3 on retinas from mice at P17 of OIR and detected NETs adjacent to pathological neovascular tufts (Fig. 2, B to D), but they were absent from normoxic controls. These structures colocalized with MPO, a neutrophil marker and a constituent of NETs (fig. S6, A and B).

Next, we sought to determine whether our findings in mice held in humans with pathological retinal vasculature. We investigated the presence of NETs in patients with PDR. Immunofluorescence on retinal cross sections from control patients with no identified vascular pathology did not show any evidence of citrullinated histone H3 (Fig. 2E). Conversely, citrullinated histone H3 was detected in preretinal ECs (isolectin B4-stained) of individuals with PDR (Fig. 2F). Patients with PDR showed protrusion of vessels at the vitreoretinal interface characteristic of preretinal NV as determined by spectral domain optical coherence tomography (fig. S6C, white arrow). To further

verify the presence of NETs in diabetic patient retinas, we analyzed the vitreous humor from patients with PDR for the presence of double-stranded DNA (dsDNA) that could be released secondary to NET production. Concentrations of dsDNA in the vitreous humor of patients with PDR were significantly higher compared with controls with nonvascular pathology such as idiopathic epiretinal membrane or macular hole (Fig. 2G). Moreover, we also detected significantly higher levels of elastase activity (associated with NET production) (41) in the vitreous humor of patients with PDR (see Table 1 for patient characteristics and Fig. 2H). Thus, NETs are associated with retinal vascular disease in mice and humans and are found at sites of pathological angiogenesis.

**Neuronal and vascular units have distinct patterns of cellular senescence and secretory phenotypes in OIR**

We next sought to elucidate the stimulus for NETosis in pathological retinal vasculature. ECs in preretinal NV as well as retinal ganglion cell (RGCs) undergo cellular senescence in OIR (17). Using GSVA on single-cell transcriptomic data

for gene sets related to cellular senescence and two gene sets related to secretory processes, we found that neurons such as RGCs were senescent but did not readily display a classical transcriptional signature of the senescence-associated secretory phenotype (SASP) and did not transcribe genes related to cytokine secretion (Fig. 3A). By contrast, ECs (green box), pericytes, astrocytes, Müller glia, and immune cells up-regulated transcripts were related to cellular senescence and triggered a SASP (Fig. 3A).

SASP expression plotted on t-SNE from retinal populations at P17 of OIR (Fig. 3, B and C), as well as hierarchical comparison of genes for the SASP (Fig. 3D), showed that astrocytes, ECs, Müller glia, and pericytes adopted a robust SASP transcriptional signature. Thus, whereas several cell populations of the retina undergo cellular senescence in retinopathy, non-neuronal and neuronal populations adopt different secretory transcriptional signatures.

**Senescent vascular endothelium triggers the release of NETs**

NETs (visualized with extracellular citrullinated H3) were regularly found adjacent to senescent isolectin-positive ECs [stained for promyelocytic leukemia (PML) protein, a key regulator of cellular senescence (42, 43)] (Fig. 4A and fig. S7A), as well as in NG2<sup>+</sup> pericytes (fig. S7B), but not in Müller cells or astrocytes [both positive for glial fibrillary acidic protein (GFAP); fig. S7C]. Thus, because several known factors of the SASP overlap with reported inducers of NETs (fig. S8), we investigated whether NETs could be triggered by senescent vascular ECs.

Classical triggers of cellular senescence include DNA damage, telomere attrition, mitochondrial dysfunction, and oncogene activation as in oncogene-induced senescence (44). The latter can be induced by various oncogenes, including sustained activation of the GTPase RAS (45), which triggered senescence through the DNA damage response and activation of p53 (46–48). We observed robust activation of the RAS pathways within preretinal pathological angiogenic sprouts either by immunostaining for phospho-ERK1/2 (a kinase downstream of RAS) (Fig. 4B and fig. S9A) or GSVA of single-cell transcriptomics (Fig. 4C). The bimodal enrichment for KRAS-associated pathways in ECs (Fig. 4C) suggested a distinct population of cells, with those in neovascular tufts likely showing higher activation (right peak) and less proliferative ECs showing lower activation (left peak). Indeed, these high-RAS ECs (red square) were not found in normoxic control retinas (fig. S9B), which suggested that senescent cells might coincide with neovascular tufts. Normoxic control retinas also showed inferior levels of RAS activation compared with those in OIR. To investigate which subsets of cells interacted with KRAS<sup>+</sup> cells in retinopathy, we performed CellPhoneDB analysis, a bioinformatics tool that

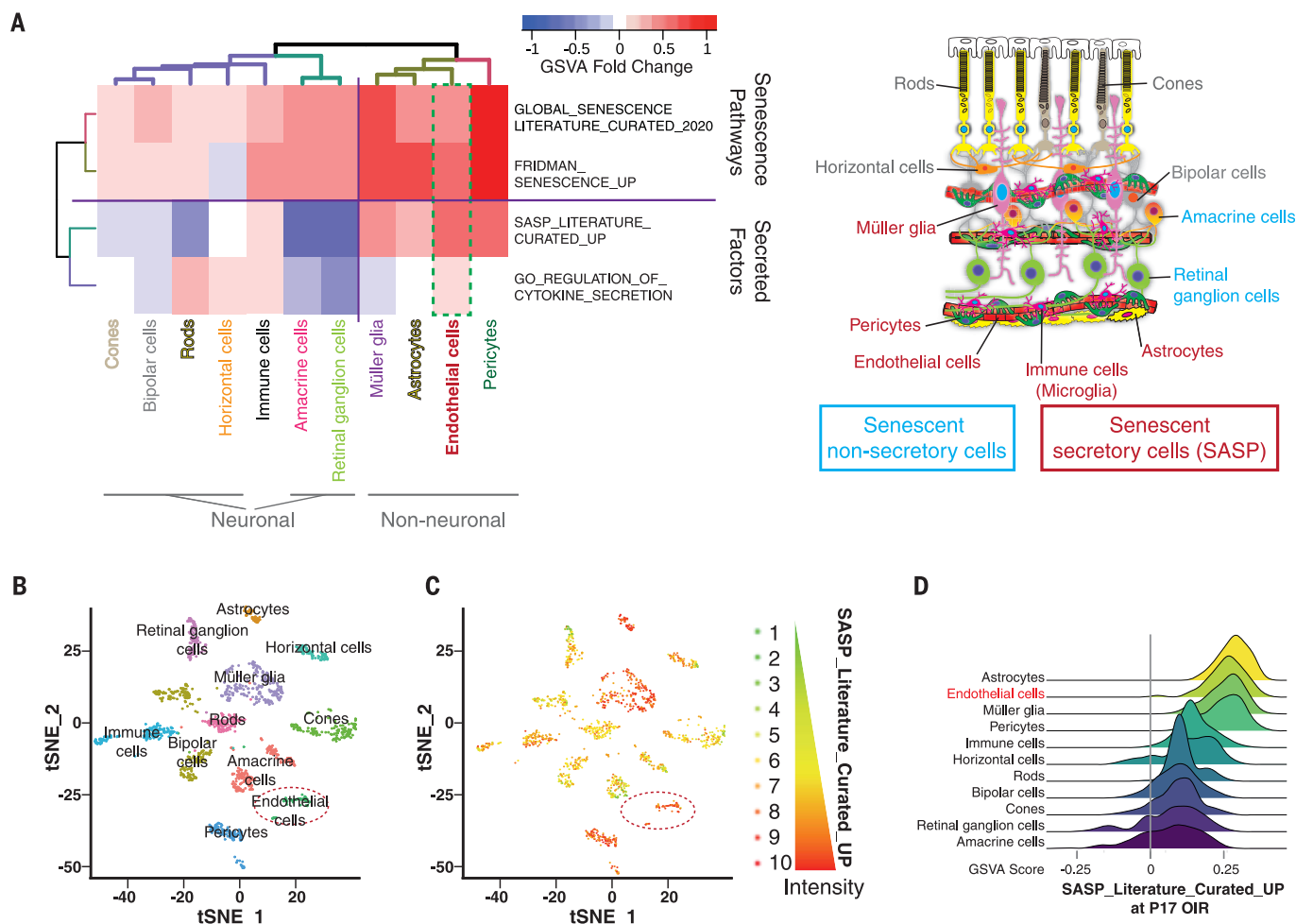


**Fig. 3. Neurons and mitotic cells display distinct gene signatures of cellular senescence in retinopathy.** (A) Fold change of GSVA score on gene sets related to cellular senescence and cytokine secretion comparing transcripts from scRNAseq of P17 normoxic and OIR retinas. (B and C) t-SNE and

(D) hierarchical clustering of cell populations from P17 retinas ranked by absolute GSVA score reveals that in OIR, astrocytes, ECs, Müller glia, and pericytes induce a SASP response compared with other cell types. Data presented were downsized to display a maximum of 1000 cells per retinal cell type.

builds cell-cell communication networks using ligand-receptor information from available single-cell transcriptomic data (49). We observed increased interactions between cluster 3 (shown to contain neutrophils; Fig. 1, C and E) and KRAS<sup>+</sup> ECs (Fig. 4D). Lower numbers of interactions were found with nonsenescent ECs. These data support the idea that neutrophils interact with senescent ECs in retinopathy.

RAS activity is elevated in active preretinal NV (50), and the expression of  $\gamma$ H2AX and PML (key modulators of RAS-induced senescence) is observed in pathological ECs during retinopathy (17). To explore the mechanism by which senescent ECs trigger NETs, we generated a model of cellular senescence in human umbilical vein endothelial vascular cells (HUEVCs) by sustained activation of the RAS pathway. Activation of RASV12 leads to a strong mitogenic signal driven by the Raf-MEK-ERK pathway, leading to a DNA damage checkpoint response, cell cycle arrest, and then senescence

(46, 47). RASV12 activation was verified (fig. S10, A to C) and induction of cellular senescence in ECs confirmed using senescence-associated  $\beta$ -galactosidase staining (SA- $\beta$ -Gal) 10 days after infection ( $67 \pm 10\%$  for RASV12-infected cells versus  $3 \pm 3\%$  for the empty vector) (fig. S10D).

To determine whether senescent ECs were able to provoke the release of NETs, we seeded senescent as well as proliferating ECs into multiwell chambers and then introduced freshly isolated human blood neutrophils colored by DiI Red to EC cultures the following day and stained with a dye labeling extracellular DNA (SYTOX Green). Time-lapse imaging revealed a modest release of extracellular DNA from neutrophils incubated with control ECs (empty vector) (Fig. 4, E and F). By contrast, neutrophils discharged loads of DNA in the presence of senescent ECs (Fig. 4, E and F). Conditioned media from RAS-overexpressing senescent ECs was sufficient to trigger NET release, suggest-

ing that a soluble factor secreted during cellular senescence was mediating NET release (Fig. 4E).

To identify factors produced by senescent cells that trigger NETosis, we performed SILAC (stable isotope labeling using amino acids in cell culture). Senescent or proliferating HUEVCs were labeled with either light or heavy arginine and lysine 13C6 and 15N2 (fig. S11A). Secreted proteins released from empty vector-transduced cells were mixed in equal proportion to those from RASV12-infected HUEVCs. The relative abundance of identified peptides was calculated after mass spectroscopy (MS)/MS analysis and MaxQuant postanalysis. We clustered the proteomic data using the Reactome database (51) and found that the secretome of senescent ECs was primarily enriched in proteins related to immune pathways (Fig. 4G), including proteins involved in cytokine signaling (Fig. 4H). These SILAC data were corroborated by the secretome of IMR90 senescent



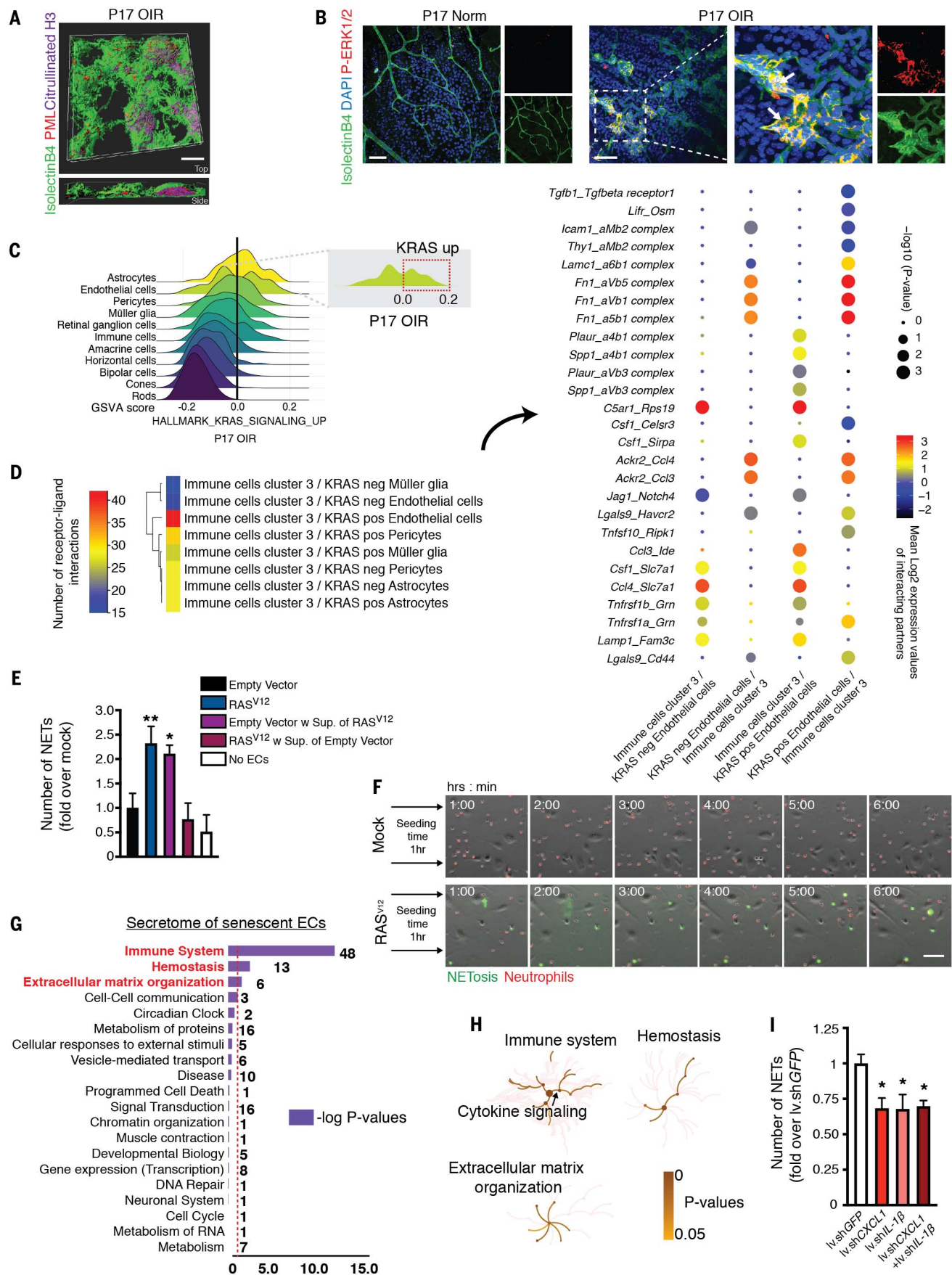


**Fig. 4. Senescent ECs trigger NETosis.** (A) Representative confocal micrograph and three-dimensional reconstruction of PML and citrullinated histone H3 at P17 of OIR. PML is mainly expressed on retinal tufts and often colocalizes with NETs (citrullinated histone H3 staining) ( $n = 3$  separate experiments). (B) Increased phosphorylation of ERK1/2 is observed by immunofluorescence in P17 OIR retinas compared with normoxic controls. Results shown are representative of three experiments. (C) Ridge plots of GSVA score for KRAS-associated transcriptional signatures of single-cell RNAseq of retinas at P17 OIR reveal enrichment primarily in astrocytes, ECs, and pericytes. Inset, ECs display bimodal distribution for KRAS-associated gene set expression. (D) CellPhoneDB analysis predicts increased interaction between immune cells of cluster 3 and KRAS<sup>+</sup> ECs gated on GSVA score [see inset in (C)]. Data are expressed as the total number of ligand-receptor interactions between immune cell cluster 3 and KRAS gated retinal cell type (see heatmap in left inset). These interactions are displayed for ECs and immune cell cluster 3 in an array of ligand-receptor couples (see dot plot in right inset), with dot color and size representing the strength and significance of the predicted interaction between cell types. (E) Quantification of NETs in (F) shows a >2-fold induction of NETosis with RAS<sup>V12</sup>-transduced cells or empty vector-infected cells with

supernatant from RAS<sup>V12</sup>-infected cells (empty vector w Sup. of RAS<sup>V12</sup>) compared with empty vector-infected cells ( $n = 3$  experiments). (F) Representative time course of human neutrophils stained with Dil Red and coincubated with RAS<sup>V12</sup>-expressing HUVECs. NETosis was visualized with SYTOX Green ( $n = 3$  experiments). (G) SILAC-based MS-MS analysis of proteins up-regulated at least 1.5-fold and analyzed through the Reactome database shows primary enrichment in peptides related to immune system regulation in RAS<sup>V12</sup>-infected senescent ECs compared with mock-infected controls. Numbers in adjacent bars represent the quantity of connections found. Top three nodes (bold) have an FDR < 0.05 (from two independent sets of labeled proteins). (H) Overrepresentation analysis showing pseudocolored nodes according to their  $P$  values. Cytokine signaling pathways are enriched in proteins from senescent RAS<sup>V12</sup>-infected ECs (black arrow). Darker colors represent nodes with lower  $P$  values (higher activation). (I) Targeted depletion of CXCL1, IL-1 $\beta$ , or both by Lv.shRNAs in RAS<sup>V12</sup>-transduced senescent ECs significantly decreases NETosis ( $n = 3$  separate experiments). Scale bars: (A) and (B), 50  $\mu$ m; (F), 20  $\mu$ m. For (E) and (I), one-way ANOVA with Bonferroni's test was used (\* $P < 0.05$ , \*\* $P < 0.01$ ). Data are shown as means  $\pm$  SEM.

fibroblasts (52), which shared the same top three enrichment clusters of immune regulation, hemostasis, and extracellular matrix reorganization (fig. S11B). On the basis of enrichment in cytokine signaling, we confirmed by real-time quantitative polymerase chain reaction (PCR) increased transcription of cytokines such as interleukin 1 $\beta$  (IL-1 $\beta$ ) or CXCL1 in RASV12-infected HUVECs (fig. S12A). To determine whether these cytokines contribute to NETosis, we generated HUVECs depleted for IL-1 $\beta$ , CXCL1, or both cytokines through lentiviral transduction of short hairpin RNAs (shRNAs) (fig. S12, B and C). Down-regulation of either IL-1 $\beta$  or CXCL1 in senescent cells led to a significant reduction in NETosis (Fig. 4I). Combined knock-down of IL-1 $\beta$  and CXCL1 did not further reduce NETosis, suggesting potential redundancy (Fig. 4I). Therefore, senescent ECs release cytokines as part of their SASP (53), which prompts neutrophils to release NETs.

#### NETs remodel retinal vasculature through apoptotic elimination of senescent ECs

Typically, cellular senescence and apoptosis are mutually exclusive cell fates. However, NETs can be cytotoxic for ECs (54, 55). In OIR retinas undergoing pruning of pathological vasculature, we noted higher numbers of apoptotic ECs (IB4<sup>+</sup> cells; Fig. 5A). Apoptotic ECs were confined to areas of pathological NV (tufts) and absent from areas outside tufts or normoxic control retinas (Fig. 5A and fig. S13). Given that senescent pathological neovasculature regresses after P17 in mouse OIR, we investigated whether NETs projected onto pathological neovasculature could influence clearance of senescent ECs (IB4<sup>+</sup> cells) in OIR. We injected DNase I into the vitreous humor of mice at P17 of OIR to promote degradation of NETs (as confirmed by immunohistological staining; fig. S14) and then analyzed the area of retinal SA- $\beta$ -Gal activity at P19. Injections of DNase I stalled the clearance of senescent cells, as seen by an enhanced proportion of SA- $\beta$ -Gal<sup>+</sup> area

in the retina at P19 of OIR (Fig. 5B). Correspondingly, DNase I treatment resulted in persistence of the senescence-associated genes *Pail* (*Serpine1*) and IL-1 $\beta$  in the retina (Fig. 5C). To investigate the role of PAD4, an essential enzyme for NETosis (56), we generated a Pad4-deficient mouse within the myeloid compartment by crossing mice expressing the Cre enzyme under the LysM promoter with mice harboring loxP sites flanking the *Pad4* gene (fig. S15A). LysM was expressed by >95% of neutrophils, as confirmed by FACS analysis (fig. S15B). Efficient diminution of PAD4 levels in LysM-cre<sup>+/+</sup>*Pad4*<sup>-/-</sup> mice was confirmed by immunoblot on mouse blood neutrophils (fig. S15C). Impeding NETosis through genetic ablation of myeloid-resident Pad4 resulted in a persistence of senescent ECs at P19 of OIR, as determined by senescence-associated markers such as PML in retinal tufts (Fig. 5D). Exposing RASV12-infected senescent ECs to NETs isolated from activated neutrophils resulted in a dose-dependent cleavage of caspase-3, suggesting that NETs could trigger apoptosis of senescent ECs (Fig. 5E). EC apoptosis upon exposure to NETs was confirmed by annexin V staining (Fig. 5F).

#### NETs participate in clearing pathological retinal vasculature

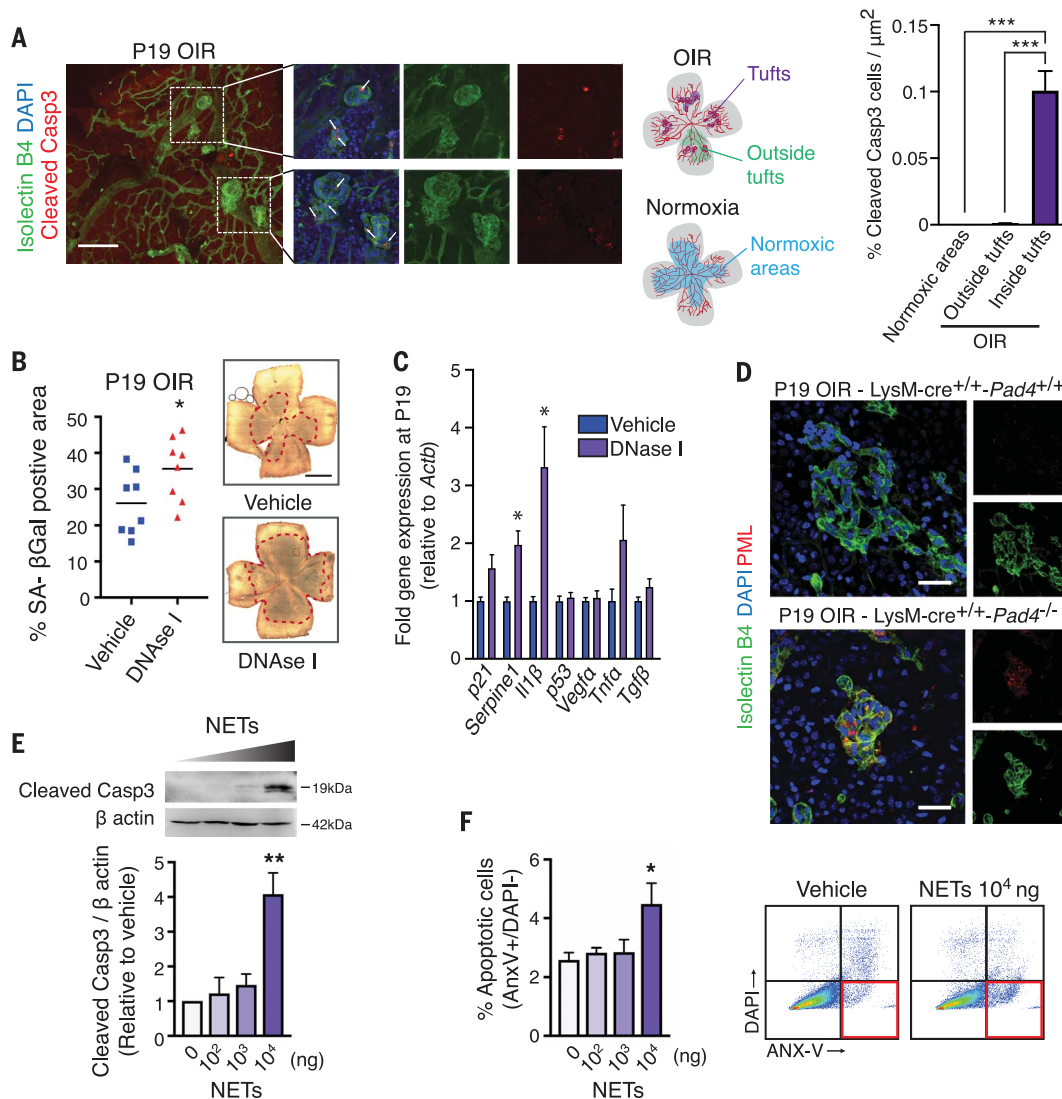
Finally, we investigated the consequences of abrogating NETosis on NV in ischemic retinopathies. First, we injected DNase I into the vitreous humor of mice subjected to OIR with the aim of degrading NETs (57) either during (P15) or after (P17) vascular tuft formation. We also used a complementary approach involving a neutrophil-depleting antibody (anti-Ly6G) (58), which abrogated neutrophils in both blood and retinas of mice without affecting other leukocyte populations (see assessment by FACS shown in fig. S16, A and B). The status of the retinal vasculature was assessed 2 days after injection for the extent of pathological preretinal angiogenesis (neovascular area) and the

extent of vascular regeneration (avascular area). These two parameters can be interdependent, with regression of neovascularization influencing the rate of revascularization (59). Treatment with either DNase I or anti-Ly6G during the phase of vascular proliferation at P12 or P15 did not influence NV (fig. S17, A and C), nor did it stimulate revascularization of avascular zones of the retina (fig. S17, B and D), compared with vehicle or isotype controls. By contrast, when DNase I or anti-Ly6G were injected at P17 of OIR during peak NV, pathological NV persisted (Fig. 6A) and vascular regeneration was impeded as assessed at P19 (Fig. 6B). Thus, various approaches to prevent NETosis in OIR by either depleting neutrophils or enzymatic removal of NETs with DNase I stalled regression of pathological vessels and consequently prevented the regeneration of functional blood vessels into the ischemic retina.

To corroborate these findings, we used cre-LysM<sup>+/+</sup>*Pad4*<sup>-/-</sup> mice. As described above, we evaluated the propensity of these mice to clear pathological NV and influence vascular regeneration in OIR. The absence of myeloid-resident PAD4 did not influence the onset or development of preretinal NV (Fig. 6C), nor did it affect vascular regeneration as assessed at P17 of OIR (Fig. 6D). However, as with the interventional approaches described above (Fig. 6, A and B), deficiency in myeloid-resident PAD4 compromised the regression of pathological preretinal blood vessels (Fig. 6E) while consequently preventing regrowth of functional vessels (Fig. 6F) as determined at P19 OIR. Similarly, inhibition of either IL-1 $\beta$  signaling with IL-1 receptor antagonist (Kineret) or CXCL1 signaling with the CXCR2 inhibitor SB265610 at the time of maximal NV (P17) reduced remodeling of pathological vasculature as determined at P19, further supporting the importance of inflammatory cytokines in mediating the clearance of pathological neovasculature (fig. S18, A to D). Inhibition of IL-1 $\beta$  before NV (P15) prevented pathological



**Fig. 5. NETs clear senescent ECs by inducing apoptosis.** (A) (Left inset) Cleaved caspase-3<sup>+</sup> apoptotic cells (white arrows) are found in P19 OIR flat mounts and colocalize with isolectin-B4<sup>+</sup> ECs almost exclusively in neovascular tuft areas (right inset) ( $n \geq 3$  separate experiments). (B) Intravitreal injection of DNase I at P17 of OIR results in persistence of SA- $\beta$ -Gal<sup>+</sup> senescent cells and (C) mRNA transcripts for certain SASP factors at P19 (both  $n = 3$  separate experiments). (D) PML<sup>+</sup> senescent cells persist in LysM-cre<sup>+/+</sup>Pad4<sup>-/-</sup> retinas at P19 of OIR as opposed to LysM-cre<sup>+/+</sup>Pad4<sup>+/+</sup> controls (results shown are representative of three separate experiments). (E) (Top) Immunoblots showing a dose-dependent induction of active cleaved caspase-3 protein in RAS<sup>V12</sup>-infected senescent HUVECs upon incubation with escalating doses of NETs with a sharp rise with  $10^4$  ng. (Bottom) Densitometric analysis of caspase-3 protein expression reveals an ~4-fold induction of cleaved caspase-3 expression with  $10^4$  ng of NETs ( $n = 3$  independent experiments). (F) Incubation of RAS<sup>V12</sup>-infected senescent HUVECs with  $10^4$  ng of NETs provokes 1.7-fold more apoptosis as assessed by annexin V surface staining ( $n = 4$  different experiments). For (B) and (C), Student's  $t$  test was used ( $*P < 0.05$ ); for (E) and (F), one-way ANOVA with Bonferroni's test was used ( $*P < 0.05$ ,  $**P < 0.01$ ). Scale bars: (A) and (D), 200  $\mu$ m; (B), 1 mm. Data are shown as means  $\pm$  SEM.



angiogenesis (fig. S18, E and F), as expected (60, 61). Therefore, neutrophils, through the release of NETs, target pathological senescent ECs for clearance and prepare the ischemic retina for reparative vascular regeneration.

## Discussion

Complex tissues of the central nervous system, consisting predominantly of postmitotic cells such as the retina and the brain, require an inherent ability to rapidly adjust to environmental stressors or to rapidly remodel after injury. Here, we tested two concepts pertaining to vascular remodeling in ischemic retinopathies. First, we investigated the idea that neutrophils, which are classically associated with a first wave of invading leukocytes, are also involved in late stages of the sterile inflammatory response during retinal vascular remodeling. Second, we investigated whether neutrophils responding to the secretome of

senescent ECs and likely other cells of the vascular unit and through extrusion of NETs eliminate diseased vasculature by triggering its apoptosis. Clearance of pathological blood vessels is a key step for tissue repair and resolution of inflammation in ischemic retinopathies and enables tissue remodeling. Conceptually, the selective removal of ECs that have engaged pathways shared with aging and cellular damage suggests an origin for programs of cellular senescence in ensuring tissue fitness. Diseased cells discharge a SASP, favoring their clearance and later restoration of functional vascular networks. Postmitotic neurons such as RGCs, which undergo postmitotic cellular senescence during OIR (62), do not readily engage a classical SASP transcriptional gene signature, suggesting that they would evade targeting by immune cells.

Cellular senescence is a dynamic response to various stressors including oxidative dam-

age, telomere attrition, ischemia, metabolic imbalances, activated oncogenes, and chemotherapy (62, 63). Pathways that lead to cellular senescence are potent tumor-suppressive mechanisms and limit the division and spread of premalignant cells (64). Moreover, in response to the secretion of immunomodulatory factors of the SASP (52), senescent cells prime neighboring cells for reprogramming (65–67) while allowing for clearance of malignant cells as part of an intrinsic program to stall tumor development and fibrosis (68–70). Collectively, these mechanisms set the stage for tissue repair and remodeling (63, 66, 67) and are consistent with the processes engaged to clear pathological vasculature in the retina (71, 72).

To date, the removal of senescent cells by the immune system has been ascribed to natural killer (NK) cells, which use the NK2GD receptor (68–70, 73) and macrophages during, for example, salamander limb regeneration (74)

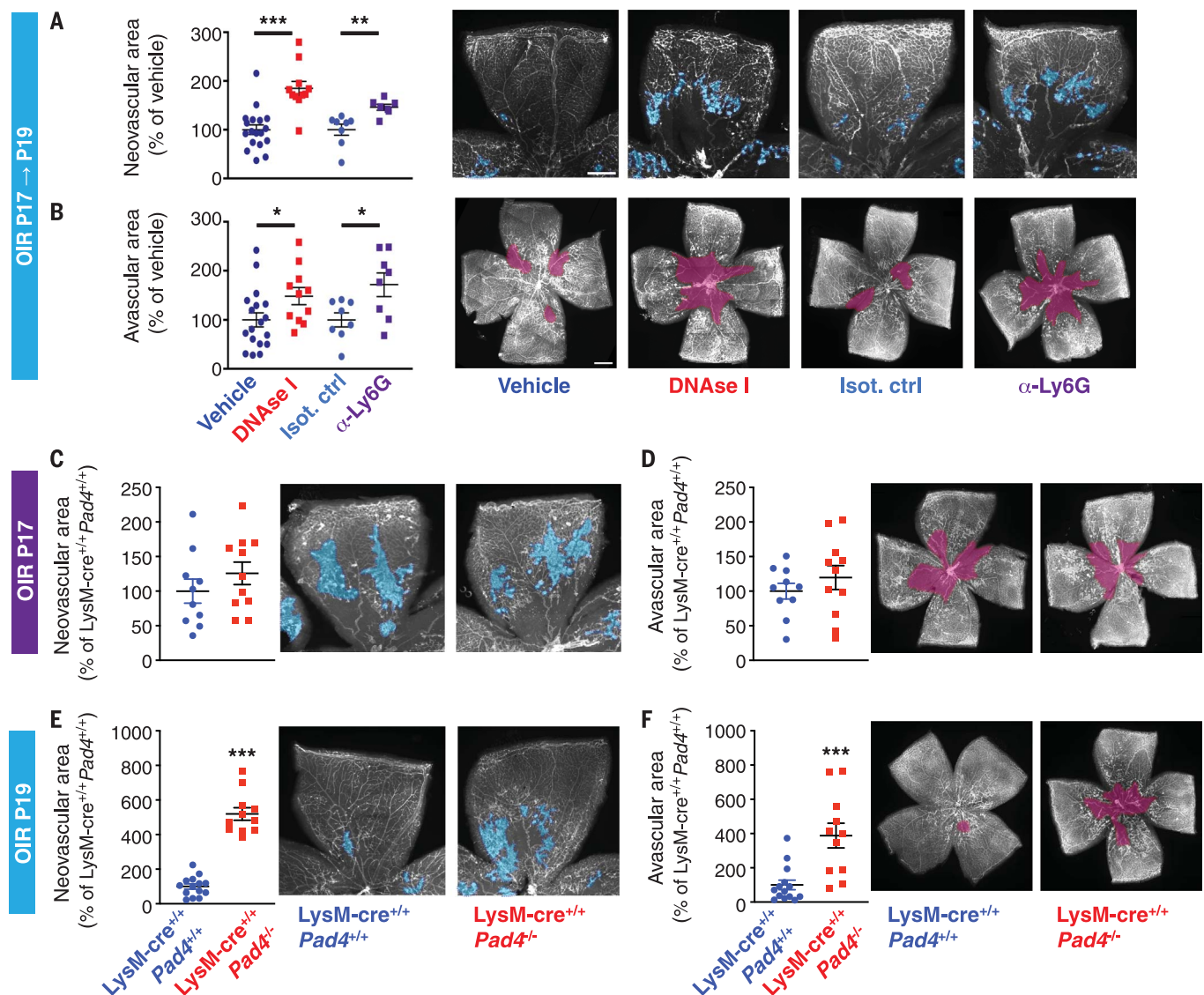


**Fig. 6. NETs promote the regression of pathological vasculature in retinopathy.** (A) Injections of DNase I or anti-Ly6G at P17 of OIR prevented regression of preretinal NV, leaving ~1.8-fold higher NV with DNase I and ~1.5-fold higher NV with anti-Ly6G at P19. (B) A similar decrease in vascular regeneration was observed with ~1.5-fold higher avascular areas with DNase I and ~1.7-fold higher avascular areas with anti-Ly6G ( $n = 8-18$  retinas). (C) LysM-cre<sup>+/+</sup>Pad4<sup>-/-</sup> and

LysM-cre<sup>+/+</sup>Pad4<sup>+/+</sup> mice developed similar amounts of preretinal NV and showed similar rates of vascular regeneration (D) at P17 of OIR, but LysM-cre<sup>+/+</sup>Pad4<sup>-/-</sup> mice showed retarded clearance of these vascular tufts at P19 (5.2-fold higher NV) (E) and ~3.7-fold larger avascular areas (F) ( $n = 10-14$  retinas). Scale bars, 0.5 mm. Data were analyzed with Student's  $t$  test (\* $P < 0.05$ , \*\* $P < 0.01$ , \*\*\* $P < 0.001$ ) and are shown as means  $\pm$  SEM.

and the clearance of senescent hepatocytes in hepatocarcinoma (68). Induction of cellular senescence in hepatic carcinomas through reactivation of p53 promotes tumor regression through the elimination of senescent tumor cells by the innate immune system, and it has been suggested that NK cells, macrophages, and neutrophils contribute to similar degrees through an unexplored mechanism (70). Our findings suggest that prolonged exposure of senescent ECs to NETs directly triggers a cytotoxic response leading to apoptotic death. This likely occurs from direct exposure to protein constituents such as histones or MPO (54).

Ultimately, neutrophil-mediated NETosis might facilitate further clearance through innate immune phagocytosis.

Quantitative proteomics using SILAC revealed that senescent ECs predominantly induce a secretome involved in immune regulation. Subsets of ECs in retinopathy adopt a SASP and excrete cytokines such as CXCL1, IL-1 $\beta$ , and others, similar to what has been described for other senescent cell populations (53). Inhibition of these cytokines or their receptors curtails senescence-induced NETosis and impedes neovascular tuft regression, highlighting the role of these inflammatory factors in vascular

remodeling. We cannot exclude that other mediators of the SASP response, such as reactive oxygen species, might contribute to NETosis. In addition to ECs, vascular-associated cells such as pericytes and Müller glia also trigger a SASP.

Although removal of diseased senescent vasculature through a neutrophil-mediated process may be an intrinsic reparative mechanism that favors tissue remodeling after vascular lesions, uncontrolled retinal neutrophils and abundant NETosis in the retina may be incompatible with proper retinal health. Retinal NETosis may potentially exacerbate retinal



vasculopathy by causing microvascular occlusions or small-vessel vasculitis secondary to the development of autoantibodies against the neutrophil elastase and MPO found in NETs (75). This is corroborated by retinal microvascular preservation in diabetes after immunodepletion of neutrophils (76, 77). Elevated systemic neutrophil counts are associated with DR (78), and elevated levels of plasma neutrophil gelatinase-associated lipocalin (NGAL) positively correlate with DR in patients with type 2 diabetes (79). Further potential detrimental effects for retinal NETs in DR are suggested by findings that neutrophils are associated with capillary closure in retinas from spontaneously diabetic monkeys (80), and circulating DNA-histone complexes and polymorphonuclear neutrophil elastase have been reported to be significantly increased in patients with DR (81). NETs are capable of forming elaborate networks of fibers that trap erythrocytes and platelets and provoke vascular occlusion, with a few hundred neutrophils capable of provoking millimeter-sized clots (82).

By triggering age-independent pathways of cellular senescence, pathological neovascularization prompts its turnover by triggering an innate immune response. These findings suggest an etiology for cellular senescence in tissue remodeling and highlight that elimination of senescent vascular cells ameliorates the outcome of neovascular retinal disease. More broadly, our findings identify an inherent mechanism whereby bouts of sterile inflammation can remodel diseased blood vessels.

## MATERIALS AND METHODS

See table S2 for a detailed description of all reagents.

### Animals

All studies were performed according to the Association for Research in Vision and Ophthalmology (ARVO) Statement for the Use of Animals in Ophthalmic and Vision Research and were approved by the Animal Care Committee of the University of Montreal in agreement with the guidelines established by the Canadian Council on Animal Care. C57BL/6 wild-type mice were purchased from The Jackson Laboratory and CD1 nursing mothers from Charles River Laboratories.

### Human samples and vitrectomy

Patients with PDR and controls (macular hole or epiretinal membrane) were followed and operated on by a single surgeon (F.A.R.). The study protocol followed the Declaration of Helsinki tenets and the institutional human clinical protocol. Informed consent was obtained from Maisonneuve-Rosemont Hospital (HMR) ethics committee (CER 13082). Human eye sections were obtained from the Human Eye Biobank (Toronto, Ontario).

### OIR and depletion of neutrophils

Mouse pups (C57BL/6, The Jackson Laboratory) and their fostering mothers (CD1 from Charles River Laboratories or S129 from The Jackson Laboratory) were exposed to 75% O<sub>2</sub> from P7 to P12 and then returned to room air. Upon return to room air, hypoxia-driven NV developed from P14 on (28). Eyes were enucleated at different time points and the retinas dissected for mRNA. Dissected retinas were flat-mounted and incubated overnight with fluoresceinated isolectin B4 (1:100) in 1 mM CaCl<sub>2</sub> to determine the extent of the avascular area or the NV area at P17. Analysis was performed using ImageJ and the SWIFT-NV method (83). Avascular areas were calculated by dividing the central capillary-free area by the total retinal area. The percentage of NV was calculated by dividing the area of neovascular tufts (saturated lectin-stained vasculature on the surface of the retina) by the total area of the retina. Neutrophils were depleted from the circulation by intraperitoneal injection of the neutrophil-specific antibody Ly6G (30 mg/kg) or a rat IgG2A isotype control antibody (30 mg/kg). Depletion efficiency was assessed after FACS analysis. Intravitreal injections (1 µl) of DNase I (10 U/µl), SB265610 (1 µM), or Kineret (150 mg/ml) were performed using a Hamilton syringe fitted with a glass capillary.

### RNA sequencing and GSEA

Preparation and analysis of total RNA from OIR and normoxic retinas were as previously described (17). Briefly, RNA was isolated using the Dynabeads mRNA Direct Micro Kit (Thermo Fisher Scientific), and whole transcriptome analysis was done with Ion Total RNA-Seq Kit version 2. Sequencing was performed on an Ion Proton Instrument (Ion Torrent, Thermo Fisher Scientific). RNA-sequencing (RNA-seq) analysis was done using the Torrent Suite software version 5.4.0 and the RNaseqAnalysis plugin (Thermo Fisher Scientific) on the mouse reference genome mm10. GSEA was performed ([www.gsea-msigdb.org/gsea/index.jsp](http://www.gsea-msigdb.org/gsea/index.jsp)) on pre-ranked lists based on shrunken log<sub>2</sub>-fold changes.

### Drop-seq

Following the same digestion procedure described by Macosko *et al.* (30), single-cell suspensions were prepared from P14 and P17 normoxic and OIR C57BL/6 mouse retinas through successive steps (digestion using papain solution, trituration, and filtration) to obtain a final concentration of 120 cells/µL. The final cell suspension was obtained from either whole or rod-depleted retinas using a CD73 magnetic column (84). Droplet generation and cDNA libraries were performed as described in the Drop-seq procedure (<http://mccarrolllab.org/dropseq/>), and sequencing was carried out on an Illumina NextSeq 500 at

an estimated read depth/cell similar to that used by Macosko *et al.* (30) (i.e., 50,000 reads/cell). Unique molecular identifier (UMI) counts from the single-cell RNA sequencing (scRNAseq) replicates of normoxic and OIR retina were merged into one single digital gene expression (DGE) matrix and processed using the “Seurat” package [spatial reconstruction of single-cell gene expression data (85)]. Cells expressing fewer than 100 genes and more than 10% of mitochondrial genes were filtered out. Single-cell transcriptomes were normalized by dividing by the total number of UMIs per cell and then multiplying by 10,000. All calculations and data were then performed in log space [i.e.,  $\ln(\text{transcripts per } 10,000 + 1)$ ].

After the whole and rod-depleted dataset were aligned using canonical correlation analysis on the most variable genes in the DGE matrix (86), the 20 most significant components were used as input for t-SNE. To identify putative cell types on the t-SNE map, a density-clustering approach was used and average gene expression was computed for each of the identified cluster based on Euclidean distances. Marker genes that were significantly enriched for each cluster were then identified, allowing cluster annotation to specific cell types. After removing the contaminant cell cluster (i.e., red blood cells and retinal pigmented epithelium), a total of 13,638 cells were obtained from normoxic retina (9191 from whole retina and 4447 from rod-depleted retina) and 17,473 cells from OIR retina (11,732 from whole retina and 5741 from rod-depleted retina). Transcriptomic differences between normoxic and OIR cell types were statistically compared using a negative binomial model and analyzed using visualization tools including Dot Plot, RidgePlot, t-SNE plot, and heatmap plot. For pathway analysis, normalized single-cell gene expression profiles from each separate cell type identified by scRNAseq (downsampled to a maximum of 1000 cells per cell cluster) were further analyzed using GSVA (87). Single-cell gene expression profiles from each separate cell type identified by scRNAseq were further analyzed using CellPhoneDB (49). The data discussed herein have been deposited in NCBI's Gene Expression Omnibus (accession no. GSE150703).

### Human neutrophil isolation

Blood was drawn from healthy volunteers in accordance with HMR guidelines. Neutrophil isolation was performed using a published protocol. Briefly, red blood cells were first removed with an Histopaque 1119 gradient. The top leukocyte fraction was separated with a 65-70-75-80-85% Percoll gradient. Neutrophils were collected in the fractions above 70%. Cells were washed twice with phosphate-buffered saline (PBS) and counted using a hemacytometer.

### Time-lapse microscopy

ECs (HUVEC, Lonza) were transduced with an RAS expressing or empty plasmid retrovirus for 2 rounds of 6-hour incubations. RAS-expressing ECs were selected after 5 days of selection with 100 µg/ml of hygromycin. Control and senescent cells were seeded in a 96-well plate the day before. Human neutrophils were isolated as described previously, labeled for 20 min with 1 µM DiI Red at 37°C, washed twice, and added to the EC layer along with Sytox Green (150 nM). Images were acquired using a Zeiss Zl live microscope equipped with a humidified chamber at 37°C at 5-min intervals. Image analysis was done using Imaris software. For imaging in live retinas, cardiac perfusion was done with 5 µg of Ly6G-FITC antibody (BioLegend) and 20 µg of lectin-rhodamine (Vector Laboratories) in mouse pups at P17 of OIR. Eyes were quickly removed and placed on ice in Ringer's solution. Retinas were dissected, flattened out on 0.4-µm cell culture inserts (Millipore), and kept humidified at all times in Ringer's solution. Images were acquired with a multiphoton Zeiss LSM880 microscope and Zeiss Zen Black software.

### Lentivirus and adenovirus production

For lentivirus production, HEK293T cells were transfected with third-generation packaging plasmids (12251, 12253, and 12259, Addgene) using polyethylenimine. Lentiviruses were collected in the supernatants after 56 hours. Supernatants were cleared by centrifugation and filtered through 0.45-µm filters to remove cell debris. For retrovirus production, Phoenix-AMPHO cells were transfected with either pWZL-HYGRO or pWZL-HYGRO-RASV12 in complete Dulbecco's modified Eagle's medium (DMEM). Thirty to 36 hours after transfection, the medium was replaced and incubated for a further 12 to 16 hours. Viruses were harvested, Phoenix-AMPHO cells were replenished with fresh DMEM for 12 hours, and viruses were collected a second time. Phoenix-AMPHO cells were purchased from ATCC (Manassas, VA, USA).

### Real-time PCR analysis

RNA was isolated using the GenElute Mammalian Total RNA Miniprep Kit (Sigma-Aldrich) and further digested with DNase I to prevent amplification of genomic DNA. RNA was reverse transcribed using M-MLV reverse transcriptase and gene expression was analyzed using SYBR Green in an ABI Biosystems Real-Time PCR machine. β-actin was used as a reference gene. All primer sequences can be found in fig. S19.

### FACS of digested retinas

Retinas from pups' eyes were dissected and homogenized with a solution of 750U/ml DNaseI (Sigma-Aldrich) and 0.5 mg/ml of

collagenase D (Roche) for 15 min at 37°C with gentle shaking. Homogenates were then filtered with a 70-µm cell strainer and washed in RPMI plus 2% fetal bovine serum. Blocking was done with an FC block (CD16/CD32) from BioLegend. A cocktail of anti-CD45.2, anti-CD11b, anti-CX3CR1, anti-CD3e, anti-Ly6C, anti-Ly6G, or anti-F4/80, and anti-Gr1 antibodies was used, as well as 7-amino-actinomycin D for detection of neutrophils. Analysis was performed using a FACSCanto flow cytometer (BD Biosciences) and the FlowJo version 7.6 software.

### Immunohistochemistry

Eyes were enucleated from mice and fixed in 4% paraformaldehyde before incubation in 30% sucrose and inclusion in optimal cutting temperature medium. Serial sections (12 µm) were taken, visualized using a confocal microscope (Olympus FV1000), and stained with 4',6-diamidino-2-phenylindole (DAPI) and lectin-rhodamine.

### MPO detection

Retinas from mice at various time points throughout OIR or during normal development were homogenized and the activity of the specific neutrophil peroxidase MPO was measured using O-dianisidine as a substrate. Briefly, retinas were homogenized in 50 mM potassium phosphate buffer, pH 6.0, containing 0.5% hexadecyltrimethylammonium bromide (HETAB), sonicated, and freeze-thawed for three cycles. The homogenates were centrifuged for 20 min at 20,000g. Analysis of MPO activity of the supernatants was done using a 50 mM potassium phosphate buffer, pH 6.0, containing 0.167 mg/ml O-dianisidine hydrochloride and 0.0005% H<sub>2</sub>O<sub>2</sub>. Absorbance was measured at 460nm at 25°C.

### dsDNA and elastase activity quantification in human vitreous

dsDNA was detected in the vitreous using the PicoGreen dsDNA reagent (Invitrogen) according to the manufacturer's instructions. Elastase activity was assessed with human neutrophil elastase substrate N-succinyl-Ala-Ala-Ala-p-nitroanilide (Sigma-Aldrich) and recorded at 405 nm for a period of 60 min.

### SA-β-Gal activity

For quantification of SA-β-Gal activity, cells or retinas were washed twice in PBS and fixed with 4% PFA for 15 min or 1 hour (retinas). After two washes in PBS with 1 mM MgCl<sub>2</sub> (adjusted to pH 5.0 for mouse retinas or 6.0 for HUVEC), incubation was done overnight in KC solution {5 mM K<sub>3</sub>[Fe(CN)<sub>6</sub>] + 6mM K<sub>4</sub>[Fe(CN)<sub>6</sub>] in PBS with 1 mM MgCl<sub>2</sub> with adjusted pH and 1 mg/ml X-Gal substrate}. Photographs were taken with a Zeiss AxioObserver Z1 motorized inverted microscope using Zeiss Blue Software.

### SILAC

HUVEC cells were grown in Lys/Arg free Iscove's modified Dulbecco's medium resupplemented with heavy or light Lys and Arg for a minimum of four population doublings before induction of senescence with retroviral expression of RASV12 or empty vector. Selection was performed with 100 µg/ml of hygromycin. At 10 days after the induction of senescence, cells were incubated in serum-free medium and supernatants collected after 24 hours. Proteins were precipitated using acetone at -20°C for 1 hour and resuspended in 8 M urea and 20 mM HEPES, pH 8.0. The extracted proteins were then digested, mixed in equal proportions, and analyzed by MS. Postanalysis was done with MaxQuant software. Incorporation of heavy and light isotopes was estimated to be >90%.

### Statistical analyses

Data are presented as mean ± SEM. Student's *t* test or ANOVA was used to compare the different groups. *P* < 0.05 was considered statistically different.

### REFERENCES AND NOTES

1. R. Lee, T. Y. Wong, C. Sabanayagam, Epidemiology of diabetic retinopathy, diabetic macular edema and related vision loss. *Eye Vis.* **2**, 17 (2015). doi: [10.1186/s40662-015-0026-2](https://doi.org/10.1186/s40662-015-0026-2); pmid: [26605370](https://pubmed.ncbi.nlm.nih.gov/26605370/)
2. J. Ding, T. Y. Wong, Current epidemiology of diabetic retinopathy and diabetic macular edema. *Curr. Diab. Rep.* **12**, 346–354 (2012). doi: [10.1007/s11892-012-0283-6](https://doi.org/10.1007/s11892-012-0283-6); pmid: [22585044](https://pubmed.ncbi.nlm.nih.gov/22585044/)
3. E. J. Duh, J. K. Sun, A. W. Stitt, Diabetic retinopathy: Current understanding, mechanisms, and treatment strategies. *JCI Insight* **2**, e93751 (2017). doi: [10.1172/jci.insight.93751](https://doi.org/10.1172/jci.insight.93751); pmid: [28724805](https://pubmed.ncbi.nlm.nih.gov/28724805/)
4. J. H. Kempen *et al.*, The prevalence of diabetic retinopathy among adults in the United States. *Arch. Ophthalmol.* **122**, 552–563 (2004). doi: [10.1001/archoph.122.4.552](https://doi.org/10.1001/archoph.122.4.552); pmid: [15078674](https://pubmed.ncbi.nlm.nih.gov/15078674/)
5. A. Hellström, L. E. Smith, O. Dammann, Retinopathy of prematurity. *Lancet* **382**, 1445–1457 (2013). doi: [10.1016/S0140-6736\(13\)60178-6](https://doi.org/10.1016/S0140-6736(13)60178-6); pmid: [23782686](https://pubmed.ncbi.nlm.nih.gov/23782686/)
6. M. E. Hartnett, J. S. Penn, Mechanisms and management of retinopathy of prematurity. *N. Engl. J. Med.* **367**, 2515–2526 (2012). doi: [10.1056/NEJMral208129](https://doi.org/10.1056/NEJMral208129); pmid: [23268666](https://pubmed.ncbi.nlm.nih.gov/23268666/)
7. E. H. Lo, A new penumbra: Transitioning from injury into repair after stroke. *Nat. Med.* **14**, 497–500 (2008). doi: [10.1038/nm1735](https://doi.org/10.1038/nm1735); pmid: [18463660](https://pubmed.ncbi.nlm.nih.gov/18463660/)
8. M. A. Moskowitz, E. H. Lo, C. Iadecola, The science of stroke: Mechanisms in search of treatments. *Neuron* **67**, 181–198 (2010). doi: [10.1016/j.neuron.2010.07.002](https://doi.org/10.1016/j.neuron.2010.07.002); pmid: [20670828](https://pubmed.ncbi.nlm.nih.gov/20670828/)
9. P. Sapieha, Eyeing central neurons in vascular growth and reparative angiogenesis. *Blood* **120**, 2182–2194 (2012). doi: [10.1182/blood-2012-04-396846](https://doi.org/10.1182/blood-2012-04-396846); pmid: [22705597](https://pubmed.ncbi.nlm.nih.gov/22705597/)
10. C. A. K. Lange, J. W. B. Bainbridge, Oxygen sensing in retinal health and disease. *Ophthalmologica* **227**, 115–131 (2012). pmid: [21952513](https://pubmed.ncbi.nlm.nih.gov/21952513/)
11. M. Oubaha *et al.*, Senescence-associated secretory phenotype contributes to pathological angiogenesis in retinopathy. *Sci. Transl. Med.* **8**, 362ra144 (2016). doi: [10.1126/scitranslmed.aaf9440](https://doi.org/10.1126/scitranslmed.aaf9440); pmid: [27797960](https://pubmed.ncbi.nlm.nih.gov/27797960/)
12. National Eye Institute, National Institutes of Health, At a glance: Retinopathy of prematurity 2014; [www.nei.nih.gov/learn-about-eye-health/eye-conditions-and-diseases/retinopathy-prematurity](http://www.nei.nih.gov/learn-about-eye-health/eye-conditions-and-diseases/retinopathy-prematurity).
13. F. Bandello, J. D. Gass, R. Lattanzio, R. Brancato, Spontaneous regression of neovascularization at the disk and elsewhere in diabetic retinopathy. *Am. J. Ophthalmol.* **122**, 494–501 (1996). doi: [10.1016/S0002-9334\(14\)72108-7](https://doi.org/10.1016/S0002-9334(14)72108-7); pmid: [8862045](https://pubmed.ncbi.nlm.nih.gov/8862045/)



14. J. R. Han, W. K. Ju, I. W. Park, Spontaneous regression of neovascularization at the disc in diabetic retinopathy. *Korean J. Ophthalmol.* **18**, 41–46 (2004). doi: [10.3341/kjo.2004.18.1.41](#); pmid: [15255236](#)
15. H. L. Little, Treatment of proliferative diabetic retinopathy. Long-term results of argon laser photocoagulation. *Ophthalmology* **92**, 279–283 (1985). doi: [10.1016/S0161-6420\(85\)34059-9](#); pmid: [2580259](#)
16. R. L. Avery *et al.*, Intravitreal bevacizumab (Avastin) in the treatment of proliferative diabetic retinopathy. *Ophthalmology* **113**, 1695.e1–1695.e15 (2006). doi: [10.1016/j.ophtha.2006.05.064](#); pmid: [17011951](#)
17. Y. Yoshikawa *et al.*, Developmental regression of hyaloid vasculature is triggered by neurons. *J. Exp. Med.* **213**, 1175–1183 (2016). doi: [10.1084/jem.20151966](#); pmid: [27325890](#)
18. I. B. Lobov *et al.*, WNT7b mediates macrophage-induced programmed cell death in patterning of the vasculature. *Nature* **437**, 417–421 (2005). doi: [10.1038/nature03928](#); pmid: [16163358](#)
19. G. A. Luttly, D. S. McLeod, Development of the hyaloid, choroidal and retinal vasculatures in the fetal human eye. *Prog. Retin. Eye Res.* **62**, 58–76 (2018). doi: [10.1016/j.preteyeres.2017.10.001](#); pmid: [29081352](#)
20. S. E. Hamrick, G. Hansmann, Patent ductus arteriosus of the preterm infant. *Pediatrics* **125**, 1020–1030 (2010). doi: [10.1542/peds.2009-3506](#); pmid: [20421261](#)
21. J. E. Girling, P. A. Rogers, Regulation of endometrial vascular remodeling: Role of the vascular endothelial growth factor family and the angiotensin-TIE signalling system. *Reproduction* **138**, 883–893 (2009). doi: [10.1530/REP-09-0147](#); pmid: [19755482](#)
22. D. F. Gilmour, Familial exudative vitreoretinopathy and related retinopathies. *Eye (Lond.)* **29**, 1–14 (2015). doi: [10.1038/eye.2014.70](#); pmid: [25323851](#)
23. E. R. Hermes-DeSantis, R. I. Clyman, Patent ductus arteriosus: Pathophysiology and management. *J. Perinatol.* **26** (Suppl 1), S14–S18, discussion S22–S23 (2006). doi: [10.1038/sj.jp.7211465](#); pmid: [16625216](#)
24. D. S. Torry, R. J. Torry, Angiogenesis and the expression of vascular endothelial growth factor in endometrium and placenta. *Am. J. Reprod. Immunol.* **37**, 21–29 (1997). doi: [10.1111/j.1600-0897.1997.tb00189.x](#); pmid: [9138450](#)
25. H. P. Gerber, N. Ferrara, Pharmacology and pharmacodynamics of bevacizumab as monotherapy or in combination with cytotoxic therapy in preclinical studies. *Cancer Res.* **65**, 671–680 (2005). pmid: [15705858](#)
26. R. K. Jain, Normalization of tumor vasculature: An emerging concept in antiangiogenic therapy. *Science* **307**, 58–62 (2005). doi: [10.1126/science.1104819](#); pmid: [15637262](#)
27. R. S. Apte, D. S. Chen, N. Ferrara, VEGF in signaling and disease: Beyond discovery and development. *Cell* **176**, 1248–1264 (2019). doi: [10.1016/j.cell.2019.01.021](#); pmid: [30849371](#)
28. L. E. Smith *et al.*, Oxygen-induced retinopathy in the mouse. *Invest. Ophthalmol. Vis. Sci.* **35**, 101–111 (1994). pmid: [7507904](#)
29. F. Binet *et al.*, Neuronal ER stress impedes myeloid-cell-induced vascular regeneration through IRE1 $\alpha$  degradation of netrin-1. *Cell Metab.* **17**, 353–371 (2013). doi: [10.1016/j.cmet.2013.02.003](#); pmid: [23473031](#)
30. E. Z. Macosko *et al.*, Highly parallel genome-wide expression profiling of individual cells using nanoliter droplets. *Cell* **161**, 1202–1214 (2015). doi: [10.1016/j.cell.2015.05.002](#); pmid: [26000488](#)
31. D. Aran *et al.*, Reference-based analysis of lung single-cell sequencing reveals a transitional profibrotic macrophage. *Nat. Immunol.* **20**, 163–172 (2019). doi: [10.1038/s41590-018-0276-y](#); pmid: [30643263](#)
32. D. Checchin, F. Sennlaub, E. Levavasseur, M. Leduc, S. Chemtob, Potential role of microglia in retinal blood vessel formation. *Invest. Ophthalmol. Vis. Sci.* **47**, 3595–3602 (2006). doi: [10.1167/iov.05-1522](#); pmid: [16877434](#)
33. Y. Kubota *et al.*, M-CSF inhibition selectively targets pathological angiogenesis and lymphangiogenesis. *J. Exp. Med.* **206**, 1089–1102 (2009). doi: [10.1084/jem.20081605](#); pmid: [19398755](#)
34. M. R. Ritter *et al.*, Myeloid progenitors differentiate into microglia and promote vascular repair in a model of ischemic retinopathy. *J. Clin. Invest.* **116**, 3266–3276 (2006). doi: [10.1172/JCI29683](#); pmid: [17111048](#)
35. B. W. Bardeol, E. F. Kenny, G. Solberger, A. Zychlinsky, The balancing act of neutrophils. *Cell Host Microbe* **15**, 526–536 (2014). doi: [10.1016/j.chom.2014.04.011](#); pmid: [24832448](#)
36. B. McDonald, P. Kubes, Chemokines: Sirens of neutrophil recruitment-but is it just one song? *Immunity* **33**, 148–149 (2010). doi: [10.1016/j.immuni.2010.08.006](#); pmid: [20732637](#)
37. V. Papayannopoulos, Neutrophil extracellular traps in immunity and disease. *Nat. Rev. Immunol.* **18**, 134–147 (2018). doi: [10.1038/nri.2017.105](#); pmid: [28990587](#)
38. A. S. Rohrbach, D. J. Slade, P. R. Thompson, K. A. Mowen, Activation of PAD4 in NET formation. *Front. Immunol.* **3**, 360 (2012). doi: [10.3389/fimmu.2012.00360](#); pmid: [23264775](#)
39. A. Warnatsch, M. Ioannou, Q. Wang, V. Papayannopoulos, Neutrophil extracellular traps license macrophages for cytokine production in atherosclerosis. *Science* **349**, 316–320 (2015). doi: [10.1126/science.aaa8064](#); pmid: [26185250](#)
40. H. Huang *et al.*, Damage-associated molecular pattern-activated neutrophil extracellular trap exacerbates sterile inflammatory liver injury. *Hepatology* **62**, 600–614 (2015). doi: [10.1002/hep.27841](#); pmid: [25855125](#)
41. V. Papayannopoulos, K. D. Metzler, A. Hakkim, A. Zychlinsky, Neutrophil elastase and myeloperoxidase regulate the formation of neutrophil extracellular traps. *J. Cell Biol.* **191**, 677–691 (2010). doi: [10.1083/jcb.201006052](#); pmid: [20974816](#)
42. M. Pearson *et al.*, PML regulates p53 acetylation and premature senescence induced by oncogenic Ras. *Nature* **406**, 207–210 (2000). doi: [10.1038/35018127](#); pmid: [10910364](#)
43. G. Ferbeyre *et al.*, PML is induced by oncogenic ras and promotes premature senescence. *Genes Dev.* **14**, 2015–2027 (2000). pmid: [10950866](#)
44. A. Hernandez-Segura, J. Nehme, M. Demaria, Hallmarks of cellular senescence. *Trends Cell Biol.* **28**, 436–453 (2018). doi: [10.1016/j.tcb.2018.02.001](#); pmid: [29477613](#)
45. M. Serrano, A. W. Lin, M. E. McCurrach, D. Beach, S. W. Lowe, Oncogenic ras provokes premature cell senescence associated with accumulation of p53 and p16INK4a. *Cell* **88**, 593–602 (1997). doi: [10.1016/S0092-8674\(00\)81902-9](#); pmid: [9054499](#)
46. R. Di Micco *et al.*, Oncogene-induced senescence is a DNA damage response triggered by DNA hyper-replication. *Nature* **444**, 638–642 (2006). doi: [10.1038/nature05327](#); pmid: [17136094](#)
47. F. A. Mallette, M. F. Gaumont-Leclerc, G. Ferbeyre, The DNA damage signaling pathway is a critical mediator of oncogene-induced senescence. *Genes Dev.* **21**, 43–48 (2007). doi: [10.1101/gad.1487307](#); pmid: [17210786](#)
48. J. Bartkova *et al.*, Oncogene-induced senescence is part of the tumorigenesis barrier imposed by DNA damage checkpoints. *Nature* **444**, 633–637 (2006). doi: [10.1038/nature05268](#); pmid: [17136093](#)
49. M. Efremova, M. Vento-Tormo, S. A. Teichmann, R. Vento-Tormo, CellPhoneDB: Inferring cell-cell communication from combined expression of multi-subunit ligand-receptor complexes. *Nat. Protoc.* **15**, 1484–1506 (2020). doi: [10.1038/s41596-020-0292-x](#); pmid: [32103204](#)
50. P. D. Westenskow *et al.*, Ras pathway inhibition prevents neovascularization by repressing endothelial cell sprouting. *J. Clin. Invest.* **123**, 4900–4908 (2013). doi: [10.1172/JCI70230](#); pmid: [24084735](#)
51. A. Fabregat *et al.*, Reactome diagram viewer: Data structures and strategies to boost performance. *Bioinformatics* **34**, 1208–1214 (2018). doi: [10.1093/bioinformatics/btx752](#); pmid: [29186351](#)
52. J. C. Acosta *et al.*, A complex secretory program orchestrated by the inflammasome controls paracrine senescence. *Nat. Cell Biol.* **15**, 978–990 (2013). doi: [10.1038/ncb2784](#); pmid: [23770676](#)
53. J. P. Coppé, P. Y. Desprez, A. Krtolica, J. Campisi, The senescence-associated secretory phenotype: The dark side of tumor suppression. *Annu. Rev. Pathol.* **5**, 99–118 (2010). doi: [10.1146/annurev-pathol-121808-102144](#); pmid: [20078217](#)
54. M. Saffarzadeh *et al.*, Neutrophil extracellular traps directly induce epithelial and endothelial cell death: A predominant role of histones. *PLOS ONE* **7**, e32366 (2012). doi: [10.1371/journal.pone.0032366](#); pmid: [22389696](#)
55. A. K. Gupta *et al.*, Activated endothelial cells induce neutrophil extracellular traps and are susceptible to NETosis-mediated cell death. *FEBS Lett.* **584**, 3193–3197 (2010). doi: [10.1016/j.febslet.2010.06.006](#); pmid: [20541553](#)
56. P. Li *et al.*, PAD4 is essential for antibacterial innate immunity mediated by neutrophil extracellular traps. *J. Exp. Med.* **207**, 1853–1862 (2010). doi: [10.1084/jem.20100239](#); pmid: [20733033](#)
57. A. Hakkim *et al.*, Impairment of neutrophil extracellular trap degradation is associated with lupus nephritis. *Proc. Natl. Acad. Sci. U.S.A.* **107**, 9813–9818 (2010). doi: [10.1073/pnas.0909927107](#); pmid: [20439745](#)
58. J. M. Daley, A. A. Thomay, M. D. Connolly, J. S. Reichner, J. E. Albina, Use of Ly6G-specific monoclonal antibody to deplete neutrophils in mice. *J. Leukoc. Biol.* **83**, 64–70 (2008). doi: [10.1189/jlb.0407247](#); pmid: [17884993](#)
59. A. Stahl *et al.*, The mouse retina as an angiogenesis model. *Invest. Ophthalmol. Vis. Sci.* **51**, 2813–2826 (2010). doi: [10.1167/iov.10-5176](#); pmid: [20484600](#)
60. S. Lavalette *et al.*, Interleukin-1 $\beta$  inhibition prevents choroidal neovascularization and does not exacerbate photoreceptor degeneration. *Am. J. Pathol.* **178**, 2416–2423 (2011). doi: [10.1016/j.ajpath.2011.01.013](#); pmid: [21514452](#)
61. J. C. Rivera *et al.*, Microglia and interleukin-1 $\beta$  in ischemic retinopathy elicit microvascular degeneration through neuronal semaphorin-3A. *Arterioscler. Thromb. Vasc. Biol.* **33**, 1881–1891 (2013). doi: [10.1161/ATVBAHA.113.301331](#); pmid: [23766263](#)
62. P. Sapiieha, F. A. Mallette, Cellular senescence in postmitotic cells: Beyond growth arrest. *Trends Cell Biol.* **28**, 595–607 (2018). doi: [10.1016/j.tcb.2018.03.003](#); pmid: [29704982](#)
63. D. Muñoz-Espín, M. Serrano, Cellular senescence: From physiology to pathology. *Nat. Rev. Mol. Cell Biol.* **15**, 482–496 (2014). doi: [10.1038/nrm3823](#); pmid: [24954210](#)
64. J. Campisi, F. d'Adda di Fagagna, Cellular senescence: When bad things happen to good cells. *Nat. Rev. Mol. Cell Biol.* **8**, 729–740 (2007). doi: [10.1038/nrm2233](#); pmid: [17667954](#)
65. M. Demaria *et al.*, An essential role for senescent cells in optimal wound healing through secretion of PDGF-AA. *Dev. Cell* **31**, 722–733 (2014). doi: [10.1016/j.devcel.2014.11.012](#); pmid: [25499914](#)
66. L. Mosteiro *et al.*, Tissue damage and senescence provide critical signals for cellular reprogramming in vivo. *Science* **354**, aaf4445 (2016). doi: [10.1126/science.aaf4445](#); pmid: [27884981](#)
67. B. Ritschka *et al.*, The senescence-associated secretory phenotype induces cellular plasticity and tissue regeneration. *Genes Dev.* **31**, 172–183 (2017). doi: [10.1101/gad.290635.116](#); pmid: [28143833](#)
68. T. W. Kang *et al.*, Senescence surveillance of pre-malignant hepatocytes limits liver cancer development. *Nature* **479**, 547–551 (2011). doi: [10.1038/nature10599](#); pmid: [22080947](#)
69. V. Krizhanovsky *et al.*, Implications of cellular senescence in tissue damage response, tumor suppression, and stem cell biology. *Cold Spring Harb. Symp. Quant. Biol.* **73**, 513–522 (2008). doi: [10.1101/sqb.2008.73.048](#); pmid: [19150958](#)
70. W. Xue *et al.*, Senescence and tumour clearance is triggered by p53 restoration in murine liver carcinomas. *Nature* **445**, 656–660 (2007). doi: [10.1038/nature05529](#); pmid: [17251933](#)
71. J. H. Sweigard *et al.*, The alternative complement pathway regulates pathological angiogenesis in the retina. *FASEB J.* **28**, 3171–3182 (2014). doi: [10.1096/fj.14-251041](#); pmid: [24668752](#)
72. M. H. Davies, A. J. Stempel, M. R. Powers, MCP-1 deficiency delays regression of pathologic retinal neovascularization in a model of ischemic retinopathy. *Invest. Ophthalmol. Vis. Sci.* **49**, 4195–4202 (2008). doi: [10.1167/iov.07-1491](#); pmid: [18487365](#)
73. A. Sagiv *et al.*, NKG2D ligands mediate immunosurveillance of senescent cells. *Aging (Albany NY)* **8**, 328–344 (2016). doi: [10.18632/aging.100897](#); pmid: [26878797](#)
74. M. H. Yun, H. Davaapil, J. P. Brookes, Recurrent turnover of senescent cells during regeneration of a complex structure. *eLife* **4**, e05505 (2015). doi: [10.7554/eLife.05505](#); pmid: [25942455](#)
75. K. Kessenbrock *et al.*, Netting neutrophils in autoimmune small-vessel vasculitis. *Nat. Med.* **15**, 623–625 (2009). doi: [10.1038/nm.1959](#); pmid: [19448636](#)
76. G. Li *et al.*, Marrow-derived cells regulate the development of early diabetic retinopathy and tactile allodynia in mice. *Diabetes* **61**, 3294–3303 (2012). doi: [10.2337/db11-1249](#); pmid: [22923475](#)
77. A. A. Veenstra, J. Tang, T. S. Kern, Antagonism of CD11b with neutrophil inhibitory factor (NIF) inhibits vascular lesions in diabetic retinopathy. *PLOS ONE* **8**, e78405 (2013). doi: [10.1371/journal.pone.0078405](#); pmid: [24205223](#)
78. S. J. Woo, S. J. Ahn, J. Ahn, K. H. Park, K. Lee, Elevated systemic neutrophil count in diabetic retinopathy and diabetes: A hospital-based cross-sectional study of 30,793 Korean subjects. *Invest. Ophthalmol. Vis. Sci.* **52**, 7697–7703 (2011). doi: [10.1167/iov.11-7784](#); pmid: [21873679](#)
79. J. O. Chung, S. Y. Park, D. H. Cho, D. J. Chung, M. Y. Chung, Plasma neutrophil gelatinase-associated lipocalin levels are positively associated with diabetic retinopathy in patients with Type 2 diabetes. *Diabet. Med.* **33**, 1649–1654 (2016). doi: [10.1111/dme.13141](#); pmid: [27100138](#)

80. S. Y. Kim *et al.*, Neutrophils are associated with capillary closure in spontaneously diabetic monkey retinas. *Diabetes* **54**, 1534–1542 (2005). doi: [10.2337/diabetes.54.5.1534](https://doi.org/10.2337/diabetes.54.5.1534); pmid: [15855343](https://pubmed.ncbi.nlm.nih.gov/15855343/)
81. J. H. Park *et al.*, Evaluation of circulating markers of neutrophil extracellular trap (NET) formation as risk factors for diabetic retinopathy in a case-control association study. *Exp. Clin. Endocrinol. Diabetes* **124**, 557–561 (2016). doi: [10.1055/s-0042-101792](https://doi.org/10.1055/s-0042-101792); pmid: [27420129](https://pubmed.ncbi.nlm.nih.gov/27420129/)
82. L. Boneschansker, Y. Inoue, R. Oklu, D. Irimia, Capillary plexuses are vulnerable to neutrophil extracellular traps. *Integr. Biol. (Camb.)* **8**, 149–155 (2016). doi: [10.1039/C5IB00265F](https://doi.org/10.1039/C5IB00265F); pmid: [26797289](https://pubmed.ncbi.nlm.nih.gov/26797289/)

## ACKNOWLEDGMENTS

We thank M. Sergeev, M. Lambert, and N. Tessier for their helpful assistance. **Funding:** This work was supported by operating grants from the Canadian Diabetes Association (grant DI-3-18-5444-PS to P.S.), the Canadian Institutes of Health Research (foundation grant 148460 to P.S.; grant PJ2-169643 to F.A.M. and P.S., grants 141956 and 390615 to J.-S. J., grant MOP-133442 to F.A.M.; grant GER-163050 to F.A.M. and K.B.; and grant MOP142425 to J.-F.C.), the Canadian the Heart & Stroke Foundation Canada (grant G-16-00014658 to P.S. and F.A.M.), the Foundation Fighting

Blindness Canada (grant to P.S. and J.-S.J.), and the Natural Sciences and Engineering Research Council of Canada (grant 418637 to P.S., grant RGPIN-2017-05227 to F.A.M., and grant RGPIN-2016-06743 to J.-S.J.). P.S. holds the Wolfe Professorship in Translational Research and a Canada Research Chair in Retinal Cell Biology. F.A.M. is the recipient of the Canada Research Chair in Epigenetics of Aging and Cancer. J.-S.J. was supported by the Burroughs Wellcome Fund Career Award for Medical Scientists (grant 1012321.01) and the Fonds de Recherche du Québec - Santé (FRQS). J.-F.C. holds the TRANSAT Chair in breast cancer research. F.B., S.C.-G., G.T.M., and A.A.T. received fellowships from the FRQS. G.C. holds a MITACs postdoctoral fellowship and is funded by the Single-Cell Academy (The Vision Health Research Network of Quebec (RRSV)) and the Antoine Turrel Foundation. M.H. holds the Banting Fellowship from the CIHR. R.D. and G.T.M. hold scholarships from the Fonds de Recherche en Ophtalmologie de l'Université de Montréal (FROUM) and the RRSV. M.N. obtained fellowships from FRQS and the Cole Foundation. C.S. obtained PhD studentships from the Cole Foundation, FRQS, and Hydro-Québec. K.B. obtained a fellowship from the Cole Foundation. **Author contributions:** P.S., F.B., and F.A.M. designed the research and study. J.S.J., G.C., S.L., J.P.H., and G.A. carried out single-cell RNAseq work. F.B., A.D., M.N., M.H., A.W., V.G., M.B., R.L., S.C.-G., G.T.M., C.S., R.D., C.P., R.J., F.P., K.B., and

A.A.T. carried out experimental work. F.A.R. performed all retinal surgeries. F.B., G.C., J.P.H., M.B., A.A.T., and J.F.C. analyzed the data. F.S. provided valuable insight on research design. P.S., F.B., and F.A.M. wrote the manuscript with valuable input from all authors. **Competing interests:** P.S. is a consultant for UNITY Biotechnology. **Data and materials availability:** All single-cell data for the study are deposited in NCBI's Gene Expression Omnibus and are accessible through GEO accession no. GSE150703. All bulk RNAseq data and gene sets used are available in the supplementary materials.

## SUPPLEMENTARY MATERIALS

[science.sciencemag.org/content/369/6506/eaay5356/suppl/DC1](https://science.sciencemag.org/content/369/6506/eaay5356/suppl/DC1)

Figs. S1 to S19

Table S1

Reproducibility Checklist

Movie S1

Databases S1 to S6

[View/request a protocol for this paper from Bio-protocol.](#)

27 June 2019; resubmitted 17 May 2020

Accepted 6 July 2020

10.1126/science.aay5356



## RESEARCH ARTICLE SUMMARY

## DRUG DEVELOPMENT

## An orally available non-nucleotide STING agonist with antitumor activity

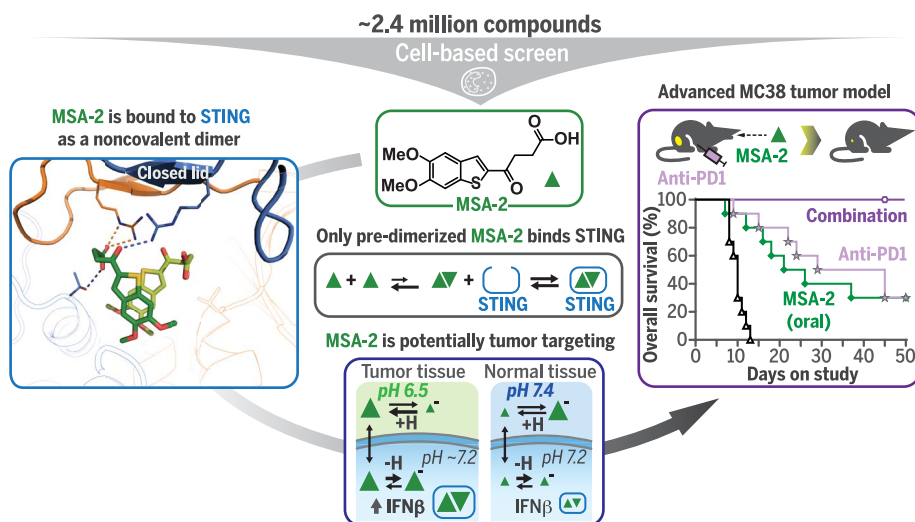
Bo-Sheng Pan\*, Samanthi A. Perera\*†, Jennifer A. Piesvaux\*, Jeremy P. Presland\*, Gottfried K. Schroeder\*†, Jared N. Cumming\*, B. Wesley Trotter\*†, Michael D. Altman, Alexei V. Buevich, Brandon Cash, Saso Cemerski, Wonsuk Chang, Yiping Chen, Peter J. Dandliker, Guo Feng, Andrew Haidle, Timothy Henderson, James Jewell, Ilona Kariv, Ian Knemeyer, Johnny Kopinja, Brian M. Lacey, Jason Laskey, Charles A. Lesburg, Rui Liang, Brian J. Long, Min Lu, Yanhong Ma, Ellen C. Minnihan, Greg O'Donnell, Ryan Otte, Laura Price, Larissa Rakhilina, Berengere Sauvagnat, Sharad Sharma, Sriram Tyagarajan, Hyun Woo, Daniel F. Wyss, Serena Xu, David Jonathan Bennett†, George H. Addona†

**INTRODUCTION:** Activation of the STING (stimulator of interferon genes) protein by its natural ligand, cyclic guanosine monophosphate-adenosine monophosphate (cGAMP), triggers signaling responses, inducing the release of type I interferons and other proinflammatory cytokines. STING-controlled interferon production is involved in antiviral defense as well as antitumor immunity. Pharmacological activation of STING is considered a promising therapeutic strategy for cancer.

**RATIONALE:** First-generation STING agonists are cyclic dinucleotide (CDN) analogs of cGAMP. When administered systemically in animal models, they induce inflammatory cytokines equipotently in tumor and normal tissues, owing to ubiquitous STING expression. Thus,

CDN-based STING agonists currently undergoing clinical trials are dosed by direct intratumor injection, which limits their application to a narrow set of tumors. To address a broad spectrum of cancers, STING agonists that are suitable for systemic administration and preferentially target tumors are needed. We identified a previously unknown compound (MSA-2) that exhibits such behavior through its distinctive mechanism of action. Moreover, MSA-2 is amenable to oral administration, a desirable delivery route because of convenience and low cost.

**RESULTS:** MSA-2 was identified in a phenotypic screen for chemical inducers of interferon- $\beta$  secretion (see the figure, top). In cell-free assays, MSA-2 binds human and mouse STING.



**STING agonist MSA-2.** Identified in a cell-based screen, MSA-2 is bound to STING as a noncovalent dimer. Extensive experimental analysis indicates that MSA-2 predimerization is required for binding. Acidic tumor microenvironments favor permeable, uncharged MSA-2. Intracellular MSA-2 is “trapped” (deprotonated) and accumulation drives MSA-2 dimerization, preferentially activating STING intratumorally. Orally dosed MSA-2 is well tolerated in mice, exhibiting STING-dependent antitumor activity, as monotherapy and combined with antibodies against PD1 (anti-PD1). Me, methyl group; IFN $\beta$ , interferon- $\beta$ .

MSA-2 is orally available, manifesting similar oral and subcutaneous exposure in mice. In tumor-bearing mice, MSA-2 induced elevations of interferon- $\beta$  in plasma and tumors by both routes of administration. Well-tolerated regimens of MSA-2 induced tumor regressions in mice bearing MC38 syngeneic tumors. Most mice that exhibited complete regression were resistant to reinoculation of MC38 cells, suggesting establishment of durable antitumor immunity. In tumor models that were moderately or poorly responsive to PD-1 blockade, combinations of MSA-2 and anti-PD-1 antibody were superior in inhibiting tumor growth and prolonging survival over monotherapy (see the figure, right).

Structural studies showed that MSA-2 was bound as a noncovalent dimer to STING in a “closed-lid” conformation (see the figure, left). Each bound MSA-2 interacted with both monomers of the STING homodimer (depicted in blue and orange). The simplest model that can account for all observed equilibrium and kinetic behaviors of MSA-2 is as follows: MSA-2 in solution exists as monomers and noncovalent dimers in an equilibrium that strongly favors monomers; MSA-2 monomers cannot bind STING, whereas the noncovalent MSA-2 dimers bind STING with nanomolar affinity (see the figure, center). The model was further supported by findings that covalently tethered dimers of MSA-2 analogs exhibited nanomolar affinity for STING.

Simulations and experimental analyses predicted that MSA-2, a weak acid, would exhibit substantially higher cellular potency in an acidified tumor microenvironment than normal tissue, owing to increased cellular entry and retention combined with the inherently steep MSA-2 concentration dependence of STING occupancy (see the figure, bottom). It is likely that preferential activation of STING by MSA-2 in tumors substantially contributes to the observed favorable in vivo antitumor activity and tolerability profile of this compound.

**CONCLUSION:** In this work, we describe the identification, in vivo antitumor properties, and mechanism of action of MSA-2, an orally available human STING agonist. MSA-2 could prove valuable for the discovery and design of human STING agonists suitable for systemic administration in the clinic. ■

The list of author affiliations is available in the full article online.

\*These authors contributed equally to this work.

†Corresponding author. Email: samanthi\_perera@merck.com

(S.A.P.); gottfried.schroeder@merck.com (G.K.S.);

wes.trotter@kronosbio.com (B.W.T.); jonathan.bennett@

merck.com (D.J.B.); george\_addona@merck.com (G.H.A.)

Cite this article as B.-S. Pan et al., *Science* 369, eaba6098

(2020). DOI: 10.1126/science.aba6098

**S** READ THE FULL ARTICLE AT  
<https://doi.org/10.1126/science.aba6098>

## RESEARCH ARTICLE

## DRUG DEVELOPMENT

## An orally available non-nucleotide STING agonist with antitumor activity

Bo-Sheng Pan<sup>1\*</sup>, Samantha A. Perera<sup>1\*†</sup>, Jennifer A. Piesvaux<sup>1\*</sup>, Jeremy P. Presland<sup>1\*</sup>, Gottfried K. Schroeder<sup>1\*†</sup>, Jared N. Cumming<sup>2\*†</sup>, B. Wesley Trotter<sup>2\*†§</sup>, Michael D. Altman<sup>2</sup>, Alexei V. Buevich<sup>2</sup>, Brandon Cash<sup>2</sup>, Saso Cemerski<sup>3¶</sup>, Wonsuk Chang<sup>2</sup>, Yiping Chen<sup>1</sup>, Peter J. Dandliker<sup>1#</sup>, Guo Feng<sup>1</sup>, Andrew Haidle<sup>2</sup>, Timothy Henderson<sup>2</sup>, James Jewell<sup>2</sup>, Ilona Kariv<sup>1</sup>, Ian Knemeyer<sup>4</sup>, Johnny Kopinja<sup>1</sup>, Brian M. Lacey<sup>1</sup>, Jason Laskey<sup>1</sup>, Charles A. Lesburg<sup>2</sup>, Rui Liang<sup>2\*\*</sup>, Brian J. Long<sup>1</sup>, Min Lu<sup>2</sup>, Yanhong Ma<sup>1</sup>, Ellen C. Minnihan<sup>5††</sup>, Greg O'Donnell<sup>1</sup>, Ryan Otte<sup>2</sup>, Laura Price<sup>1</sup>, Larissa Rakhilina<sup>1</sup>, Berengere Sauvagnat<sup>1</sup>, Sharad Sharma<sup>3‡‡</sup>, Sriram Tyagarajan<sup>2</sup>, Hyun Woo<sup>4</sup>, Daniel F. Wyss<sup>2</sup>, Serena Xu<sup>1</sup>, David Jonathan Bennett<sup>2†</sup>, George H. Addona<sup>1†</sup>

Pharmacological activation of the STING (stimulator of interferon genes)–controlled innate immune pathway is a promising therapeutic strategy for cancer. Here we report the identification of MSA-2, an orally available non-nucleotide human STING agonist. In syngeneic mouse tumor models, subcutaneous and oral MSA-2 regimens were well tolerated and stimulated interferon- $\beta$  secretion in tumors, induced tumor regression with durable antitumor immunity, and synergized with anti-PD-1 therapy. Experimental and theoretical analyses showed that MSA-2 exists as interconverting monomers and dimers in solution, but only dimers bind and activate STING. This model was validated by using synthetic covalent MSA-2 dimers, which were potent agonists. Cellular potency of MSA-2 increased upon extracellular acidification, which mimics the tumor microenvironment. These properties appear to underpin the favorable activity and tolerability profiles of effective systemic administration of MSA-2.

Recent clinical experience with new cancer therapies that block immune checkpoint pathways, such as antibodies to PD-1 (anti-PD-1), has led to intense efforts focused on other immune pathways that may be pharmacologically modulated to enhance the therapeutic benefits of checkpoint inhibitors (1). STING (stimulator of interferon genes) is an endoplasmic reticulum-associated homodimeric protein and the receptor for 2',3'-cyclic guanosine monophosphate-adenosine monophosphate (cGAMP) (Fig. 1A), which is a second messenger produced by cGAMP synthase, a cytosolic double-stranded DNA sensor (2, 3). Crystallographic (4) and cryo-electron microscopy (5, 6) studies have revealed that cGAMP binding to STING induces

a pronounced conformational change from the open form of the ligand-free structure (Fig. 1B) to a closed-form complex that completely sequesters the bound ligand from solution (Fig. 1C). Activation of STING by cGAMP triggers downstream signaling events initially via interactions of the closed-form complex with TBK1 kinase (5, 6) and later by the transcription factors IRF3 and NF- $\kappa$ B, culminating in increased synthesis and secretion of type I interferons and proinflammatory cytokines (3). Type I interferons are essential to the development of robust adaptive antitumor immunity owing to their ability to stimulate T cell cross-priming (7), potentially rendering tumors more susceptible to checkpoint blockade (8). The therapeutic potential of STING agonism has been demonstrated in preclinical studies with syngeneic mouse tumor models in which a cyclic dinucleotide (CDN) STING agonist exhibited marked antitumor activity when administered intratumorally either alone or in combination with an inhibitor of PD-1 or PD-L1 (7, 9–12). However, owing to ubiquitous STING expression, systemically administered CDN-based STING agonists induced inflammatory cytokines in both tumor and normal tissues. Thus, the dosing routes of CDN-based STING agonists are largely limited to direct intratumor injection (7), which restricts their application to a subset of tumors.

To address a broad range of malignancies, STING agonists that are suitable for systemic administration are required. Feasibility of

treating tumors with a systemically dosed STING agonist has been demonstrated in vivo with the xanthone DMXAA, a mouse-specific STING agonist (13–15) that binds mouse STING in the same closed form as that induced by cGAMP (4) but does not activate human STING (16). Unfortunately, efforts to use DMXAA as a starting point for medicinal chemistry have thus far not succeeded (17). Recently, a non-CDN-based human STING agonist intended for intravenous administration was reported (18). Herein, we describe a previously unknown non-nucleotide STING agonist (MSA-2) that preferentially targets tumor tissue, owing to its distinctive mechanism of action. Moreover, MSA-2 can be dosed by oral administration, which is a convenient, low-cost delivery route.

## Discovery of the non-CDN STING agonist MSA-2

To identify cell-permeable STING agonists, we developed a high-throughput, cell-based phenotypic screen to detect stimulation of

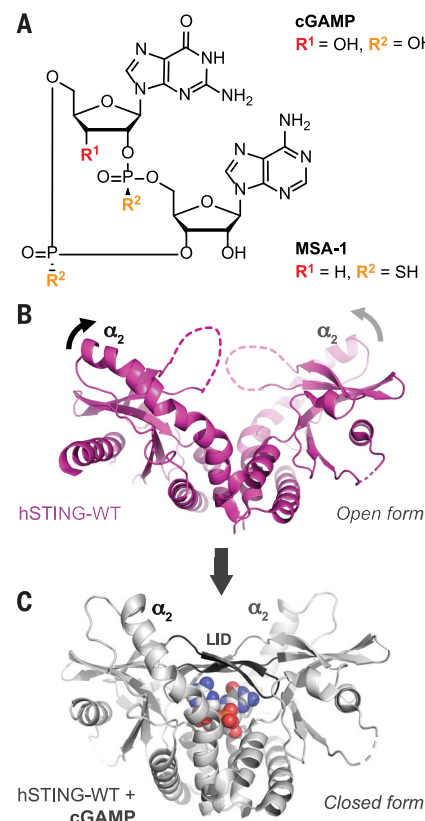


**Fig. 1. Structures of CDN ligands and human STING.** (A) Chemical structures of human endogenous STING agonist cGAMP and synthetic analog MSA-1. (B and C) The ligand-free open-form structure (magenta) (B) of the STING homodimer (PDB ID 4EF5) undergoes conformational change to a closed form (gray) (C) upon binding cGAMP (PDB ID 4KSY). In the closed form, the angle between the central helices ( $\alpha_2$ ) becomes more acute, and the lid residues form a four-stranded  $\beta$  sheet atop the binding site.

<sup>1</sup>Department of Quantitative Biosciences, Merck & Co., Inc., Kenilworth, NJ, USA. <sup>2</sup>Department of Discovery Chemistry, Merck & Co., Inc., Kenilworth, NJ, USA. <sup>3</sup>Department of Discovery Oncology, Merck & Co., Inc., Kenilworth, NJ, USA. <sup>4</sup>Department of Pharmacokinetics, Merck & Co., Inc., Kenilworth, NJ, USA. <sup>5</sup>Department of Discovery Pharmaceutical Sciences, Merck & Co., Inc., Kenilworth, NJ, USA. \*These authors contributed equally to this work. †Corresponding author. Email: samanthi\_perera@merck.com (S.A.P.); gottfried.schroeder@merck.com (G.K.S.); wes.trotter@kronosbio.com (B.W.T.); jonathan.bennett@merck.com (D.J.B.); george\_addona@merck.com (G.H.A.)

‡Present address: LifeMine Therapeutics, Cambridge, MA, USA. §Present address: Kronos Bio, Inc., Cambridge, MA, USA. ¶Present address: Cue Biopharma, Cambridge, MA, USA. #Present address: Dewpoint Therapeutics, Inc., Boston, MA, USA. \*\*Present address: Tri-Institutional Therapeutics Discovery Institute, New York, NY, USA. ††Present address: Bill & Melinda Gates Medical Research Institute, Cambridge, MA, USA. ‡‡Present address: Sanofi US, Cambridge, MA, USA.



interferon- $\beta$  (IFN- $\beta$ ) secretion, a known effect of STING agonism. Using human monocytic THP-1 cells that express the naturally occurring human HAQ STING isoform (hSTING-HAQ) (19), we screened a diverse library of ~2.4 million compounds and identified a small number of molecules, including MSA-2 (benzothiophene oxobutanoic acid) (Fig. 2A), that induced IFN- $\beta$  production in THP-1 cells (Fig. 2B). MSA-2 did not exhibit such activity in STING<sup>-/-</sup> THP-1 cells (fig. S1A). Moreover, treatment of THP-1 cells with MSA-2 induced phosphorylation of both TBK1 and IRF-3, consistent with STING pathway activation (fig. S1B). MSA-2 also induced IFN- $\beta$  in mouse macrophages (Fig. 2C). In biochemical assays, MSA-2 inhibited binding

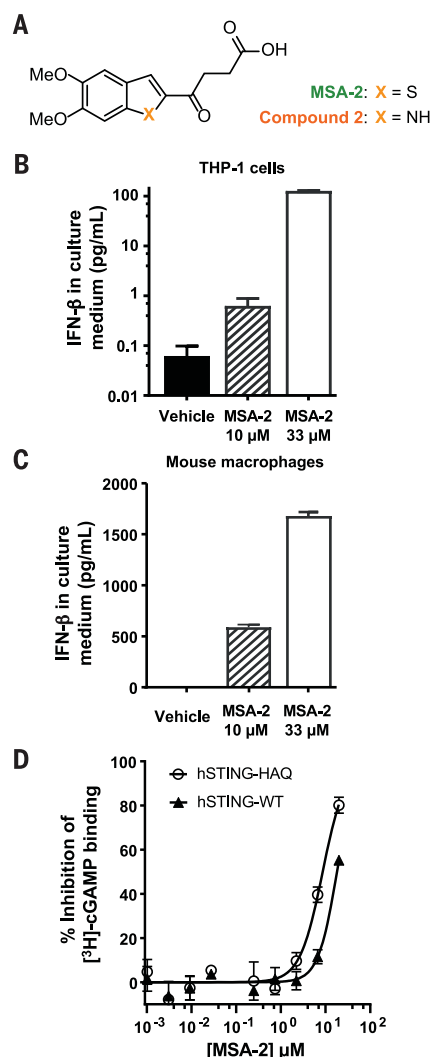


**Fig. 2. Confirmation of MSA-2 as a STING ligand.** (A) Chemical structures of MSA-2 and compound 2. Me, methyl group. (B) In vitro evidence of STING agonism included induction of IFN- $\beta$  in human THP-1 monocytes and (C) mouse macrophages. (D) MSA-2 displaces [<sup>3</sup>H]-cGAMP from hSTING-WT and hSTING-HAQ membranes in a filtration-based competition assay. Error bars indicate SD.

of radiolabeled cGAMP to full-length, membrane-anchored wild-type human STING (hSTING-WT) and hSTING-HAQ (Fig. 2D). Additionally, MSA-2 appeared to be selective, exhibiting no significant effect in binding assays against a panel of 108 receptor, transporter, ion channel, and enzyme assays when tested at 10  $\mu$ M (table S1). Consistent with its small size, MSA-2 also exhibited higher permeability than CDNs such as the phosphorothioate analog MSA-1 (Fig. 1A) in an in vitro permeability assay (apparent permeability =  $23.7 \times 10^{-6}$  cm/s versus undetected in LLC-PK1 cells).

### Orally dosed MSA-2 exhibits durable STING-dependent antitumor activity in vivo

To evaluate the in vivo pharmacokinetic and pharmacodynamic properties and antitumor activity of MSA-2, it was administered by intratumoral (IT), subcutaneous (SC), or oral (PO) routes in the MC38 (colon carcinoma) syngeneic mouse tumor model (Fig. 3A). Pharmacokinetic studies (Fig. 3, B and C) demonstrated that MSA-2 dosed via either PO or SC regimens achieved comparable exposure in both tumor and plasma (table S2). MSA-2 also exhibited dose-dependent antitumor activity when administered by IT, SC, or PO routes, and dosing regimens were identified that induced complete tumor regressions in 80 to 100% of treated animals (Fig. 3, D to F). Well-tolerated (assessed by body weight loss and recovery; Fig. 3G and fig. S2, A to C) PO or SC doses of MSA-2 that effectively inhibited tumor growth induced substantial elevations of IFN- $\beta$ , interleukin-6 (IL-6), and tumor necrosis factor- $\alpha$  (TNF- $\alpha$ ) in tumor and plasma (Fig. 3, H to J, and fig. S2, D and E), with peak levels at 2 to 4 hours and a return to baseline within ~24 hours (Fig. 3, I to J, and fig. S2, D and E).

All mice that experienced complete tumor regression were subsequently rechallenged with MC38 cells. Tumors did not grow in 95% of rechallenged animals (Fig. 3K), which suggests that MSA-2 induced long-term antitumor immunity. Furthermore, in MC38 tumor-bearing STING<sup>gt/gt</sup> (Goldenticket) mice, which lack detectable STING protein (20), MSA-2 exhibited no antitumor activity, weight loss, or cytokine induction (fig. S2, F to H), demonstrating that the observed MSA-2 activity is STING dependent. Moreover, as evaluated by in vivo antitumor activity and tolerability, MSA-2 administered orally in mice was equal to or better than MSA-1 (cGAMP analog; Fig. 1A) dosed by IT or SC routes (fig. S3). Orally dosed MSA-1 [10 mg per kilogram of body weight (mg/kg)] exhibited poor exposure and was undetectable in plasma (<0.01  $\mu$ M).

### MSA-2 predimerizes in solution before binding to STING

The x-ray crystal structure of MSA-2 bound to human STING (Fig. 4A) shows a closed conformation of STING, with the “lid” residues

(disordered in the ligand-free protein) forming a four-stranded  $\beta$  sheet atop two MSA-2 molecules and the two  $\alpha_2$  helices forming a smaller angle (Fig. 5A) than in the open conformation (Fig. 1B), similar to the cGAMP complex (Fig. 1C). Binding in the same site as cGAMP, the two MSA-2 molecules make substantial contact with each other via their aromatic cores [ $316 \text{ \AA}^2$  of total buried solvent-accessible surface area (SASA); table S3] and stack against Tyr<sup>167</sup> from each STING subunit (Fig. 4A). Bound MSA-2 also forms polar interactions with a network of water molecules and several surrounding side chains such as Ser<sup>162</sup> (Fig. 4A; pink dashed lines to methoxy oxygen atoms). Each MSA-2 ketone forms a hydrogen bond (green dashed lines) with the Arg<sup>238</sup> guanidinium group of the proximal STING monomer (e.g., chain A), and the carboxylate forms a hydrogen bond with the proximal Thr<sup>263</sup> (e.g., chain A). These same carboxylate groups additionally form hydrogen bonds (yellow dashed lines) with the Arg<sup>238</sup> side chain across the STING homodimer (e.g., chain B), noncovalently cross-linking the protein homodimer and stabilizing the “closed-lid” conformation. This binding mode is a distinctive characteristic of MSA-2 and is not observed in structures with other STING agonists (4, 18). Thus, the MSA-2 dimer fills the CDN binding pocket as effectively as cGAMP (MSA-2 dimer:  $1047 \text{ \AA}^2$ , cGAMP:  $1145 \text{ \AA}^2$  of total buried SASA; table S3) and functions as a STING agonist despite having a markedly lower molecular weight than that of cGAMP (294 versus 674 Da).

The solution <sup>1</sup>H nuclear magnetic resonance (NMR) spectrum of <sup>15</sup>N-labeled hSTING-HAQ (Fig. 4B, magenta) exhibits several well-separated resonances below 0 parts per million (ppm). When incubated with either cGAMP (black) or MSA-2 (blue), these resonances undergo analogous upfield shifts relative to ligand-free protein (Fig. 4B, dashed lines), suggesting a similar environment for these unassigned protein protons. Moreover, two-dimensional (2D) <sup>1</sup>H-<sup>15</sup>N heteronuclear correlation NMR spectra of hSTING (Fig. 4C) exhibited several distinct diagnostic peak shifts (or “fingerprints”) corresponding to the open conformation (ligand-free, magenta) or closed conformation (with bound cGAMP or MSA-2, black or blue, respectively). Substantial chemical shift perturbations were observed for lid residues such as Gly<sup>230</sup> and Gly<sup>234</sup>, consistent with the pronounced changes in local environment predicted for the “closed-lid” conformation versus the largely unstructured lid of the ligand-free state (Fig. 1B).

Conceptually, the STING-MSA-2 complex may be formed by one of the three mechanisms depicted in Fig. 5C. In Model 1, monomeric MSA-2 molecules bind independently to two identical, noninteracting ligand-binding sites

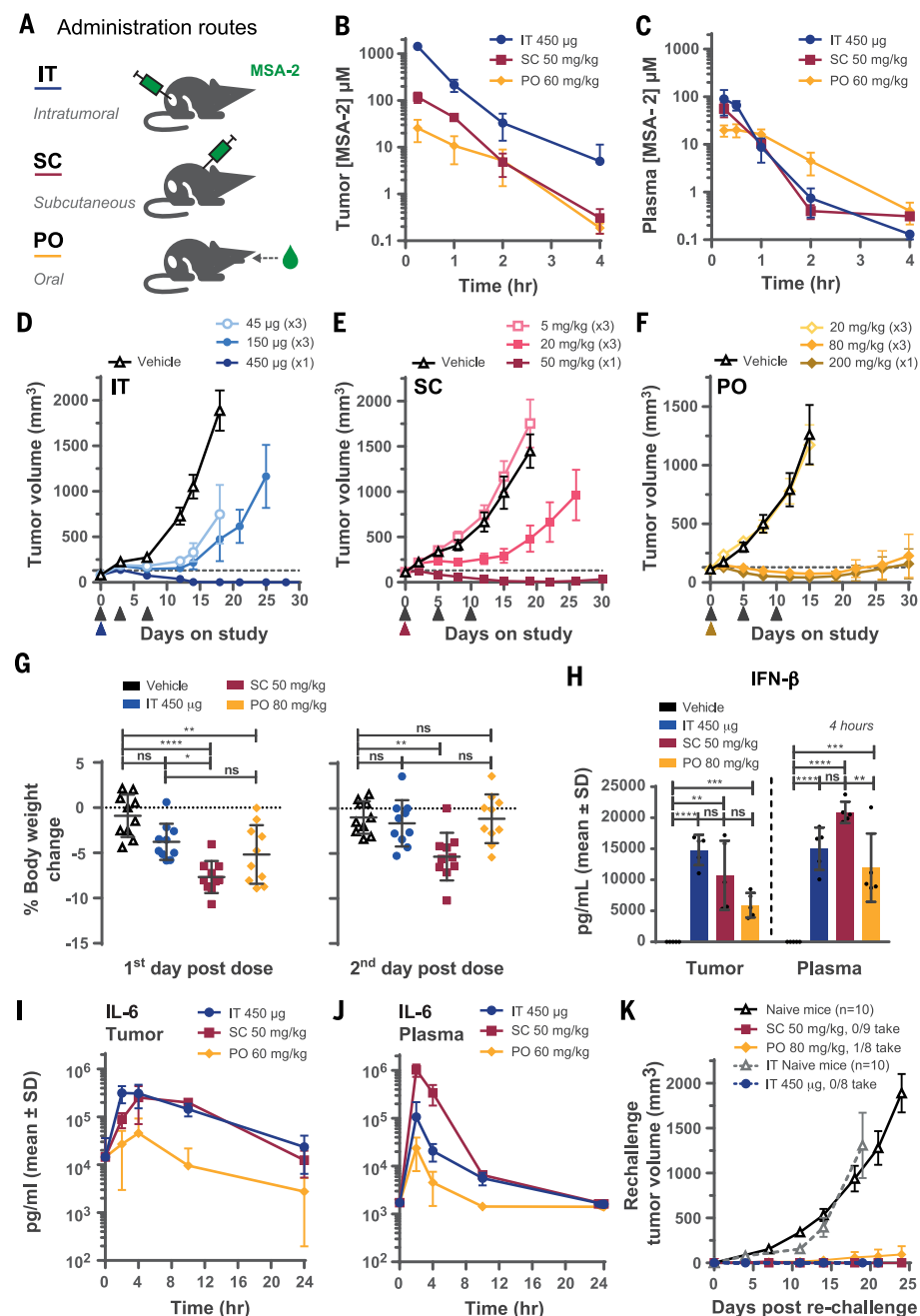


**Fig. 3. MSA-2 is an orally bioavailable STING agonist with in vivo antitumor activity.** (A) Illustration of administration routes. (B and C) Pharmacokinetics of indicated MSA-2 doses in tumors (B) and plasma (C) after single intratumoral (IT; blue circles), subcutaneous (SC; red squares), and oral (PO; yellow diamonds) administration in MC38 tumor-bearing C57BL/6 mice ( $n = 3$  to 6). (D to F) Effect of indicated IT (D), SC (E), and PO (F) regimens of MSA-2 (triangles below the x axis indicate dosing days) on MC38 tumor growth (initial volume  $\sim 100 \text{ mm}^3$ ,  $n = 10$  mice per group). Dashed lines indicate tumor start size of  $81 \text{ mm}^3$  (D) or  $112 \text{ mm}^3$  (E and F). (G) Tolerability, illustrated by percentage of body weight change of mice in (D) to (F), on days 1 and 2 for the indicated MSA-2 doses. (H to J) IFN- $\beta$  (H) and IL-6 (I to J) levels in MC38 tumors and plasma from C57BL/6 mice after 4 hours or over 24 hours after the indicated single doses of MSA-2 ( $n = 3$  to 5). (K) Tumor-growth kinetics and tumor-take frequency after reinoculation of MC38 tumors in mice from (D) to (F) that had previously experienced complete regression in response to indicated IT, SC, or PO regimens of MSA-2. Treatment-naive mice ( $n = 10$ ) were used as positive controls (triangles). Data points in (B), (C), and (G) to (J) represent mean  $\pm$  SD and in (D) to (F) and (K) represent mean  $\pm$  SEM. Statistical significance was determined by one-way analysis of variance (ANOVA). ns, not significant; \* $P < 0.05$ ; \*\* $P < 0.01$ ; \*\*\* $P < 0.001$ ; \*\*\*\* $P < 0.0001$ .

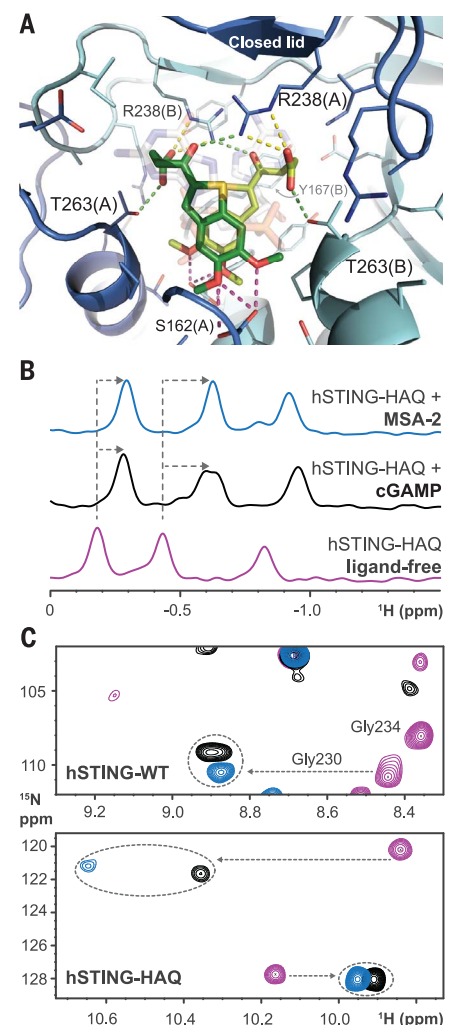
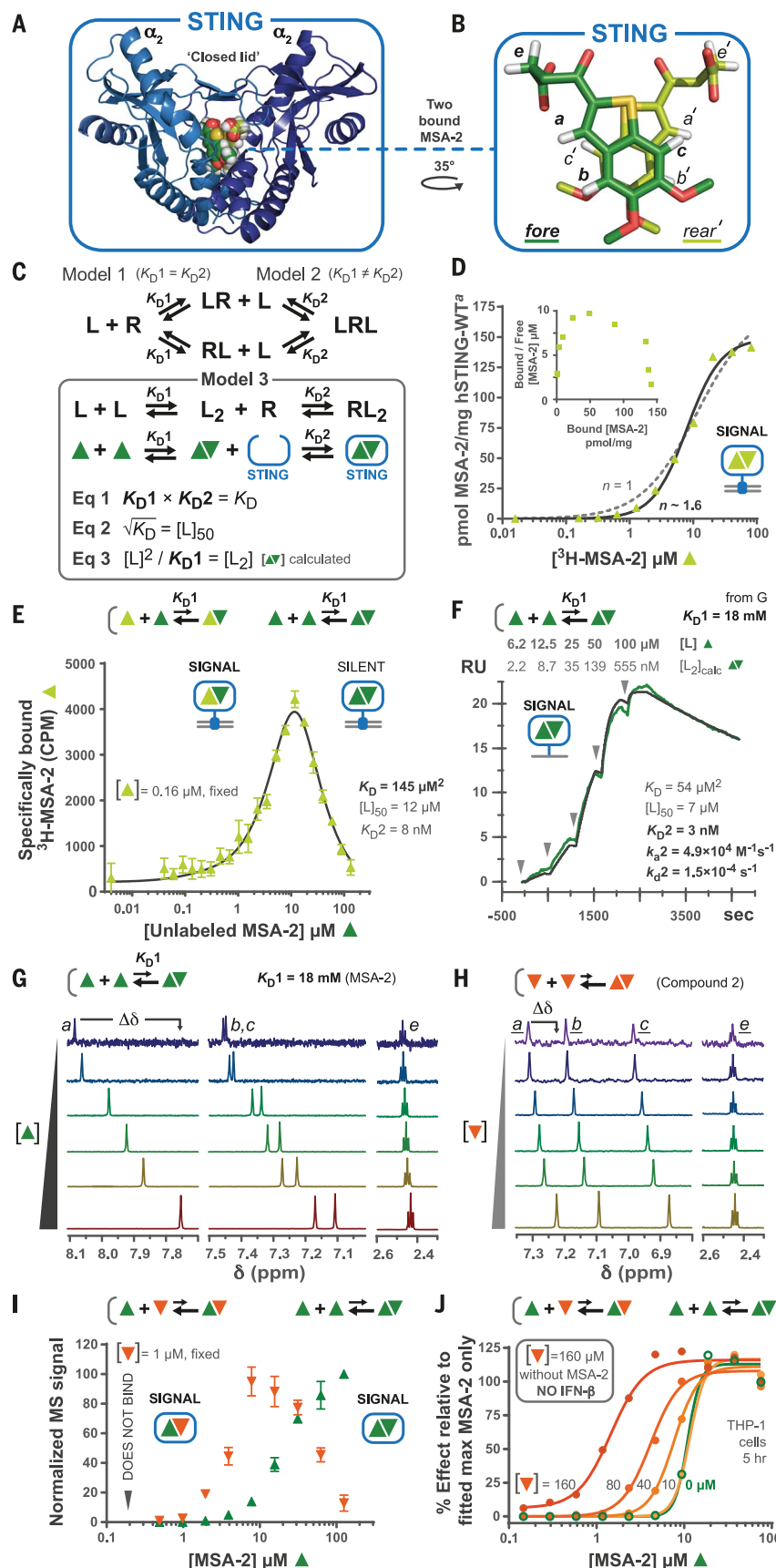


**Fig. 4. MSA-2 is bound to a closed form of hSTING.** (A) The 1.7-Å x-ray structure of an MSA-2: hSTING-HAQ complex shows two copies of MSA-2 (dark and light green) in the CDN binding site of human hSTING-HAQ. cGAMP (from PDB ID 4KSY) is depicted as faint transparent sticks to illustrate the overlapping binding site. Interactions between MSA-2 and the surrounding protein are shown as dashed lines. Lid interactions are shown in green (proximal) and yellow (cross-linking). Interactions at the base of the binding site are shown in pink. Specifically, MSA-2 forms both proximal and cross-linking interactions with lid residue Arg<sup>238</sup>. Residue Tyr<sup>167</sup>(A) has been removed for clarity. R, Arg; S, Ser; T, Thr; Y, Tyr. (B) Solution  $^1\text{H}$  NMR spectra of hSTING-HAQ shows that multiple well-resolved chemical shift perturbations in the presence of MSA-2 (blue, top spectrum) are more closely aligned with those in the presence of cGAMP (black, middle) than ligand-free protein (magenta, bottom). (C) Solution  $^1\text{H}$ - $^{15}\text{N}$  heteronuclear correlation NMR spectra of hSTING-WT and hSTING-HAQ (magenta, ligand-free; black, cGAMP; blue, MSA-2), highlighting resonances of lid residues Gly<sup>230</sup> and Gly<sup>234</sup> for hSTING-WT (top) and unassigned resonances for hSTING-HAQ (bottom), which undergo marked chemical shift perturbations when human STING adopts the closed form.



**Fig. 5. Mode of MSA-2–STING interaction.**

(A) Structure (PDB ID 6UKM) of hSTING-HAQ dimer (blue) with MSA-2 (green spheres). (B) Close-up of bound MSA-2. NMR-relevant protons (white) are annotated. (C) Three models in which L, L<sub>2</sub>, and R denote monomeric MSA-2 (dark green triangles), dimeric MSA-2, and dimeric STING, respectively. Visual depiction of Model 3 and equations are used throughout this figure. (D) Saturation binding of [<sup>3</sup>H]-MSA-2 (light green triangles) to full-length, membrane-anchored hSTING-WT (graphic). *n*, Hill coefficient; <sup>a</sup>, total membrane protein. (Inset) Corresponding Scatchard plot. (E) Homologous competition experiment with [<sup>3</sup>H]-MSA-2 (fixed), hSTING-WT, and unlabeled MSA-2 fitted with an equation based on Model 3 (solid line, *K<sub>D</sub>*). *K<sub>D</sub>*2 and [L]<sub>50</sub> were calculated from Eqs. 1 and 2 in (C) with *K<sub>D</sub>*1 = 18 mM. Visualizations and graphics (inset) depict predominant equilibria and STING complexes, respectively, per concentration. CPM, counts per minute. Error bars indicate SD. (F) Binding kinetics (SPR) of MSA-2 to hSTING-WT (green trace). *K<sub>D</sub>*2 was determined by fitting (1:1, black line) using dimeric [MSA-2] (L<sub>2</sub>) calculated from Eq. 3 in (C) with *K<sub>D</sub>*1 = 18 mM. Visualizations and graphics (inset) depict predominant equilibria and STING complexes, respectively, per concentration. CPM, counts per minute. Error bars indicate SD. (G) Proton NMR of MSA-2 titration to estimate *K<sub>D</sub>*1 (18 mM; fig. S6). Proton annotations correspond to those in (B).  $\delta$ , chemical shift. (H) Same as (G) for compound 2 (inverted triangles). (I) Simultaneous observation of hSTING-WT cytosolic domain (graphic)–bound MSA-2 (triangles, titration) and compound 2 (inverted triangles), monitored by affinity selection mass spectrometry (MS) and normalized independently (fig. S7 and text S2). Error bars indicate SD. (J) IFN- $\beta$  production in response to MSA-2 titrations (alone; green) at multiple concentrations of compound 2 (orange) fit to a four-parameter model (lines).



in a STING dimer. In Model 2, binding of a monomeric MSA-2 molecule to one STING subunit alters the MSA-2 affinity of the unoccupied STING subunit. In Model 3, MSA-2 exists as monomers and dimers in equilibrium, but only dimers can bind STING. These mechanistic models were probed experimentally.

Saturation binding of [<sup>3</sup>H]-MSA-2 to hSTING-WT yielded a Hill coefficient >1 (*n* ~ 1.6; solid line in Fig. 5D) and a concave downward Scatchard plot (Fig. 5D). Furthermore, homologous radioligand competition experiments exhibited a bell-shaped relationship between specific [<sup>3</sup>H]-MSA-2 binding to hSTING-WT and unlabeled MSA-2 concentration (Fig. 5E). These behaviors are incompatible with Model 1, which would have yielded a Hill coefficient of unity (dashed line in Fig. 5D), a linear Scatchard plot, and a homologous competition curve that decreased monotonically with increasing unlabeled [MSA-2]. Furthermore, Model 1 failed to account for the kinetics of MSA-2 interaction with human and mouse STING observed by surface plasmon resonance (SPR) (Fig. 5F and fig. S4). On the basis of these

findings, Model 1 was ruled out. Simulations showed that both Model 2 and Model 3 could, under certain conditions, display a concave downward Scatchard plot and a bell-shaped homologous competition curve (fig. S5). However, fitting the kinetic SPR results with Model 2 failed to satisfactorily account for the data (fig. S4B and text S1).

To further differentiate Models 2 and 3, we focused on experimental validation of the defining feature of Model 3: dimerization of MSA-2 in the absence of STING. <sup>1</sup>H-NMR of MSA-2 alone in aqueous buffer showed that several nonexchangeable MSA-2 benzothiophene ring protons underwent chemical shift perturbations in a concentration-dependent manner (Fig. 5G), consistent with a reversible dimerization process ( $K_D1 \approx 18$  mM; fig. S6). The observed chemical shift perturbations were substantially larger for protons *a* to *c* than for proton *e*, mirroring the changes in local environment experienced by the bioactive MSA-2 dimer seen in the crystal structure (Fig. 5B; larger shielding effects are expected for protons *a* to *c* because of aromatic group overlap). This was interpreted as supporting evidence that most MSA-2 dimers in solution are in a bioactive configuration capable of binding STING.

As shown in Fig. 5, E and F, both the equilibrium and kinetic properties of the MSA-2 and hSTING-WT interaction can be accommodated by Model 3, where monomeric and dimeric MSA-2 are in equilibrium ( $K_D1 \approx 18$  mM) and only MSA-2 dimers are capable of binding hSTING-WT with single-digit nanomolar potency (defined as  $K_D2$ ) and a slow off-rate ( $t_{1/2} = 1.3$  hours). Using Model 3, we were also able to determine equilibrium and kinetic constants for the interaction of MSA-2 with mouse STING (mSTING) and two common human STING variants (19): hSTING-HAQ and human STING-H232 (hSTING-H232) (tables S4 and S5 and fig. S4, D, F, and H). The rank order of dimeric MSA-2 affinity for the four STING variants is mSTING > hSTING-HAQ > hSTING-WT >> hSTING-H232.

Compound **2** (Fig. 2A), an MSA-2 analog in which the sulfur of the thiophene ring is replaced by nitrogen, exhibited a weaker tendency to homodimerize in solution than did MSA-2 (Fig. 5, G and H, and fig. S6). Compound **2** also appeared to bind both hSTING-WT and hSTING-HAQ more weakly than MSA-2 (fig. S7, A to D, and text S2) when assessed with a mass spectrometry-based technique that isolates and identifies protein-bound compounds [automated ligand identification system (ALIS)] (21). When the hSTING-WT (or hSTING-HAQ) cytosolic domain was incubated with **2** at a concentration insufficient to elicit detectable binding (fig. S7, C and D), inclusion of MSA-2 in the incubation caused concurrent binding of both MSA-2 and **2** to STING. As shown in Fig. 5I (or fig. S7E), in-

creasing [MSA-2] caused a bell-shaped increase (and decrease) in bound **2** (orange), whereas bound MSA-2 (green) concurrently increased in a sigmoidal fashion. These observations were interpreted as mass-action-driven formation of MSA-2:**2** heterodimers capable of binding STING and competition between these heterodimers and MSA-2 homodimers for binding to STING (Fig. 5I, top). To determine whether the MSA-2:**2** heterodimer is a functional agonist, cellular experiments were conducted to assess the agonist potency of MSA-2 in the presence of several fixed concentrations of compound **2**, which alone did not have any detectable agonist activity. Compound **2** increased the apparent potency of MSA-2 as much as 10-fold in a concentration-dependent manner when measuring IFN- $\beta$  secretion from THP-1 cells (Fig. 5J). These results suggest that (i) the MSA-2:**2** heterodimer is a functional agonist, and (ii) the equilibrium dissociation constant for heterodimer formation must be lower than that for compound **2** homodimerization. Taken together, the observed interactions between MSA-2 and **2** constitute powerful evidence for the basic premise of Model 3—namely, that the bioactive molecule is a noncovalent dimer.

### Design of covalent MSA-2 dimers, which are potent STING agonists

The central tenet of Model 3 is that MSA-2 must form a noncovalent dimer in solution to gain STING binding activity, whereas monomeric MSA-2 is incapable of binding STING. This model therefore predicts that a stable compound dimer would be a good ligand. We thus used this compound as the starting point for development of a more potent class of STING agonists. Although various substitutions of the heterocycle and oxobutanoic acid regions of the molecule did not improve potency, analysis of the x-ray cocrystal structure with STING suggested the possibility of synthetically linking the two closely packed MSA-2 units to produce a single molecule, a covalent dimer, that would bind with reduced entropic penalty.

To predict the optimal linkers for this design, we developed a computational method in which thousands of tethered benzothiophene cores were generated in silico (enumerated). Each of their conformations was scored for the estimated free energy required for selection out of the conformational ensemble versus the quality of overlay on the crystal structure of MSA-2 bound to STING (Fig. 6A). The results highlight linking between the 5-positions—especially replacement of both 5-methoxy groups with a propane linker (Fig. 6A, teal circle labeled **3**)—as particularly promising.

We thus synthesized covalent dimer **3** (Fig. 6C) and found that it is a highly potent STING agonist. Confirmation that the binding mode of **3** was similar to the MSA-2 noncovalent

pose was provided by an x-ray cocrystal structure with human STING (Fig. 6B), which illustrated that the key interactions of both the ketone and carboxylic acid moieties with STING lid residues replicate those of MSA-2. Notably, the loss of the 5-methoxy groups and their interactions with the side chains of Ser<sup>162</sup> did not abrogate cellular potency.

Having demonstrated the viability of a covalent linking strategy with a three-atom, all-carbon propyl linker in **3**, we investigated a diverse set of modifications and found that both homologation to four- and five-atom linkers and incorporation of oxygen at the linker attachment points were generally well tolerated, particularly when one or both benzothiophene cores were fluorinated alpha to the 5-position linker attachment point (Fig. 6C and fig. S8A). This effect was particularly evident for the 1,2-dioxoethane linker, for which fluorination of the core was required for potency (e.g., **6** and **7** versus **5**). Within the computational analysis, linkers with oxygen attachment points were predicted to have increased strain due to the required out-of-plane geometry. Fluorination at the neighboring position helps eliminate this strain through preorganization, consistent with observation.

In addition to linker composition, we also observed a surprisingly broad accommodation of different linker attachment points on the benzothiophene cores (Fig. 6C and fig. S8), with both 5,6- and 6,6-linked analogs of **9** providing potent agonists. With these data validating additional permutations beyond 5,5-tethers, we revisited the x-ray structure of MSA-2 bound to STING and noted the proximity of the 6-methoxy group of one MSA-2 unit to the 4-position of the benzothiophene core of its partner. On the basis of modeling that suggested that a shorter tether would be preferred, we prepared the 4,6-propyl linked analog **12**, which again demonstrated potent STING agonism.

X-ray crystallographic data obtained for a number of these covalent dimers bound to STING revealed that the oxobutanoic acid moiety is the dominant feature in determining the binding pose for these molecules (Fig. 6D, fig. S8B, and table S6). Notably, all analogs preserve the same configuration and interactions of the ketone and carboxylic acid portions of the oxobutanoic acid moieties, regardless of linker attachment points. To preserve these interactions, tethered molecules adopted benzothiophene conformations to maintain symmetric or pseudosymmetric  $\pi$ -stacking arrangements that conserve the oxobutanoic acid interaction with STING.

Taken together, the results described for MSA-2 and its covalent dimer analogs establish that presentation of two oxobutanoic acid substructures in a specific conformation—either through noncovalent interactions or linked by various methods and modified by



**Fig. 6. Identification of covalently linked MSA-2 analogs.**

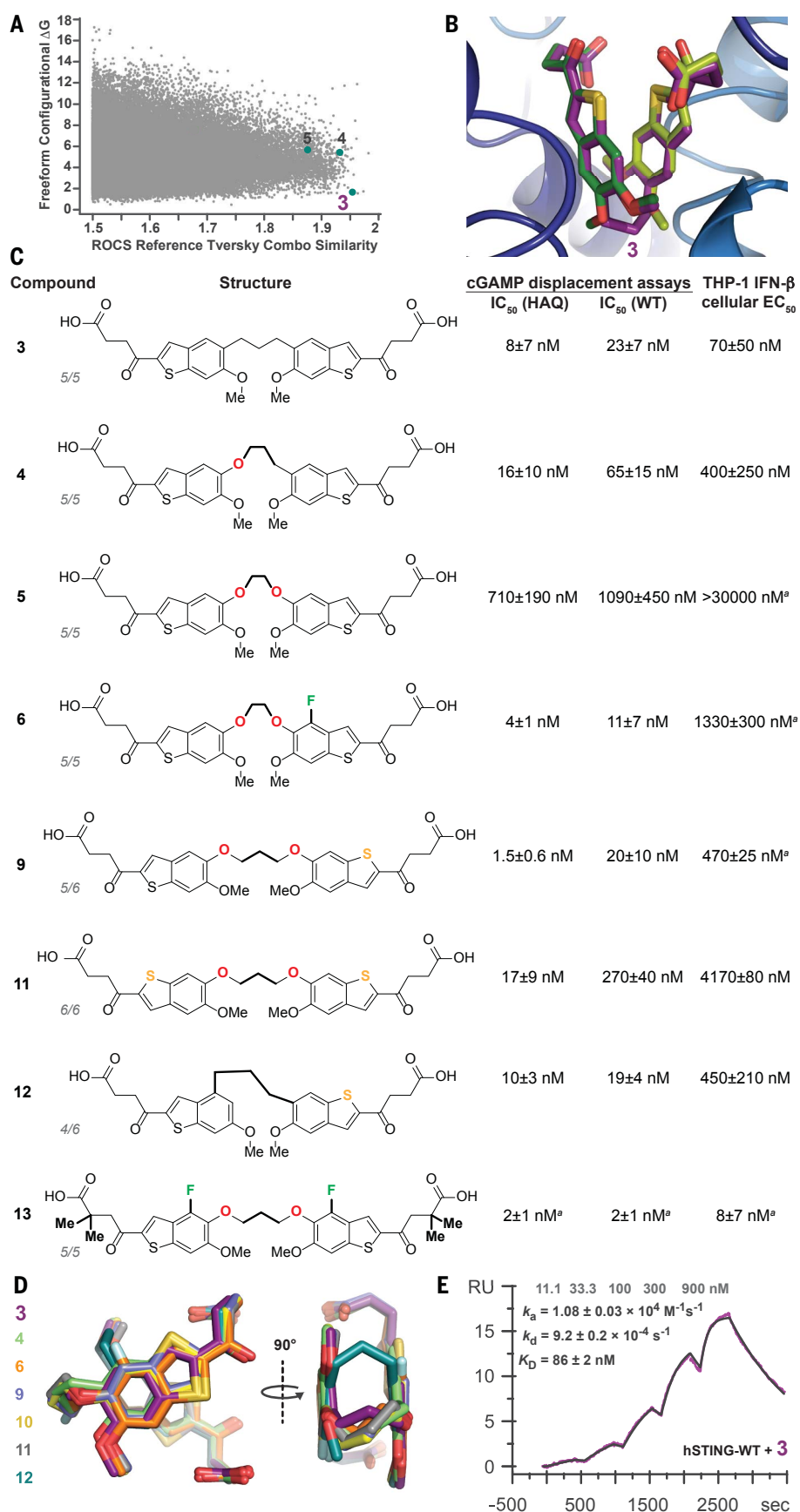
**(A)** Enumeration of thousands of possible linked benzothiophene core dimers identified linkage arrangements predicted to adopt low-energy conformations that provide optimal overlay with the MSA-2 STING-bound structure. Teal circles, predicted optimal conformations of **3**, **4**, and **5**;  $\Delta G$ , Gibbs free energy. **(B)** X-ray crystal structure of dimer **3** (purple) confirms adoption of an MSA-2 (dark and light green overlay)–like conformation in the STING binding site. **(C)** Variation of linker composition and attachment positions with assay data summary (mean  $\pm$  SD,  $n = 2$  unless noted with superscript  $a$ , in which case  $n \geq 3$ ). IC<sub>50</sub>, half-maximal inhibitory concentration; EC<sub>50</sub>, half-maximal effective concentration. **(D)** Superposition of crystal structures of STING in complex with seven covalent dimeric MSA-2 analogs with various combinations of linker length (three, four, or five atoms), C-linked or O-linked, symmetric or asymmetric, and substitution positions (5/5, 6/6, 5/6, 4/6). Each compound binds in the same location and positions the  $\gamma$ -ketoacid group for identical interactions with Arg<sup>238</sup> (see Fig. 4A), even if this requires the benzothiophene group to be flipped relative to the parental MSA-2 orientation. **(E)** SPR sensorgram for the interaction of compound **3** with hSTING-WT (purple line), successfully fitted with a direct 1:1 binding model (black line). Resultant kinetic parameters are summarized ( $n = 3$ ), and tested concentrations are noted in gray (top). RU, resonance units.

various substitutions—represents a general pharmacophore for potent STING agonism.

We selected compound **3** as the most reasonable surrogate for the noncovalent dimer of MSA-2 (Fig. 6, B and C) and determined the kinetic parameters by SPR. Compound **3** exhibited 1:1 binding with hSTING-WT and a slow on-rate ( $k_a = 1.1 \times 10^4 \text{ M}^{-1} \text{ s}^{-1}$ ) that is very similar to that calculated for the noncovalent MSA-2 dimer based on Model 3 ( $k_a = 4.9 \times 10^4 \text{ M}^{-1} \text{ s}^{-1}$ ; Fig. 5F). These observations further support our interpretation that the NMR-derived equilibrium constant for MSA-2 homodimerization ( $K_D$ ) predominately reflects formation of a bioactive dimer. In summary, the relatively simple Model 3 can fully account for all of the data. To our knowledge, MSA-2 is currently the only small molecule reported to undergo reversible, noncovalent dimerization in solution to become a pharmacologically active ligand.

#### Enhanced cellular potency of MSA-2 predicted in acidic tumor microenvironments

Considering physiologically relevant conditions, the fraction of uncharged MSA-2 molecules ( $\text{p}K_a = 4.78 \pm 0.05$ , where  $K_a$  is the acid dissociation constant) at pH 7.4 is  $\sim 0.2\%$  and increases with decreasing pH (fig. S9A). Assuming that cellular influx and efflux of MSA-2



is primarily by passive diffusion of uncharged MSA-2, we hypothesized that acidification of the extracellular environment, such as occurs often in tumors (22), would facilitate cellular entry and retention of MSA-2, thereby increasing its intracellular concentration and enhancing its apparent cellular potency. Employing the algorithms of Scott *et al.* (23) and a binding equation based on Model 3 {fraction saturation = [free MSA-2]<sup>2</sup>/(K<sub>D</sub> + [free MSA-2]<sup>2</sup>)}, we simulated the theoretical effects of extracellular pH on the intracellular [MSA-2] and fractional saturation of STING. The simulations predicted that when the ratio of cell membrane permeability of uncharged to charged MSA-2 ≥ 50, varying extracellular pH within the pathophysiological range (6 to 7.5) will have substantial effects on the intracellular concentrations of monomeric and dimeric MSA-2 (Fig. 7A) and will thereby shift the cellular potency of MSA-2 (Fig. 7B). This observation implies that in vivo, systemic doses of MSA-2 that are insufficient to induce detectable STING activation in normal tissues may elicit substantial STING activation in tissues with an acidified microenvironment.

These predictions were validated qualitatively by observations that stepwise reductions of extracellular pH from 7.5 to 6 increased MSA-2 potency in both THP-1 cells and mouse macrophages (Fig. 7, C and D). By contrast, in THP-1 cells the potency of cGAMP, which is 100% anionic over the same pH range, was essentially unchanged (Fig. 7E). Direct pH measurement in vivo confirmed that relevant syngeneic mouse tumors were more acidic than nontumor regions (Fig. 7F). Moreover, higher MSA-2 concentrations were observed in tumors than in plasma or other nontumor tissues (Fig. 7G) and were used to calculate theoretical bioactive MSA-2 dimer levels (dotted line). The increase in proinflammatory cytokine (IFN-β, IL-6, and TNF-α) levels also trends higher in tumors than in various nontumor tissues after administration of MSA-2 by SC or PO routes (Fig. 7H and fig. S9, B and C).

### MSA-2 enhances in vivo antitumor activity of anti-PD-1 antibody

We also investigated whether MSA-2 could enhance antitumor activity of anti-PD-1 in syngeneic tumor models that are either moderately or poorly responsive to PD-1 blockade. Combinations of systemically administered MSA-2 with anti-PD-1 were evaluated in four syngeneic mouse tumor models: advanced MC38 (colorectal), CT26 (colorectal), B16F10 (melanoma), and LL-2 (lung) tumors. For each tumor model, one or more combinations of anti-PD-1 dosed intraperitoneally and MSA-2 (dosed subcutaneously or orally) were found to be synergistic in inhibiting tumor growth and prolonging overall survival compared with the corresponding monotherapy (Fig. 8, A to

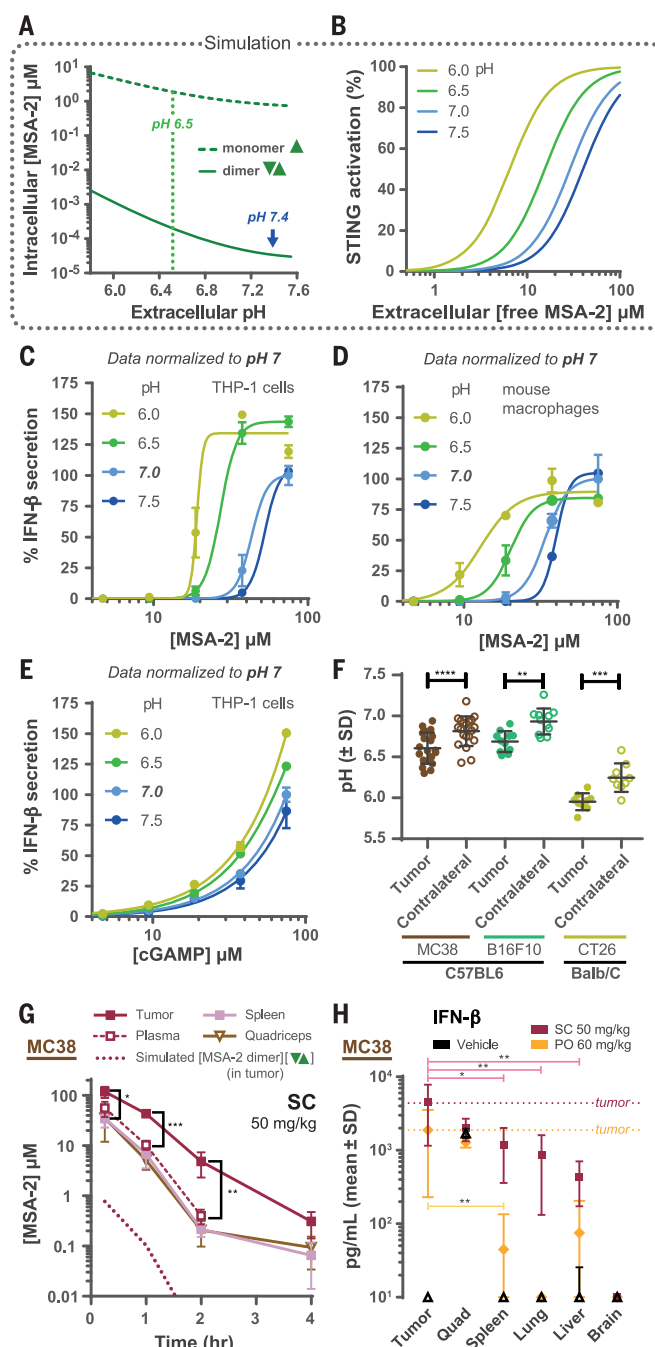


**Fig. 7. Simulated and observed effect of extracellular pH on MSA-2-induced STING activation.**

(A) Simulated effect of extracellular pH on intracellular concentration of dimeric and monomeric MSA-2 when total extracellular [free MSA-2] = 3 μM. Assumptions: membrane potential = -40 mV, intracellular pH = 7.2, permeability ratio of uncharged to charged free MSA-2 = 50. (B) Simulated effect of extracellular pH on relationship between extracellular [free MSA-2] and STING occupancy (K<sub>D</sub> = 100 μM<sup>2</sup>) in cells. Same assumptions as in (A); see materials and methods. (C and D) Observed effect of extracellular pH on potency of MSA-2 in stimulating IFN-β secretion in THP-1 cells and mouse macrophages, respectively. (E) Observed effect of extracellular pH on cGAMP potency in THP-1 cells. (F) In vivo pH measurements from tumors (solid circles) and contralateral skin area (open circles) (n = 9 to 11) in three different syngeneic tumor models. (G) Time course of MSA-2 concentrations in various tissues after a single SC dose of 50 mg/kg to MC38 tumor-bearing C57BL/6 mice (n = 3). Data were collected from the same experiment depicted in Fig. 3, B and C. Simulated upper limit for bioactive [dimeric MSA-2] in tumors (dotted line) calculated using Model 3 (Eq. 3 from Fig. 5C). (H) IFN-β levels in various tissues of MC38 tumor-bearing C57BL/6 mice (n = 5, mean ± SD) 4 hours after the indicated doses of MSA-2 by SC or PO administration. Statistical significance was determined by paired *t* test (F) or one-way ANOVA [(G) and (H)]. \**P* < 0.05; \*\**P* < 0.01; \*\*\**P* < 0.001; \*\*\*\**P* < 0.0001.



D, and fig. S10). Combination regimens with lower MSA-2 levels achieved the same efficacy end point with improved tolerability (body weight) compared with the higher MSA-2 monotherapies required for regression in these anti-PD-1 refractory models (Fig. 8E). Further, combinations of MSA-2 and anti-PD-1 increased tumor CD8<sup>+</sup> T cell infiltration in the LL-2 tumor model (Fig. 8F). Moreover, T cell and immunodeficient mice (Ncr nude and NSG) bearing MC38 tumors exhibited only partial tumor regression in response to MSA-2 doses that are typically sufficient to induce complete regression in C57BL6 mice (Fig. 8G), despite evident target engagement (changes in both cytokine levels and body weight; fig. S11). These observations, combined with the MC38 rechallenge results (Fig. 3K), suggest that both innate and adaptive immune function contribute to STING agonist-driven tumor regression. However, further in vitro and in vivo studies are required to more fully understand the immunopharmacology and toxicology of MSA-2 and related compounds.

## Outlook

We report the identification of an orally available, non-nucleotide-based STING agonist, MSA-2, in a high-throughput cell-based phenotypic screen. When used as a single agent in mice, systemically administered MSA-2 induced tumor regression with durable anti-tumor immunity and was well tolerated. In mouse tumor models that are poorly responsive to PD-1 blockade, combinations of MSA-2 with an anti-PD-1 immune checkpoint inhibitor were superior to monotherapy in inhibiting tumor growth and prolonging survival. Experiments with STING-deficient and immunodeficient mice showed that the immunogenic and anti-tumor activities of MSA-2 are mediated by STING and involve both the innate and adaptive immune systems. These observations strongly support the concept that induction of host adaptive antitumor immunity via pharmacological activation of STING can overcome tumor resistance to checkpoint inhibitors.

First-generation CDN-based STING agonists currently undergoing clinical trials are dosed by intratumor injection. A recent study by Sivick *et al.* (9) highlighted the challenges associated with attaining optimum drug levels by direct intratumor dosing, a critical requirement to balance the immunogenic and cell-ablative effect of STING activation. The ease of MSA-2 PO administration and the corresponding pharmacokinetic profile allow fine-tuning of the magnitude of STING agonism in various tissues in vivo.

Notably, MSA-2 preferentially targets tumor tissue because of its distinctive mechanism of action. In-depth molecular mechanism of action studies revealed that MSA-2 is not an

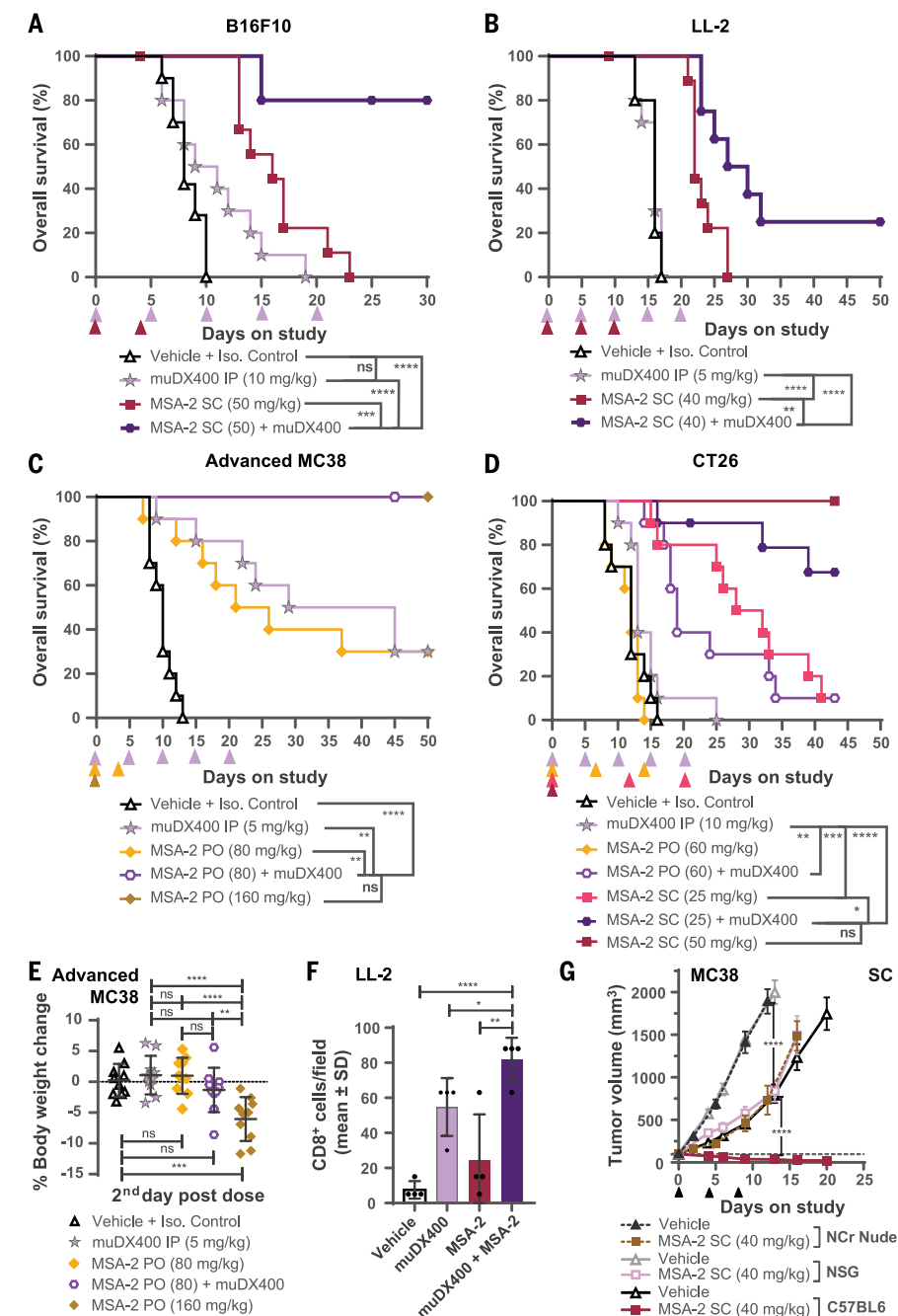


**Fig. 8. Therapeutic activity of systemic MSA-2 regimens combined with PD-1 blockade in mouse tumor models.** Survival curves of B16F10 (A), LL-2 (B), advanced MC38 (C), and CT-26 (D) tumor-bearing mice treated with vehicle + Iso. control (anti-mouse IgG1 monoclonal antibody), muDX400 (anti-mouse PD-1 monoclonal antibody), or MSA-2 at the indicated doses (SC or PO; colored as in Fig. 1) alone or in combination with muDX400 ( $n = 10$  per group). Vehicle was dosed SC or PO and antibodies were dosed intraperitoneally (IP). (E) Tolerability, illustrated by percentage of body weight change of mice in (C), on day 2 for the indicated doses. (F) Quantification of CD8<sup>+</sup> T cell infiltration into LL-2 tumors treated as in (B) ( $n = 4$ ). (G) Tumor volume in T cell-deficient NCr nude and NSG or immune-competent C57BL6 mice after vehicle or MSA-2 administration ( $n = 10$ , mean  $\pm$  SEM). Statistical significance was determined by log-rank Mantel-Cox test for (A) to (D), one-way ANOVA for (E), and unpaired Student's *t* test for (F) and (G). ns, not significant; \* $P < 0.05$ ; \*\* $P < 0.01$ ; \*\*\* $P < 0.001$ ; \*\*\*\* $P < 0.0001$ .

active ligand of STING but rather a prodrug of sorts. In solution, monomeric MSA-2 exists in equilibrium with a noncovalent dimer of MSA-2, which is a potent STING agonist. In fact, covalently tethered dimers of MSA-2 ana-

logs, another previously unidentified class of STING agonists, exhibited nanomolar affinity for STING. Simulations and experimental analyses predicted that MSA-2, a weak acid, would exhibit substantially higher cellular potency

in an acidified tumor microenvironment (versus normal tissue), owing to increased cellular entry and retention combined with its inherent mode of interaction with STING. It is likely that preferential activation of STING by MSA-2 in tumors substantially contributes to the observed favorable in vivo antitumor activity and tolerability profile of this compound. MSA-2 is a small molecule that undergoes reversible, noncovalent dimerization in solution to become a pharmacologically active ligand. MSA-2, an orally available human and mouse STING agonist, should be a valuable tool in the endeavor to discover and design human STING agonists suitable for systemic administration in the clinic.

## Materials and methods summary

### High-throughput screening and follow-up assays

In the primary screen, THP-1 (ATCC TIB-202) cells were incubated, in 1536-well plates, with test compounds (20  $\mu$ M) in a RPMI1640-based assay medium in the presence of 5% carbon dioxide at 37°C for 5 hours. IFN- $\beta$  levels were determined using an AlphaLISA assay and an EnVision Reader (PerkinElmer, Waltham, MA) and expressed as percentages of IFN- $\beta$  induced by cGAMP (100  $\mu$ M, positive control). In follow-up assays, the cellular activity of hits from the primary screen was confirmed in THP-1 and mouse macrophage cells by using the Meso Scale Human Interferon- $\beta$  assay kit (Meso Scale Discovery) or the mouse IFN- $\beta$  Verikine ELISA (enzyme-linked immunosorbent assay) (PBL Assay Science, Piscataway, NJ), respectively. STING binding activity of compounds was evaluated with a competitive radioligand binding assay using tritiated cGAMP and membrane embedded full-length recombinant human and mouse STING generated in insect cells. STING pathway activation by MSA-2 was assessed by Western blotting, probing phosphorylation status and total protein levels of STING, TBK-1, and IRF3 by using commercially available antibodies (Cell Signaling Technology, Danvers, MA).

### Biochemical and biophysical methods

In saturation binding experiments, insect microsomes expressing full-length STING were incubated with serially diluted tritiated MSA-2 for 18 hours at 25°C. Reactions were terminated by filtration, and filter-bound radioactivity was measured by a TopCount NXT instrument (Perkin Elmer). Nonspecific binding was determined in the presence of cGAMP (20  $\mu$ M). In homologous competition binding experiments, insect microsomes expressing hSTING-WT or mSTING were incubated for 16 hours (25°C) with serially diluted unlabeled MSA-2 (with or without 100  $\mu$ M cGAMP) at a fixed concentration of tritiated MSA-2 (0.16  $\mu$ M). Levels of STING-bound tritiated MSA-2 were determined as described above. N-terminal

tagged recombinant cytosolic domain STING constructs were cloned into the pET47b plasmid, expressed in *Escherichia coli*, and purified by affinity and size exclusion chromatography. Affinity tags were removed for proteins intended for crystallography and protein NMR. STING intended for SPR experiments was biotinylated using BirA Biotin-Protein Ligase Bulk Reaction Kit (Avidity, Aurora, CO). STING used in NMR experiments was generated using expression media containing [ $^{15}$ N]-ammonium sulfate (Cambridge Isotope Laboratories, Tewksbury, MA). For crystallography, cocrystals of hSTING-HAQ complexed with MSA-2 or covalent dimers were prepared by hanging-drop vapor diffusion with streak seeding at 18°C. Samples were prepared for synchrotron data collection by swishing through perfluoropolyether cryo oil (Hampton Research) before plunging into liquid nitrogen. Structures were solved by molecular replacement using PDB ID 4KSY as a probe. Protein NMR experiments (1D  $^1$ H methyl and 2D  $^1$ H- $^{15}$ N SOFAST-HMQC) using  $^{15}$ N-labeled STING (50  $\mu$ M) were conducted at 30°C on an 800-MHz Bruker Ascend Four Channel AVANCE III HD NMR spectrometer equipped with a TCI 5-mm CryoProbe (automatic tuning and matching). Proton ( $^1$ H) NMR experiments to determine dimerization properties of MSA-2 or compound **2** were collected on a Varian VNMRs 600-MHz instrument at 25°C. For SPR (Biacore T200, GE Healthcare) experiments, biotinylated cytosolic domain STING variants (1 to 3  $\mu$ M, molecular weight ~31 kDa) were captured on a streptavidin chip (Series S Sensor Chip SA, GE Healthcare) to a final level of ~3100 resonance units. Serially diluted compound solutions were analyzed using single-cycle injection mode at a flow rate of 50  $\mu$ L/min in HBS-EP+ buffer (GE Healthcare) with 1 mM dithiothreitol and 3% v/v dimethyl sulfoxide. For ALIS experiments, human STING (5  $\mu$ M) was preincubated with MSA-2 and/or compound **2** for 30 min before injection into the ALIS system. Both protein and protein-ligand complexes were separated from unbound ligand by using a proprietary size exclusion chromatography column and were subsequently directed to a reverse-phase C18 column (40°C) equilibrated with aqueous 0.2% formic acid. Dissociated ligands were resolved using a solvent gradient (0 to 95% acetonitrile in 2.5 min) and eluted directly into a high-resolution Exactive mass spectrometer (ThermoFisher Scientific, San Jose, CA).

### In vivo methods

All animal experimental procedures were performed according to the guidelines approved by the Institutional Animal Care and Use Committee of Merck & Co., Inc., Kenilworth, NJ, USA, following the guidance of the Association for Assessment and Accreditation of Laboratory Animal Care. C57BL/6J and NSG (NOD.

Cg-Prkdc<sup>scid</sup> Il2rg<sup>tm1Wjl</sup>/SzJ) mice were obtained from The Jackson Laboratory (Bar Harbor, ME), whereas BALB/c and nude NCr mice were obtained from Taconic Biosciences (Germantown, NY). Tumor cells were inoculated subcutaneously into the lower flank. MSA-2 or vehicle was dosed by IT injection, SC injection, or PO gavage. Tumor and body-weight measurements were performed twice per week using calipers and a weigh scale, respectively. Mice were euthanized when tumor volume approached ~2000 mm<sup>3</sup>, weight loss exceeded 20%, or tumors ulcerated. When necessary, plasma and tumor samples were collected at specific time points and frozen for pharmacokinetics and pharmacodynamics studies. MSA-2 concentration was then determined by liquid chromatography and mass spectroscopy (API5000, Applied Biosystems). IFN- $\beta$  was measured by ELISA (PBL Assay Science, Piscataway, NJ), and IL-6 and TNF- $\alpha$  were measured using a Meso Scale kit (custom U-plex kit, Meso Scale Discovery, Rockland, MD). Tumor pH was measured using a bevel-needle-tipped combination microelectrode (Orion 9863BN Micro pH Electrode) inserted up to 1.3 cm into the center of the tumor.

### Chemistry

Tritiated cGAMP was synthesized via a biocatalytic reaction in which recombinant cGAMP synthase preactivated with herring DNA was incubated with [ $^3$ H]-ATP (Perkin Elmer) and [ $^3$ H]-GTP (Perkin Elmer) overnight at 37°C. The reaction was then filtered to remove protein, and [ $^3$ H]-cGAMP was purified by anion exchange chromatography. MSA-2 was synthesized in three steps using 5,6-dimethoxybenzo[b]thiophene-2-carboxylic acid as the starting material and (3-ethoxy-3-oxopropyl)zinc(II) bromide. Tritiated MSA-2 (4-(5-methoxy-6-(methoxy-*t*-<sub>3</sub>)benzo[b]thiophen-2-yl)-4-oxobutanoic acid) was synthesized in five steps using MSA-2 as the starting material.

See the supplementary materials for more details about the experimental materials and methods.

### REFERENCES AND NOTES

1. S. A. Patel, A. J. Minn, Combination cancer therapy with immune checkpoint blockade: Mechanisms and strategies. *Immunity* **48**, 417–433 (2018). doi: [10.1016/j.immuni.2018.03.007](https://doi.org/10.1016/j.immuni.2018.03.007); pmid: [29562193](https://pubmed.ncbi.nlm.nih.gov/29562193/)
2. P. Gao et al., Cyclic [G(2',5')pA(3',5')p] is the metazoan second messenger produced by DNA-activated cyclic GMP-AMP synthase. *Cell* **153**, 1094–1107 (2013). doi: [10.1016/j.cell.2013.04.046](https://doi.org/10.1016/j.cell.2013.04.046); pmid: [23647843](https://pubmed.ncbi.nlm.nih.gov/23647843/)
3. X. Zhang et al., Cyclic GMP-AMP containing mixed phosphodiester linkages is an endogenous high-affinity ligand for STING. *Mol. Cell* **51**, 226–235 (2013). doi: [10.1016/j.molcel.2013.05.022](https://doi.org/10.1016/j.molcel.2013.05.022); pmid: [23747010](https://pubmed.ncbi.nlm.nih.gov/23747010/)
4. P. Gao et al., Structure-function analysis of STING activation by c[G(2',5')pA(3',5')p] and targeting by antiviral DMXAA. *Cell* **154**, 748–762 (2013). doi: [10.1016/j.cell.2013.07.023](https://doi.org/10.1016/j.cell.2013.07.023); pmid: [23910378](https://pubmed.ncbi.nlm.nih.gov/23910378/)
5. G. Shang, C. Zhang, Z. J. Chen, X. C. Bai, X. Zhang, Cryo-EM structures of STING reveal its mechanism of activation by cyclic GMP-AMP. *Nature* **567**, 389–393 (2019). doi: [10.1038/s41586-019-0998-5](https://doi.org/10.1038/s41586-019-0998-5); pmid: [30842659](https://pubmed.ncbi.nlm.nih.gov/30842659/)



6. C. Zhang *et al.*, Structural basis of STING binding with and phosphorylation by TBK1. *Nature* **567**, 394–398 (2019). doi: [10.1038/s41586-019-1000-2](https://doi.org/10.1038/s41586-019-1000-2); pmid: [30842653](https://pubmed.ncbi.nlm.nih.gov/30842653/)
7. L. Corrales *et al.*, Direct Activation of STING in the Tumor Microenvironment Leads to Potent and Systemic Tumor Regression and Immunity. *Cell Rep.* **11**, 1018–1030 (2015). doi: [10.1016/j.celrep.2015.04.031](https://doi.org/10.1016/j.celrep.2015.04.031); pmid: [25959818](https://pubmed.ncbi.nlm.nih.gov/25959818/)
8. T. L. Whiteside, S. Demaria, M. E. Rodriguez-Ruiz, H. M. Zarour, I. Melero, Emerging Opportunities and Challenges in Cancer Immunotherapy. *Clin. Cancer Res.* **22**, 1845–1855 (2016). doi: [10.1158/1078-0432.CCR-16-0049](https://doi.org/10.1158/1078-0432.CCR-16-0049); pmid: [27084738](https://pubmed.ncbi.nlm.nih.gov/27084738/)
9. K. E. Sivick *et al.*, Magnitude of Therapeutic STING Activation Determines CD8<sup>+</sup> T Cell-Mediated Anti-tumor Immunity. *Cell Rep.* **25**, 3074–3085.e5 (2018). doi: [10.1016/j.celrep.2018.11.047](https://doi.org/10.1016/j.celrep.2018.11.047); pmid: [30540940](https://pubmed.ncbi.nlm.nih.gov/30540940/)
10. A. Sallets, S. Robinson, A. Kardosh, R. Levy, Enhancing immunotherapy of STING agonist for lymphoma in preclinical models. *Blood Adv.* **2**, 2230–2241 (2018). doi: [10.1182/bloodadvances.2018020040](https://doi.org/10.1182/bloodadvances.2018020040); pmid: [30194137](https://pubmed.ncbi.nlm.nih.gov/30194137/)
11. G. Berger, M. Marloye, S. E. Lawler, Pharmacological Modulation of the STING Pathway for Cancer Immunotherapy. *Trends Mol. Med.* **25**, 412–427 (2019). doi: [10.1016/j.molmed.2019.02.007](https://doi.org/10.1016/j.molmed.2019.02.007); pmid: [30885429](https://pubmed.ncbi.nlm.nih.gov/30885429/)
12. S. Yum, M. H. Li, A. E. Frankel, Z. J. J. Chen, Roles of the cGAS-STING Pathway in Cancer Immunoregulation and Immunotherapy. *Annu. Rev. Cancer Biol.* **3**, 323–344 (2019). doi: [10.1146/annurev-cancerbio-030518-055636](https://doi.org/10.1146/annurev-cancerbio-030518-055636)
13. J. Conlon *et al.*, Mouse, but not human STING, binds and signals in response to the vascular disrupting agent 5,6-dimethylxanthone-4-acetic acid. *J. Immunol.* **190**, 5216–5225 (2013). doi: [10.4049/jimmunol.1300097](https://doi.org/10.4049/jimmunol.1300097); pmid: [23585680](https://pubmed.ncbi.nlm.nih.gov/23585680/)
14. D. Prantner *et al.*, 5,6-Dimethylxanthone-4-acetic acid (DMXAA) activates stimulator of interferon gene (STING)-dependent innate immune pathways and is regulated by mitochondrial membrane potential. *J. Biol. Chem.* **287**, 39776–39788 (2012). doi: [10.1074/jbc.M112.382986](https://doi.org/10.1074/jbc.M112.382986); pmid: [23027866](https://pubmed.ncbi.nlm.nih.gov/23027866/)
15. S. Kim *et al.*, Anticancer flavonoids are mouse-selective STING agonists. *ACS Chem. Biol.* **8**, 1396–1401 (2013). doi: [10.1021/cb400264n](https://doi.org/10.1021/cb400264n); pmid: [23683494](https://pubmed.ncbi.nlm.nih.gov/23683494/)
16. J. M. Weiss *et al.*, The STING agonist DMXAA triggers a cooperation between T lymphocytes and myeloid cells that leads to tumor regression. *Oncolimmunology* **6**, e1346765 (2017). doi: [10.1080/2162402X.2017.1346765](https://doi.org/10.1080/2162402X.2017.1346765); pmid: [29123960](https://pubmed.ncbi.nlm.nih.gov/29123960/)
17. J. Hwang, T. Kang, J. Lee, B. S. Choi, S. Han, Design, synthesis, and biological evaluation of C7-functionalized DMXAA derivatives as potential human-STING agonists. *Org. Biomol. Chem.* **17**, 1869–1874 (2019). doi: [10.1039/C8OB01798K](https://doi.org/10.1039/C8OB01798K); pmid: [30117503](https://pubmed.ncbi.nlm.nih.gov/30117503/)
18. J. M. Ramanjulu *et al.*, Design of amidobenzimidazole STING receptor agonists with systemic activity. *Nature* **564**, 439–443 (2018). doi: [10.1038/s41586-018-0705-y](https://doi.org/10.1038/s41586-018-0705-y); pmid: [30405246](https://pubmed.ncbi.nlm.nih.gov/30405246/)
19. G. Yi *et al.*, Single nucleotide polymorphisms of human STING can affect innate immune response to cyclic dinucleotides. *PLOS ONE* **8**, e77846 (2013). doi: [10.1371/journal.pone.0077846](https://doi.org/10.1371/journal.pone.0077846); pmid: [24204993](https://pubmed.ncbi.nlm.nih.gov/24204993/)
20. J. D. Sauer *et al.*, The N-ethyl-N-nitrosourea-induced Goldenticket mouse mutant reveals an essential function of Sting in the in vivo interferon response to *Listeria monocytogenes* and cyclic dinucleotides. *Infect. Immun.* **79**, 688–694 (2011). doi: [10.1128/IAI.00999-10](https://doi.org/10.1128/IAI.00999-10); pmid: [21098106](https://pubmed.ncbi.nlm.nih.gov/21098106/)
21. D. A. Annis, E. Nickbarg, X. Yang, M. R. Ziebell, C. E. Whitehurst, Affinity selection-mass spectrometry screening techniques for small molecule drug discovery. *Curr. Opin. Chem. Biol.* **11**, 518–526 (2007). doi: [10.1016/j.cbpa.2007.07.011](https://doi.org/10.1016/j.cbpa.2007.07.011); pmid: [17931956](https://pubmed.ncbi.nlm.nih.gov/17931956/)
22. B. A. Webb, M. Chimenti, M. P. Jacobson, D. L. Barber, Dysregulated pH: A perfect storm for cancer progression. *Nat. Rev. Cancer* **11**, 671–677 (2011). doi: [10.1038/nrc3110](https://doi.org/10.1038/nrc3110); pmid: [21833026](https://pubmed.ncbi.nlm.nih.gov/21833026/)
23. D. O. Scott, A. Ghosh, L. Di, T. S. Maurer, Passive drug permeation through membranes and cellular distribution. *Pharmacol. Res.* **117**, 94–102 (2017). doi: [10.1016/j.phrs.2016.11.028](https://doi.org/10.1016/j.phrs.2016.11.028); pmid: [27890815](https://pubmed.ncbi.nlm.nih.gov/27890815/)

## ACKNOWLEDGMENTS

We thank B. Andresen, D. Hesk, T. Ho, D. Levorse, N. Rivera, and X. Song for generation of custom reagents and molecular characterization needed for these studies; H. Hatch and E. DiNunzio for support in developing certain biochemical and cell-based assays used in this work; C. Li for assistance with coordinating in vivo studies; and A. Beard, H.-Y. Kim, L. Nogle, C. Pickens, J. Sauri, D. Sloman, D. Smith, and WuXi AppTec for contributions to synthesis, purification, and characterization of the molecules described herein. This research used resources at the Industrial Macromolecular Crystallography Association Collaborative Access Team (IMCA-CAT) beamline 17-ID, supported by the companies of the Industrial Macromolecular Crystallography Association through a contract with Hauptman-Woodward Medical Research Institute. This research used resources of the Advanced

Photon Source, a U.S. Department of Energy (DOE) Office of Science User Facility operated for the DOE Office of Science by Argonne National Laboratory under contract no. DE-AC02-06CH11357. We acknowledge the Paul Scherrer Institut, Villigen, Switzerland, for provision of synchrotron radiation beamtime at beamline PXI\_X06SA of the Swiss Light Source. **Funding:** This work was supported by Merck Sharp & Dohme Corp., a subsidiary of Merck & Co., Inc., Kenilworth, NJ, USA. **Author contributions:** B.-S.P., S.A.P., J.A.P., J.P.P., G.K.S., B.W.T., B.M.L., M.D.A., A.V.B., J.N.C., P.J.D., A.H., I.Ka., I.Kn., B.J.L., D.J.B., L.R., S.C., S.S., C.A.L., L.P., D.F.W., and G.H.A. conceived, designed, or planned the studies. B.-S.P., S.A.P., J.A.P., J.P.P., G.K.S., M.D.A., A.V.B., Y.C., J.J., J.K., J.L., C.A.L., A.H., L.R., S.S., E.C.M., B.S., Y.M., B.C., W.C., Y.C., G.F., T.H., R.L., M.L., G.O., R.O., L.P., S.T., H.W., D.F.W., and S.X. contributed to the design and synthesis of molecules and/or acquisition, analysis, or interpretation of the data. B.-S.P., S.A.P., J.A.P., J.P.P., G.K.S., B.W.T., J.N.C., M.D.A., C.A.L., and D.F.W. drafted the manuscript. All authors critically reviewed or revised the manuscript for intellectual content and approved the final version. **Competing interests:** Merck & Co., Inc., has filed patent applications related to this manuscript, including: PCT International Patent Application nos. PCT/US2016/046444, PCT/US2017/054688, PCT/US2017/066557, PCT/US2018/044275, PCT/US2018/044276, and PCT/US2019/025088. All authors are employees or former employees of Merck Sharp & Dohme Corp., a subsidiary of Merck & Co., Inc., Kenilworth, NJ, USA, and may hold stock or stock options in Merck & Co., Inc., Kenilworth, NJ, USA. **Data and materials availability:** All data are available in the main text or the supplementary materials. The structure factors and coordinates have been deposited with the Protein Data Bank (IDs 6UKM, 6UKU, 6UKV, 6UKW, 6UKX, 6UKY, 6UKZ, and 6ULO).

## SUPPLEMENTARY MATERIALS

[science.sciencemag.org/content/369/6506/eaba6098/suppl/DC1](https://science.sciencemag.org/content/369/6506/eaba6098/suppl/DC1)  
Materials and Methods  
Supplementary Text S1 and S2  
Figs. S1 to S11  
Tables S1 to S6  
References (24–39)

[View/request a protocol for this paper from Bio-protocol.](#)

17 December 2019; accepted 13 July 2020  
[10.1126/science.aba6098](https://doi.org/10.1126/science.aba6098)

## RESEARCH ARTICLE

## CANCER IMMUNOLOGY

# Cross-reactivity between tumor MHC class I-restricted antigens and an enterococcal bacteriophage

Aurélien Fluckiger<sup>1,2</sup>, Romain Daillière<sup>1,2,3</sup>, Mohamed Sassi<sup>4</sup>, Barbara Susanne Sixt<sup>5,6,7,8,9,10</sup>, Peng Liu<sup>6,7,8,9,10</sup>, Friedemann Loos<sup>6,7,8,9,10</sup>, Corentin Richard<sup>11,12,13</sup>, Catherine Rabu<sup>14,15</sup>, Maryam Tidjani Alou<sup>12,16</sup>, Anne-Gaëlle Goubet<sup>12</sup>, Fabien Lemaître<sup>13</sup>, Gladys Ferrere<sup>12</sup>, Lisa Derosa<sup>12,17</sup>, Connie P. M. Duong<sup>12</sup>, Meriem Messaoudene<sup>18</sup>, Andréanne Gagné<sup>18</sup>, Philippe Joubert<sup>18</sup>, Luisa De Sordi<sup>19,20</sup>, Laurent Debarbieux<sup>19</sup>, Sylvain Simon<sup>14,15</sup>, Clara-Maria Scarlata<sup>21</sup>, Maha Ayyoub<sup>21</sup>, Belinda Palermo<sup>22</sup>, Francesco Facciolo<sup>23</sup>, Romain Boidot<sup>24</sup>, Richard Wheeler<sup>25</sup>, Ivo Gomperts Boneca<sup>25</sup>, Zsófia Sztupinszki<sup>26</sup>, Krisztian Papp<sup>27</sup>, Istvan Csabai<sup>27</sup>, Edoardo Pasoli<sup>28</sup>, Nicola Segata<sup>29</sup>, Carlos Lopez-Otin<sup>7,8,9,10,30</sup>, Zoltan Szallasi<sup>26,31,32,33</sup>, Fabrice Andre<sup>34,35</sup>, Valerio Iebba<sup>12,36</sup>, Valentin Quiniou<sup>37,38</sup>, David Klatzmann<sup>37,38</sup>, Jacques Boukhalil<sup>16</sup>, Saber Khelaifia<sup>16</sup>, Didier Raoult<sup>16</sup>, Laurence Albiges<sup>1,39</sup>, Bernard Escudier<sup>1,39,40</sup>, Alexander Eggermont<sup>1,41</sup>, Fathia Mami-Chouaib<sup>42</sup>, Paola Nistico<sup>22,23</sup>, François Ghiringhelli<sup>43</sup>, Bertrand Routy<sup>18,44</sup>, Nathalie Labarrière<sup>14,15</sup>, Vincent Cattoir<sup>4,45,46</sup>, Guido Kroemer<sup>6,7,8,9,10,47,48,49,50\*</sup>, Laurence Zitvogel<sup>1,2,17,49\*</sup>

Intestinal microbiota have been proposed to induce commensal-specific memory T cells that cross-react with tumor-associated antigens. We identified major histocompatibility complex (MHC) class I-binding epitopes in the tail length tape measure protein (TMP) of a prophage found in the genome of the bacteriophage *Enterococcus hirae*. Mice bearing *E. hirae* harboring this prophage mounted a TMP-specific H-2K<sup>b</sup>-restricted CD8<sup>+</sup> T lymphocyte response upon immunotherapy with cyclophosphamide or anti-PD-1 antibodies. Administration of bacterial strains engineered to express the TMP epitope improved immunotherapy in mice. In renal and lung cancer patients, the presence of the enterococcal prophage in stools and expression of a TMP-cross-reactive antigen by tumors correlated with long-term benefit of PD-1 blockade therapy. In melanoma patients, T cell clones recognizing naturally processed cancer antigens that are cross-reactive with microbial peptides were detected.

**U**nleashing immune responses against tumor-associated antigens through chemotherapy, radiotherapy, targeted therapies, or immune checkpoint inhibitors has formed the basis of successful cancer treatments (1, 2). The recent discovery that

the gut microbiota affects the cancer-immune set point, thus influencing the clinical outcome of cancer therapies, has rekindled the concept that microbes or their products modulate not only intestinal but also systemic immunity (3, 4). Indeed, memory responses by

interferon- $\gamma$  (IFN $\gamma$ )-secreting CD4<sup>+</sup> and CD8<sup>+</sup> T cells specific for *Enterococcus hirae*, *Bacteroides fragilis*, and *Akkermansia muciniphila* are associated with favorable clinical outcome in cancer patients (5–8), suggesting that microbe-specific T lymphocytes may contribute to anti-tumor immune responses. The mechanisms through which microbes trigger chronic intestinal inflammation and systemic autoimmune disease have not been resolved (9). The theory of “molecular mimicry” (10–15) posits that T cells elicited by bacteria or viruses accidentally recognize autoantigens as they “escape” from self-tolerance-inducing mechanisms (such as clonal deletion or inactivation). Although major histocompatibility complex (MHC) class I- and class II-binding epitopes encoded by bacterial genomes may be immunogenic (10–14), very few reports have demonstrated that microbe-specific CD4<sup>+</sup> or CD8<sup>+</sup> T lymphocytes attack normal or neoplastic tissues (16–18).

Cyclophosphamide (CTX) is a chemotherapeutic drug that can induce the translocation of *E. hirae* from the gut lumen to the mesenteric and splenic immune tissues. This results in CD4<sup>+</sup> and CD8<sup>+</sup> T lymphocytes producing interleukin-17 (IL-17) and IFN $\gamma$  and correlates with improved anticancer immune responses in mice (6, 19). Broad-spectrum antibiotics abolished the therapeutic efficacy of CTX unless *E. hirae* was supplied by oral gavage (6). When comparing a panel of distinct *E. hirae* strains (table S1 and fig. S1A) for their capacity to restore the antibiotic-perturbed anticancer effects of CTX, we found that only a few *E. hirae* isolates (such as 13144 and IGR11) were efficient to reduce MCA205 tumor size (Fig. 1, A and B) (6). Given that the therapeutic efficacy of the combination of CTX and *E. hirae* 13144 is abrogated by the depletion of CD8<sup>+</sup> T cells or the neutralization of IFN $\gamma$  (6), we

<sup>1</sup>Gustave Roussy Cancer Campus (GRCC), Villejuif, France. <sup>2</sup>Institut National de la Santé et de la Recherche Médicale, U1015, Institut Gustave Roussy, Villejuif, France. <sup>3</sup>everImmune, Gustave Roussy Cancer Center, Villejuif, France. <sup>4</sup>Université Rennes 1, Laboratoire de Biochimie Pharmaceutique, Inserm U1230 - UPRES EA 2311, Rennes, France. <sup>5</sup>Laboratory for Molecular Infection Medicine Sweden, Umeå Centre for Microbial Research, Department of Molecular Biology, Umeå University, 90187, Umeå, Sweden. <sup>6</sup>Cell Biology and Metabolomics Platforms, Gustave Roussy Cancer Campus, Villejuif, France. <sup>7</sup>Equipe 11 labellisée Ligue contre le Cancer, Centre de Recherche des Cordeliers, Paris, France. <sup>8</sup>INSERM U1138, Paris, France. <sup>9</sup>Université de Paris, Paris, France. <sup>10</sup>Sorbonne Université, Paris, France. <sup>11</sup>Research Platform in Biological Oncology, Dijon, France. <sup>12</sup>GIMI Genetic and Immunology Medical Institute, Dijon, France. <sup>13</sup>University of Burgundy-Franche Comté, Dijon, France. <sup>14</sup>CRClNA, INSERM, Université d'Angers, Université de Nantes, Nantes, France. <sup>15</sup>LabEx IGO “Immunotherapy, Graft, Oncology,” Nantes, France. <sup>16</sup>UMR MEPHI, Aix-Marseille Université, IRD, AP-HM, Institut Hospitalo-Universitaire Méditerranée-Infection, 19-21 Boulevard Jean Moulin, 13385, Marseille cedex 05, France. <sup>17</sup>Université Paris-Saclay, Villejuif, F-94805, France. <sup>18</sup>Institut Universitaire de Cardiologie et de Pneumologie de Québec, Research Center and Department of Cytology and Pathology, Québec City, Québec, Canada. <sup>19</sup>Bacteriophage, Bacterium, Host Laboratory, Institut Pasteur, F-75015 Paris, France. <sup>20</sup>Sorbonne Université, Centre de Recherche Saint Antoine, INSERM UMR5\_938, Paris, France. <sup>21</sup>Cancer Research Centre of Toulouse, INSERM UMR 1037, 31037 Toulouse, France; Université Toulouse III Paul Sabatier, 31330 Toulouse, France; Institut Universitaire du Cancer de Toulouse-Oncopole, 31100 Toulouse, France. <sup>22</sup>Unit of Tumor Immunology and Immunotherapy, Department of Research, Advanced Diagnostics and Technological Innovation, IRCCS Regina Elena National Cancer Institute, Rome, Italy. <sup>23</sup>Thoracic Surgery Unit, Department of Surgical Oncology, IRCCS Regina Elena National Cancer Institute, Rome, Italy. <sup>24</sup>Unit of Molecular Biology, Department of Biology and Pathology of Tumors, Georges-François Leclerc Anticancer Center, UNICANCER, Dijon, France. <sup>25</sup>Institut Pasteur, Unit Biology and Genetics of the Bacterial Cell Wall, Paris, France. <sup>26</sup>Computational Health Informatics Program (CHIP), Boston Children's Hospital, Boston, MA, USA. <sup>27</sup>Department of Physics of Complex Systems, ELTE Eötvös Loránd University, Budapest, Hungary. <sup>28</sup>Department of Agricultural Sciences, University of Naples Federico II, Naples, Italy. <sup>29</sup>Department CIBIO, University of Trento, Trento, Italy. <sup>30</sup>Departamento de Bioquímica y Biología Molecular, Instituto Universitario de Oncología (IUOPA), Universidad de Oviedo, Oviedo, Spain. <sup>31</sup>Harvard Medical School, Boston, MA, USA. <sup>32</sup>Danish Cancer Society Research Center, Copenhagen, Denmark. <sup>33</sup>MTA-SE-NAP, Brain Metastasis Research Group, 2nd Department of Pathology, Semmelweis University, Budapest, Hungary. <sup>34</sup>Department of Cancer Medicine, Breast Cancer Committee, Gustave Roussy, Villejuif, France. <sup>35</sup>INSERM Unit 981, Gustave Roussy, Villejuif, France. <sup>36</sup>Department of Medical Sciences, University of Trieste, 34137 Trieste, Italy. <sup>37</sup>AP-HP, Hôpital Pitié-Salpêtrière, Clinical Investigation Center in Biotherapy (CIC-BTI) and Immunology-Inflammation-Infectiology and Dermatology Department (3iD), F-75651, Paris, France. <sup>38</sup>Sorbonne Université, INSERM, Immunology-Immunopathology-Immunotherapy (i3), F-75651, Paris, France. <sup>39</sup>Department of Medical Oncology, Gustave Roussy, Villejuif, France. <sup>40</sup>INSERM U981, GRCC, Villejuif, France. <sup>41</sup>Princess Maxima Center, CS 3584 Utrecht, the Netherlands. <sup>42</sup>INSERM UMR 1186, Integrative Tumor Immunology and Immunotherapy, Gustave Roussy, Fac. de Médecine - Univ. Paris-Sud, Université Paris-Saclay, 94805, Villejuif, France. <sup>43</sup>Department of Medical Oncology, Center GF Leclerc, Dijon, France. <sup>44</sup>Division d'Hémostase-Oncologie, Département de Médecine, Centre Hospitalier de l'Université de Montréal (CHUM), Montréal, Québec, Canada. <sup>45</sup>CHU de Rennes - Hôpital Ponchaillou, Service de Bactériologie-Hygiène Hospitalière, Rennes, France. <sup>46</sup>CNR de la Résistance aux Antibiotiques (laboratoire associé “Entérocoques”), Rennes, France. <sup>47</sup>Pôle de Biologie, Hôpital Européen Georges Pompidou, Assistance Publique-Hôpitaux de Paris, Paris, France. <sup>48</sup>Department of Women's and Children's Health, Karolinska University Hospital, 1 Stockholm, Sweden. <sup>49</sup>Suzhou Institute for Systems Biology, Chinese Academy of Medical Sciences, Suzhou, China. <sup>50</sup>Institut Universitaire de France, Paris, France.

\*Corresponding author. Email: laurence.zitvogel@gustaveroussy.fr (L.Z.); kroemer@orange.fr (G.K.)



screened the differential capacity of *E. hirae* strains to elicit memory T cell responses after priming of the host, measured as the ex vivo recall response (IFN $\gamma$  secretion) of splenic CD8 $^{+}$  T cells against various *E. hirae* strains loaded onto dendritic cells (DCs) (fig. S2A). Whereas *E. hirae* 13144 triggered specific CD8 $^{+}$  T cell responses (that were not cross-reactive against irrelevant enterococci), *E. hirae* 708 and 13344 (two prototypic inefficient strains) (6) failed to do so (fig. S2A).

To identify relevant T cell epitopes, we aligned the sequences of bacterial genes encoding putative cell wall and secreted proteins for immunogenic (13144) versus nonimmunogenic (708 and 13344) *E. hirae* strains, followed by the in silico identification of 13144-specific nonapeptides with strong affinity (<50 nM) for the MHC class I H-2K $^{b}$  protein (table S2). Subsequently, we recovered splenic CD8 $^{+}$  T cells from mice that had been exposed to *E. hirae* 13144 and CTX (Fig. 1C), restimulated them in vitro with pools of potentially immunogenic nonapeptides from *E. hirae* 13144 to measure IFN $\gamma$  production (table S2 and fig. S2B), and then split the most efficient pool (no. 7) into individual

peptides (Fig. 1D). This approach led to the identification of one dominant epitope (one-letter amino acid code: TSLARFANI, abbreviation TMP1) in position 187 to 197 of the amino acid sequence of the bacteriophage tail length tape measure protein (TMP, 1506 amino acids) from a 39.2-kb prophage of *E. hirae* 13144 (Fig. 1D, fig. S3, and tables S2 and S3). Temperate and lytic bacteriophages are bacterial viruses that transfer virulence, antimicrobial resistance genes, and immunogenic sequences to new bacterial hosts with a strict specificity (20). The TMP protein, which contains a variable number of tandem repeats with highly conserved tryptophan and phenylalanine residues at fixed positions, is encoded by the genome of *Siphoviridae* phages (21, 22).

The 39.2-kb prophage (i.e., bacteriophage genome) encodes 65 genes, including one shared between all 18 *E. hirae* genomes and 38 specific to *E. hirae* 13144 (fig. S1B), encoding capsid, portal, and tail structures characteristic of *Siphoviridae* bacteriophages. The TMP1 epitope of the 39.2-kb prophage from *E. hirae* 13144 and the prophage fragment contained in *E. hirae* IGR11 showed 100% se-

quence identity (figs. S3 and S4A). Accordingly, *E. hirae* IGR11 was as efficient as *E. hirae* 13144 in reducing the growth of MCA205 sarcomas treated with CTX (Fig. 1, A and B). By contrast, the absence of a bona fide TMP1 epitope (observed in *E. hirae* 708 and 13344) (fig. S1B) and a mutation in position 3 of the TSLARFANI peptide (L $\rightarrow$ F observed in *E. hirae* ATCC9790) (fig. S4A) correlated with the lack of anticancer effects of these *E. hirae* strains (Fig. 1B) (6). Enzyme-linked immunosorbent spot (ELISpot) assays designed to detect peptide-specific IFN $\gamma$ -producing T cells revealed that mice gavaged with *E. hirae* 13144 or IGR11 mounted a CD8 $^{+}$  T cell response against TMP1 (but not against the control peptides TMP2 and TMP3), but mice receiving *E. hirae* strains lacking TMP1 (strains 708 and 13344) or a strain possessing a mutated TMP1 (strain ATCC9790) were unable to stimulate a response (Fig. 1D). We used a fluorescent H-2K $^{b}$ /TSLARFANI tetrameric complex [and its negative control H-2K $^{b}$ /SIINFEKL binding to ovalbumin (OVA) specific CD8 $^{+}$  T cells] to detect the frequency and distribution of TMP1-specific cytotoxic T lymphocytes (CTLs) in naive and MCA205 sarcoma-bearing C57BL/6 mice. We observed

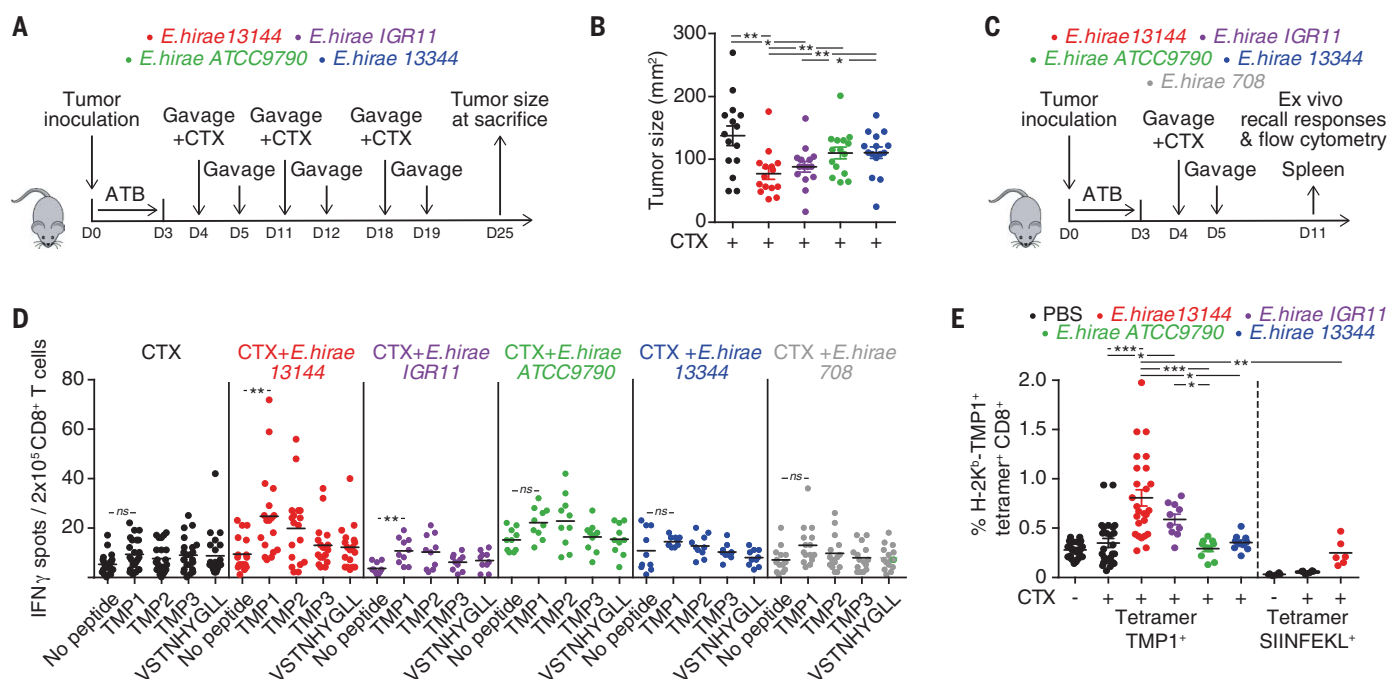


**Fig. 1. Phage tail length TMP is a specific antigenic sequence in *E. hirae* 13144.** (A and B) C57BL/6 mice bearing MCA205 sarcomas were conditioned with broad-spectrum antibiotics (ATB) (streptomycin, colistin, ampicillin, vancomycin) for 3 days before performing oral gavages with *E. hirae* strain 13144 and intraperitoneal injections of CTX. (B) Tumor size was recorded for each mouse at sacrifice on day 25. Mean tumor sizes at sacrifice are depicted. (C to E). Naive C57BL/6 mice were conditioned with antibiotics, gavaged with indicated *E. hirae* strains and treated with CTX (C). (D) Day 11 purified CD8 $^{+}$  T splenocytes [from (C)] were restimulated ex vivo in a recall assay with bone marrow-derived DCs loaded with the indicated peptides

(group 7 in table S2) to quantify IFN $\gamma$ -secreting CD8 $^{+}$  T cells. The number of IFN $\gamma$ -producing cells per  $2 \times 10^5$  CTL is depicted for three independent experiments. (E) H-2K $^{b}$ /TMP1 (TSLARFANI) or H-2K $^{b}$ /SIINFEKL tetramer-binding CD8 $^{+}$  splenocytes [from (C)] were detected by cytofluorometry at day 11. The percentages of tetramer-binding CTL in the CD8 $^{+}$  T cell gate are depicted for three independent experiments. Also, fig. S2D presents tetramer stainings in tumor-draining LNs. Each graph assembles results from two to three independent experiments containing groups of five to six mice. ANOVA statistical analyses (Kruskal-Wallis test): \* $P < 0.05$ , \*\* $P < 0.01$ , \*\*\* $P < 0.001$ . The statistical report is in the supplementary materials.

a specific increase in splenic CD8<sup>+</sup> T cells that recognized the TMP1 peptide (but not the OVA peptide SIINFEKL) at day 7 after treatment with CTX and gavage with *E. hirae* 13144 (Fig. 1E), as well as in tumor-draining lymph nodes (LNs) of tumor-bearing mice at day 14 after treatment with CTX and gavage with *E. hirae* 13144 (fig. S2, C and D). Splenic TMP1 (but not OVA)-specific (H-2K<sup>b</sup>/TSLARFANI tetramer-positive) CTLs also increased in their frequency after gavage with *E. hirae* IGR11 (but not 13344 or ATCC9790) (Fig. 1E). The H-2K<sup>b</sup>/TSLARFANI tetramer-positive CTLs were specifically enriched in the CXCR3<sup>+</sup>CCR9<sup>+</sup> fraction of CD8<sup>+</sup> T cells from secondary lymphoid organs (fig. S2C). Even in mice colonized with human fecal materials, CTX administration and oral gavage with *E. hirae* 13144 induced an anticancer effect (fig. S2E) and an expansion of H-2K<sup>b</sup>/TSLARFANI tetramer-positive CTL in tumor-draining LNs

at day 7 and in tumor beds at day 17 but were not detectable in mesenteric LNs (fig. S2, F and H). Hence, immunogenic *E. hirae* elicits an H-2K<sup>b</sup>-restricted CTL response against the TMP-derived peptide TMP1/TSLARFANI.

To explore the capacity of TMP1-specific H-2K<sup>b</sup>-restricted T cells to control the growth of MCA205 cancers, we subcutaneously (sc) immunized naive C57BL/6 mice with DCs loaded with heat-inactivated *E. hirae* 13144 (positive control), the naturally occurring TMP1/TSLARFANI peptide from 13144 and IGR11, the L→F mutant from *E. hirae* ATCC9790 (mut3) (Fig. 2A and fig. S4A), or other non-immunogenic bacterial peptides (group 1 in fig. S2B). In this prophylactic setting, DCs pulsed with TMP1 (but not mut3) were as efficient as the whole *E. hirae* extract in reducing tumor growth (Fig. 2, B and C). Next, we explored whether the TMP1 peptide would be able to confer immunogenicity to the usually

inefficient bacterium *Escherichia coli* strain DH5α in the therapeutic setting, in which antibiotic treatment is followed by gavage with different bacterial strains and CTX-based chemotherapy (Fig. 1A) (6). *E. coli* engineered to express TMP1 (fig. S5) was as efficient as *E. hirae* 13144 in restraining MCA205 tumor growth (fig. S4B and Fig. 2D) and eliciting tetramer-binding CTL in the spleen (Fig. 2E). By contrast, *E. coli* expressing an irrelevant sequence [encoding mouse enhanced green fluorescent protein (EGFP) protein], mut3, or mutant TMP1 bearing an S→A exchange in the anchor position 2 (mut2) (Fig. 2A) failed to induce such a cancer-protective immune response (Fig. 2, D and E).

To explore the mechanism by which TMP1 exerts its anticancer activity against MCA205 tumors in C57BL/6 mice, we investigated whether H-2K<sup>b</sup>-restricted mouse tumor antigens with high identity to the TMP1 peptide (TSLARFANI) exist. Using the National Center for Biotechnology Information (NCBI) BLASTP suite, we found that the peptide (GSLARFRNI) belonging to the proteasome subunit beta type-4 (PSMB4) located at amino acid positions 76 to 84 shared a strong homology with TMP1 (seven out of nine amino acids with identical amino acids at the MHC class I anchoring positions 2 and 9) (Fig. 3A). We queried for potential neoepitopes of MCA205 but found no significant homology with TMP1, prompting us to focus on the nonmutated PSMB4 peptide. Some mouse tumors (such as MCA205 sarcomas and TC1 lung cancers) overexpress the PSMB4 antigen compared with their normal tissues of origin, whereas others (such as MC38 colon cancers) failed to do so (Fig. 3B). This correlates with the fact that MCA205 and TC1 tumors respond to the treatment with CTX+*E. hirae* 13144, whereas MC38 tumors do not (fig. S6, A and B). PSMB4 is an oncogenic driver involved in proliferation and invasion (23) in a variety of malignancies such as glioblastoma (24), melanoma (25), and breast cancers (26), associated with poor prognosis (23, 24, 26). CRISPR-Cas9-mediated genomic knock-in of the PSMB4 sequence in MCA205 cells, replacing GSLARFRNI by GALARFRNI (with an S→A exchange in position 2) or GSFARFRNI (with an L→F exchange in position 3 equivalent to mut3 of TSLARFANI) (fig. S7) significantly affected tumor growth kinetics (fig. S6, C and D), suggesting that this PSMB4 epitope contributes to the oncogenic activity of PSMB4. Whereas these knock-in mutations did not interfere with the efficacy of CTX treatment alone, they substantially blunted the anticancer effects of *E. hirae* 13144 (Fig. 3, C and D). We extended these findings to a second tumor model in which the anticancer effects of the combination of CTX+*E. hirae* 13144 were additive even in the absence of antibiotic-

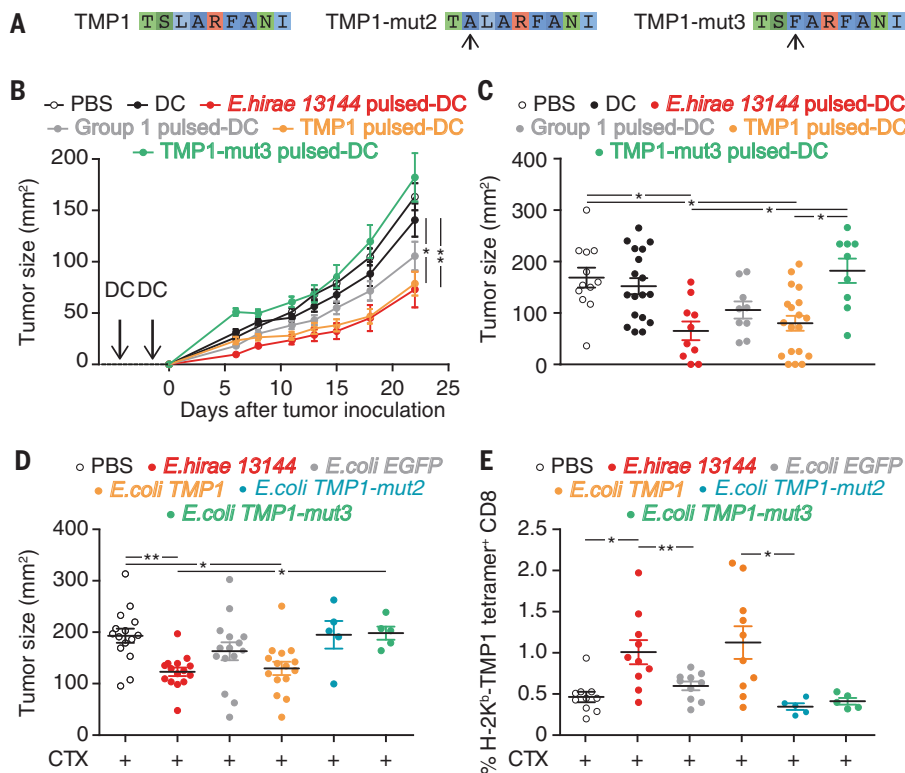


**Fig. 2. Prophylactic and therapeutic immunization using phage tail length TMP against murine sarcomas.** (A) Sequence of the immunogenic epitope TMP1 (TSLARFANI) with the engineered and naturally occurring mutations in positions 2 and 3, respectively. (B and C) Prophylactic vaccination: TLR3 ligand-exposed DCs were pulsed with peptides or heat-inactivated bacteria and then inoculated (sc) twice into mice. One month later, MCA205 sarcomas were implanted in the opposite flank, and tumor size was monitored [mean  $\pm$  SEM are in (B), individual results are in (C)]. (D and E) Therapeutic vaccination: MCA205 tumor-bearing mice were treated with CTX and gavaged with *E. hirae* 13144 or *E. coli* (as shown in Fig. 1A) that were genetically modified to express the indicated peptides or EGFP as a negative control. (D) Tumor size at sacrifice (each dot representing one tumor per mouse) and (E) the frequency of H-2K<sup>b</sup>/TMP1 tetramer-binding splenic CD8<sup>+</sup> T cells were monitored (each dot representing one flow cytometric staining). Results are shown for 12 to 18 animals, gathered from two to three independent experiments. ANOVA statistical analyses (Kruskal-Wallis test) were used: \* $P < 0.05$ , \*\* $P < 0.01$ . The statistical report is in the supplementary materials.



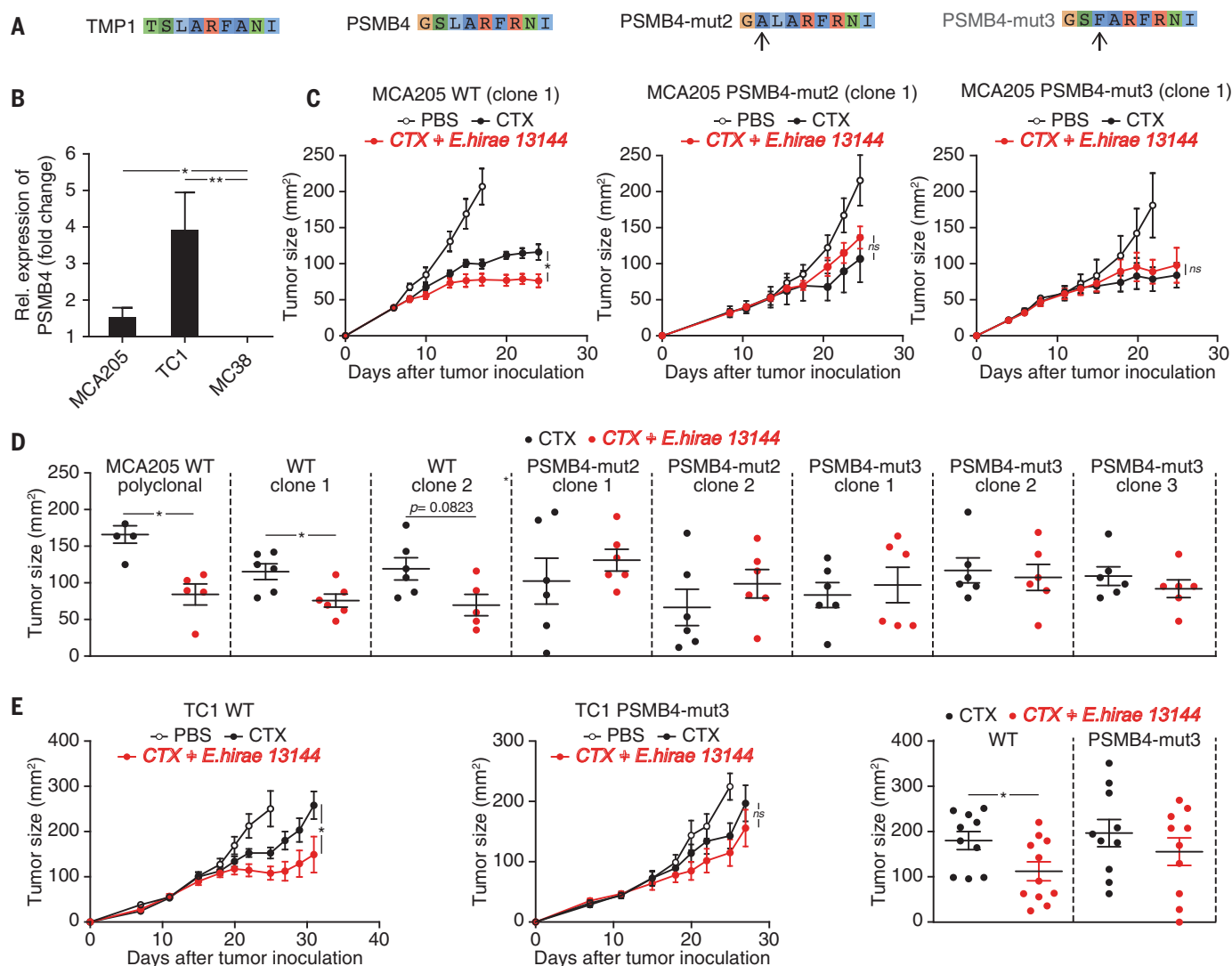


**Fig. 3. Molecular mimicry between phage tail length TMP and the oncogenic PSMB4 epitope in murine tumors.** (A) Sequence alignment of the enterophage TMP1 peptide and a PSMB4 epitope with its two experimental mutants. (B) Relative (Rel.) expression of PSMB4 mRNA in MCA205 sarcoma, TC1 lung cancer, and MC38 colon carcinomas as compared with their healthy tissue of origin (mean ratio  $\pm$  SEM,  $n = 3$ ). (C and D) Therapeutic response of wild type (WT) versus knock-in mutants of MCA205 to CTX alone or in combination with immunogenic *E. hirae* strain 13144 (as outlined in Fig. 1A).

Results are shown as tumor growth kinetics (mean  $\pm$  SEM) for (C) selected MCA205 clones or as (D) individual results (one data point corresponds to one mouse) on day 25. (E) Therapeutic response of WT versus mutated TC1 lung cancers to CTX alone or in combination with *E. hirae* 13144 (as outlined in Fig. 1A, but without antibiotic preconditioning), reflected by tumor growth kinetics and individual tumor sizes at sacrifice. Results are shown as mean  $\pm$  SEM. Mann-Whitney test or ANOVA statistical analyses (Kruskal-Wallis test) were used: \* $P < 0.05$ , \*\* $P < 0.01$ . The statistical report is in the supplementary materials.

induced dysbiosis. Introducing a knock-in mutation in position 3 of PSMB4 into TC1 lung cancer cells again compromised the anti-tumor effects of CTX (Fig. 3E). Moreover, in the setting of PD-1 blockade, administration of *E. hirae* 13144 without prior conditioning with antibiotics reduced the growth of parental but not PSMB4-mutated MCA205 cancers (fig. S6E). These results support the idea that the TSLARFANI TMP1 peptide encoded by *E. hirae* 13144 induces T cell responses against the PSMB4-derived GSLARFRNI peptide across different tumor types and therapy modalities.

Reinforcing the notion of molecular mimicry between phage-encoded and cancer antigens, flow cytometric analyses using fluorescently-labeled tetramers H-2K<sup>b</sup>/TSLARFANI (from TMP1) and H-2K<sup>b</sup>/GSLARFRNI (from PSMB4) identified a subset of double-positive CTLs that infiltrate MCA205 tumors from CTX and *E. hirae* 13144-treated mice (fig. S6F) and that was as frequent as CTLs recognizing the PSMB4 peptide only (Fig. 4A). We purified the splenic CD8<sup>+</sup> T cells using either the TMP1-H-2K<sup>b</sup>- or PSMB4-H-2K<sup>b</sup>-specific tetramers and stimulated them with irrelevant (OVA-derived SIINFEKL) versus relevant

(TMP-derived TSLARFANI or PSMB4-derived GSLARFRNI) peptides (Fig. 4B). CD8<sup>+</sup> T cells binding H-2K<sup>b</sup>-TMP1 tetramers produced IFN $\gamma$  not only in response to TMP1 (up to fivefold increase in IFN $\gamma$ -secreting T cells) but also in response to the PSMB4 epitope (twofold increase, as much as with heat-killed *E. hirae* 13144 processed by DCs) (Fig. 4C, fig. S6G). Similarly, CD8<sup>+</sup> T cells binding H-2K<sup>b</sup>-PSMB4 tetramers functionally recognized TMP1, albeit less efficiently than the PSMB4 epitope (fig. S6G). We analyzed the T cell receptor (TCR) repertoire of these two tetramer-reactive CD8<sup>+</sup> T cell subsets. In accordance with the

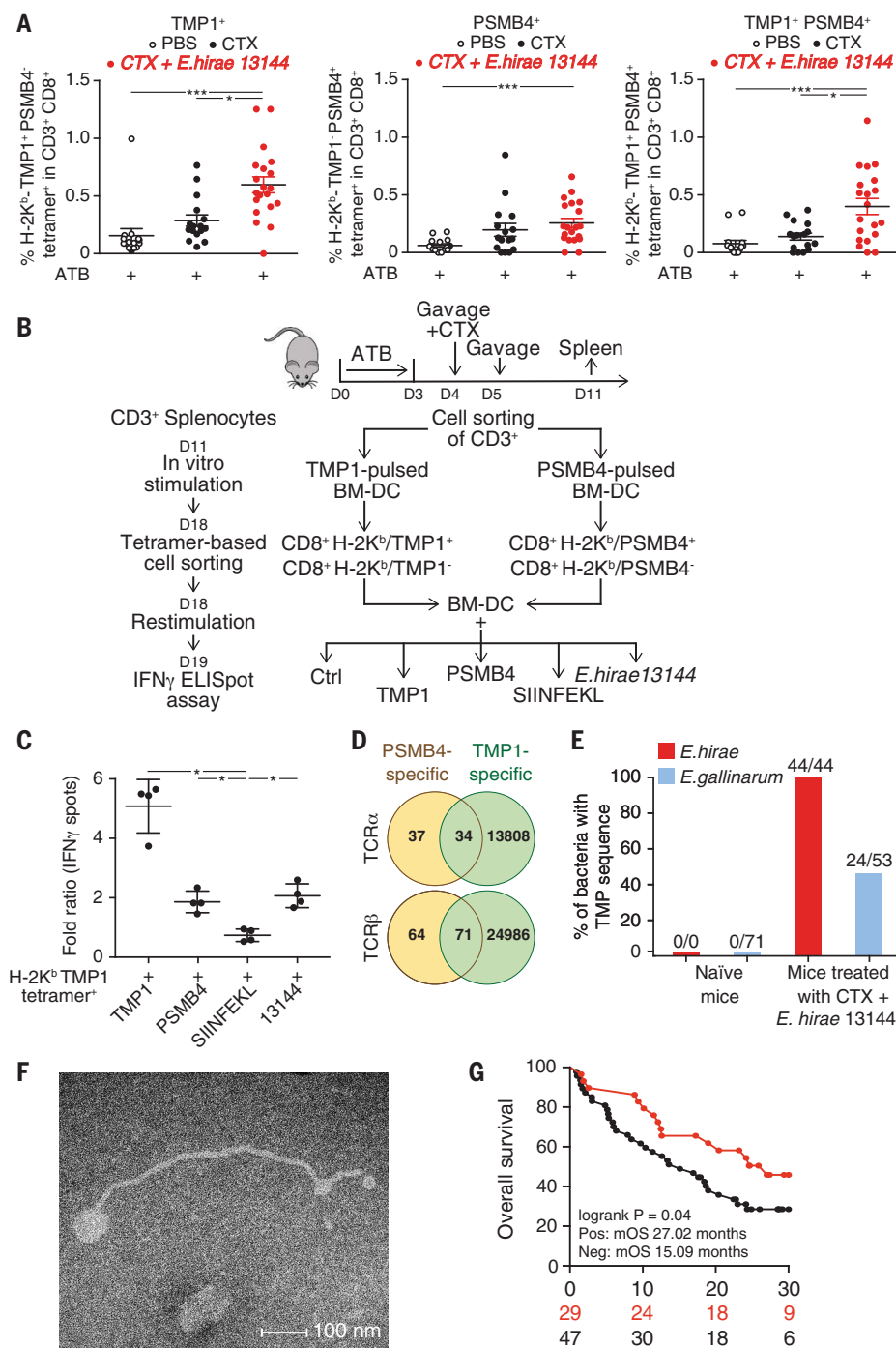


**Fig. 4. Phage tail length TMP cross-reacts with the PSMB4 cancer epitope. (A)** Flow cytometry analysis of CD8<sup>+</sup> tumor-infiltrating lymphocytes (from tumors treated as outlined in Fig. 1A) after costaining with two different tetramers (H-2K<sup>b</sup>/TMP1 and H-2K<sup>b</sup>/PSMB4, sequences in Fig. 3A). Each data point indicates one tumor, and error bars indicate SEM. The graphs represent compiled results of three independent experiments with five mice per group. **(B and C)** Purified CD3<sup>+</sup> T splenocytes from animals treated with CTX and *E. hirae* 13144 were restimulated ex vivo with bone marrow-derived DCs (BM-DC) loaded with TMP1 or PSMB4 peptide. One week after ex vivo restimulation, peptide-specific CD8<sup>+</sup> T cells were purified after staining with the corresponding tetramer to measure IFN<sub>γ</sub> secretion in response to DC loaded with peptides (TMP1, PSMB4, SIINFEKL as negative control) or heat-inactivated *E. hirae* 13144. These results were performed in parallel on the tetramer-binding versus nonbinding fraction and were normalized to the PBS controls (Ctrl). Each dot represents one culture, and error bars represent SEM. Mann-Whitney test or ANOVA statistical analyses (Kruskal-Wallis test) were used: \**P* < 0.05, \*\*\**P* < 0.001. **(D)** Venn diagram of TCRα and β chains from tetramer-positive CD8<sup>+</sup> T cells specific for PSMB4 (yellow) or TMP1 (green). **(E)** Lysogenic conversion of *E. gallinarum* by the *E. hirae* Siphoviridae phage in vivo. Ileal content was obtained from naïve mice or from mice receiving *E. hirae* together with CTX, followed by cultivation and isolation of bacterial colonies, MALDI-TOF identification, and PCR-based detection of TMP. Results are from five mice per group, and SEMs within the five ilea are indicated for the CTX+*E. hirae* 13144 group. **(F)** Transmission electron microscopy of the phage produced by *E. hirae* 13144. **(G)** Kaplan-Meier survival plots of 76 patients with NSCLC or renal cell cancer subjected to PD-1-targeting immunotherapy, stratified according to the presence or absence of TMP in at least five *E. faecalis* or *E. hirae* colonies per patient. Univariate log-rank (Mantel-Cox) analysis was used. The statistical report is in the supplementary materials. mOS, mean overall survival; Neg, TMP phage negative; Pos, TMP phage positive.

functional data, half of the CD8<sup>+</sup> T cells labeled with PSMB4-H-2K<sup>b</sup> tetramers shared clonotypes with the much wider TCR repertoire of T cells labeled with the TMP1-H-2K<sup>b</sup>-specific tetramers (Fig. 4D and tables S4 and S5), but not with the negative fraction (fig. S6H). Therefore, T cells recognizing the TMP1 epitope of immunogenic *E. hirae* can cross-react with a peptide contained in the oncogenic driver PSMB4 and vice versa.

Some bacteriophages have the potential to transfer immunogenic sequences to other

strains in the host ecosystem (20–22). To investigate the capacity of the *E. hirae* 13144 prophage to lysogenize other bacterial species in vivo, we performed culturomic analyses of the ileal content from C57BL/6 mice subjected to oral gavage with *E. hirae* 13144 and systemic CTX therapy, followed by polymerase chain reaction (PCR) analyses seeking TMP sequences (fig. S8, A and B). We tested 7 to 18 bacterial colonies from each animal and a total of 76 colonies. We only found lysogenic conversion of *Enterococcus gallinarum*

by the *E. hirae*-temperate phage in vivo, as confirmed by sequencing of the phage genome in the second host (Fig. 4E and fig. S8, B and C). By contrast, none of the 90 colonies (mostly of *E. gallinarum*) isolated from naïve mice harbored the TMP sequence (fig. S8A) and table S6. Similarly, in vitro coculture of TMP<sup>+</sup> *E. hirae* 13144 together with TMP<sup>−</sup> *E. gallinarum* spp. at a 1:1 ratio uncovered a significant (~15%) rate of lysogenic conversion (fig. S8D). Examination of a preparation admixing *E. hirae* 13144 and *E. gallinarum* at a 1:10 ratio by



means of transmission electron microscopy revealed numerous phages with the typical *Siphoviridae* morphology in the medium, whereas control cultures (bacteria separately) were free of such phages (Fig. 4F). These results indicate that the TMP1 peptide-encoding *Siphoviridae* prophage of *E. hirae* 13144 disseminates within enterococci.

We next explored the possible pathophysiological relevance of these findings. We first screened a total of 3027 adult and mother-infant metagenomes (27), validated by a second independent metagenomic assembly-based screening of 9428 metagenomes (28), to assess the breadth of coverage (BOC) of the *E. hirae* genome and its phages (fig. S9A). *E. hirae* was present with 100% confidence (BOC > 80%) in fewer than 150 fecal samples from disparate geography, age, and datasets. This phage (and its host) can be vertically transmitted from mothers to infants and then colonizes the neonate. There was an increased prevalence of the phage (57%) in fecal microbiomes from children (representing 16% of all metagenomes, Fisher's test  $P$  value < 0.00001) (table S7). The *E. hirae* 13144 phage was detectable in many samples lacking the presence of the *E. hirae* core genome, suggesting that other bacteria in addition to *E. hirae* can host this phage (table S7). All host genomes belonged to the *Enterococcus* genus (except two assigned to *Coprobacillus*), in particular *Enterococcus faecalis* (80 genomes), *Enterococcus faecium* (23 genomes), and *E. hirae* (15 genomes), suggesting that phage 13144 (and its homologs from *E. hirae* 708, and 13344) are genus-specific but not species-specific (table S8).

Contrasting with metagenomics that has a low sensitivity to detect poor abundance species, culturomics followed by MALDI-TOF (matrix-assisted laser desorption ionization time-of-flight mass spectrometry) provides a technology for detecting rare *E. hirae* colonies in the stool of healthy individuals (29) or cancer patients (8). PCR analyses of each single cultivatable enterococcal colony (up to five per species and individual) from 76 cancer patients led to the detection of the TMP sequence encompassing the TMP1 peptide in 34% of the patients, only in *E. faecalis* and *E. hirae* (figs. S9B and S10). Advanced renal and lung cancer patients [cohort described in Ref. (8)] with detectable fecal TMP at diagnosis exhibited prolonged overall survival after therapy with immune checkpoint inhibitors targeting PD-1 (Fig. 4G). Therefore, we screened 16 TMP-derived nonapeptides predicted to bind the human MHC class I human leukocyte antigen (HLA)-A\*0201 with high affinity for their ability to prime naive CD8<sup>+</sup> T cells from six healthy volunteers in vitro. We found 6 out of 16 epitopes capable of triggering significant peptide-specific IFN $\gamma$  release

that were located in two distinct regions of the TMP protein (504 to 708 and 1397 to 1462) (fig. S11, A and B, and table S9). Using the NCBI BLASTP suite, we searched the human cancer peptidome [of the Cancer Genome Atlas (TCGA) database] for a high degree of homology with these six HLA-A\*0201-restricted immunogenic nonapeptides. We found that only the TMP-derived peptide KLAKFASVV (amino acids 631 to 639) shared significant homology (seven out of nine amino acids, with identical residues at the MHC anchoring positions 2 and 9) with a peptide contained in the protein glycerol-3-phosphate dehydrogenase 1-like (GPD1-L) (fig. S11C). GPD1-L reportedly counteracts the oncogenic hypoxia-inducible factor 1 $\alpha$ -dependent adaptation to hypoxia, and its expression is associated with favorable prognosis in head and neck squamous cell carcinomas (30–32). The TCGA transcriptomics database unveiled that high expression of GPD1-L is associated with improved overall survival in lung adenocarcinoma and kidney cancers (fig. S11D). Moreover, high expression of GPD1-L mRNA by tumors at diagnosis was associated with improved progression-free survival in three independent cohorts of non-small cell lung cancer (NSCLC) patients ( $n = 157$ ) (table S10) treated with anti-PD1 antibodies (fig. S11, E and F). Expression of GPD1-L failed to correlate with that of PD-L1 in NSCLC (fig. S11G). Mutations in or adjacent to the 631 to 639 amino acid sequence of GPD1-L gene could rarely be identified in several types of neoplasia (fig. S12).

We derived an HLA-A\*0201-restricted, phage peptide (KLAKFASVV)-specific T cell line from peripheral blood mononuclear cells (PBMCs) of a human volunteer. Clones from this line also recognized the HLA-A\*0201-restricted GPD1-L epitope (KLQKFASVV) (fig. S13, A to C). Moreover, we detected CD8<sup>+</sup> T cells binding HLA-A\*0201/KLAKFASVV tetramers exhibiting hallmarks of effector functions after in vitro stimulation of PBMCs with the KLAKFASVV phage epitope in three out of six NSCLC patients (fig. S13, D to F). In the reverse attempt, searching for molecular mimicry between well-known and naturally processed non-mutated melanoma differentiation antigens recognized by human T cell clones (such as HLA-A\*0201-binding MART-1 or MELOE epitopes) and gut commensal antigens, we found microbial analogs in the public microbiome databases (figs. S14 and S15 and tables S11 and S13). Some of these microbial peptides are recognized by the corresponding TCR (tables S11 and S13) with similar affinities as the parental (tumoral) epitope.

Altogether, our results suggest that microbial genomes code for MHC class I-restricted antigens that induce a memory CD8<sup>+</sup> T cell response, which, in turn, cross-reacts with cancer antigens. Several lines of evidence plead in

favor of this interpretation, as exemplified for the TMP1 epitope found in a phage that infects enterococci. First, naturally occurring (mut3 in *E. hirae* strain ATCC9790) or artificial mutations (mut2 or mut3 in *E. coli*) introduced into the TMP1 epitope suppressed the tumor-prophylactic and therapeutic potential of bacteria expressing TMP1. Second, transfer of the TMP1-encoding gene into *E. coli* conferred immunogenic capacity to this proteobacterium, which acquired the same anti-tumor properties as TMP1-expressing *E. hirae*. Third, when cancer cells were genetically modified to remove the TMP1-cross-reactive peptide in the PSMB4 protein, they formed tumors that could no longer be controlled upon oral gavage with TMP1-expressing *E. hirae*. Fourth, cancer patients carrying the TMP phage sequence in fecal enterococci or the GPD1-L tumoral antigen homologous to TMP epitopes exhibited a better response to PD-1 blockade, suggesting that this type of microbe-cancer cross-reactivity might be clinically relevant.

Recent reports point to the pathological relevance of autoantigen-cross-reactive, microbiota-derived peptides for autoimmune disorders such as myocarditis, lupus, and rheumatoid arthritis (15, 33, 34). Given the enormous richness of the commensal proteome (35), we expect the existence of other microbial antigens mimicking auto- and tumor antigens. We have extended these findings to naturally processed melanoma-specific antigens that have microbial orthologs recognized by the same TCRs (figs. S14 and 15 and tables S10 to S12). Global phage numbers have been estimated to reach as high as 10<sup>31</sup> particles with the potential of 10<sup>25</sup> phage infections occurring every second (36, 37). Thus, the perspective opens that in the microbiota, bacteriophages may enrich the therapeutic armamentarium for modulating the intestinal flora and for stimulating systemic anticancer immune responses.

## REFERENCES AND NOTES

1. P. Sharma, J. P. Allison, *Cell* **161**, 205–214 (2015).
2. L. Galluzzi, A. Buqué, O. Kepp, L. Zitvogel, G. Kroemer, *Cancer Cell* **28**, 690–714 (2015).
3. L. Zitvogel, Y. Ma, D. Raoult, G. Kroemer, T. F. Gajewski, *Science* **359**, 1366–1370 (2018).
4. T. Tanoue et al., *Nature* **565**, 600–605 (2019).
5. M. Vétizou et al., *Science* **350**, 1079–1084 (2015).
6. R. Daillère et al., *Immunity* **45**, 931–943 (2016).
7. Y. Rong et al., *Exp. Cell Res.* **358**, 352–359 (2017).
8. B. Routy et al., *Science* **359**, 91–97 (2018).
9. N. R. Rose, *Curr. Opin. Immunol.* **49**, 51–55 (2017).
10. V. Rubio-Godoy et al., *J. Immunol.* **169**, 5696–5707 (2002).
11. L. Vujanovic, M. Mandic, W. C. Olson, J. M. Kirkwood, W. J. Storkus, *Clin. Cancer Res.* **13**, 6796–6806 (2007).
12. M. E. Perez-Muñoz, P. Joglekar, Y.-J. Shen, K. Y. Chang, D. A. Peterson, *PLOS ONE* **10**, e0144382 (2015).
13. Y. Yang et al., *Nature* **510**, 152–156 (2014).
14. J. N. Chai et al., *Sci. Immunol.* **2**, eaal5068 (2017).
15. C. Gil-Cruz et al., *Science* **366**, 881–886 (2019).
16. Q. Ji, A. Perchellet, J. M. Goverman, *Nat. Immunol.* **11**, 628–634 (2010).
17. V. P. Balachandran et al., *Nature* **551**, 512–516 (2017).

18. C. P. Bradley *et al.*, *Cell Host Microbe* **22**, 697–704.e4 (2017).
19. S. Viaud *et al.*, *Science* **342**, 971–976 (2013).
20. M. G. Weinbauer, *FEMS Microbiol. Rev.* **28**, 127–181 (2004).
21. M. Piuri, G. F. Hatfull, *Mol. Microbiol.* **62**, 1569–1585 (2006).
22. M. Belcaid, A. Bergeron, G. Poisson, *BMC Bioinformatics* **12** (Suppl 9), S10 (2011).
23. G. Y. Lee *et al.*, *Cancer Res.* **74**, 3114–3126 (2014).
24. Y.-C. Cheng, W.-C. Tsai, Y.-C. Sung, H.-H. Chang, Y. Chen, *Cell. Physiol. Biochem.* **45**, 819–831 (2018).
25. X. Zhang *et al.*, *Tumour Biol.* **39**, 1010428317705767 (2017).
26. H. Wang *et al.*, *Oncol. Rep.* **40**, 2343–2352 (2018).
27. E. Pasolli *et al.*, *Nat. Methods* **14**, 1023–1024 (2017).
28. E. Pasolli *et al.*, *Cell* **176**, 649–662.e20 (2019).
29. B. Samb-Ba *et al.*, *PLOS ONE* **9**, e87419 (2014).
30. T. J. Kelly, A. L. Souza, C. B. Clish, P. Puigserver, *Mol. Cell. Biol.* **31**, 2696–2706 (2011).
31. Z. Feng *et al.*, *Histopathology* **64**, 348–355 (2014).
32. S.-C. Liu *et al.*, *Cell Death Dis.* **5**, e1485 (2014).
33. T. M. Greiling *et al.*, *Sci. Transl. Med.* **10**, eaan2306 (2018).
34. M. F. König *et al.*, *Sci. Transl. Med.* **8**, 369ra176 (2016).
35. J. Li *et al.*, *Nat. Biotechnol.* **32**, 834–841 (2014).
36. M. L. Pedulla *et al.*, *Cell* **113**, 171–182 (2003).
37. K. E. Wommack, R. R. Colwell, *Microbiol. Mol. Biol. Rev.* **64**, 69–114 (2000).

## ACKNOWLEDGMENTS

We are thankful to the animal facility team of Gustave Roussy and all the technicians from Centre GF Leclerc. We are indebted to O. Kepp for figure design and to H. G. Rammensee (University of Tübingen, Germany) for his careful guidance in peptide selection and reading of the paper. **Funding:** L.Z. and G.K. were supported

by RHU Torino Lumière (ANR-16-RHUS-0008), ONCOBIOME H2020 network, the Seerave Foundation, the Ligue contre le Cancer (équipe labellisée); Agence Nationale de la Recherche (ANR) – Projets blancs; ANR Francogermanique ANR-19-CE15-0029 under the frame of E-Rare-2, the ERA-Net for Research on Rare Diseases; Association pour la recherche sur le cancer (ARC); Cancéropôle Ile-de-France; Fondation pour la Recherche Médicale (FRM); a donation by Elior; the European Research Council (ERC); Fondation Carrefour; High-end Foreign Expert Program in China (GDW20171100085 and GDW20181100051), Institut National du Cancer (INCa); Inserm (HTE); Institut Universitaire de France; LeDucq Foundation; the LabEx Immuno-Oncology; the SIRIC Stratified Oncology Cell DNA Repair and Tumor Immune Elimination (SOCRATE); CARE network (directed by X. Mariette, Kremlin Bicêtre AP-HP), and the SIRIC Cancer Research and Personalized Medicine (CARPEM). The results shown here are based upon data generated by the TCGA Research Network: <http://cancergenome.nih.gov/>. I.C. was supported by National Research, Development and Innovation Fund of Hungary Project (no. FIEK\_16-1-2016-0005). Z.S. was supported by the Research and Technology Innovation Fund (NAP2-2017-1.2.1-NKP-0002) and Breast Cancer Research Foundation (BCRF-17-156). Z.S. and I.C. were supported by the Novo Nordisk Foundation Interdisciplinary Synergy Programme Grant (NNF15OC0016584). P.N. was supported by the Italian Association for Cancer Research (AIRC IG 19822). Mouse TCR sequencing was performed by the TRiPoD ERC-Advanced EU (322856) grants to D.K. N.S. is supported by the European Research Council (project ERC- STG MetaPG-716575). L.D.S. is funded by a Roux-Cantarini fellowship from the Institut Pasteur (Paris, France). Bristol-Myers-Squibb provided resources to support translational research related to the NIVOREN clinical trial enrolling kidney cancer patients. **Competing interests:** R.D., D.R., L.Z., and G.K. are cofounders of everImmune, a biotech company devoted to the use of commensal microbes for the

treatment of cancers. R.D. is a full-time employee of everImmune. L.Z., A.F., V.C., and R.D. are inventors on a patent application (WO/2019/129753) submitted by Institute Gustave Roussy/INSERM/University Paris Saclay that covers “Immunogenic sequences from a Phage Tail Length Tape Measure Protein, bacteria expressing the same and their use in treating a cancer.”

**Data and materials availability:** *E. hirae* 13144 isolate and *E. hirae* isolates IGR4 and IGR11 are available from U1015 INSERM under a material transfer agreement (with Gustave Roussy Technology Transfer) or from the repository of Institut Pasteur listed as *Enterococcus hirae* deposited at the Collection Nationale de Cultures de Microorganismes (CNCM) of Pasteur Institute, Paris: strains 13144 (EHFS001), deposited on November 7, 2013, under the number I-4815; IGR4 deposited on November 27, 2017, under the number CNCM I-5260; and IGR11 deposited on November 27, 2017, under the number CNCM I-5261. Bacteria genomes sequenced in this study have been deposited in the NCBI GenBank under the accession number PRNJA639126. Microbiome-related mass spectrometry data have been deposited (<https://doi.org/10.35081/bd5t-nm23>).

## SUPPLEMENTARY MATERIALS

[science.sciencemag.org/content/369/6506/936/suppl/DC1](https://science.sciencemag.org/content/369/6506/936/suppl/DC1)  
Materials and Methods  
Figs. S1 to S15  
Tables S1 to S12  
Statistical Report  
References (38–52)

[View/request a protocol for this paper from Bio-protocol.](#)

19 March 2019; resubmitted 28 February 2020  
Accepted 23 June 2020  
10.1126/science.aax0701



## CANCER IMMUNOLOGY

# BTN3A1 governs antitumor responses by coordinating $\alpha\beta$ and $\gamma\delta$ T cells

Kyle K. Payne<sup>1</sup>, Jessica A. Mine<sup>1</sup>, Subir Biswas<sup>1</sup>, Ricardo A. Chaurio<sup>1</sup>, Alfredo Perales-Puchalt<sup>2</sup>, Carmen M. Anadon<sup>1</sup>, Tara Lee Costich<sup>1</sup>, Carly M. Harro<sup>1,3</sup>, Jennifer Walrath<sup>2</sup>, Qianqian Ming<sup>4</sup>, Evgenii Tcyganov<sup>2</sup>, Andrea L. Buras<sup>5</sup>, Kristen E. Rigolizzo<sup>1</sup>, Gunjan Mandal<sup>1</sup>, Jason Lajoie<sup>6</sup>, Michael Ophir<sup>6</sup>, Julia Tchou<sup>7</sup>, Douglas Marchion<sup>8</sup>, Vincent C. Luca<sup>4</sup>, Piotr Bobrowicz<sup>6</sup>, Brooke McLaughlin<sup>6</sup>, Ugur Eskicak<sup>6</sup>, Michael Schmidt<sup>6</sup>, Juan R. Cubillos-Ruiz<sup>9</sup>, Paulo C. Rodriguez<sup>1</sup>, Dmitry I. Gabrilovich<sup>2\*</sup>, Jose R. Conejo-Garcia<sup>1,5†</sup>

Gamma delta ( $\gamma\delta$ ) T cells infiltrate most human tumors, but current immunotherapies fail to exploit their in situ major histocompatibility complex-independent tumoricidal potential. Activation of  $\gamma\delta$  T cells can be elicited by butyrophilin and butyrophilin-like molecules that are structurally similar to the immunosuppressive B7 family members, yet how they regulate and coordinate  $\alpha\beta$  and  $\gamma\delta$  T cell responses remains unknown. Here, we report that the butyrophilin BTN3A1 inhibits tumor-reactive  $\alpha\beta$  T cell receptor activation by preventing segregation of N-glycosylated CD45 from the immune synapse. Notably, CD277-specific antibodies elicit coordinated restoration of  $\alpha\beta$  T cell effector activity and BTN2A1-dependent  $\gamma\delta$  lymphocyte cytotoxicity against BTN3A1<sup>+</sup> cancer cells, abrogating malignant progression. Targeting BTN3A1 therefore orchestrates cooperative killing of established tumors by  $\alpha\beta$  and  $\gamma\delta$  T cells and may present a treatment strategy for tumors resistant to existing immunotherapies.

The advent of immune checkpoint inhibitors has revolutionized the management of certain cancers (1–3). However, most solid tumors remain poorly responsive to existing immunotherapies, and the successes of PD-1-targeting antibodies for melanoma and lung cancer are not frequently observed in other tumor types. Whereas most immunotherapeutic approaches focus on boosting  $\alpha\beta$  T cell responses, other leukocyte subsets with antitumor potential infiltrate tumor beds. In ovarian cancer, a disease resistant to single checkpoint blockade, ~6% of hematopoietic cells in solid tumors (>20% of CD3<sup>+</sup> T cells) represent  $\gamma\delta$  T cells (4), which include V $\gamma$ 9V $\delta$ 2 lymphocytes, the most abundant  $\gamma\delta$  T cells in peripheral blood (5–8). Although  $\gamma\delta$  T cells spontaneously exhibit regulatory activity at tumor beds through the production of galectin-1 (4), there is a strong rationale for

rescuing their antitumor activity in coordination with effector  $\alpha\beta$  T cells to expand the range of immunotherapy-sensitive tumors.

The extracellular domains of butyrophilin (BTN) and butyrophilin-like (BTNL) molecules are structurally related to the B7 family of costimulatory ligands, which includes PD-L1, B7-H3, and B7-H4 (9). Polymorphisms of several BTN and BTNL molecules are associated with inflammatory diseases (9–11), and it has been suggested that the BTN3A family of BTNs could modulate antigen-specific  $\alpha\beta$  T cell responses, though the mechanism(s) is currently unknown (12–15). More recently, BTN and BTNL molecules have been found to play critical roles in modulating  $\gamma\delta$  T cell functions (16, 17), for which concurrent BTN3A1–BTN2A1 interactions are essential for T cell receptor (TCR)-dependent activation of human V $\gamma$ 9V $\delta$ 2<sup>+</sup> T cells (5, 6, 18–20). In vivo, this is dependent on the binding of phosphorylated metabolites to the B30.2 intracellular domain (21, 22). However, these effects can be mimicked by stabilizing the extracellular domain of BTN3A1 with CD277 (BTN3A1-3)-specific antibodies (23), possibly through multimerization of BTN3A1 and conformational changes from its spontaneous V-shaped conformation (19, 22, 23).

We hypothesized that the suppressive function of BTN3A1 against  $\alpha\beta$  T cells occurs only in its spontaneous conformation without BTN2A1 and that antibodies targeting BTN3A1 would overcome the suppression of  $\alpha\beta$  T cells and simultaneously induce  $\gamma\delta$  T cell antitumor cytotoxicity. We report that antibodies against CD277 (anti-CD277) transform BTN3A1 from an immunosuppressive to an immunostimu-

latory molecule, thus dynamically eliciting coordinated  $\alpha\beta$  and  $\gamma\delta$  T cell-driven anti-tumor immunity to abrogate the progression of established ovarian cancer.

## RESULTS

## BTN3A1 is overexpressed in aggressive human tumors to suppress T cell activity

To investigate the potential role of BTN3A1 in cancer, we first performed Western blot assays using protein lysates from 42 stage III/IV human high-grade serous ovarian carcinomas (HGSOCs). As shown in Fig. 1A, BTN3A1 is heavily overexpressed in malignant tissues, compared with benign ovarian tumors and normal tissues. Slightly lower amounts of a specific (~53-kDa) BTN3A1 band were found in four triple-negative breast cancers analyzed (Fig. 1B), supporting that BTN3A1 expression is not restricted to ovarian malignancies. Fluorescence-activated cell sorting (FACS) analysis of freshly dissociated ovarian and breast carcinomas showed that CD277 expression was high among myeloid and tumor cells, with weaker expression found among lymphocytes (Fig. 1, C and D). Lower CD277 expression was retained on peripheral blood mononuclear cells from healthy donors, without differences between myeloid cells and lymphocytes (fig. S1A).

Immunohistochemical analysis of 398 additional HGSOCs and 19 breast cancers of mixed histology confirmed that BTN3A1 is universally expressed at tumor beds, where it is commonly localized to the membrane and cytoplasm within epithelial cells (Fig. 1E and fig. S1B). Consistent with its immunosuppressive role, higher average BTN3A1 expression in 200 ovarian cancers with clinical annotations was significantly associated with reduced patient survival (Fig. 1F). FACS analysis of an additional 13 HGSOCs confirmed that V $\gamma$ 9V $\delta$ 2 lymphocytes constituted up to 2.5% of total T cells (Fig. 1G), and  $\gamma\delta$  T cell infiltration was associated with improved patient outcome (Fig. 1, H and I).

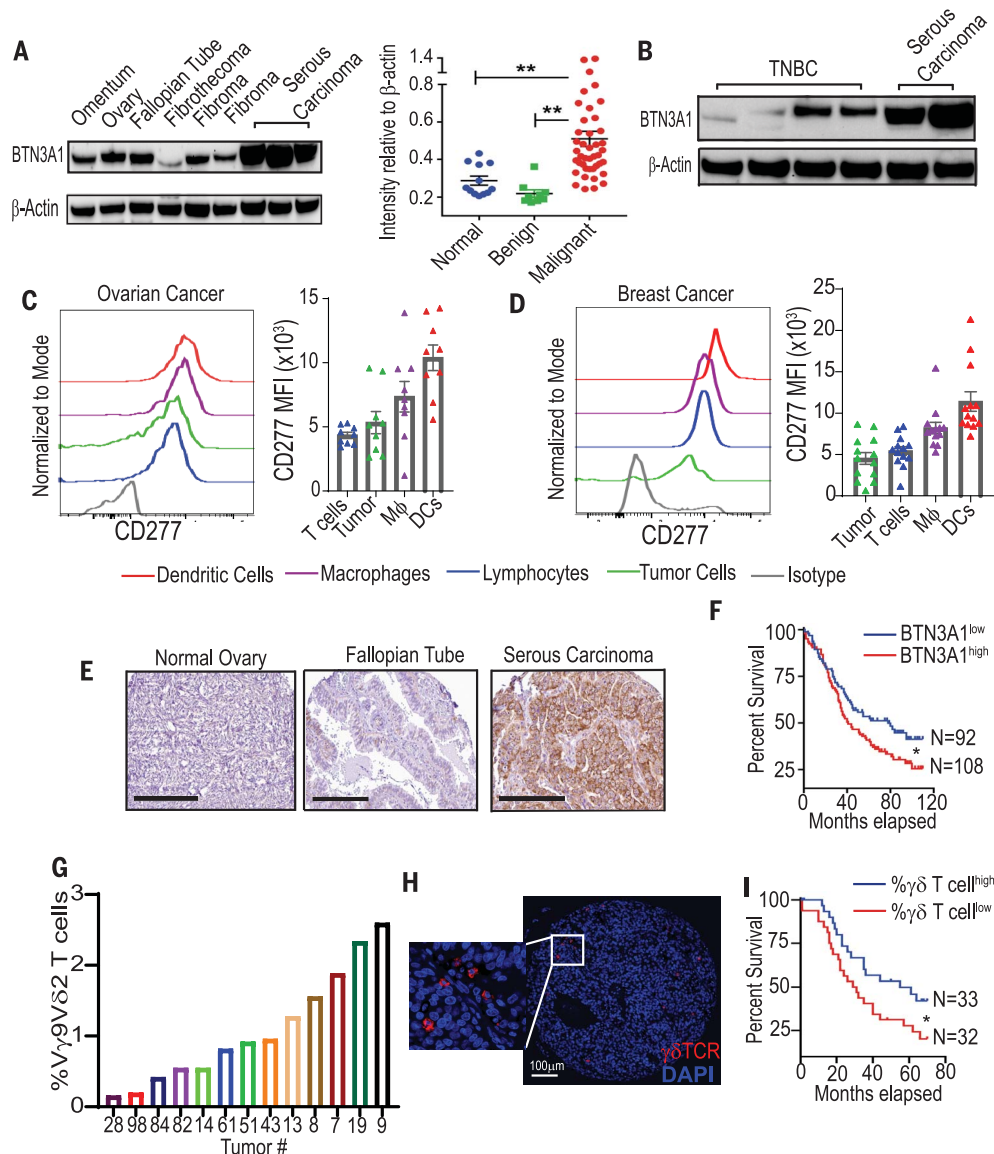
As predicted from its similarity to other B7 family members, BTN3A1 retrovirally expressed on the surface of major histocompatibility complex class I-negative (MHC-I<sup>-</sup>) CD32<sup>+</sup> K562 artificial antigen-presenting cells (BTN-K32 aAPCs) (24) abrogated OKT3-induced activation of both CD4<sup>+</sup> and CD8<sup>+</sup>  $\alpha\beta$  T cells sorted from the peripheral blood of multiple donors (Fig. 2A). Similarly, HLA-A2-transduced BTN-K32 aAPCs pulsed with the NY-ESO-1 peptide SLLMWITQC (BTN-K32<sup>A2</sup>) elicited similar blunting on specific TCR-transduced  $\alpha\beta$  T cells (25) (Fig. 2B and fig. S1C).  $\alpha\beta$  T cell suppression was independent of  $\gamma\delta$  T cells (fig. S1D) and was not due to phenotypic alterations in K562 cells, because similar inhibitory effects were observed using multiple clones of BTN3A1 mock-transduced aAPCs (fig. S1E). Therefore,

<sup>1</sup>Department of Immunology, H. Lee Moffitt Cancer Center and Research Institute, Tampa, FL 33612, USA. <sup>2</sup>Immunology, Microenvironment and Metastasis Program, The Wistar Institute, Philadelphia, PA 19104, USA. <sup>3</sup>Department of Cell Biology, Microbiology, and Molecular Biology and Cancer Biology PhD Program, University of South Florida, Tampa, FL 33620, USA. <sup>4</sup>Drug Discovery, H. Lee Moffitt Cancer Center and Research Institute, Tampa, FL 33612, USA. <sup>5</sup>Department of Gynecologic Oncology, H. Lee Moffitt Cancer Center and Research Institute, Tampa, FL 33612, USA. <sup>6</sup>Compass Therapeutics, Cambridge, MA 02142, USA. <sup>7</sup>Division of Endocrine and Oncologic Surgery, Department of Surgery, University of Pennsylvania, Philadelphia, PA 19104-1693, USA. <sup>8</sup>Department of Pathology, H. Lee Moffitt Cancer Center and Research Institute, Tampa, FL 33612, USA. <sup>9</sup>Department of Obstetrics and Gynecology, Sandra and Edward Meyer Cancer Center, Weill Cornell Medicine, New York, NY 10065, USA.

\*Present address: Cancer Immunology, AstraZeneca, Gaithersburg, MD 20878, USA.

†Corresponding author. Email: jose.conejo-garcia@moffitt.org

**Fig. 1. BTN3A1 is abundantly expressed in ovarian cancer and is associated with poor outcome.** (A) Relative expression of BTN3A1 in normal tissue ( $n = 12$  tissue samples), benign ovarian tumors ( $n = 9$ ), and ovarian serous carcinoma ( $n = 42$ ). Data represent means  $\pm$  SEM. (B) Expression of BTN3A1 in triple-negative breast cancer (TNBC;  $n = 4$ ). (C and D) Expression of CD277 within dissociated human HGSOs ( $n = 9$ ) (C) or breast cancer of mixed histology ( $n = 13$ ) (D) of dendritic cells (DCs; CD45<sup>+</sup>CD1c<sup>+</sup>CD11c<sup>+</sup>MHC-II<sup>+</sup>Zbtb46<sup>+</sup>), macrophages (M $\phi$ ; CD45<sup>+</sup>CD1c<sup>+</sup>CD11c<sup>+</sup>MHC-II<sup>+</sup>), tumor cells (CD45<sup>+</sup>EpCAM<sup>+</sup>), and lymphocytes (CD45<sup>+</sup>CD1c<sup>+</sup>CD11c<sup>+</sup>MHC-II<sup>+</sup>) after normalization against the isotype control. Data represent means  $\pm$  SEM. MFI, median fluorescence intensity. (E) Representative BTN3A1 expression in indicated tissue samples as determined by immunohistochemistry. Scale bars represent 200  $\mu$ m. (F) Survival outcome associated with the intensity of BTN3A1 expression within ovarian cancer specimens as assessed by immunohistochemistry of tissue microarrays corresponding to 200 independent ovarian cancer patients with clinical annotations. (G) Frequency of HGSOc-infiltrating V $\gamma$ 9V $\delta$ 2 T cells among total CD3<sup>+</sup> cells ( $n = 13$ ). (H) Multiplex immunofluorescence detailing the presence of  $\gamma\delta$  T cells (red) within HGSOs. DAPI, 4',6-diamidino-2-phenylindole. (I) Survival outcome associated with the frequency of  $\gamma\delta$  T cells within 65 HGSOs with clinical annotations. Statistical analysis was performed as follows: for (A), one-way analysis of variance (ANOVA); for (F) and (I), log-rank (Mantel-Cox) test for survival. \* $P < 0.05$ ; \*\* $P \leq 0.01$ .



prognostically relevant BTN3A1 effectively suppress  $\alpha\beta$  T cell responses.

#### Human anti-CD277 prevent BTN3A1-mediated inhibition of T cells while inducing T cell activation

To block the immunosuppressive activity of BTN3A1, a panel of 15 BTN3A1-reactive, full-length monoclonal antibodies were obtained by screening a combinatorial human library expressed in a yeast presentation system (26). To avoid cross-linking, antibody-dependent T cell cytotoxicity, and complement activation, these antibodies were generated on an aglycosylated human IgG1 backbone (27). Clone CTX-2026 was the most effective at restoring pMHC TCR (Fig. 2C and fig. S1F) and OKT3 activation (fig. S1, G and H) of CD4<sup>+</sup> and CD8<sup>+</sup>  $\alpha\beta$  T cells, and this clone advanced as the lead compound. As expected, CTX-2026 had no effect on T cell proliferation in mock-transduced

(BTN3A1<sup>-</sup>) K32 or K32<sup>A2</sup> aAPCs (fig. S1, G and I). In addition, zoledronate treatment, which activates V $\gamma$ 9V $\delta$ 2 T cells (19), and CD277-specific V $\gamma$ 9V $\delta$ 2-agonistic [clone 20.1 (23)] and antagonistic [clone 103.2 (28)] antibodies restored BTN3A1-dependent  $\alpha\beta$  T cell activation (Fig. 2C and fig. S1J). Accordingly, zoledronate and anti-CD277 also enhanced antigen-specific killing of NY-ESO-1-transduced, HLA-A2<sup>+</sup>BTN3A1<sup>+</sup> OVCAR3 cells (NY-OVCAR3) (Fig. 2D and fig. S1K) and heightened cytotoxic elimination of BTN3A1<sup>+</sup> primary cancer cells from three HGSOs by autologous tumor-infiltrating lymphocytes (Fig. 2E and fig. S1L).

To gain insights into the mechanism of CTX-2026 action, we determined the crystal structure of the CTX-2026:BTN3A1 complex (fig. S2A). Notably, the F(ab) binds to the IgV domain of CD277 with a stoichiometry of 1:1. All three CDR loops of the heavy chain are involved in the paratope, with a minimal

contribution from CDRL2 (Fig. 2F). We superimposed this complex with the 20.1:CD277 complex (PDB 4F9L) to gain insight into the relative binding position of 20.1 and CTX-2026 (fig. S2B). Epitope evaluation of CTX-2026 further revealed partial spatial and sequential overlap with clone 20.1 (Fig. 2F, fig. S2C, and files S1 and S2). Accordingly, in vitro, CTX-2026 (but not 103.2) redirected the cytotoxic activity of V $\gamma$ 9V $\delta$ 2 T cells from multiple donors against BTN3A1<sup>+</sup> OVCAR3 cells (Fig. 2G) or primary HGSOc cells (Fig. 2H and fig. S3A) with the same efficacy as clone 20.1 or zoledronate.

In support of other recent reports (19, 20), CRISPR-mediated ablation of *BTN2A1* in BTN-K32 aAPCs (Fig. 2I and fig. S3B) abrogated antibody- and zoledronate-dependent interferon- $\gamma$  (IFN- $\gamma$ ) production by V $\gamma$ 9V $\delta$ 2 T cells (Fig. 2J). However, BTN2A1-ablated BTN-K32 aAPCs maintained their ability to suppress  $\alpha\beta$  T cell activation



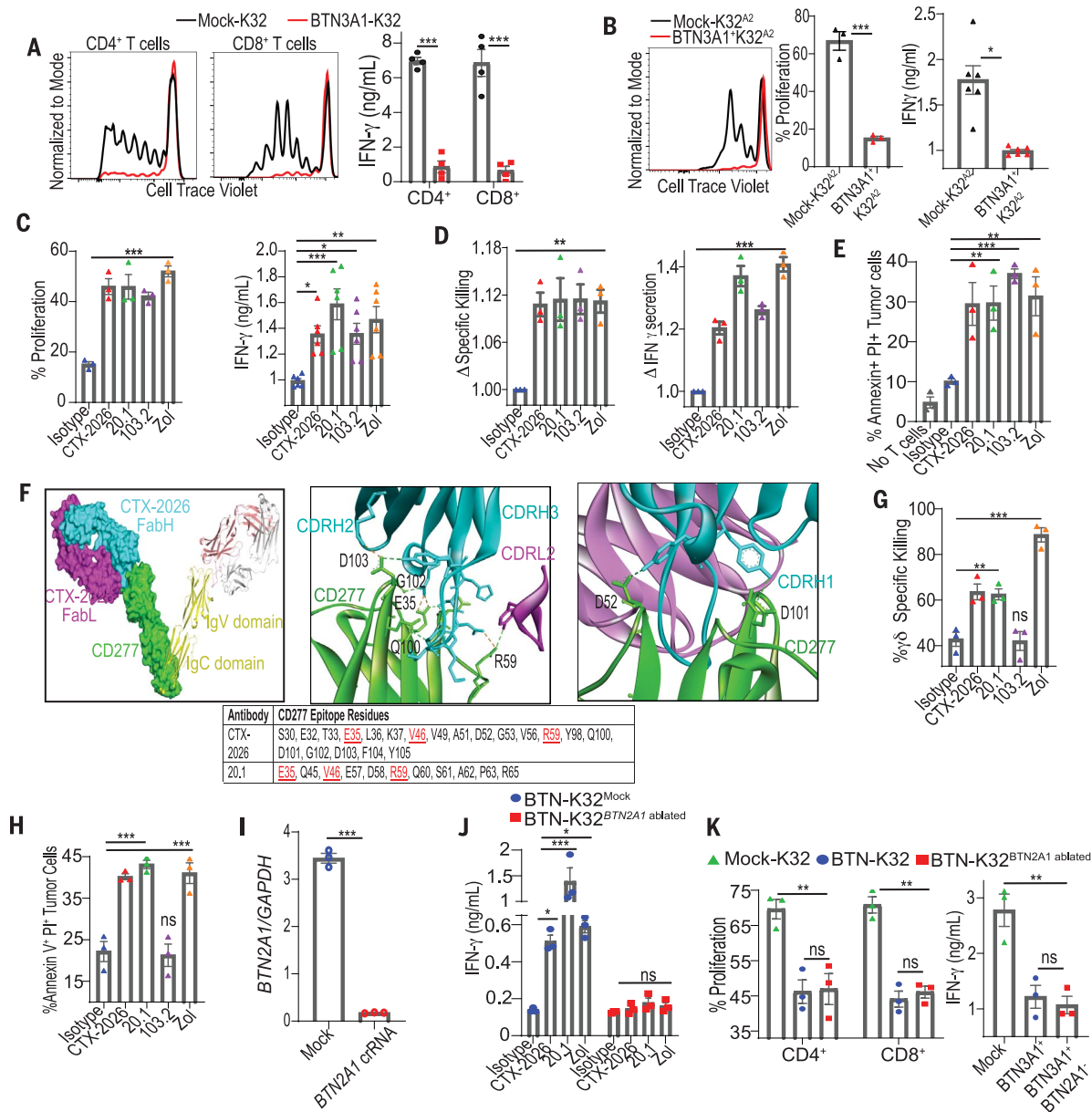
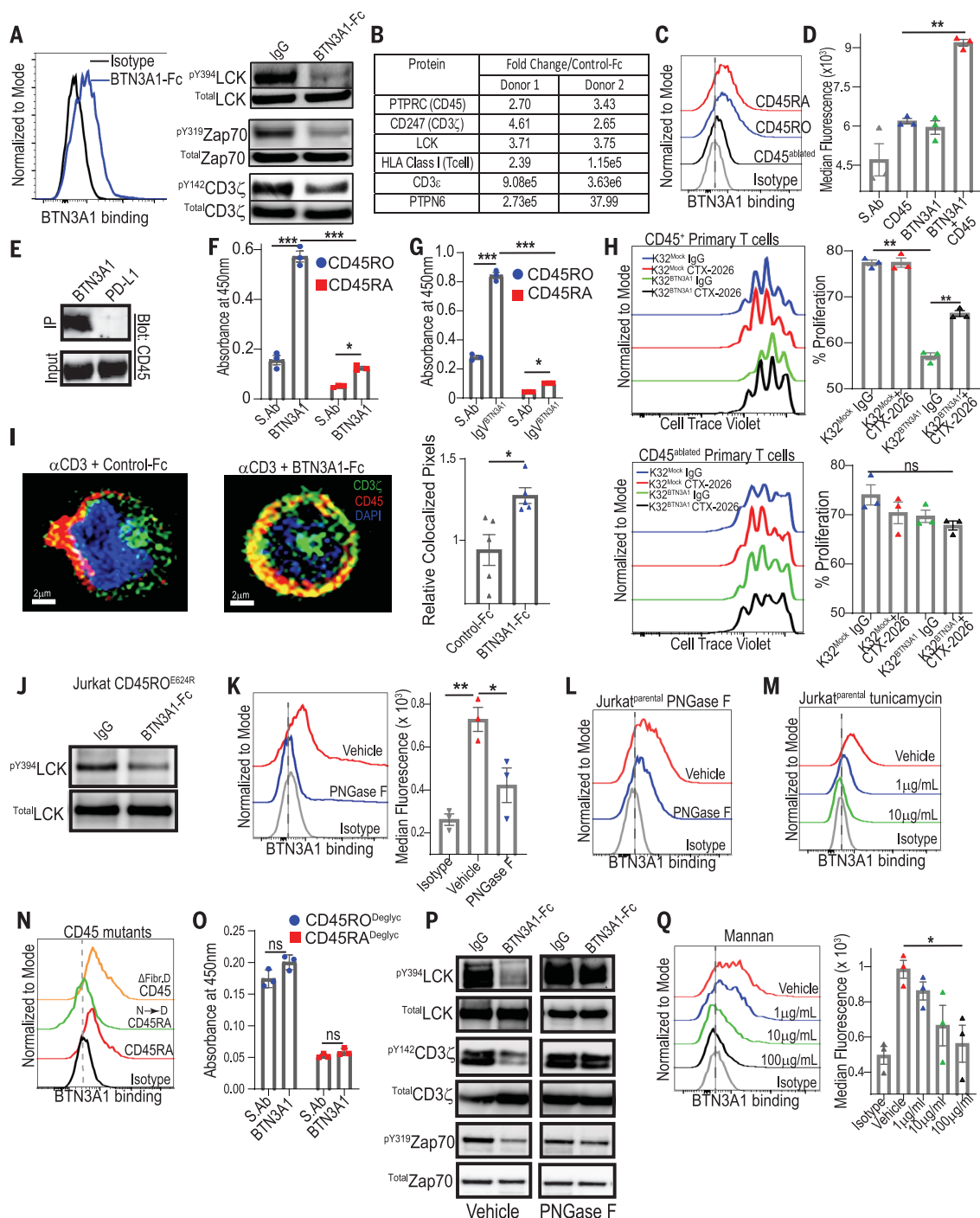


**Fig. 2. BTN3A1-specific antibodies relieve  $\alpha\beta$  T cell inhibition and activate V $\gamma$ 9V $\delta$ 2 T cells.** (A) Proliferation and IFN- $\gamma$  release of CD4<sup>+</sup> and CD8<sup>+</sup> T cells cultured with OKT3-loaded (500 ng/ml) BTN3A1-K32 or mock-K32 cells at a 10:1  $\alpha\beta$  T cell:K32 ratio after 6 days. (B) Proliferation and IFN- $\gamma$  release of NY-ESO-1 TCR<sup>+</sup> T cells cultured with HLA-A2<sup>+</sup> BTN3A1-K32 cells, or HLA-A2<sup>+</sup> mock-K32 cells, loaded with 1  $\mu$ M SLLMWITQV peptide at a 10:1 T cell:K32 ratio after 6 days. (C) Proliferation and IFN- $\gamma$  release after 6 days of NY-ESO-1 TCR<sup>+</sup> T cells cultured at a 10:1 T cell:K32 ratio with HLA-A2<sup>+</sup> BTN3A1-K32 cells previously treated, or not, with zoledronate (Zol; 1  $\mu$ M), loaded with 1  $\mu$ M SLLMWITQV peptide, and preincubated with 1  $\mu$ g/ml isotype control or anti-CD277 (CTX-2026, 20.1, or 103.2). (D) Specific killing of NY-ESO-1 TCR<sup>+</sup> T cells cocultured with OVCAR3<sup>Luciferase</sup> cells pretreated with 1  $\mu$ M zoledronate, or not, and preincubated with 1  $\mu$ g/ml isotype control or anti-CD277 (CTX-2026, 20.1, or 103.2) at a 10:1  $\alpha\beta$  T cell:target cell ratio for 6 hours. Data are presented as the fold change relative to isotype control. (E) Cytotoxicity of immunopurified tumor-infiltrating CD3<sup>+</sup>  $\alpha\beta$  T cells from three HGSOC samples after coculturing with matched tumor cells pretreated with 1  $\mu$ M zoledronate, or not, and preincubated with 1  $\mu$ g/ml isotype control or anti-CD277 (CTX-2026, 20.1, or 103.2) at a 5:1  $\alpha\beta$  T cell:target cell ratio for 12 hours. (F, left) Crystal structure of the CTX-2026 interaction with CD277 homodimer in space-fill and ribbon diagram. (Middle and right) Interface highlighting hydrogen bonds between CD277 and CDRH2, CDRH3, and CDRL2 of CTX-2026 (middle) or CDRH1 of CTX-2026 (right). (Bottom) Epitopes of CTX-2026 and 20.1 are shown, with common residues highlighted in red (bottom). (G) Similar to the experiment shown in (D), except immunopurified  $\gamma\delta$  T cells were used at a 5:1  $\gamma\delta$  T cell:target cell ratio for 24 hours. (H) Similar to the experiment in (E), except immunopurified  $\gamma\delta$  T cells were used at a 5:1  $\gamma\delta$  T cell:target cell ratio for 24 hours. (I) Relative quantity of *BTN2A1* mRNA in BTN-K32 cells electroporated with CRISPR RNA targeting *BTN2A1*, or not. (J) IFN- $\gamma$  release from immunopurified  $\gamma\delta$  T cells cocultured with BTN3A1-K32 cells, or BTN3A1-K32<sup>BTN2A1 ablated</sup> cells previously treated, or not, with zoledronate (1  $\mu$ M) and preincubated with 1  $\mu$ g/ml isotype control or anti-CD277 (CTX-2026, 20.1, or 103.2) at a 5:1  $\gamma\delta$  T cell:K32 ratio after 72 hours. (K) Proliferation and IFN- $\gamma$  release of immunopurified  $\alpha\beta$  T cells cultured with OKT3-loaded (500 ng/ml) BTN3A1-K32 or BTN3A1-K32<sup>BTN2A1 ablated</sup> cells at a 10:1  $\alpha\beta$  T cell:K32 ratio after 6 days. For all histogram panels, data are representative of three independent experiments with similar results, and data represent means  $\pm$  SEM. Statistical analysis was performed as follows: for (B) and (I), two-tailed Student's *t* test; for (A), (J), and (K), two-way analysis of variance (ANOVA); for (C), (D), (E), (G), (H), and (K), one-way ANOVA. ns, not significant; \**P* < 0.05; \*\**P*  $\leq$  0.01; \*\*\**P*  $\leq$  0.001.

### Fig. 3. BTN3A1 interacts with the CD45 phosphatase, blunting proximal T cell signaling.

**(A)** Binding of BTN3A1-Fc to the surface of primary human T cells (left); immunoblot of purified  $\alpha\beta$  T cells after TCR cross-linking by plate-bound OKT3 in the presence of BTN3A1-Fc or control immunoglobulin G (IgG)-Fc proteins (all at 10  $\mu\text{g}/\text{ml}$ ) for 1 min (right). **(B)** LC-MS/MS readout of BTN3A1-specific pulldowns after incubation with activated  $\alpha\beta$  T cells. **(C)** Binding of BTN3A1-Fc to the surface of CD45<sup>+</sup> Jurkat cells or CD45<sup>-</sup> Jurkat cells with rescued expression of CD45RA or CD45RO. **(D)** In situ proximity ligation far red median fluorescence between BTN3A1 and CD45, single-stained controls, or detection probes alone (S. Ab), using purified primary T cells. **(E)** Immunoblot of CD45 after primary T cells were coated with either BTN3A1-Fc or PD-L1-Fc (10  $\mu\text{g}/\text{ml}$ ), lysed, and Fc protein immunoprecipitation (IP). **(F)** Absorbance at 450 nm after immobilized BTN3A1 proteins (10  $\mu\text{g}/\text{ml}$ ) were incubated with CD45RA or CD45RO proteins (20  $\mu\text{g}/\text{ml}$ ) and CD45RA and CD45RO detection antibodies (20  $\mu\text{g}/\text{ml}$ ), or after incubation of CD45RA or CD45RO proteins (10  $\mu\text{g}/\text{ml}$ ) and CD45RA and CD45RO detection antibodies (20  $\mu\text{g}/\text{ml}$ ) without BTN3A1 immobilization (S. Ab). **(G)** Similar to the experiment shown in (F), except only the IgV domain of BTN3A1 was immobilized. **(H)** Proliferation



of CD45<sup>+</sup> and CD45<sup>-</sup> ablated primary  $\alpha\beta$  T cells cultured with BTN3A1-K32 cells or mock-K32 cells in the presence or absence of 1  $\mu\text{g}/\text{ml}$  CTX-2026 or isotype control for 6 days. **(I, left)** Segregation of CD45 from CD3 $\zeta$  in the presence of control-Fc or BTN3A1-Fc proteins (10  $\mu\text{g}/\text{ml}$ ) after TCR cross-linking in the presence of plate-bound OKT3 (10  $\mu\text{g}/\text{ml}$ ) for 3 min. **(Right)** Cumulative quantification of CD3 $\zeta$  and CD45 colocalization in the presence of BTN3A1-Fc or control-Fc proteins is shown from five fields per condition with ~120 cells per field. Scale bars represent 2  $\mu\text{m}$ . **(J)** Immunoblot of CD45<sup>-</sup> Jurkat cells expressing CD45RO<sup>E624R</sup> after TCR cross-linking by plate-bound OKT3 in the presence of BTN3A1-Fc or control IgG-Fc proteins (all at 10  $\mu\text{g}/\text{ml}$ ) for 1 min. **(K)** Binding (left) and median fluorescence (right) of BTN3A1-Fc proteins after primary T cells were treated overnight with 100 U/ml of PNGase F or vehicle. **(L)** Binding of BTN3A1-Fc proteins to CD45<sup>+</sup> Jurkat cells after treatment overnight with 100 U/ml PNGase F or vehicle. **(M)** Binding of BTN3A1-Fc proteins to CD45<sup>+</sup> Jurkat cells after treatment with the indicated concentrations of tunicamycin, or vehicle, for 72 hours. **(N)** Binding of BTN3A1-Fc proteins to CD45<sup>-</sup> Jurkat cells or CD45<sup>-</sup> Jurkat cells expressing CD45RO<sup>N→D</sup>, or CD45RO<sup>ΔFibr.D</sup>. **(O)** Absorbance measurements, similar to those for the experiment shown in (F), except N-linked glycans were removed from both CD45RA and CD45RO prior to the assay by overnight treatment with PNGase F. **(P)** Immunoblot assay similar to that shown in (A), except a portion of the primary T cells was treated with PNGase F overnight (100 U/ml) before the assay. **(Q)** Binding (left) and median fluorescence (right) of BTN3A1-Fc proteins after primary T cells were preincubated with increasing concentrations of mannan polysaccharides or vehicle. For all histogram panels, data are representative of three independent experiments with similar results and represent means  $\pm$  SEM. Statistical analysis was performed as follows: for (I), two-tailed Student's *t* test; for (F), (G), and (O), two-way ANOVA; for (D), (H), (K), and (Q), one-way ANOVA. ns, not significant; \**P* < 0.05; \*\**P* ≤ 0.01; \*\*\**P* ≤ 0.001.



**Fig. 4. Targeting CD277 in vivo rescues anti-gen-specific  $\alpha\beta$  T cell responses and leverages the cytotoxic potential of  $\gamma\delta$  T cells.**

(A) Experimental schema. (B, left) Progression of NY-OVCAR3 tumors in NSG mice treated with  $1.5 \times 10^6$  NY-ESO-1-TCR-transduced  $\alpha\beta$  T cells and treated every third day with zoledronate (Zol; 0.05 mg/kg; intra-peritoneally (ip)) or CTX-2026, 20.1, or control IgG (5 mg/kg; ip). (Right) Quantification of tumor weight from each group after 15 days. Data represent means  $\pm$  SEM with five mice per treatment group, representative of three independent experiments with similar results. (C) Absolute number of GFP<sup>+</sup> CD8<sup>+</sup>  $\alpha\beta$  T cells within NY-OVCAR3 tumors treated with zoledronate, CTX-2026, 20.1, or control IgG. (D) Progression of NY-OVCAR3 tumors in NSG mice treated with NY-ESO-1-TCR  $\alpha\beta$  T cells and then nivolumab, CTX-2026, or control IgG every third day (5 mg/kg; ip). Data represent means  $\pm$  SEM with five mice per treatment group, representative of three independent experiments with similar results. (E) Progression of NY-OVCAR3 tumors in NSG mice treated with CTX-2026 or treated with  $3 \times 10^5$  purified  $\gamma\delta$  T cells and then CTX-2026 or control IgG every third day. Data represent means  $\pm$  SEM with three mice per treatment group, representative of three independent experiments with similar results. (F) Absolute number of  $\gamma\delta$  T cells within NY-OVCAR3 tumors treated with CTX-2026, 20.1, or control IgG. (G) Progression of NY-OVCAR3 tumors in NSG mice treated with purified  $\gamma\delta$  T cells and CTX-2026 or control IgG,  $\alpha\beta$  T cells with CTX-2026 or control IgG, or the combination of antigen-specific  $\alpha\beta$  T cells and autologous  $\gamma\delta$  T cells (ratio of 6:1) with CTX-2026 or control IgG. Data represent means  $\pm$  SEM with three mice per treatment group, representative of three independent experiments with similar results. (H) Representative formation of cystic cavities in NY-OVCAR3 tumors treated with the combination of antigen (Ag)-specific  $\alpha\beta$  T cells,  $\gamma\delta$  T cells, and CTX-2026. Scale bars represent 3 mm. Statistical analysis was performed as follows: for (B) (left), (D), (E), (F), and (G), two-tailed Student's *t* tests; for (B) (right) and (C), one-way ANOVA. \**P* < 0.05; \*\**P*  $\leq$  0.01; \*\*\**P*  $\leq$  0.001.

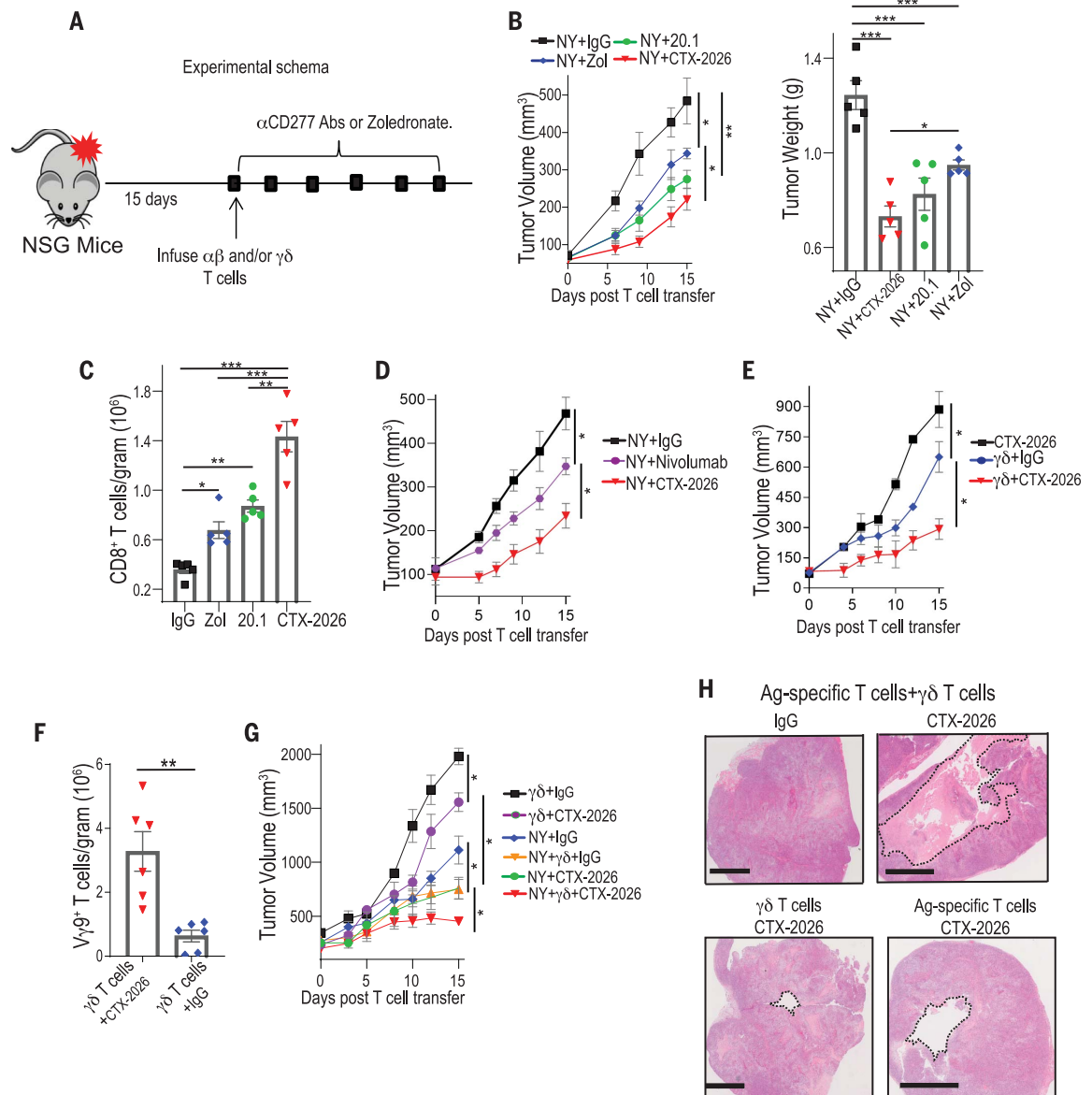


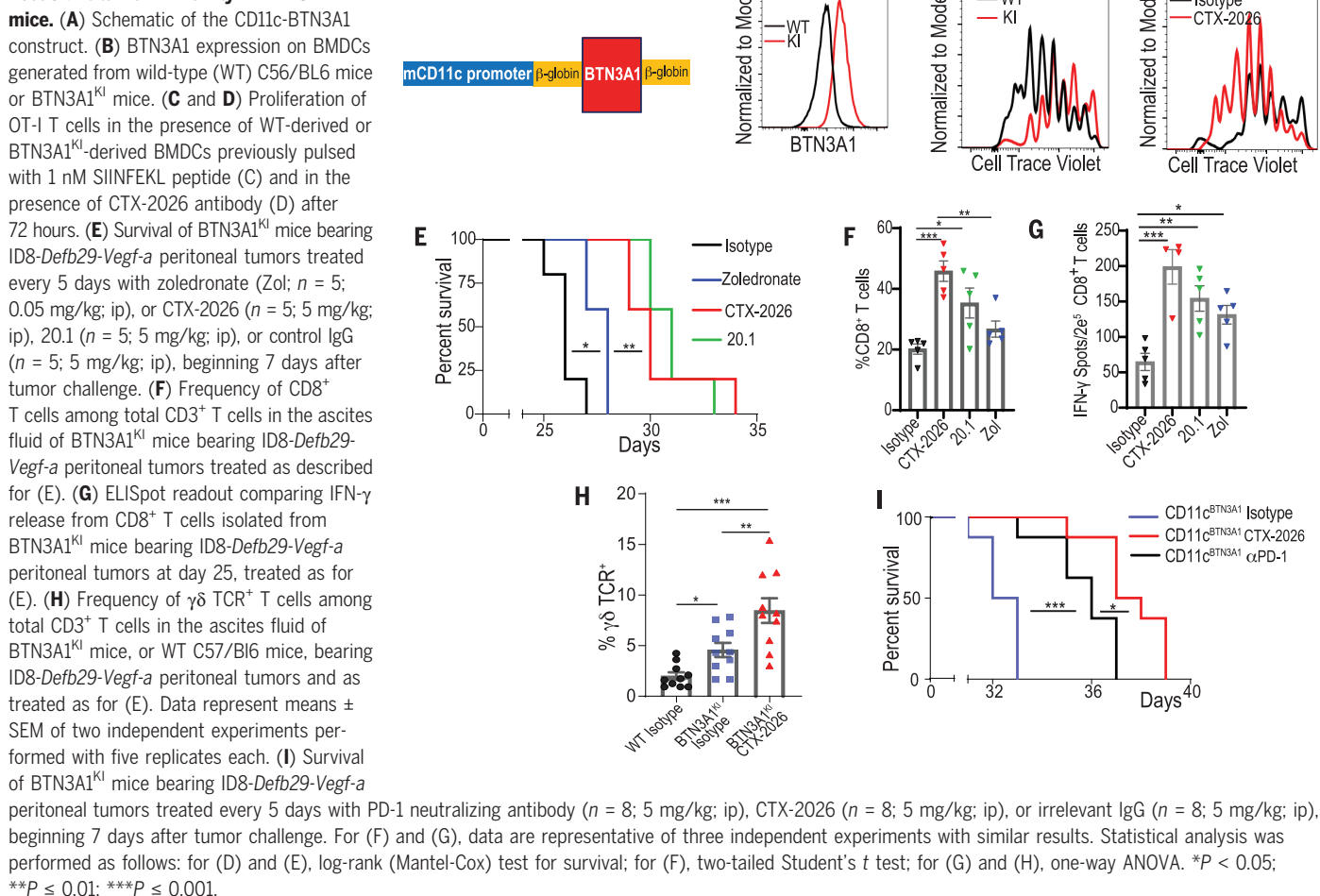
(Fig. 2K and fig. S3C), suggesting that the switch between the  $\alpha\beta$ -immunosuppressive and  $V\gamma 9V\delta 2$ -immunostimulatory activities of BTN3A1 is regulated by BTN2A1 signaling.

#### BTN3A1 suppresses T cells by preventing the segregation of CD45 from the immune synapse

To elucidate the mechanism by which BTN3A1 inhibits  $\alpha\beta$  T cell activity, we confirmed that upon TCR activation, homodimeric BTN3A1-

Fc binding (fig. S3D) to the surface of activated primary T cells blunts the phosphorylation of TCR proximal signaling molecules, as at activating residues in LCK<sup>Y394</sup>, Zap70<sup>Y319</sup>, and CD3 $\zeta$ <sup>Y142</sup> (Fig. 3A). We excluded binding to potential immunosuppressive receptors by comparing the binding of recombinant GPR174, NRP1, and NRP2 Fc proteins to BTN-K32 with that of mock-transduced aAPCs (fig. S3E). We next used BTN3A1-Fc proteins to coimmuno-

precipitate the binding partner(s) of BTN3A1 on OKT3-activated primary  $\alpha\beta$  T cells from multiple donors. In three independent experiments, liquid chromatography-tandem mass spectrometry (LC-MS/MS) showed BTN3A1 coimmunoprecipitated with a complex that consistently included only four T cell proteins with an extracellular domain—CD3 $\epsilon$ , CD3 $\zeta$ , HLA-A, and the phosphatase CD45—and also the intracellular TCR signaling protein LCK

**Fig. 5. Targeting *BTN3A1* results in spontaneous antitumor immunity in *BTN3A1*<sup>tg</sup> mice.**

and the phosphatase PTPN6 (SHP-1) (Fig. 3B and file S3). CD45 similarly consistently coimmunoprecipitated with BTN3A1 from nonactivated primary αβ T cells and CD45<sup>+</sup> Jurkat cells (fig. S3F and file S4). By contrast, BTN3A1 did not reproducibly coimmunoprecipitate with other heavily glycosylated or abundant surface molecules, including CD44, CD5, or CD2. Accordingly, BTN3A1-Fc proteins bound to CD45<sup>+</sup> Jurkat cells but not to CD45-ablated Jurkat cells (fig. S3G), whereas ectopic expression of CD45RA or CD45RO (fig. S3H) rescued BTN3A1-Fc binding (Fig. 3C and fig. S3I). Furthermore, in situ proximity ligation confirmed CD45-BTN3A1 interactions within ≤30 to 40 nm on the T cell surface (Fig. 3D and fig. S3J), whereas BTN3A1-Fc proteins (but not control PD-L1-Fc) pulled down CD45 from activated αβ T cells (Fig. 3E). Although both CD45RA and CD45RO were found to directly bind to immobilized BTN3A1 proteins, binding to CD45RO was significantly stronger (Fig. 3F). Notably, the extracellular IgV domain of BTN3A1 was sufficient to engage both isoforms (Fig. 3G).

CD45-BTN3A1 interactions specifically drive αβ T cell suppression, because CRISPR ablation of *PTPRC* in primary αβ T cells (fig. S3K) abrogated both the inhibitory effect of BTN3A1 and the rescuing effect of CTX-2026, whereas nonablated CD45<sup>+</sup> T cells in the same cultures were effectively suppressed and rescued (Fig. 3H and fig. S3L).

Given these findings, we hypothesized that BTN3A1 might disrupt TCR triggering by preventing the segregation of CD45 from the immune synapse. To test this, a CD3ζ-green fluorescent protein (GFP) fusion protein was generated and was used to monitor the degree of CD3ζ-CD45 colocalization after OKT3-induced TCR triggering in the presence of BTN3A1-Fc versus control-Fc. As predicted, CD45 segregated from CD3ζ after TCR activation in the presence of control-Fc (Fig. 3I). In contrast, the presence of BTN3A1 impeded the segregation of CD45 from CD3ζ in multiple independent experiments with different donors, further supporting that BTN3A1 abrogates αβ T cell responses by effectively dismantling the immune synapse (Fig. 3I and fig. S4). We observed that αβ T cells

activated in the presence of BTN3A1-Fc proteins (but not PD-L1-Fc) generated CD45-specific peptides approximately double the predicted size of monomeric CD45 under nonreducing conditions (fig. S5A and file S5), which are indicative of inhibitory CD45 dimerization (29). However, whereas CD45<sup>+</sup> Jurkat cells were not sensitive to BTN3A1 suppression at TCR-proximal residues as expected (fig. S5B), CD45<sup>+</sup> Jurkat cells expressing CD45RO with an inactivating mutation in the cytoplasmic inhibitory wedge (CD45RO<sup>E624R</sup>) remained sensitive to BTN3A1 inhibition at Y394-LCK, which is consistent with localized CD45 within the immune synapse inhibiting pMHC-TCR ligation independent of its protein tyrosine phosphatase potential (Fig. 3J).

#### BTN3A1 binds to N-mannosylated residues in CD45

To elucidate how BTN3A1 binds to different isoforms of CD45, we focused on its heavily N-glycosylated residues (30). Peptide N-glycosylase (PNGase) F-treated (N-deglycosylated) primary T cells (Fig. 3K), CD45<sup>+</sup> Jurkat cells (Fig. 3L



and fig. S5C), and CD45<sup>+</sup> Jurkat cells with ectopic expression of CD45RA and CD45RO (fig. S5, D and E) all showed significantly reduced binding to BTN3A1-Fc proteins, whereas surface level expression of CD45 remained intact (fig. S5, C and F). Similar results were obtained using the N-glycan inhibitor tunicamycin (Fig. 3M and fig. S5G), although conservative replacement of asparagine with aspartic acid in the extracellular domain of CD45RA also abrogated BTN3A1-Fc–Jurkat cell interactions (Fig. 3N and fig. S5H); these results are all indicative of an N-glycosylation-dependent mechanism. Accordingly, N-deglycosylation by PNGase F or tunicamycin decreased CD45 coimmunoprecipitated with BTN3A1-Fc from activated  $\alpha\beta$  T cells (fig. S5I), whereas N-deglycosylation of either CD45RO or CD45RA by PNGase F abrogated their binding to immobilized BTN3A1 proteins (Fig. 3O) and treatment of primary  $\alpha\beta$  T cells with PNGase F abrogated the ability of BTN3A1 to blunt TCR proximal signaling in primary T cells (Fig. 3P). Corresponding results were observed using CD45<sup>+</sup> Jurkat cells transduced or not with CD45RO and CD45RA (fig. S5B). However, PNGase F-mediated deglycosylation of BTN3A1-Fc did not abrogate binding to CD45RO (fig. S5J), indicating BTN3A1-specific N-glycan recognition.

CD45 mutants expressing only the membrane-proximal fibronectin domains in CD45<sup>+</sup> Jurkat cells restored BTN3A1-Fc binding to an even greater extent than expression of CD45RA (Fig. 3N), suggesting increased accessibility to proximal N-mannosylated oligosaccharides (30). Accordingly, mannan polysaccharides inhibited binding of BTN3A1-Fc proteins to  $\alpha\beta$  T cells in a dose-dependent manner (Fig. 3Q). Collectively, these data suggest that BTN3A1 recognizes N-mannosylated oligosaccharides within the membrane-proximal domains of CD45, which anchors dimeric CD45 near the TCR and blunts effective TCR signaling, possibly by physically blocking pMHC–TCR ligation (31–34).

#### **Anti-BTN3A1 elicit coordinated and T cell responses to impede growth of established human ovarian tumors in vivo**

To assess the potential of targeting BTN3A1 by utilizing CTX-2026 to rescue human  $\alpha\beta$  T cell responses against advanced tumors in vivo, we implemented the NY-OVCAR3/ $\alpha\beta$  NY-ESO-1-specific TCR T cell system (25) (Fig. 4A and fig. S1, C and K). Adoptive transfer of these ( $\gamma\delta$  T cell-free) SLLMWTQC-reactive  $\alpha\beta$  T cells had only modest effects in preventing the growth of established (75 to 250 mm<sup>3</sup>) NY-OVCAR3 tumors compared to mock-transduced T cells (fig. S6A). In contrast, BTN3A1 blockade with CTX-2026 antibodies delayed malignant progression from nine different donors (in 10 independent experiments) and was more effective than zoledronate and 20.1 (Fig. 4B and fig. S6, B and C). Superior therapeutic effects elicited

by CTX-2026 were associated with significant increases in the accumulation of intratumoral antigen-reactive CD8<sup>+</sup> T cells, compared with control IgG-treated mice (Fig. 4C). CTX-2026 was more effective than the anti-PD-1 antibody nivolumab when combined with tumor-reactive T cells (Fig. 4D and fig. S6D), despite PD-L1 upregulation by NY-OVCAR3 tumor cells in vivo (fig. S6E). Of note, tumors in all experiments were allowed to grow for at least 15 days and were treated with a single T cell injection, with significant growth delays for tumors as large as 300 mm<sup>3</sup> at the time of adoptive transfer (Fig. 4A and fig. S4, A and B).

Notably, the protective effects of CTX-2026 in vivo were not restricted to tumor-reactive  $\alpha\beta$  T cells, because  $\gamma\delta$  T cells from eight different donors also elicited tumor growth reduction, albeit only in combination with CTX-2026 antibodies (Fig. 4E and fig. S6F). Accordingly, BTN3A1 targeting resulted in a greater accumulation of V $\gamma$ 9 T cells within tumor beds (Fig. 4F). However, maximal antitumor responsiveness against established tumors was only achieved upon coadministration of  $\gamma\delta$  and tumor-specific  $\alpha\beta$  T cells into NY-OVCAR3 tumor-bearing NSG mice in combination with CTX-2026 administration (Fig. 4G and fig. S6G) and was superior to zoledronate treatment (fig. S6H). This treatment provoked the formation of cystic cavities within the tumor (Fig. 4H), which indicate partial tumor rejection. Thus, targeting BTN3A1 orchestrates coordinated responses between tumor-reactive  $\alpha\beta$  T cells rescued from BTN3A1-mediated immunosuppression and cytotoxic V $\gamma$ 9V $\delta$ 2 T cells that are redirected to kill BTN3A1<sup>+</sup> tumors.

#### **Preexisting antitumor immune responses in immunocompetent hosts are restored by anti-CD277**

To confirm the antitumor effectiveness of blocking BTN3A1 in myeloid cells in immunocompetent hosts, we engineered a knock-in mouse expressing human BTN3A1 under the control of the mouse *Itga $\alpha$ /Cd11c* promoter (BTN3A1<sup>KI</sup>) (Fig. 5A). As expected, CD11c<sup>+</sup> bone marrow-derived dendritic cells (BMDCs) from BTN3A1<sup>KI</sup> mice expressed human BTN3A1 on the cell surface (Fig. 5B). Equally important, activation of murine T cells in the presence of BTN3A1-Fc fusion proteins decreased IFN- $\gamma$  release compared with controls (fig. S7A), whereas proliferation of OT-I T cells in response to SIINFEKL-pulsed CD11c<sup>+</sup>BTN3A1<sup>+</sup> BMDCs was significantly lower than in response to BTN3A1<sup>−</sup> BMDCs from littermates (Fig. 5C and fig. S7B). Thus, although mouse CD45 has a somewhat different pattern of glycosylation near the N terminus, human BTN3A1 can also functionally suppress mouse  $\alpha\beta$  T cells. Accordingly, treatment with anti-CD277 CTX-2026 also blocked human BTN3A1-mediated suppression of mouse  $\alpha\beta$  T cells (Fig. 5D and fig. S7C).

To test the role of BTN3A1 in an immunocompetent syngeneic ovarian cancer model, BTN3A1<sup>KI</sup> mice were challenged intraperitoneally with orthotopic ID8-*Defb29/Vegf-a* tumors, an aggressive model that responds to checkpoint inhibitors (35) and provokes the accumulation of tumor-promoting CD11c<sup>+</sup> myeloid cells (36). Predictably, compared with control littermates, BTN3A1<sup>KI</sup> recipients accumulated BTN3A1<sup>+</sup> dendritic cells in the ascites fluid (fig. S7D) and showed accelerated malignant progression (fig. S7E). Targeting tumor-bearing BTN3A1<sup>KI</sup> recipient mice with zoledronate extended their survival, but to a lesser extent than treatment with CTX-2026 and 20.1 antibodies (Fig. 5E), with corresponding differences in intratumoral CD8<sup>+</sup> T cell accumulation (Fig. 5F). Consequently, the frequencies of peritoneal T cells responding to cognate tumor antigen in IFN- $\gamma$  enzyme-linked immunosorbent spot (ELISpot) analyses were increased by all BTN3A1-targeting therapeutics, with the highest readout for CTX-2026 (Fig. 5G). Murine  $\gamma\delta$  T cells accumulated in the ascites fluid of BTN3A1<sup>KI</sup> tumor-bearing mice in a CTX-2026-dependent manner (Fig. 5H). As in our humanized model, targeting BTN3A1 was demonstrably more effective in delaying malignant progression than neutralizing the PD-L1/PD-1 checkpoint (Fig. 5I). Thus, targeting of BTN3A1 overcomes the highly immunosuppressive microenvironment of ovarian cancer, a disease that, thus far, has been resistant to existing checkpoint inhibitors.

## **DISCUSSION**

We report that targeting BTN3A1 with certain human antibodies is sufficient to elicit coordinated  $\alpha\beta$  and  $\gamma\delta$  T cell antitumor responses against established tumors, and we have demonstrated that BTN3A1 targeting in validated orthotopic xenograft and syngeneic models of ovarian cancer is superior to PD-1 checkpoint therapy. Most human malignancies remain resistant to existing checkpoint inhibitors, which are aimed to rescue  $\alpha\beta$  T cell responses. Yet,  $\gamma\delta$  T cells also infiltrate multiple human cancers, where they primarily play regulatory roles (4, 37). Engaging the cooperation of these two T cell subsets could therefore extend the range of cancer patients benefiting from immunotherapy. In addition, BTN3A1 targeting was more effective than PD-1 neutralization in  $\alpha\beta$  T cells in our PD-L1<sup>+</sup> humanized systems, and it is possible that anti-CD277 also block  $\alpha\beta$  T cell inhibition by the nearly identical BTN3A2 and BTN3A3. Because  $\gamma\delta$  T cells also express PD-1, it will be interesting to determine whether coordinated action also takes place in patients that respond to checkpoint inhibitors. Nevertheless, unlike PD-L1, BTN3A1 does not require a specific receptor to mediate its immunosuppressive activity. Rather, BTN3A1, independently of BTN2A1, inhibits  $\alpha\beta$  T cells

by binding to N-mannosylated residues in human CD45, preventing its segregation from the immune synapse and promoting its dimerization, and thus abrogating effective TCR activation. At least in ovarian cancer, BTN3A overexpression in myeloid and tumor cells is associated with accelerated malignant progression; thus, it is possible that BTN3A1 targeting might be combined with other checkpoint inhibitors to enhance immunotherapeutic responses.

An interesting finding in our study is that both phosphometabolites and CTX-2026 antibodies transform BTN3A1 from an immunosuppressive to an immunostimulatory mediator. Recent work showed that phosphometabolite-driven cosignaling by BTN3A1 and BTN2A1 promotes V $\gamma$ 9V $\delta$ 2 activation, whereas BTN2A1 is also required for the agonistic activity of antibody 20.1 (19). The structure of CTX-2026 bound to BTN3A1 is similar to that of mouse scFv 20.1:BTN3A complexes (23), in which both antibodies partially share an overlapping epitope. This supports the results of Adams and colleagues that agonistic antibodies modify the extracellular domains of BTN3A molecules, mimicking the effect of phosphoantigens (23). It is tempting to speculate that antibody-phosphoantigen-induced clustering separates BTN3A1 from MHC:antigen complexes, allowing robust engagement with specific  $\alpha\beta$  TCRs. However, BTN2A1 is essential for antibody-driven switching of BTN3A1 from an immunosuppressive to immunostimulatory action, suggesting that CD277 clustering could release a BTN2A1 partner additionally required for V $\gamma$ 9V $\delta$ 2 activation. Perhaps these mechanisms might be effectively elicited in vivo and in situ at tumor beds as an anticancer intervention.

## REFERENCES AND NOTES

1. M. D. Hellmann *et al.*, *N. Engl. J. Med.* **378**, 2093–2104 (2018).
2. R. J. Motzer *et al.*, *N. Engl. J. Med.* **378**, 1277–1290 (2018).
3. L. Horn *et al.*, *N. Engl. J. Med.* **379**, 2220–2229 (2018).
4. M. R. Rutkowski *et al.*, *Cancer Cell* **27**, 27–40 (2015).
5. S. Vavassori *et al.*, *Nat. Immunol.* **14**, 908–916 (2013).
6. A. Sandstrom *et al.*, *Immunity* **40**, 490–500 (2014).
7. H. Wang *et al.*, *J. Immunol.* **191**, 1029–1042 (2013).
8. S. Meraviglia *et al.*, *Clin. Exp. Immunol.* **161**, 290–297 (2010).
9. D. A. Rhodes, W. Reith, J. Trowsdale, *Annu. Rev. Immunol.* **34**, 151–172 (2016).
10. H. A. Arnett *et al.*, *J. Immunol.* **178**, 1523–1533 (2007).
11. L. Abeler-Dörner, M. Swamy, G. Williams, A. C. Hayday, A. Bas, *Trends Immunol.* **33**, 34–41 (2012).
12. J. R. Cubillos-Ruiz *et al.*, *Oncotarget* **1**, 329–338 (2010).
13. T. Yamazaki *et al.*, *J. Immunol.* **185**, 5907–5914 (2010).
14. K. Sarter *et al.*, *J. Exp. Med.* **213**, 177–187 (2016).
15. N. Messal *et al.*, *Eur. J. Immunol.* **41**, 3443–3454 (2011).
16. J. L. Blazquez, A. Benyamine, C. Pasero, D. Olive, *Front. Immunol.* **9**, 1601 (2018).
17. R. Di Marco Barros *et al.*, *Cell* **167**, 203–218.e17 (2016).
18. P. Vantourout *et al.*, *Proc. Natl. Acad. Sci. U.S.A.* **115**, 1039–1044 (2018).
19. M. Rigau *et al.*, *Science* **367**, eaay5516 (2020).
20. M. M. Karunakaran *et al.*, *Immunity* **52**, 487–498.e6 (2020).
21. S. Gu *et al.*, *Proc. Natl. Acad. Sci. U.S.A.* **114**, E7311–E7320 (2017).
22. Y. Yang *et al.*, *Immunity* **50**, 1043–1053.e5 (2019).
23. A. Palakodeti *et al.*, *J. Biol. Chem.* **287**, 32780–32790 (2012).
24. M. V. Maus *et al.*, *Nat. Biotechnol.* **20**, 143–148 (2002).
25. P. F. Robbins *et al.*, *J. Clin. Oncol.* **29**, 917–924 (2011).
26. A. Jemal *et al.*, *CA Cancer J. Clin.* **59**, 225–249 (2009).
27. M. S. Ju, S. T. Jung, *Curr. Opin. Biotechnol.* **30**, 128–139 (2014).
28. C. Harly *et al.*, *Blood* **120**, 2269–2279 (2012).
29. R. Majeti, A. M. Bilwes, J. P. Noel, T. Hunter, A. Weiss, *Science* **279**, 88–91 (1998).
30. L. A. Earl, L. G. Baum, *Immunol. Cell Biol.* **86**, 608–615 (2008).
31. V. T. Chang *et al.*, *Nat. Immunol.* **17**, 574–582 (2016).
32. Y. Razvag, Y. Neve-Oz, J. Sajman, M. Reches, E. Sherman, *Nat. Commun.* **9**, 732 (2018).
33. J. Irie-Sasaki *et al.*, *Nature* **409**, 349–354 (2001).
34. R. R. Hovis *et al.*, *Science* **260**, 544–546 (1993).
35. T. L. Stephen *et al.*, *Immunity* **46**, 51–64 (2017).
36. A. J. Tesone *et al.*, *Cell Rep.* **14**, 1774–1786 (2016).
37. C. Fleming, S. Morrissey, Y. Cai, J. Yan, *Trends Cancer* **3**, 561–570 (2017).

## ACKNOWLEDGEMENTS

We are grateful to Chemical Biology, Analytic Microscopy, Advanced CLIA Tissue Imaging, Proteomics, and Flow Cytometry Shared Resources at Moffitt Cancer Center, as well as E. Larson of HarkerBio, for exceptional support. **Funding:** Support for shared resources was provided by Cancer Center Support Grant (CCSG) CA076292 to H. Lee Moffitt Cancer Center. This study was supported by the National Institutes of Health (R01CA157664, R01CA124515, R01CA178687, R01CA211913, and U01CA232758 to J.R.C.-G.; R01CA184185 to P.C.R.; and R01NS114653 and R21CA248106 to J.R.C.-R.); the U.S. Department of Defense Ovarian Cancer Research Program (W81XWH-16-1-0438 and W81XWH-20-1-0191 to J.R.C.-R.), and Stand Up to Cancer (SU2C-AACR-IRG-03-16 and SU2C-AACR-PS24 to J.R.C.-R.). K.K.P. was supported by T32CA009140 and an American Cancer Society Postdoctoral Fellowship. **Competing interests:** J.R.C.-G. and D.I.G. are members of the External Advisory Board of Compass Therapeutics and receive consulting fees and stock options from the company. J.R.C.-G. additionally receives consulting fees from Anixa Bioscience and Leidos. A.P.-P. is the Vice President for Research & Development at Geneos Therapeutics. J.L., M.O., P.B., B.M., U.E., and M.S. were employees of Compass Therapeutics. J.R.C.-G., K.K.P., M.S., B.M., and P.B. are inventors on patent application WO202003923A1 submitted by Compass Therapeutics LLC, The Wistar Institute of Anatomy and Biology, and H. Lee Moffitt Cancer Center; this patent covers a method for reducing CD277-mediated inhibition of  $\alpha\beta$  T cells, as well as a method for inducing or enhancing CD277-mediated  $\gamma\delta$  T cell stimulation. **Data and materials availability:** The crystal structure of the human BTN3A1 ectodomain in complex with the CTX-2026 Fab was deposited in wwPDB (accession code PDB ID 6XLQ). The humanized BTN3A1 transgenic mouse, as well as CD45-ablated Jurkat cells transduced with CD45RA or CD45RO, are available from J.R.C.-G. under a material transfer agreement with Moffitt Cancer Center.

## SUPPLEMENTARY MATERIALS

science.sciencemag.org/content/369/6506/942/suppl/DC1  
Materials and Methods  
Figs. S1 to S7  
Tables S1 to S3  
References (38–48)  
Files S1 to S7

[View/request a protocol for this paper from Bio-protocol.](#)

12 June 2019; resubmitted 11 May 2020  
Accepted 30 June 2020  
10.1126/science.aay2767



## LIQUID CRYSTALS

# Shaping colloidal bananas to reveal biaxial, splay-bend nematic, and smectic phases

Carla Fernández-Rico<sup>1</sup>, Massimiliano Chiappini<sup>2</sup>, Taiki Yanagishima<sup>1</sup>, Heidi de Sousa<sup>1</sup>, Dirk G. A. L. Aarts<sup>1</sup>, Marjolijn Dijkstra<sup>2</sup>, Roel P. A. Dullens<sup>1\*</sup>

Understanding the impact of curvature on the self-assembly of elongated microscopic building blocks, such as molecules and proteins, is key to engineering functional materials with predefined structure. We develop model “banana-shaped” colloidal particles with tunable dimensions and curvature, whose structure and dynamics are accessible at the particle level. By heating initially straight rods made of SU-8 photoresist, we induce a controllable shape deformation that causes the rods to buckle into banana-shaped particles. We elucidate the phase behavior of differently curved colloidal bananas using confocal microscopy. Although highly curved bananas only form isotropic phases, less curved bananas exhibit very rich phase behavior, including biaxial nematic phases, polar and antipolar smectic-like phases, and even the long-predicted, elusive splay-bend nematic phase.

Curvature has an enormous impact on the functionality and self-assembly of elongated microscopic building blocks (1, 2). In the biological world, for instance, curved, rod-shaped bacteria outperform their straight counterparts in surface-colonization and swimming efficiency, which makes them ubiquitous in marine environments (3, 4). Many cellular functions, such as cell division or endocytosis, rely on the ability of “banana-shaped” proteins to generate curvature in cell membranes (5, 6). Curvature is also of key importance at the molecular scale where, for example, banana-shaped or bent-core molecules exhibit a fascinating range of new liquid crystalline phases with distinctive features such as supramolecular chirality and polarity (7–9). This has led to a surge of interest in banana-shaped liquid crystals from both a fundamental and technological point of view. They are not only ideal systems to study, for example, the spontaneous chiral symmetry breaking in systems of achiral molecules (10–13) but also excellent candidates for achieving faster switching speeds in display technologies (14, 15).

Over the past two decades, more than 50 new banana-shaped liquid crystalline phases have been reported, depending primarily on the molecular curvature (7–9). The vast majority of these are smectic (Sm) phases, because the curved shape of the constituting molecules promotes their locking into smectic layers (8, 9). The large stability of Sm phases has also been observed in experiments of colloidal “boomerang-like” particles (16) and in com-

puter simulations of similarly shaped particles (17). The rather uncommon observation of nematic phases in banana-shaped systems (18, 19) has been of interest for the past 20 years, not least because of their potential to form chiral and biaxial nematic phases (13, 17, 20, 21). Examples of chiral and biaxial nematic phases are the twist-bend ( $N_{TB}$ ) and the splay-bend ( $N_{SB}$ ) nematic phases, respectively, in both of which the particle orientation is modulated in space. Whereas in the  $N_{TB}$  phase the particles exhibit a periodic twist in space resulting in a chiral phase, the  $N_{SB}$  phase exhibits periodic splay and bend modulations of the particle orientation in a single plane, thus showing biaxiality but not chirality (12).

The  $N_{TB}$  and  $N_{SB}$  phases were postulated more than 40 years ago by Meyer (22), and later independently by Dozov (12), who suggested that bend deformations in the orientation field of banana-shaped particles should be accompanied either by twist or splay deformations to fill three-dimensional (3D) space. Whereas the  $N_{TB}$  phase has been observed in thermotropic liquid crystals [see, e.g., (23–25)], the existence of the  $N_{SB}$  phase has yet to be confirmed experimentally. Computer simulations suggested that the  $N_{SB}$  phase can be found in systems of hard boomerangs—that is, rod-like particles with a sharp kink—if the Sm phase is destabilized by polydispersity in the particle length or by smooth curvature in the particle shape (17). Experimentally studying the impact of features such as the curvature on the structure of banana-shaped systems at the particle level is thus crucial for a deeper understanding of the formation and properties of these phases. However, banana-shaped liquid crystals are typically characterized using birefringence and x-ray diffraction techniques, where direct information about structural details is not available at the molecular scale. This prompts the need for a colloidal analog, where such microscopic structural information is readily accessible using optical microscopy. However, despite the abundance of liquid crystal-forming colloidal particles such as rods, boomerangs, and platelets (26–28), there is no system of smoothly curved colloidal rods available. As such, the rich phase behavior predicted for banana-shaped particles has yet to be experimentally uncovered at the particle level.

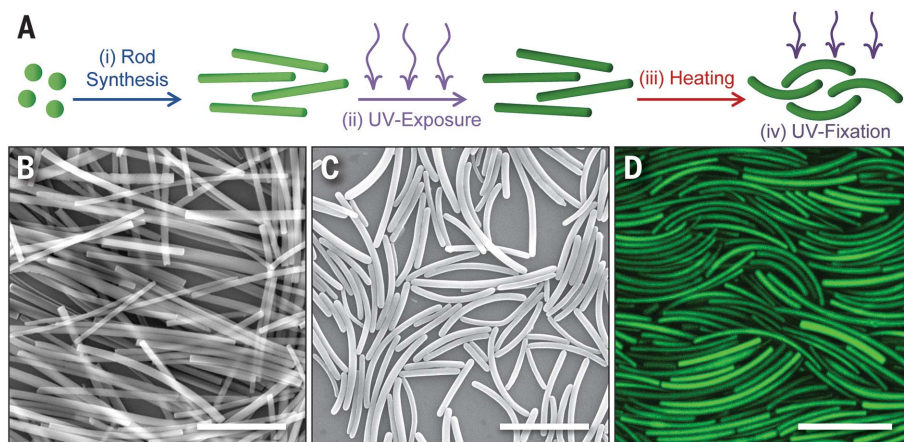


**Fig. 1. Synthesis of colloidal SU-8 banana-shaped particles.** (A) Schematic showing the synthesis of SU-8 banana-shaped particles. In the first step, straight SU-8 rods are synthesized by shearing an emulsion of SU-8 droplets (29, 30). In the second step, the rods are partially cross-linked through exposure to UV light. In the third step, the partially cross-linked rods are heated to induce a shape deformation into banana-shaped particles, before they are UV-cured in the fourth step. (B and C) Scanning electron microscopy images of (B) the rods obtained after the synthesis with no heating and (C) the colloidal SU-8 bananas ( $t_{UV} = 45$  min) obtained with heating. (D) Confocal microscopy image of the fluorescent colloidal SU-8 bananas. Scale bars are 10  $\mu$ m.

<sup>1</sup>Department of Chemistry, Physical and Theoretical Chemistry Laboratory, University of Oxford, South Parks Road, Oxford OX1 3QZ, UK. <sup>2</sup>Soft Condensed Matter, Debye Institute for Nanomaterials Science, Department of Physics, Utrecht University, Princetonplein 1, 3584 CC Utrecht, Netherlands.

\*Corresponding author. Email: roel.dullens@chem.ox.ac.uk

In this work, we develop a method to produce, in bulk, fluorescent curved colloidal rods—colloidal bananas—with tunable dimensions and curvature. Our method relies on the temperature-driven buckling of initially straight rods made of SU-8 photoresist into colloidal bananas. The extent of the shape deformation, and hence the final curvature of the particles, is controlled by the rigidity of

the SU-8 rods during the heating. Using confocal microscopy, we elucidate the phase behavior of three differently curved banana-shaped particles at the single-particle level. Although isotropic phases are found for highly curved bananas, very rich phase behavior—including biaxial nematic, splay-bend nematic, and polar and antipolar smectic-like structures—is observed for less curved bananas.

### Shaping colloidal SU-8 particles: From rods to banana-shaped particles

Our method to produce colloidal SU-8 banana-shaped particles consists of four main steps, which are illustrated in Fig. 1A: (i) synthesis of rods, (ii) ultraviolet (UV) exposure, (iii) heating, and (iv) UV curing. In the first step, polydisperse straight SU-8 rods of  $\sim 20\ \mu\text{m}$  in length (Fig. 1B) are synthesized by vigorously

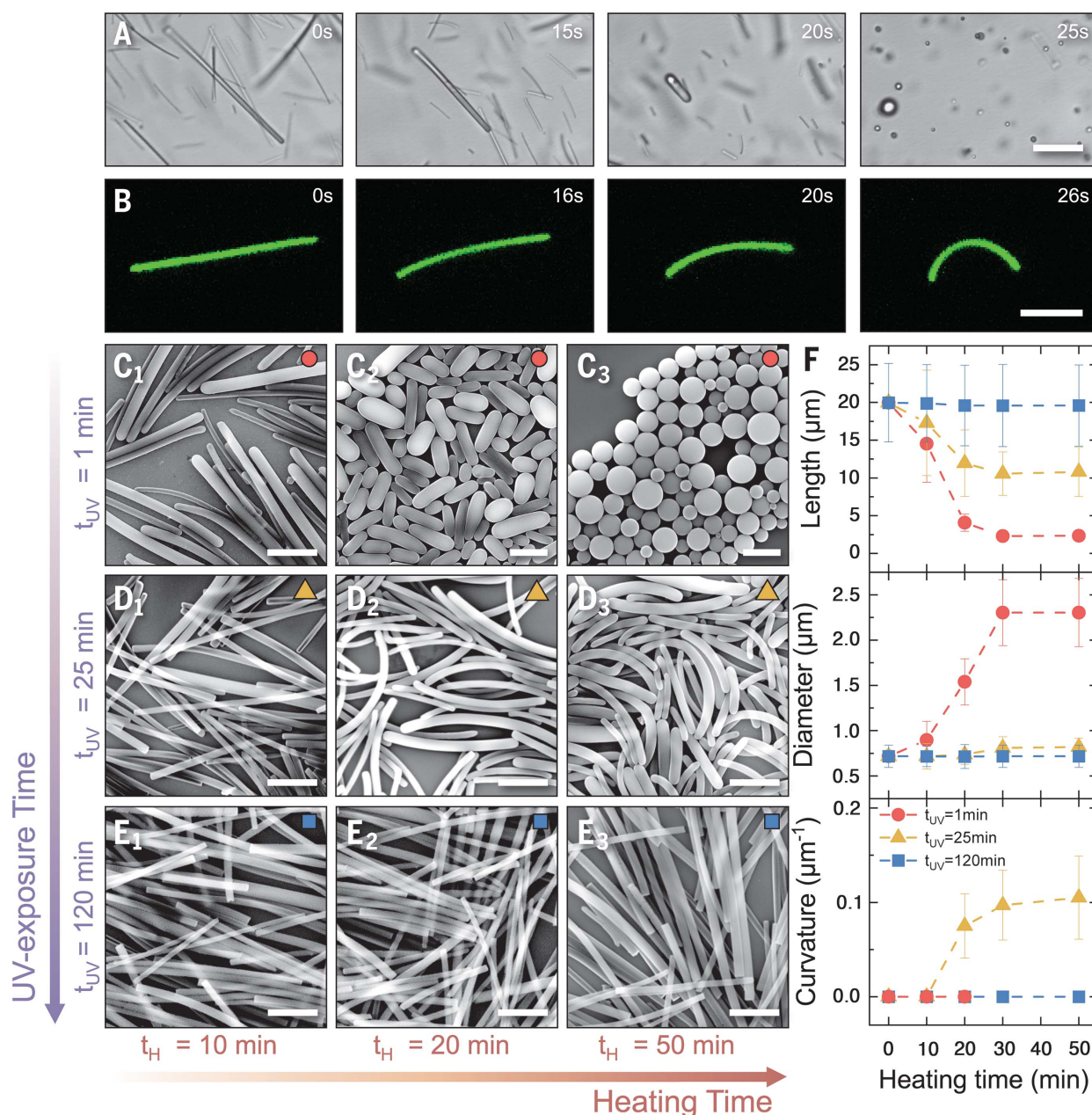
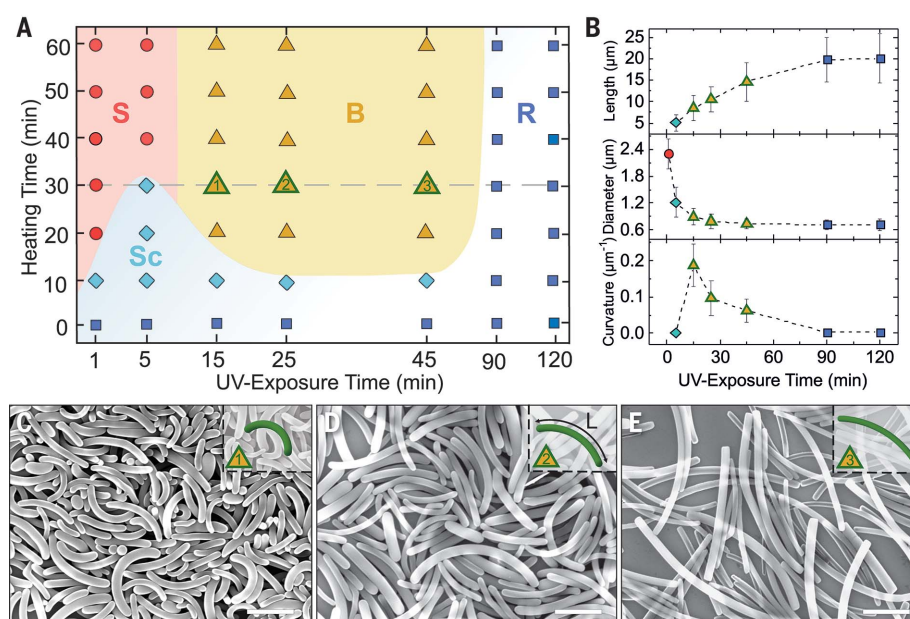


**Fig. 2. Particle shape deformations during heating.** (A and B) (A) Bright-field and (B) confocal microscopy snapshots of the deformation of an SU-8 rod during heating at  $95^\circ\text{C}$  using a heating stage; for (A),  $t_{UV} = 1\text{ min}$ , and for (B),  $t_{UV} = 25\text{ min}$ . (C to E) Representative SEM images of the shape evolution of the SU-8 rods during heating in a  $95^\circ\text{C}$  oven for (C)  $t_{UV} = 1\text{ min}$ , (D)

$t_{UV} = 25\text{ min}$ , and (E)  $t_{UV} = 120\text{ min}$ . (F) Evolution of the dimensions and curvature of the originally straight SU-8 rods during heating in a  $95^\circ\text{C}$  oven for  $t_{UV} = 1\text{ min}$  (circles),  $t_{UV} = 25\text{ min}$  (triangles), and  $t_{UV} = 120\text{ min}$  (squares). Error bars represent the standard deviation of the mean value. Scale bars are  $10\ \mu\text{m}$  in (A) and (B) and  $5\ \mu\text{m}$  in (C) to (E).



**Fig. 3. Tuning particle shape and controlling the curvature and dimensions of banana-shaped particles.** (A) Morphological state diagram of the SU-8 polymer particles as a function of UV exposure and heating times with a heating temperature of 95°C, where S, B, R, and Sc denote the sphere, banana, rod, and spherocylinder regimes, respectively. (B) Length, diameter, and curvature of the SU-8 particles after heating for 30 min, see dashed line in (A), in a 95°C oven for  $t_{UV} = 5, 15, 25, 45, 90,$  and 120 min. Error bars represent the standard deviation of the mean value, and the different colors of the symbols correspond to the different regimes in (A). (C to E) SEM images of banana-shaped particles with decreasing curvature obtained when  $t_{UV} = 15, 25,$  and 45 min, respectively. The insets show schematics of the bananas with their mean curvatures: (C)  $0.25 \mu\text{m}^{-1}$ , (D)  $0.10 \mu\text{m}^{-1}$ , and (E)  $0.07 \mu\text{m}^{-1}$ . Scale bars are 5  $\mu\text{m}$ .



shearing an emulsion of SU-8 droplets in a viscous medium (29, 30). During the second step, the resulting rods are partially cross-linked through the ring-opening reaction of the epoxy groups under low-intensity UV light (supplementary materials section 2). The degree of cross-linking in the rods is controlled by the UV exposure time,  $t_{UV}$ , as confirmed by the infrared spectra shown in fig. S3, where the peak corresponding to the epoxy groups decreases with increasing exposure time. In the third step, the deformation into banana-shaped particles is induced by heating the rods in a 95°C oven, resulting in smoothly curved polydisperse colloidal bananas (Fig. 1, C and D;  $t_{UV} = 45$  min). Finally, the particles are fully cross-linked by means of high-intensity UV light exposure, yielding highly stable particles that can be dispersed in both aqueous and nonaqueous solvents.

The formation of banana-shaped particles is controlled by the interplay between the cross-linking density of the SU-8 rods, tuned by the UV exposure time, and the interfacial forces induced during the heating step. The cross-linking density of SU-8 dictates its rigidity and glass transition temperature, and both increase with longer UV exposures (31, 32). In our experiments, we observe three distinct responses after heating, depending on the UV exposure time. At short exposure times ( $t_{UV} = 1$  min; Fig. 2A), i.e., low cross-linking densities, the heating of the rods results in the rounding of their sharp edges (Fig. 2C), suggesting that the rods are heated to a temperature above their glass transition temperature. The interfacial forces associated with the hemispherical particle ends drive the collapse of the rods into spheres, rather than bananas, to

minimize their surface energy (33–35). This collapse takes place via a spherocylindrical intermediate state, as shown by the snapshots taken during heating in Fig. 2A (see also movie S1). From the corresponding scanning electron microscopy (SEM) images shown in Fig. 2C, we find that the particle length decreases and the diameter increases (Fig. 2F) but that the particle volume remains constant during heating (see fig. S5). At intermediate exposure times ( $t_{UV} = 25$  min; Fig. 2B), the heating of the rods still results in the formation of round edges (Fig. 2D), which leads to an initial decrease of the rod length and an increase of the rod diameter (Fig. 2F). However, the increased cross-linking density of the rods, i.e., the higher rigidity, leads to the formation of banana-shaped particles through buckling, as directly visualized during the heating process using confocal microscopy (Fig. 2B and movie S2). The buckling manifests itself by the appearance of curvature after heating for 20 min, where the particle length and diameter no longer change considerably (Fig. 2F). At long exposure times ( $t_{UV} = 120$  min; Fig. 2E), i.e., high cross-linking densities, no rounding of the edges is observed, suggesting that the rods are heated to temperatures below their glass transition temperature. Consequently, no shape deformation is observed, and the length, diameter, and curvature are all constant during the heating (Fig. 2F). Finally, carrying out the experiments in the dark, i.e., no cross-linking takes place, always results in the formation of spheres (fig. S4), which thus confirms the crucial role of the interplay between interfacial forces and the differing UV-induced rigidity of the rods on controlling the final particle shape.

### Morphological state diagram

The ability to systematically control the final particle shape using both UV exposure and heating time (supplementary materials section 1) is summarized in the morphological state diagram shown in Fig. 3A. Within the banana regime, we show that both the dimensions and curvature of the resulting banana-shaped particles can be controlled by tuning the UV exposure time. This is observed in the SEM images presented in Fig. 3, C to E, where the bananas obtained using UV exposure times of 15, 25, and 45 min, respectively, are shown for a constant heating time of 30 min. We find that with longer UV exposure times, the mean particle length  $L$  (inset in Fig. 3D) increases from 8 to 14  $\mu\text{m}$ , whereas the mean diameter and curvature decrease from 1 to 0.7  $\mu\text{m}$  and from 0.25 to  $0.07 \mu\text{m}^{-1}$ , respectively (Fig. 3B and fig. S6). This corroborates the fact that the rigidity of the rods increases and thus the extent of buckling decreases with UV exposure time. Inherent to the polydisperse nature of the initial SU-8 rods (29, 30), the resulting colloidal bananas are also polydisperse in length, diameter, and curvature, with typical polydispersities of 30, 20, and 30%, respectively (table S1).

### Phase behavior of colloidal bananas

We study the phase behavior of banana-shaped particles, and how this is affected by curvature, by preparing concentrated samples of three differently curved colloidal bananas and imaging them using confocal microscopy. Although the 3D samples are typically  $\sim 50 \mu\text{m}$  thick, we image the system relatively close to the bottom wall of



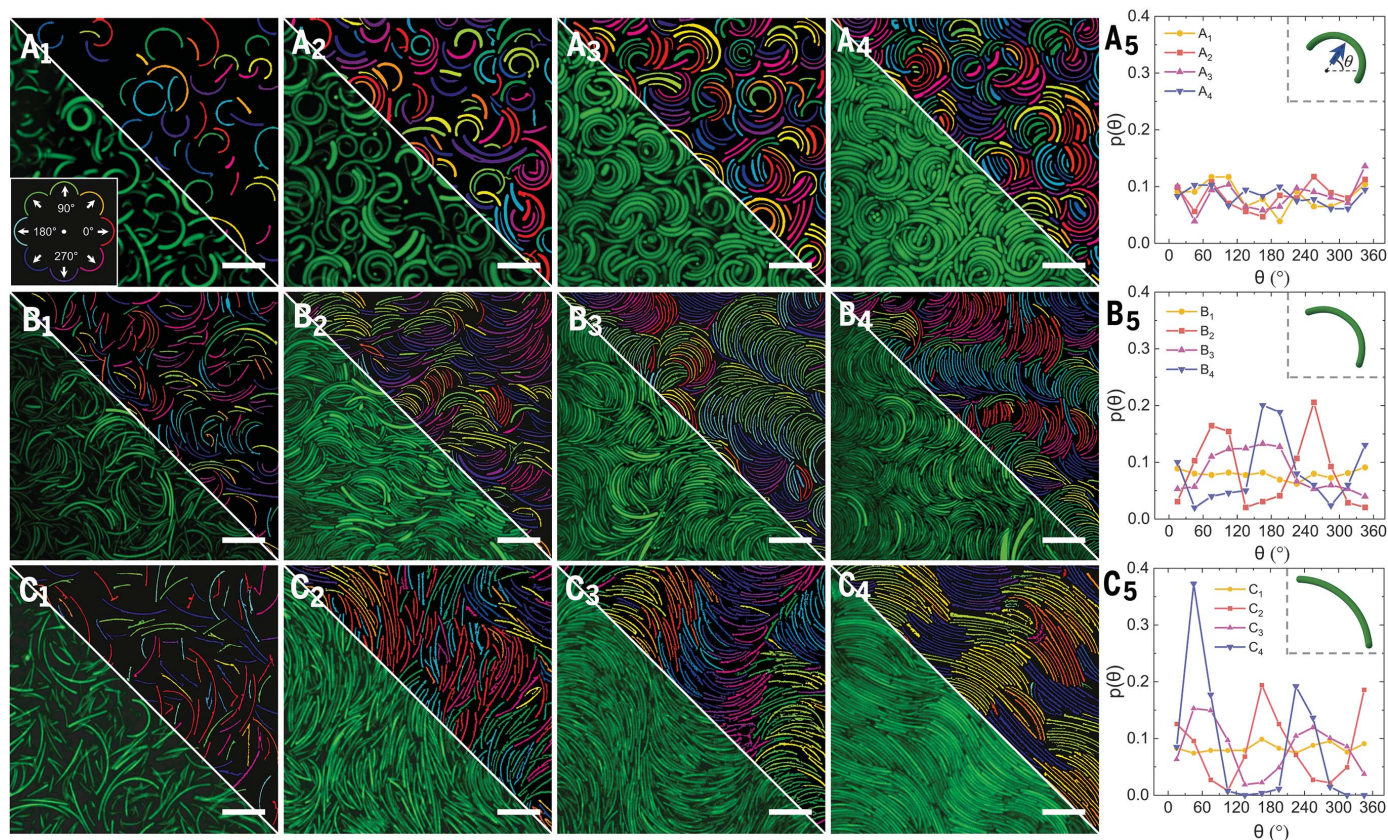


**Fig. 4. Phase behavior of banana-shaped colloidal particles with different curvatures.** (A to C) Confocal microscopy images of colloidal bananas with an average curvature of [(A<sub>1</sub>) to (A<sub>4</sub>)]  $\kappa = 0.25 \mu\text{m}^{-1}$  and packing fractions  $\phi = 0.12, 0.26, 0.61,$  and  $0.84$ , respectively; [(B<sub>1</sub>) to (B<sub>4</sub>)]  $\kappa = 0.10 \mu\text{m}^{-1}$  and  $\phi = 0.27, 0.63, 0.79,$  and  $0.82$ , respectively; and [(C<sub>1</sub>) to (C<sub>4</sub>)]  $\kappa = 0.07 \mu\text{m}^{-1}$  and  $\phi = 0.29,$

$0.60, 0.67,$  and  $0.79$ , respectively. The top-right overlays on the images show the bananas colored according to their polar orientation  $\theta$  as defined in the inset in (A<sub>5</sub>) and the color legend in (A<sub>1</sub>). (A<sub>5</sub>), (B<sub>5</sub>), and (C<sub>5</sub>) show the polar angle distributions of the corresponding confocal microscopy images. The insets show schematics of the bananas with their mean curvatures. Scale bars are  $10 \mu\text{m}$ .

the sample container to which the bananas align because this facilitates a quantitative 2D structural analysis at the particle level (supplementary materials section 4.2 for details). In Fig. 4, we present confocal microscopy images of the structures formed by the three differently curved colloidal bananas at different packing fractions  $\phi$ . The most curved bananas [curvature ( $\kappa$ ) =  $0.25 \mu\text{m}^{-1}$ ] only display isotropic phases (I) at all packing fractions, as shown in Fig. 4A (see fig. S9 for confocal images of the system at all packing fractions studied). Although small smectic domains are observed at high packing fractions, the combination of polydispersity and small opening angles of these bananas (table S1) suppresses the formation of any ordering at larger length scales. This is corroborated by the flat distribution of polar orientation  $\theta$  (inset in Fig. 4A<sub>5</sub>) of the bananas,  $p(\theta)$ , in Fig. 4A<sub>5</sub> and the lack of orientational correlations over space in the overlays in Fig. 4, A<sub>1</sub> to A<sub>4</sub>, where the bananas are colored according to their polar orientation. Note that because of the alignment of the bananas to the wall, the

orientation of the long axis is directly related to the polar orientation through a  $\pi/2$  rotation (fig. S7).

The bananas with intermediate curvature,  $\kappa = 0.10 \mu\text{m}^{-1}$ , also exhibit isotropic ordering at low packing fractions (Fig. 4B<sub>1</sub>) but self-assemble into biaxial nematic and polar and antipolar smectic-like phases at higher packing fractions, as shown in Fig. 4, B<sub>2</sub> to B<sub>4</sub> (see fig. S12 for images at all packing fractions). The onset of orientational ordering in the nematic and smectic phases manifests itself as the emergence of peaks in  $p(\theta)$  above  $\phi = 0.63$ , as shown in Fig. 4B<sub>5</sub>. The biaxial nature of this ordering is inherent to the orthogonality of the long and polar axes of the bananas because of their alignment to the wall (see fig. S7). In particular, the biaxial nematic phase (N<sub>b</sub>) observed at  $\phi = 0.63$  (Fig. 4B<sub>2</sub>) is characterized by two peaks in  $p(\theta)$ , which correspond to the two polar orientations that the bananas show in this phase. At higher packing fractions,  $\phi = 0.79$  (Fig. 4B<sub>3</sub>), the emergence of smectic domains, with some local polar smectic order-

ing, is observed (36). The polydomain structure at this packing fraction is likely due to kinetic effects (supplementary materials section 4.2) and results in a single broad peak in  $p(\theta)$ . Antipolar smectic ordering is observed at  $\phi = 0.82$  (Fig. 4B<sub>4</sub>), which leads to a double peak in  $p(\theta)$  due to the neighboring layers exhibiting alternating polar orientation, as is also evident from the overlay in Fig. 4B<sub>4</sub>.

Even richer phase behavior is observed for the least curved bananas ( $\kappa = 0.07 \mu\text{m}^{-1}$ ), as shown in Fig. 4C (see fig. S15 for images at all packing fractions). As expected, the isotropic phase is observed at low packing fractions. On increasing packing fraction, the system starts to exhibit biaxial nematic ordering (Fig. 4, C<sub>2</sub> and C<sub>3</sub>), as is evident from the development of peaks in  $p(\theta)$  (Fig. 4C<sub>5</sub>), and eventually forms layered antipolar biaxial smectic structures at  $\phi = 0.79$  (Fig. 4C<sub>4</sub>). We also observe different types of defects as shown in fig. S24. Most interestingly, however, the biaxial nematic phase of bananas with this curvature (Fig. 4C<sub>3</sub>) exhibits a strong spatial modulation of the particle orientations,



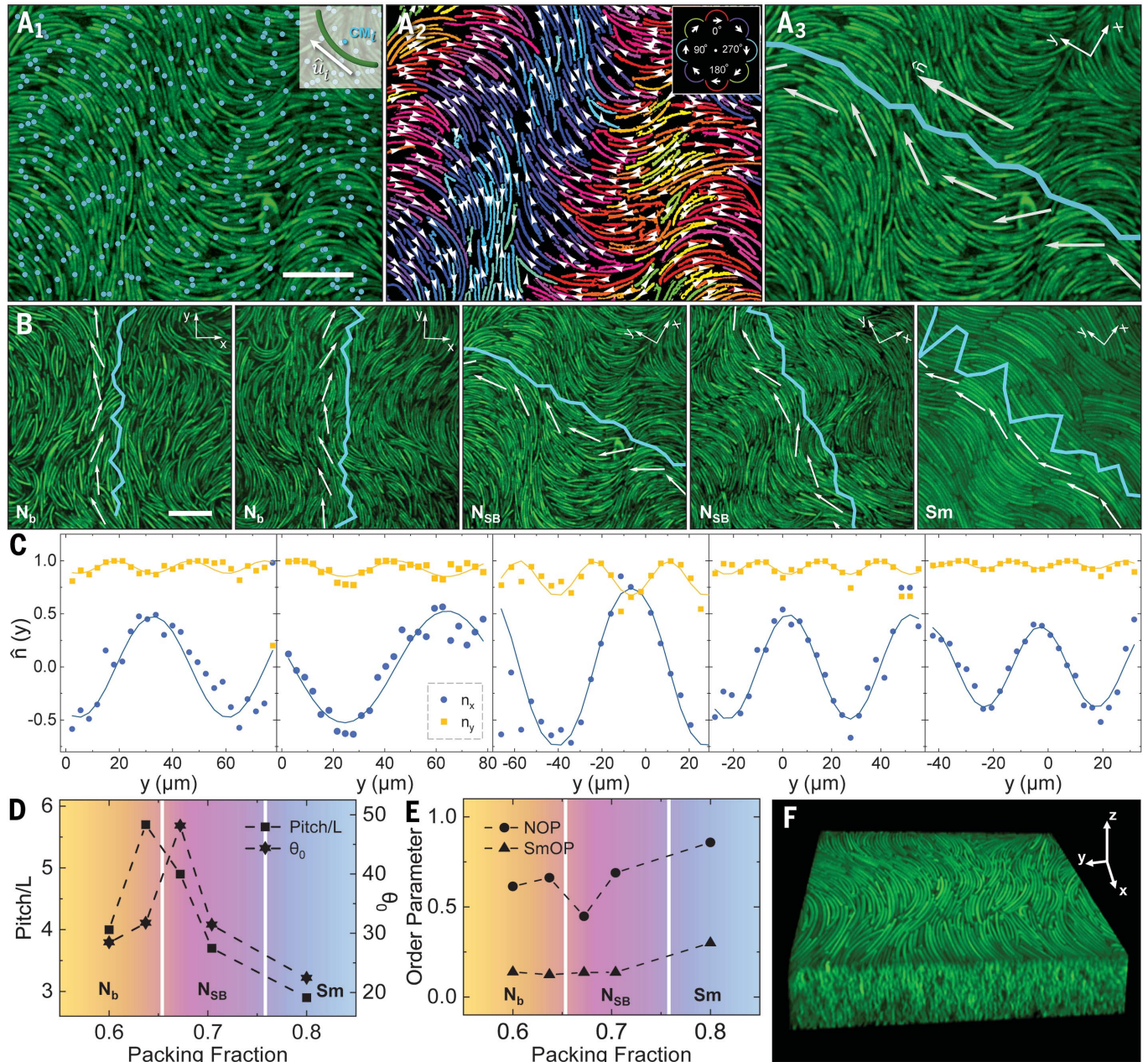


**Fig. 5. Observation of the splay-bend nematic phase.** (A<sub>1</sub>) Center of mass (CM)<sub>i</sub> positions of all the bananas. The inset shows a schematic of the center of mass and orientation of a banana. (A<sub>2</sub>) Bananas colored according to the particle orientation as indicated by the white arrows. The inset shows the color legend used for the particle orientation. (A<sub>3</sub>) The density profile  $\rho(y)$  (blue line) and nematic director field  $\hat{n}(y)$  (white arrows) along the nematic director,  $\hat{n}$ , of the system shown in Fig. 4C<sub>3</sub>. Note that the  $y$  axis is parallel to  $\hat{n}$ . (B) Confocal microscopy images of the colloidal bananas with curvature

$\kappa = 0.07 \mu\text{m}^{-1}$  for packing fractions  $\phi = 0.6, 0.64, 0.67, 0.70$ , and  $0.79$ , with  $\rho(y)$  and  $\hat{n}(y)$  overlaid. (C) Modulation of the  $x$  and  $y$  components of the measured nematic director field along  $\hat{n}$ . The solid lines are fits according to the theoretical expression for  $\hat{n}(y)$  (see main text). (D) Pitch-length (in units of the particle length  $L$ ) and amplitude  $\theta_0$  as a function of the packing fraction. (E) Global nematic (NOP) and smectic (SmOP) parameters as a function of the packing fraction. (F) 3D confocal microscopy image ( $70 \mu\text{m}$  by  $70 \mu\text{m}$  by  $15 \mu\text{m}$ ) of the splay-bend nematic phase. Scale bars are  $10 \mu\text{m}$ .

which is reminiscent of the elusive biaxial splay-bend nematic phase.

#### Splay-bend nematic phase in colloidal bananas

To distinguish the splay-bend nematic phase from the biaxial nematic and smectic phases, we measure the spatial modulation of both the particle positions and orientations along

the nematic director  $\hat{n}$ , defined as the average particle orientation of the phase (supplementary materials section 7). To this end, we determine the center of mass positions and the particle orientations  $\hat{u}_i$  (inset in Fig. 5, A<sub>1</sub> and A<sub>2</sub>, respectively, for the least curved bananas at  $\phi = 0.67$ . From these, we

extract the number density profile and the nematic director field along the nematic director  $\hat{n}$  (supplementary materials section 7), which are shown as the blue line and the white arrows in Fig. 5A<sub>3</sub>, respectively. Note that the  $y$  axis is defined to be parallel to  $\hat{n}$ . In Fig. 5B, we present these measurements for the five highest packing fractions

( $\phi = 0.60$  to  $0.79$ ) for the bananas with the lowest curvature ( $\kappa = 0.07 \mu\text{m}^{-1}$ ). First, we observe that the number density profiles,  $\rho(y)$ , are mostly flat, characteristic for nematic phases, except for the highest packing fraction ( $\phi = 0.79$ ), where clear peaks develop owing to the organization of the bananas into positionally ordered smectic layers. Consistently, the global smectic order parameter (supplementary materials section 7) only increases at  $\phi = 0.79$ , as shown in Fig. 5E, confirming the smectic nature of this phase. Second, we observe a clear modulation of the nematic director field,  $\hat{\mathbf{n}}(y)$ , for all five packing fractions, as is evident from the periodic fluctuations in the orientations of the white arrows in Fig. 5B.

A detailed characterization of the measured  $\hat{\mathbf{n}}(y)$  is shown in Fig. 5C, where the spatial modulations of its components parallel ( $n_y$ ) and perpendicular ( $n_x$ ) to the nematic director are shown for all five packing fractions. To unambiguously identify the splay-bend nature of these phases, we fit the measured nematic director field with the theoretical expression for the director field of a splay-bend nematic phase (12), given by  $\hat{\mathbf{n}}(y) = \left\{ \sin \left[ \theta_0 \sin \left( \frac{2\pi}{p} y \right) \right], \cos \left[ \theta_0 \sin \left( \frac{2\pi}{p} y \right) \right] \right\}$ , where  $\theta_0$  and  $p$  are the amplitude and pitch-length of the modulation, respectively (12) (fig. S18).

As shown in Fig. 5C, we find that our experimental data for  $n_x$  and  $n_y$  are notably well described by the expression for  $\hat{\mathbf{n}}(y)$  for all packing fractions in the range  $\phi = 0.60$  to  $0.79$ , confirming the splay-bend nature of the director field. However, for  $\phi < 0.67$ , the amplitude  $\theta_0$  and pitch-length  $p$ , obtained from these fits, increase with increasing  $\phi$  (Fig. 5D), in contrast to what is expected for the splay-bend nematic phase (17). Only for  $\phi \geq 0.67$ ,  $\theta_0$  and  $p$  are directly proportional to each other and decrease with increasing  $\phi$  (Fig. 5D), in agreement with computer simulations of the splay-bend nematic phase (17), suggesting that the splay-bend nematic phase forms at  $\phi \geq 0.67$ . This is corroborated by the decrease in the global nematic order parameter (supplementary materials section 7) at  $\phi = 0.67$ , consistent with the onset of substantial splay-bend modulations of the particle orientations, resulting in a decrease of the global alignment of particles (Fig. 5E). For our least curved colloidal bananas ( $\kappa = 0.07 \mu\text{m}^{-1}$ ), it is thus clear that they undergo a transition from the biaxial nematic phase to the modulated splay-bend nematic phase at  $\phi \approx 0.67$ , before going into the smectic phase at  $\phi \approx 0.79$ . As far as we are aware, this is the first experimental observation of the splay-bend nematic phase (see also fig. S23 and movie S4), which was predicted in 1976

(22). Finally, we demonstrate the 3D nature of the splay-bend nematic phase in Fig. 5F, where a 3D confocal microscopy image shows the splay-bend deformations up to 15 particle diameters into the bulk of our sample (see also fig. S26).

The following picture of the phase behavior for our differently curved colloidal bananas emerges: For the most curved bananas ( $\kappa = 0.25 \mu\text{m}^{-1}$ ), only the isotropic phase is observed; for the bananas with intermediate curvature ( $\kappa = 0.10 \mu\text{m}^{-1}$ ), a phase sequence of I-N<sub>b</sub>-Sm is found; and the least curved bananas ( $\kappa = 0.07 \mu\text{m}^{-1}$ ) exhibit a I-N<sub>b</sub>-N<sub>SB</sub>-Sm phase sequence as a function of the packing fraction (fig. S27). The experimental observation of the splay-bend nematic phase confirms the importance of a smooth particle curvature or polydispersity for the stability of this phase (17) and also suggests that the typical sharp kink and purity of bent-core molecules could be one of the reasons as to why this phase has not yet been observed in molecular systems. Although our results for the least curved bananas are largely consistent with the phase behavior found in computer simulations of similar banana-shaped particles (17), we do not observe the N<sub>TB</sub> phase, which is predicted to occur between the nematic and N<sub>SB</sub> phases (17). We attribute the absence of the N<sub>TB</sub> phase in the experimental phase behavior to a combination of the effect of gravity and the presence of a flat bottom wall in our sample cell. An external field like a gravitational or electric field may transform the N<sub>TB</sub> phase into a N<sub>SB</sub> phase in the case that the nematic director is perpendicular to the external field (25). In addition, the presence of a flat wall favors biaxial order, and hence the N<sub>SB</sub> rather than the N<sub>TB</sub> phase may form close to the wall. The direct observation of the colloidal analog of the N<sub>TB</sub> phase therefore still remains an exciting experimental challenge.

## REFERENCES AND NOTES

1. S. C. Glotzer, M. J. Solomon, *Nat. Mater.* **6**, 557–562 (2007).
2. V. N. Manoharan, *Science* **349**, 1253751 (2015).
3. A. Persat, H. A. Stone, Z. Gitai, *Nat. Commun.* **5**, 3824 (2014).
4. R. Schuech, T. Hoehfurner, D. J. Smith, S. Humphries, *Proc. Natl. Acad. Sci. U.S.A.* **116**, 14440–14447 (2019).
5. B. Qualmann, D. Koch, M. M. Kessels, *EMBO J.* **30**, 3501–3515 (2011).
6. M. Simunovic, G. A. Voth, A. Callan-Jones, P. Bassereau, *Trends Cell Biol.* **25**, 780–792 (2015).
7. H. Takezoe, Y. Takanishi, *Jpn. J. Appl. Phys.* **45**, 597–625 (2006).
8. R. A. Reddy, C. Tschierske, *J. Mater. Chem.* **16**, 907–961 (2006).
9. A. Jákli, O. D. Lavrentovich, J. V. Selinger, *Rev. Mod. Phys.* **90**, 045004 (2018).
10. D. R. Link *et al.*, *Science* **278**, 1924–1927 (1997).
11. T. Sekine *et al.*, *J. Mater. Chem.* **7**, 1307–1309 (1997).
12. I. Dozov, *Europhys. Lett.* **56**, 247–253 (2001).

13. C. Greco, A. Ferrarini, *Phys. Rev. Lett.* **115**, 147801 (2015).
14. N. A. Clark, S. T. Lagerwall, *Appl. Phys. Lett.* **36**, 899–901 (1980).
15. F. T. Niori, T. Sekine, J. Watanabe, T. Furukawa, H. Takezoe, *J. Mater. Chem.* **6**, 1231 (1996).
16. Y. Yang *et al.*, *Sci. Adv.* **4**, eaas8829 (2018).
17. M. Chiappini, T. Drwenski, R. van Roij, M. Dijkstra, *Phys. Rev. Lett.* **123**, 068001 (2019).
18. M. Mathews, S. Kang, S. Kumar, Q. Li, *Liq. Cryst.* **38**, 31–40 (2011).
19. A. Jákli, *Liq. Cryst. Rev.* **1**, 65–82 (2013).
20. L. A. Madsen, T. J. Dingemans, M. Nakata, E. T. Samulski, *Phys. Rev. Lett.* **92**, 145505 (2004).
21. C. Tschierske, D. J. Photinos, *J. Mater. Chem.* **20**, 4263 (2010).
22. R. B. Meyer, in *Molecular Fluids*, R. Balian, G. Weill, Eds. (Gordon and Breach, 1976), pp. 271–343.
23. K. Adlem *et al.*, *Phys. Rev. E* **88**, 022503 (2013).
24. D. Chen *et al.*, *Phys. Rev. E* **89**, 022506 (2014).
25. G. Paják, L. Longa, A. Chrzanowska, *Proc. Natl. Acad. Sci. U.S.A.* **115**, E10303–E10312 (2018).
26. F. M. van der Kooij, K. Kassapidou, H. N. W. Lekkerkerker, *Nature* **406**, 868–871 (2000).
27. Y. Yang *et al.*, *J. Am. Chem. Soc.* **138**, 68–71 (2016).
28. C. Fernández-Rico, T. Yanagishima, A. Curran, D. G. A. L. Aarts, R. P. A. Dullens, *Adv. Mater.* **31**, e1807514 (2019).
29. R. G. Alargova, K. H. Bhatt, V. N. Paunov, O. D. Velev, *Adv. Mater.* **16**, 1653–1657 (2004).
30. R. G. Alargova, V. N. Paunov, O. D. Velev, *Langmuir* **22**, 765–774 (2006).
31. R. Feng, R. J. Farris, *J. Micromech. Microeng.* **13**, 80–88 (2002).
32. K. I. Schiffrmann, C. Brill, *Int. J. Mater. Res.* **98**, 397–403 (2007).
33. M. Caggioni, J. Lenis, A. V. Bayles, E. M. Furst, P. T. Spicer, *Langmuir* **31**, 8558–8565 (2015).
34. R. W. Style, A. Jagota, C.-Y. Hui, E. R. Dufresne, *Annu. Rev. Fluid Mech.* **8**, 99–118 (2016).
35. J. Bico, E. Reyssat, B. Roman, *Annu. Rev. Fluid Mech.* **50**, 629–659 (2018).
36. Y. Lansac, P. K. Maiti, N. A. Clark, M. A. Glaser, *Phys. Rev. E* **67**, 011703 (2003).

## ACKNOWLEDGMENTS

We thank A. E. Stones and L. Cortes for assistance with the image analysis. **Funding:** The ERC (ERC Consolidator Grant no. 724834 – OMCIDC) is acknowledged for financial support. M.C. and M.D. acknowledge financial support from the EU H2020-MSCA-ITN-2015 project MULTIMAT (Marie Skłodowska-Curie Innovative Training Networks) (project no. 676045). **Author contributions:** C.F.-R. and R.P.A.D. conceived the project and designed the experiments. D.G.A.L.A. contributed to initiating the project and provided general expertise. C.F.-R. and H.d.S. synthesized the colloidal bananas, and T.Y. contributed to the interpretation of the synthesis mechanism. C.F.-R. performed the microscopy experiments. C.F.-R., M.C., M.D., and R.P.A.D. initiated the phase behavior study. C.F.-R. and M.C. wrote the image analysis routines and analyzed the phase behavior data. C.F.-R., M.C., T.Y., M.D., and R.P.A.D. interpreted the data. M.D. and R.P.A.D. supervised the analysis of the phase behavior. C.F.-R. and R.P.A.D. wrote the manuscript, and all co-authors commented on the manuscript. R.P.A.D. supervised the project. **Competing interests:** The authors declare no competing interests. **Data and materials availability:** All data are available in the main text or the supplementary materials.

## SUPPLEMENTARY MATERIALS

science.sciencemag.org/content/369/6506/950/suppl/DC1  
Materials and Methods  
Figs. S1 to S27  
Table S1  
References (37–39)  
Movies S1 to S4

25 February 2020; resubmitted 1 May 2020  
Accepted 9 July 2020  
10.1126/science.abb4536



## CORONAVIRUS

# Isolation of potent SARS-CoV-2 neutralizing antibodies and protection from disease in a small animal model

Thomas F. Rogers<sup>1,2\*</sup>, Fangzhu Zhao<sup>1,3,4\*</sup>, Deli Huang<sup>1\*</sup>, Nathan Beutler<sup>1\*</sup>, Alison Burns<sup>1,3,4</sup>, Wan-ting He<sup>1,3,4</sup>, Oliver Limbo<sup>3,5</sup>, Chloe Smith<sup>1,3</sup>, Ge Song<sup>1,3,4</sup>, Jordan Woehl<sup>3,5</sup>, Linlin Yang<sup>1</sup>, Robert K. Abbott<sup>4,6</sup>, Sean Callaghan<sup>1,3,4</sup>, Elijah Garcia<sup>1</sup>, Jonathan Hurtado<sup>1,4,7</sup>, Mara Parren<sup>1</sup>, Linghang Peng<sup>1</sup>, Sydney Ramirez<sup>6</sup>, James Ricketts<sup>1</sup>, Michael J. Ricciardi<sup>8</sup>, Stephen A. Rawlings<sup>2</sup>, Nicholas C. Wu<sup>9</sup>, Meng Yuan<sup>9</sup>, Davey M. Smith<sup>2</sup>, David Nemazee<sup>1</sup>, John R. Tejjaro<sup>1</sup>, James E. Voss<sup>1</sup>, Ian A. Wilson<sup>3,4,9</sup>, Raiees Andrabi<sup>1,3,4</sup>, Bryan Briney<sup>1,4,7</sup>, Elise Landais<sup>1,3,4,5</sup>, Devin Sok<sup>1,3,4,5,†</sup>, Joseph G. Jardine<sup>3,5,†</sup>, Dennis R. Burton<sup>1,3,4,10,†</sup>

Countermeasures to prevent and treat coronavirus disease 2019 (COVID-19) are a global health priority. We enrolled a cohort of severe acute respiratory syndrome coronavirus 2 (SARS-CoV-2)-recovered participants, developed neutralization assays to investigate antibody responses, adapted our high-throughput antibody generation pipeline to rapidly screen more than 1800 antibodies, and established an animal model to test protection. We isolated potent neutralizing antibodies (nAbs) to two epitopes on the receptor binding domain (RBD) and to distinct non-RBD epitopes on the spike (S) protein. As indicated by maintained weight and low lung viral titers in treated animals, the passive transfer of a nAb provides protection against disease in high-dose SARS-CoV-2 challenge in Syrian hamsters. The study suggests a role for nAbs in prophylaxis, and potentially therapy, of COVID-19. The nAbs also define protective epitopes to guide vaccine design.

**T**he novel coronavirus disease 2019 (COVID-19) has had devastating global health consequences, and there is currently no cure or licensed vaccine. Neutralizing antibodies (nAbs) to the causative agent of the disease, severe acute respiratory syndrome coronavirus 2 (SARS-CoV-2), represent potential prophylactic and therapeutic options and could help guide vaccine design. A nAb to another respiratory virus, respiratory syncytial virus (RSV), is in widespread clinical use prophylactically to protect vulnerable infants (7). Furthermore, nAbs prevent death from the emerging Ebola virus in macaques, even when given relatively late in infection, and thus have

been proposed for use in outbreaks (2, 3). Generally, nAbs with outstanding potency (known as super-antibodies) (4) can be isolated by deeply mining antibody responses of a sampling of infected donors. Outstanding potency coupled with engineering to extend antibody half-life from weeks to many months brings down the effective costs of antibodies and suggests more opportunities for prophylactic intervention. At the same time, outstanding potency can permit antiviral therapeutic efficacy that is not observed for less potent antibodies (4). Here, we present the isolation of highly potent nAbs to SARS-CoV-2 and demonstrate their in vivo protective efficacy in a small animal model, suggesting their potential utility as a medical countermeasure.

To investigate the antibody response against SARS-CoV-2 and discover nAbs, we adapted our pipeline to rapidly isolate and characterize monoclonal antibodies (mAbs) from convalescent donors (Fig. 1). A cohort of previously swab-positive SARS-CoV-2 donors was recruited for peripheral blood mononuclear cell (PBMC) and plasma collection. In parallel, we developed both live replicating and pseudovirus neutralization assays using a HeLa-ACE2 (angiotensin-converting enzyme 2) cell line that gave robust and reproducible virus titers. Convalescent serum responses were evaluated for neutralization activity against SARS-CoV-1 and SARS-CoV-2, and eight donors were selected for mAb discovery. Single antigen-specific memory B cells were sorted, and their corresponding variable genes were recovered

and cloned using a high-throughput production system that enabled antibody expression and characterization in under 2 weeks. Promising mAbs were advanced for further biophysical characterization and in vivo testing.

## Development of viral neutralization assays

Two platforms were established to evaluate plasma neutralization activity against SARS-CoV-2, one using replication-competent virus and another using pseudovirus (PSV). Vero-E6 cells were first used as target cells for neutralization assays, but this system was relatively insensitive at detecting replicating virus compared with a HeLa cell line that stably expressed the cell surface ACE2 receptor (fig. S1A). The HeLa-ACE2 target cells gave reproducible titers and were used for the remainder of the study. In certain critical instances, HeLa-ACE2 and Vero cells were compared.

The live replicating virus assay used the Washington strain of SARS-CoV-2, USA-WA1/2020 (BEI Resources NR-52281) and was optimized to a 384-well format to measure plaque formation. In parallel, a PSV assay was established for both SARS-CoV-1 and SARS-CoV-2 using murine leukemia virus-based PSV (MLV-PSV) (5). The assay used single-cycle infectious viral particles bearing a firefly luciferase reporter for high-throughput screening. Unlike MLV-PSV, which buds at the plasma membrane, coronaviruses assemble in the endoplasmic reticulum (ER)-Golgi intermediate compartment, so the C terminus of the SARS-CoV-1 spike (S) protein contains an ER retrieval signal (6). The alignment of SARS-CoV-1 and SARS-CoV-2 S proteins showed that this ER retrieval signal is conserved in SARS-CoV-2 (fig. S1B). To prepare high titers of infectious SARS-CoV-1 and SARS-CoV-2 PSV particles, various truncations of SARS-CoV-1 and SARS-CoV-2 S protein were expressed in which the ER retrieval signal was removed to improve exocytosis of the virus. Pseudovirion versions carrying SARS-CoV-1-Δ28 and SARS-CoV-2-Δ18S protein efficiently transduced ACE2-expressing target cells but not control HeLa or A549 cells (fig. S1C). Control VSV-G pseudotyped virions showed a similar transduction efficiency in all target cells. Luciferase expression in transduced cells proved to be proportional to viral titer over a wide range (fig. S1D).

## Establishment of a SARS-CoV-2 cohort

In parallel to the development of neutralization assays, a cohort was established in San Diego, California, of 17 donors who had previously been infected with SARS-CoV-2 (Fig. 2A, fig. S2A, and table S1). The cohort was 47% female, and the average age was 50 years. Infection was determined by a positive SARS-CoV-2 polymerase chain reaction (PCR) test from a nasopharyngeal swab. All donors also had symptoms consistent

<sup>1</sup>Department of Immunology and Microbiology, The Scripps Research Institute, La Jolla, CA 92037, USA.

<sup>2</sup>Division of Infectious Diseases, Department of Medicine, University of California, San Diego, La Jolla, CA 92037, USA.

<sup>3</sup>IAVI Neutralizing Antibody Center, The Scripps Research Institute, La Jolla, CA 92037, USA. <sup>4</sup>Consortium for HIV/AIDS Vaccine Development (CHAVD), The Scripps Research Institute, La Jolla, CA 92037, USA.

<sup>5</sup>IAVI, New York, NY 10004, USA. <sup>6</sup>Center for Infectious Disease and Vaccine Research, La Jolla Institute for Immunology (LJI), La Jolla, CA 92037, USA. <sup>7</sup>Center for Viral Systems Biology, The Scripps Research Institute, La Jolla, CA 92037, USA. <sup>8</sup>Department of Pathology, George Washington University, Washington, DC 20052, USA. <sup>9</sup>Department of Integrative Structural and Computational Biology, The Scripps Research Institute, La Jolla, CA 92037, USA. <sup>10</sup>Ragon Institute of Massachusetts General Hospital, Massachusetts Institute of Technology, and Harvard University, Cambridge, MA 02139, USA.

\*These authors contributed equally to this work.

†Corresponding author. Email: dsok@iavi.org (D.S.); jjardine@iavi.org (J.G.J.); burton@scripps.edu (D.R.B.)

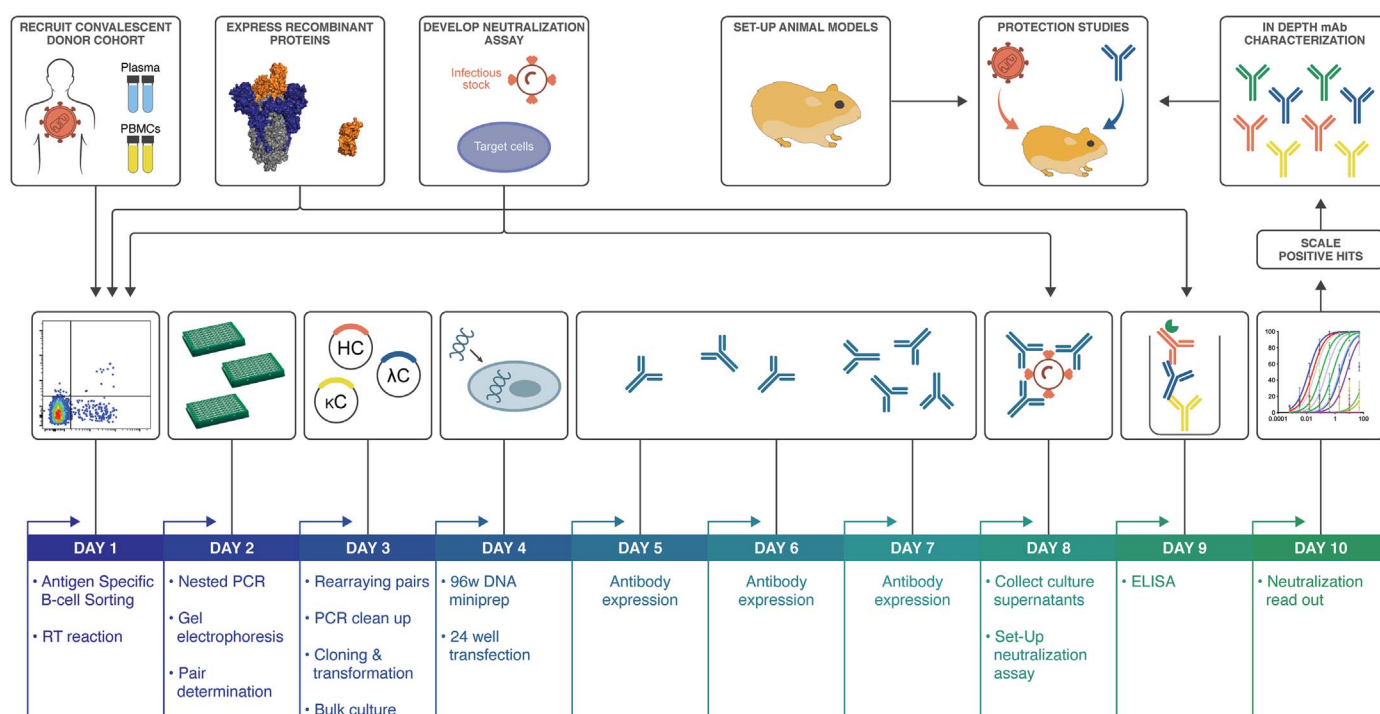


**Fig. 1. SARS-CoV-2 neutralizing antibody isolation strategy.** A natural infection cohort was established to collect plasma and PBMC samples from individuals who recovered from COVID-19. In parallel, functional assays were developed to rapidly screen plasma samples for SARS-CoV-2 neutralizing activity. SARS-CoV-2 recombinant surface proteins were also produced for use as baits in single-memory B cell sorting and downstream functional characterization of isolated mAbs. Finally, a Syrian hamster animal model was set up to evaluate mAb passive immunization and protection. The

standard mAb isolation pipeline was optimized to facilitate high-throughput amplification, cloning, expression, and functional screening of hundreds of unpurified Ab heavy and light chain pairs isolated from each of several selected neutralizers in only 10 days. Selected pairs were scaled up to purify IgG for validation and characterization experiments. Potent neutralizing mAbs were selected to evaluate protection in the Syrian hamster model. HC, heavy chain; κC, kappa light chain; λC, lambda light chain; RT, reverse transcriptase.

with COVID-19, and disease severity ranged from mild to severe, including intubation in one case, although all donors recovered. Donor plasma were tested for binding to recombinant SARS-CoV-2 and SARS-CoV-1 S and receptor binding domain (RBD) proteins, for binding to cell surface-expressed spikes, and for neutralization in both live replicating virus and PSV assays [Fig. 2, B to D, and fig. S2B; three donors (CC6, CC12, and CC25) that are further discussed below are highlighted]. Binding titers to SARS-CoV-2 S protein varied considerably, reaching a half-maximal effective concentration ( $EC_{50}$ ) at serum dilutions of  $\sim 10^4$ , with titers against the RBD about an order of magnitude less. Titers against SARS-CoV-1 S protein were notably less than those for SARS-CoV-2 S protein, and titers against SARS-CoV-1 RBD were only detected in a small number of donors. Neutralizing titers in the PSV assay varied over a wide range for SARS-CoV-2 (Fig. 2D and fig. S2A) and were low or undetectable against SARS-CoV-1. RBD binding and PSV neutralization were notably well correlated (Fig. 2E). There was also a positive correlation between cell surface spike binding and live replicating virus neutralization (fig. S2C). The

titers in the PSV assay and the replicating virus assay were largely similar (figs. S2 and S3). In most later measurements, the PSV assay was preferred owing to its higher throughput.

#### Antibody isolation and preliminary functional screens for down-selection

Cryopreserved PBMCs from eight donors were stained for memory B cells markers ( $CD19^+/IgG^+$ ; IgG, immunoglobulin G) and both AviTag biotinylated RBD and SARS-CoV-2 S antigen baits before single-cell sorting.  $S^+$  and  $S^+/RBD^+$  memory B cells were present at an average frequency of 2.0 and 0.36%, respectively, across the eight donors (fig. S4A). In total, 3160 antigen-positive ( $Ag^+$ ) memory B cells were sorted to rescue native heavy and light chain pairs for mAb production and validation (fig. S4B). A total of 2045 antibodies were cloned and expressed, which represents, on average, a 65% PCR recovery of paired variable genes and >86% estimated recovery of fully functional cloned genes (fig. S4C). The bulk-transformed ligation products for both the heavy chain and light chain were transfected and tested for binding to RBD and S protein and for neutral-

ization in the SARS-CoV-2 PSV assay using HeLa-ACE2 target cells (fig. S5).

The majority of transfected pairs (92%) resulted in IgG expression. Of these, 43% showed binding only to S protein, while 5.9% bound to both S and RBD proteins and 0.1% bound only to RBD. The supernatants were also screened for binding to an unrelated HIV antigen (BG505 SOSIP) to eliminate nonspecific or polyreactive supernatants. The supernatants were next evaluated for neutralization activity using SARS-CoV-2 and SARS-CoV-1 pseudoviruses. A small proportion of the binding antibodies showed neutralization activity, and, unexpectedly, that activity was equally distributed between  $RBD^+/S^+$  and  $S^+$ -only binders, despite a much larger number of  $S^+$ -only binding supernatants, as exemplified by the three donors, CC6, CC12, and CC25 (Fig. 3A). These data indicate that viral infection generates a strong response against the non-RBD regions of the S protein, but only a small proportion of that response is neutralizing. In contrast, there are fewer RBD-binding antibodies, but a larger proportion of these neutralize SARS-CoV-2 pseudovirus. Antibodies that tested positive for neutralization in the



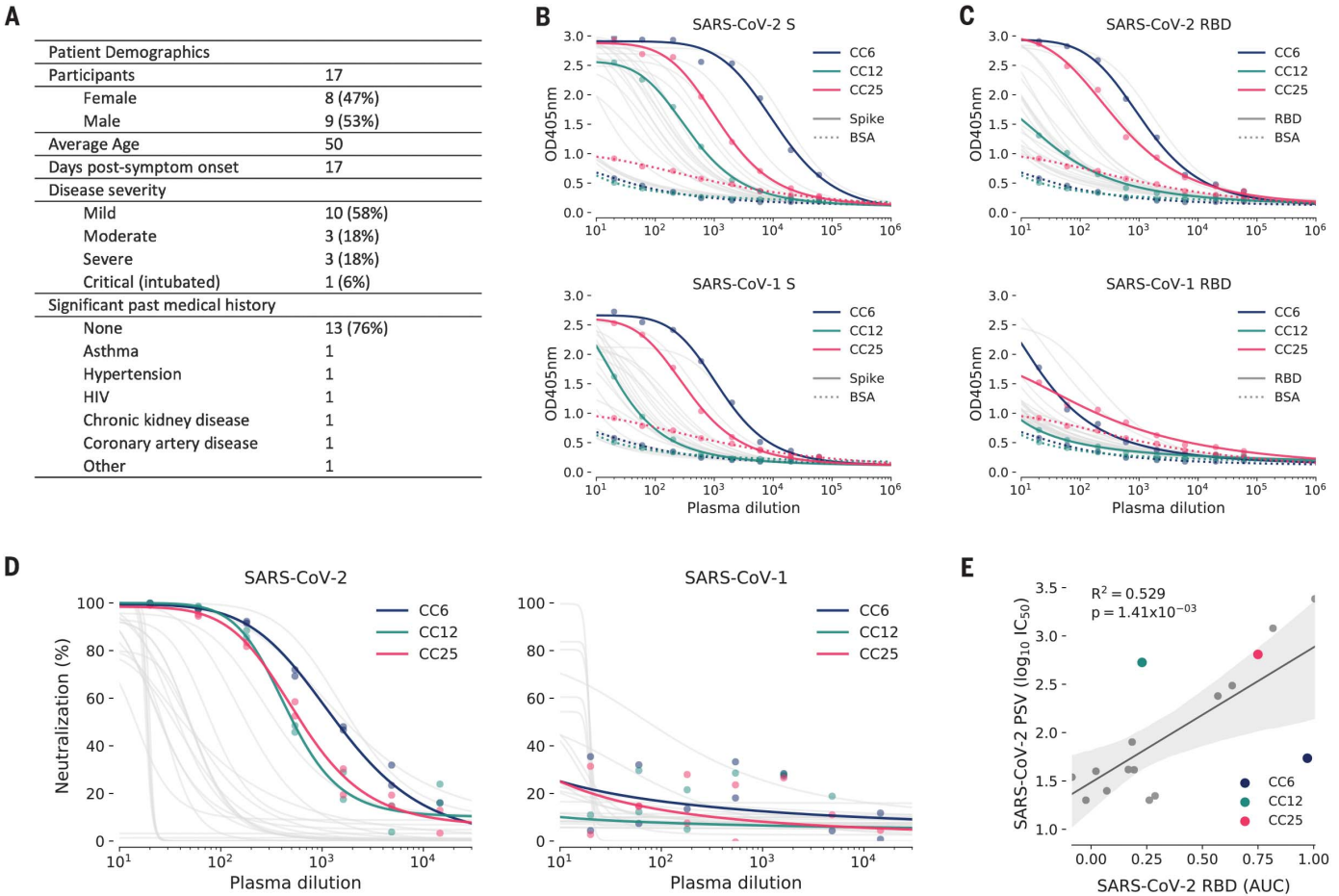


**Fig. 2. COVID-19 cohort functional screening.** (A) Demographics of the University of California, San Diego (UCSD) COVID-19 cohort (CC) participants. CC plasma was tested for binding to SARS-CoV-1 and SARS-CoV-2 S proteins (B) and RBD subunits (C) by ELISA. Background binding of plasma to bovine serum albumin-coated plates is represented by a dotted line. OD405nm, optical density for wavelength of 405 nm. (D) Plasma was also tested for neutralization of pseudotyped (PSV) SARS-CoV-1 and SARS-CoV-2 virions. (E) Correlation

between PSV SARS-CoV-2 neutralization and RBD subunit ELISA binding AUC (area under the curve). AUC was computed using Simpson's rule. The 95% confidence interval of the regression line is shown by the gray shaded area and was estimated by performing 1000 bootstrap resamplings.  $R^2$  (coefficient of determination) and  $P$  values of the regression are also indicated. CC participants from whom mAbs were isolated are specifically highlighted in blue (CC6), green (CC12), and pink (CC25).

high-throughput screening were sequence-confirmed and advanced for large-scale expression for additional characterization. Thirty-three antibodies were prioritized for in-depth characterization from the three donors, CC6, CC12, and CC25. Within that subset, we identified 25 distinct lineages, with 23 containing a single member (table S2). VH1 and VH3 gene families were notably prominent in these Abs, and there was a diversity of CDR3 lengths (Fig. 3, B and C). There was one prominent example of a clonally expanded lineage, with eight recovered clonal members that averaged 4.3 and 2.8% mutations from germ-line at the nucleotide level in the heavy chain and light chain, respectively (Fig. 3D). The remaining clones were relatively unmutated, averaging just above 1% mutation at the nucleotide level, suggesting that these antibodies were primed by the ongoing COVID

infection and likely not recalled from a previous endemic human coronavirus exposure. All antibodies that were expressed at scale were evaluated in standard enzyme-linked immunosorbent assay (ELISA)-based polyreactivity assays with solubilized Chinese hamster ovary (CHO) membrane preparations, single-stranded DNA, and insulin (7, 8), and none were poly-reactive (fig. S6).

**Functional activity of down-selected antibodies**

The antibody hits that were identified in the high-throughput screening were next evaluated for epitope specificity by biolayer interferometry using S and RBD proteins as capture antigens. The antigens were captured on anti-HIS biosensors before addition of saturating concentrations (100  $\mu\text{g/ml}$ ) of antibodies that were then followed by competing antibodies at a lower concentration (25  $\mu\text{g/ml}$ ). Accordingly,

only antibodies that bind to a noncompeting site would be detected in the assay. Among the antibodies evaluated, the results reveal three epitope bins for RBD (designated RBD-A, RBD-B, and RBD-C) and three epitope bins for the S protein (designated S-A, S-B, and S-C) (Fig. 4A and fig. S7). The mAb CC12.19 appears to compete with antibodies targeting two different epitopes, RBD-B and S-A (fig. S7), which might indicate that this mAb targets an epitope spanning RBD-B and S-A. To evaluate epitope specificities further, we next assessed binding of the antibodies to extended RBD constructs with subdomains (SD) 1 and 2, including the independently folding RBD-SD1 and RBD-SD1-2 and the N-terminal domain (NTD) (Fig. 4B and fig. S8, A and B). None of the antibodies showed binding to the NTD. CC12.19 binds to all other constructs, which supports the epitope binning data described in Fig. 4A. The

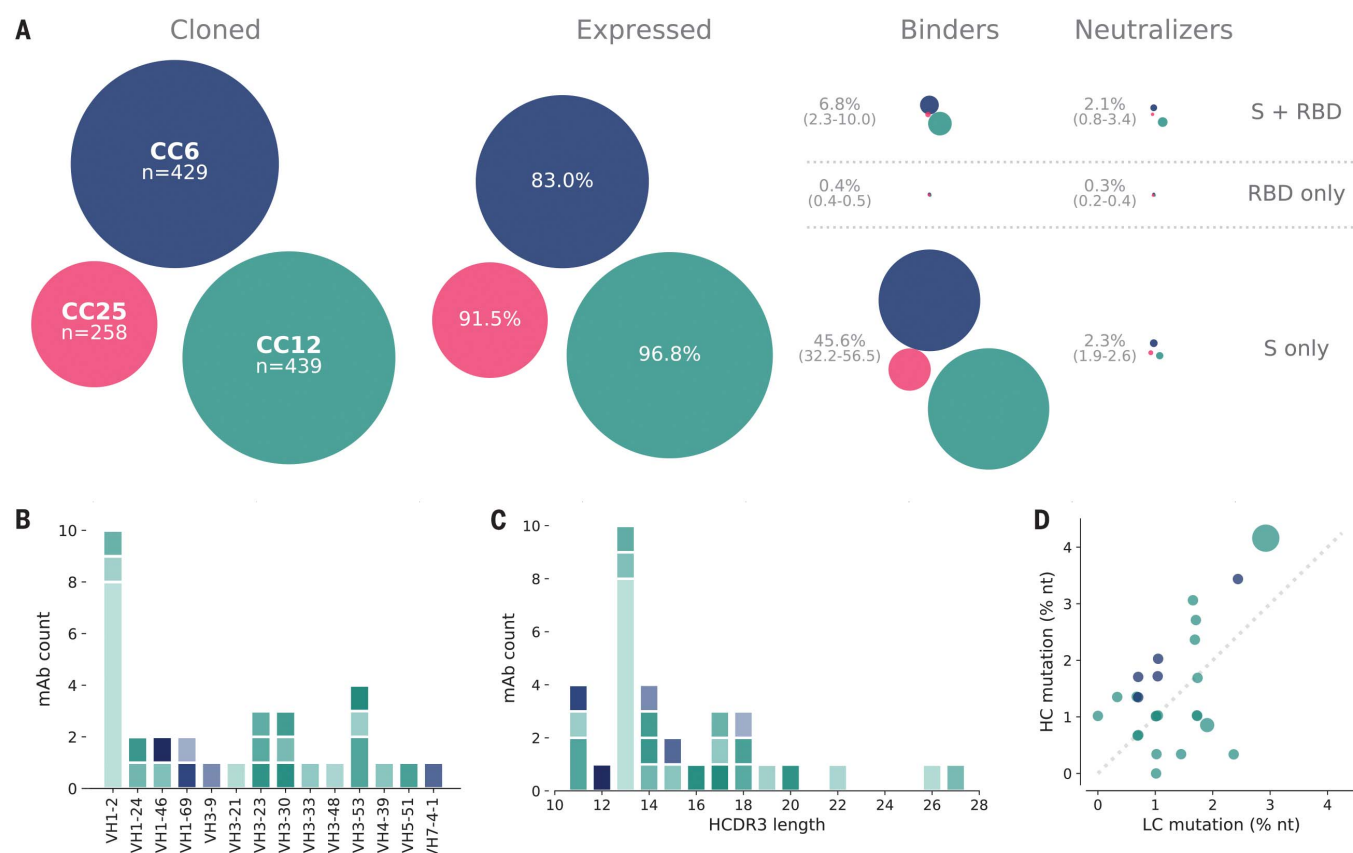


**Fig. 3. Antibody isolation and functional screening for SARS-CoV antigen binding and neutralization.** (A) Antibody down-selection process from three donors, presented as bubble plots. The areas of the bubbles for each donor are sized according to the number of antibodies (n) that were cloned and transfected, then scaled according to the number that were positive in subsequent assays. All antibodies that expressed at measurable levels were tested for binding to S protein and RBD to determine their

specificity and then screened for neutralization. (B) VH gene distribution of down-selected mAbs. (C) Heavy chain CDR3 lengths of down-selected mAbs. Antibodies in (B) and (C) are colored according to their respective clonal lineages. (D) Mutation frequency of down-selected mAb lineages. Bubble position represents the mean mutation frequency for each lineage, with a bubble area that is proportional to lineage size. LC, light chain; nt, nucleotides.

other antibodies grouped in the S-A epitope bin that compete with CC12.19 either showed no binding to RBD or RBD-SD constructs (CC12.20 and CC12.21) or showed binding to RBD-SD1 and RBD-SD1-2 but not RBD (CC12.23). These data suggest two competing epitopes within the S-A epitope bin: one that is confined to the non-RBD region of the S protein, and one that includes some element of RBD-SD1-2. This interpretation will require further investigation by structural studies.

We next evaluated the mAbs for neutralization activity against SARS-CoV-2 and SARS-CoV-1 pseudoviruses. The neutralization half-maximal inhibitory concentration ( $IC_{50}$ ) potencies of these antibodies are shown in Fig. 4C, and their associated maximum neutralization plateaus (MNP) are shown in Fig. 4D. A comparison of neutralization potencies between pseudovirus (fig. S8C) and live replicating virus (fig. S8D) is also included. The most potent neutralizing antibodies were those directed to RBD-A epitope, including two antibodies, CC6.29 and CC6.30, that neutralize SARS-CoV-2

pseudovirus with an  $IC_{50}$  of 2 ng/ml and 1 ng/ml, respectively (Fig. 4C). In comparison, antibodies directed to RBD-B tended to have a higher  $IC_{50}$  and many plateaued below 100% neutralization. Despite this trend, CC6.33 is directed against RBD-B and showed complete neutralization of SARS-CoV-2 with an  $IC_{50}$  of 39 ng/ml and also neutralized SARS-CoV-1 with an  $IC_{50}$  of 162 ng/ml. CC6.33 was the only antibody that showed potent neutralization of both pseudoviruses. The antibodies that do not bind to RBD and are directed to non-RBD epitopes on the S protein all showed poor neutralization potencies and MNPs well below 100%.

To evaluate whether the RBD-A epitope might span the ACE2 binding site, we next performed cell surface competition experiments. Antibodies were premixed with biotinylated S (Fig. 4E) or RBD (Fig. 4F) proteins at a 4:1 molar ratio of antibodies to target antigen. The mixture was then incubated with the HeLa-ACE2 cell line and the percent competition against ACE2 receptor was recorded by comparing percent binding of the target antigen with and without

antibody present (fig. S8E). The antibodies targeting the RBD-A epitope competed best against the ACE2 receptor, and the neutralization  $IC_{50}$  correlated well with the percent competition for ACE2 receptor binding for both S protein (Fig. 4E) and RBD (Fig. 4F). We also assessed the affinity of all RBD-specific antibodies to soluble RBD by surface plasmon resonance (SPR) and found a poor correlation between affinity and neutralization potency (Fig. 4G and fig. S9). However, the correlation is higher when limited to antibodies targeting the RBD-A epitope. The lack of a correlation between RBD binding and neutralization for mAbs contrasts with the strong correlation described earlier for serum RBD binding and neutralization. Overall, the data highlight epitope RBD-A as the preferred target for eliciting neutralizing antibodies and suggest that corresponding increases in affinity of mAbs to RBD-A will likely result in corresponding increases in neutralization potency.

SARS-CoV-2 has shown some propensity for mutation as it has circulated worldwide, as



evidenced, for example, in the emergence of the D614G variant (9). We investigated the activity of five nAbs against six viral variants that have been reported. The three sera studied

above (CC6, CC12, and CC25) neutralized all the variants (fig. S10A). All five nAbs neutralized the D614G variant. However, one variant with a mutation in the ACE2 binding site

[Gly<sup>476</sup>→Ser (G476S)] did show effectively complete resistance to one of the nAbs, and another variant (V367F) showed a 10-fold higher IC<sub>50</sub> than the WA1 strain (fig. S10B).

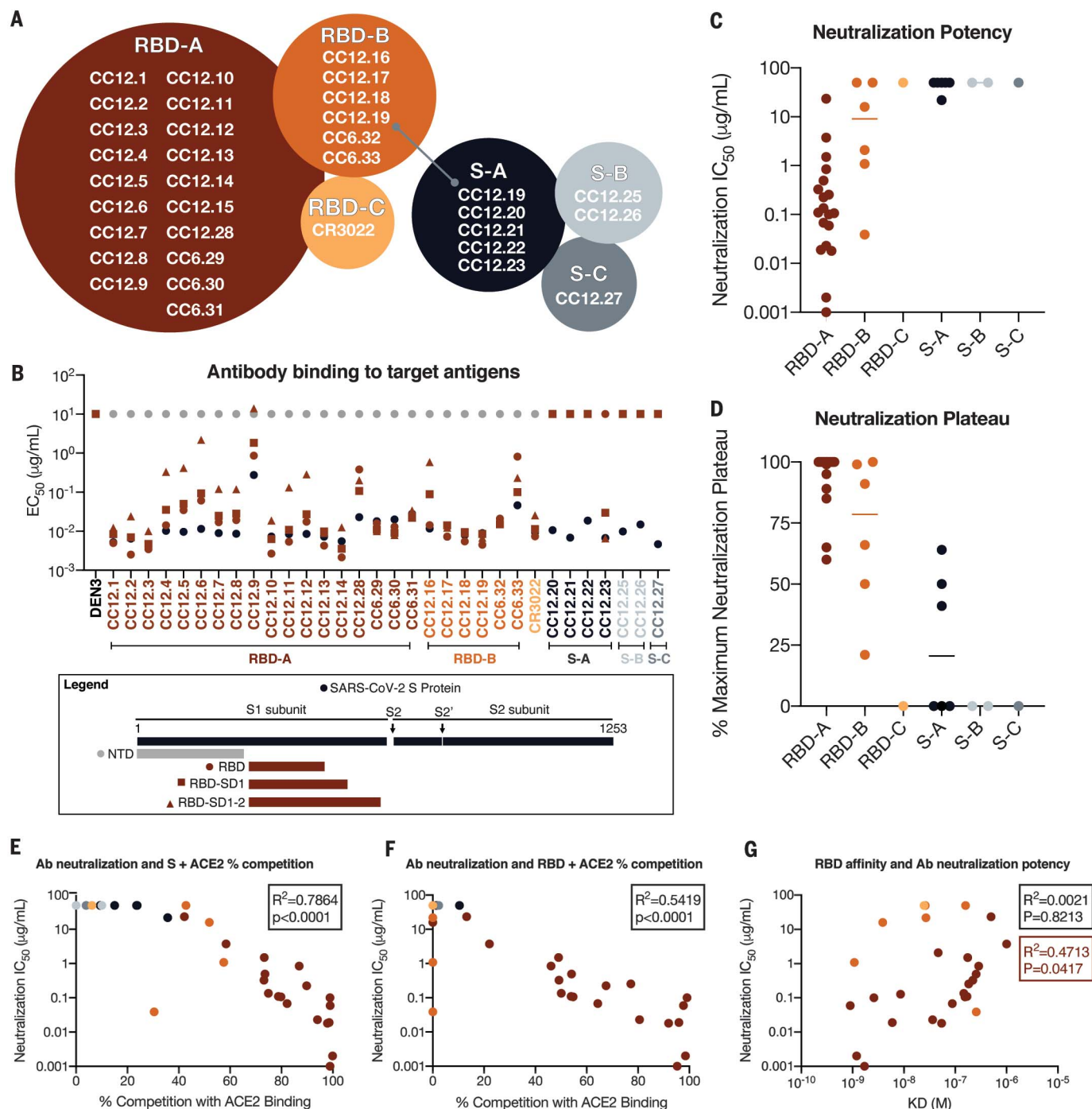


**Fig. 4. Antibody functional activity by epitope specificities.** Monoclonal antibody epitope binning was completed using RBD and SARS-CoV-2 S protein as target antigens. **(A)** A total of three noncompeting epitopes for RBD (RBD-A, RBD-B, and RBD-C) and three noncompeting epitopes for S (S-A, S-B, and S-C) were identified. **(B)** MAbs were evaluated for binding to different target antigens (S, NTD, RBD, RBD-SD1, and RBD-SD1-2) by ELISA and apparent EC<sub>50</sub> values are reported in micrograms per milliliter. **(C)** MAbs were evaluated for neutralization of SARS-CoV-2 pseudovirus

using HeLa-ACE2 target cells. Antibodies are grouped according to epitope specificities, and neutralization IC<sub>50</sub> values are reported in micrograms per milliliter. **(D)** The MNP is reported for each mAb and grouped by epitope specificity. MAbs were mixed with **(E)** S or **(F)** RBD protein and measured for binding to HeLa-ACE2 target cells as a measure of competition to the cell surface ACE-2 receptor. **(G)** mAb neutralization potencies (IC<sub>50</sub>) are plotted as a function of dissociation constants (KD) measured by SPR to RBD target antigen.

### Passive transfer of neutralizing antibodies and SARS-CoV-2 challenge in Syrian hamsters

To investigate the relationship between in vitro neutralization and protection in vivo against SARS-CoV-2, we selected two mAbs for passive transfer and challenge experiments in a Syrian hamster animal model on the basis of a summary of the nAb data (table S3 and fig. S11). The experimental design for the passive transfer study is shown in Fig. 5A. In the first experiment, we tested nAb CC12.1, which targets the RBD-A epitope and has an in vitro  $IC_{50}$  neutralization of 0.019  $\mu\text{g/ml}$  against pseudovirus, and in the second experiment, we tested nAb C12.23, which targets the S-B epitope with an  $IC_{50}$  neutralization of 22  $\mu\text{g/ml}$ . In both experiments, an unrelated antibody to dengue virus, Den3, was used as a control. The anti-SARS-CoV-2 nAbs were delivered at five different concentrations to evaluate dose-dependent protection, starting at 2 mg per animal (average: 16.5 mg/kg) at the highest dose and 8  $\mu\text{g}$  per animal at the lowest dose. The Den3 control antibody was delivered at a single dose of 2 mg per animal. Sera were collected from each animal 12 hours after intraperitoneal infusion of the antibody, and all animals were subsequently challenged with a dose of  $1 \times 10^6$  plaque forming units (PFU) of SARS-CoV-2 (USA-WA1/2020) by intranasal administration 12 hours after antibody infusion (Fig. 5A).

Syrian hamsters typically clear virus within 1 week after SARS-CoV-1 infection, and observations made in that model system determined the strategy adopted here (10). The hamsters were weighed daily as a measure of disease due to infection. Lung tissues were collected to measure viral load on day 5. A data summary is presented in Fig. 5B and fig. S12A for animals that received CC12.1, which targets the RBD-A epitope. The control animals that received Den3 lost, on average, 13.6% of body weight by day 5 after virus challenge. In comparison, the animals that received the neutralizing RBD-A antibody at a dose of 2 mg (average: 16.5 mg/kg) or 500  $\mu\text{g}$  (average: 4.2 mg/kg) exhibited no weight loss. However, animals that received a dose of 125  $\mu\text{g}$  (average: 0.9 mg/kg) had an average body weight loss of 8%, while animals that received a dose of 31  $\mu\text{g/ml}$  (average: 0.2 mg/kg) and 8  $\mu\text{g/ml}$  (average: 0.06 mg/kg) lost 15.8 and 16.7% of body weight, respectively. Although these animals showed a trend for greater weight loss than did control animals, this trend did not achieve statistical significance (table S4). Given concerns about antibody-mediated enhanced disease in SARS-CoV-2 infection, this observation merits further attention using larger animal group sizes. The weight loss data are further corroborated by quantification of lung viral load measured by real-time PCR (Fig. 5C), which showed a moderate correlation to weight loss. The data

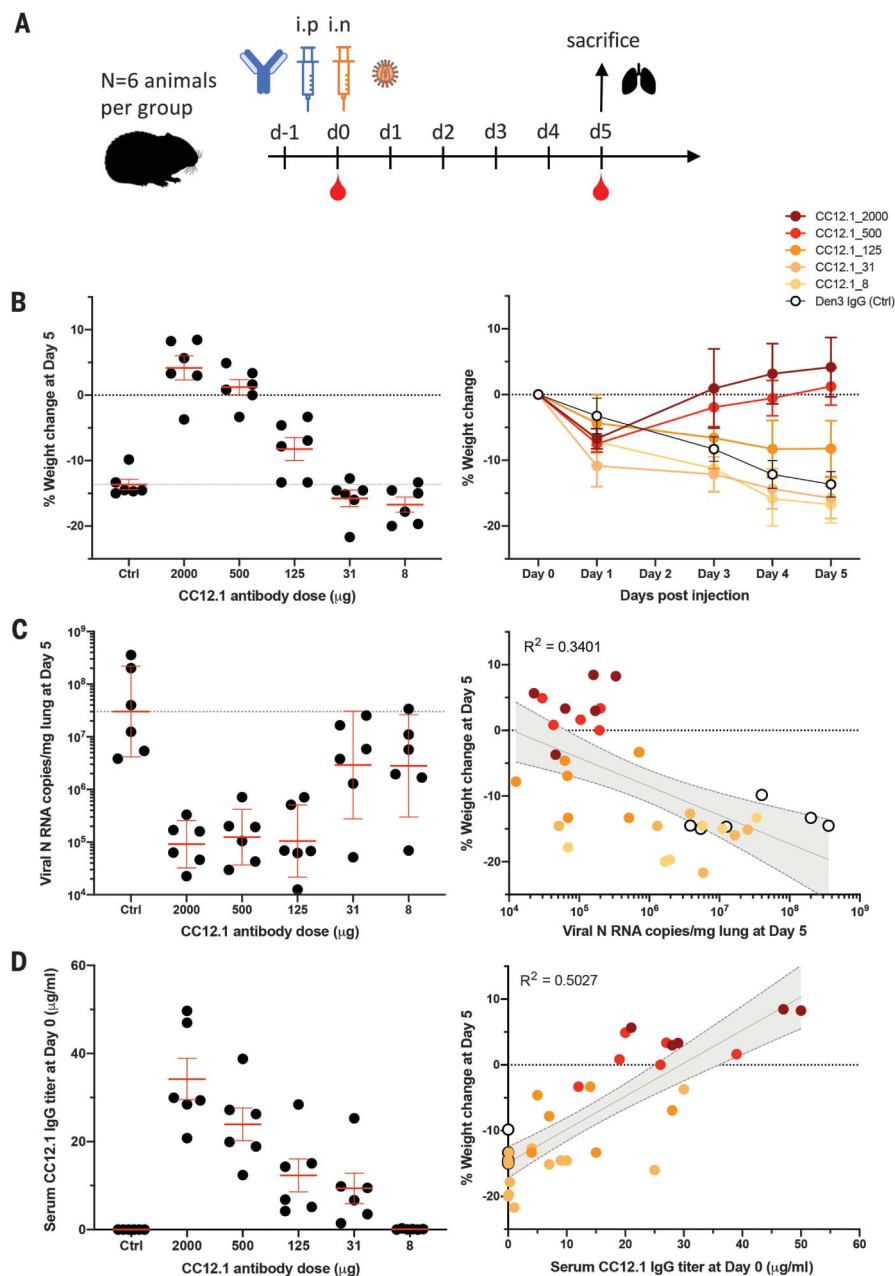


**Fig. 5. A potent SARS-CoV-2 RBD-specific neutralizing mAb protects against weight loss and lung viral replication in Syrian hamsters.** (A) SARS-CoV-2-specific human neutralizing mAb CC12.1 isolated from natural infection was administered at a starting dose of 2 mg per animal (average: 16.5 mg/kg) and subsequent serial fourfold dilutions. Control animals received 2 mg of Den3. Each group of six animals was challenged intranasally (i.n.) 12 hours after infusion with  $1 \times 10^6$  PFU of SARS-CoV-2. Serum was collected at the time of challenge (day 0), and animal weight was monitored as an indicator of disease progression. On day 5, lung tissue was collected for viral burden assessment. (B) Percent weight change was calculated from day 0 for all animals. (C) Viral load, as assessed by nucleocapsid RNA quantitative polymerase chain reaction (qPCR) from lung tissue at day 5 after infection. (D) Serum titers of the passively administered mAb, as assessed by ELISA at the time of challenge [12 hours after intraperitoneal (i.p.) administration]. Correlation analyses with 95% confidence intervals indicated by the gray shaded area.

indicate comparable viral loads between the three higher doses (2 mg, 500  $\mu\text{g}$ , and 125  $\mu\text{g}$ ) of nAbs. In contrast, equivalent viral loads were observed between the control group receiving Den3 and the low-dose groups receiving 31 or 8  $\mu\text{g}$  of nAb. In contrast to the nAb to RBD-A,

the less potent and incompletely neutralizing antibody to the S-B epitope showed no evidence of protection at any concentration when compared with control animals (fig. S12B).

To determine the antibody serum concentrations that may be required for protection



against disease from SARS-CoV-2 infection, we also measured the antibody serum concentrations just before intranasal virus challenge (Fig. 5D). The data highlight that an antibody serum concentration of ~22 µg/ml of nAb (1160 × PSV neutralization IC<sub>50</sub>) enables full protection and a serum concentration of 12 µg/ml (630 × PSV neutralization IC<sub>50</sub>) is adequate for a 50% reduction in disease, as measured by weight loss. The effective antibody concentration required at the site of infection to protect from disease remains to be determined. Sterilizing immunity at serum concentrations that represent a large multiplier of the in vitro neutralizing IC<sub>50</sub> is observed for many viruses (11).

## Discussion

Using a high-throughput rapid system for antibody discovery, we isolated more than 1000 mAbs from three convalescent donors by memory B cell selection using SARS-CoV-2 S or RBD recombinant proteins. About half of the mAbs isolated could be expressed, and they also bound effectively to S and/or RBD proteins. Only a small fraction of these Abs were neutralizing, which highlights the value of deep mining of responses to access the most potent Abs (4).

A range of nAbs were isolated to different sites on the S protein. The most potent Abs, reaching single-digit nanogram per milliliter IC<sub>50</sub> values in PSV assays, are targeted to a site that, judged by competition studies, overlaps the ACE2 binding site. Only one of the Abs, directed to RBD-B, neutralized SARS-CoV-1 PSV, as may be anticipated given the differences in ACE2 contact residues between the two viruses (fig. S13) and given that the selections were performed with SARS-CoV-2 target proteins. Abs that are directed to the RBD but not competitive with soluble ACE2 (although they may be competitive in terms of an array of membrane-bound ACE2 molecules interacting with an array of S proteins on a virion) are generally less potent neutralizers and tend to show incomplete neutralization, plateauing well below 100% neutralization. The one exception is the cross-reactive RBD-B antibody, mentioned above. Similarly low potency and incomplete neutralization are observed for Abs to the S protein that are not reactive with recombinant RBD. The cause(s) of these incomplete neutralization phenomena is unclear but presumably originates in some S protein heterogeneity that is either glycan, cleavage, or conformationally based. Regardless, the RBD-A nAbs that directly compete with ACE2 are clearly the most preferred for prophylactic and therapeutic applications and as reagents to define nAb epitopes for vaccine design. Note that, even for a small sampling of naturally occurring viral variants, two were identified that showed notable resistance to individual

potent nAbs to the WA1 strain, which suggests that neutralization resistance will need to be considered in planning for clinical applications of nAbs. Cocktails of nAbs may be required.

In terms of nAbs as passive reagents, the efficacy of a potent anti-RBD nAb in vivo in Syrian hamsters is promising in view of the positive attributes of this animal model (12) and suggests that human studies are merited. Nevertheless, as for any animal model, there are many limitations, including, in the context of antibody protection, differences in effector cells and Fc receptors between humans and hamsters. The failure of the non-RBD S-protein nAb to protect in the animal model is consistent with its lower potency and, likely most importantly, its inability to fully neutralize challenge virus. In the context of human studies, the following antibody engineering goals could be considered: improving the potency of protective nAbs by enhancing binding affinity to the identified RBD epitope, improving half-life, and reducing Fc receptor binding to minimize potential antibody-dependent enhancement (ADE) effects if they are identified. As observed for heterologous B cell responses against different serotypes of flavivirus infection, there is a possibility, but no current experimental evidence, that subtherapeutic vaccine serum responses or subtherapeutic nAb titers could potentially exacerbate future coronavirus infection disease burden by expanding the viral replication and/or cell tropism of the virus. If ADE is found for SARS-CoV-2 and operates at subneutralizing concentrations of neutralizing antibodies, as it can for dengue virus (13), then it would be important, from a vaccine standpoint, to carefully define the full range of nAb epitopes on the S protein, as we have begun to do here. From a passive antibody standpoint, it would be important to maintain high nAb concentrations or appropriately engineer nAbs.

The nAbs described here have very low somatic hypermutation (SHM), typically only one or two mutations in the VH gene and one or two in the VL gene. Such low SHM may be associated with the isolation of the nAbs relatively soon after infection, perhaps before affinity-maturation has progressed. Low SHM has also been described for potent nAbs to Ebola virus, RSV, Middle East respiratory syndrome coronavirus, and yellow fever virus (14–17) and may indicate that the human naïve repertoire is often sufficiently diverse to respond effectively to many pathogens with little mutation. Of course, nAb efficacy and titer may increase over time, as described for other viruses, and it will be interesting to see if even more potent nAbs to SARS-CoV-2 evolve in our donors in the future.

What do our results suggest for SARS-CoV-2 vaccine design? First, they suggest a focus on the RBD—strong nAb responses have indeed

been demonstrated by immunizing mice with a multivalent presentation of RBD (18). The strong preponderance of non-neutralizing antibodies and the very few nAbs to S protein that we isolated could arise for a number of reasons, including the following: (i) The recombinant S protein that we used to select B cells is a poor representation of the native spike on virions. In other words, there may be many nAbs to the S protein, but we failed to isolate them because of the selecting antigen. (ii) The recombinant S protein that we used is close to native, but non-neutralizing antibodies bind to sites on the S protein that do not interfere with viral entry. (iii) The S protein in natural infection disassembles readily, generating a strong Ab response to viral debris that is non-neutralizing, because the antibodies recognize protein surfaces that are not exposed on the native spike. The availability of both neutralizing and non-neutralizing antibodies generated in this study will facilitate evaluation of S protein immunogens for presentation of neutralizing and non-neutralizing epitopes and will promote effective vaccine design. The design of an immunogen that improves on the quality of nAbs elicited by natural infection may well emerge as an important goal of vaccine efforts (19).

In summary, we describe the very rapid generation of neutralizing antibodies to a newly emerged pathogen. The antibodies can find clinical application and will aid in vaccine design.

## REFERENCES AND NOTES

1. The Impact-RSV Study Group, *Pediatrics* **102**, 531–537 (1998).
2. D. Corti et al., *Science* **351**, 1339–1342 (2016).
3. J. Misasi et al., *Science* **351**, 1343–1346 (2016).
4. L. M. Walker, D. R. Burton, *Nat. Rev. Immunol.* **18**, 297–308 (2018).
5. T. Giotou et al., *J. Virol.* **78**, 9007–9015 (2004).
6. C. E. McBride, J. Li, C. E. Machamer, *J. Virol.* **81**, 2418–2428 (2007).
7. T. Jain et al., *Proc. Natl. Acad. Sci. U.S.A.* **114**, 944–949 (2017).
8. J. G. Jardine et al., *PLoS Pathog.* **12**, e1005815 (2016).
9. CoV-Glue, Amino acid replacements; <http://cov-glue.cvr.gla.ac.uk/#/replacement>.
10. A. Roberts et al., *J. Virol.* **79**, 503–511 (2005).
11. P. W. Parren, D. R. Burton, *Adv. Immunol.* **77**, 195–262 (2001).
12. J. F.-W. Chan et al., *Clin. Infect. Dis.* **ciaa325** (2020).
13. S. B. Halstead, *Microbiol. Spectr.* **2**, (2014).
14. C. W. Davis et al., *Cell* **177**, 1566–1582.e17 (2019).
15. T. Ying et al., *Nat. Commun.* **6**, 8223 (2015).
16. E. Goodwin et al., *Immunity* **48**, 339–349.e5 (2018).
17. A. Z. Wee et al., *Proc. Natl. Acad. Sci. U.S.A.* **117**, 6675–6685 (2020).
18. B. D. Quinlan et al., *bioRxiv* 2020.04.10.036418 [Preprint].  
12 April 2020. <https://doi.org/10.1101/2020.04.10.036418>.
19. D. R. Burton, L. M. Walker, *Cell Host Microbe* **27**, 695–698 (2020).

## ACKNOWLEDGMENTS

We thank T. Gilman, A. Salazar, and Biosero for their contribution to high-throughput pipeline generation. We also thank B. Graham and J. S. McLellan for provision of materials. We thank L. Walker for valuable manuscript discussions. We thank all the COVID-19 cohort participants for donating samples. **Funding:** This work was supported by the NIH CHAVD (UM1 AI144462 to I.A.W., B.B., D.S., and D.R.B.), R01 (AI132317 and AI073148 to D.N.), and K99 (AI145762 to R.K.A.) awards; the IAVI Neutralizing Antibody Center; and the Bill and Melinda Gates Foundation (OPP1170236 to I.A.W. and D.R.B., OPP1183956 to J.E.V., and OPP1196345/INV-008813 to D.S. and D.R.B.). This work was also supported by the John and Mary Tu Foundation and the Pendleton Trust. **Author contributions:** T.F.R., E.L., D.S., J.G.J., and D.R.B. conceived of and designed the study. T.F.R., N.B., E.G., M.P., S.R., S.A.R., and D.M.S. recruited donors and collected and processed

plasma and PBMC samples. F.Z., A.B., L.Y., M.P., and G.S. performed ELISA and cell binding assays. F.Z., D.H., N.B., L.Y., M.P., L.P., J.E.V., and J.R. developed and performed neutralization experiments. F.Z., A.B., O.L., C.S., J.W., R.K.A., E.L., D.S., and J.G.J. performed antibody isolation, cloning, expression, and competition experiments. W.-t.H., G.S., S.C., R.A., N.C.W., M.Y., and I.A.W. generated recombinant antigens. T.F.R., L.Y., M.J.R., and J.R.T. carried out animal studies and qPCR viral load measurements. T.F.R., F.Z., D.H., N.B., G.S., J.W., J.H., M.J.R., D.N., J.R.T., R.A., B.B., E.L., D.S., J.G.J., and D.R.B. designed the experiments and analyzed the data. E.L., D.S., J.G.J., and D.R.B. wrote the paper, and all authors reviewed and edited the paper.

**Competing interests:** D.R.B., D.H., J.G.J., E.L., T.F.R., D.S., and F.Z. are listed as inventors on pending patent applications describing the SARS-

CoV-2 antibodies. D.R.B. is a consultant for IAVI. All other authors have no competing interests to declare. **Data and materials availability:** Antibody sequences have been deposited in GenBank under accession numbers MT594038 to MT594103. Antibody plasmids are available from D.R.B. under an MTA from the Scripps Research Institute. This work is licensed under a Creative Commons Attribution 4.0 International (CC BY 4.0) license, which permits unrestricted use, distribution, and reproduction in any medium, provided the original work is properly cited. To view a copy of this license, visit <https://creativecommons.org/licenses/by/4.0/>. This license does not apply to figures/photos/artwork or other content included in the article that is credited to a third party; obtain authorization from the rights holder before using such material.

## SUPPLEMENTARY MATERIALS

[science.sciencemag.org/content/369/6506/956/suppl/DC1](https://science.sciencemag.org/content/369/6506/956/suppl/DC1)  
Materials and Methods  
Figs. S1 to S13  
Tables S1 to S4  
References (20–27)  
MDAR Reproducibility Checklist

[View/request a protocol for this paper from Bio-protocol.](#)

12 May 2020; accepted 11 June 2020  
Published online 15 June 2020  
10.1126/science.abc7520



## GLOBAL CLIMATE CHANGE

# Synchronous timing of abrupt climate changes during the last glacial period

Ellen C. Corrick<sup>1,2\*</sup>, Russell N. Drysdale<sup>1,2</sup>, John C. Hellstrom<sup>3</sup>, Emilie Capron<sup>4,5</sup>, Sune Olander Rasmussen<sup>5</sup>, Xu Zhang<sup>6,7,8</sup>, Dominik Fleitmann<sup>9</sup>, Isabelle Couchoud<sup>2,1</sup>, Eric Wolff<sup>10</sup>

Abrupt climate changes during the last glacial period have been detected in a global array of palaeoclimate records, but our understanding of their absolute timing and regional synchrony is incomplete. Our compilation of 63 published, independently dated speleothem records shows that abrupt warmings in Greenland were associated with synchronous climate changes across the Asian Monsoon, South American Monsoon, and European-Mediterranean regions that occurred within decades. Together with the demonstration of bipolar synchrony in atmospheric response, this provides independent evidence of synchronous high-latitude-to-tropical coupling of climate changes during these abrupt warmings. Our results provide a globally coherent framework with which to validate model simulations of abrupt climate change and to constrain ice-core chronologies.

Climate records from Greenland ice cores spanning the last glacial cycle (115,000 to 11,700 years ago) reveal a series of centennial- to millennial-scale cold-warm oscillations called Dansgaard-Oeschger (DO) events (1–3). In Greenland, each event commenced with a rapid transition to warm conditions [a “Greenland Interstadial” (GI)] followed by a gradual, then abrupt, return to a cold climate state [a “Greenland Stadial” (GS)] (2, 3). This pattern is widely accepted to be associated with changes in the strength of the Atlantic Meridional Overturning Circulation (AMOC), which regulates interhemispheric oceanic heat flux, as captured in the thermal oceanic bipolar seesaw theory (4–7). During the DO warm phase, a strong AMOC exports heat from the south and tropics to the high latitudes of the North Atlantic, leading to cooling of the global ocean north of the Antarctic Circumpolar Current (ACC) and reduced temperatures over Antarctica (6). At times of DO cooling, a weakened AMOC reduces northward ocean heat transport and results in heat accumulation in the Southern Ocean, leading to Antarctic warming. These changes are broadly reflected in ocean-sediment records across the Atlantic (8–10) as far south as the mid-latitude South Atlantic, where both

surface (4) and deep-ocean signals (11) show a similar abruptness and timing to those seen in the North Atlantic but of opposite sign in surface ocean temperature. Further poleward, the abruptness is dampened by the ACC, which influences heat flux into and out of the Southern Ocean (4–6). This ultimately leads to less abrupt air-temperature changes over Antarctica (12), whose onsets lag the Greenland counterparts by around  $200 \pm 100$  years (13). The Antarctic changes are therefore symptomatic of a slow-oceanic response to the abrupt changes recorded north of the ACC (6, 14).

Changes to the cross-hemisphere ocean-temperature difference induced by switches in AMOC mode drive meridional shifts in the atmospheric mean state, particularly the position of the Intertropical Convergence Zone (ITCZ) (14, 15). This is most vividly observed in terrestrial monsoon records from both sides of the equator (16, 17) at times when Greenland climate switches abruptly from a stadial to an interstadial (called here an “interstadial onset”), and is supported by numerical climate model outputs (Fig. 1) (18–20). These higher-amplitude warming episodes correspond to air-temperature increases over the Greenland ice sheet of up to  $16^{\circ}\text{C}$  (21), typically in around 80 years. Such a strong high-latitude-to-tropical teleconnection indicates widespread atmospheric reorganization at the onset of interstadials. However, there is uncertainty over the exact phasing: Were climate responses synchronous between different monsoon regions, and between the wider tropical realm and Greenland? Recent reassessments of ice-core data (22, 23) suggest that atmospheric changes associated with abrupt warming and cooling in Greenland were transmitted more or less synchronously as far south as the Antarctic ice sheet, indicating rapid reorganization of atmospheric circulation. Such bipolar synchrony implies that mid-latitude and tropical regions also responded rapidly as Green-

land temperatures changed abruptly. This has been the assumption in previous studies (24, 25) but has yet to be rigorously tested. Answering these questions will deepen our understanding of the underlying dynamics of global climate teleconnections during abrupt climate changes, which serves as a basis to test climate models used for future projections (26).

Testing the large-scale synchrony of stadial-interstadial changes to augment the suggestion of bipolar synchrony is hampered by the limited availability of independently dated palaeoclimate time series with sufficiently constrained chronologies ( $2\sigma$  age uncertainties in the range of decades to centuries). The chronologies of many last-glacial records are aligned to other marine, ice-core, or speleothem age models under the assumption that abrupt events did occur synchronously between sites at least to within the resolution of the records in question (25, 27, 28). This prevents any independent assessments of potential regional leads and lags between these records (29). The current Greenland Ice Core Chronologies (GICC05 and its extension GICC05modelext) (30–32) provide the chronological framework for the latest event stratigraphy of abrupt climate changes (3), but published age uncertainties in the annual-layer counting accumulate with increasing age, reaching  $\pm 2600$  years at 60,000 years before 1950 [before the present (B.P.)]. Beyond this, age uncertainties of the flow-model extension to the chronology, GICC05modelext, are unquantified (32). Thus, any comparison of the timing of interstadials and stadials between ice cores and other archives becomes less certain through time, even though the incremental nature of the ice-core counting errors produces high-precision constraints on the time difference between successive events—that is, the duration of and spacing between events (fig. S1).

## Speleothem records of interstadial onset

To test the global synchrony of these events, we investigated the timing of the abrupt interstadial onset for 25 major and 28 minor interstadial events (3, 33) using 63 published, high-resolution, and precisely dated speleothem records covering the last glacial period (Fig. 1 and table S1) (34). Speleothems (secondary mineral deposits found in caves) have great potential because they can be radiometrically dated with great accuracy with uranium-series methods to a precision of 0.1 to 1% ( $2\sigma$ ) over last-glacial time scales [for example, (35)]. Numerous speleothem stable oxygen isotope ( $\delta^{18}\text{O}$ ) records spanning the Northern Hemisphere (NH) mid-latitudes to the Southern Hemisphere (SH) subtropics capture stadial-interstadial transitions, particularly the more pronounced interstadial onsets, where local precipitation and/or temperature changes lead to prominent changes in  $\delta^{18}\text{O}$  (17, 36, 37).

<sup>1</sup>School of Geography, The University of Melbourne, Melbourne, Victoria, Australia. <sup>2</sup>EDYTEM, CNRS, Université Savoie Mont Blanc, Université Grenoble Alpes, Chambéry, France. <sup>3</sup>School of Earth Science, The University of Melbourne, Melbourne, Victoria, Australia. <sup>4</sup>British Antarctic Survey, Cambridge, UK. <sup>5</sup>Physics of Ice, Climate and Earth, Niels Bohr Institute, University of Copenhagen, Copenhagen, Denmark. <sup>6</sup>Key Laboratory of Western China's Environmental Systems (Ministry of Education), College of Earth and Environmental Sciences, Center for Pan Third Pole Environment (Pan-TPE), Lanzhou University, Lanzhou, 730000, China. <sup>7</sup>Alfred Wegener Institute, Helmholtz Centre for Polar and Marine Research, D-27570 Bremerhaven, Germany. <sup>8</sup>CAS Center for Excellence in Tibetan Plateau Earth Sciences, Chinese Academy of Sciences (CAS), Beijing 100101, China. <sup>9</sup>Department of Environmental Sciences, University of Basel, 4056 Basel, Switzerland. <sup>10</sup>Department of Earth Sciences, University of Cambridge, Cambridge, UK. \*Corresponding author. Email: ecorrick@student.unimelb.edu.au

We standardized all speleothem time series to avoid methodological bias in age calculations and depth-age model construction then identified the onset of each interstadial by adapting a technique applied to the ice-core record (fig. S2) (3, 34). Because of the nature of speleothem growth, variability is exhibited in the temporal span of each record, with the majority covering a few tens of thousands of years, although some are much shorter (fig. S3). Within a single record, the temporal resolution may vary greatly owing to changes in the growth rate of the speleothem. All records are dated directly by using uranium-thorium (U-Th) methods, and each time series is free of synchronization to any tuning target. The isotope records for all speleothems are shown in data file S3 and provided in data file S7. Of the 53 interstadials identified in the ice cores (3), 39 could be confidently resolved in at least two records in the speleothem dataset, with the overwhelming majority of records falling into either the Asian Summer Monsoon (ASM), the South American Monsoon (SAM), or the Europe-Mediterranean (EM) domains (Fig. 1) (34). The speleothem  $\delta^{18}\text{O}$  in these three regions exhibits well-documented changes across interstadial onsets (Fig. 2), with patterns gen-

erally well reproduced in DO-type transient climate-model simulations (Fig. 1, background maps). In the ASM domain, warming in the North Atlantic is associated with a strengthening of both the Indian and East Asian Summer Monsoon subsystems, which produces decreased  $\delta^{18}\text{O}$  values driven by variations in rainout, air-mass trajectories, and/or rainfall amounts (Fig. 1A) (36–38). The  $\delta^{18}\text{O}$  in the SAM domain increases because of the same processes under a weakened monsoon (Fig. 1B) (39). This “monsoon-seesaw pattern” over interstadial onsets is consistent with a northward shift of the ITCZ (10, 17). In the EM region, the speleothem  $\delta^{18}\text{O}$  response to interstadial onsets is slightly more complex. Sites situated around the Alps and western Turkey (Sofular) show increased isotopic values (40, 41) as the climate warms, which is consistent with the dominating temperature effect (Fig. 1C) on the  $\delta^{18}\text{O}$  of local precipitation (42), whereas seasonal changes in moisture source and the source effect cause  $\delta^{18}\text{O}$  values in northeastern Turkey (Karaca) to decrease (43). Around the Mediterranean, regional warming increases the amount of rainfall reaching cave sites (44), leading to decreasing  $\delta^{18}\text{O}$  values owing to the rainfall amount effect (42). This effect

also occurs in the eastern Mediterranean, where it may be modified by changes in local seawater  $\delta^{18}\text{O}$  composition related to higher Nile discharge (45). The abruptness of speleothem  $\delta^{18}\text{O}$  change at the onset of the interstadials (Fig. 2) is, in most cases, comparable with what is observed in the ice-core record (41), when accounting for differences in temporal resolution, speleothem age-model uncertainties, and the smoothing of atmospheric signals in speleothems due to groundwater transport and mixing processes in the karst aquifer (46).

### Testing the synchrony of interstadial onset

In restricting our comparison to the three regions best represented by the speleothem data, we first tested the intraregional synchrony of an interstadial onset, hypothesizing that abrupt changes within a single region should be recorded practically simultaneously by speleothems at each cave site. Second, we tested the synchrony between the three regions for each interstadial onset. We assessed the degree of intra- and interregional synchrony using the reduced  $\chi^2$  statistic, known in geochronology as the mean-square weighted deviation (MSWD) (47, 48), which tests whether a group of radiometric ages belong to a single population (34). Where we found statistical agreement between speleothem ages from the same region, we calculated the error-weighted mean (EWM) (34) and assigned this as the “regional age.” These regional ages were used to test the synchrony between regions and to derive a composite speleothem age for each interstadial onset in cases for which data from multiple regions were available. These age estimates for interstadial onsets form the Speleothem Interstadial Onset Compilation data set (SIOC19). We also assessed the extent to which an age estimate for the timing of an interstadial onset based on data from only one region could be used as a wider event-age indicator. We then compared the SIOC19 age estimates for each interstadial onset with their timing in the ice-core GICC05 and GICC05modelext chronologies (3). Last, we investigated the regional age offset over interstadial onsets for which two or more speleothem records from the same region were available.

For 34 of the 37 interstadials recorded in multiple speleothem records, there is strong intraregional agreement (within  $2\sigma$  uncertainties), comprising cases in which one (nine interstadials) or multiple (25 interstadials) regions are represented (Fig. 2, fig. S4, and table S2). The three remaining onsets (into interstadials 12a, 14e, and 23.1) show disagreement within all of the represented regions [the MSWD lies outside the accepted range (34)], and we assigned an indeterminate result to these (table S2D). Three of the 34 transitions show disagreement within one or more of the regions represented (interstadials 4,

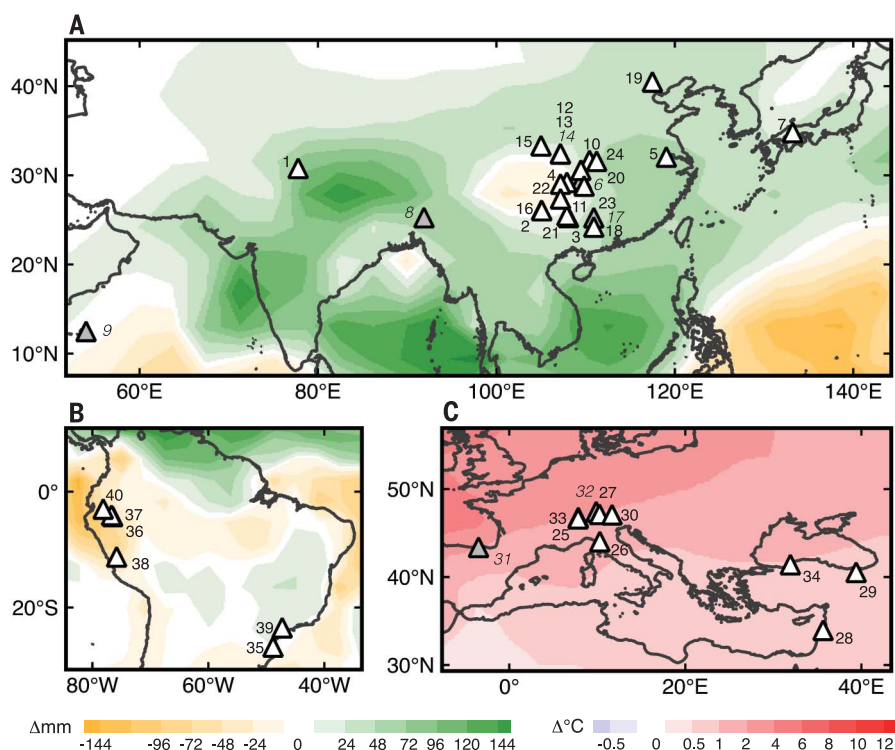


**Fig. 1. Location of last glacial speleothem records included in the compilation. (A to C)** Cave sites for records from the (A) Asian Summer Monsoon region, (B) South American Monsoon region, (C) Europe-Mediterranean region. Gray triangles and italicized font represent records that were used in the comparison but are not represented in the age estimates for the synchronous events shown in Table 1. Reference to the numbering is provided in table S1, which shows the complete list of speleothem records and citation to the original publication. Shaded backgrounds are composite anomalies of [(A) and (B)] annual mean precipitation and (C) surface air temperature between interstadial and stadial states in DO-type transient experiments (19, 20, 34, 52).



ASM and EM; 12c, ASM; and 24.2, ASM), so we excluded the data from the anomalous region from further (interregional) comparisons (table S2, A and B, region listed as “unresolved”). The strong overall intraregional agreement validates the assumption of intraregional synchrony. This enables us to treat the records from each region as a single population and combine them into a single regional age, based on the EWM, with a reduced uncertainty relative to the individual records. It is likely that statistically significant age differences within a region may be due to either sample and/or site-specific processes affecting the registration of the climate signal (for example, competing mechanisms driving local  $\delta^{18}\text{O}$ ) or chronological issues such as undetected growth hiatuses, uranium leaching (49), and/or suboptimal positioning of U-Th age or stable isotope samples.

In comparing the regional EWM ages, we found strong evidence of synchronous onset for 23 of the 25 interstadials for which we were able to make interregional comparisons (Fig. 2; Table 1, entries denoted with an asterisk; fig. S4; and table S2). In the case of onsets younger than 40,000 years B.P., the difference in the mean age between any region represented by multiple speleothem records (thus giving greater confidence and narrowing the regional uncertainty) ranges from 3 to 72 years (table S2), with an uncertainty that spans zero. This indicates that the onset of interstadials is likely synchronous within decades. It also highlights that the major limiting factor in deriving more precise constraints of event synchrony is related to the magnitude of the U-Th dating errors of individual speleothem records rather than scatter in the ages themselves.

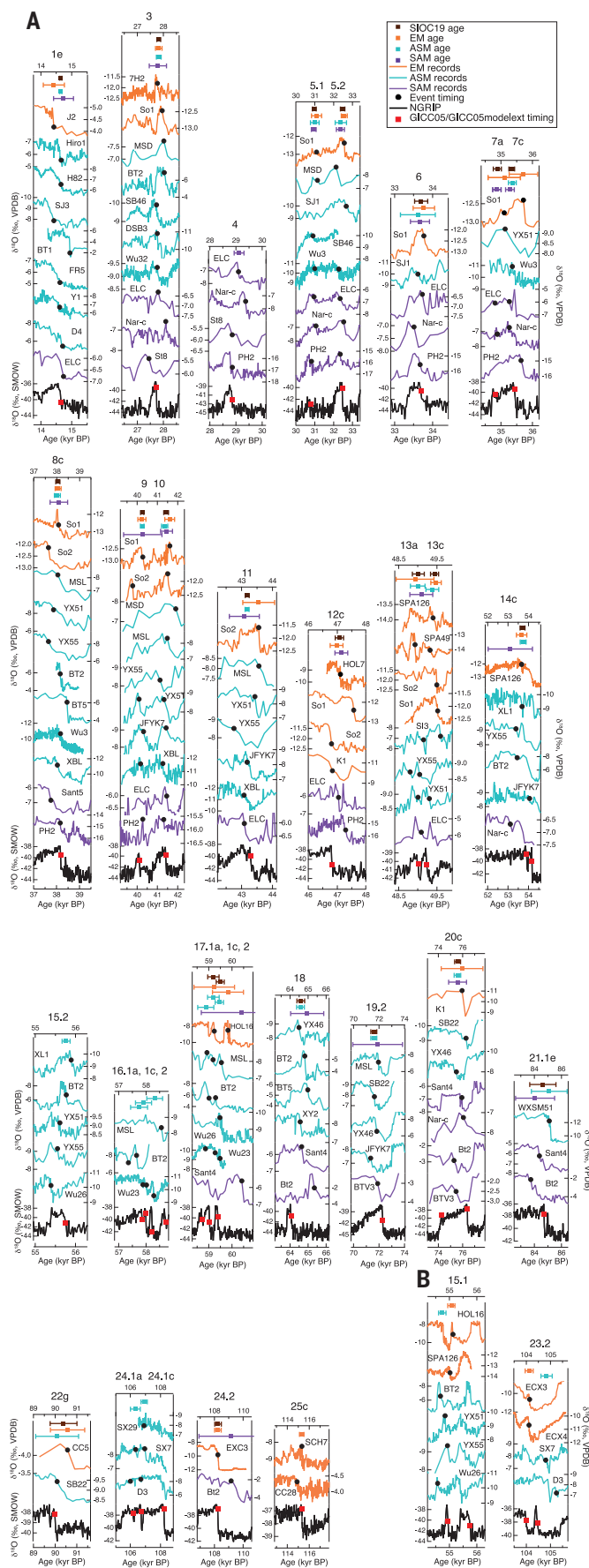


**Fig. 2. Stable isotope records of individual speleothems for each interstadial onset. (A and B)** Each speleothem record displayed has met screening and event identification criteria (34) and is color-coded according to region (EM, orange; ASM, blue; and SAM, purple). All records are plotted on the recalculated chronology (34). Plots are provided for interstadial onsets found to be (A) synchronous and (B) non-synchronous. (A) includes interstadials for which we have data from only one region. The North Greenland Ice Core Project (NGRIP)  $\delta^{18}\text{O}$  series on the GICC05 or GICC05modelext chronology is plotted in black, with each event position (3) indicated with a red square. The corresponding event position in each speleothem record is indicated with a solid black circle (timing and uncertainty are provided in data file S1). Markers with error bars at the top of (A) and (B) indicate the age and  $2\sigma$  uncertainty of the interregional age estimate (brown) and intraregional age estimates (EM, orange; ASM, blue; and SAM, purple). Lettering provides the name of each speleothem record. The full details and original reference for each record are provided in table S1. VPDB, Vienna Pee Dee belemnite; SMOW, standard mean ocean water; kyr, thousand years.

The onset of the two interstadials that are not recorded synchronously between regions are those to interstadial 15.1 (recorded 334 ± 185 years earlier in the EM compared with the ASM) and interstadial 23.2 (recorded 716 ± 287 years later in the EM compared with the ASM); in both cases, there were no high-quality records from the SAM region (Fig. 2B and table S2C). These anomalies could reflect a genuine asynchrony, implying that these interstadials are

of an unusual nature in the context of the other 23. However, such asynchrony may reflect varying sensitivity to these short-lived interstadials, which is also suggested by some structural difference to the very sharp peaks in Greenland. The regional lead-lag is not consistent, however, so does not suggest a systematic regionally asynchronous response to interstadials of this type.

Given that the great majority of interstadial onsets tested for interregional synchrony (23

out of 25) show chronological agreement, it is reasonable to assume that an EWM age estimate for an interstadial onset in which only a single region is represented (the case for nine interstadials) (Table 1, entries denoted with “+”, and table S2B) is also indicative of a transition’s broader timing. We tested this assumption by comparing the spacing of consecutive interstadial onsets in the speleothems with the corresponding annual-layer-counted intervals in the GICC05 ice-core chronology (Fig. 3) (3, 31, 50). As noted above, although the precision on the absolute ages of the GICC05 chronology decreases back in time, the interval between the onset of consecutive interstadials over the layer-counted section (0 to 60,000 years B.P.) can be estimated with relatively high precision [the average 2[σ] error for all consecutive intervals in this period is 5.0 ± 1.3 (1[σ]) (Fig. 3 and fig. S1). Interstadial duration estimates based on the SIOC19 age estimates (including those based on data from only one region) agree within uncertainty with those from the GICC05 chronology, with the exception of one interval out of 22 (interval 12c to 11, GICC05 estimate 3520 ± 176 years, SIOC19 3886 ± 158 years) (Fig. 3). Beyond the layer-counted section (>60,000 years B.P.), only two out of nine intervals show discrepancies outside of the uncertainty estimate of SIOC19 (interval 19.2 to 18, GICC05modelxt 8240 years, SIOC19 6998 ± 312 years; interval 18 to 17.2, GICC05modelxt 4660 years, SIOC19 5107 ± 273 years) (Fig. 3). Overall, however, the agreement between SIOC19 and the GICC05 and GICC05modelxt chronologies for the duration of consecutive interstadials validates the accuracy of the relative ages (within uncertainties) of the single-region estimates and thus their inclusion alongside the multiregional EWM ages. Nevertheless, we suggest that the timing estimates of interstadial onsets based on data from only a single region (denoted by † in Table 1) should be treated cautiously until they are verified by additional high-quality speleothem records from other regions.

The regional speleothem ages of interstadial onsets from three geographically diverse areas being likely synchronous to well within a century suggests that the timing should agree—within the same uncertainty—with corresponding events in Greenland. We next evaluated the GICC05 and GICC05modelxt chronologies by comparing speleothem and ice-core ages for the 32 interstadials in Table 1. The multiregion (23 interstadials) and single-region (nine interstadials) speleothem age estimates are all within 1.1% of the ice-core mean ages (Table 1 and fig. S6A). Three of the four largest offsets (20c, 19.2, and 18) are observed beyond the layer-counted interval (fig. S6A), for which ice-core chronological control is less secure owing to uncertainties associated with the glaciological modeling that underpins this section (GICC05modelxt) (32).

**Table 1. The timing of each interstadial onset in the combined speleothem records (SIOC19) and the corresponding ages in the Greenland ice-core chronology.** The combined speleothem age is the error-weighted mean (and the corresponding 2σ uncertainty) of multiple individual speleothem records that have been grouped at a regional level (Asian Summer Monsoon, South American Monsoon, and Europe-Mediterranean regions). *n* denotes the total number of speleothem records contributing to the age. The corresponding GICC05/GICC05modelxt age (3) is shown, including the maximum counting error for the annual layer-counted section (back to 60,000 years B.P.). No errors are shown beyond 60,000 years B.P. because the uncertainty on this section of the chronology (GICC05modelxt) is not quantified (32). The age difference between the ice core and composite speleothem ages is given as both a percentage and absolute difference. The ages in GICC05 are from (3) and were identified in a 20-year resolution multicore ice-core dataset. All ages are reported in years B.P. (before 1950).

Interstadial number	Combined speleothem SIOC19 age	<i>n</i>	GICC05/GICC05modelxt age	Age difference (%)	Age difference (years)
1e	14,646 ± 34*	9	14,642 ± 186	−0.03	−4
3	27,822 ± 72*	10	27,730 ± 832	−0.33	−92
4	29,117 ± 189†	4	28,850 ± 898	−0.93	−267
5.1	30,980 ± 103*	7	30,790 ± 1024	−0.62	−190
5.2	32,477 ± 115*	7	32,450 ± 1132	−0.08	−27
6	33,699 ± 174*	5	33,690 ± 1212	−0.03	−9
7a	34,884 ± 130†	3	34,830 ± 1293	−0.16	−54
7c	35,342 ± 90*	6	35,430 ± 1321	0.25	88
8c	38,044 ± 88*	11	38,170 ± 1449	0.33	126
9	40,251 ± 81*	6	40,110 ± 1580	−0.35	−141
10	41,431 ± 119*	10	41,410 ± 1633	−0.05	−21
11	43,185 ± 64*	7	43,290 ± 1736	0.24	105
12c	47,071 ± 145†	6	46,810 ± 1912	−0.56	−261
13a	49,015 ± 154*	5	49,010 ± 2021	−0.01	−5
13c	49,439 ± 106†	7	49,230 ± 2031	−0.43	−209
14c	53,713 ± 124*	6	53,910 ± 2289	0.37	197
15.2	55,770 ± 98†	5	55,750 ± 2368	−0.04	−20
16.1a	57,746 ± 311†	2	57,870 ± 2492	0.21	124
16.1c	57,910 ± 293†	2	57,990 ± 2497	0.14	80
16.2	58,315 ± 288†	2	58,230 ± 2511	−0.15	−85
17.1a	58,870 ± 346†	2	58,730 ± 2540	−0.24	−140
17.1c	59,199 ± 241†	4	59,030 ± 2557	−0.29	−169
17.2	59,489 ± 173*	6	59,390 ± 2569	−0.17	−99
18	64,596 ± 211†	6	64,050	−0.85	−546
19.2	71,594 ± 230†	5	72,290	0.96	696
20c	75,583 ± 248*	7	76,390	1.06	807
21.1e	84,621 ± 971†	3	84,710	0.11	89
22g	90,386 ± 617†	2	89,990	−0.44	−396
24.1a	106,328 ± 325†	2	106,170	−0.15	−158
24.1c	106,918 ± 204†	3	106,700	−0.20	−218
24.2	108,254 ± 235†	2	108,230	−0.02	−24
25c	115,310 ± 209†	2	115,320	0.01	10

\*All three regions are represented by the corresponding speleothem records. †One region is represented by the corresponding speleothem records. ‡Two of the three regions are represented by the corresponding speleothem records.



We do not detect any systematic GICC05-to-SI0C19 age difference that could be linked to either background climate state or interstadial duration, amplitude, and rate of warming (fig. S6, C to F).

Because the interstadial onsets captured by the speleothems are sufficient in number and encompass the entire range of interstadial types for the last glacial period (for example, including longer-duration events and rebound-type events), they can therefore be regarded as a representative sample of the population of all last glacial interstadial onsets. On the basis of this assumption, we quantified the GICC05-to-SI0C19 age difference across all 23 events younger than 60,000 years using robust regression (GICC05 versus SI0C19 ages) (34). The regression yields a slope of 1.000 and a  $y$  intercept (mean age difference) of  $-48$  ( $-160/+240$ ) years (fig. S6B), providing compelling evidence that the speleothem and ice-core ages agree to within, at a maximum, a couple of centuries. These radiometric-age com-

parisons provide strong support for the accuracy of both the GICC05 and GICC05modelext chronologies throughout the duration of the last glacial period and suggest that the quoted uncertainties are too conservative. On the basis of our time points for the time period, we do not find strong support for GICC05 being too young over the period 45,000 to 15,000 years B.P. as is suggested by linking the GICC05 and U-Th time scales through the use of cosmogenic radionuclides (51), nor can we confirm the 0.63% counting bias correction found by correlation to Hulu cave U-Th dates during the dating of the West Antarctic Ice Sheet (WAIS) Divide ice core (24). Such differences may arise because of the methodological approach, including the choice of detrital-thorium correction and depth-age modeling (34). The effect of compiling multiple speleothem records is also likely to be substantial, in that the influence of potentially younger or older individual records is not as dominant. Our study also looks across the whole of the last

glacial period rather than subsections or the individual temporal span of selected records.

Although overall synchrony between individual monsoon regions, and between Europe and the monsoon regions, has been assumed [for example, (25, 41)], it has yet to be fully tested quantitatively. To examine this further, we undertook two steps. First, we computed the EWM (and 95% uncertainties) of the differences between the Asian and South American Monsoon speleothem age estimates for each interstadial onset, where a 0 mean would indicate perfect synchrony (table S3A). We included only the interstadial onsets in which both monsoon regions were represented by two or more speleothem records (the case for eight interstadials) on the grounds that multiple speleothem records for an onset provide a more robust age estimate. The results give an EWM age difference (ASM minus SAM) of  $19 \pm 113$  years (MSWD = 0.26) [Fig. 4A, blue probability density function (PDF) curve, and table S3A]. This strong degree of synchrony suggests that the ASM and SAM regions can be treated as a single category to yield “monsoon” EWM ages (and 95% uncertainties). Second, we then determined the age difference between the EM and combined monsoon regions for the same onsets. There are six interstadials (3, 8c, 9, 10, 12c, and 13c) for which there are at least two records from the EM region and at least two monsoon records (regardless of their origin). The mean onset-age difference and uncertainty (EM minus Monsoon) is  $25 \pm 84$  years (MSWD = 0.90) (Fig. 4A, red PDF curve, and table S3B). This implies that the 95th percentile EM lead and EM lag over the monsoon regions is 109 and 59 years, respectively.

### Comparison with model output and implications

We then compared the regional phasing of the onset of interstadials as indicated by the speleothems with modeling simulations and previous research (12, 13, 15, 23) to attain an overall picture regarding global climate teleconnections during an abrupt interstadial onset associated with AMOC recovery. We used long-term North Atlantic hosing experiments (52), in which a  $\sim 0.2$  sverdrup freshwater flux was released to the Ruddiman Belt for 1000 years to mimic a cold “stadial” climate state. As the freshwater flux is removed at the 501st model year (1st model year in Fig. 4), the AMOC starts increasing instantly and reaches its “interstadial” state within a century (Fig. 4). We acknowledge that other forcing factors (such as ice-sheet height and atmospheric  $\text{CO}_2$ ) are also able to mimic DO-type abrupt AMOC changes (19, 20), and freshwater flux may not be a realistic forcing factor for all interstadials (for example, those that follow non-Heinrich stadials). However, freshwater forcing is the ideal surrogate to evaluate the role of AMOC changes on the

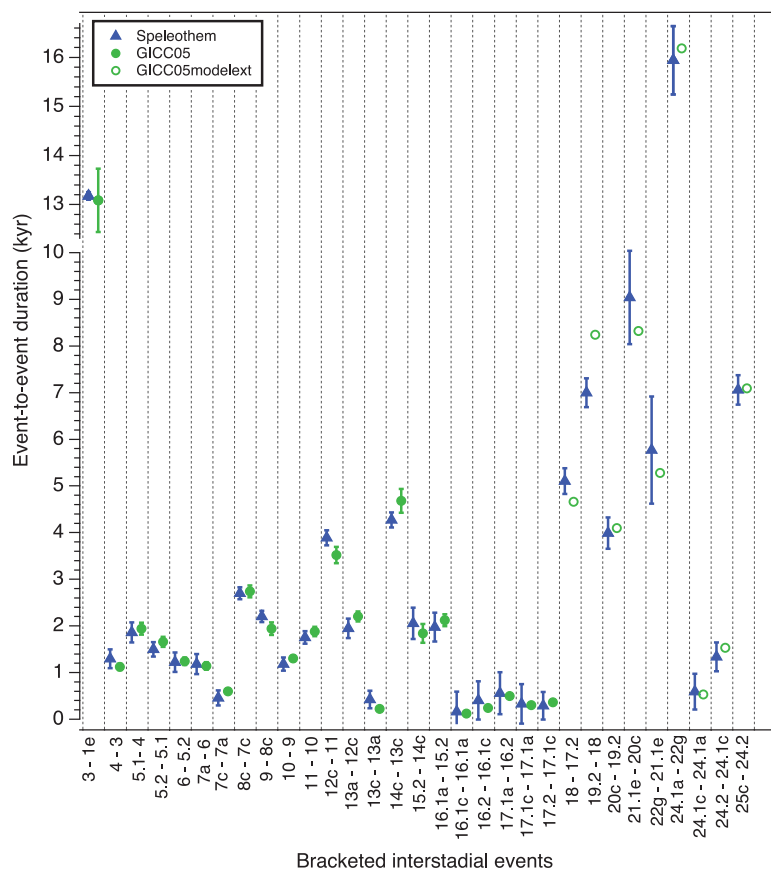
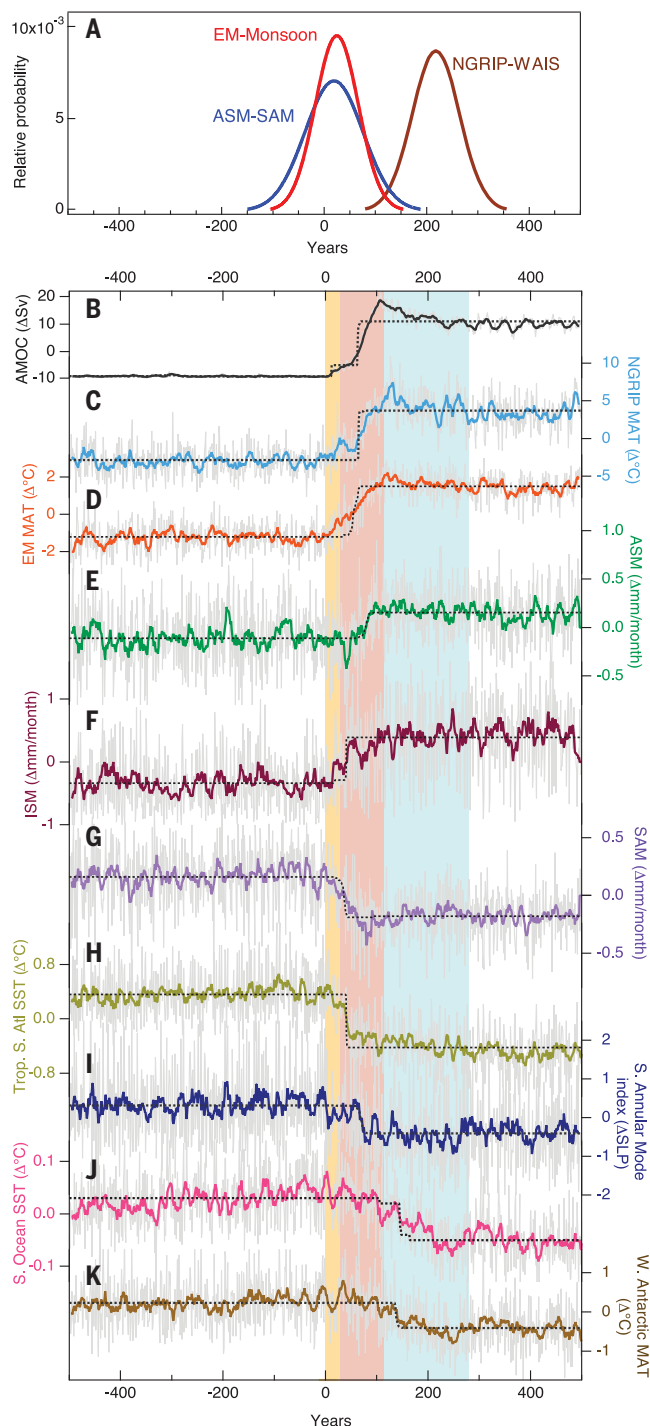


**Fig. 3. Years between the onset of consecutive interstadials.** The time interval between the onset of consecutive interstadials in the GICC05/GICC05modelext chronology is compared with the corresponding interval based on the SI0C19 ages. Error bars represent the  $2\sigma$  age uncertainties on the interval. For the GICC05 chronology, this was calculated as the change in the accumulated layer-counting uncertainty between events (fig. S1); errors are not shown for events within the GICC05modelext section because they are not quantified (32). For the speleothems, the error bar is the uncertainty of the consecutive SI0C19 age estimates in quadrature. The timing between interstadial onsets is shown for those interstadials demonstrated to be synchronous in the speleothems, including estimates based on data from only one region.

**Fig. 4. Spatial synchrony of climate changes during interstadial onsets.** (A) PDFs of spatial age offsets between the two monsoon regions (ASM minus SAM, blue) and between Europe and both monsoon regions (EM minus Monsoon, red) based on composite speleothem data (table S3). Also shown (brown) is the previously determined offset between the WAIS ice core  $\delta^{18}\text{O}$  and NGRIP  $\delta^{18}\text{O}$  (13). (B to K) Simulated climate changes in a DO-type hosing simulation, each expressed as anomalies from the mean of the simulation (fig. S6 and table S4) (34). (B) AMOC index (defined as maximal meridional stream function at the water depth of 1500 to 3000 m north of 45°N in the North Atlantic). (C) Annual mean surface air temperature over the NGRIP drilling site (NGRIP MAT). (D) Annual mean surface air temperature over the Europe-Mediterranean region (30°N to 45°N, 25°E to 40°E) (EM MAT). [(E) to (G)] Mean annual precipitation over the (E) Eastern Asian (20°N to 30°N, 108°E to 120°E), (F) Indian (25°N to 35°N, 75°E to 85°E), and (G) South American regions (5°S to 10°S, 30°W to 75°W). (H) Annual mean sea-surface temperature (SST) in the tropical-subtropical South Atlantic (5°S to 30°S, 60°W to 10°E). (I) Southern Annular Mode index reflecting changes in sea-level pressure from 20°S to 90°S. (J) Annual mean SST in the Atlantic sector of the Southern Ocean (55°S to 75°S, 60°W to 10°E). (K) MAT over West Antarctica (75°S to 82°S, 90°W to 135°W) taken to be representative of the WAIS ice core site. Yellow shading indicates the period of fast atmospheric response in which the Atlantic ITCZ starts migrating toward the subtropical North Atlantic. Pink shading indicates the period of further strengthening of the AMOC and NH warming. Blue shading indicates the start of the AMOC interstadial mode. The gray series are raw model outputs, and the color series are 11-year running averages. The black dotted lines are model series derived from the application of a Bayesian, least-squares change-point analysis (58) to each raw time series. For (B) to (K), the x axis shows model years, with year 1 reset to the year of the removal of the freshwater flux (34). For (A), the year scale refers to the age offset for each PDF. The NGRIP-WAIS PDF curve is therefore in its approximate correct position with respect to the model-year scale in (B) to (K) (34).



in sea-level pressure from 20°S to 90°S. (J) Annual mean SST in the Atlantic sector of the Southern Ocean (55°S to 75°S, 60°W to 10°E). (K) MAT over West Antarctica (75°S to 82°S, 90°W to 135°W) taken to be representative of the WAIS ice core site. Yellow shading indicates the period of fast atmospheric response in which the Atlantic ITCZ starts migrating toward the subtropical North Atlantic. Pink shading indicates the period of further strengthening of the AMOC and NH warming. Blue shading indicates the start of the AMOC interstadial mode. The gray series are raw model outputs, and the color series are 11-year running averages. The black dotted lines are model series derived from the application of a Bayesian, least-squares change-point analysis (58) to each raw time series. For (B) to (K), the x axis shows model years, with year 1 reset to the year of the removal of the freshwater flux (34). For (A), the year scale refers to the age offset for each PDF. The NGRIP-WAIS PDF curve is therefore in its approximate correct position with respect to the model-year scale in (B) to (K) (34).

spatial phasing of climate changes (53) because changes in ice-sheet height and atmospheric  $\text{CO}_2$  will exert additional regional and global climate responses that are not associated with AMOC changes (fig. S7) (19, 20, 34).

The climate response to AMOC reinvigoration expressed in the modeled regional climate anomalies is consistent with the observations from the regional array of speleothems (Fig. 4). Furthermore, the degree of synchrony shown by the speleothems between the ASM and SAM and between EM and the combined Monsoon agrees with the timing of modeled regional precipitation and temperature anomalies in the Monsoon and EM, respectively (Fig. 4). On the basis of this, we can summarize the pattern of climate changes during the interstadial onsets in three stages (Fig. 4, B to K). At the beginning, AMOC recovery (Fig. 4B) will lead to an initial warming anomaly in the northern North Atlantic (Fig. 4, C and D), causing thermal asymmetry between the North and South Atlantic. This would drive a fast atmospheric response in which the Atlantic ITCZ starts migrating toward the subtropical North Atlantic (Fig. 4, yellow shading). As the AMOC is strengthened further, the entire NH warms, pulling the ITCZ further northward globally (Fig. 4, E to H, pink shading). This strengthening and weakening of the ASM and SAM, respectively, leads to the observed respective decrease and increase in speleothem  $\delta^{18}\text{O}$  records (37–39). Over Europe and the Mediterranean, warming drives increased speleothem  $\delta^{18}\text{O}$  at sites where the local rainfall is most sensitive to mean atmospheric temperature changes (40, 41) and lower speleothem  $\delta^{18}\text{O}$  at sites where warmer ocean temperatures drive higher rainfall amounts (44). Meanwhile, Antarctica starts perceiving the northern signal by way of the atmospheric bridge (6, 22). This is evident in the model output of changes to the Southern Annular Mode index, a proxy for meridional changes in the position of the westerlies: As interstadial onset commences, and the ITCZ shifts northward, the index becomes more negative over a similar time frame to the ITCZ changes (Fig. 4I). This is consistent with a northward migration of the southern mid-latitude westerlies and supports the conceptual model proposed by (23) to explain the changes in the  $d$ -excess of Antarctic ice across the warming transitions. Once the AMOC reaches interstadial mode (Fig. 4, blue shading), atmospheric circulation assumes its interstadial mean state, leading to a cascade of processes that alters heat transport across the ACC, leading to an Antarctic temperature decrease (Fig. 4K) (6) that lags the AMOC recovery [and Greenland warming (Fig. 4C)] by approximately  $200 \pm 100$  years (Fig. 4A, brown PDF curve) (13). The compilation of precise speleothem records now lends support to this pattern of changes



and provides crucial empirical evidence for the synchronous response to these changes in the mid-latitudes.

The SIOC19 age estimates (Table 1) constitute the most precise, absolute dating of interstadial onsets yet produced. Using the full range of interstadial types across the whole last glacial period, and incorporating as much speleothem information as possible from the target regions, we demonstrate that synchronous climate changes (within a century) occurred between Europe and the Asian and South American monsoon domains at the onset of interstadials. A similar level of synchrony is observed between Europe and both monsoon regions (Fig. 4A). Given the proximity of Greenland to EM, compared with the proximity of the EM to both monsoon domains, it is highly likely that such synchrony extends across the North Atlantic to Greenland. A recent comparison, based on four speleothem records, of interstadials in the latter part of the last glacial (<45,000 years B.P.) also shows the timing of the onset to be synchronous within uncertainties (57). Our findings are also consistent with a previous study of a single interstadial, where synchrony between tropical (using methane as a proxy) and Greenland temperatures took place within 24 years (54). Thus, our study strongly supports the long-held, but theretofore untested, assertions of practically synchronous high-latitude-to-tropical climate changes during abrupt interstadial onsets (24, 25, 28). Recent results from Antarctica suggest that changes in the source location of moisture reaching the ice sheet were abrupt and occurred within decades of DO warmings (and coolings) in Greenland (22), implying an inter polar atmospheric teleconnection. Our results provide crucial, independent supporting evidence of near-synchronous atmospheric propagation of abrupt climate changes during interstadial onsets that were global in scale by providing spatial detail between the NH mid-latitudes and the SH subtropics.

The prospect of future abrupt climate change due to anthropogenic forcing, and the importance of reliable climate-model predictions, has brought past abrupt changes, such as DO events, into sharp focus in recent years. Our study provides precise chronological information on the timing of climate changes during stadial-interstadial transitions, reveals the wide-

spread synchrony of their response, and provides radiometric validation and constraint for refining ice-core chronologies. The triggering mechanism for DO events (and the associated AMOC changes), however, remains an open question, and discriminating between external forcing (such as ice-sheet height, greenhouse gases, meltwater, and volcanism) (18–20, 55, 56) and “self-oscillation” mechanisms (57) as drivers of AMOC-mode transitions rests with future studies that take advantage of state-of-the-art Earth-system models and well-dated, high-resolution palaeoclimate records.

## REFERENCES AND NOTES

- W. Dansgaard et al., *Nature* **364**, 218–220 (1993).
- NGRIP Members, *Nature* **431**, 147–151 (2004).
- S. O. Rasmussen et al., *Quat. Sci. Rev.* **106**, 14–28 (2014).
- S. Barker et al., *Nature* **457**, 1097–1102 (2009).
- T. F. Stocker, S. J. Johnsen, *Paleoceanography* **18**, 1087 (2003).
- J. B. Pedro et al., *Quat. Sci. Rev.* **192**, 27–46 (2018).
- W. S. Broecker, *Paleoceanography* **13**, 119–121 (1998).
- J. P. Sachs, S. J. Lehman, *Science* **286**, 756–759 (1999).
- S. Barker et al., *Nature* **520**, 333–336 (2015).
- L. C. Peterson, G. H. Haug, K. A. Hughen, U. Röhl, *Science* **290**, 1947–1951 (2000).
- J. Gottschalk et al., *Nat. Geosci.* **8**, 950–954 (2015).
- EPICA Community Members, *Nature* **444**, 195–198 (2006).
- WAIS Divide Project Members, *Nature* **520**, 661–665 (2015).
- I. Cvijanovic, P. L. Langen, E. Kaas, P. D. Ditlevsen, *J. Clim.* **26**, 4121–4137 (2013).
- A. J. Broccoli, K. A. Dahl, R. J. Stouffer, *Geophys. Res. Lett.* **33**, L01702 (2006).
- L. C. Kanner, S. J. Burns, H. Cheng, R. L. Edwards, *Science* **335**, 570–573 (2012).
- X. Wang et al., *Quat. Sci. Rev.* **25**, 3391–3403 (2006).
- A. Ganopolski, S. Rahmstorf, *Nature* **409**, 153–158 (2001).
- X. Zhang, G. Lohmann, G. Knorr, C. Purcell, *Nature* **512**, 290–294 (2014).
- X. Zhang, G. Knorr, G. Lohmann, S. Barker, *Nat. Geosci.* **10**, 518–523 (2017).
- C. Lang, M. Leuenberger, J. Schwander, S. Johnsen, *Science* **286**, 934–937 (1999).
- B. R. Markle et al., *Nat. Geosci.* **10**, 36–40 (2016).
- C. Buizert et al., *Nature* **563**, 681–685 (2018).
- C. Buizert et al., *Clim. Past* **11**, 153–173 (2015).
- K. A. Hughen, J. Southon, S. Lehman, C. Bertrand, J. Turnbull, *Quat. Sci. Rev.* **25**, 3216–3227 (2006).
- G. Flato et al., *Evaluation of Climate Models: Climate Change The Physical Science Basis. Contribution of Working Group I to the Fifth Assessment Report of the Intergovernmental Panel on Climate*, T. F. Stocker et al., Eds. (Cambridge Univ. Press, 2013).
- G. Bond et al., *Nature* **365**, 143–147 (1993).
- N. J. Shackleton, Michael A. Hall, E. Vincent, *Paleoceanography* **15**, 565–569 (2000).
- M. Blaauw, *Quat. Sci. Rev.* **36**, 38–49 (2010).
- K. K. Andersen et al., *Quat. Sci. Rev.* **25**, 3246–3257 (2006).
- A. Svensson et al., *Clim. Past* **4**, 47–57 (2008).
- E. W. Wolff, J. Chappellaz, T. Blunier, S. O. Rasmussen, A. Svensson, *Quat. Sci. Rev.* **29**, 2828–2838 (2010).
- E. Capron et al., *Clim. Past* **6**, 345–365 (2010).
- Materials and methods are available as supplementary materials.
- W. Duan, H. Cheng, M. Tan, R. L. Edwards, *Sci. Rep.* **6**, 20844–20846 (2016).
- H. Cheng et al., *Nature* **534**, 640–646 (2016).
- G. Kathayat et al., *Sci. Rep.* **6**, 24374–24377 (2016).
- S. Chen et al., *Sci. Rep.* **6**, 32995 (2016).
- H. Cheng et al., *Nat. Commun.* **4**, 1411–1416 (2013).
- G. E. Moseley et al., *Geology* **42**, 1043–1046 (2014).
- D. Fleitmann et al., *Geophys. Res. Lett.* **36**, L19707–L5 (2009).
- W. Dansgaard, *Tellus A, Dyn. Meteorol. Oceanogr.* **16**, 436–468 (1964).
- P. J. Rowe et al., *Quat. Sci. Rev.* **45**, 60–72 (2012).
- R. N. Drysdale et al., *Geology* **35**, 77–80 (2007).
- H. Cheng et al., *Geophys. Res. Lett.* **42**, 8641–8650 (2015).
- E. Hodge et al., *Radiocarbon* **53**, 345–357 (2011).
- I. Wendt, C. Carl, *Chem. Geol.* **86**, 275–285 (1991).
- P. W. Reiners et al., *Geochronology and Thermochronology* (John Wiley and Sons, 2018).
- P. Bajo et al., *Quat. Sci. Rev.* **148**, 17–28 (2016).
- A. Svensson et al., *Quat. Sci. Rev.* **25**, 3258–3267 (2006).
- F. Adolphi et al., *Clim. Past* **14**, 1755–1781 (2018).
- X. Zhang, G. Lohmann, G. Knorr, X. Xu, *Clim. Past* **9**, 2319–2333 (2013).
- M. Kageyama et al., *Clim. Past* **9**, 935–953 (2013).
- J. L. Rosen et al., *Nat. Geosci.* **7**, 459–463 (2014).
- G. Knorr, G. Lohmann, *Nature* **424**, 532–536 (2003).
- J. U. L. Baldini, R. J. Brown, J. N. McElwaine, *Sci. Rep.* **5**, 17442–17449 (2015).
- W. R. Peltier, G. Vettoretti, *Geophys. Res. Lett.* **41**, 7306–7313 (2014).
- E. Ruggieri, *Int. J. Climatol.* **33**, 520–528 (2012).

## ACKNOWLEDGMENTS

We thank all authors of the published speleothem records who made their data available online, shared their data, or provided further information about their records. **Funding:** E.C.C. was supported by an Australian Government Research Training Program Scholarship. J.C.H. was supported by an Australian Research Council Future Fellowship (FT130100801). E.C. is funded by the European Union's Seventh Framework Program for research and innovation under the Marie Skłodowska-Curie grant agreement 600207. S.O.R. and E.C. acknowledge the support of the Carlsberg Foundation. X.Z. is supported by Helmholtz Postdoc Program (PD-301), the National Key R&D Program of China (grant 2018YFA0606403), and Qingdao National Laboratory for Marine Science and Technology (QMLM201703). D.F. was supported by the Swiss National Science Foundation (PP002-110554/1). E.W. is supported by a Royal Society professorship. **Author contributions:** R.N.D., D.F., and E.W. proposed the initial research idea. E.C.C. collated and standardized the data sets, with assistance from J.C.H. and R.N.D. The analysis and interpretation of the results was performed by E.C.C., R.N.D., and J.C.H., with input from all authors. X.Z. designed and performed the model simulations. E.C.C. led the write up of the manuscript, with contributions from all authors. **Competing interests:** The authors declare no competing interests. **Data and materials availability:** The data reported in this paper are available in the supplementary materials.

## SUPPLEMENTARY MATERIALS

science.sciencemag.org/content/369/6506/963/suppl/DC1  
Materials and Methods  
Figs. S1 to S8  
Tables S1 to S4  
References (59–117)  
Data Files S1 to S7

17 July 2019; accepted 9 July 2020  
10.1126/science.aay5538

## REPORT

## ORGANIC CHEMISTRY

## Asymmetric remote C–H borylation of aliphatic amides and esters with a modular iridium catalyst

Ronald L. Reyes<sup>1,2</sup>, Miyu Sato<sup>2</sup>, Tomohiro Iwai<sup>2</sup>, Kimichi Suzuki<sup>1,2</sup>, Satoshi Maeda<sup>1,2</sup>, Masaya Sawamura<sup>1,2\*</sup>

Site selectivity and stereocontrol remain major challenges in C–H bond functionalization chemistry, especially in linear aliphatic saturated hydrocarbon scaffolds. We report the highly enantioselective and site-selective catalytic borylation of remote C(sp<sup>3</sup>)–H bonds  $\gamma$  to the carbonyl group in aliphatic secondary and tertiary amides and esters. A chiral C–H activation catalyst was modularly assembled from an iridium center, a chiral monophosphite ligand, an achiral urea-pyridine receptor ligand, and pinacoloboryl groups. Quantum chemical calculations support an enzyme-like structural cavity formed by the catalyst components, which bind the substrate through multiple noncovalent interactions. Versatile synthetic utility of the enantioenriched  $\gamma$ -borylcarboxylic acid derivatives was demonstrated.

Aliphatic carboxylic acids constitute one of the most fundamental and widespread compound classes in nature and serve as major feedstock chemicals. Metal-catalyzed activation and functionalization reactions of unactivated C(sp<sup>3</sup>)–H bonds in the saturated hydrocarbon frameworks of these substances have emerged as a straightforward methodology to access valuable chemicals and build up molecular complexity (1–10). Among those, the reactivities of  $\beta$ -C(sp<sup>3</sup>)–H

(1–6) bonds or  $\gamma$ -C(sp<sup>3</sup>)–H bonds (7–10) have been demonstrated under chelation-assisted strategies to form five- or six-membered metal-lacycles, respectively (Fig. 1A). In the  $\gamma$ -C–H functionalizations, however, the targeted C–H bonds belonged to terminal methyl groups branching from the aliphatic chains of the substrates. Thus far, the activation and subsequent functionalization of remote  $\gamma$ -methylene C–H bonds remain elusive, and hence their enantioselective transformations are highly challenging (Fig. 1A). The pioneering work of Breslow in the development of P-450 mimics for the hydroxylation of remote C(sp<sup>3</sup>)–H bonds in steroids using cyclodextrin-modified metalloporphyrins (11) inspired the creation

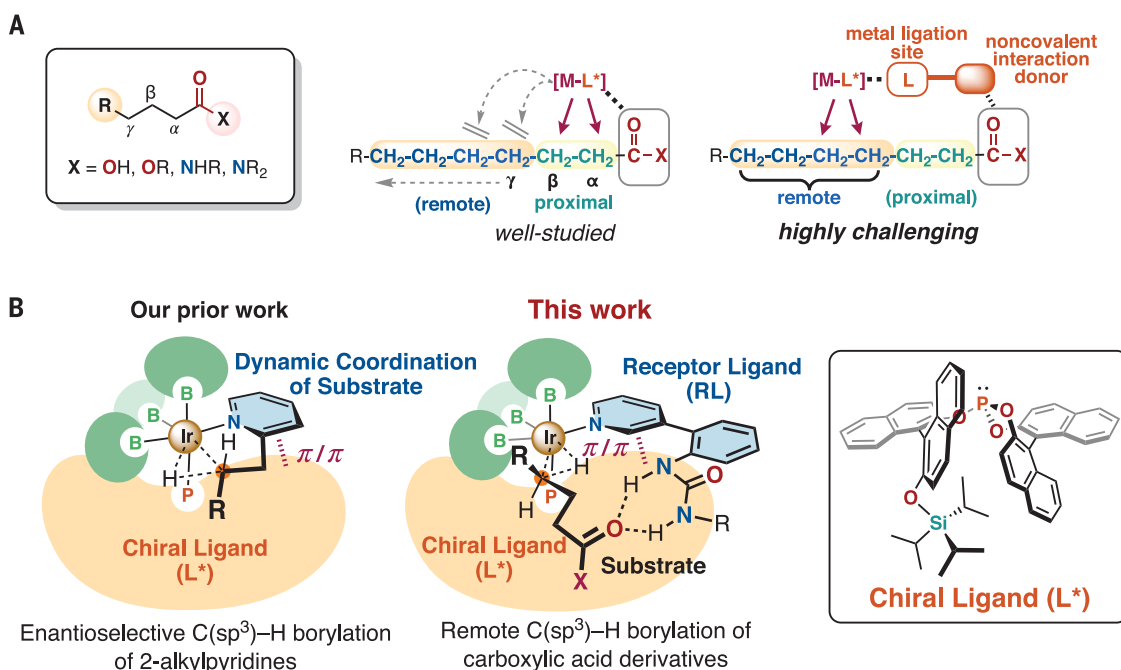
of various biomimetic systems (12, 13). Despite the conceptual advances of these systems, the elaborate preparations and limited substrate scopes hinder their utility in organic synthesis.

As another challenge for C–H activation, remote C(sp<sup>2</sup>)–H bond activation in arenes has also gained momentum recently. For instance, Yu reported the remote C(sp<sup>2</sup>)–H alkenylation of 3-phenylpyridines enabled by a template that binds to two metal centers (14). Kanai and Kuninobu introduced receptor ligands composed of a bipyridine metal-chelation moiety, derived from a well-established C–H borylation catalyst (15, 16), linked by an aromatic spacer to a urea-based hydrogen-bonding moiety, resulting in excellent regioselectivity for the Ir-catalyzed meta-selective C(sp<sup>2</sup>)–H borylation of benzamides and esters (17). More recently, Phipps demonstrated the viability of using ion-pairing interactions between a chiral cation and an anionic group linked to a bipyridine ligand bound to the iridium center for the desymmetrization of geminal diaryl motifs through meta-selective and enantioselective C(sp<sup>2</sup>)–H borylation (18).

We recently developed an enantioselective borylation of unactivated methylene C(sp<sup>3</sup>)–H bonds in 2-alkylpyridines (19) (Fig. 1B) with bis(pinacolato)diboron (pinB–Bpin) and further extended the reactivity to the enantioselective borylation of N-adjacent C(sp<sup>3</sup>)–H bonds in carboxamides and related compounds (20). We proposed that this catalytic system, consisting of a chiral monophosphite ligand (**L**<sup>\*</sup>) (21) and tris(boryl)iridium Ir(Bpin)<sub>3</sub> (15, 16), generates a binding cavity resembling an enzyme active site. The Ir catalyst recognizes the

**Fig. 1. Proximal and distal functionalizations of C–H bonds.** (A) Conceptual framework in the functionalization of both proximal and remote C–H bonds.

(B) Our proposed strategy for the borylation of a remote C(sp<sup>3</sup>)–H bond in aliphatic carboxylic acid derivatives.





pyridine moiety of the substrate through  $\pi/\pi$  interactions with one of the naphthalene rings of the phosphite, coupled with C-H/ $\pi$  and nonclassical C-H...O hydrogen bonds. This coordination leads to the differentiation of enantiotopic C(sp<sup>3</sup>)-H bonds (5, 6). Inspired by this reactivity and the outcome of quantum chemical calculations, we envisaged that

the metal-coordinating pyridine and the metal-activated C-H bond site linked intramolecularly within the chiral catalytic pocket might be replaced with a heterodimer composed of a pyridine-based receptor ligand and a noncovalent interaction donor moiety and a C(sp<sup>3</sup>)-H borylation substrate with a complementary functional group (Fig. 1B). Here, we report that

a modular approach for producing a chiral catalyst (22, 23) using a new urea-pyridine receptor ligand (**RL**) in combination with the chiral monophosphite-Ir catalyst system [Ir(Bpin)<sub>3</sub>-**L\***] led to the discovery of the highly enantioselective C(sp<sup>3</sup>)-H borylation of aliphatic carboxylic amides and esters that occurs specifically at the  $\gamma$ -methylene group.

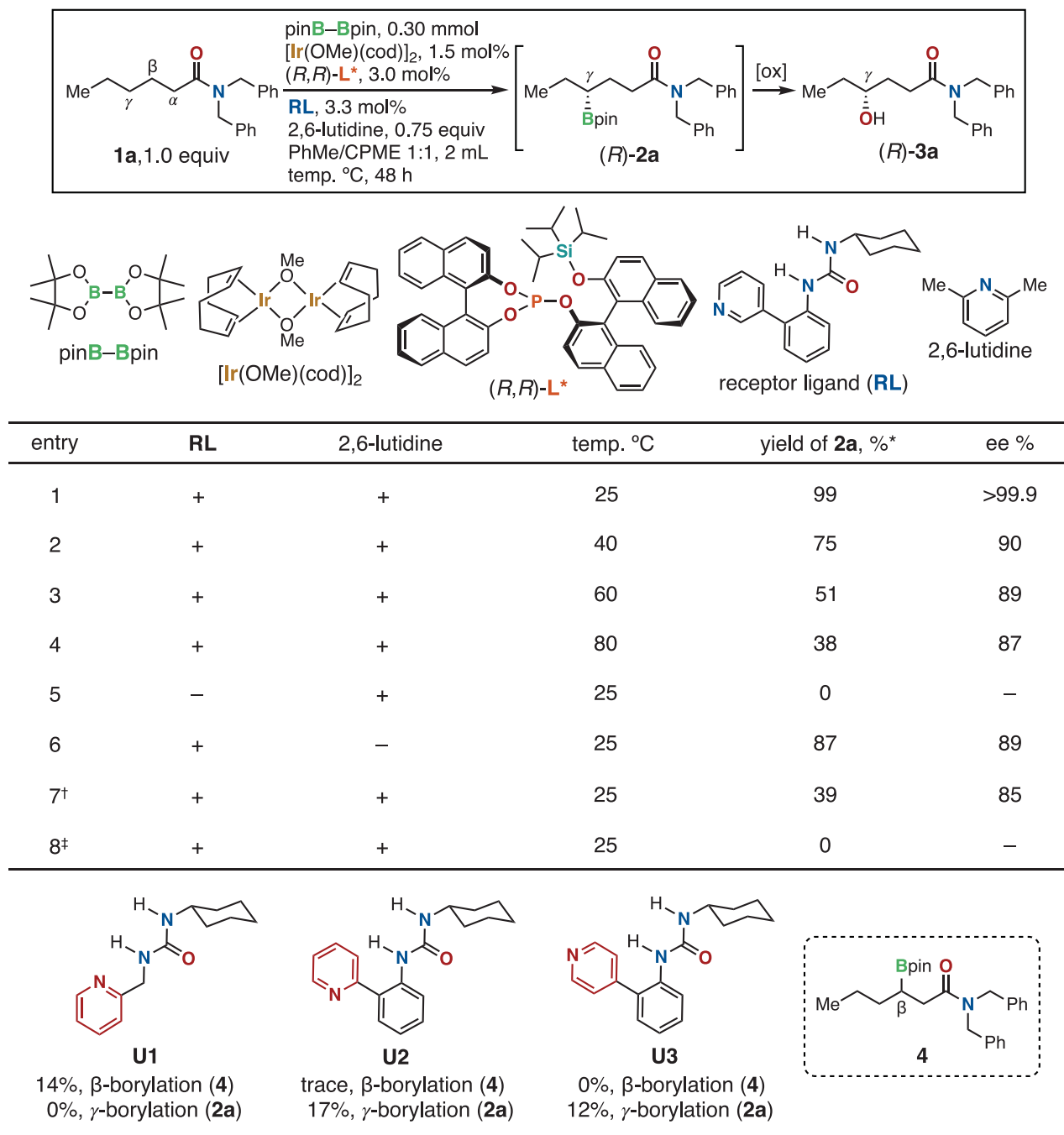


**Fig. 2. Enantioselective  $\gamma$ -C-H borylation of **1a** catalyzed by an Ir-**L\***-**RL** system.** Conditions: **1a** (0.30 mmol), [Ir(OMe)(cod)]<sub>2</sub> (1.5 mol %), **L\*** (3.0 mol %), urea-pyridine ligand **RL**, **U1–3** (3.3 mol %), pinB-Bpin (1 equiv), 2,6-lutidine (0.75 equiv), PhMe/CPME 1:1 (2 mL), temperature as stated above. In the cases when **U1–3** were used, the reactions were conducted at 25°C, 48 hours, in PhMe/

CPME 1:1 (2 mL). (+) and (–) indicate the presence or absence of **RL** or additive in the catalytic reaction, respectively. \*Yields of **2a** and **4** determined by <sup>1</sup>H NMR. †Reaction with 6 mol % **RL**. ‡Reaction conducted in the absence of **L\*** using 6 mol % **RL**. Conditions for the oxidation of **2a** to **3a**: NaBO<sub>3</sub>·4H<sub>2</sub>O (3.0 equiv), THF (tetrahydrofuran)/H<sub>2</sub>O 1:1 (2 mL), room temperature, 3 hours.

Preliminary molecular modeling based on our previous computational work (19) on the enantioselective borylation of 2-propylpyridine predicted that a simple urea-pyridine conjugate with an ortho-phenylene linker connected to one of the N atoms of urea and the 3-position of the pyridine such as **RL** would produce a chemical space suitable for the binding of aliphatic carboxylic acid derivatives that positioned one of the  $\gamma$ -C-H bonds in proximity to the Ir center (Fig. 1B). We then synthesized **RL** and found its exceptional utility as a receptor ligand to create an enantioselective  $\gamma$ -C-H borylation catalyst.

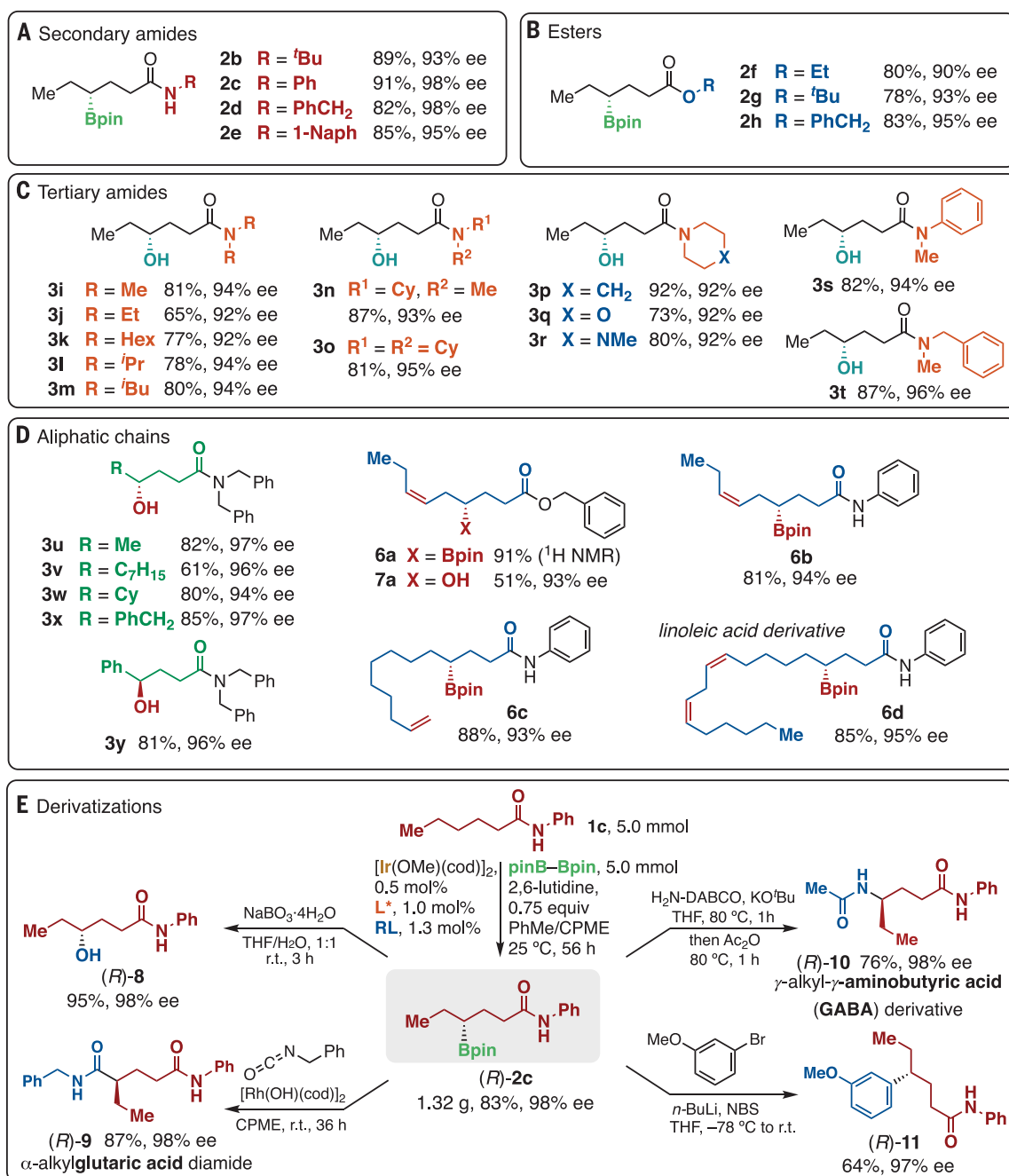
Specifically, the reaction between *N,N*-dibenzylhexanamide **1a** (0.3 mmol) and pinB-Bpin (1 equiv) in the presence of 2,6-lutidine additive (0.75 equiv) and an iridium catalyst prepared in situ from [Ir(OMe)(cod)]<sub>2</sub> (1.5 mol %), **L\*** (3 mol %), and **RL** (3.3 mol %) in toluene (PhMe)/cyclopentyl methyl ether (CPME) mixed solvent (PhMe/CPME 1:1, 2 ml) at 25°C over 48 hours occurred with complete substrate conversion and with exclusive site selectivity (>99:1) at the remote position  $\gamma$  to the carbonyl group of the aliphatic chain to produce alkylboronate **2a** [99% <sup>1</sup>H nuclear magnetic resonance (NMR) yield]. Virtually perfect

enantiocontrol was obtained as judged by high-performance liquid chromatography (HPLC) analysis of the corresponding secondary alcohol [(*R*)-**3a**, >99.9% enantiomeric excess (ee)] (Fig. 2, entry 1) (see table S4 for solvent effects).

The reactivity was hampered and the enantiocontrol was notably diminished by increasing the reaction temperature from 25°C over a range up to 80°C (Fig. 2, entries 1 to 4, no side product was detected). The observed negative temperature-reactivity correlation is supportive of the postulated substrate binding through the urea-carbonyl hydrogen bonding, which should be less favorable at higher

**Fig. 3. Substrate scope of the enantioselective  $\gamma$ -methylene C-H borylation and product transformation.** Reaction conditions for (A) to (D) Substrates

**1b-y**, **5a-d** (0.30 mmol), pinB-Bpin (1 equiv), [Ir(OMe)(cod)]<sub>2</sub> (1.5 mol %), **L\*** (3.0 mol %), **RL** (3.3 mol %), PhMe/CPME 1:1 (2 ml), 25°C, 48 hours. For the reactions of **1v** and **5a-d**, the reaction time was 56 hours. Yields are those for the isolated products (**2b-h**, **3i-y**, **6a-d**). Conditions for the oxidation reaction in the case of tertiary amides: NaBO<sub>3</sub>·4H<sub>2</sub>O (3.0 equiv), THF/H<sub>2</sub>O 1:1 (2 ml), room temperature, 3 hours. (A) Secondary carboxamides, (B) ester derivatives, (C) tertiary amides, and (D) aliphatic carboxylic acid derivatives with different alkanoil groups. (E) Gram-scale preparation of (*R*)-**2c** (Ir-**L\***: 1 mol %) and its derivatizations. DABCO, 1,4-diazabicyclo [2.2.2]octane. NBS, *N*-bromosuccinimide.





temperature. The borylation did not proceed at all in the absence of **RL** (entry 5). Unfavorable effects on the yield and enantioselectivity were apparent in the absence of 2,6-lutidine (entry 6) in accord with our prior works (19, 20). Increasing the **RL** loading (6 mol %) led to diminished yield and enantioselectivity (entry 7). The absence of **L\*** in the presence of **RL** (6 mol %, two equiv to Ir) fully impeded the reaction (entry 8). The catalytic reaction of **1a** using the antipode of the ligand, (*S,S*)-**L\*** gave the identical result but with the opposite absolute configuration of the product.

Effects of the structure of the urea-pyridine ligands are also summarized in Fig. 2 (see fig. S1 for the effects of other derivatives). The use of a pyridine-urea ligand (**U1**) with a methylene linker at the pyridine 2-position instead of **RL** redirected the site selectivity toward the borylation of a proximal  $\beta$ -methylene C–H bond (14%  $^1\text{H}$  NMR yield for **4**). Changing the linker from the methylene group in **U1** back to the *ortho*-phenylene group in **U2** led again to activation of the  $\gamma$ -C–H bond, giving **2a** (17%) but still with a trace amount of the  $\beta$ -borylation product. The 4-pyridyl isomer **U3** delivered only  $\gamma$ -C–H borylation product **2a** but with a low product yield (12%).

The enantioselective borylation also occurred in high yields and excellent site- and enantioselectivities with secondary carboxamides (**1b–e**, Fig. 3A, see caption) and esters (**1f–h**, Fig. 3B, see caption). In these cases, the secondary alkylboronate products (**2b–h**) were sufficiently stable to be isolated by silica gel column chromatography. *N*-(*t*-Butyl)hexanamide was borylated site selectively at the  $\gamma$ -methylene C–H bond of the aliphatic hydrocarbon backbone, giving **2b** (93% ee). The *N*-*t*-butyl group, which has terminal  $\text{C}(\text{sp}^3)\text{--H}$  bonds  $\gamma$  to the carbonyl group, remained intact. Hexanoic acid anilide similarly gave **2c** with excellent enantioselectivity (98% ee). The  $\text{C}(\text{sp}^2)\text{--H}$  bonds in the *N*-phenyl group, which are also located  $\gamma$  to the carbonyl group, stayed unaffected. Likewise, *N*-benzyl and *N*-1-naphthylhexanamide derivatives delivered **2d** (98% ee) and **2e** (95% ee) as the sole products, respectively. Esters were equally amenable. Ethyl hexanoate gave **2f** (90% ee) exclusively, resulting from the activation of a methylene  $\gamma\text{-C}(\text{sp}^3)\text{--H}$  bond in the aliphatic acyl group rather than the terminal methyl C–H bonds in the alkoxy group. Enhanced enantioselectivities were observed in the case of *t*-butyl and benzyl hexanoic acid esters, giving **2g** (93% ee) and **2h** (95% ee), respectively.

Complementary to the reactivity of **1a**, various *N,N*-disubstituted hexanamides with different *N*-substituents were suitable substrates (Fig. 3C). Thus, substrates with linear or branched *N,N*-dialkylamino groups, including methyl (**1i**), ethyl (**1j**), hexyl (**1k**),

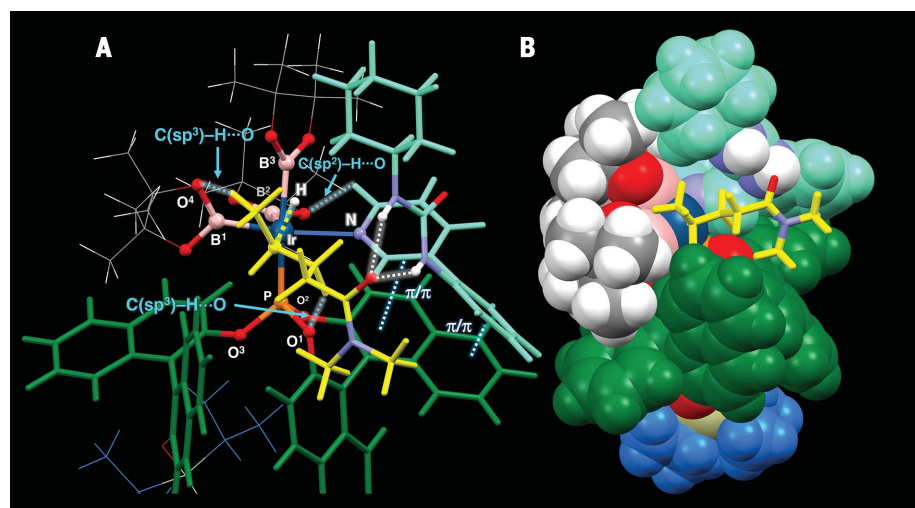


**Fig. 4. Three-dimensional representation of the calculated transition state (TS) leading to the major enantiomer. (A)** The geometrical features of TS-R showing  $\text{C}(\text{sp}^3)\text{--H}\cdots\text{O}$  and  $\pi/\pi$  noncovalent interactions between the substrate and the modular catalyst. **(B)** The space-filling model shows the reaction cavity and the efficient fitting of the substrate within the catalytic pocket. The binaphthyl frameworks of **L\*** are shown in green, the isopropyl (*iPr*) groups in the triisopropylsilyl (TIPS) moiety of **L\*** in blue, the **RL** in cyan, and the substrate in yellow.

isopropyl (**1l**), and isobutyl (**1m**) groups, underwent the borylation followed by the mild stereoretentive oxidation with  $\text{NaBO}_3$  with exclusive site selectivity to the  $\gamma$ -C–H bond (92 to 94% ee) of the hexanamide chain. *N*-Cyclohexyl-*N*-methyl- and *N,N*-dicyclohexylhexanamides were converted to **3n** (93% ee) and **3o** (95% ee), respectively. Hexanamides with cyclic amine moieties, including piperidine (**1p**), morpholine (**1q**), and *N*-methylpiperazine (**1r**), likewise participated in the reaction (92% ee). Hexanamides bearing *N*-methylaniline and *N*-methyl-*N*-benzylamine moieties similarly gave **3s** (94% ee) and **3t** (96% ee) as the sole products, respectively.

The applicability of the protocol toward various carboxamides with different aliphatic chains was investigated for *N,N*-dibenzyl-substituted amide derivatives (Fig. 3D). The valeric acid derivative, one carbon shorter than **1a**, gave **3u** with excellent enantioselectivity (97% ee). The undecylic acid derivative underwent the borylation at the C-4,  $\gamma$ -C–H bond to deliver product **3v** (96% ee). The borylation of more congested substrates with cyclohexyl (**1w**), benzyl (**1x**), or phenyl (**1y**) groups at the  $\gamma$ -methylene carbon also proceeded smoothly (94 to 97% ee), demonstrating the substantial tolerance of this protocol toward steric hindrance, whereas the sense of enantioselection was reversed for the reaction of the phenyl-substituted amide (**3y**).

The protocol was also applicable to unsaturated alkenoic acid derivatives (**5a–d**) (Fig. 3D). Thus, the benzyl ester (**5a**) of 6-nonenic acid gave the homoallylic alcohol **7a** (93% ee) upon oxidation of the  $\gamma$ -boryl product (**6a**), whereas the anilide (**5b**) delivered the  $\gamma$ -boryl- $\omega$ -3-*N*-phenylnonenamide **6b** (94% ee). Fur-

thermore, the anilide (**5c**) of 12-tridecenoic acid with a distal terminal alkene moiety gave **6c** (93% ee) as the only product. The reaction of the anilide (**5d**) of linoleic acid gave **6d** (95% ee) exclusively without any trace of side reactions such as alkene migration in either the product (85%) or the recovered substrate (12%).

Figure 3E showcases the synthetic utility of the borylation protocol by the transformations of the  $\gamma$ -borylhexanoic acid anilide (*R*)-**2c**. A lower loading (1 mol %) of the Ir-**L\*** catalyst enabled the gram-scale synthesis of (*R*)-**2c** (1.32 g, 83%) from **1c** without erosion of the enantioselectivity. Subsequently, mild oxidation of (*R*)-**2c** provided the corresponding alcohol (*R*)-**8**. The Rh-catalyzed stereoretentive carboboration (19) of (*R*)-**2c** to benzyl isocyanate gave the enantioenriched  $\alpha$ -alkylglutaric acid diamide (*R*)-**9**. The amination of (*R*)-**2c** allowed direct access to a pharmacologically interesting  $\gamma$ -alkyl- $\gamma$ -aminobutyric acid (GABA) derivative [(*R*)-**10**] (24). The transition-metal free cross-coupling between (*R*)-**2c** and 3-bromoanisole (25) furnished the  $\gamma$ -arylated derivative (*R*)-**11** (98% ee).

To gain insight into the structural features of the modular chiral catalyst as proposed in Fig. 1B, we performed preliminary quantum chemical calculations, focusing on C–H bond cleavage by the catalyst, employing *N,N*-dimethylpentanamide as a model substrate, Ir(Bpin)<sub>3</sub>-**L\*** as the catalyst backbone, and **RL** as the receptor ligand. We used the GFN2-xTB method (26) and the artificial force-induced reaction (AFIR) method (27, 28) to explore various conformations of **RL** and the amide substrate associated with the cleavage of the C–H bonds of the hydrogen-bonded

substrate. A three-dimensional (3D) representation of the transition state leading to the major enantiomer, which was optimized without artificial force at the GFN2-xTB level of theory and further refined by the M06-L density functional including D3 empirical dispersion correction (SDD for Ir, 6-31G\*), is shown in Fig. 4A. The space-filling representation is given in Fig. 4B. An accessible surface is formed as a deep cavity created by the modular catalyst that presents the urea hydrogen-bonding site at the outer rim with the Ir atom at the bottom of the groove. One of the naphthalene rings of **L\*** has  $\pi/\pi$  interactions not only with the pyridine moiety but also with the *ortho*-phenylene linker of **RL**, forming a well-defined multicomponent catalyst assembly (see fig. S12 for a plot of noncovalent interactions and movies S1 and S2 for overall views of the calculated transition state).

The amide substrate, which adopts a normal extended conformation, is bound in the cavity not only through hydrogen bonding with the urea moiety, but also through other noncovalent interactions with the inner surface of the cavity (Fig. 4). The urea donates two N–H bonds to the amide carbonyl group, resulting in bidentate hydrogen bonding. The noncovalent interactions donated by the catalyst surface include two C(sp<sup>3</sup>)–H...O interactions (19, 29): one between the  $\beta$ -C–H bond and O<sup>1</sup> of the phosphite ligand **L\***, and the other between the C–H bond of the terminal Me group and O<sup>4</sup> of the B<sup>1</sup>pin ligand. In addition, London dispersion interactions seem to contribute to the substrate binding in the catalytic cavity. The 3D representations highlight that whereas the *pro-R*- $\gamma$ -C–H bond of

the substrate is activated by the Ir atom, the terminal methyl substituent at the stereogenic center is situated at the topmost vicinity of the reaction pocket, thereby avoiding any steric clash with the catalyst.

## REFERENCES AND NOTES

- V. G. Zaitsev, D. Shabashov, O. Daugulis, *J. Am. Chem. Soc.* **127**, 13154–13155 (2005).
- Y. Zhu *et al.*, *Nat. Commun.* **8**, 14904 (2017).
- Z. Zhuang *et al.*, *J. Am. Chem. Soc.* **140**, 10363–10367 (2018).
- Z. Zhuang, J.-Q. Yu, *Nature* **577**, 656–659 (2020).
- T. G. Saint-Denis, R.-Y. Zhu, G. Chen, Q.-F. Wu, J.-Q. Yu, *Science* **359**, eaao4798 (2018).
- C. G. Newton, S.-G. Wang, C. C. Oliveira, N. Cramer, *Chem. Rev.* **117**, 8908–8976 (2017).
- S. Li, G. Chen, C.-G. Feng, W. Gong, J.-Q. Yu, *J. Am. Chem. Soc.* **136**, 5267–5270 (2014).
- S. Li, R.-Y. Zhu, K.-J. Xiao, J.-Q. Yu, *Angew. Chem. Int. Ed.* **55**, 4317–4321 (2016).
- N. Thrimurtulu, S. Khan, S. Maity, C. M. R. Volla, D. Maiti, *Chem. Commun.* **53**, 12457–12460 (2017).
- P. Dolui, J. Das, H. B. Chandrashekar, S. S. Anjana, D. Maiti, *Angew. Chem. Int. Ed.* **58**, 13773–13777 (2019).
- R. Breslow, X. Zhang, Y. Huang, *J. Am. Chem. Soc.* **119**, 4535–4536 (1997).
- S. Das, C. D. Incavito, R. H. Crabtree, G. W. Brudvig, *Science* **312**, 1941–1943 (2006).
- G. Olivo *et al.*, *Angew. Chem. Int. Ed.* **56**, 16347–16351 (2017).
- Z. Zhang, K. Tanaka, J.-Q. Yu, *Nature* **543**, 538–542 (2017).
- T. Ishiyama *et al.*, *J. Am. Chem. Soc.* **124**, 390–391 (2002).
- T. M. Boller *et al.*, *J. Am. Chem. Soc.* **127**, 14263–14278 (2005).
- Y. Kuninobu, H. Ida, M. Nishi, M. Kanai, *Nat. Chem.* **7**, 712–717 (2015).
- G. R. Genov, J. L. Douthwaite, A. S. K. Lahdenperä, D. C. Gibson, R. J. Phipps, *Science* **367**, 1246–1251 (2020).
- R. L. Reyes, T. Iwai, S. Maeda, M. Sawamura, *J. Am. Chem. Soc.* **141**, 6817–6821 (2019).
- R. L. Reyes, M. Sato, T. Iwai, M. Sawamura, *J. Am. Chem. Soc.* **142**, 589–597 (2020).
- R. L. Reyes, M. Sawamura, (2020). Dinaphtho[2,1-d':1',2'-f][1,3,2]dioxaphosphin, 4-[[[(1*R*)-2'-[(triisopropylsilyl)oxy][1,1'-binaphthalen]-2-yl]oxy]-, (1*lbR*)-(9*Cl*). In *Encyclopedia of Reagents for Organic Synthesis*. doi: 10.1002/047084289X.rm02326
- J. Wieland, B. Breit, *Nat. Chem.* **2**, 832–837 (2010).

- M. Raynal, P. Ballester, A. Vidal-Ferran, P. W. N. M. van Leeuwen, *Chem. Soc. Rev.* **43**, 1660–1733 (2014).
- X. Liu *et al.*, *Angew. Chem. Int. Ed.* **59**, 2745–2749 (2020).
- G. Wang *et al.*, *Angew. Chem. Int. Ed.* **58**, 8187–8191 (2019).
- C. Bannwarth, S. Ehlert, S. Grimme, *J. Chem. Theory Comput.* **15**, 1652–1671 (2019).
- S. Maeda, Y. Harabuchi, M. Takagi, T. Taketsugu, K. Morokuma, *Chem. Rec.* **16**, 2232–2248 (2016).
- S. Maeda, K. Ohno, K. Morokuma, *Phys. Chem. Chem. Phys.* **15**, 3683–3701 (2013).
- M. C. Schwarzer *et al.*, *Chem. Sci.* **9**, 3484–3493 (2018).

## ACKNOWLEDGMENTS

**Funding:** This work was supported by JSPS KAKENHI grant no. JP15H05801 in Precisely Designed Catalysts with Customized Scaffolding and JSPS KAKENHI grant no. JP18H03906 in Grant-in-Aid for Scientific Research (A) to M. Sawamura, by JSPS KAKENHI grant no. 20K15269 in Grant-in-Aid for Early Career Scientists to R.L.R., and by the Uehara Memorial Foundation to T.I. **Author contributions:** M. Sawamura, T.I., and R.L.R. conceived and designed the experiments. R.L.R. and M. Sato performed the experiments along with the preparation of the supplementary materials. K.S. and S.M. performed the quantum chemical calculations. M. Sawamura supervised the entire project. All authors discussed the results and helped in writing the manuscript. **Competing interests:** M.S., R.L.R., T.I., and S.M. are inventors of patent application JP, 2020-133238 submitted by Hokkaido University that covers urea-pyridine-type monodentate ligands, borylation catalysts, and methods for preparation of organoboron compounds using the catalysts. The authors declare no other competing interests. **Data and materials availability:** Characterization data for all compounds in this study, along with details of the calculations and optimization of transition states, are available in the supplementary materials.

## SUPPLEMENTARY MATERIALS

science.sciencemag.org/content/369/6506/970/suppl/DC1  
Materials and Methods  
Figs. S1 to S12  
Tables S1 to S4  
HPLC Data  
NMR Spectra  
Movies S1 and S2  
References (30–70)

16 May 2020; accepted 29 June 2020  
10.1126/science.abc8320



## CHEMICAL PHYSICS

## Attosecond spectroscopy of liquid water

Inga Jordan, Martin Huppert\*, Dominik Rattenbacher†, Michael Peper, Denis Jelovina, Conaill Perry, Aaron von Conta, Axel Schild, Hans Jakob Wörner‡

Electronic dynamics in liquids are of fundamental importance, but time-resolved experiments have so far remained limited to the femtosecond time scale. We report the extension of attosecond spectroscopy to the liquid phase. We measured time delays of 50 to 70 attoseconds between the photoemission from liquid water and that from gaseous water at photon energies of 21.7 to 31.0 electron volts. These photoemission delays can be decomposed into a photoionization delay sensitive to the local environment and a delay originating from electron transport. In our experiments, the latter contribution is shown to be negligible. By referencing liquid water to gaseous water, we isolated the effect of solvation on the attosecond photoionization dynamics of water molecules. Our methods define an approach to separating bound and unbound electron dynamics from the structural response of the solvent.

The study of liquid water has been at the heart of physical sciences since their emergence. Although undoubtedly the most studied liquid, water has properties that are still not entirely understood. Water displays more than 70 anomalies in its physical properties (1–3), such as density, heat capacity, or thermal conductivity. Even the structure of liquid water with its rapidly fluctuating hydrogen-bond network remains an object of intense debate (4–7). Many open questions are associated with liquid water, and their far-reaching implications explain the considerable attention that it has always attracted. A wide variety of experimental techniques have therefore been applied to its study, including nuclear magnetic resonance (8), infrared (IR) spectroscopy (9), x-ray spectroscopies (10), and x-ray scattering (11).

Despite these considerable efforts, many properties of liquid water remain mysterious. This fact is partially the consequence of a mismatch between the temporal resolution of the available techniques and the ultrafast dynamics of liquid water. A prominent example is the observation of a splitting in the x-ray emission spectrum of the outermost valence band of liquid water, which is assigned either to two structural motifs of liquid water, differing in their hydrogen-bond structure (12), or to dynamics in the core-hole state (13). Differentiation of these two interpretations would require subfemtosecond temporal resolution. Hence, probing liquid water on ever shorter time scales may allow for a better understanding of at least some of its unusual properties.

Here, we used attosecond spectroscopy to study liquid water. Whereas isolated molecules of increasing complexity have been studied

with attosecond temporal resolutions (14–17), a deeper understanding of electronic dynamics in real chemical and biological processes requires an extension of attosecond science to the liquid phase. As the main distinguishing feature relative to most femtosecond spectroscopies, the inherent time scale of the present measurements freezes all types of structural dynamics, leaving only the fastest electronic dynamics as possible contributions.

We concentrated on the measurement of time delays in photoemission. Previous measurements on atoms (18, 19) and molecules (17, 20), with supporting theoretical work (21–23), established that such experiments access photoionization delays caused by the propagation of the photoelectron through the potential created by the parent ion. Similar measurements on metals (24–26) revealed the dominant influence of the electron transport time from the point of ionization to the surface. The additional role of initial-state and final-state effects was highlighted in (27–29). Recent work on nanoparticles (30) interpreted the time delays as being dominantly sensitive to inelastic scattering times on the basis of purely classical simulations that neglected the time delays due to photoionization and scattering. Here, we developed a model that describes such time delays on a fully quantum mechanical level and combined it with a semiclassical-trajectory Monte Carlo simulation of electron transport, which includes elastic and inelastic electron scattering, the quantum mechanical phase accumulated along all possible electron trajectories, and the resulting interference effects. We show that, in general, the measured time delays encode both scattering delays and mean free paths in addition to the photoemission delay.

The concept of our measurement is illustrated in Fig. 1. We used attosecond interferometry to measure the time delay between the photoemission from liquid water and that from gaseous water. Liquid water was introduced into a vacuum chamber through a

quartz nozzle with an inner diameter of ~25  $\mu\text{m}$ . Evaporation from the jet created the surrounding gas phase. An extreme ultraviolet (XUV) attosecond pulse train (APT), obtained through high-harmonic generation of a ~30-fs near-IR laser pulse in an argon gas cell, was focused onto the liquid microjet (spot size ~50  $\mu\text{m}$ ) together with a strongly attenuated replica of the IR laser pulse. This resulted in the detection of electrons from both phases simultaneously. [See (31) for details of the experimental setup.]

The photoelectron signals from the liquid phase were shifted and broadened relative to the gas-phase signals, which enabled their discrimination. Photoemission induced by the APT created several replicas of the photoelectron spectra (Fig. 1, blue). The simultaneous presence of the APT and IR pulses resulted in the formation of sideband spectra (Fig. 1, red). Because these sidebands can be created through two different quantum pathways, their intensity oscillates as a function of the delay between the APT and IR pulses.

A general challenge in attosecond time-resolved measurements originates from the spectral bandwidth of attosecond pulses. The resulting spectral congestion is considerably reduced by using an APT (17, 32). Nonetheless, most complex systems usually have broad photoelectron spectra, which makes the application of attosecond photoelectron spectroscopy difficult. This challenge has been addressed by using metallic filters to reduce the spectral overlap (17, 19) and additionally performing an energy-dependent analysis of the sideband oscillation phases (32, 33). In the general case of broad overlapping photoelectron spectra, these approaches are no longer sufficient. We therefore combined these ideas with a general approach: the complex-valued principal components analysis (CVPCA) that was numerically validated in (34).

Figure 2 shows the experimental results obtained with APTs transmitted through Sn or Ti filters, respectively, resulting in a spectral restriction to harmonic orders 11, 13, and 15 (Sn) or 17, 19, and 21 (Ti). Shown in Fig. 2, A and B, are the photoelectron spectra recorded in the absence (blue circles) or presence (orange circles) of the IR field; Fig. 2, C and D, shows the difference spectrum (“IR on” – “IR off”; black circles) recorded on a single-shot basis by chopping the IR beam at half of the laser repetition rate. The spectra are dominated by the photoelectrons originating from the highest valence band of liquid water (light blue), the highest occupied molecular orbital (HOMO) of isolated water molecules (dark blue), and the respective sidebands (light and dark orange, respectively).

To achieve the highest accuracy, we based the analysis on principal component spectra

Laboratorium für Physikalische Chemie, ETH Zürich, Zürich, Switzerland.

\*Present address: Paul Scherrer Institut, CH-5232 Villigen PSI, Switzerland. †Present address: Max Planck Institute for the Science of Light, D-91058 Erlangen, Germany.

‡Corresponding author. Email: hwoerner@ethz.ch

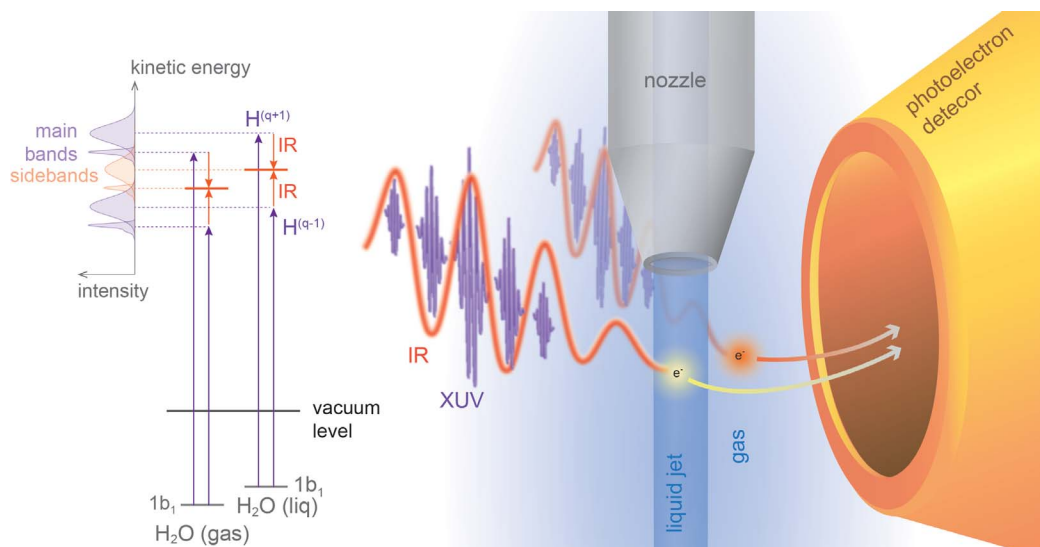


**Fig. 1. Attosecond time-resolved photoelectron spectroscopy of liquid water.**

A spectrally filtered attosecond pulse train composed of a few high-harmonic orders (such as  $H^{(q-1)}$  and  $H^{(q+1)}$ ), superimposed with a near-IR femtosecond laser pulse, interacts with a microjet of liquid water. Photoelectrons are simultaneously emitted from the liquid and the surrounding gas phase. The resulting photoelectron spectra are measured as a function of the time delay between the overlapping pulses.

that were measured with the same liquid-microjet photoelectron spectrometer (35), but replacing the APT with isolated high-order harmonics selected in a time-preserving monochromator (36). [See (31) and fig. S1 for the corresponding photoelectron spectra obtained with harmonics 11 to 21.] These principal components were used to decompose the photoelectron and difference spectra in Fig. 2 into the individual contributions of the high-harmonic orders and the two phases of water. Positive contributions in the difference spectra (Fig. 2, C and D) represent sidebands, whereas the negative contributions originate from the depletion of the main photoelectron bands.

Figure 2, E and F, shows the difference spectra as a function of the APT-IR delay. Distinct oscillations with a period of 1.33 fs can be observed in both spectrograms in the spectral regions corresponding to both gas- and liquid-phase contributions. Figure 2, G and H, shows the power spectrum of the Fourier transform of Fig. 2, E and F. These images reveal the presence of the expected  $2\omega$  oscillations (where  $\omega$  is the angular frequency of the IR laser).

Figure 2, I and J, shows the complex-valued Fourier transform of Fig. 2, E and F, obtained by integration over the width of the  $2\omega$  peak. Note that the phases (blue circles in Fig. 2, I and J) are not flat but vary across most energy ranges, as do the amplitudes (green triangles). We find that our CVPCA fully reproduces the complex-valued Fourier transform by attributing a unique phase shift and modulation depth to each of the principal components (37).

This analysis reliably provides the time delays between photoemission from the liquid and gas phases as  $\Delta\tau = \tau_{\text{liq}} - \tau_{\text{gas}} = (\phi_{\text{liq}} - \phi_{\text{gas}})/2\omega$ . In the case of sideband 14 (21.7 eV photon energy), we obtain  $\Delta\tau = 69 \pm 20$  as; in the case of sideband 20 (31.0 eV photon energy), we

obtain  $\Delta\tau = 49 \pm 16$  as. The statistical analyses leading to these results are given in table S1 and figs. S4 and S5 (37). The positive sign of the relative delays indicates that the electrons from liquid water appear to be emitted later than those from water vapor.

The modulation depth  $M$ , where  $M = 1$  signifies a perfect contrast of the sideband oscillation, is also observable. In the gas phase, values of  $M \geq 0.95$  are usually observed [see, e.g., figures 1 and 2 of (17) for an experiment using the same apparatus and nearly identical experimental conditions]. In the gas phase, deviations of  $M$  from unity are caused by the incoherent superposition of oscillations with different phase shifts, experimental imperfections, and/or small differences in the amplitudes of the two quantum paths leading to the same sideband state. Here, we concentrated on the analysis of the relative modulation depths between the liquid- and gas-phase signals, which eliminates the latter two effects. The relative modulation depths, defined as  $M_r = M_{\text{liq}}/M_{\text{gas}}$ , amount to  $0.17 \pm 0.03$  and  $0.45 \pm 0.06$  in the case of sidebands 14 and 20, respectively.

The near-field distributions around the liquid microjet were calculated with finite-element time-dependent methods (see figs. S6 and S7). The near-field distributions make a negligible contribution to the delay of  $\tau_{\text{liq}} - \tau_{\text{gas}} = -5$  as. Moreover, they cause a reduction of the modulation contrast of 3% for the liquid phase and 6% for the gas phase. Both effects are opposite in trend to the measured results and are much smaller in magnitude.

Attosecond interferometry in liquids can be understood as a fully coherent combination of photoionization and electron scattering during transport to the surface of the jet (Fig. 3). Our previous analysis (37) has shown that such experiments can be rationalized by combining

the laser-assisted photoelectric effect (LAPE) with laser-assisted electron scattering (LAES). We distinguish “local” pathways, when the XUV and IR fields act at the same location in space, from “nonlocal” pathways where the XUV interaction (photoionization) and IR interaction (LAES) take place at different spatial positions.

For clarity we first discuss the one-dimensional case, modeling photoionization with an attractive potential and electron-water scattering with a shallower repulsive potential (Fig. 4). For sufficiently high photon energies, a single collision results in a total delay that oscillates between  $\tau^{\text{PI}} + \tau^{\text{sca}}$  and  $\tau^{\text{PI}} - \tau^{\text{sca}}$ , where  $\tau^{\text{PI}}$  and  $\tau^{\text{sca}}$  are the Wigner delays for photoionization and scattering, respectively, as a function of the distance between the locations of LAPE and LAES with a spatial period  $L = 4\pi/(k_{q+1} - k_{q-1})$  as shown in Fig. 4B. This oscillation is caused by the interference between local and nonlocal pathways along which the photoelectron wave packets have accumulated different amounts of phase because of their different central momenta ( $k_{q-1}$ ,  $k_q$ , or  $k_{q+1}$ ). In the presence of an exponential distribution of path lengths, corresponding to a given elastic mean free path (EMFP), the observed delay monotonically decays from  $\tau^{\text{PI}} + \tau^{\text{sca}}$  to  $\tau^{\text{PI}}$  (37). In the case of  $n = \text{IMFP}/\text{EMFP}$  elastic collisions, where IMFP is the inelastic mean free path, the total delay decays from  $\tau^{\text{PI}} + \tau^{\text{sca}}$  to  $\tau^{\text{PI}}$  about  $n$  times faster (Fig. 4C).

We hence draw the (general) conclusion that in the limit  $\text{EMFP} \ll L/n$  (or  $\text{IMFP} \ll L$ ), the classical limit is reached and the total delay is simply the sum of the photoionization and all scattering delays. In the opposite limit ( $\text{EMFP} \gg L/n$ , i.e.,  $\text{IMFP} \gg L$ ), the effects of the scattering delays cancel, such that the total delay becomes equal to the photoionization delay.



The MFPs of slow ( $\leq 50$  eV) electrons in liquid water are extremely difficult to calculate and no reliable experimental measurements exist, as summarized in (38). Therefore, we developed an approach to determine the elastic and inelastic MFPs based on first-principles

electron-molecule scattering calculations to determine the differential scattering cross section (DCS) for electron scattering with liquid water (39). These DCSs are used in a trajectory Monte Carlo simulation to uniquely determine the unknown EMFPs and IMFPs,

required to describe electron scattering event by event, from two recent experimental measurements (40, 41). Details of this procedure are given in (39). The EMFP amounts to 0.56 nm and the IMFP to 3.8 nm at the kinetic energy corresponding to sideband 14. At the kinetic

**Fig. 2. Attosecond photoelectron spectra of liquid and gaseous water.** Data were acquired with a Sn-filtered APT (left) or a Ti-filtered APT (right).

(A and B) Photoelectron spectra in the absence (blue) and presence (orange) of the IR field with their principal components fit (full lines) and decomposition (filled curves). (C and D) Difference spectra (circles), principal components fit (line), and decomposition (filled curves) into sidebands (orange) and depletion (blue). (E and F) Difference spectra as a function of the APT-IR time delay. (G and H) Fourier-transform power spectrum of (E) and (F). (I and J) Amplitude and phase of the  $2\omega$  component of the Fourier transform.

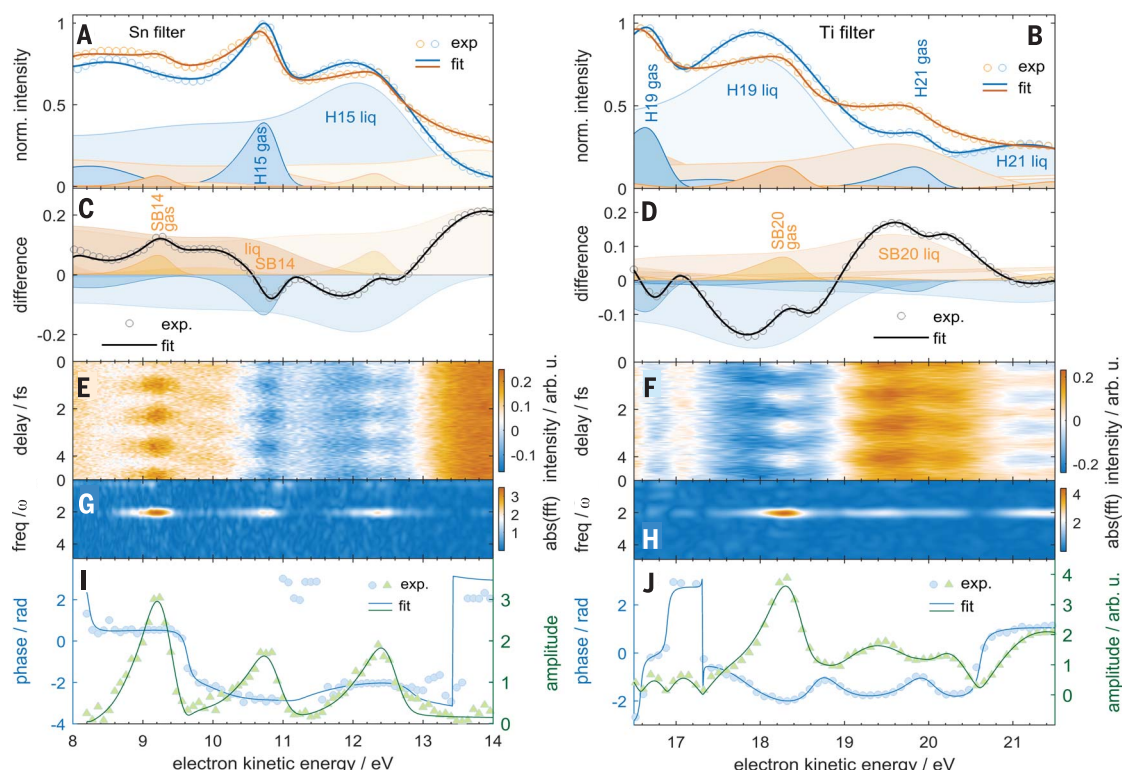
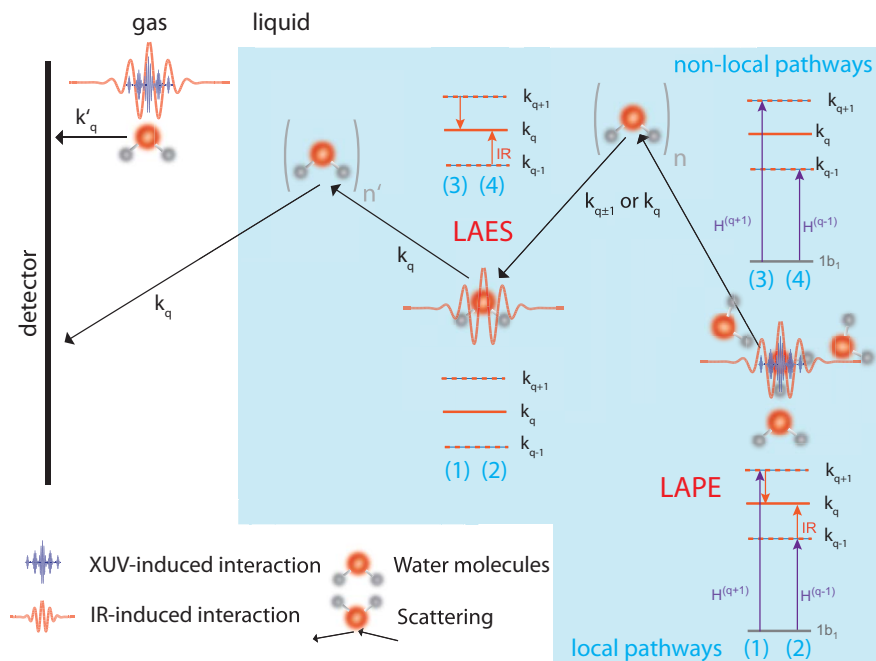


**Fig. 3. Physical mechanisms of attosecond interferometry in liquid water.** In the gas phase, the XUV- and IR-induced interactions are both localized to the same molecule.

In the condensed phase, we distinguish “local” pathways [(1) and (2)], followed by additional scattering events without exchange of photons, from “nonlocal” pathways [(3) and (4)], consisting of ionization followed by one laser-assisted scattering event (including exchange of one photon with the IR field) among  $n + n'$  non-laser-assisted collisions. Along the local pathways, photoelectron wave packets with central momenta  $k_q$  are launched. The nonlocal pathways correspond to the launch of wave packets with central momenta  $k_{q-1}$  and  $k_{q+1}$  that are converted to a central momentum  $k_q$  through a remote LAES interaction.



energy corresponding to sideband 20, the EMFP amounts to 0.84 nm and the IMFP to 4.6 nm. These MFPs are thus sufficiently large to cancel the scattering contributions to the total delays (Fig. 4C). Consequently, even larger values of the MFPs will not modify our results.

We further verified this conclusion through a complete three-dimensional calculation, which is described in (31) and implements all physical mechanisms shown in Fig. 3. Our model is based on semiclassical Monte Carlo trajectory calculations, but includes the phases and amplitudes derived from a quantum mechanical treatment of photoionization, electron scattering, LAPE, LAES, and transport in three dimensions, which were derived from our earlier one-dimensional model (37). The Monte Carlo trajectory calculations rely on accurate complex-valued scattering factors obtained from ab initio scattering calculations of electrons with water clusters of increasing size, and they use the associated values of the EMFP and IMFP (39). More than  $10^8$  classical trajectories were launched from at least  $10^3$  randomly selected initial positions with a momentum of either  $k_{q-1}$  or  $k_{q+1}$  (where  $q = 14$  or 20 is realized in different sets of calculations). The results of these calculations are given in fig. S11. The contribution of electron scattering during transport amounts to 0 to 6 as, depending on the depth from which the electrons originate, which averages to  $\sim 2$  as over all probed depths. Hence, these contributions are negligible in comparison to the measured delays of  $\sim 50$  to 70 as.

Having excluded the contributions from electron scattering and the near-field distributions, we now turn to the photoionization delays. Figure 5 shows the calculated photoionization delays of the isolated water molecule, a water pentamer, corresponding to one complete solvation shell and a  $(\text{H}_2\text{O})_{11}$  cluster, which possesses a partial second solvation shell (31). A tetrahedral coordination of each water molecule with an O-O distance of 2.75 Å, corresponding to the averaged structure of liquid water, was chosen. The delays systematically increase with the addition of the first solvation shells. The increase of the delay from  $\text{H}_2\text{O}$  to  $(\text{H}_2\text{O})_{11}$  amounts to 61 as at 21.7 eV and 30 as at 31.0 eV. These numbers compare well with the experimentally measured relative delays of  $69 \pm 20$  as and  $49 \pm 16$  as (Fig. 5, red box), particularly when noticing the slower convergence of the delay with cluster size at the higher photon energy.

Because the solvation structure of liquid water is an important and still controversial topic [see, e.g., (4–7)], we studied the sensitivity of the delays to local structural distortions. Using the most representative solvation structures identified in x-ray absorption spectroscopy (4, 12), we stretched one O-O distance in the water pentamer from 2.75 Å

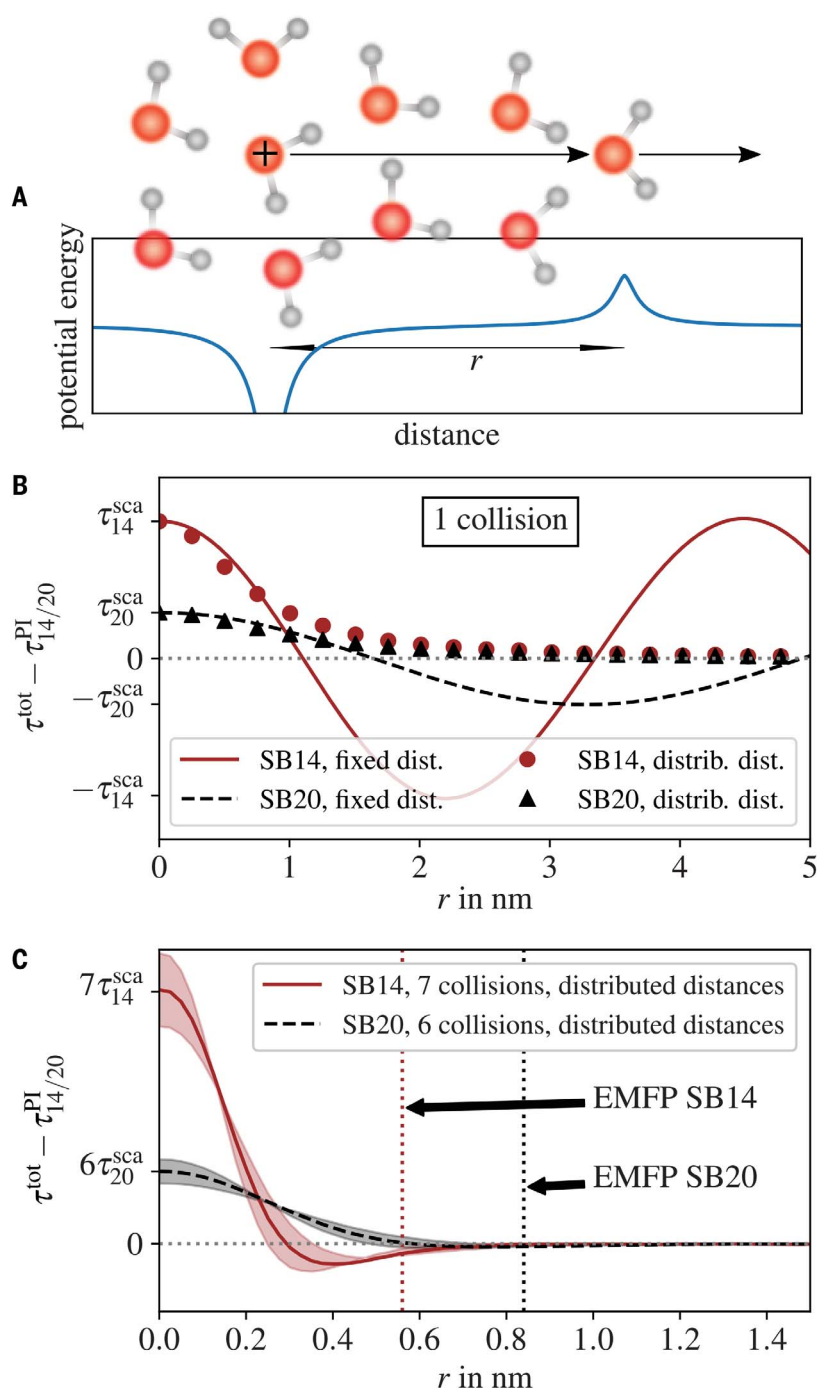


**Fig. 4. Contributions of photoionization and scattering to the measured delays.** (A) Schematic representation of the potentials used in the time-dependent Schrödinger equation (TDSE) calculations. (B) Total delays ( $\tau^{\text{tot}}$ ) for the case of a single collision at a fixed distance (lines) or an exponential path-length distribution with average  $r$  (symbols). (C) The case of  $n$  elastic collisions, sampled according to an exponential path-length distribution with average  $r$ . The shaded areas represent one standard deviation of the corresponding MFPs.

to 3.50 Å (Fig. 5, arrow labeled “stretched”) or rotated one water molecule by  $50^\circ$  around the central molecule. In the case of  $(\text{H}_2\text{O})_{11}$ , the same operations were applied to one group of three water molecules attached to the central

one. Our measured delays are consistent with both the unperturbed tetrahedral coordination (see Fig. 5, red box) and with a single hydrogen bond being broken by stretching (Fig. 5, dashed red box), but not by bending. Photoionization



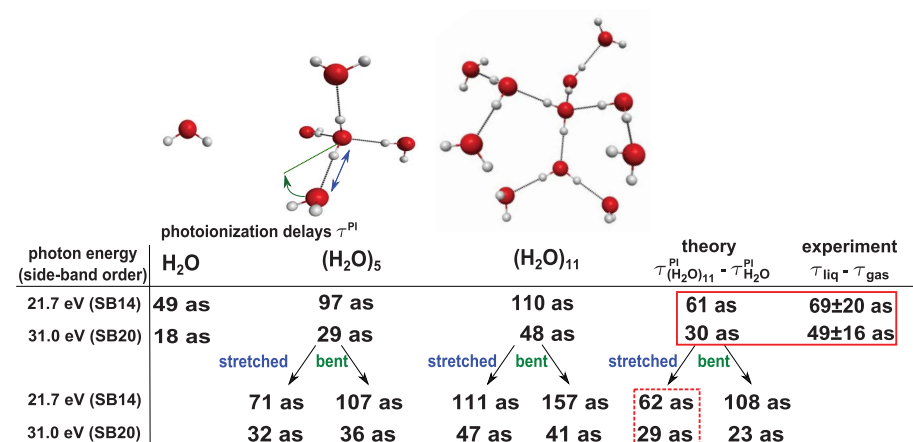


**Fig. 5. Effect of the local solvation structure on photoionization delays.** Calculated photoionization delays for  $\text{H}_2\text{O}$ ,  $(\text{H}_2\text{O})_5$ , and  $(\text{H}_2\text{O})_{11}$  are shown. The bottom two rows indicate delays obtained by stretching (arrow labeled “stretched”) or bending (arrow labeled “bent”) one hydrogen bond in the clusters.  $(\text{H}_2\text{O})_{11}$  was the largest entity for which fully converged delay calculations were possible, with a typical computational cost of 180 CPU days per calculation.

delays therefore discriminate between stretched or bent solvation structures, which yield indistinguishable x-ray absorption spectra [curves c and e of figure 3A in (4)]. Our measurements are thus consistent with a dominantly tetrahedral coordination of liquid water; they do not exclude the contribution of stretched hydrogen bonds, but they do exclude a dominant fraction of hydrogen bonds being broken by bending. Moreover, these sensitivities motivate the application of attosecond interferometry to ice and supercooled water, which are structurally more or less homogeneous than liquid water, respectively.

We now return to the interpretation of the reduced modulation depths observed for the liquid phase. According to Fig. 5, these finite contrasts most likely originate from a distribution of local solvation structures, which results in a distribution of photoionization delays. The superposition of interferometric oscillations with a distribution of phase shifts will indeed result in a reduced contrast of the interferometric oscillation. The larger sensitivity of the delays calculated at 21.7 eV (ranging from 110 to 157 as) compared to 31.0 eV (41 to 48 as) is consistent with the lower relative modulation depth of  $0.17 \pm 0.03$  and  $0.45 \pm 0.06$ , respectively. An additional possible contribution to the reduced contrast comes from decoherence of electrons in liquid water. In the case of the nonlocal pathways (see Fig. 3), the collisions taking place between photoionization and LAES can cause decoherence of the propagating electron wave packet, which would also result in a reduced modulation contrast. Nonlocal attosecond interferometry therefore offers a possible approach to measuring the loss of electronic phase coherence during electron transport in matter.

The time delays determined in our work reflect the effect of the solvation environment on (i) the electronic structure of water molecules and (ii) the multiple scattering of the outgoing photoelectron. This assignment is confirmed by the dominant influence of the first two solvation shells (i and ii) and the decrease of the solvation-induced delays with the kinetic energy (ii). The measurement of photoemission time delays from liquids can thus be viewed as an attosecond time-resolved, fully coherent, electron scattering experiment from within. Relative to diffraction techniques based on external sources, it has the advantage of selectively probing the immediate environment of the ionized species. Relative to x-ray spectroscopy, it offers a temporal resolution reaching down to a few attoseconds. These aspects open new perspectives in solvation science, such as the measurement of the purely electronic solvent response after electronic excitation, relaxation, or large-amplitude chemical dynamics. They additionally offer the perspective of time-resolving both local and nonlocal electronic relaxations in the liquid phase, such as Auger decay, intermolecular coulombic decay (42, 43), and electron transfer-mediated decay (44).

Our work shows that, relative to the photoemission from the HOMO of the isolated molecule, photoemission from the most weakly bound valence band of liquid water is delayed by 50 to 70 as. Detailed calculations indicate that the contributions of electron transport to the measured delays are negligible and identify solvation as the main contribution to the measured delays. The measured delays are dominated by the first two solvation shells of water and are sensitive to the local solvation structure. Although demonstrated on practically

pure liquid water, our techniques are directly applicable to other liquids and solutions, thereby establishing the applicability of attosecond spectroscopy to solvated species. This development has the potential of expanding attosecond science into the realms of chemistry, materials science, and biology.

## REFERENCES AND NOTES

1. F. H. Stillinger, *Science* **209**, 451–457 (1980).
2. J. R. Errington, P. G. Debenedetti, *Nature* **409**, 318–321 (2001).
3. A. Nilsson, L. G. Pettersson, *Nat. Commun.* **6**, 8998 (2015).
4. P. Wernet et al., *Science* **304**, 995–999 (2004).
5. J. D. Smith et al., *Science* **306**, 851–853 (2004).
6. G. N. I. Clark, G. L. Hura, J. Teixeira, A. K. Soper, T. Head-Gordon, *Proc. Natl. Acad. Sci. U.S.A.* **107**, 14003–14007 (2010).
7. K. Yamazoe, J. Miyawaki, H. Niwa, A. Nilsson, Y. Harada, *J. Chem. Phys.* **150**, 204201 (2019).
8. J. Ropp, C. Lawrence, T. C. Farrar, J. L. Skinner, *J. Am. Chem. Soc.* **123**, 8047–8052 (2001).
9. H. J. Bakker, J. L. Skinner, *Chem. Rev.* **110**, 1498–1517 (2010).
10. T. Fransson et al., *Chem. Rev.* **116**, 7551–7569 (2016).
11. T. Head-Gordon, G. Hura, *Chem. Rev.* **102**, 2651–2670 (2002).
12. T. Tokushima et al., *Chem. Phys. Lett.* **460**, 387–400 (2008).
13. O. Fuchs et al., *Phys. Rev. Lett.* **100**, 027801 (2008).
14. G. Sansone et al., *Nature* **465**, 763–766 (2010).
15. S. Biswas et al., *Nat. Phys.* **16**, 778–783 (2020).
16. P. M. Kraus et al., *Science* **350**, 790–795 (2015).
17. M. Huppert, I. Jordan, D. Baykusheva, A. von Conta, H. J. Wörner, *Phys. Rev. Lett.* **117**, 093001 (2016).
18. M. Schultze et al., *Science* **328**, 1658–1662 (2010).
19. K. Klünder et al., *Phys. Rev. Lett.* **106**, 143002 (2011).
20. V. Loriot et al., *J. Phys. Photonics* **2**, 024003 (2020).
21. J. M. Dahlström, A. L’Huillier, A. Maquet, *J. Phys. B* **45**, 183001 (2012).
22. R. Pazourek, S. Nagele, J. Burgdörfer, *Rev. Mod. Phys.* **87**, 765–802 (2015).
23. D. Baykusheva, H. J. Wörner, *J. Chem. Phys.* **146**, 124306 (2017).
24. A. L. Cavalieri et al., *Nature* **449**, 1029–1032 (2007).
25. S. Neppl et al., *Nature* **517**, 342–346 (2015).
26. M. Ossiannder et al., *Nature* **561**, 374–377 (2018).
27. R. Locher et al., *Optica* **2**, 405 (2015).
28. Z. Tao et al., *Science* **353**, 62–67 (2016).
29. F. Siek et al., *Science* **357**, 1274–1277 (2017).
30. L. Seifert et al., *Nat. Phys.* **13**, 766–770 (2017).
31. See supplementary materials.
32. M. Isinger et al., *Science* **358**, 893–896 (2017).
33. V. Gruson et al., *Science* **354**, 734–738 (2016).
34. I. Jordan, H. J. Wörner, *J. Opt.* **20**, 024013 (2018).
35. I. Jordan, M. Huppert, M. A. Brown, J. A. van Bokhoven, H. J. Wörner, *Rev. Sci. Instrum.* **86**, 123905 (2015).
36. A. von Conta, M. Huppert, H. J. Wörner, *Rev. Sci. Instrum.* **87**, 073102 (2016).
37. D. Rattenbacher, I. Jordan, A. Schild, H. J. Wörner, *Phys. Rev. A* **97**, 063415 (2018).
38. H. Shinotsuka et al., *Surf. Interface Anal.* **49**, 238–252 (2017).
39. A. Schild, M. Peper, C. Perry, D. Rattenbacher, H. J. Wörner, *J. Phys. Chem. Lett.* **11**, 1128–1134 (2020).
40. S. Thürmmer et al., *Phys. Rev. Lett.* **111**, 173005 (2013).
41. Y. Suzuki, K. Nishizawa, N. Kurahashi, T. Suzuki, *Phys. Rev. E* **90**, 010302 (2014).
42. T. Jahnke et al., *Nat. Phys.* **6**, 139–142 (2010).
43. M. Mucke et al., *Nat. Phys.* **6**, 143–146 (2010).
44. I. Unger et al., *Nat. Chem.* **9**, 708–714 (2017).
45. I. Jordan et al., Data for “Attosecond Spectroscopy of Liquid Water,” Zenodo (2020); <http://doi.org/10.5281/zenodo.3934437>.

## ACKNOWLEDGMENTS

We thank A. Schneider, M. Kerellaj, and A. Laso for technical support; T. Gaumnitz for help with the operation of the laser system; A. Jain for preliminary calculations of photoionization delays; J. Richardson and Z. Yin for discussions; and T. Fennel and L. Seifert for their contributions to the near-field calculations and their initial support with the 1D calculations presented in this work. Results were partially calculated on the Euler- and NCCR-cluster supercomputers. **Funding:**

Supported by an ERC Starting Grant (project 307270-ATTOSCOPE); an ERC Consolidator Grant (project 772797-ATTOLIQ); the NCCR-MUST, a funding instrument of the Swiss National Science Foundation; an Ambizione grant of the Swiss National Science Foundation (A.S.); and the European Union's Horizon 2020 research and innovation programme under the Marie Skłodowska-Curie grant agreement no. 801459 - FP-RESOMUS (D.J.). **Author contributions:** I.J. and M.H. built the experimental setup and performed the measurements; I.J. analyzed the data; A.v.C. contributed to the measurements of the

monochromatic photoelectron spectra; D.R., M.P., I.J., and C.P. contributed to the development of the theoretical model and calculations; A.S. performed the Monte Carlo trajectory simulations; D.J. realized the photoionization-delay calculations; and H.J.W. supervised the project and wrote the manuscript with input from all coauthors. **Competing interests:** None to declare. **Data and materials availability:** All data needed to evaluate the conclusions in the paper are present in the paper or the supplementary materials, as well as online at Zenodo (45).

#### SUPPLEMENTARY MATERIALS

[science.sciencemag.org/content/369/6506/974/suppl/DC1](https://science.sciencemag.org/content/369/6506/974/suppl/DC1)  
Materials and Methods  
Figs. S1 to S12  
Tables S1 and S2  
References (46–59)

29 January 2020; accepted 10 July 2020  
10.1126/science.abb0979



## SURFACE CHEMISTRY

# Covalent surface modifications and superconductivity of two-dimensional metal carbide MXenes

Vladislav Kamysbayev<sup>1</sup>, Alexander S. Filatov<sup>1</sup>, Huicheng Hu<sup>1</sup>, Xue Rui<sup>2</sup>, Francisco Lagunas<sup>2</sup>, Di Wang<sup>1</sup>, Robert F. Klie<sup>2</sup>, Dmitri V. Talapin<sup>1,3\*</sup>

Versatile chemical transformations of surface functional groups in two-dimensional transition-metal carbides (MXenes) open up a previously unexplored design space for this broad class of functional materials. We introduce a general strategy to install and remove surface groups by performing substitution and elimination reactions in molten inorganic salts. Successful synthesis of MXenes with oxygen, imido, sulfur, chlorine, selenium, bromine, and tellurium surface terminations, as well as bare MXenes (no surface termination), was demonstrated. These MXenes show distinctive structural and electronic properties. For example, the surface groups control interatomic distances in the MXene lattice, and  $Ti_{n+1}C_n$  ( $n = 1, 2$ ) MXenes terminated with telluride ( $Te^{2-}$ ) ligands show a giant (>18%) in-plane lattice expansion compared with the unstrained titanium carbide lattice. The surface groups also control superconductivity of niobium carbide MXenes.

**T**wo-dimensional (2D) transition-metal carbides and nitrides (MXenes) (1) have been actively studied for applications in supercapacitors (2), batteries (3), electromagnetic interference shielding (4), composites (5, 6), and catalysts (7). MXenes are typically synthesized from the corresponding MAX phases (Fig. 1A), where M stands for the transition metal (e.g., Ti, Nb, Mo, V, W, etc.) and X stands for C or N, by selectively etching the main group element A (e.g., Al, Ga, Si, etc.). The etching is usually performed in aqueous hydrofluoric (HF) solutions, rendering MXenes terminated with a mixture of F, O, and OH functional groups, commonly denoted as  $T_x$ . These functional groups can be chemically modified, unlike the surfaces of other 2D materials such as graphene and transition-metal dichalcogenides. Recent theoretical studies predict that selective terminations of MXenes with different surface groups can lead to remarkable properties, such as opening or closing bandgap (8), room-temperature electron mobility exceeding  $10^4$  cm<sup>2</sup>/V·s (9), widely tunable work functions (10), half-metallicity, and 2D ferromagnetism (11). Covalent functionalization of MXene surfaces is expected to uncover new directions for rational engineering of 2D functional materials.

The surface of MXene sheets is defined during MAX phase etching. Electrochemical and hydrothermal methods have been recently applied for etching MAX phases without resorting to HF solutions, but the use of

aqueous solutions introduces a mixture of Cl, O, and OH surface groups (12, 13). The etching of  $Ti_3AlC_2$  MAX phase in molten  $ZnCl_2$  and several other Lewis acidic molten salts above 500°C results in  $Ti_3C_2Cl_2$  MXene with a pure Cl termination (14, 15). Because etching of MAX phases in molten salts eliminates unwanted oxidation and hydrolysis, we used a variation of this method for synthesis of  $Ti_3C_2Cl_2$ ,  $Ti_2CCl_2$ , and  $Nb_2CCl_2$  MXenes in  $CdCl_2$  molten salt (figs. S1 to S5). Moreover, the use of Lewis acidic  $CdBr_2$  allowed us to extend the molten salt etching route beyond chlorides to prepare the first Br-terminated  $Ti_3C_2Br_2$  and  $Ti_2CBr_2$  MXenes (Fig. 1, B and C, and figs. S6 and S7). The morphology, structure, and composition of all newly synthesized MXenes were characterized using high-resolution scanning transmission electron microscopy (STEM), Raman spectroscopy, and a combination of x-ray methods, including energy-dispersive elemental mapping, diffraction (XRD), atomic pair distribution function (PDF), fluorescence, extended x-ray absorption fine structure (EXAFS), and photoelectron spectroscopy (XPS).

We show that Cl-terminated and especially Br-terminated MXenes can efficiently engage in a new type of surface reaction wherein halide ions exchange for other atoms and functional groups. The exchange reactions enable unprecedented control over the surface chemistry, structure, and properties of MXene materials.

The transition-metal atoms from the outer layers of MXene sheets (Ti, Mo, Nb, and V) form relatively weak M-Cl and M-Br bonds, in comparison to M-F and M-OH bonds typical for MXenes with  $T_x$  surface groups. This point can be demonstrated by the enthalpies of formation for  $TiBr_4$  (−617 kJ mol<sup>−1</sup>)

and  $TiCl_4$  (−804 kJ mol<sup>−1</sup>) versus  $TiF_4$  (−1649 kJ mol<sup>−1</sup>), as well as by direct comparison of the bond energies (table S1). Strong Ti-F and Ti-O bonds make it difficult to perform any postsynthetic covalent surface modifications of MXenes (16). In contrast, Cl- and Br-terminated MXenes with labile surface bonding act as versatile synthons for further chemical transformations.

MXene surface exchange reactions typically require temperatures of 300° to 600°C, which are difficult to achieve using traditional solvents. We instead used molten alkali metal halides as solvents with unmatched high-temperature stability, high solubility of various ionic compounds, and wide electrochemical windows (17–19). For example,  $Ti_3C_2Br_2$  MXene (Fig. 1B) dispersed in CsBr-KBr-LiBr eutectic (melting point: 236°C) reacted with  $Li_2Te$  and  $Li_2S$  to form  $Ti_3C_2Te$  (Fig. 1D and figs. S8 to S10) and  $Ti_3C_2S$  (Fig. 1E and fig. S11) MXenes, respectively. The reactions of  $Ti_3C_2Cl_2$  and  $Ti_3C_2Br_2$  with  $Li_2Se$ ,  $Li_2O$ , and  $NaNH_2$  yielded  $Ti_3C_2Se$ ,  $Ti_3C_2O$ , and  $Ti_3C_2(NH)$  MXenes, respectively (figs. S12 to S16). The multilayers of  $Ti_3C_2T_n$  MXenes ( $T = Cl, S, NH$ ) were further treated with *n*-butyl lithium (*n*-BuLi) resulting in  $Li^+$  intercalated sheets (fig. S17) with a negative surface charge (Fig. 2A and fig. S18). Subsequent dispersion in a polar organic solvent such as *N*-methyl formamide (NMF) resulted in stable colloidal solutions of single-layer flakes (Fig. 2, B and C). Raman spectroscopy and elemental analysis showed that delaminated MXenes preserve their original  $T_n$  surface groups (figs. S18 to S20). The x-ray diffraction pattern of spin-coated films showed a single (0002) diffraction peak corresponding to the center-to-center separation (*d*) between two adjacent MXene sheets (Fig. 2D). The absence of (10 $\bar{1}$ l) and (11 $\bar{2}$ 0) reflections is consistent with the alignment of delaminated flakes parallel to the substrate (20), which is also confirmed by the grazing incidence wide-angle x-ray scattering patterns (fig. S19).

Similar covalent surface modifications were achieved for  $Ti_2CCl_2$ ,  $Ti_2CBr_2$ , and  $Nb_2CCl_2$  MXenes (Fig. 3A and figs. S21 to S34). The ability to perform surface exchange reactions on the thinnest MXenes demonstrated that the 2D sheets remained intact during all stages of the transformation. The exact metal to surface group elemental ratios for newly synthesized MXenes were near the expected values, as summarized in table S2.

The reactions of  $Ti_3C_2Br_2$  and  $Ti_2CBr_2$  with LiH at 300°C produced bare  $Ti_3C_2$  (Fig. 1F and fig. S14) and  $Ti_2C$  MXenes (fig. S21), where □ stands for the vacancy site. Because H-terminations are difficult to observe by STEM and other methods, we based this conclusion on the experimental value of the center-to-center distance between the  $Ti_3C_2$  sheets

<sup>1</sup>Department of Chemistry and James Franck Institute, University of Chicago, Chicago, IL 60637, USA. <sup>2</sup>Department of Physics, University of Illinois at Chicago, Chicago, IL 60607, USA. <sup>3</sup>Center for Nanoscale Materials, Argonne National Laboratory, Argonne, IL 60439, USA.  
\*Corresponding author. Email: dvtalapin@uchicago.edu

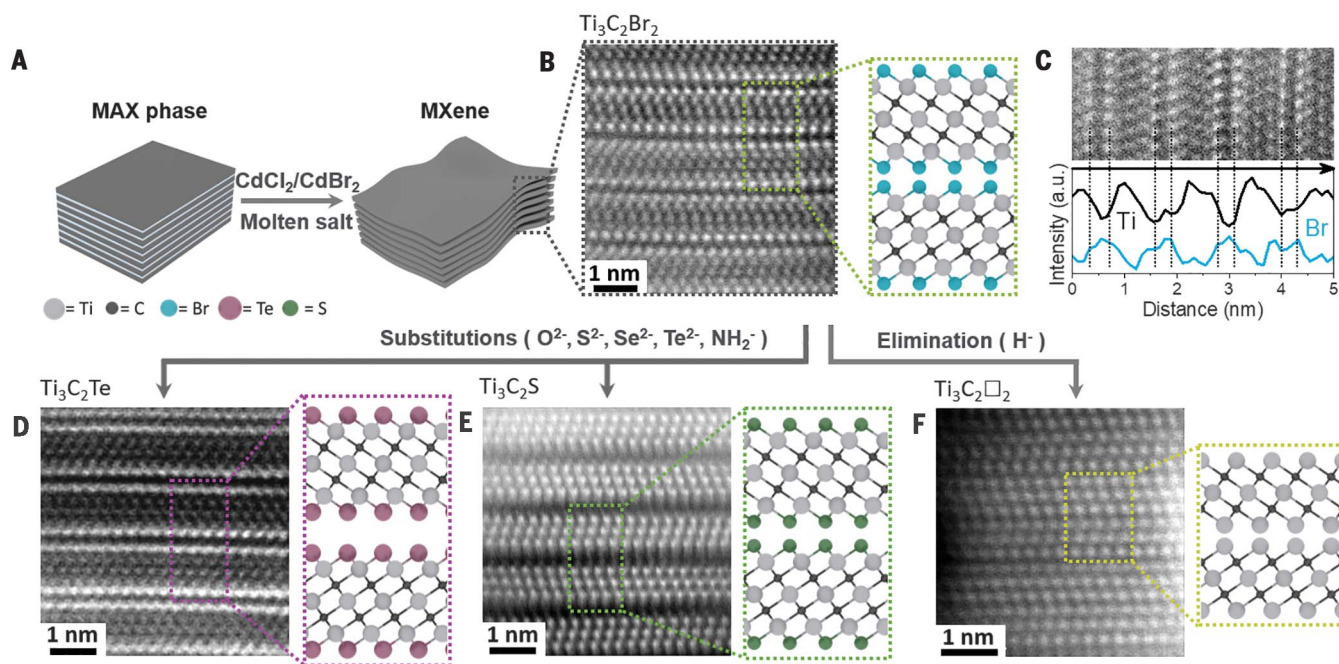


**Fig. 1. Surface reactions of MXenes in molten inorganic salts.** (A) Schematics for etching of MAX phases in Lewis acidic molten salts. (B) Atomic-resolution high-angle annular dark-field (HAADF) image of Ti<sub>3</sub>C<sub>2</sub>Br<sub>2</sub> MXene sheets synthesized by etching Ti<sub>3</sub>AlC<sub>2</sub> MAX phase in CdBr<sub>2</sub> molten salt. The electron beam is parallel to the [210] zone axis. (C) Energy-dispersive

x-ray elemental analysis (line scan) of Ti<sub>3</sub>C<sub>2</sub>Br<sub>2</sub> MXene sheets. a.u., arbitrary units. HAADF images of (D) Ti<sub>3</sub>C<sub>2</sub>Te and (E) Ti<sub>3</sub>C<sub>2</sub>S MXenes obtained by substituting Br for Te and S surface groups, respectively. (F) HAADF image of Ti<sub>3</sub>C<sub>2</sub>□<sub>2</sub> MXene (□ stands for the vacancy) obtained by reductive elimination of Br surface groups.

(7.59 Å), which was substantially smaller than the theoretical prediction for Ti<sub>3</sub>C<sub>2</sub>H<sub>2</sub> MXene (8.26 Å) and near the smallest theoretically possible spacing of 7.23 Å (21). Because XPS showed reduction of Ti (fig. S16), this process could be formally described as a reductive elimination of the hydride groups after the exchange reaction.

The chemical transformations of solids are generally impeded by slow diffusion, which severely limits the scope of synthesizable solid-state compounds (22). The complete exchange of surface groups in stacked MXenes is also expected to be kinetically cumbersome, especially if the entering ions are bulkier than the leaving ones, as in the case of Cl<sup>-</sup> (the ionic radius  $R_i = 1.81$  Å) exchanged for Te<sup>2-</sup> ( $R_i = 2.21$  Å). Counterintuitively, the reactions of Ti<sub>3</sub>C<sub>2</sub>Cl<sub>2</sub> and Ti<sub>2</sub>CCl<sub>2</sub> MXenes with O<sup>2-</sup>, S<sup>2-</sup>, Se<sup>2-</sup>, and Te<sup>2-</sup> occurred at similar temperatures and with comparable reaction rates.

To understand this reactivity, we followed the evolution of the (0002) diffraction peak during surface exchange reactions. In the initial state, Ti<sub>3</sub>C<sub>2</sub>Cl<sub>2</sub> sheets formed stacks (fig. S1) with  $d = 11.25$  Å, and the van der Waals (vdW) gap between MXenes was  $\sim 2.8$  Å (table S3), which is smaller than the dimensions of entering or leaving ions. No measurable changes of the  $d$ -spacing were detected upon heating Ti<sub>3</sub>C<sub>2</sub>Cl<sub>2</sub> in KCl-LiCl molten salt to 500°C (fig. S35). However, heating MXene in the same molten salt but in the presence of Li<sub>2</sub>O re-

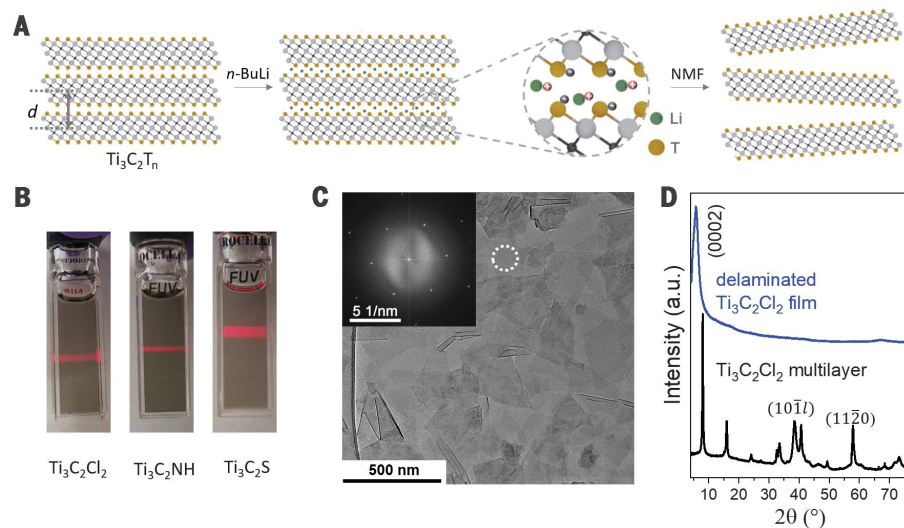


**Fig. 2. Delamination of multilayer Ti<sub>3</sub>C<sub>2</sub>T<sub>n</sub> MXenes.** (A) Schematic of delamination process. (B) Photographs of stable colloidal solutions of Ti<sub>3</sub>C<sub>2</sub>T<sub>n</sub> MXenes (T = Cl, S, NH) in NMF exhibiting Tyndall effect. (C) TEM image of Ti<sub>3</sub>C<sub>2</sub>Cl<sub>2</sub> MXene flakes deposited from a colloidal solution. (Inset) Fast Fourier transform of the circled region, showing crystallinity and hexagonal symmetry of the individual flake. (D) XRD patterns of multilayer MXene and delaminated flakes in a film spin coated on a glass substrate.

sulted in  $d = 13.2$  Å (fig. S36), which corresponds to a 4.7-to-6.3-Å vdW gap between the surface atoms on adjacent MXene sheets, depending on the local surface terminations (see supplementary materials). A similar  $d$

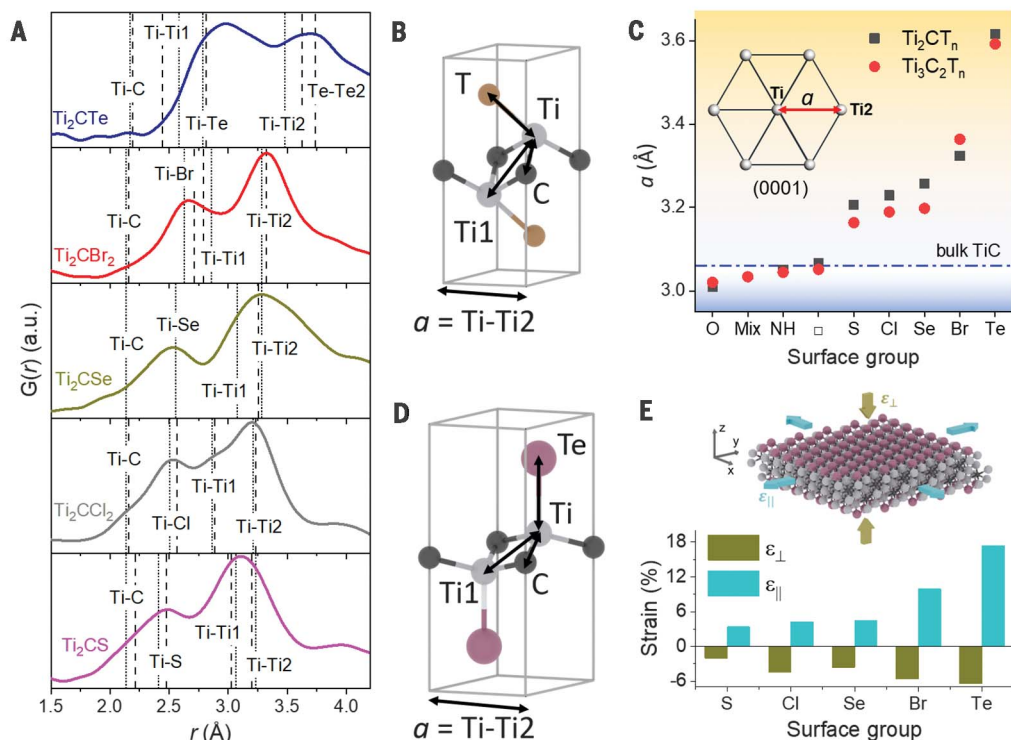
of 13.5 Å was observed during reaction of Ti<sub>3</sub>C<sub>2</sub>Cl<sub>2</sub> MXene with Li<sub>2</sub>Se, although with a larger disorder (fig. S37).

The unstacking of MXene sheets in molten salts greatly facilitated diffusion of ions



**Fig. 3. Surface groups can induce giant strain in the MXene lattice.**

**(A)** Local interatomic distances in  $\text{Ti}_2\text{CT}_n$  MXenes ( $T = \text{S, Cl, Se, Br, Te}$ ) probed by small  $r$  region of the atomic pair distribution functions,  $G(r)$ . The vertical lines show the Ti-C and Ti-T bond lengths and Ti-Ti1 and Ti-Ti2 interatomic distances obtained from the Rietveld refinement of powder XRD patterns (dashed lines) and EXAFS analysis (dotted lines). **(B)** The unit cells of  $\text{Ti}_2\text{CT}_n$  MXenes ( $T = \text{S, Cl, Se, Br}$ ) obtained from the Rietveld refinement. **(C)** Dependence of the in-plane lattice constant  $a$  [equivalent to the Ti-Ti2 distance in (A)] for  $\text{Ti}_2\text{CT}_n$  and  $\text{Ti}_3\text{C}_2\text{T}_n$  MXenes on the chemical nature of the surface group ( $T_n$ ). **(D)** Proposed unit cell of  $\text{Ti}_2\text{CTe}$  MXene (see fig. S39). **(E)** Biaxial straining of  $\text{Ti}_3\text{C}_2\text{T}_n$  MXene lattice induced by the surface groups. The in-plane ( $\epsilon_{\parallel}$ ) and out-of-plane ( $\epsilon_{\perp}$ ) strain components are evaluated with respect to the bulk cubic TiC lattice with  $a_{\text{TiC}} = 4.32 \text{ \AA}$ .



and made MXene surfaces sterically accessible. The interaction potential of MXenes in a molten salt was likely defined by surface-templated ion layering, which created an exponentially decaying oscillatory interaction energy (23). We speculate that the free energy released in the surface exchange reaction caused MXene sheets to “swell” into one of the energy minima and stay in this state during chemical transformation.

Moreover, the nature of the surface groups had an unusually strong impact on the MXene structure. The XRD patterns of  $\text{Ti}_3\text{C}_2\text{T}_n$  and most of the  $\text{Ti}_2\text{CT}_n$  MXenes were modeled using the space group of the parent  $\text{Ti}_3\text{AlC}_2$  and  $\text{Ti}_2\text{AlC}$  MAX phases ( $P6_3/mmc$ ) (24). Because of the simpler structure of thinner  $\text{Ti}_2\text{CT}_n$  MXenes, their representative XRD patterns were further modeled using the Rietveld refinement. The fitting of the experimental Fourier-transformed EXAFS functions of  $\text{Ti}_2\text{CT}_n$  MXenes (fig. S26) demonstrated that the local structure around Ti atoms was consistent with the respective crystallographic models. The real-space interatomic PDFs,  $G(r)$ , showed systematic shifts of Ti-T and Ti-Ti2 distances to larger values in S to Te series of  $\text{Ti}_2\text{CT}_n$  MXenes (Fig. 3, A and B, and fig. S27). In MXenes, the Ti-Ti2 distance is equal to the nearest-neighbor distance between Ti atoms in the basal (0001) plane, and hence it represents the in-plane  $a$  lattice constant (Fig. 3, B and C). For example, for  $\text{Ti}_2\text{CBr}_2$ , the Rietveld, EXAFS, and PDF methods converged on  $a = 3.32 \text{ \AA}$ . After exchanging  $\text{Br}^-$  for  $\text{O}^{2-}$ , the re-

sultant MXene showed  $a = 3.01 \text{ \AA}$ , and the reaction with  $\text{Te}^{2-}$  produced MXene with  $a = 3.62 \text{ \AA}$  (Fig. 3C). The simulated XRD patterns of  $\text{Ti}_2\text{CT}_n$  MXenes (figs. S38 and S39) suggest that large  $\text{Te}^{2-}$  groups are likely positioned on top of the neighboring Ti atoms (Fig. 3D). This arrangement is distinctively different from the MXenes with smaller surface groups, which are positioned between hexagonally packed Ti surface atoms, on top of the opposite Ti atoms of the same  $\text{Ti}_2\text{CT}_n$  sheet (Fig. 3B), in accordance with recent theoretical studies (25).

The vdW radii and packing density of surface atoms had a huge effect on  $a$  (Fig. 3C), and fig. S40 compares these values with available computational predictions. For comparable ion radii, e.g., S versus Cl and Se versus Br, halido-terminated MXenes showed larger  $a$ , likely because of the smaller number of chalcogenide ions required for charge compensation of the MXene surface. To estimate the in-plane strain ( $\epsilon_{\parallel}$ ) imposed on the titanium carbide lattice by surface groups in the newly synthesized MXene species, we compared  $a$  to the nearest-neighbor distance between Ti atoms in the (111) plane of bulk cubic TiC that is structurally equivalent to the basal (0001) MXene plane. For  $\text{Ti}_3\text{C}_2\text{T}_n$  and  $\text{Ti}_2\text{CT}_n$  MXene families, the mixed ( $T_x = \text{F, O, OH}$ ) and pure  $\text{O}^{2-}$  terminations resulted in a compressive  $\epsilon_{\parallel}$ . Bare ( $\square$ ) and NH-terminated MXenes were nearly strain-free, whereas Cl-, S-, Se-, and Br-terminated MXenes all had tensile  $\epsilon_{\parallel}$ . The thinner  $\text{Ti}_2\text{CT}_n$  MXenes had,

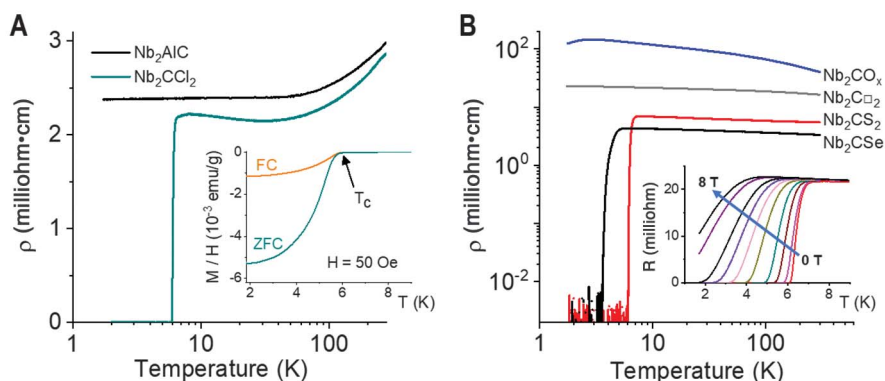
on average, a slightly larger in-plane expansion or contraction with respect to the bulk TiC lattice than did the thicker  $\text{Ti}_3\text{C}_2\text{T}_n$  MXenes. The  $\text{Ti}_2\text{CTe}$  MXene (Fig. 3, A and C, and fig. S24) had the largest magnitude of tensile  $\epsilon_{\parallel}$  (18.2%), in accordance with  $\text{Te}^{2-}$  having the largest vdW radius among all groups used in this study. This degree of lattice expansion in a crystalline solid is very unusual. For comparison, the lattice of bulk TiC expands by only 2.5% when heated from room temperature to  $2700^\circ\text{C}$  (26).

Because the out-of-plane  $c$  lattice constant is strongly affected by the intercalation of ions and solvent molecules between MXene sheets (27), we used high-resolution STEM images to assess the distances between the Ti planes along the  $c$  axis of the unit cell (table S3). The magnitude of the out-of-plane strain in the MXene core ( $\epsilon_{\perp}$ ) was calculated by referencing experimental distances between Ti planes inside the MXene sheets ( $M_{\perp}$ ) to the distance between the (111) planes of bulk TiC (table S3). Figure 3E shows that the expansion of the  $a$ -lattice parameter in  $\text{Ti}_3\text{C}_2\text{T}_n$  MXenes functionalized with S, Cl, Se, Br, and Te atoms was accompanied by the corresponding contraction of the  $\text{Ti}_3\text{C}_2$  layers along the  $c$  axis.

This observation is consistent with the behavior of the  $\text{Ti}_3\text{C}_2$  layers as an elastic 2D sheet under tensile stress imposed by the surface atoms (Fig. 3E). The Poisson effect can account for the relations between the stress and the strain components reflected by

**Fig. 4. Electronic transport and superconductivity in Nb<sub>2</sub>CT<sub>n</sub> MXenes.**

**(A)** Temperature-dependent resistivity for the cold-pressed pellets of Nb<sub>2</sub>AlC MAX phase and Nb<sub>2</sub>CCl<sub>2</sub> MXene. (Inset) Magnetic susceptibility (i.e., ratio of magnetization to magnetizing field strength) of Nb<sub>2</sub>CCl<sub>2</sub> MXene as a function of temperature. FC and ZFC correspond to the field cooled and zero-field cooled measurements, respectively. emu, electromagnetic unit. **(B)** Temperature-dependent resistivity for the cold-pressed pellets of Nb<sub>2</sub>CT<sub>n</sub> MXenes. (Inset) Resistance as a function of temperature at different applied magnetic fields (0 to 8 T) for the cold-pressed pellets of Nb<sub>2</sub>CS<sub>2</sub> MXene.



observed changes of  $a$  and  $M_{\perp}$  distances. Unfortunately, our atomic-resolution STEM images of MXenes measured  $M_{\perp}$  values with relatively large error bars (caused by projection effects and bending of the MXene sheets), which interfered with accurate estimation of the Poisson's ratio ( $\nu$ ) for newly synthesized MXenes. A simple elastic model (see supplementary materials) applied to Ti<sub>3</sub>C<sub>2</sub>T<sub>n</sub> yields  $\nu \sim 0.22$  for T = S and Br, which is comparable to the recently predicted  $\nu$  value for Ti<sub>3</sub>C<sub>2</sub>T<sub>x</sub> (2*I*). However, Ti<sub>3</sub>C<sub>2</sub>Te showed  $\nu = 0.16 \pm 0.06$ , likely caused by the additional stiffening of the Ti<sub>3</sub>C<sub>2</sub> layers under very large in-plane stress.

The above examples show that the composition and structure of MXenes can be engineered with previously unattainable versatility. Chemical functionalization of MXene surfaces is expected to affect nearly every property of these materials, and we found that the surface groups defined the nature of electronic transport in Nb<sub>2</sub>CT<sub>n</sub> MXenes. Figure 4, A and B, shows temperature-dependent four-probe resistivity ( $\rho$ ) measured on cold-pressed pellets of Nb<sub>2</sub>CT<sub>n</sub> (T = □, Cl, O, S, Se) MXenes (fig. S41), all synthesized by the procedures described above. Figure 4A also compares the conductivity of the parent Nb<sub>2</sub>AlC MAX phase with that of Nb<sub>2</sub>CCl<sub>2</sub> MXene. Above 30 K, both MAX phase and MXene samples showed similar specific resistivity, which decreased when the sample was cooled. This temperature dependence is often associated with metallic conductivity. The ultraviolet photoelectron spectroscopy (UPS) confirmed nonzero density of electronic states at the Fermi energy  $E_F$  (fig. S42), which is also consistent with a metallic state.

However, when the Nb<sub>2</sub>CCl<sub>2</sub> MXene was cooled below 30 K, the resistivity started increasing, possibly indicating the onset of localization. A sharp drop of resistivity by several orders of magnitude occurred at a critical temperature  $T_c \sim 6.0$  K (Fig. 4A), which is reminiscent of a superconductive transition. The magnetic susceptibility measurements

showed the development of a strong diamagnetism below 6.3 K that we interpreted as the Meissner effect (Fig. 4A). From the magnitude of zero-field cooled data at 1.8 K, we estimated the lower bound for the superconducting volume fraction of Nb<sub>2</sub>CCl<sub>2</sub> MXene as  $\sim 35\%$ . Consistent with superconductivity, the transition broadened, and  $T_c$  shifted to lower temperatures with the application of an external magnetic field (Fig. 4B and fig. S43). In contrast, the parent Nb<sub>2</sub>AlC MAX phase exhibited normal metal behavior down to the lowest measured temperature (1.8 K), which is consistent with a previously reported  $T_c \sim 0.44$  K for Nb<sub>2</sub>AlC (28). For reference, Nb<sub>2</sub>CT<sub>x</sub> MXene with mixed O, OH, and F termination prepared by the traditional aqueous HF etching route shows two orders of magnitude higher resistivity and no superconductivity (fig. S44) (29).

In contrast to the Nb<sub>2</sub>CCl<sub>2</sub> MXene, the resistivity of MXenes terminated with chalcogenide ions (O, S, Se) gradually increased when the sample was cooled (Fig. 4B), which is consistent with the activated transport regime. Given that UPS showed the finite density of states at  $E_F$  in Nb<sub>2</sub>CS<sub>2</sub> (fig. S42), we hypothesized that the localization was controlled by the tunneling rates for charge carriers between metallic MXene sheets. The oxo-terminated Nb<sub>2</sub>CT<sub>n</sub> MXene showed the highest resistivity, and the seleno-terminated MXene showed the lowest resistivity, consistent with the reduction of the tunneling barrier heights between the MXene sheets.

In the low-temperature region, we observed superconducting transitions in Nb<sub>2</sub>CS<sub>2</sub> ( $T_c \sim 6.4$  K), Nb<sub>2</sub>CSe ( $T_c \sim 4.5$  K), and Nb<sub>2</sub>C(NH) ( $T_c \sim 7.1$  K) (fig. S34), whereas Nb<sub>2</sub>CO<sub>x</sub> did not enter the superconducting state (fig. S45). In granular metals, the development of macroscopic superconductivity can be suppressed by weak coupling of individual superconducting domains, which is also reflected by the high resistivity in the normal state (30). The upper critical field ( $\mu_0 H_{c2}$ ) showed a strong dependence on the surface functional group.

For example, Nb<sub>2</sub>CS<sub>2</sub> MXene exhibited higher  $\mu_0 H_{c2}$  compared with Nb<sub>2</sub>CCl<sub>2</sub> (Fig. 4B, inset, and fig. S46). Bare Nb<sub>2</sub>C□<sub>2</sub> MXenes, on the other hand, showed no transition to the superconducting state down to 1.8 K (Fig. 4B). Thus, surface groups were not spectators but active contributors to the MXene superconductivity, which is consistent with surface groups affecting biaxial lattice strain, phonon frequencies, and the strength of electron-phonon coupling.

The MXene exchange reactions represent an exciting counterexample to the traditional perception of solids as entities that are difficult to postsynthetically modify. We showed that chemical bonds inside an extended MXene stack can be rationally designed in a way that is more typical for molecular compounds. Other MXene structures could be enabled by the combinations of etching and substitution reactions using Lewis acidic and Lewis basic molten salts, respectively.

## REFERENCES AND NOTES

1. B. Anasori, M. R. Lukatskaya, Y. Gogotsi, *Nat. Rev. Mater.* **2**, 16098 (2017).
2. Y. Xia et al., *Nature* **557**, 409–412 (2018).
3. C. J. Zhang et al., *Nat. Commun.* **10**, 849 (2019).
4. F. Shahzad et al., *Science* **353**, 1137–1140 (2016).
5. V. Kamysbayev et al., *ACS Nano* **13**, 12415–12424 (2019).
6. J. Guo et al., *Adv. Mater.* **30**, e1801846 (2018).
7. J. Zhang et al., *Nat. Catal.* **1**, 985–992 (2018).
8. M. Khazaei et al., *Adv. Funct. Mater.* **23**, 2185–2192 (2013).
9. L. Zhou, Y. Zhang, Z. Zhuo, A. J. Neukirch, S. Tretiak, *J. Phys. Chem. Lett.* **9**, 6915–6920 (2018).
10. Y. Liu, H. Xiao, W. A. Goddard 3rd, *J. Am. Chem. Soc.* **138**, 15853–15856 (2016).
11. C. Si, J. Zhou, S. Sun, *ACS Appl. Mater. Interfaces* **7**, 17510–17515 (2015).
12. S.-Y. Pang et al., *J. Am. Chem. Soc.* **141**, 9610–9616 (2019).
13. T. Li et al., *Angew. Chem. Int. Ed.* **57**, 6115–6119 (2018).
14. M. Li et al., *J. Am. Chem. Soc.* **141**, 4730–4737 (2019).
15. Y. Li et al., *Nat. Mater.* **19**, 894–899 (2020).
16. D. Kim et al., *ACS Nano* **13**, 13818–13828 (2019).
17. V. Srivastava et al., *J. Am. Chem. Soc.* **140**, 12144–12151 (2018).
18. A. Dash, R. Vaßen, O. Guillon, J. Gonzalez-Julian, *Nat. Mater.* **18**, 465–470 (2019).
19. X. Liu, N. Fechner, M. Antonietti, *Chem. Soc. Rev.* **42**, 8237–8265 (2013).



20. M. Ghidui, M. W. Barsoum, *J. Am. Ceram. Soc.* **100**, 5395–5399 (2017).
21. Z. H. Fu *et al.*, *Phys. Rev. B* **94**, 104103 (2016).
22. M. Jansen, *Angew. Chem. Int. Ed.* **41**, 3746–3766 (2002).
23. H. Zhang *et al.*, *Nature* **542**, 328–331 (2017).
24. M. Sokol, V. Natu, S. Kota, M. W. Barsoum, *Trends Chem.* **1**, 210–223 (2019).
25. Y. Qin *et al.*, *J. Phys. Condens. Matter* **32**, 135302 (2019).
26. J. H. Richardson, *J. Am. Ceram. Soc.* **48**, 497–499 (1965).
27. O. Mashtalir *et al.*, *Nat. Commun.* **4**, 1716 (2013).
28. T. H. Scabarozzi *et al.*, *Thin Solid Films* **517**, 2920–2923 (2009).
29. J. Halim *et al.*, *J. Phys. Condens. Matter* **31**, 165301 (2019).
30. I. S. Beloborodov, A. V. Lopatin, V. M. Vinokur, K. B. Efetov, *Rev. Mod. Phys.* **79**, 469–518 (2007).

#### ACKNOWLEDGMENTS

We thank Y. Gogotsi and B. Anasori (Drexel University) for sharing the early samples of  $\text{Ti}_3\text{AlC}_2$  MAX phase and introducing us to the exciting field of MXenes. T. Witten, J. Anderson, J. Park, and B. Tian (University of Chicago) are acknowledged for many stimulating discussions. We also thank C. Malliakas (Northwestern

University) and A. Yakovenko [17-BM-B, Advanced Photon Source (APS)] for transmission powder XRD, O. Borkiewicz (11-ID-B, APS) for x-ray total scattering, C.-J. Sun (20-BM-B, APS) for XAS, and J. Xie (University of Chicago) for magnetization measurements. **Funding:** V.K., H.H., D.W., and D.V.T. were supported by the Department of Defense (DOD) Air Force Office of Scientific Research grant FA9550-18-1-0099; by the Office of Basic Energy Sciences, U.S. Department of Energy, award no. DE-SC0019375; and by the National Science Foundation awards nos. DMR-1611371 and DMR-2004880. X.R., F.L., and R.F.K. were supported by the National Science Foundation (DMREF CBET-1729420). The JEOL JEM ARM200CF in the UIC Research Resources Center was acquired and upgraded using grants from the National Science Foundation (DMR-0959470 and DMR-1626065). This research used resources of the Center for Nanoscale Materials and the Advanced Photon Source, an Office of Science User Facilities operated for the U.S. Department of Energy (DOE) Office of Science by Argonne National Laboratory, supported by the U.S. DOE under contract no. DE-AC02-06CH11357, and the Canadian Light Source and its funding partners. **Author contributions:** V.K. designed and performed the experiments, analyzed data, and cowrote the paper. A.S.F. contributed to the x-ray data analysis. X.R., F.L., and R.F.K. performed high-resolution STEM studies and image analysis. H.H.

and D.W. carried out MAX phase synthesis and delamination of MXenes. D.V.T. conceived of and designed experiments, analyzed data, cowrote the paper, and supervised the project. All authors discussed the results and commented on the manuscript.

**Competing interests:** V.K. and D.V.T. are inventors on patent application U.S. 63/020,885 submitted by the University of Chicago, which covers surface modifications of MXenes and methods.

**Data and materials availability:** All data needed to evaluate the conclusions in the paper are present in the paper or the supplementary materials.

#### SUPPLEMENTARY MATERIALS

science.sciencemag.org/content/369/6506/979/suppl/DC1  
Materials and Methods  
Supplementary Text  
Figs. S1 to S46  
Tables S1 to S15  
References (31–59)

9 January 2020; accepted 2 June 2020  
Published online 2 July 2020  
10.1126/science.aba8311

## IMMUNOLOGY

# SOSTDC1-producing follicular helper T cells promote regulatory follicular T cell differentiation

Xin Wu<sup>1</sup>, Yun Wang<sup>1</sup>, Rui Huang<sup>1</sup>, Qujing Gai<sup>1</sup>, Haofei Liu<sup>1</sup>, Meimei Shi<sup>1</sup>, Xiang Zhang<sup>1</sup>, Yonglin Zuo<sup>1</sup>, Longjuan Chen<sup>1</sup>, Qiwen Zhao<sup>1</sup>, Yu Shi<sup>1</sup>, Fengchao Wang<sup>2</sup>, Xiaowei Yan<sup>3</sup>, Huiping Lu<sup>4</sup>, Senlin Xu<sup>1</sup>, Xiaohong Yao<sup>1</sup>, Lin Chen<sup>2</sup>, Xia Zhang<sup>1</sup>, Qiang Tian<sup>3\*</sup>, Ziyang Yang<sup>5</sup>, Bo Zhong<sup>6</sup>, Chen Dong<sup>4</sup>, Yan Wang<sup>1†</sup>, Xiu-Wu Bian<sup>1†</sup>, Xindong Liu<sup>1†</sup>

Germinal center (GC) responses potentiate the generation of follicular regulatory T (T<sub>FR</sub>) cells. However, the molecular cues driving T<sub>FR</sub> cell formation remain unknown. Here, we show that sclerostin domain-containing protein 1 (SOSTDC1), secreted by a subpopulation of follicular helper T (T<sub>FH</sub>) cells and T-B cell border-enriched fibroblastic reticular cells, is developmentally required for T<sub>FR</sub> cell generation. Fate tracking and transcriptome assessment in reporter mice establishes SOSTDC1-expressing T<sub>FH</sub> cells as a distinct T cell population that develops after SOSTDC1<sup>+</sup> T<sub>FH</sub> cells and loses the ability to help B cells for antibody production. Notably, *Sostdc1* ablation in T<sub>FH</sub> cells results in substantially reduced T<sub>FR</sub> cell numbers and consequently elevated GC responses. Mechanistically, SOSTDC1 blocks the WNT- $\beta$ -catenin axis and facilitates T<sub>FR</sub> cell differentiation.

Unlike follicular helper T (T<sub>FH</sub>) cells, which initiate germinal center (GC) reactions (1–4), follicular regulatory T (T<sub>FR</sub>) cells, a recently identified subset of Foxp3-expressing regulatory T (T<sub>reg</sub>) cells, constrain GC reactions (5–10). Thymus-derived T<sub>reg</sub> cells give rise to T<sub>FR</sub> cells through the up-regulation of T<sub>FH</sub> cell-related signature molecules (5, 11, 12). T<sub>FR</sub> cells thus share chimeric

features with both T<sub>FH</sub> and T<sub>reg</sub> cells simultaneously (11, 13–15). However, the environmental cues attributed to T<sub>FR</sub> cell commitment remain unclear.

We recently observed that sclerostin domain-containing protein 1 (SOSTDC1), a secreted protein containing a C-terminal cysteine knot-like domain, was selectively expressed in T<sub>FH</sub> cells (16). The *Sostdc1* locus in T<sub>FH</sub> cells was

marked with the active marker trimethylated histone H3 lysine 4 (H3K4me3) and lacked the repressive marker H3K27me3, as compared with other CD4<sup>+</sup> T cell subsets (fig. S1A). *Sostdc1* mRNA was expressed in T<sub>FH</sub> cells but not in other T cell populations (Fig. 1A). SOSTDC1 protein was highly expressed in cells that localized in B cell follicles, especially at the T–B cell border (fig. S1B). In *Sostdc1*<sup>EGFP</sup> reporter mice challenged with either influenza viruses or antigen immunization, SOSTDC1 expression in CD4<sup>+</sup> T cells was confined to CXCR5<sup>+</sup>PD-1<sup>+</sup> T<sub>FH</sub> cells (fig. S2, A to E). Anatomically, enhanced green fluorescent protein (EGFP)<sup>+</sup> cells were enriched at T–B cell border and B cell follicle regions (fig. S3, A and B). At T–B cell border regions, *Sostdc1*<sup>+</sup> cells comprised both EGFP<sup>+</sup> CD4<sup>+</sup> T and podoplanin<sup>+</sup> fibroblastic reticular cells (FRCs) (fig. S3B). Notably, the number of *Sostdc1*<sup>+</sup> CD4<sup>+</sup> T cells located at the T–B cell border was second only to that in the B cell follicle (fig. S3C). Thus, *Sostdc1* is preferentially expressed in T<sub>FH</sub> cells and T–B cell border-resident FRCs in peripheral lymphoid organs.

SOSTDC1 expression in T<sub>FH</sub> cells was initiated at day 3, gradually increased from day 3 to 7, and maintained until at least day 15 at ~12% (Fig. 1B). On day 8, SOSTDC1-EGFP<sup>+</sup> T<sub>FH</sub> cells were located in B cell follicles and at T–B cell borders (Fig. 1C). Additionally, phenotyping

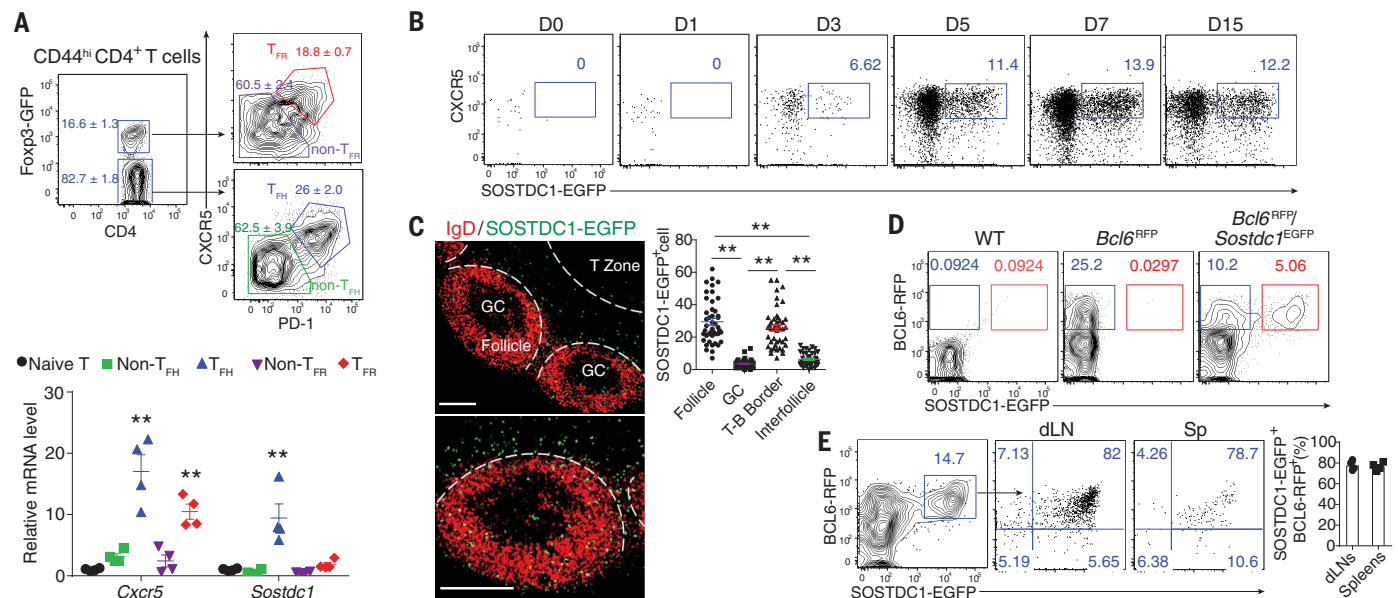


**Fig. 1. SOSTDC1 is selectively expressed in a subpopulation of T<sub>FH</sub> cells.** (A) *Cxcr5* and *Sostdc1* mRNA levels in naive CD4<sup>+</sup> T, as well as T<sub>FR</sub>, non-T<sub>FR</sub>, T<sub>reg</sub>, T<sub>FH</sub>, and non-T<sub>FH</sub> cells that were sorted from KLH- and complete Freund's adjuvant (CFA)-immunized Foxp3<sup>EGFP</sup> mice. (B) Flow cytometric analysis of donor cells from CD45.1<sup>+</sup> mice that received naive *Sostdc1*<sup>EGFP</sup>/OT-II cells, followed by immunization with ovalbumin (OVA) and CFA. (C) Immunofluorescent staining of dLNs from mice that received *Sostdc1*<sup>EGFP</sup>/OT-II cells, followed by immunization with OVA in CFA subcutaneously for 8 days. Green: SOSTDC1-GFP; Red: IgD; scale bars: 200  $\mu$ m. The dashed lines demarcate the

distribution of donor cells in the follicles, GCs, and interfollicular region. (D) Flow cytometric analysis of CD4<sup>+</sup> T cells with red fluorescent protein (RFP) and EGFP gating from WT, *Bcl6*<sup>RFP</sup>, and *Bcl6*<sup>RFP</sup>/*Sostdc1*<sup>EGFP</sup> mice immunized subcutaneously with KLH in CFA for 7 days. (E) Flow cytometric analysis of donor T<sub>FH</sub> cells in congenic mice that received SOSTDC1-EGFP<sup>+</sup> Bcl6-RFP<sup>+</sup> T<sub>FH</sub> OT-II cells, followed by immunization with OVA in incomplete Freund's adjuvant subcutaneously for 7 days. Sp, spleens. Error bars indicate SEM. Statistical tests: Student's *t* test. \*\**P* < 0.01. Data represent at least two independent experiments with three to five mice per group.



of *Sostdc1*<sup>EGFP</sup>/*Bcl6*<sup>RFP</sup> dual-reporter mice demonstrated that SOSTDC1<sup>+</sup> T<sub>FH</sub> cells (~5%) coexisted distinctly from SOSTDC1<sup>-</sup> T<sub>FH</sub> cells (~10%) in the draining lymph nodes (dLNs) (Fig. 1D). Furthermore, most SOSTDC1<sup>+</sup> T<sub>FH</sub> cells were able to maintain their phenotype during a recall response (Fig. 1E). Thus, a distinctive subpopulation of T<sub>FH</sub> cells exists that is defined by SOSTDC1 expression.

Gene expression analysis revealed that the SOSTDC1<sup>+</sup> T<sub>FH</sub> cells were distinct from those of SOSTDC1<sup>-</sup> T<sub>FH</sub> and non-T<sub>FH</sub> cells (Fig. 2, A and B). In comparison with non-T<sub>FH</sub> cells,

although both SOSTDC1<sup>+</sup> and SOSTDC1<sup>-</sup> T<sub>FH</sub> cells expressed equivalent levels of the T<sub>FH</sub> cell signature genes *Ascl2*, *Bcl6*, and *Cxcr5* and reduced expression of *Gata3*, *Ifng*, *Rorc*, and *Tbx21*, SOSTDC1<sup>+</sup> T<sub>FH</sub> cells distinguished themselves from SOSTDC1<sup>-</sup> T<sub>FH</sub> cells by overexpression of *Sostdc1* and *Zfp703* and reduction of *Il4*, *Il21*, and *Cd154*, as well as WNT-related genes, such as *Wnt3a* and *Lrp5* (Fig. 2C). Single-cell RNA sequencing (scRNA-seq) analysis confirmed differential transcriptome between SOSTDC1<sup>+</sup> (cluster 4) and SOSTDC1<sup>-</sup> (cluster 2) T<sub>FH</sub> cells (fig. S4, A and B). Further pseudo-

temporal ordering analysis demonstrated a developmental transition from *Sostdc1*<sup>-</sup> to *Sostdc1*<sup>+</sup> T<sub>FH</sub> cell (fig. S4C). In vivo fate mapping showed that *Sostdc1*<sup>+</sup> T<sub>FH</sub> cell appears to develop from plastic precursor SOSTDC1<sup>-</sup> T<sub>FH</sub> cells (fig. S4D). Although both populations of SOSTDC1<sup>+</sup> and SOSTDC1<sup>-</sup> T<sub>FH</sub> cells were predominantly distributed in follicle and T-B cell interface regions, higher percentages of SOSTDC1<sup>+</sup> T<sub>FH</sub> cells were located in follicles and GC regions than SOSTDC1<sup>-</sup> T<sub>FH</sub> cells (fig. S4E). Functionally, unlike SOSTDC1<sup>-</sup> T<sub>FH</sub> cells, SOSTDC1<sup>+</sup> T<sub>FH</sub> cells were unable to help B cells

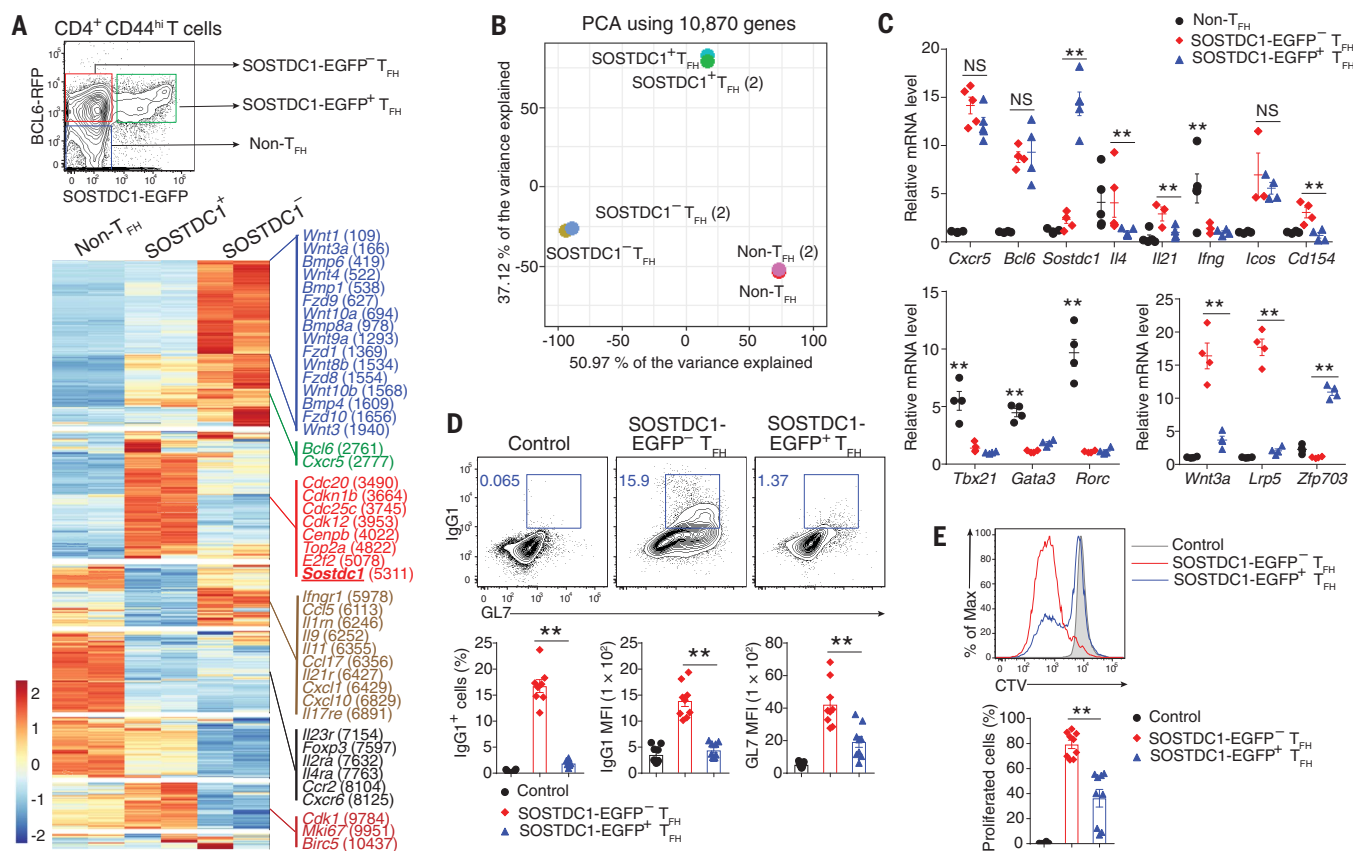


**Fig. 2. SOSTDC1-expressing T<sub>FH</sub> cells represent a distinct subpopulation of T<sub>FH</sub> cells that do not help B cells to promote antibody production.**

(A to C) RNA-seq assessment of sorted CD44<sup>hi</sup> CD4<sup>+</sup> BCL6-RFP<sup>+</sup> SOSTDC1-EGFP<sup>-</sup> T<sub>FH</sub> cells, BCL6-RFP<sup>+</sup> SOSTDC1-EGFP<sup>+</sup> T<sub>FH</sub> cells, and BCL6-RFP<sup>-</sup> SOSTDC1-EGFP<sup>-</sup> non-T<sub>FH</sub> cells from *Sostdc1*<sup>EGFP</sup>/*Bcl6*<sup>RFP</sup> dual-reporter mice that were immunized subcutaneously with KLH and CFA for 7 days.

(A) Heatmap of genes expressed differentially in these three populations of cells. (B) Principle components analysis (PCA) of their transcriptomes.

(C) Quantitative reverse transcription polymerase chain reaction (qRT-PCR) measurement of gene expression by these three populations. NS, no

significance. (D and E) Assessment of the role of T<sub>FH</sub> cells in regulating B cell responses. Non-T<sub>FH</sub> (control), SOSTDC1-EGFP<sup>-</sup> T<sub>FH</sub>, and SOSTDC1-EGFP<sup>+</sup> T<sub>FH</sub> cells were sorted from *Sostdc1*<sup>EGFP</sup> mice that received immunization with KLH and CFA subcutaneously for 7 days and cocultured separately with B220<sup>+</sup> IgD<sup>+</sup> B cells for 6 days. (D) Flow cytometric analysis of class-switched (IgG1<sup>+</sup>GL7<sup>+</sup>) B cells from cocultures. MFI, mean fluorescence intensity. (E) B cell proliferation measured by Cell Trace Violet (CTV) at day 6. Max, maximum. Data represent at least two independent experiments with five to seven mice per group. Error bars indicate SEM. Statistical tests: one-way analysis of variance (ANOVA). \*\*P < 0.01.

<sup>1</sup>Institute of Pathology and Southwest Cancer Center, Southwest Hospital, Third Military Medical University (Army Medical University), Chongqing 400038, P. R. China. <sup>2</sup>State Key Laboratory of Trauma, Burns and Combined Injury, Third Military Medical University (Army Medical University), Chongqing 400038, P. R. China. <sup>3</sup>Institute for Systems Biology, Seattle, WA 98103, USA.

<sup>4</sup>Institute for Immunology and School of Medicine, Tsinghua University, Beijing 100084, P. R. China. <sup>5</sup>Department of Obstetrics and Gynecology, Qilu Hospital of Shandong University, Jinan, 250012, P. R. China. <sup>6</sup>Medical Research Institute, School of Medicine, Wuhan University, Wuhan, 430071, P. R. China.

\*Present address: National Research Center for Translational Medicine (Shanghai), Ruijin Hospital, School of Medicine, Shanghai Jiao Tong University, Shanghai, 200240, P. R. China.

†Corresponding author. Email: xindongliu@hotmail.com (X.L.); bianxiuwu@263.net (X.-W.B.); wang\_yan1977@hotmail.com (Y.W.)

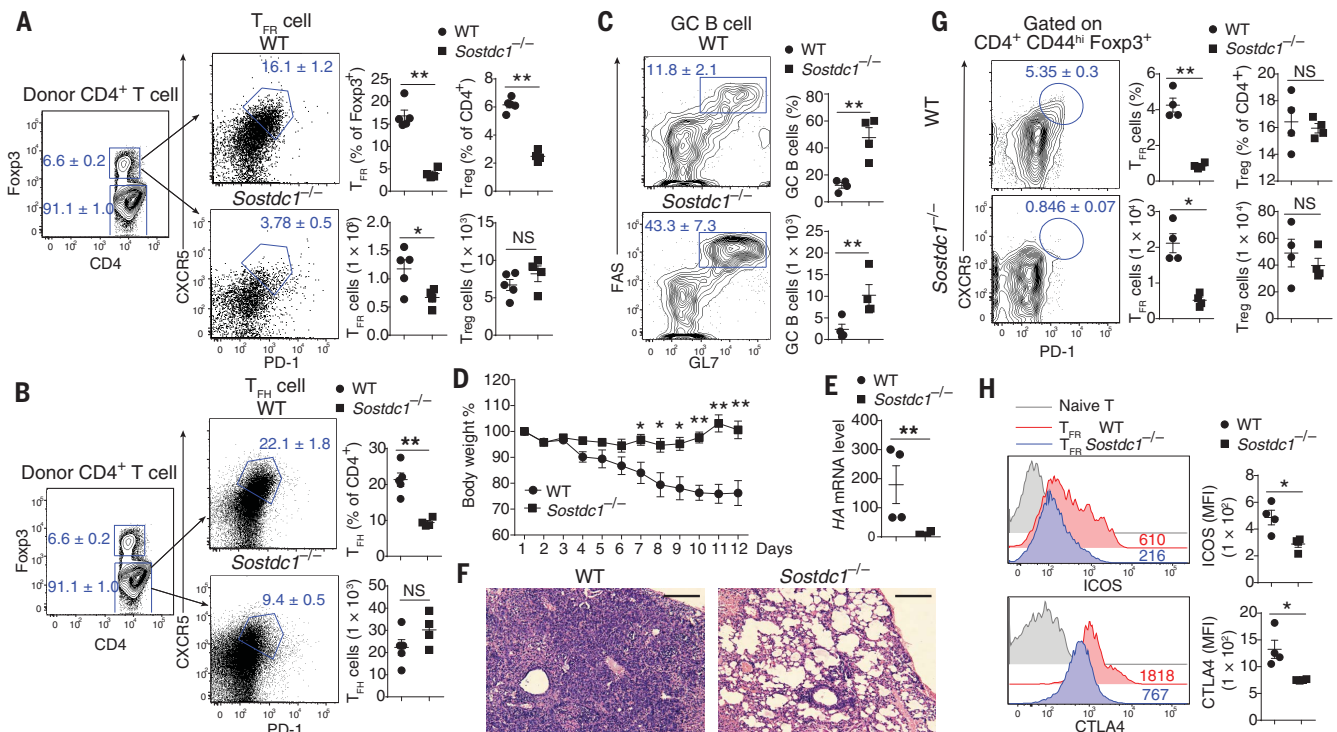


**Fig. 3. T<sub>FR</sub> cell-derived SOSTDC1 is required for T<sub>FR</sub> cell generation.**

(A to C) Sorted Foxp3-GFP<sup>+</sup> nT<sub>Reg</sub> and B1.8 B cells were cotransferred with naïve WT or *Sostdc1*<sup>-/-</sup> OT-II cells into *Rag1*<sup>-/-</sup> recipient mice, followed by immunization with NP-OVA and CFA subcutaneously for 7 days. Flow cytometric analysis and quantification of T<sub>FR</sub> and T<sub>Reg</sub> cells (A), T<sub>FR</sub> cells (B), and GC B cells (C) in dLNs. (D to H) WT and *Sostdc1*<sup>-/-</sup> mice were infected intranasally with influenza virus A/PR8 for 15 days. Their body weights (D) were measured and lung viral titers were assessed by

hemagglutinin (HA) gene expression with qRT-PCR (E). (F) Representative hematoxylin and eosin images of lung sections. Scale bars, 200 μm. Flow cytometric analysis and quantification of T<sub>FR</sub> cells numbers (G) as well as T<sub>FR</sub> cell ICOS and CTLA4 expression (H) in lung dLNs. Red, WT T<sub>FR</sub> cells; blue, *Sostdc1*<sup>-/-</sup> T<sub>FR</sub> cells; gray, naïve CD4<sup>+</sup> T cells. Data are representative of at least two independent experiments, with three to five mice per group. Error bars indicate SEM. Statistical tests: two-way ANOVA [(A) to (D)] and Student's *t* test [(E), (G), and (H)]; \**P* < 0.05, \*\**P* < 0.01.

for antibody production, partially because of lower levels of *Il4* and *Il21*, as well as surface *Cd154* (CD40L) (Fig. 2, C to E, and fig. S5, A to C). Thus, SOSTDC1-expressing T cells are a distinct subpopulation of T<sub>FR</sub> cells that develop from SOSTDC1<sup>+</sup> T<sub>FR</sub> cells and lose their ability to provide help for B cells.

During the course of keyhole limpet hemocyanin (KLH) immunization, *Sostdc1* deficiency substantially increased the percentage of GC B cells and serum levels of KLH-specific immunoglobulin G2c (IgG2c) and IgG2b while leaving the T<sub>FR</sub> cell population unchanged (fig. S6, A to C). By contrast, T<sub>FR</sub> cells were significantly reduced as a percentage of total cells and in comparison with T<sub>FR</sub> cells (fig. S6, C and D). Furthermore, we adapted a cotransfer mouse model and found *Sostdc1* deficiency in donor OT-II cells blocked T<sub>FR</sub> cell generation and consequentially enhanced GC responses (Fig. 3, A to C). *Sostdc1* deficiency reduced the percentage, but not number, of T<sub>FR</sub> cells (Fig. 3B and fig. S7, A and B). In the context of influenza viral infection, *Sostdc1*<sup>-/-</sup> mice displayed substantially reduced weight loss, viral loads, and lung tissue damage compared with wild-type (WT) mice (Fig. 3, D to F). Consistent with

these KLH immunization data, *Sostdc1* deficiency largely increased GC responses, concomitant with reduced T<sub>FR</sub> cell numbers and impaired expression of ICOS and CTLA4 by T<sub>FR</sub> cells (Fig. 3, G and H, and fig. S8, A to C). Thus, *Sostdc1* ablation results in T<sub>FR</sub> defects, which, in turn, enhances humoral immunity against viruses.

To delineate the roles of T<sub>FR</sub> cell- and FRC-derived SOSTDC1 in T<sub>FR</sub> cell differentiation, we first generated mixed bone marrow chimeras by transferring WT bone marrow cells to *Sostdc1*<sup>-/-</sup> recipient mice and vice versa. This demonstrated that SOSTDC1-expressing cells of both hematopoietic and nonhematopoietic origin support T<sub>FR</sub> cell generation. (fig. S9, A to D). Furthermore, bone marrow chimeras reconstituted with either WT + *Sostdc1*<sup>-/-</sup> or *Bcl6*<sup>ΔB/Δ</sup>/Cd4<sup>Cre</sup> + *Sostdc1*<sup>-/-</sup> bone marrow cells revealed that T<sub>FR</sub>-derived SOSTDC1 was critical for T<sub>FR</sub> cell formation (fig. S10, A to C). Thus, SOSTDC1-expressing T<sub>FR</sub> cells may function with nonhematopoietic FRCs to support T<sub>FR</sub> cell generation through SOSTDC1.

To rule out the possibility that defective features of T<sub>FR</sub> cells by *Sostdc1* ablation are potentially inherited from thymic T cells, we

analyzed and compared T cell populations and activation status between WT and *Sostdc1*<sup>-/-</sup> mice. The percentages of CD4<sup>+</sup>, CD4<sup>+</sup>CD8<sup>+</sup>, and CD8<sup>+</sup> T cells in the thymus and Foxp3<sup>+</sup> T<sub>Reg</sub> cell in the lymph nodes were unaffected by *Sostdc1* ablation (fig. S11, A and B). Additionally, in chimeric mice reconstituted with WT and *Sostdc1*<sup>-/-</sup> bone marrow, *Sostdc1* deficiency did not affect thymic T cell development and peripheral T cell homeostasis (fig. S11, C and D).

SOSTDC1 inhibits the canonical WNT-β-catenin pathway (17–19). The most pronounced difference between SOSTDC1<sup>+</sup> and SOSTDC1<sup>+</sup> T<sub>FR</sub> cell subsets was the overexpression of WNT ligand genes in SOSTDC1<sup>+</sup> T<sub>FR</sub> cells, whereas WNT-antagonistic genes were elevated in SOSTDC1<sup>+</sup> T<sub>FR</sub> cells (Fig. 4A). Given that canonical WNT signaling inhibits T<sub>Reg</sub> cells (20, 21), we hypothesized that the defective T<sub>FR</sub> cells observed in *Sostdc1* deficiency are due to the dysregulation of the WNT-β-catenin signaling axis. *Sostdc1* ablation increased β-catenin levels in T<sub>FR</sub> cells significantly more than in T<sub>FR</sub> and Foxp3<sup>+</sup>CXCR5<sup>+</sup> T<sub>Reg</sub> cells (Fig. 4B and fig. S12A). Consistent with this, the global transcriptional changes by *Sostdc1* ablation in



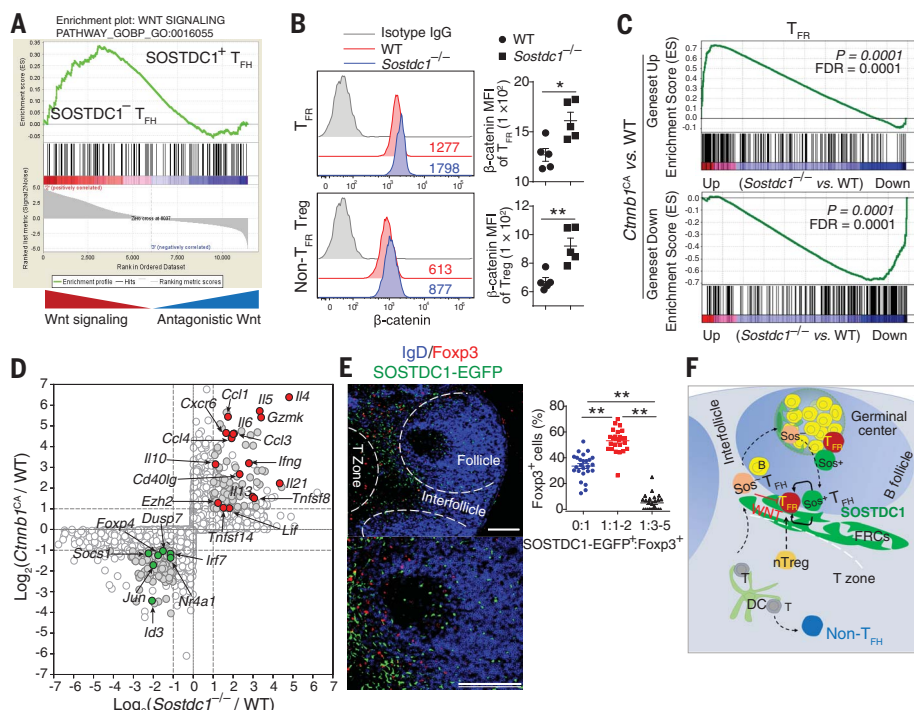


**Fig. 4. SOSTDC1 promotes T<sub>FR</sub> cell generation through blockade of the WNT-β-catenin pathway.**

(A) Gene set enrichment analysis (GSEA) of transcriptomes in SOSTDC1-EGFP<sup>-</sup> and SOSTDC1-EGFP<sup>+</sup> T<sub>FR</sub> cells. (B) β-catenin expression in T<sub>FR</sub> and non-T<sub>FR</sub> T<sub>reg</sub> cells from WT and *Sostdc1*<sup>-/-</sup> mice immunized subcutaneously with KLH and CFA for 7 days. (C and D) RNA-seq analyses of GITR<sup>hi</sup> T<sub>FR</sub> cells and GITR<sup>hi</sup> non-T<sub>FR</sub> T<sub>reg</sub> cells were sorted from WT or *Sostdc1*<sup>-/-</sup> mice immunized subcutaneously with KLH and CFA for 7 days. These populations were valuated with Foxp3 staining. (C) GSEA of altered genes in T<sub>FR</sub> (*Sostdc1*<sup>-/-</sup> versus WT) in the context of gene set from T<sub>reg</sub> (*Cttnb1*<sup>CA</sup> versus WT) (21). FDR, false discovery rate. (D) Gene expression scatter plot of 8245 genes altered similarly between T<sub>FR</sub> (*Sostdc1*<sup>-/-</sup> versus WT) and T<sub>reg</sub> (*Cttnb1*<sup>CA</sup> versus WT) cells. Red, up-regulated effectors; green, down-regulated transcriptional repressors. (E) Immunofluorescent staining and assessment of Foxp3<sup>+</sup> and EGFP<sup>+</sup> cells in dLNs sections from *Sostdc1*<sup>EGFP</sup> mice immunized with KLH and CFA subcutaneously for 7 days. Red, Foxp3<sup>+</sup>; blue, IgD; and green, SOSTDC1-EGFP. Scale bars, 200 μm. (F) Schematic model for the differentiation and function of SOSTDC1<sup>-</sup> T<sub>FR</sub> cells. The data are representative of at least two independent experiments, with three to five mice per group. Error bars indicate SEM. Statistical tests: two-way ANOVA, \*P < 0.05, \*\*P < 0.01.

T<sub>FR</sub>, but not CXCR5<sup>-</sup> T<sub>reg</sub>, cells were positively correlated with that in β-catenin-stabilized T<sub>reg</sub> cells (21) (Fig. 4C and fig. S12, B to D). Specifically, *Sostdc1* deficiency significantly up-regulated the expression of effector cytokines (*Il4*, *Il5*, *Il6*, *Il13*, *Il21*, and *Ifng*) and down-regulated transcriptional repressors (*Nr4a1*, *Id3*, and *Foxp4*) in T<sub>FR</sub> cells (Fig. 4D). Furthermore, *Sostdc1* ablation enriched β-catenin-lymphoid enhancer factor-T cell factor binding motif while reducing KLF family binding in T<sub>FR</sub> cells (fig. S12E). Last, there were comparable levels of bone morphogenetic protein (BMP) pathway-related Smad4 and phosphorylated Smad1 and Smad5 in WT and *Sostdc1*<sup>-/-</sup> T<sub>FR</sub> cells (fig. S12F), excluding the possible correlation of SOSTDC1 with the BMP signaling cascade (22, 23). Thus, *Sostdc1* ablation predominantly augments the β-catenin-controlled transcriptome, which blocks T<sub>FR</sub> cell differentiation.

To specify the role of β-catenin in T<sub>FR</sub> cells, we generated chimeric mice containing WT or *Cttnb1*<sup>ex3/ERT2</sup> Cre nT<sub>reg</sub> cells in which β-catenin can be stabilized by tamoxifen (fig. S13A). Assessment of donor cells revealed that stabilization of β-catenin impaired T<sub>FR</sub> cell generation significantly (fig. S13B). Additionally, in chimeras transduced with WT and *Cttnb1*<sup>fl/fl</sup>/*Cd4*<sup>Cre</sup> bone marrow, *Cttnb1*<sup>fl/fl</sup>/*Cd4*<sup>Cre</sup> bone marrow-derived T<sub>FR</sub> cells predominated over WT bone marrow-derived counterparts (fig. S13C). Thus, β-catenin plays a negative role in regulating T<sub>FR</sub> cell differentiation.

SOSTDC1-EGFP<sup>+</sup> cells were localized proximally to Foxp3<sup>+</sup> T cells in B cell follicle and T-B cell border regions. Furthermore, more than 60% of Foxp3<sup>+</sup> T cells were surrounded by at least one SOSTDC1-EGFP<sup>+</sup> neighbor cell with a distance of less than one cell diameter (Fig. 4E), suggesting that SOSTDC1<sup>+</sup> cells func-

tion by aiding nearby T<sub>FR</sub> cells in B cell follicle and T-B cell border regions. Last, in vitro coculture assays demonstrated that SOSTDC1<sup>+</sup> T<sub>FR</sub> cells helped maintain the T<sub>FR</sub> cell phenotype (fig. S14). Thus, SOSTDC1-expressing T<sub>FR</sub> cells have the capacity to promote T<sub>FR</sub> cell formation and maintenance.

Previous studies have shown that SOSTDC1 is capable of modulating the WNT-β-catenin signaling pathway through WNT receptors, including LRP4, LRP5, and LRP6 (17, 19). Only Lrp5 and Lrp6 were highly expressed in T<sub>FR</sub> and T<sub>reg</sub> cells (fig. S15A). When stimulating T cells with Wnt3a plus increased dosage of SOSTDC1, SOSTDC1 attenuated the levels of β-catenin and phosphorylated LRP6 in a dose-dependent manner (fig. S15B). Furthermore, double disruption of LRP5 and LRP6 appreciably rescued both Foxp3<sup>+</sup> T<sub>reg</sub> cell and Foxp3<sup>+</sup> CXCR5<sup>+</sup> T<sub>FR</sub> cell subsets in the context of heightened WNT ligands (fig. S15, C to E). Thus, SOSTDC1 can govern T<sub>FR</sub> cell differentiation by neutralizing extrinsic WNT ligands.

Uncontrolled WNT-β-catenin signaling plays a critical role in autoimmune diseases (20, 24–27). SOSTDC1, produced by a subpopulation of T<sub>FR</sub> cells and T-B cell interface-resident stromal FRCs, is able to promote commitment to the T<sub>FR</sub> cell fate by means of the blockade of WNT stimuli. Both this T<sub>FR</sub> cell subpopulation and resident FRCs form a negative regulatory layer to curtail humoral immunity (Fig. 4F). Consequently, manipulation of the reciprocal SOSTDC1-WNT signaling axis may have clinical benefits for vaccine development and the treatment of autoimmune diseases.

## REFERENCES AND NOTES

- C. G. Vinuesa, M. A. Linterman, D. Yu, I. C. MacLennan, *Annu. Rev. Immunol.* **34**, 335–368 (2016).
- S. Crotty, *Annu. Rev. Immunol.* **29**, 621–663 (2011).
- Z. Shulman et al., *Science* **341**, 673–677 (2013).
- G. D. Victora, M. C. Nussenzweig, *Annu. Rev. Immunol.* **30**, 429–457 (2012).
- Y. Chung et al., *Nat. Med.* **17**, 983–988 (2011).
- M. A. Linterman et al., *Nat. Med.* **17**, 975–982 (2011).
- I. Wollenberg et al., *J. Immunol.* **187**, 4553–4560 (2011).
- P. T. Sage, A. H. Sharpe, *Immunol. Rev.* **271**, 246–259 (2016).
- J. B. Wing, W. Ise, T. Kurosaki, S. Sakaguchi, *Immunity* **41**, 1013–1025 (2014).
- W. Fu et al., *J. Exp. Med.* **215**, 815–825 (2018).
- D. Botta et al., *Nat. Immunol.* **18**, 1249–1260 (2017).
- B.-H. Yang et al., *Cell Rep.* **27**, 3629–3645.e6 (2019).
- J. B. Wing et al., *Proc. Natl. Acad. Sci. U.S.A.* **114**, E6400–E6409 (2017).
- I. Sayin et al., *J. Exp. Med.* **215**, 1531–1542 (2018).
- C. Jandl et al., *Nat. Commun.* **8**, 14647 (2017).
- X. Liu et al., *J. Exp. Med.* **209**, 1841–1852 (2012).
- Y. Ahn, B. W. Sanderson, O. D. Klein, R. Krumlauf, *Development* **137**, 3221–3231 (2010).
- S. W. Cho et al., *Development* **138**, 1807–1816 (2011).
- N. Itasaki et al., *Development* **130**, 4295–4305 (2003).
- J. van Loosdregt et al., *Immunity* **39**, 298–310 (2013).
- T. Sumida et al., *Nat. Immunol.* **19**, 1391–1402 (2018).
- J. Laurikkala, Y. Kassai, L. Pakkasjärvi, I. Thesleff, N. Itoh, *Dev. Biol.* **264**, 91–105 (2003).
- Y. Yoshioka, M. Ono, M. Osaki, I. Konishi, S. Sakaguchi, *Eur. J. Immunol.* **42**, 749–759 (2012).
- S. Keerthivasan et al., *Sci. Transl. Med.* **6**, 225ra28 (2014).

25. N. Macías-Segura *et al.*, *PLOS ONE* **13**, e0194205 (2018).  
26. N. Harada *et al.*, *EMBO J.* **18**, 5931–5942 (1999).  
27. T. Reya *et al.*, *Immunity* **13**, 15–24 (2000).

ACKNOWLEDGMENTS

We thank T. Sumida from Yale University for sharing RNA-seq data and J. He from Yan Wang’s laboratory for his help with immunofluorescent staining. **Funding:** The study was supported by the National Key Research and Development Program of China (2016YFA0101200 to X.L. and X.-W.B.) and the National Natural

Science Foundation of China (31770973 to X.L., 81703531 to X.W., and 81101982 to Z.Y.) **Author contributions:** Conceptualization: X.L.; Investigation: X.W., Yu.W., R.H., Q.G., M.S., Ha.L., Xiaow.Y., Xiang Z., Y.S., S.X., Lo.C., Xia Z., Z.Y., F.W., Hu.L., and Xiaoh.Y.; Mouse strain provider: B.Z., F.W., Li.C., and C.D.; Supervision: X.L., X.-W.B., and Ya.W. **Competing interests:** The authors declare no competing interests. **Data and materials availability:** RNA-seq, scRNA-seq, and ATAC-seq (assay for transposase-accessible chromatin using sequencing) data have been deposited in the Gene Expression Omnibus (GSE142523).

SUPPLEMENTARY MATERIALS

science.sciencemag.org/content/369/6506/984/suppl/DC1  
Materials and Methods  
Figs. S1 to S15  
References (28–35)

[View/request a protocol for this paper from Bio-protocol.](#)

20 December 2019; accepted 12 June 2020  
10.1126/science.aba6652



## NEUROSCIENCE

# Julich-Brain: A 3D probabilistic atlas of the human brain's cytoarchitecture

Katrin Amunts<sup>1,2\*,†</sup>, Hartmut Mohlberg<sup>1\*,†</sup>, Sebastian Bludau<sup>1</sup>, Karl Zilles<sup>1</sup>

Cytoarchitecture is a basic principle of microstructural brain parcellation. We introduce Julich-Brain, a three-dimensional atlas containing cytoarchitectonic maps of cortical areas and subcortical nuclei. The atlas is probabilistic, which enables it to account for variations between individual brains. Building such an atlas was highly data- and labor-intensive and required the development of nested, interdependent workflows for detecting borders between brain areas, data processing, provenance tracking, and flexible execution of processing chains to handle large amounts of data at different spatial scales. Full cortical coverage was achieved by the inclusion of gap maps to complement cortical maps. The atlas is dynamic and will be adapted as mapping progresses; it is openly available to support neuroimaging studies as well as modeling and simulation; and it is interoperable, enabling connection to other atlases and resources.

**M**aps of the microstructural segregation of the human brain can offer improved understanding of the biological substrates of brain functions, dysfunctions, and behavior. Cytoarchitecture—the arrangement of cells, their distribution, composition, and layering—is a major principle of microstructural brain organization. It is closely linked to the connectivity pattern of a region and its function (1). Furthermore, cytoarchitecture allows multiple aspects of brain organization (such as myeloarchitecture, molecular architecture, gene expression, and activation or resting-state networks) to be referenced to a common ground that serves as the interface to represent and integrate the different aspects of brain organization (2). It is widely accepted that a multifaceted but integrated approach is a prerequisite for research into brain organization (3, 4).

Brodmann's cytoarchitectonic map from 1909 was one of the first maps of its kind and is still widely used. It has several limitations; for example, it shows only the left hemisphere of a single brain and therefore cannot account for intersubject variability. Evidence has been obtained that the number of cortical areas is in the range of 180 or more (2, 5, 6), as compared to 43 areas in Brodmann's map. Subcortical structures have been mapped with the same level of detail (7) but are not part of the Brodmann atlas. Without analyzing and processing thousands of histological sections per brain with consistently high quality, the variable cytoarchitecture of areas and nuclei in a cytoarchitectonic map cannot be captured with sufficient spatial resolution (8).

We created the Julich-Brain atlas in our labs in Jülich and Düsseldorf (Fig. 1). It is a cytoarchitectonic atlas containing probabilistic maps of cortical areas and subcortical nuclei. Having started this endeavor in the mid-1990s, we more recently resorted to “crowdsourcing” strategies (but on a high professional level and based on profound expertise), which in turn required Big Data-capable processing workflows. All of the necessary steps—preparation of human brain tissue, microstructural mapping, analysis, and complex data processing—are data-, time-, and labor-intensive, all the more so with increasing sample sizes and higher spatial resolution. It is thus impossible to provide whole-brain maps with sufficient detail by single researchers or small teams in an acceptable time frame. Increased computing power and storage capacities, as well as improved algorithms and workflows for data processing, now enable much faster and more robust processing at high spatial resolution.

However, not all datasets and analyses benefit equally from improved data acquisition techniques. Our cytoarchitectonic mapping efforts started more than 25 years ago. The brains have already been histologically processed, and neither new high-field magnetic resonance imaging (MRI) data nor high-resolution blockface images can be acquired afterward. The quality of MRI data is thus constrained by the quality available at the time of acquisition. This may sometimes restrict the use of modern imaging tools and techniques, because these are often geared toward currently available data quality. Specific data processing strategies considering both recent and older datasets are mandatory. To ensure accuracy, reproducibility, and consistency of data and processing steps over the entire data life cycle, automated and reproducible workflows governed by provenance tracking are necessary.

We therefore developed a modular, flexible, and adaptive framework to create probabilistic cytoarchitectonic maps, resulting from the analysis of 10 postmortem human brains, for each area (Fig. 2). Maps were aligned to two widely used stereotaxic spaces, MNI-Colin27 and ICBM152casym space (9), and superimposed. The Julich-Brain atlas allows comparison of functional activations, networks, genetic expression patterns, anatomical structures, and other data obtained across different studies in a common stereotaxic reference space (Fig. 3). The framework relies on long-standing expertise for handling whole human postmortem brains, cytoarchitectonic mapping of a variety of cortical and subcortical regions, and computational expertise to develop robust and adaptive tools, using both local clusters and supercomputers. All of these aspects have changed over time, and the creation of a uniform, reproducible, and probabilistic brain atlas depends on their convergence.

The Julich-Brain atlas is based on histological sections of 23 postmortem brains (11 female, 12 male; mean age = 64 years, age range = 30 to 86 years; mean postmortem delay = 12 hours; table S1) acquired from the body donor programs of the Anatomical Institute of the University of Düsseldorf. The brains were fixed in formalin or Bodian solution, subjected to MRI, embedded in paraffin, and serially cut with a microtome into 20- $\mu$ m sections (10). Cell bodies were stained using a modified Merker method. Histological sections were digitized with flatbed scanners at 10  $\mu$ m, reduced to an isotropic resolution of 20  $\mu$ m, framed to a fixed picture size, and stored as lossless compressed gray-level images. Two brains constitute complete series [the “BigBrain datasets,” one of which was published in (11)], where every single section was stained and digitized. The other brains were stained with intervals of up to 15 sections. This resulted in more than 24,000 histological sections. Histological processing and staining, including mounting of sections and removal of small wrinkles and folds, entailed some degree of local deformation, damage, or staining inhomogeneity. Although this was unavoidable, fewer than 1% of the sections showed irretrievable damage (e.g., loss of substantial parts of the tissue), and 20 to 30% had small, local damages. To correct for distortions in histological sections, we used the corresponding MRI datasets for 3D reconstruction (Fig. 2). Rather severe areas of damage in images of histological sections were manually and, where applicable, semiautomatically corrected (11) (fig. S1A).

The time-consuming repairs and the considerable amount of computing time for processing the BigBrain datasets required a workflow using supercomputers. The large number of

<sup>1</sup>Institute of Neuroscience and Medicine (INM-1), Research Centre Jülich, Jülich, Germany. <sup>2</sup>C. and O. Vogt Institute for Brain Research, University Hospital Düsseldorf, Heinrich Heine University Düsseldorf, Düsseldorf, Germany.

\*Corresponding author. Email: k.amunts@fz-juelich.de (K.A.); h.mohlberg@fz-juelich.de (H.M.)

†These authors contributed equally to this work.

datasets, in combination with the complexity and diversity of the overall reconstruction workflow, required time- and resource-effective computational processing. This in turn required advanced management of big datasets, computing, and provenance tracking (fig. S1). On the basis of the reconstruction of BigBrain 1 (11), an adapted workflow was developed for the reconstruction of BigBrain 2, which includes an elaborate data provenance tracking system. It served as the basis for a general-purpose dataflow management system that allowed restricting the recalculation to only those images that were affected by subsequent repairs (fig. S1A), resulting in a substantial reduction of computing time (12). In addition, the pipeline of the BigBrain 2 dataset was closely linked to the overall workflow and was used in a similar way as for the other 21 postmortem brains. To recover the original shape and topology of the brain volume, we computed a 3D reconstruction of histological sections (fig. S3); for a recent survey of methods, see (13). The approach is based on a multistep procedure starting from an initially 3D dataset at a resolution of  $0.3 \text{ mm}^3$  and is explained in the supplementary materials.

Human brains show a variable pattern of sulci and gyri, plus intersubject variability in shape, localization, and extent of cytoarchitectonic regions (2). To make brains comparable, we initially transferred 3D reconstructed histological datasets to the stereotaxic space of the single-subject MNI-Colin27 template (fig. S3). In contrast to templates resulting from an “average” of many brain datasets [e.g., the MNI305 template (9)], the individual reference brain shows a detailed (but not representative) anatomy, thus allowing a precise registration of the gross anatomy of the postmortem brains to that space. Because mean group datasets are well accepted in the neuroimaging community, nonlinear transformations into the ICBM2009casym space were also computed. This template represents a compromise between the detailed but specific anatomy of the MNI-Colin27 brain and the more generic but smoother MNI305 template. The representation of the maps in these two spaces makes Julich-Brain interoperable with other atlases and resources [e.g., (6, 7, 14, 15)] and connects it to large cohort studies such as the Human Connectome Project (HCP; [www.humanconnectome.org](http://www.humanconnectome.org)) and UK Biobank ([www.ukbiobank.ac.uk](http://www.ukbiobank.ac.uk)) (see also supplementary materials).

Different approaches are available to register postmortem brains to each other [for an overview, see (13)]. To develop an atlas with both cortical areas and subcortical nuclei, we started with a volume-based approach, which provided a consistent registration framework for both cortical and subcor-

tical structures. An elastic 3D registration was applied with a well-matched parameter set that was also used for the 2D registrations. The method showed high reliability in both postmortem and in vivo datasets. The registration of all postmortem brains to the MNI-Colin27 and the ICBM152casym reference brains resulted in a similar folding pattern and shape of the 3D-reconstructed datasets and the template (fig. S3). The 3D vector field transformations of each 3D-reconstructed histological dataset were stored and were later applied to the mapped cytoarchitectonic areas.

To date, 41 projects have resulted in maps of 248 cytoarchitectonic areas (Fig. 1). Projects were carried out by doctoral students, researchers, and guest scientists and have been published in peer-reviewed scientific journals [for an overview, see (2)]. These publications provide details of cytoarchitecture, localization with respect to sulci/gyri and stereotaxic space, intersubject variability, and other features; some of them also refer to the relationship of the areas to functional imaging studies, receptor architecture, and/or area-specific gene expression.

Each map is based on analyses of 10 postmortem brains (5 male, 5 female), which were selected from the pool of 23 brains on the basis of their folding pattern, the presence of already mapped neighboring areas, the orientation of the cutting plane, etc. Consequently, overlapping and sometimes similar samples were analyzed for different regions.

Depending on the size and shape of a structure, every 15th to 60th section was mapped over the whole extent of a cytoarchitectonic region. Borders between cortical areas were identified using image analysis and statistical criteria to make mapping reproducible (16). The positions of borders were labeled in the digitized sections, and a closed polygon (contour line) marked its extent in the section (fig. S4). For subcortical nuclei, the outer boundaries of nuclei were identified in histological sections and labeled as closed polygonal lines. Contour lines were also used for a quality check of each map over its full extent (fig. S4).

As a next step, individual shrinkage-corrected volumes for each area/nucleus, hemisphere, and brain were calculated (see supplementary materials). The analysis of the 120 currently available areas showed considerable

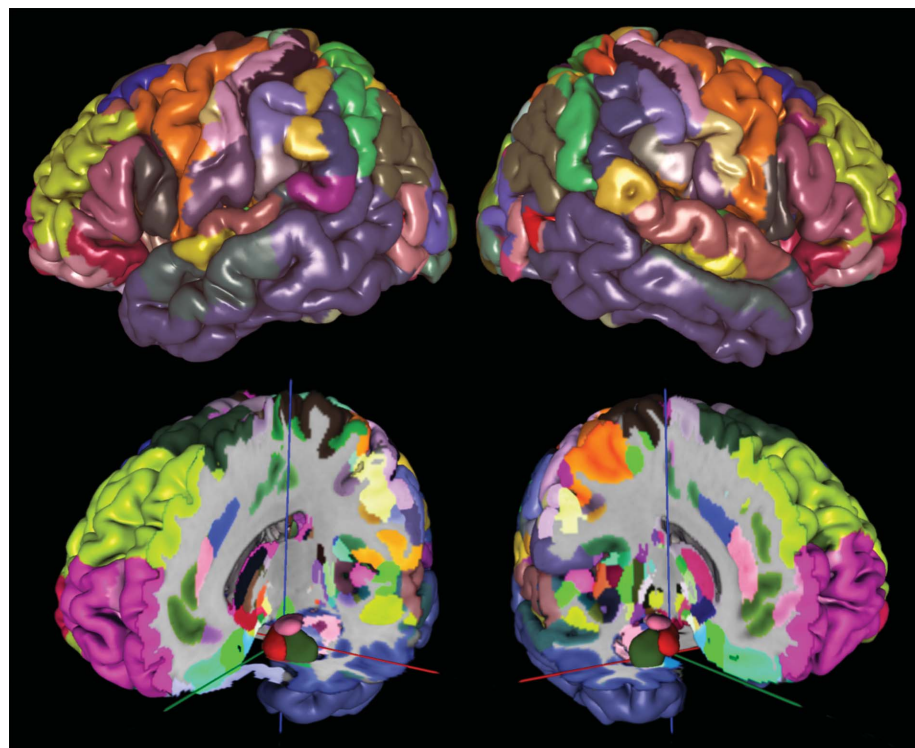


**Fig. 1. Cytoarchitectonic maximum probability maps of Julich-Brain in MNI-Colin27 reference space.**

Areas have different colors; views of the left and right hemispheres are shown. The lower panel shows structures located in the depths of the brain. Datasets of published areas are freely available through the Julich-Brain and HBP data portals. Both web-based interfaces allow the visualization and inspection of probabilistic and maximum probability maps as surface (pial, smoothed white matter, inflated) and volume representations.



intersubject differences in volume (fig. S5), but differences between the two hemispheres were not significant at a global level, nor were differences between male and female brains (see table S2 for full information on these volumes). The list of volumes is a growing resource together with the probabilistic maps of areas and nuclei, made available and constantly updated through the Knowledge graph of the European Human Brain Project (HBP; see <https://ebrains.eu>).

The comparison of the degree of intersubject variability suggests differences between brain regions (fig. S5). For example, we found high variability (i.e., low values for probability) in Broca's region with areas 44 and 45 and the superior parietal lobule, whereas the occipital pole with the primary and secondary visual cortices (BA17/18) and area Te3 in the temporal lobe appeared less variable.

Previous and ongoing mapping projects resulted in more than 10,616 XML files con-

taining 85,210 contour lines with 3,737,771 points and a total length of 1961 m. Stacks with contour lines were managed using the open-source version control software Subversion, which automatically manages files and directories so as to document the complete history of how the localization of an areal border might have changed over its life cycle (fig. S1B). Changes may occur when a new mapping project requires reanalysis of an already existing map, but these have been small in the past.

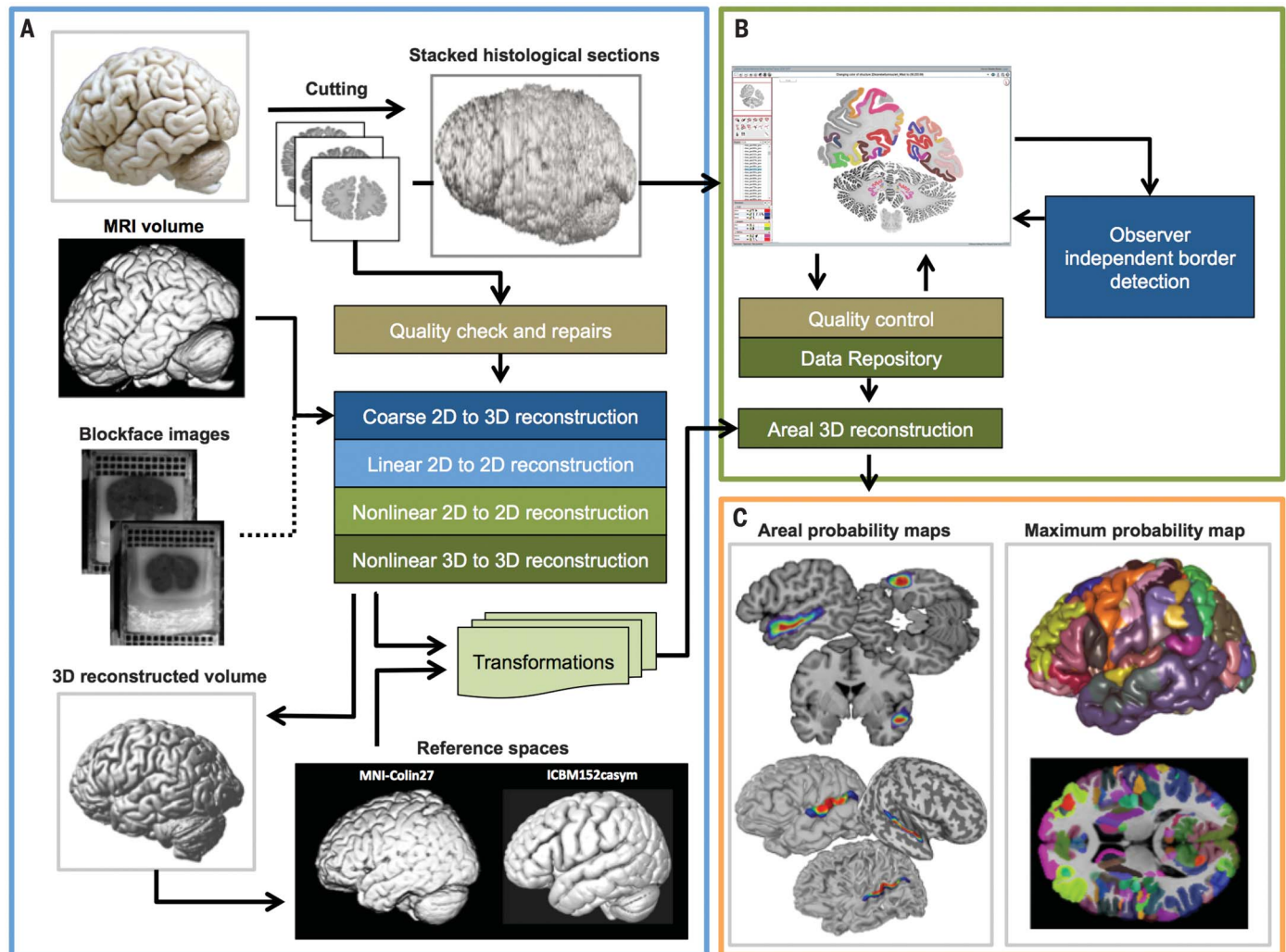


**Fig. 2. Workflow of the 3D reconstruction of serial histological sections and alignment of brain data to a reference space, cytoarchitectonic analysis in 2D images, and the computing of the probabilistic Julich-Brain atlas.**

(A) To recover the 3D shape of a postmortem brain, we applied a combination of linear and nonlinear processing steps at different scales based on the undistorted MRI dataset, and optional on blockface images, obtained during sectioning. The digitized histological images were repaired and corrected for illumination and optical imbalances. A rigid section-to-section alignment was computed to create a first approximate 3D reconstruction. It served to align the MRI dataset to the corresponding section planes by a rigid-body transformation. The sections were nonlinearly registered to the sections of the MRI by an elastic method. The alignment was improved by re-registering the output several times, section

by section, to a median filtered version. (B) The cytoarchitecture was analyzed in consecutive histological sections covering the complete extent of an area and characterized by the gray-level index (16). Contour lines of the areas were submitted to a data repository, 3D-reconstructed, and topologically normalized. Linear and nonlinear transformations were applied to the areas, and areas were superimposed to form the cytoarchitectonic probability map. (C) Volume- and surface-based maximum probability maps of the Julich-Brain atlas were computed. To effectively organize the intensive computations, we implemented a data processing management system that allowed distributed processing of a large number of datasets across multiple CPU cores. It was designed to scale up well from a single core computer system up to thousands of computing nodes in a high-performance computing environment (12). See fig. S1, A to C, for details.

The areas and nuclei were also transformed to the stereotaxic *MINI-Colin27* and *ICBM2009* asym reference space, using the computed whole-brain transformations, and superimposed (see supplementary materials). The resulting probabilistic, cytoarchitectonic maps were stored as volume data files. By projecting the probability values onto the surface, a surface-based representation of cytoarchitectonic cortical maps was computed (Fig. 1 and fig. S6). The result-

ing values, indicating the probability of an area or nucleus being localized in a given voxel (0% to 100% overlap), range from 0.0 to 1.0; this number provides a measure for variations of a given area in localization and extent from brain to brain (i.e., intersubject variability). These probabilistic maps overlap with each other; that is, voxels in reference space can usually be assigned to more than one area, each with a well-defined probability, summing up to 100%

(fig. S6). We found that about 50% of the voxels were associated with a single area or nucleus, 35% with two, and 15% with three or more.

To reduce complexity and to visualize the extent of areas comparable to Brodmann's map, we calculated a maximum probability map (MPM). Each voxel in the reference brain was assigned to the cytoarchitectonic area with the highest probability at that position (17). The average overlap fraction of all currently

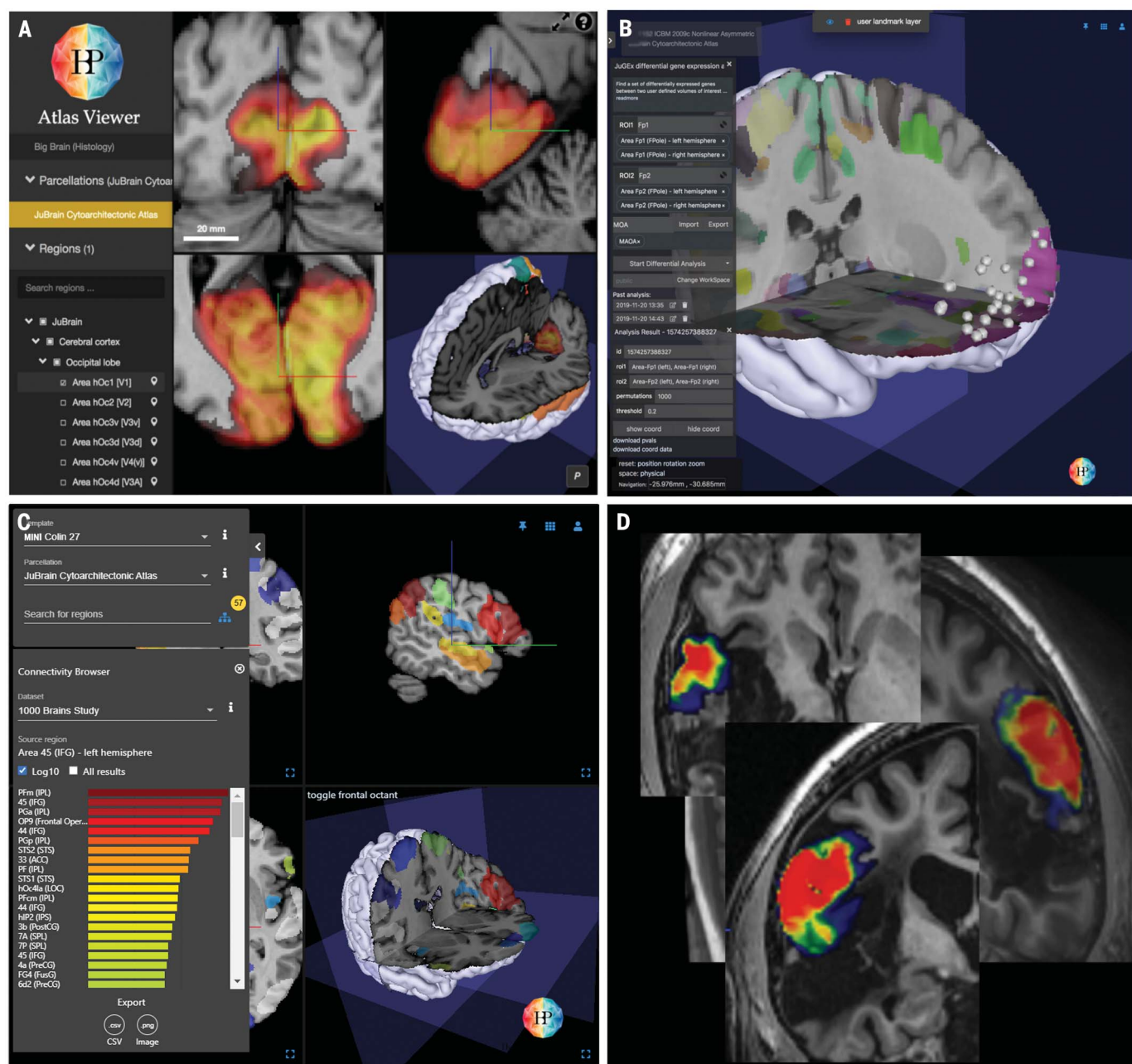


**Fig. 3. Examples of applications of the Julich-Brain atlas.** (A) Screenshot of the web-based atlas tool in the Human Brain Atlas of the HBP showing probability maps in different views. (B and C) JuGEx enables analysis of differential gene expression in cytoarchitectonic maps (B) and linkage and exploration of DTI-based

connectivity (e.g., left Broca's area 45) (C). (D) Superposition of the probabilistic map of Broca's area 44 on a dataset of a patient with a brain lesion and aphasia. The maps allow precise statements about the microanatomical location of a neuroimaging finding, and are a tool to quantify these findings by using the maps as a mask.



mapped and adjacent areas results in a threshold value of about 35%. Under the assumption that this threshold also applies to MPM borders to yet unmapped areas, this threshold is used to cut the MPM toward unmapped regions. The visualization of neighboring areas demonstrates that gyri may be occupied by one or more areas that differ in cytoarchitecture and function. Conversely, single areas may be found on more than one gyrus; examples are given for the auditory cortex in fig. S7. The manifold of relationships between areas and sulci/gyri illustrates the advantage and higher precision of cytoarchitectonic probabilistic maps as compared to macroscopic brain maps.

At present, about 70% of the cortical surface has been covered by completed and published mapping projects. However, there are still areas that have not been mapped and represent projects for future research. To provide whole-brain coverage for the cortex (fig. S8), we have combined parts of the cortex that have not yet been charted into several “gap maps,” pooling these uncharted areas in a given brain region (see supplementary materials and fig. S9). The distributions were modeled so that probabilistic gap maps were computed in analogy to the other maps. As mapping progresses, new maps are continuously replacing gap maps while the process is captured and documented by provenance tracking. Consequently, the atlas is not static (as is, e.g., Brodmann’s map) but rather represents a “living map”—a concept that is known, for example, from geography for navigating complex spaces.

Gap maps allow computation of a parcellation covering the entire cortical surface and the unambiguous assignment of each position to a cortical region. Together with the increasing number of probabilistic maps of subcortical nuclei, gap maps contribute to a whole-brain human atlas. Maps in Julich-Brain can be combined with findings in other atlases and maps; one example involves the study of microstructural correlates of activations from neuroimaging studies of healthy subjects and patients (Fig. 3). Moreover, Julich-Brain contributes to brain modeling and simulation through informing the model by a functionally sound microstructural parcellation. It is expected that this will open new avenues to generate models of brain activity such as those used in the treatment of epilepsy, where personalized brain models are used to predict the propagation of seizures (18).

The modular, flexible, and extensible workflows cover a broad range of steps from image acquisition to 3D reconstruction and the generation of probabilistic maps, which can be found in several areas of research. The methodical framework (or parts of it) can be extended to brains of other species, and it can be used to process section images labeled by other techniques (e.g., immunohistology). New modules can be added to the workflows for applications such as mapping brain areas on the basis of deep learning (19).

The Julich-Brain atlas is a freely available resource ([www.julich-brain.org](http://www.julich-brain.org)). Maps have been made available through different tools and websites such as the SPM anatomy toolbox ([www.fz-juelich.de/inm/inm-7/JuelichAnatomyToolbox](http://www.fz-juelich.de/inm/inm-7/JuelichAnatomyToolbox)), FSL (<https://fsl.fmrib.ox.ac.uk>), FreeSurfer (<https://surfer.nmr.mgh.harvard.edu>), and the EBRAINS research infrastructure of the HBP (<https://ebrains.eu/services/atlas>). The maps can be linked to diffusion tensor imaging (DTI)-based connectivity data (Fig. 3C) and to gene expression data provided by the Allen Institute for Brain Science (<https://alleninstitute.org/what-we-do/brain-science>) through the JuGEx tool (20) to enable a multimodal perspective on human brain organization (Fig. 3B).

Julich-Brain represents a new kind of human brain atlas that is (i) cytoarchitectonic to reflect a basic principle of the brain’s microstructural parcellation; (ii) whole-brain, to cover both the cerebral cortex and subcortical nuclei; (iii) 3D-probabilistic, to consider variations between individual brains in stereotaxic space; (iv) dynamic, a living atlas, to be supplemented by maps of new areas or subdivision of existing maps of areas (e.g., when new studies suggest a finer or new parcellation); (v) flexible, to allow for modifications of modules in the workflows for other data modalities, organs, or species; (vi) open-access and based on FAIR principles, to contribute to studies by other researchers addressing structure-function relationships and network organization; and (vi) interoperable, to link it to other atlases and resources that provide complementary information about brain organization.

## REFERENCES AND NOTES

1. A. Goulas, K. Zilles, C. C. Hilgetag, *Trends Neurosci.* **41**, 775–788 (2018).
2. K. Amunts, K. Zilles, *Neuron* **88**, 1086–1107 (2015).
3. D. C. Van Essen *et al.*, *Proc. Natl. Acad. Sci. U.S.A.* **116**, 26173–26180 (2019).
4. B. Fischl, M. I. Sereno, *Neuroimage* **182**, 219–231 (2018).

5. R. Nieuwenhuys, C. A. J. Broere, *Brain Struct. Funct.* **222**, 465–480 (2016).
6. M. F. Glasser *et al.*, *Nature* **536**, 171–178 (2016).
7. J. K. Mai *et al.*, *Atlas of the Human Brain* (Academic Press, ed. 4, 2015).
8. K. Zilles, K. Amunts, *Nat. Rev. Neurosci.* **11**, 139–145 (2010).
9. A. C. Evans, A. L. Janke, D. L. Collins, S. Baillet, *Neuroimage* **62**, 911–922 (2012).
10. K. Amunts *et al.*, *J. Neurosci.* **27**, 1356–1364 (2007).
11. K. Amunts *et al.*, *Science* **340**, 1472–1475 (2013).
12. H. Mohlberg *et al.*, in *Brain-Inspired Computing: Second International Workshop, BrainComp 2015*, K. Amunts *et al.*, Eds. (Springer, 2016), pp. 15–27.
13. J. Pichat, J. E. Iglesias, T. Yousry, S. Ourselin, M. Modat, *Med. Image Anal.* **46**, 73–105 (2018).
14. H. Damasio, *Human Brain Anatomy in Computerized Images* (Oxford Univ. Press, ed. 2, 2005).
15. S. L. Ding *et al.*, *J. Comp. Neurol.* **524**, 3127–3481 (2016).
16. A. Schleicher *et al.*, *Anat. Embryol.* **210**, 373–386 (2005).
17. S. B. Eickhoff *et al.*, *Neuroimage* **25**, 1325–1335 (2005).
18. T. Proix, F. Bartolomei, M. Guye, V. K. Jirsa, *Brain* **140**, 641–654 (2017).
19. H. Spitzer *et al.*, in *Medical Image Computing and Computer Assisted Intervention—MICCAI 2018, Part III*, A. F. Frangi *et al.*, Eds. (Springer, 2018), pp. 663–671.
20. S. Bludau *et al.*, *Brain Struct. Funct.* **223**, 2335–2342 (2018).

## ACKNOWLEDGMENTS

We thank more than 41 postdocs, doctoral students, guests, and colleagues who contributed to the mapping of 248 cytoarchitectonic areas and nuclei; the technical assistants of the C. and O. Vogt Institute of Heinrich Heine University Düsseldorf and Research Centre Jülich; S. Eickhoff, R. Hübbers, P. Pieperhoff, N. Palomero-Gallagher, S. Caspers, T. Dickseid, and A. C. Evans for intensive discussions; A. Schleicher for developing the original observer-independent mapping approach; our partners of the International Consortium for Human Brain Mapping who stimulated and actively supported this research; and our colleagues at the Jülich Supercomputing Centre, in particular B. Tweddell and T. Lippert. **Funding:** Supported by the Portfolio Theme “Supercomputing and Modeling for the Human Brain” of the Helmholtz Association, the European Union Seventh Framework Programme (FP7/2007-2013, HBP), and the European Union’s Horizon 2020 Research and Innovation Programme, grant agreements 604102 (HBP SGA1), 785907 (HBP SGA2), and 945539 (HBP SGA3). **Author contributions:** K.A. and K.Z. developed the concept of 3D probabilistic cytoarchitectonic brain mapping and atlas. K.A. is overseeing the atlas projects, contributed to methodological developments, and drafted the manuscript. H.M. developed and adapted the methodology and the software for data processing and atlas building, and drafted the manuscript. S.B. developed new tools for analysis and mapping of cytoarchitectonic areas. All authors contributed to the writing of the manuscript. **Competing interests:** The authors declare no competing interests. **Data and materials availability:** All data are available in the main text or the supplementary materials. Various data modalities of the already published maps of brain areas and the complete atlas are available online at [www.julich-brain.org](http://www.julich-brain.org) and via EBRAINS (<https://ebrains.eu/>) (DOI: 10.25493/TAKY-64D). Previously developed parts of the workflows were published earlier; new scripts for computing the Julich-Brain Atlas and for analyzing contour lines and gap maps (<https://doi.org/10.5281/zenodo.3906413>) are provided via the git repository, <https://github.com/JulichBrainAtlas>.

## SUPPLEMENTARY MATERIALS

[science.sciencemag.org/content/369/6506/988/suppl/DC1](https://science.sciencemag.org/content/369/6506/988/suppl/DC1)  
Materials and Methods  
Figs. S1 to S9  
Tables S1 and S2  
References (21–56)

27 February 2020; accepted 24 June 2020  
Published online 30 July 2020  
10.1126/science.abb4588

## DRUG DEVELOPMENT

# Antitumor activity of a systemic STING-activating non-nucleotide cGAMP mimetic

Emily N. Chin<sup>1</sup>, Chenguang Yu<sup>1,2\*</sup>, Vincent F. Vartabedian<sup>3\*</sup>, Ying Jia<sup>1,3\*</sup>, Manoj Kumar<sup>2</sup>, Ana M. Gamo<sup>2</sup>, William Vernier<sup>2</sup>, Sabrina H. Ali<sup>1</sup>, Mildred Kissai<sup>1</sup>, Daniel C. Lazar<sup>3</sup>, Nhan Nguyen<sup>3</sup>, Laura E. Pereira<sup>1</sup>, Brent Benish<sup>2</sup>, Ashley K. Woods<sup>2</sup>, Sean B. Joseph<sup>2</sup>, Alan Chu<sup>2</sup>, Kristen A. Johnson<sup>2</sup>, Philipp N. Sander<sup>1</sup>, Francisco Martínez-Peña<sup>1</sup>, Eric N. Hampton<sup>2</sup>, Travis S. Young<sup>2</sup>, Dennis W. Wolan<sup>4</sup>, Arnab K. Chatterjee<sup>2</sup>, Peter G. Schultz<sup>1,2</sup>, H. Michael Petrassi<sup>2†</sup>, John R. Teijaro<sup>3†</sup>, Luke L. Lairson<sup>1†</sup>

Stimulator of interferon genes (STING) links innate immunity to biological processes ranging from antitumor immunity to microbiome homeostasis. Mechanistic understanding of the anticancer potential for STING receptor activation is currently limited by metabolic instability of the natural cyclic dinucleotide (CDN) ligands. From a pathway-targeted cell-based screen, we identified a non-nucleotide, small-molecule STING agonist, termed SR-717, that demonstrates broad interspecies and interallelic specificity. A 1.8-angstrom cocrystal structure revealed that SR-717 functions as a direct cyclic guanosine monophosphate–adenosine monophosphate (cGAMP) mimetic that induces the same “closed” conformation of STING. SR-717 displayed antitumor activity; promoted the activation of CD8<sup>+</sup> T, natural killer, and dendritic cells in relevant tissues; and facilitated antigen cross-priming. SR-717 also induced the expression of clinically relevant targets, including programmed cell death 1 ligand 1 (PD-L1), in a STING-dependent manner.

The cyclic guanosine monophosphate (GMP)–adenosine monophosphate (AMP) synthase (cGAS)–stimulator of interferon genes (STING) (cGAS–STING) signaling pathway plays a critical role in the innate response to infection (1, 2). It also serves as a direct link between inflammation and diverse physiological processes, including micronuclei surveillance in the context of DNA damage (3, 4), age-associated inflammation (5), mitochondrial DNA-related inflammatory phenotypes (6), and microbiome-dependent intestinal homeostasis (7). STING is an endoplasmic reticulum signaling protein, partially localized to mitochondria-associated membranes, that is broadly expressed in both immune and nonimmune cell types. STING binds cyclic dinucleotides (CDNs)—including 2',3'-cyclic GMP–AMP (2',3'-cGAMP) produced by cGAS in response to cytosolic DNA (8)—and the scaffolding function rapidly induces type I interferon (IFN) and proinflammatory cytokines in a TBK1–IRF3-dependent fashion (9, 10). STING has been demonstrated to play essential roles in antitumor immunity. For example, efficient tumor-initiated T cell activation requires STING pathway–

dependent IFN- $\beta$  expression, as well as expression of STING in dendritic cells (DCs) (11, 12).

Initial STING agonist small molecules were synthesized as derivatives of the CDN natural ligand; however, because of poor stability properties, CDN-based agonist administration is limited to intratumoral delivery. Although intratumoral delivery of CDN agonists has consistently shown regression of established tumors in syngeneic models (13, 14), intratumoral CDN administration in humans has been met with mixed success. Activation of the STING pathway has also been demonstrated to contribute notably to the antitumor effect of radiation and chemotherapeutics (4, 15, 16). As such, a systemic STING-activating agent has considerable potential utility, not only as a therapeutic for cancer and infectious disease but also as a pharmacological probe to enable mechanistic discovery in the context of STING-dependent antitumor immunity and diverse STING-dependent biological processes.

We used a cGAS–STING pathway-targeted cell-based phenotypic screening approach to identify functional non-nucleotide small-molecule STING agonists. Human monocytic THP-1 cells, harboring an interferon regulatory factor (IRF)–inducible luciferase reporter construct (ISG-THP1), were used to screen a collection of ~100,000 commercially available structurally diverse druglike small molecules in 1536-well plate format [5  $\mu$ M, 0.1% dimethyl sulfoxide (DMSO)]. Confirmed primary hits (plate-based  $z$  score >3) were evaluated in secondary assays involving STING knockout (ISG-THP1 STING-KO) or cGAS knockout

(ISG-THP1 cGAS KO) cell lines (fig. S1) to determine pathway specificity and potential target identity, respectively. Protein thermal shift assays, involving recombinant human and mouse STING protein (hSTING and mSTING), were used to profile compounds for direct on-target binding activity, cross-species activity, and human allele specificity. This resulted in the identification of SR-001 (Fig. 1A), which was found to robustly induce reporter signal in ISG-THP1 cells [fig. S2A; mean effective concentration (EC<sub>50</sub>) ~1.1  $\mu$ M] and ISG-THP1 cGAS KO cells (fig. S2B) but was completely inactive in ISG-THP1 STING KO cells (fig. S2, A to C), suggesting that the compound acts downstream of cGAS with a dependence on STING expression. Commercial SR-001 was also found to increase the thermal stability of the soluble C-terminal CDN-binding domain of recombinant human STING protein (hSTING<sup>REF</sup>) (fig. S2E), which is responsible for recruiting downstream signaling proteins. Chemical resynthesis of SR-001 afforded a compound that was consistently active in cell-based assays (fig. S2D) but was now devoid of activity in the STING thermal shift binding assay (fig. S2E). Analytical characterization of the commercial material revealed the presence of a minor but notable amount of the de-esterified derivative SR-012 (Fig. 1A). This suggested that SR-001 was acting as a prodrug, with ester substitution being a requisite for cell permeability and the active STING-binding species being the carboxylic acid.

Consistent with this hypothesis, synthetic SR-012 was found to bind both recombinant hSTING and mSTING protein (fig. S2E) but was inactive in cell-based assays (fig. S2D). SR-001 was also observed to be rapidly converted to SR-012 in cells (fig. S2F). To address the cell permeability of SR-012 and intracitable rodent exposure properties of the SR-001 prodrug, we completed a medicinal chemistry effort focused on improved prodrug stability or bioisosteric replacement of the carboxylic acid or improved cell permeability for the carboxylic acid. This resulted in the identification of a carboxylic acid-containing analog, containing difluoro-substitution of the aniline ring system (SR-717; Fig. 1B), which was found to possess equivalent cell-based activity when compared with SR-001 prodrug (Fig. 1C; ISG-THP1, EC<sub>50</sub> = 2.1  $\mu$ M; ISG-THP1 cGAS KO, EC<sub>50</sub> = 2.2  $\mu$ M; ISG-THP1 STING KO, no activity up to the limit of solubility). Critically, SR-717 increased the thermal stability of the common human alleles of hSTING (Fig. 1D and fig. S3A), as well as that of recombinant soluble mSTING protein (Fig. 1D), suggesting that the binding mode of SR-717 is not affected by interallelic or interspecies differences in amino acid sequence. This latter issue was ultimately

<sup>1</sup>Department of Chemistry, The Scripps Research Institute, 10550 North Torrey Pines Road, La Jolla, CA 92037, USA.

<sup>2</sup>California Institute for Biomedical Research, 11119 North Torrey Pines Road, La Jolla, CA 92037, USA. <sup>3</sup>Department of Immunology and Microbiology, The Scripps Research Institute, 10550 North Torrey Pines Road, La Jolla, CA 92037, USA. <sup>4</sup>Department of Molecular Medicine, The Scripps Research Institute, 10550 North Torrey Pines Road, La Jolla, CA 92037, USA.

\*These authors contributed equally to this work.

†Corresponding author. Email: petrassi@scripps.edu (H.M.P.); jteijaro@scripps.edu (J.R.T.); llairson@scripps.edu (L.L.L.)



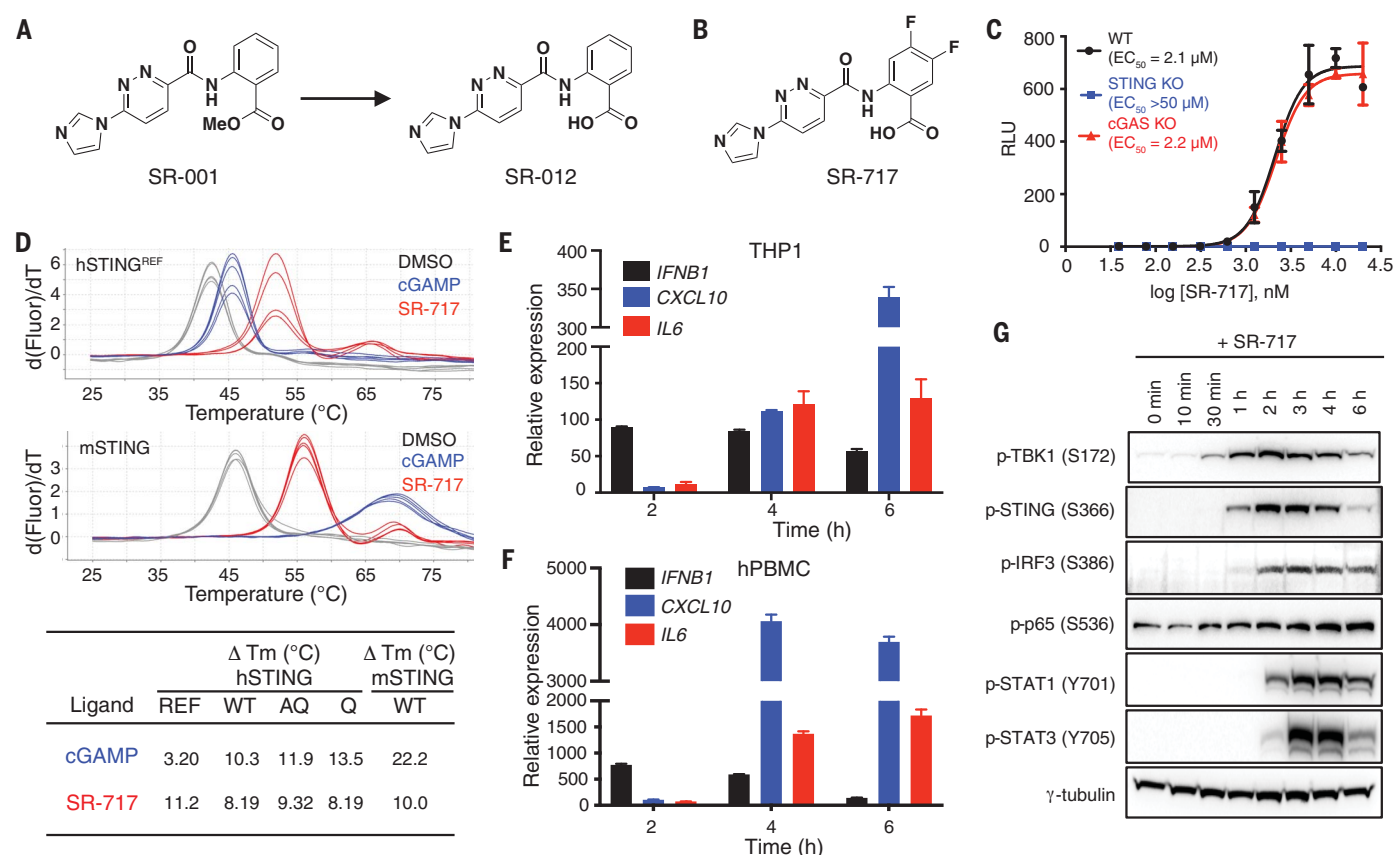


**Fig. 1. Discovery and profile of small-molecule STING agonist SR-717.**

(A) Structure of prodrug screening hit SR-001 and elucidated STING agonist SR-012. Me, methyl. (B) Structure of optimized STING agonist SR-717. (C) Cell-based activity of SR-717 in ISG-THP1 (WT), ISG-THP1 cGAS KO (cGAS KO), and ISG-THP1 STING KO (STING KO) cell lines was quantified by normalizing SR-717-induced reporter activity to DMSO-treated reporter activity for each cell and reported as relative light units (RLU). (D) Impact of SR-717 (100  $\mu$ M) or cGAMP (100  $\mu$ M) on the melting temperature ( $\Delta T_m$ ) of recombinant common human alleles of STING protein (hSTING), as well as recombinant mSTING. REF, R232H; AQ, G230A, R293Q; Q, R293Q; d(Fluor)/dT, first derivative of

fluorescence melt curve. (E) Quantitative reverse transcription polymerase chain reaction (qRT-PCR) analysis of time-dependent target gene expression in THP1 cells treated with SR-717 ( $EC_{80} = 3.6$   $\mu$ M) normalized to DMSO-treated control. (F) qRT-PCR analysis of time-dependent target gene expression in freshly isolated human PBMCs treated with SR-717 (10  $\mu$ M) normalized to DMSO-treated control. (G) Western blot analysis of the kinetics of activation of the cGAS-STING and FN- $\alpha/\beta$  receptor (IFNAR) signaling pathways in THP1 cells stimulated with SR-717 ( $EC_{80} = 3.6$   $\mu$ M).  $\gamma$ -Tubulin was used as a loading control. Data are representative of three independent experiments [(C) to (G)], and values are the mean of three replicates  $\pm$  SD [(C) to (F)].

responsible for the clinical failure of 5,6-dimethylxanthone-4-acetic acid (DMXAA), a vascular disrupting agent that can function as a murine STING agonist but fails to bind to the human form of the protein (17, 18). Characterization of SR-717 in a homogeneous time-resolved fluorescence-based cGAMP competition assay, involving wild-type (WT) human STING protein, revealed that SR-717 binds to STING with an apparent affinity [mean inhibitory concentration ( $IC_{50}$ ) = 7.8  $\mu$ M; fig. S3B] that is comparable to its observed cell-based potency. Compound washout experiments revealed that a robust induction of reporter signal is achieved within 1 hour of exposure (fig. S3C). Further, SR-717 was found to possess mouse pharmacokinetic properties that would enable its in vivo characterization in the context of systemic administration (fig. S4A). Cell-free profiling of SR-717 at a concen-

tration of 5  $\mu$ M against a panel of 468 kinases revealed the compound to be exceptionally selective, with only a single kinase (serine/threonine kinase PIM3) being identified as an interacting partner (fig. S5; percent of control < 35). Kinetic characterization of the cell-based activity of SR-717, at the calculated  $EC_{80}$  concentration (3.6  $\mu$ M), revealed that interferon-stimulated response element (ISRE)-luciferase reporter activity translated to activation of target gene expression. Specifically, SR-717 stimulates *IFNB1* expression within 1 hour of incubation and achieves maximal activation by 2 hours of treatment, whereas activation of *CXCL10*, a transcript activated by both IRF3 and IFN- $\beta$  signaling, peaks at 6 hours (Fig. 1E). Importantly, these kinetics of activation are maintained in primary human peripheral blood mononuclear cells (PBMCs) (Fig. 1F). On-target pathway acti-

vation by SR-717 was further validated by analyzing the phosphorylation of TBK1, IRF3, and p65 signal transduction proteins (Fig. 1G), which are downstream of STING, as well as the secondary activation of STAT1 and STAT3 (Fig. 1G), which are downstream of IFN- $\beta$  and IL-6 signaling, respectively. Further, inhibition of the downstream effector TBK1, using small molecule inhibitor BX795, was observed to block the induction of reporter signal (fig. S6, A and B) and downstream IRF-3 and secondary STAT1 phosphorylation events (fig. S6C) by SR-717.

The soluble cytosolic C-terminal region of hSTING exists in solution as a dimer and binds to naturally occurring and synthetic CDNs with varying degrees of affinity. X-ray crystallographic analysis of this CDN-binding domain has revealed that STING exists as a closely associated dimer that takes the shape

of a “pair of wings,” with an approximate antiparallel four-helix bundle making up an extensive buried dimer interface (19, 20). The solved cocrystal structures of cGAMP bound to hSTING revealed that cGAMP binds in a deep cleft at the dimer interface and causes a substantial conformational change, which leads to the formation of an antiparallel four-strand  $\beta$ -sheet overhead cap element that serves to completely envelop the CDN [fig. S7A, (18, 21)]. In the cGAMP-bound “closed” conformation, the distance between the tips of the symmetry-related  $\alpha 2$  helices is substantially reduced when compared with the unbound protein structure [fig. S7B; Protein Data Bank (PDB) ID 4F9E (19)]. By contrast, binding of di-GMP CDN induces an increase in the angle and distance between the tips of the  $\alpha 2$  helices, leading to the formation of an “open” conformation that lacks the  $\beta$ -sheet overhead cap element [fig. S7C; PDB ID 4F9G (19)]. Mechanistic and structural studies involving cGAMP and DMXAA (18, 21) suggested that ligands that induce the closed conformation lead to STING activation. Interestingly, diABZI-2 was recently described as eliciting the phosphorylation of IRF3 and downstream target expression leading to antitumor immunity by binding to STING and inducing an open conformation akin to that induced by di-GMP [fig. S7D; PDB ID 6DXL (22)]. It is intriguing that CDNs produced directly by bacteria (i.e., di-GMP) can activate STING by stabilizing an open conformation that is so substantially different to that of the closed conformation, which is induced by the endogenously produced secondary message of cytosolic double-stranded DNA (i.e., cGAMP). The biological consequences of differing CDN-induced conformation-dependent STING scaffolding functions remain to be fully characterized.

The 1.8-Å cocrystal structure of SR-717 bound to hSTING<sup>R232</sup> (residues 155 to 341) is shown in Fig. 2A (supporting crystallography statistics are shown in table S1), with simulated anneal omit maps of unbiased electron density for bound ligands shown in fig. S8A. Binding of two molecules of SR-717 at the base of the STING dimer intersubunit cleft closely mimics the binding mode of cGAMP. It induces the same closed conformation (Fig. 2B and fig. S7A), involving a near identical characteristic reduction in distance between the tips of the  $\alpha 2$  helices (Fig. 2C and fig. S7A), as well as the formation of the four-strand  $\beta$ -sheet overhead cap element (Fig. 2, A, B, and D; and fig. S7A). As occurs with both purine bases of bound cGAMP (18, 21), the pyridazine ring of each molecule of SR-717 is “bracketed” by stacking interactions with the side chains of Tyr<sup>167</sup> (Y167) and Arg<sup>238</sup> (R238) from opposing monomers (Fig. 2, D and F, and fig. S9A). The structure of SR-717 facilitates a binding mode in which Thr<sup>263</sup> (T263) side chain hydroxyls from both

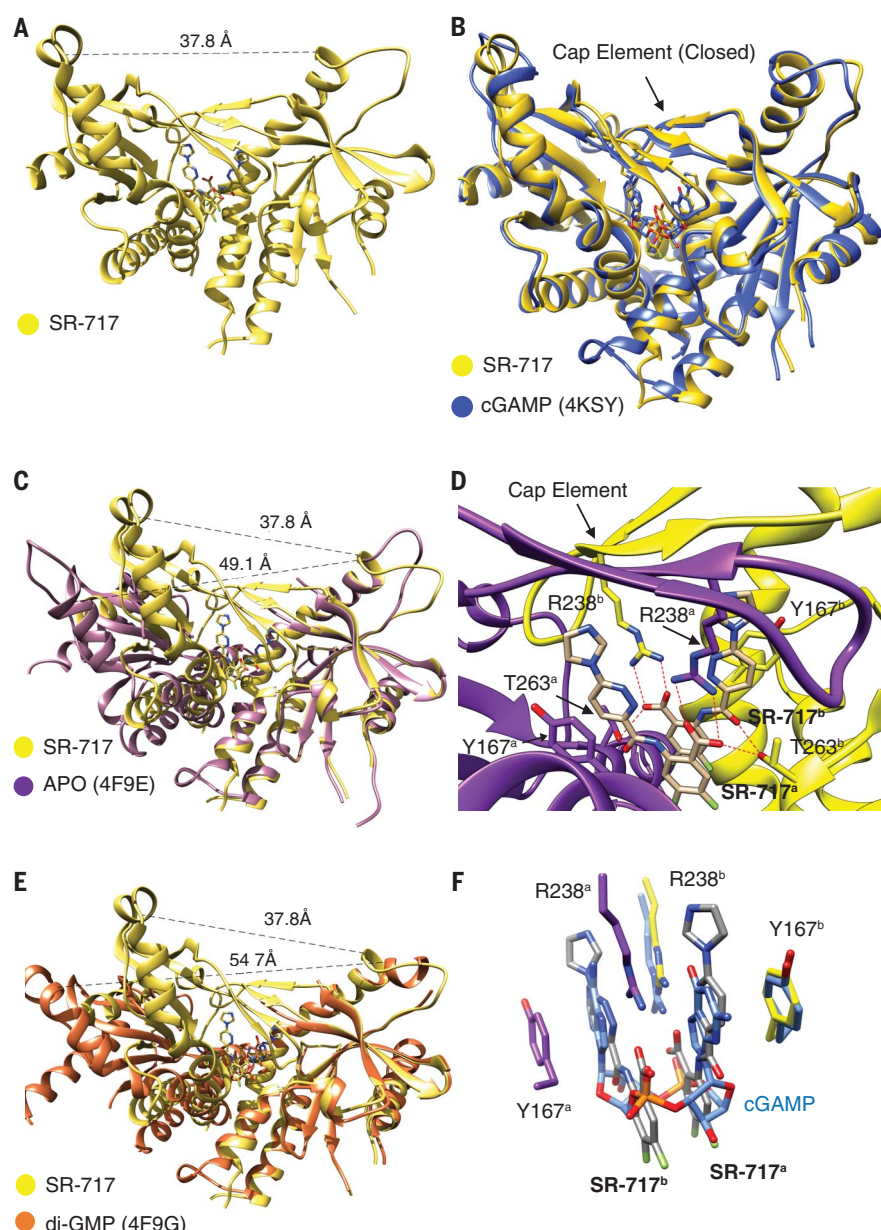


**Fig. 2. Crystal structure of SR-717 bound to hSTING<sup>R232</sup> and comparison to existing hSTING structures and intermolecular contacts.** (A) The 1.8-Å structure of SR-717 bound to hSTING<sup>R232</sup> (residues 155 to 341). Ribbon representation of the symmetrical hSTING<sup>R232</sup> dimer and stick representations of SR-717 are shown. (B) Superposition of the structure of SR-717 bound to hSTING<sup>R232</sup> with the structure of cGAMP bound to hSTING [PDB ID 4KSY (21)], shown as yellow or blue ribbon representations, respectively, highlighting near identical closed conformations and associated formation of characteristic  $\beta$ -sheet overhead cap elements. Stick representations of bound SR-717 or cGAMP are shown. (C) Superposition of the structure of SR-717 bound to hSTING<sup>R232</sup> with the unbound (APO) structure of hSTING [PDB ID 4F9E (19)], shown as yellow or purple ribbon representations, respectively. (D) Details of the intermolecular contacts and hydrogen-bond (dashed red line) network associated with the binding of two molecules of SR-717 to the cGAMP binding site of hSTING<sup>R232</sup>. Residues from individual monomers of the hSTING<sup>R232</sup> dimer are shown in stick format in yellow and purple. The a and b superscripts indicate protein monomer or individual ligand identity. (E) Superposition of the structure of SR-717 bound to hSTING<sup>R232</sup> with the structure of di-GMP bound to hSTING [PDB ID 4F9G (19)], shown as yellow or orange ribbon representations, respectively. Stick representations of SR-717 and di-GMP are shown. (F) Detailed view of the overlay and conserved intermolecular contacts of bound SR-717 and cGAMP ligands from the overlaid hSTING structures shown in (B). Side chains from the SR-717-bound hSTING<sup>R232</sup> structure are shown in yellow or purple, and those from the cGAMP structure are shown in blue. Stick representations of two molecules of SR-717 are shown in gray, and cGAMP is shown in light blue.



monomers are positioned to form hydrogen-bond interactions with both the carboxylic acid of one bound molecule of SR-717 and the amide carbonyl of the other bound SR-717

molecule (Fig. 2D and fig. S9B). These side chains, at the base of the cGAMP binding site, form hydrogen-bonding interactions with the purine bases of bound cGAMP (PDB ID 4KSY).

Consistent with the observed requisite of a carboxylic acid for binding (fig. S2E), the carboxylic acid of each molecule of bound SR-717 is directly positioned in the location of a

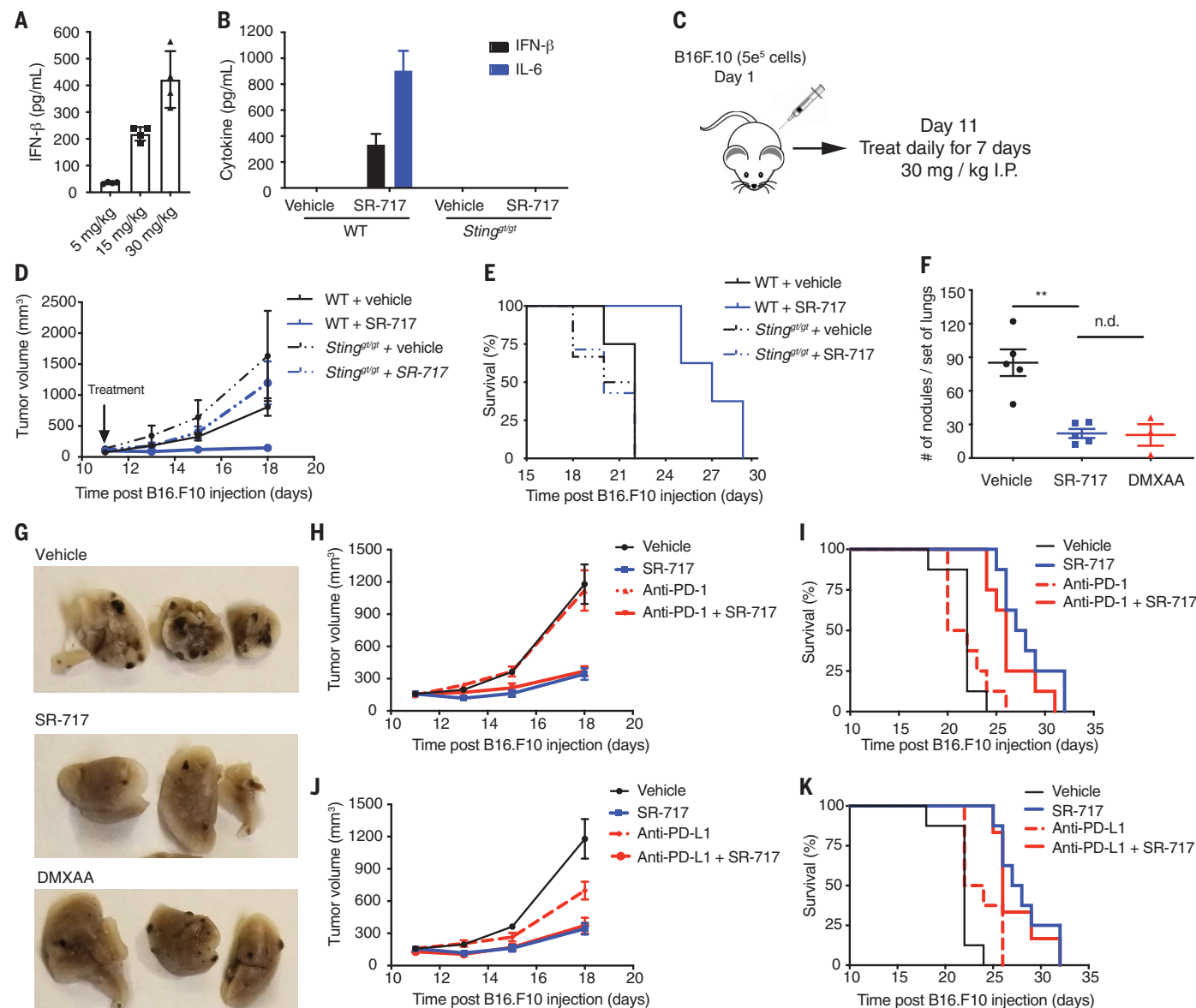


**Fig. 3. STING-dependent pharmacodynamic and antitumor activities of systemic SR-717.** (A) Dose escalation of SR-717 by intraperitoneal injection and corresponding plasma IFN- $\beta$  levels in C57BL/6 mice (n = 4) 4 hours after dosing, after 4 days of daily dosing (n = 4). (B) Plasma concentrations of cGAS-STING signaling target cytokines after dosing with SR-717 (15 mg/kg intraperitoneally) in WT (n = 4) or *Sting*<sup>et/et</sup> mice (n = 4). (C) Schematic of therapeutic treatment strategy of B16.F10 tumor-bearing mice used to evaluate SR-717. I.P., intraperitoneal. (D) Impact of SR-717 [30 mg/kg intraperitoneally, using dosing regimen described in (C)] on B16.F10 tumor growth in WT (n = 8) or *Sting*<sup>et/et</sup> mice (n = 8). (E) Kaplan-Meier survival curve of WT (n = 8) or *Sting*<sup>et/et</sup> B16.F10 tumor-bearing mice (n = 8) after treatment with SR-717 as described in (D). Mice were euthanized when tumor area exceeded 2000 mm<sup>3</sup>. (F) Impact of SR-717 or DMXAA positive control (both dosed at 15 mg/kg intraperitoneally, once per day) on metastasized B16.F10 lung nodule formation in C57BL/6 mice. Pulmonary nodules were quantified 7 days after intravenous

tail vein administration of B16.F10 cells (n = 5 mice for vehicle, n = 5 for SR-717, and n = 3 for DMXAA). Each data point represents the number of nodules per set of lungs in each mouse. \*\*P  $\leq$  0.01; n.d., no difference. (G) Representative images of isolated lungs from studies described in (F). (H) Impact of SR-717 [n = 8, 30 mg/kg intraperitoneally, using dosing regimen described in (C)] starting on day 10; anti-PD-1 antibody (n = 8, 200  $\mu$ g on days 10, 14, and 17); or combination SR-717 plus anti-PD-1 treatment (n = 8) on B16.F10 tumor growth in WT C57BL/6 mice. (I) Kaplan-Meier survival curve of WT B16.F10 tumor-bearing mice (n = 8) after treatments described in (H). (J) Impact of SR-717 [30 mg/kg intraperitoneally, using dosing regimen described in (C)] starting on day 11] (n = 8); anti-PDL1 antibody (200  $\mu$ g on days 11, 14, and 17) (n = 8); or combination thereof (n = 8) on B16.F10 tumor growth in WT C57BL/6 mice. (K) Kaplan-Meier survival curve of WT B16.F10 tumor-bearing mice (n = 8) after treatments described in (J). Data are representative of three independent experiments, and values are the mean  $\pm$  SEM [(A), (B), and (D) to (K)].

backbone phosphate of bound cGAMP (Fig. 2F). This facilitates formation of direct hydrogen-bond contacts with the guanidinium side chains of R238 from both STING monomers (Fig. 2, D and F). These residues are located on opposing ends of the  $\beta$  strands from each monomer that make the intersubunit interactions within the  $\beta$ -sheet cap element (Fig. 2D). By inducing compaction at the base of the binding site (i.e., through interactions with both T263 side chains), mimicking intersubunit stacking interactions and orientating both R238 side chains to induce formation of the  $\beta$ -sheet cap element, SR-717 is able to serve as a direct cGAMP mimetic that activates STING by inducing it to adopt the closed conformation. SR-717 also forms hydrogen-bond interactions with the side chain of R232 from only one monomer (fig. S9B), exactly as is observed for bound cGAMP (PDB ID 4KSY). Additional stabilizing interactions are derived from a water-mediated hydrogen-bond network involving Val<sup>239</sup> (V239), Ser<sup>241</sup> (S241), Asn<sup>242</sup> (N242), and Y240 (fig. S9B). The near identical conformational change induced by SR-717, as well as its ability to directly mimic the binding mode of cGAMP, is highlighted by an overlay of the SR-717-bound hSTING cocrystal structure with the cGAMP-bound complex (Fig. 2, B and F). By contrast, the SR-717 complex clearly does not correspond to the open conformation induced by di-GMP (Fig. 2E; PDB ID 4F9G). Consistent with the observed impact of SR-717 on the thermal stability of mSTING (Fig. 1D), the 2.5-Å cocrystal structure of SR-717 bound to mSTING (residues 154 to 340) (figs. S8B and S10A) is nearly identical to the induced closed-conformation hSTING complex (figs. S10B and S11). SR-717 is a stable cGAMP mimetic that activates STING by inducing the same closed conformation, which thereby provides an avenue to explore this class of systemic STING agonist in diverse contexts, including antitumor immunity.

We used IFN- $\beta$  protein concentrations in circulating plasma as a pharmacodynamic marker of STING target engagement by SR-717, which displayed favorable mouse pharmacokinetic properties (fig. S4A), as well as robust antitumor activity after intratumoral delivery in syngeneic B16.F10 melanoma or MC38 colorectal adenocarcinoma mouse models (fig. S12, A and B, respectively). Dose-dependent induction of IFN- $\beta$  was observed after intraperitoneal administration of SR-717 in WT C57BL/6 mice (Fig. 3A). By contrast, SR-717 did not affect circulating IFN- $\beta$  or associated proinflammatory cytokine expression in *Sting*<sup>gt/gt</sup> mice (Fig. 3B and fig. S16A), thereby demonstrating its selective on-target in vivo activity. Based on the known ability of cGAS-STING pathway activation in DCs to

stimulate CD8 T cell priming (11, 12, 23), we elected to use the poorly immunogenic and highly aggressive syngeneic B16.F10 murine melanoma model (24) to evaluate and characterize the antitumor activities of systemically delivered closed conformation-inducing STING agonists. A therapeutic mode of treatment was modeled by initiating treatment with SR-717 on day 11 when B16.F10 melanoma tumors are well established (Fig. 3C). Notably, efficacious doses of diABZI-2 (22), an open conformation-inducing STING agonist that induces equivalent maximal levels of cell-based activity when compared with SR-717 (fig. S13, A to C), were found to induce ~20 ng/ml of IFN- $\beta$  (fig. S13D). By contrast, systemic dosing regimens of the closed conformation-inducing STING agonist SR-717 that resulted in the induction of >0.2 ng/ml of circulating IFN- $\beta$  (Fig. 3A and fig. S13D) were found to be well tolerated and efficacious. Specifically, a 30 mg/kg intraperitoneal once-per-day regimen of SR-717 for 1 week (Fig. 3C) was found to maximally inhibit tumor growth (Fig. 3D), as well as lengthen survival time in tumor-bearing mice (Fig. 3E). The antitumor efficacy of SR-717 displayed an obligatory dependence on STING expression, based on the observed lack of activity in *Sting*<sup>gt/gt</sup> host mice (Fig. 3, D and E).

To establish if efficacy was restricted to subcutaneous tumors, as well as to determine utility in the context of metastasis, we treated C57BL/6 mice that had been injected intravenously with B16.F10 cells, which are reported to home to and colonize lung tissue (25). SR-717 was observed to significantly inhibit the formation of pulmonary nodules in this model of metastasis (Fig. 3, F and G), consistent with the ability of a systemic STING agonist to control metastasis and B16.F10 tumorigenesis in a manner that is independent of tissue type. We investigated the efficacy of this compound series in the context of oral delivery, using the active STING agonist analog SR-301 (fig. S14, A and B; EC<sub>50</sub> = 0.6  $\mu$ M), which has appreciable bioavailability (%F = 32.2) and suitable rodent exposure properties (fig. S4B).

Encouragingly, 15 mg/kg oral once-per-day dosing with SR-301 for 18 days was found to maximally reduce tumor burden in the B16.F10 model (fig. S14, C to E). Based on the more favorable physicochemical properties, as well as enhanced uniformity with respect to dosage to pharmacodynamic relationships, intraperitoneal administration of SR-717 was used to further characterize antitumor immunity. Using the B16.F10 model, we compared the antitumor activity of SR-717 to that observed for anti-programmed cell death 1 (anti-PD-1) or anti-programmed cell death 1 ligand 1 (anti-PD-L1) antibody therapy. Under the constraints and limitations of this model,

maximal achievable efficacy was observed with a single-agent therapy consisting of SR-717 STING agonist. Specifically, SR-717 displayed a better level of efficacy to that achieved by anti-PD-1 or anti-PD-L1 antibody therapy in this model, with respect to tumor burden (Fig. 3, H and J, respectively) or overall survival (Fig. 3, I and K, respectively). The observed activity profiles of PD-1-based checkpoint blockade in this poorly immunogenic model is consistent with previous reports (24, 26).

We investigated the impact of effective systemic exposure levels of SR-717 on immune cell activation and immunological mechanisms, in the context of tumor-bearing mice. Consistent with previous reports associated with intratumoral injection of 2'3'-cGAMP (13, 27), systemic delivery of SR-717 increased the frequency of activated CD69<sup>+</sup>CD8 T cells among isolated tumor infiltrating lymphocytes (TILs) and within isolated spleens and inguinal lymph nodes (Fig. 4A). A similar increase was observed in the frequency of activated CD69<sup>+</sup> natural killer (NK) cells within isolated spleens and inguinal lymph nodes (Fig. 4B), consistent with previous findings describing the ability of the STING pathway to activate this cell type (28). Within the CD45.2<sup>+</sup> population, SR-717 treatment resulted in a significant increase in the frequency of CD8 T cells among TILs and a decrease in the frequencies of NK cells within the draining lymph node (dLN) and spleen (fig. S16B). Because of the potential for STING agonism to induce pathological consequences, we next assessed the infiltration of CD8 T cells into peripheral tissues. We observed no significant differences in lymphocyte or CD8 T cell infiltration into the lung after SR-717 treatment (30 mg/kg intraperitoneally for 7 days) (fig. S15, A and D), although a small but statistically significant increase in frequencies of CD44<sup>+</sup>PD-1<sup>+</sup> T cells was observed (fig. S15A). In the liver, a small but statistically significant increase in CD8 T cell infiltration was observed (fig. S15, B and D). Measurement of liver enzymes revealed a transient up-regulation of alanine aminotransferase (ALT) levels on day 4 after treatment, which returned to vehicle levels by day 7 after treatment, and no impact on aspartate transaminase (AST) levels was observed (fig. S15C). Further assessment of T cell function revealed that SR-717 treatment significantly increased the frequency of granzyme B and CD107a<sup>+</sup> CD8 T cells in both spleen and tumor (Fig. 4, C and E). Although we did not observe increases in granzyme B<sup>+</sup> NK cells in spleen or tumor (Fig. 4D), we did detect increases in CD107a expression in NK cells in both tissues (Fig. 4F), suggesting that at the time of analysis, NK cells had already degranulated in SR-717-treated animals. Analysis of cytokine-producing



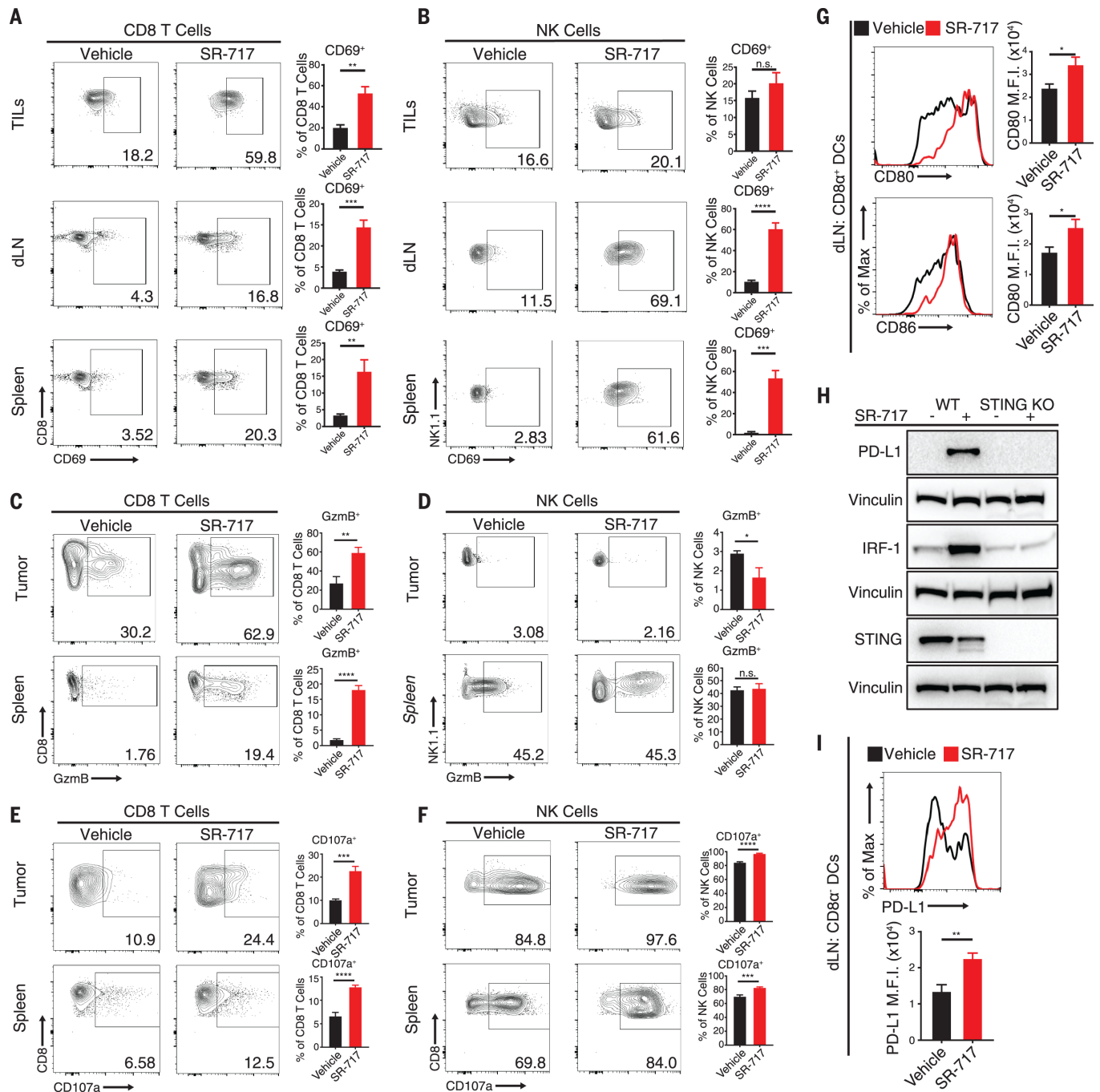


**Fig. 4. Impact of systemic SR-717 administration on antitumor immunity in mice.** (A) Impact of systemic SR-717 delivery (administered as described in Fig. 3C) on surface CD69 expression, assessed by flow cytometry, on CD8 T cells isolated from tumors (TILs), spleens, or dLN of B16.F10 tumor-bearing mice ( $n = 4$ ). (B) Impact of systemic SR-717 delivery (administered as described in Fig. 3C) on surface CD69 expression, assessed by flow cytometry, on NK cells isolated from tumors (TILs), spleens, or dLN of B16.F10 tumor-bearing mice ( $n = 4$ ). (C) Impact of systemic SR-717 delivery (administered as described in Fig. 3C) on granzyme B expression, assessed by flow cytometry, on restimulated intratumoral and splenic CD8 T cells ( $n = 5$ ). (D) Impact of systemic SR-717 delivery (administered as described in Fig. 3C) on granzyme B expression, assessed by flow cytometry, on restimulated intratumoral and splenic NK cells ( $n = 5$ ). (E) Impact of systemic SR-717 (administered as described in Fig. 3C) on surface CD107a

expression on restimulated intratumoral and splenic CD8 T cells ( $n = 5$ ). (F) Impact of systemic SR-717 (administered as described in Fig. 3C) on surface CD107a expression on restimulated intratumoral and splenic NK cells ( $n = 5$ ). (G) Impact of systemic SR-717 delivery (administered as described in Fig. 3C) on surface expression of CD80 and CD86, determined by flow cytometry, and on CD8α<sup>+</sup> DCs from dLN of B16.F10 tumor-bearing mice ( $n = 4$ ). (H) Western blot analysis of the impact of SR-717 delivery (3.8 μM) on PD-L1 expression in WT THP1 or ISG-THP1 STING KO (STING KO) cells. Vinculin was used as a loading control. (I) Impact of systemic SR-717 delivery (administered as described in Fig. 3C) on PD-L1 surface expression on CD8α<sup>+</sup> DCs from the dLN of B16.F10 tumor-bearing mice ( $n = 4$ ). Data are representative of three independent experiments, and values indicate mean ± SEM with the exception of values in (I), which indicate mean ± SD. \* $P \leq 0.05$ ; \*\* $P \leq 0.01$ ; \*\*\* $P \leq 0.001$ ; \*\*\*\* $P \leq 0.0001$ ; n.d., no difference.

NK cells revealed significantly reduced IFN- $\gamma$ <sup>+</sup> NK cells in TLNs (fig. S16C), with a modest but significant increase of IFN- $\gamma$ <sup>+</sup> NK cells in spleen (fig. S16C). Moreover, SR-717 treatment had no significant effect on the frequency of polyfunctional CD8 T cell responses (fig. S16D). We also observed increases in the frequencies of CD8 T cells undergoing apoptosis within the dLN (fig. S16E), the magnitude of which being consistent with those previously reported for efficacious doses of cGAMP after intratumoral injection (14). The antitumor activity derived from STING activation is dependent on CD11c<sup>+</sup>CD8 $\alpha$  DCs (12) and involves tumor antigen cross-presentation leading to the activation of CD8 T cells within the draining lymph node, as well as the activation of type I interferon signaling (11, 23). Systemic SR-717 administration induces the activation of CD11c<sup>+</sup>CD8 $\alpha$  DCs, as determined by CD80 and CD86 staining intensity (Fig. 4G), and enhances cross-priming of CD8 T cells, as determined by monitoring the in vivo proliferation of transferred Thy1.1<sup>+</sup> OT-I CD8 T cells isolated from mice pretreated with SR-717 and subsequently injected with ovalbumin protein (fig. S16, F and G). At this stage of treatment, OT-I CD8 T cell activation state was determined to be significantly enhanced by treatment with SR-717, as determined based on the evaluation of CD44<sup>+</sup>PD-1<sup>+</sup> and granzyme B<sup>+</sup> CD8 T cell populations, as well as polyfunctional CD8 T cell responses (fig. S16, H to J).

Finally, we examined the impact of SR-717 on the expression of critical targets associated with antitumor immunity. STING pathway activation can induce mechanisms known to regulate immune checkpoint protein expression. STING activation, and the subsequent induction of type I interferon, can induce STAT3 phosphorylation (29), a key regulator of interferon-dependent PD-L1 expression (30, 31). SR-717 was found to induce the expression of PD-L1 in THP1 cells (Fig. 4H and fig. S17A) and in primary human PBMCs (fig. S17B) in a STING-dependent manner (Fig. 4H). Consistent with previous findings describing the impact of cGAMP on STING protein levels (32), and indicative of negative feedback mechanisms associated with pathway activation, total STING protein levels were observed to decrease after treatment with SR-717 (Fig. 4H). In vivo, we observed that intraperitoneal injection of SR-717 resulted in increased cell-surface levels of PD-L1 on CD11c<sup>+</sup>CD8<sup>+</sup> DCs but not on CD8<sup>+</sup> DCs isolated from the inguinal lymph nodes of B16.F10 tumor bearing mice (Fig. 4I), even though SR-717 clearly activates CD8<sup>+</sup> DCs, which suggests cell type-selective differences in downstream STING-dependent signaling. Indoleamine 2,3-dioxygenase 1 (IDO1) in vivo expression has been demonstrated to be induced in a STING-dependent manner

(33). SR-717 STING agonist was found to induce IDO1 expression in primary human PBMCs (fig. S17C). Taken together, our results demonstrate that although STING activation with SR-717 induces the expected stimulatory events, a corresponding induction of molecules known to suppress immune responses was also elicited, albeit in a cell type-selective manner. These observations have important implications for the selection of agents and the temporal design of combination-based clinical trials involving a systemically delivered STING agonist.

To address the limitations of intratumoral delivery, we have identified the SR-717 chemical series of functional cGAMP mimetic STING agonists, which, after systemic administration, were demonstrated to promote antitumor immunity and activate CD8<sup>+</sup> T cells within tumors and the dLN, as well as activate NK cells within the dLN. The systemic administration of SR-717 reduced tumor burden in the B16.F10 melanoma model with a level of efficacy that was observed to be superior than what is observed for anti-PD-1 or anti-PD-L1 therapy in this particular poorly immunogenic model. Importantly, systemic administration of SR-717 produced substantial efficacy despite inducing modest levels of IFN- $\beta$ , suggesting that the threshold for efficacy in tumor models may be far lower than previously reported and can be achieved without considerable toxicity. It is also of potential critical importance that STING activation by SR-717 was found to induce the expression of PD-L1 in a STING-dependent fashion. These results have important implications for the choice of agent to be combined with a STING agonist, as well as the relative timing of a dosing regimen, in the context of cancer treatment. Presumably, it would be unproductive to treat with an agent that increases the relative abundance of the target of the second agent. The ability of SR-717 to induce the cGAMP-induced closed STING conformation, in contrast to open conformation-inducing ligands, enables exploration of the relative importance of different potential scaffolding functions in vivo and in the context of systemic distribution in settings of antitumor immunity and beyond. Differential pathway activation associated with the recognition of bacterial-derived CDNs [e.g., di-GMP derived from commensal bacteria (34)] as compared with endogenously produced cGAMP, derived from cytosolic DNA as a result of diverse pathological events (e.g., genomic instability), is readily conceivable and most likely probable. Each class of agonist may provide differential therapeutic benefits depending on the setting.

## REFERENCES AND NOTES

- Q. Chen, L. Sun, Z. J. Chen, *Nat. Immunol.* **17**, 1142–1149 (2016).

- M. H. Christensen, S. R. Paludan, *Cell. Mol. Immunol.* **14**, 4–13 (2017).
- K. J. Mackenzie et al., *Nature* **548**, 461–465 (2017).
- S. M. Harding et al., *Nature* **548**, 466–470 (2017).
- M. De Cecco et al., *Nature* **566**, 73–78 (2019).
- D. A. Sliter et al., *Nature* **561**, 258–262 (2018).
- M. C. C. Canesso et al., *Mucosal Immunol.* **11**, 820–834 (2018).
- L. Sun, J. Wu, F. Du, X. Chen, Z. J. Chen, *Science* **339**, 786–791 (2013).
- H. Ishikawa, Z. Ma, G. N. Barber, *Nature* **461**, 788–792 (2009).
- H. Ishikawa, G. N. Barber, *Nature* **455**, 674–678 (2008).
- M. B. Fuertes et al., *J. Exp. Med.* **208**, 2005–2016 (2011).
- S. R. Woo et al., *Immunity* **41**, 830–842 (2014).
- L. Corrales et al., *Cell Rep.* **11**, 1018–1030 (2015).
- K. E. Sivick et al., *Cell Rep.* **29**, 785–789 (2019).
- C. Vanpouille-Box et al., *Nat. Commun.* **8**, 15618 (2017).
- C. Pantelidou et al., *Cancer Discov.* **9**, 722–737 (2019).
- J. Conlon et al., *J. Immunol.* **190**, 5216–5225 (2013).
- P. Gao et al., *Cell* **154**, 748–762 (2013).
- Q. Yin et al., *Mol. Cell* **46**, 735–745 (2012).
- S. Ouyang et al., *Immunity* **36**, 1073–1086 (2012).
- X. Zhang et al., *Mol. Cell* **51**, 226–235 (2013).
- J. M. Ramanjulu et al., *Nature* **564**, 439–443 (2018).
- M. S. Diamond et al., *J. Exp. Med.* **208**, 1989–2003 (2011).
- M. A. Curran, W. Montalvo, H. Yagita, J. P. Allison, *Proc. Natl. Acad. Sci. U.S.A.* **107**, 4275–4280 (2010).
- A. Raz et al., *Cancer Res.* **40**, 1645–1651 (1980).
- S. Kleffel et al., *Cell* **162**, 1242–1256 (2015).
- O. Demaria et al., *Proc. Natl. Acad. Sci. U.S.A.* **112**, 15408–15413 (2015).
- A. Marcus et al., *Immunity* **49**, 754–763.e4 (2018).
- J. Ahn, S. Son, S. C. Oliveira, G. N. Barber, *Cell Rep.* **21**, 3873–3884 (2017).
- A. Garcia-Diaz et al., *Cell Rep.* **19**, 1189–1201 (2017).
- T. L. Song et al., *Blood* **132**, 1146–1158 (2018).
- H. Konno, K. Konno, G. N. Barber, *Cell* **155**, 688–698 (2013).
- H. Lemos et al., *J. Immunol.* **192**, 5571–5578 (2014).
- O. Danilchanka, J. J. Mekalanos, *Cell* **154**, 962–970 (2013).

## ACKNOWLEDGMENTS

We thank A. Theofilopoulos for invaluable discussion and insight. **Author contributions:** L.L.L. and E.N.C. conceived of, initiated, and coordinated the project. L.L.L., E.N.C., J.R.T., H.M.P., P.G.S., and A.K.C. contributed to conceptualization. E.N.C., C.Y., V.F.V., Y.J., M.K., A.M.G.A., W.V., S.A., D.L., N.N., L.P., B.B., P.S., F.M.-P., and E.H. conducted research. L.L.L., J.R.T., H.M.P., P.G.S., A.C., T.Y., K.J., S.J., and A.K.W. were involved with project administration. L.L.L., E.N.C., J.R.T., V.F.V., H.M.P., P.G.S., C.Y., D.W., and M.Ki. were involved with the interpretation of data. L.L.L. and E.N.C. wrote the original draft. L.L.L., E.N.C., J.R.T., V.F.V., and H.M.P. were involved with review and editing. **Competing interests:** L.L.L., E.N.C., A.K.C., M.Ku., A.M.G.A., H.M.P., P.G.S., C.Y., and W.V. are inventors on patent application PCT/US2019/018899 submitted by The Scripps Research Institute that covers small-molecule agonists of STING. **Data and materials availability:** All data are available in the manuscript or in the supplementary materials. Noncommercial reagents described in this manuscript are available from L.L.L., H.M.P., or J.R.T. under a material transfer agreement with The Scripps Research Institute. Coordinates for the following crystal structure complexes have been deposited in the RCSB Protein Data Bank: hSTING:SR-717 (PDB ID 6XNP) and mSTING:SR-717 (PDB ID 6XNN).

## SUPPLEMENTARY MATERIALS

science.sciencemag.org/content/369/6506/993/suppl/DC1  
Materials and Methods  
Figs. S1 to S19  
Table S1  
References

[View/request a protocol for this paper from Bio-protocol.](#)

24 February 2020; accepted 9 July 2020  
10.1126/science.abb4255



## GLOBAL CARBON CYCLE

# Abrupt CO<sub>2</sub> release to the atmosphere under glacial and early interglacial climate conditions

C. Nehrbass-Ahles<sup>1,2,3\*</sup>, J. Shin<sup>4</sup>, J. Schmitt<sup>1,2</sup>, B. Bereiter<sup>1,2,5</sup>, F. Joos<sup>1,2</sup>, A. Schilt<sup>1,2</sup>, L. Schmidely<sup>1,2</sup>, L. Silva<sup>1,2</sup>, G. Teste<sup>4</sup>, R. Grilli<sup>4</sup>, J. Chappellaz<sup>4</sup>, D. Hodell<sup>3</sup>, H. Fischer<sup>1,2</sup>, T. F. Stocker<sup>1,2</sup>

Pulse-like carbon dioxide release to the atmosphere on centennial time scales has only been identified for the most recent glacial and deglacial periods and is thought to be absent during warmer climate conditions. Here, we present a high-resolution carbon dioxide record from 330,000 to 450,000 years before present, revealing pronounced carbon dioxide jumps (CDJ) under cold and warm climate conditions. CDJ come in two varieties that we attribute to invigoration or weakening of the Atlantic meridional overturning circulation (AMOC) and associated northward and southward shifts of the intertropical convergence zone, respectively. We find that CDJ are pervasive features of the carbon cycle that can occur during interglacial climate conditions if land ice masses are sufficiently extended to be able to disturb the AMOC by freshwater input.

**A**nalyses of Antarctic ice cores have demonstrated that atmospheric CO<sub>2</sub> has been a major driver of Earth's climate on orbital to millennial time scales (1–3). However, evidence of submillennial-scale CO<sub>2</sub> variability is only available for the past ~60 thousand years (ka), that is, not beyond the last glacial period (4–6). Climate-carbon cycle perturbations during previous interglacial periods serve as first-order templates for the natural response of Earth's climate system to warmer climatic background conditions (7), but the use of CO<sub>2</sub> records to decipher submillennial-scale variations has thus far been hampered by insufficient temporal resolution of existing ice core records.

Previous research identified two principal modes of CO<sub>2</sub> variability on millennial to centennial time scales: (i) millennial-scale carbon dioxide maxima (CDM) frequently occurring during the last glacial period (4, 5, 8) and (ii) centennial-scale carbon dioxide jumps (CDJ) caused by pulse-like CO<sub>2</sub> releases to the atmosphere, most prominently occurring during the last deglaciation (6, 9).

CDM are characterized by a triangular shape of evolving CO<sub>2</sub> changes. They closely covary with Antarctic temperature proxy records on millennial time scales, as evidenced by the Antarctic isotope maxima (4, 8, 10). During cold periods (stadials) in the Northern Hemisphere (NH), CO<sub>2</sub> is observed to increase gradually and in parallel to the bipolar see-

saw response in Antarctic temperature (11) at typical rates of ~1 part per million (ppm) per century (4, 8). CDM reach amplitudes of up to 30 ppm before their trends are reversed in connection with a sudden strengthening of the Atlantic meridional overturning circulation (AMOC) linking the onset of Dansgaard-Oeschger (DO) events (i.e., abrupt warming over Greenland) and the start of slow cooling in the Southern Ocean (SO) region (4, 8, 11).

In contrast, abrupt CDJ do not directly correspond to variations in Antarctic temperature but are associated with either DO events or Heinrich stadials (HS) in the NH (6, 12, 13). The latter are characterized by extended cold periods in the NH associated with a weakened AMOC (14–16). The few CDJ identified so far are superimposed on gradually increasing millennial CO<sub>2</sub> trends connected to CDM or glacial terminations and lead to a sudden 10 to 15 ppm CO<sub>2</sub> rise within less than ~250 years at rates of ~10 ppm per century, about 10 times faster than CDM. As of yet, CDJ have only been identified during the most recent deglaciation (Termination I) (6, 9) and for HS 4 (12, 13), occurring at 39.5 ka BP (thousand years before present, with the present defined as 1950 CE). CDJ are synchronous with either major methane (CH<sub>4</sub>) rises linked to DO events or small CH<sub>4</sub> peaks associated with HS, suggesting a link with sudden AMOC changes and poleward shifts of the intertropical convergence zone (ITCZ) (6, 17, 18). Here, we address whether CDJ also occur during glacial growth phases and interglacial climate conditions and therefore whether they are a pervasive feature of the past carbon cycle.

Centennial- to millennial-scale CO<sub>2</sub> variability between ~150 and 400 ka BP could not be explored because of insufficient measurement precision and low temporal resolution of the existing CO<sub>2</sub> record for this period (1). Here, we investigate the older part of this in-

terval by presenting a high-resolution record of CO<sub>2</sub> mole fractions covering a full glacial-interglacial cycle from 330 to 450 ka BP [i.e., marine isotope stage (MIS) 9e to MIS 12a (19)], measured on samples from the European Project for Ice Coring in Antarctica (EPICA) Dome C (EDC) ice core using an improved dry-extraction technique (20). In comparison to earlier data (1, 2), we enhance the precision by a factor of three (now ~1 ppm) and increase temporal resolution between four- and sixfold (now ~300 years on average).

Additionally, we improve the resolution of the existing EDC CH<sub>4</sub> record (21) to an average of ~250 years at periods of abrupt changes (20). This improvement permits a direct comparison of the CH<sub>4</sub> imprint of fast climate changes in the NH with the Southern Hemisphere bipolar seesaw response in Antarctic temperature and atmospheric CO<sub>2</sub> (4, 8). We combine our ice core data with new records of benthic  $\delta^{13}\text{C}$  and  $\delta^{18}\text{O}$  of *Cibicides wuellerstorfi* (22) and planktic  $\delta^{18}\text{O}$  of *Globigerina bulloides* (23). These stable isotope data are measured on marine sediment core samples from the International Ocean Discovery Program (IODP) site U1385 located on the Iberian margin off the coast of Portugal at a water depth of ~2600 m below sea level (20). A temporal resolution of ~150 years on average enables us to directly compare our ice core data with this independent paleoclimatic archive of hydrological change in the North Atlantic (NA).

On orbital time scales, our CO<sub>2</sub> record reveals generally high CO<sub>2</sub> levels persisting above 260 ppm (24) over ~35 ka during the exceptionally long interglacial period MIS 11c to 11e, from 427 to 393 ka BP (Fig. 1B), extending over more than one precessional cycle (25). The minimum CO<sub>2</sub> value of  $187.6 \pm 1.0$  ppm is reached at 358 ka BP, coinciding with the lowest sea surface temperature (SST) (Fig. 2, D, G, and H) (26). However, the onset of the deglacial CO<sub>2</sub> rise toward MIS 9e (Termination IV) only takes place ~13.5 ka later, at 344.5 ka BP. The end of this deglacial CO<sub>2</sub> increase (~335 ka BP) is marked by a peak CO<sub>2</sub> value of  $300.4 \pm 1.0$  ppm, representing the highest natural CO<sub>2</sub> mole fraction derived from Antarctic ice cores over the past 800 ka. We identify, superimposed on this orbital trend, different types of millennial- to centennial-scale CO<sub>2</sub> variability, occurring most frequently during, but not limited to, the glacial growth phase.

On millennial time scales, the CO<sub>2</sub> record mirrors the variability in the EDC temperature proxy (Figs. 1A and 2A) (10) and dust flux records (Fig. 2B) (27), a feature previously observed over the past 800 ka in lower-resolution CO<sub>2</sub> data (2, 3). Our new benthic  $\delta^{18}\text{O}$  record from IODP site U1385 follows the same pattern (Fig. 2C), indicating the influence of southern-sourced deep water, as first noted for the last

<sup>1</sup>Climate and Environmental Physics, Physics Institute, University of Bern, Bern, Switzerland. <sup>2</sup>Oeschger Centre for Climate Change Research, University of Bern, Bern, Switzerland. <sup>3</sup>Godwin Laboratory for Palaeoclimate Research, Department of Earth Sciences, University of Cambridge, Cambridge, UK. <sup>4</sup>Institute of Environmental Geosciences (IGE), Grenoble INP, IRD, CNRS, Université Grenoble Alpes, Grenoble, France. <sup>5</sup>Laboratory for Air Pollution/Environmental Technology, Empa—Swiss Federal Laboratories for Materials Science and Technology, Dübendorf, Switzerland.

\*Corresponding author. Email: cn425@cam.ac.uk

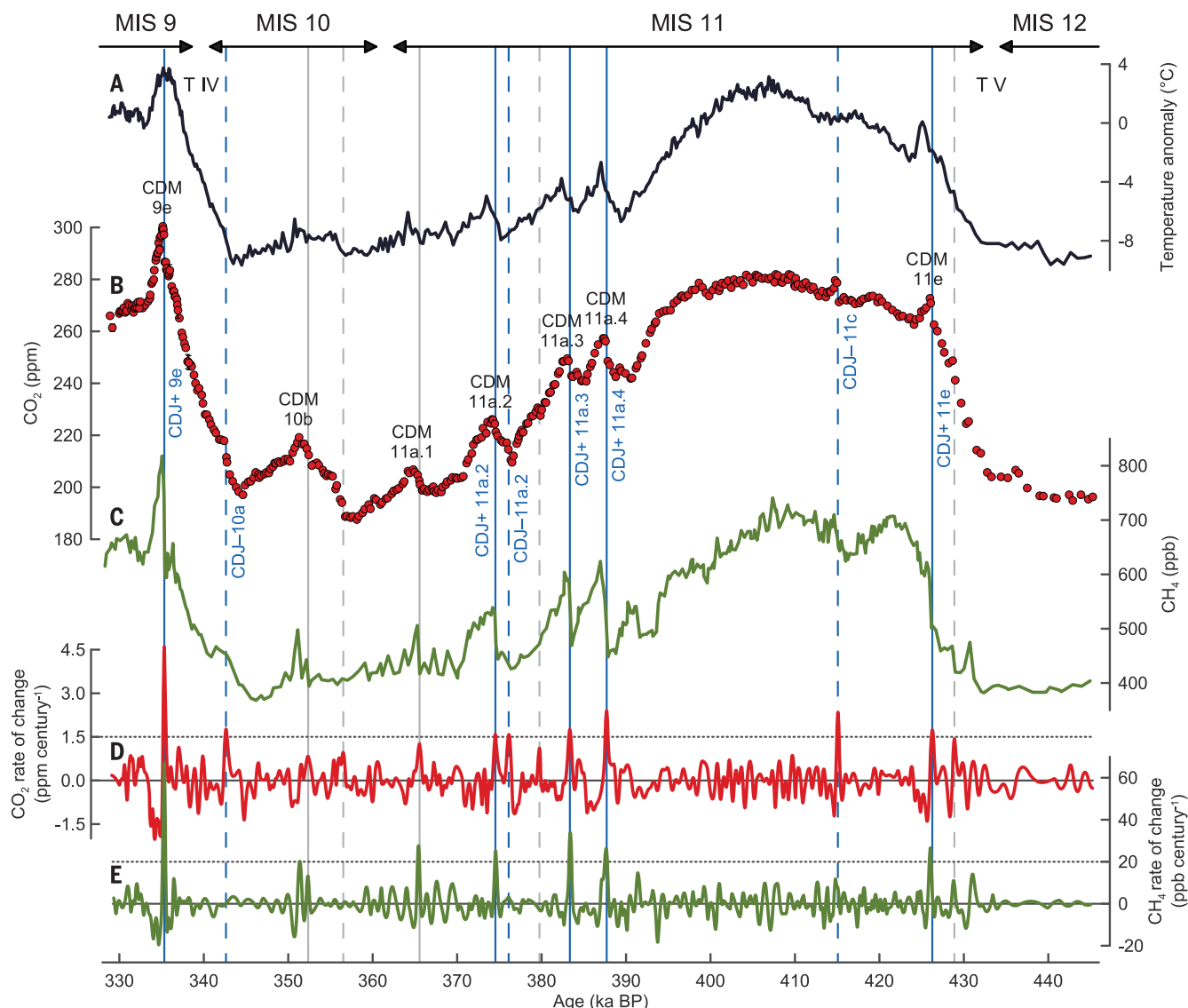


**Fig. 1. High-resolution CO<sub>2</sub> and improved CH<sub>4</sub> records compared with Antarctic temperature during MIS 9e to 12a.** (A) Antarctic temperature anomalies (10). (B) CO<sub>2</sub> record (this study). (C) CH<sub>4</sub> compilation (this study) (20). (D) Rate of change of CO<sub>2</sub> in the ice core record derived from a smoothed version of (B) (20). (E) Rate of change of CH<sub>4</sub> in the ice core record derived from a smoothed version of (C) (20). All data are based on measurements of EDC ice core samples and are plotted on the Antarctic Ice Core Chronology 2012 (AICC2012) age scale (34).

Identified CDM and CDJ are labeled according to the MIS assignment in (19). Distinct CDJ in the CO<sub>2</sub> record are indicated with blue vertical lines, positioned at the peaks in (D) exceeding a threshold value of 1.5 ppm per century (20). CDJ+ (solid blue lines) coincide with major CH<sub>4</sub> rises greater than 50 ppb at growth rates greater than 20 ppb per century (E), whereas CDJ- (dashed blue lines) do not. Further potential events with positive rates below 1.5 ppm per century (D) are indicated with gray vertical lines but not labeled. T IV, Termination IV; T V, Termination V.

glacial period (MIS 3) (28). Our results demonstrate that this correlation also applies to MIS 10a to 11a, thereby emphasizing the key role of SO processes in the bipolar seesaw (4, 11) and associated global-scale climate regime shifts in shaping atmospheric CO<sub>2</sub> on millennial time scales. We identify a total of seven CDM events (Fig. 1B). The two youngest events (CDM 9e and 10b) were reported previously (7), but the oldest five (CDM 11a.1, 11a.2, 11a.3, 11a.4, and 11e) were not. Furthermore, our record shows that the covariation of CO<sub>2</sub> and the Antarctic temperature proxy (10) also holds for the extended interglacial pe-

riod MIS 11c (Fig. 1, A and B), where both Antarctic temperatures and CO<sub>2</sub> gradually increase along with the summer insolation at 65°N (25). The time at which CO<sub>2</sub> and Antarctic temperature cease to covary in our record is at the end of MIS 11c, when Antarctic temperature leads the CO<sub>2</sub> decrease by several thousand years, similar to what is observed for the glacial inception after the penultimate interglacial (29).

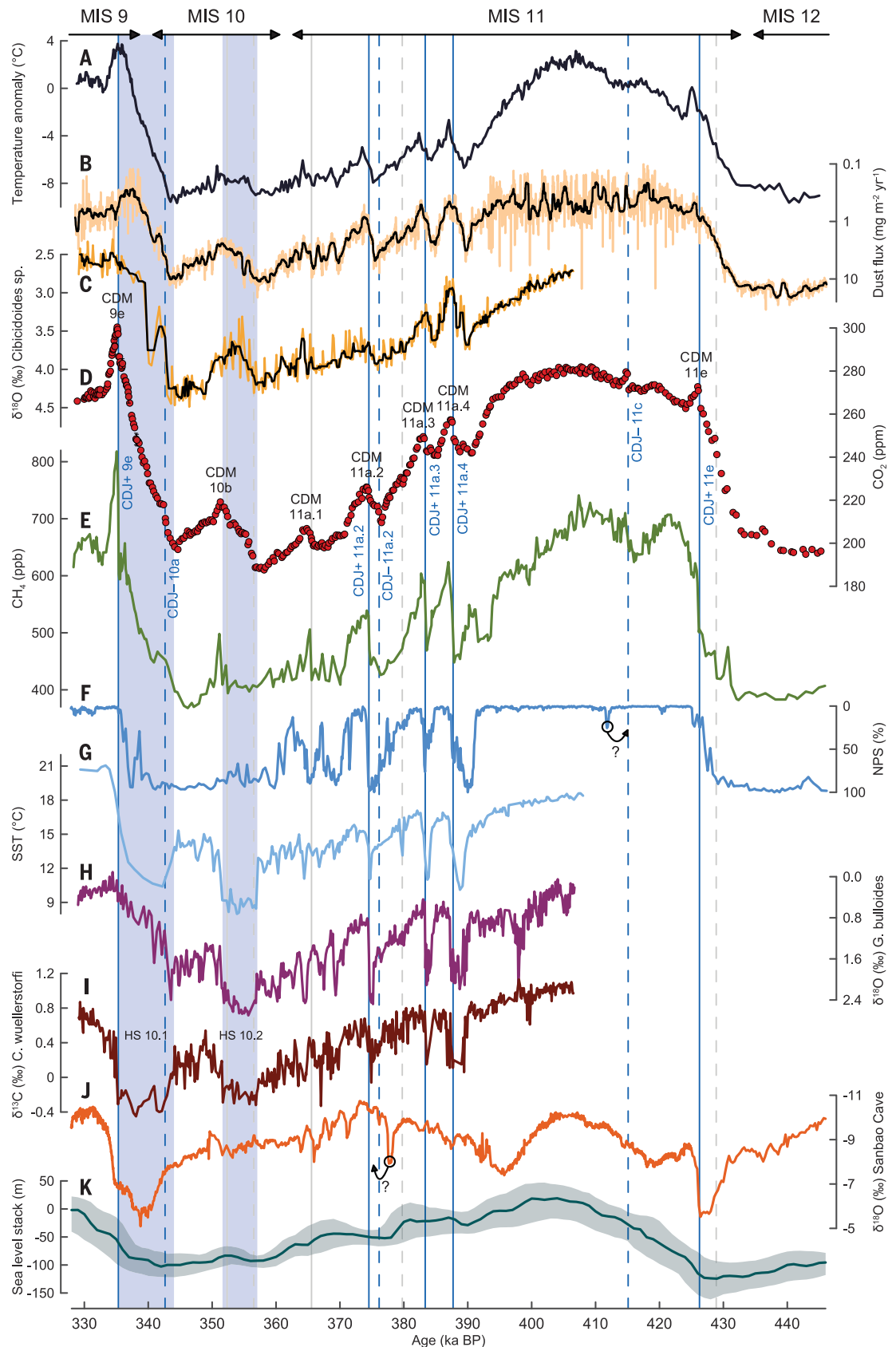
On the centennial time scale, we detect eight CDJ occurring under very different climate boundary conditions (Fig. 1B). They are marked by centennial-scale peaks in the rate

of change of CO<sub>2</sub> exceeding a threshold of 1.5 ppm per century in the ice core record (Fig. 1D) (20). The close correlation of millennial-scale CO<sub>2</sub> variability with Antarctic temperature (Fig. 1A) does not hold for CDJ (Fig. 3A and fig. S1A). While all CDJ lead to an abrupt rise in CO<sub>2</sub> of ~10 ppm (table S1), their underlying causes may differ (13, 30). We distinguish two varieties of CDJ on the basis of the presence or absence of a major simultaneous CH<sub>4</sub> rise at the same depth level of the ice core (20).

The first variety of CDJ is synchronous with rapid rises in the CH<sub>4</sub> record greater than



**Fig. 2. Comparison of high-resolution CO<sub>2</sub> and improved CH<sub>4</sub> records with marine sediment and speleothem data covering MIS 9e to 12a.** (A) EDC temperature anomalies (10). (B) EDC dust flux (27), including an ~500-year running median. (C) Benthic  $\delta^{18}\text{O}$  *C. wuellerstorfi* from IODP site U1385 on the Iberian margin (this study), including an ~500-year running median. (D) EDC CO<sub>2</sub> record (this study). (E) EDC CH<sub>4</sub> compilation (this study) (20). (F) Relative proportion of the polar planktic foraminifera *Neogloboquadrina pachyderma* (NPS) from ODP site 983 (38). (G) U<sup>K</sup><sub>37</sub>-based SST from IODP site U1385 (26). (H) Planktic  $\delta^{18}\text{O}$  *G. bulloides* from IODP site U1385 (this study). (I) Benthic  $\delta^{13}\text{C}$  *C. wuellerstorfi* from IODP site U1385 (this study). (J)  $\delta^{18}\text{O}$  Sanbao Cave record in Hubei, China (35). (K) Global sea level stack (probability maximum) including 95% probability intervals (37). All records are given on the AICC2012 age scale (34) or are transferred to AICC2012 (20), with the exception of (J) and (K). Arrows in (F) and (J) highlight potential age-scale inconsistencies. Labeling and vertical line styles are identical to those in Fig. 1. Vertical blue bands indicate HS 10.1 and HS 10.2 (see text for details).



50 parts per billion (ppb) (Figs. 1C and 3C) and growth rates exceeding 20 ppb per century, as recorded in the EDC ice core (Figs. 1E and 3E). We dub these pulse-like CO<sub>2</sub> release events CDJ+. Using this definition, we identify five CDJ+ (9e, 11a.2, 11a.3, 11a.4, and 11e) (Fig. 1B). The major CH<sub>4</sub> rises associated with CDJ+ indicate abrupt DO-like warming in the NH directly linked to AMOC invigorations (6, 17). Direct evidence for such AMOC strengthening comes from associated abrupt rises in SST in the NH (Fig. 2, F to H) and increases of benthic  $\delta^{13}\text{C}$  values (Fig. 2I), indicative of the inflow of NA deep-water masses at IODP site U1385. These findings are consistent with the two previously identified CDJ+ events during the last deglaciation, at the onsets of the Bølling-Allerød and Preboreal periods (6, 9).

The most pronounced CDJ+ (CDJ+ 9e) takes place during early interglacial conditions, when CO<sub>2</sub> values are already above 285 ppm, a level that is higher than typical peak-CO<sub>2</sub> mole fractions during interglacial conditions over the past 800 ka (3). The time resolution for CDJ+ 9e is better than 90 years and shows an exceptionally fast CO<sub>2</sub> increase of ~10 ppm per century, as measured on the two neighboring ice samples (Fig. 3B). Accounting for

the smoothing of atmospheric signals by the bubble enclosure process, we estimate an original rate of atmospheric CO<sub>2</sub> increase of  $26.2 \pm 17.6$  ppm per century (Fig. 3B and table S1) (20), which provides a benchmark for the possible range and speed of positive carbon cycle feedbacks connected to AMOC variations during the deglaciation. This rate exceeds previous estimates of maximum preindustrial atmospheric increase rates (31) by a factor of seven but is still a factor of nine lower than recent anthropogenic growth rates over the past decade (32). The CO<sub>2</sub> decrease after CDJ+ 9e shows that natural processes during interglacial conditions allowed for a sustained CO<sub>2</sub> removal from the atmosphere estimated at ~2 ppm per century for ~2 ka (Figs. 1B and 3B).

The second variety of CDJ occurs independently from major responses in the EDC CH<sub>4</sub> record (Fig. 1, C and E) (see supplementary text section of the supplementary materials) and is dubbed CDJ-. We identify two CDJ- (10a and 11a.2), which share similar characteristics with the two CDJ- events associated with HS 1 during the last deglaciation (~16 ka BP) and HS 4 (6, 12, 13). We speculate that CDJ- can be attributed to carbon cycle processes caused by AMOC weak-

ening. Although direct AMOC records do not yet exist for MIS 9e to 12a, abrupt decreases of benthic  $\delta^{13}\text{C}$  indicate intrusions of Antarctic bottom water masses at IODP site U1385 (Fig. 2I) likely due to AMOC weakening, similar to what occurred during HS in the last glacial period (14, 15). Note that major HS (HS 10.1 and 10.2) are identified in Fig. 2 by the drop in alkenone saturation index ( $U^{K_{37}}$ )-based SST (Fig. 2G) and the decrease in benthic  $\delta^{13}\text{C}$  (Fig. 2I) indicative of a reduced state of the AMOC. Whereas CDJ- 10a is likely related to carbon cycle responses to an AMOC slowdown caused by massive ice discharge during HS 10.1 (Fig. 2I), there exists only ambiguous evidence for CDJ- 11a.2 being associated with freshwater forcing. Low CH<sub>4</sub> levels (Fig. 2E) and cold SST in the NA (Fig. 2F) indicate stadial conditions in the NH associated with CDJ- 11a.2. Given the relative age uncertainties between our ice core and independently dated records (33, 34), the  $\delta^{18}\text{O}$  calcite record from Sanbao Cave (Fig. 2J) (35) indicates a major shift of the ITCZ that may be associated with CDJ- 11a.2 (18, 36).

Most notably, the new CO<sub>2</sub> record reveals the clearly distinguishable CDJ 11c ( $12.9 \pm 2.7$  ppm increase within  $191 \pm 123$  years) (Fig.

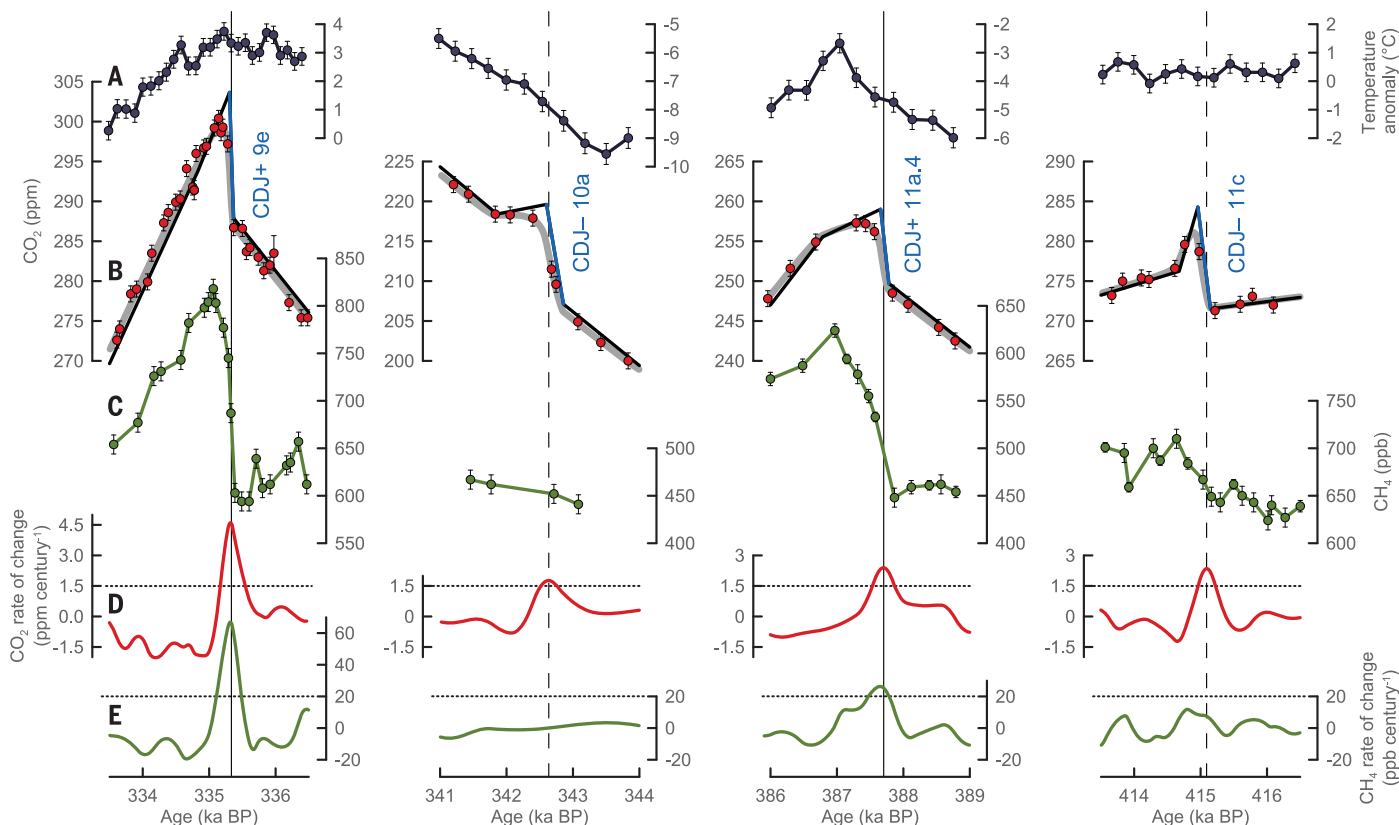


**Fig. 3. Detailed view of the two varieties of CDJ.** (A to E) Identical to Fig. 1. The black linear segments in (B) indicate first-order approximations of the atmospheric CO<sub>2</sub> evolution. The blue segment highlights the actual CDJ event. These approximations for the atmospheric trajectories are optimized so that the

CO<sub>2</sub> curve after smoothing by the bubble enclosure process (gray lines) fits the ice core data (red dots) best. The firn smoothing is realized by applying improved gas enclosure characteristics for the EDC ice core (20). See table S1 for details. All remaining CDJ are shown in fig. S1.



3B and table S1) at 415 ka BP, occurring ~10 ka into interglacial temperature conditions at Dome C, but still at a time of considerable sea level rise (Fig. 2K) (37). A hiatus in the section older than 407 ka BP at IODP site U1385 obscures potential signals related to this event (20). A distinct peak found in a proxy for SST conditions at 412 ka BP (Fig. 2F) (38) is indicative of hydrographic disturbance in the NA. A possible perturbation of the AMOC at the same time (39) may be connected to this event, both of which may be attributed to a major freshwater forcing at the time of near-deglaciation of the southern Greenland Ice Sheet in the early part of MIS 11c (40). Another recent study suggests a major ice sheet discharge event into the SO that might also coincide with this CDJ at 415 ka BP (41), but dating uncertainties do not permit an unambiguous attribution. While there is limited evidence supporting an AMOC perturbation around 415 ka BP, it remains unclear whether CDJ 11c is associated with an AMOC weakening or strengthening. Given the lack of a major CH<sub>4</sub> rise in our record (Fig. 3, C and E), we classify this event as CDJ- (CDJ- 11c); however, it could mechanistically also be CDJ+, with an atypical CH<sub>4</sub> response caused by already warm climate conditions in the NH.

Invigorations of the AMOC during DO events lead to abrupt increases in cross-equatorial heat transport to the NH (15, 42), which may be a necessary (yet insufficient) condition for the occurrence of CDJ+ events (6, 43). As a direct consequence of this energy imbalance, the ITCZ shifts northward and promotes a poleward shift and intensification of westerlies in the NH (18, 42). Driven by this shift in the ITCZ, new tropical wetlands are formed in the NH, which leads to an extended increase in CH<sub>4</sub> production (17, 18).

Conversely, we presume that CDJ- are associated with a weakening of the AMOC, causing a southward shift of the ITCZ, which promotes the formation of wetlands in the SH. The latter results in an initial overshoot in the CH<sub>4</sub> production that coincides with CDJ- during HS 1 and HS 4 (18). These small, short-lived CH<sub>4</sub> peaks of amplitudes smaller than ~50 ppb are distinct from major CH<sub>4</sub> rises associated with CDJ+; however, both CH<sub>4</sub> responses proceed at comparable growth rates. The absence of any short-lived CH<sub>4</sub> peaks related to CDJ- in our record (Fig. 3C and fig. S1C), similar to those found for HS 1 and HS 4 (18), can be explained by a combination of relatively low sample resolution and the bubble enclosure process that smooths the EDC gas record. The latter results in the obliteration of any potential CH<sub>4</sub> peaks smaller than ~50 ppb lasting for less than 200 years (see supplementary text). Accordingly, we use the absence of a major CH<sub>4</sub> rise as a criterion to distinguish CDJ- from CDJ+. Whereas the climate condi-

tions for CDJ+ are characteristic for DO events in the NH, CDJ- appear to be connected with major freshwater forcing and stadial conditions in the NH (6, 13, 18).

The strong correspondence of the CO<sub>2</sub> record with Antarctic temperature and benthic δ<sup>18</sup>O at the Iberian margin on the millennial time scale (Fig. 2, A, C, and D) suggests a causal link of CDM formation with SO processes (8). Proposed CDM-generating mechanisms include perturbations in the carbon cycle owing to changes in deep SO ventilation related to changes in stratification, buoyancy forcing, and Southern Hemisphere westerlies (44, 45); variations of the southern sea ice edge (46); and efficiency of the biological pump caused by either changes in the magnitude of dust-induced iron fertilization (44) or mode changes in the AMOC (47).

In contrast, the underlying CO<sub>2</sub> release mechanisms for the CDJ are poorly understood. Suggested marine mechanisms include outgassing due to increasing SST (30), rapid ventilation of accumulated respired carbon from intermediate-depth Atlantic (43, 48), or SO deep-water masses (49, 50). Despite the coherence of CDJ with AMOC changes and associated deep-water reorganizations in the NA (Fig. 2I) (6, 43), the carbon source for CDJ may not necessarily originate from the ocean. Proposed terrestrial sources include permafrost thawing in the NH (51), drought-induced biomass decomposition (6, 30), and changes in precipitation and vegetation distribution connected to ITCZ shifts (18, 36). To explain a 10-ppm CDJ in the atmosphere caused by carbon release from the land biosphere, ~80 Pg of carbon are needed (52). For most of these processes, a shift of the position of the ITCZ and resulting changes in the mid- to high-latitude westerly winds (53) are necessary to couple the cross-equatorial heat transport in the NA to the global carbon cycle (11, 42).

Our CO<sub>2</sub> record from the EDC ice core provides evidence for centennial-scale CDJ during glacial, deglacial, and early interglacial conditions. The CDJ identified here suggest fast, pulse-like CO<sub>2</sub> releases to the atmosphere during MIS 9e to 12a that are likely related to abrupt changes in AMOC (Fig. 2I) and shifts in the position of the ITCZ (Fig. 2E). Our data imply that CDJ are a pervasive feature of the natural carbon cycle that may go undetected in CO<sub>2</sub> records of insufficient temporal resolution and precision. We stress that such CDJ also occur during interglacial temperature conditions, as long as freshwater discharge from remnant ice sheets persists and is able to disturb ocean circulation. Anthropogenic warming and the committed ice sheet melting and associated sea level rise over the coming millennia (54) constitute new drivers that might trigger ocean circulation changes, and hence, pulse-like CO<sub>2</sub> releases such as those detected in our record

during an earlier interglacial period when AMOC was perturbed.

## REFERENCES AND NOTES

1. J. R. Petit *et al.*, *Nature* **399**, 429–436 (1999).
2. U. Siegenthaler *et al.*, *Science* **310**, 1313–1317 (2005).
3. D. Lüthi *et al.*, *Nature* **453**, 379–382 (2008).
4. B. Bereiter *et al.*, *Proc. Natl. Acad. Sci. U.S.A.* **109**, 9755–9760 (2012).
5. J. Ahn, E. J. Brook, *Nat. Commun.* **5**, 3723 (2014).
6. S. A. Marcott *et al.*, *Nature* **514**, 616–619 (2014).
7. H. Fischer *et al.*, *Nat. Geosci.* **11**, 474–485 (2018).
8. J. Ahn, E. J. Brook, *Science* **322**, 83–85 (2008).
9. E. Monnin *et al.*, *Science* **291**, 112–114 (2001).
10. J. Jouzel *et al.*, *Science* **317**, 793–796 (2007).
11. T. F. Stocker, S. J. Johnsen, *Paleoceanography* **18**, 1087 (2003).
12. J. Ahn, E. J. Brook, A. Schmittner, K. Kreutz, *Geophys. Res. Lett.* **39**, 5 (2012).
13. T. K. Bauska *et al.*, *Geophys. Res.* **45**, 7731–7740 (2018).
14. S. R. Hemming, *Rev. Geophys.* **42**, RG1005 (2004).
15. L. G. Henry *et al.*, *Science* **353**, 470–474 (2016).
16. Heinrich stadials are directly linked to massive glacial ice and meltwater discharges from the Hudson Strait known as Heinrich events.
17. M. Baumgartner *et al.*, *Clim. Past* **10**, 903–920 (2014).
18. R. H. Rhodes *et al.*, *Science* **348**, 1016–1019 (2015).
19. L. B. Railsback, P. L. Gibbard, M. J. Head, N. R. G. Voarintsoa, S. Toucanne, *Quat. Sci. Rev.* **111**, 94–106 (2015).
20. Materials and methods are available as supplementary materials.
21. L. Loulergue *et al.*, *Nature* **453**, 383–386 (2008).
22. Benthic δ<sup>13</sup>C of *C. wuellerstorfi* reflects changes in deep-water ventilation related to reorganization of deep-ocean circulation and remineralization of organic carbon. The δ<sup>18</sup>O signal of the same species indicates variations in deep-water temperatures.
23. Millennial-scale changes in the planktic δ<sup>18</sup>O record of *G. bulloides* follow changes in the sea surface temperature in the North Atlantic.
24. P. C. Tzedakis *et al.*, *Nat. Geosci.* **2**, 751–755 (2009).
25. P. C. Tzedakis *et al.*, *Clim. Past* **8**, 1473–1485 (2012).
26. T. Rodrigues *et al.*, *Quat. Sci. Rev.* **172**, 118–130 (2017).
27. F. Lambert, M. Bigler, J. P. Steffensen, M. Hutterli, H. Fischer, *Clim. Past* **8**, 609–623 (2012).
28. N. J. Shackleton, M. A. Hall, E. Vincent, *Paleoceanography* **15**, 565–569 (2000).
29. R. Schneider, J. Schmitt, P. Köhler, F. Joos, H. Fischer, *Clim. Past* **9**, 2507–2523 (2013).
30. T. K. Bauska *et al.*, *Proc. Natl. Acad. Sci. U.S.A.* **113**, 3465–3470 (2016).
31. F. Joos, R. Spahni, *Proc. Natl. Acad. Sci. U.S.A.* **105**, 1425–1430 (2008).
32. P. Tans, R. Keeling, Annual mean CO<sub>2</sub> growth rate for Mauna Loa, Hawaii (NOAA/ESRL and Scripps Institution of Oceanography, 2020); [www.esrl.noaa.gov/gmd/ccgg/trends/gr.html](http://www.esrl.noaa.gov/gmd/ccgg/trends/gr.html).
33. T. Exter *et al.*, *Quat. Sci. Rev.* **185**, 244–257 (2018).
34. L. Bazin *et al.*, *Clim. Past* **9**, 1715–1731 (2013).
35. H. Cheng *et al.*, *Nature* **534**, 640–646 (2016).
36. A. Bozbiyik, M. Steinacher, F. Joos, T. F. Stocker, L. Menviel, *Clim. Past* **7**, 319–338 (2011).
37. R. M. Spratt, L. E. Lisiecki, *Clim. Past* **12**, 1079–1092 (2016).
38. S. Barker *et al.*, *Nature* **520**, 333–336 (2015).
39. A. J. Dickson *et al.*, *Nat. Geosci.* **2**, 428–433 (2009).
40. R. G. Hatfield *et al.*, *Earth Planet. Sci. Lett.* **454**, 225–236 (2016).
41. D. J. Wilson *et al.*, *Nature* **561**, 383–386 (2018).
42. J. B. Pedro *et al.*, *Quat. Sci. Rev.* **192**, 27–46 (2018).
43. T. Chen *et al.*, *Science* **349**, 1537–1541 (2015).
44. S. L. Jaccard, E. D. Galbraith, A. Martínez-García, R. F. Anderson, *Nature* **530**, 207–210 (2016).
45. C. Basak *et al.*, *Science* **359**, 900–904 (2018).
46. B. B. Stephens, R. F. Keeling, *Nature* **404**, 171–174 (2000).
47. A. Schmittner, E. D. Galbraith, *Nature* **456**, 373–376 (2008).
48. M. Lacerra, D. Lund, J. Yu, A. Schmittner, *Paleoceanography* **32**, 780–795 (2017).
49. L. Menviel *et al.*, *Nat. Commun.* **9**, 2503 (2018).
50. J. W. B. Rae *et al.*, *Nature* **562**, 569–573 (2018).
51. P. Köhler, G. Knorr, E. Bard, *Nat. Commun.* **5**, 5520 (2014).
52. A. Jeltsch-Thömmes, F. Joos, *Clim. Past* **16**, 423–451 (2020).
53. C. Buizert *et al.*, *Nature* **563**, 681–685 (2018).

54. P. U. Clark *et al.*, *Nat. Clim. Chang.* **6**, 360–369 (2016).
55. C. Nehrbass-Ahles *et al.*, High-resolution atmospheric CO<sub>2</sub> and CH<sub>4</sub> records derived from the EPICA Dome C ice core and stable isotope records from marine sediment core IODP Site U1385 covering MIS 9e – 12a, PANGAEA (2020); <https://doi.org/10.1594/PANGAEA.915146>.

#### ACKNOWLEDGMENTS

We thank M. Häberli, O. Eicher, S. Eggleson, C. Bréant, J. Beck, and B. Seth for assistance with sample acquisition. We acknowledge the support of G. Aufresne, who conducted additional CH<sub>4</sub> measurements at IGE. Samples from site U1385 were provided by the International Ocean Discovery Program (IODP). J. Booth, S. Crowhurst, J. Nicolson, J. Rolfe, and M. Mleneck-Vautravers provided laboratory support. Thanks to R. Walther, S. Marending, K. Grossenbacher, H. P. Moret, and R. Bleisch for technical assistance and E. Brook for helpful comments on an earlier version of the manuscript. **Funding:** This work is a contribution to the European Project for Ice Coring in Antarctica (EPICA), a joint

European Science Foundation and European Commission scientific program, funded by the European Union and by national contributions from Belgium, Denmark, France, Germany, Italy, the Netherlands, Norway, Sweden, Switzerland, and the United Kingdom. Main logistic support was provided by IPEV and PNRA. This is EPICA publication no. 315. C.N.-A., J.Sc., B.B., F.J., A.S., L.Sc., L.Si., H.F., and T.F.S. acknowledge long-term financial support from the Swiss National Science Foundation (SNF project numbers 200020\_159563, 200020\_172745, 200020\_172506, 200020\_172476, and 20FI21\_189533). This project is TiPES (Tipping Points in the Earth System) contribution no. 17. This project has received funding from the European Union's Horizon 2020 research and innovation program under grant 820970 and from the European Community's Seventh Framework Programmes ERC-2011-AdG under grant agreement 291062 (ERC ICE&LASERS). J.Sh. is supported by the LabEX OSUG@2020 project of the Grenoble Observatory of Sciences of the Universe (OSUG). **Author contributions:** C.N.-A., J.Sc., B.B., J.C., D.H., H.F., and T.F.S. designed the research. C.N.-A. performed the measurements

with contributions from J.Sh., A.S., G.T., and R.G. Data analyses were led by C.N.-A. with contributions from J.Sc., B.B., F.J., L.Sc., L.Si., D.H., H.F., and T.F.S. C.N.-A. and T.F.S. led the writing of the manuscript, with input from all authors. **Competing interests:** The authors declare no competing interests. **Data and materials availability:** All data are available online in the supplementary materials and through the PANGAEA data depository (55).

#### SUPPLEMENTARY MATERIALS

[science.sciencemag.org/content/369/6506/1000/suppl/DC1](https://science.sciencemag.org/content/369/6506/1000/suppl/DC1)  
Materials and Methods  
Supplementary Text  
Figs. S1 to S9  
Table S1  
References (56–87)  
Data S1 and S2

2 August 2019; accepted 9 July 2020  
10.1126/science.aay8178



## MICROBIOLOGY

# Architecture and function of human uromodulin filaments in urinary tract infections

Gregor L. Weiss<sup>1\*</sup>, Jessica J. Stanisich<sup>1\*</sup>, Maximilian M. Sauer<sup>1\*†</sup>, Chia-Wei Lin<sup>2‡</sup>, Jonathan Eras<sup>1</sup>, Dawid S. Zyla<sup>1</sup>, Johannes Trück<sup>3</sup>, Olivier Devuyst<sup>4,5</sup>, Markus Aebi<sup>2</sup>, Martin Pilhofer<sup>1§</sup>, Rudi Glockshuber<sup>1</sup>

Uromodulin is the most abundant protein in human urine, and it forms filaments that antagonize the adhesion of uropathogens; however, the filament structure and mechanism of protection remain poorly understood. We used cryo-electron tomography to show that the uromodulin filament consists of a zigzag-shaped backbone with laterally protruding arms. N-glycosylation mapping and biophysical assays revealed that uromodulin acts as a multivalent ligand for the bacterial type 1 pilus adhesin, presenting specific epitopes on the regularly spaced arms. Imaging of uromodulin-uropathogen interactions in vitro and in patient urine showed that uromodulin filaments associate with uropathogens and mediate bacterial aggregation, which likely prevents adhesion and allows clearance by micturition. These results provide a framework for understanding uromodulin in urinary tract infections and in its more enigmatic roles in physiology and disease.

**T**he glycoprotein uromodulin (UMOD) is secreted in the kidney and is the most abundant urinary protein (1). A UMOD promoter variant present in ~80% of the human population drives a twofold increase in urinary UMOD concentration (2), which results in reduced susceptibility to bacterial urinary tract infections (UTIs) (3). Uropathogenic *Escherichia coli* (UPEC) utilize adhesive type 1 pili to attach to high-mannose-type N-glycans displayed on the uroepithelial surface (4). It has been suggested that UMOD acts as a soluble adhesion antagonist for UPEC (5–11).

Mature UMOD consists of three epidermal growth factor (EGF)-like domains (EGF I to III), a cysteine-rich domain (D8C), a fourth EGF domain (EGF IV), and the bipartite zona pellucida (ZP) module (subdomains ZP-N and ZP-C) (Fig. 1A) (1). Produced as a glycosylphosphatidylinositol-anchored precursor, UMOD is then cleaved by the protease hepsin and assembles into homopolymeric filaments with an average length of ~2.5  $\mu\text{m}$  (12, 13). Despite its multiple roles in human health and disease (1), the molecular architecture and interactions of UMOD in urine are poorly understood.

We first developed a protocol to purify stable UMOD filaments from urine (table S1 and fig. S1A). Mass spectrometry (MS) of dissociated UMOD monomers from different donors revealed highly similar, broad mass-distribution profiles (fig. S1, B to D), which showed that UMOD glycosylation was gender- and genotype-independent. Next, we established a site-specific N-glycosylation map of UMOD using liquid chromatography with tandem mass spectrometry (LC-MS/MS) of tryptic glycopeptides (Fig. 1A, figs. S2 to S6, and tables S2 and S3). We identified individual N-glycans attached to asparagine (Asn) residues 38, 76, 80, 232, 275, 322, 396, and 513 (figs. S2 to S6 and tables S2 and S3). High-mannose N-glycans were found at Asn<sup>275</sup> and Asn<sup>513</sup>, whereas other N-glycans were confirmed to be di-, tri-, or tetra-antennary complex types. Because UPEC adhere to uroepithelial cells by means of type 1 pili that specifically recognize high-mannose N-glycans (4, 14), both glycans at Asn<sup>275</sup> and Asn<sup>513</sup> were candidates for mediating UMOD's antiadhesive activity.

To contextualize the glycan arrangement within UMOD polymers, we imaged UMOD filaments using cryo-electron tomography (cryo-ET) (15) (Fig. 1B and movie S1). One orientation (Fig. 1C) was consistent with the previously observed zigzag shape (12, 13, 16, 17), though filaments showed different degrees of curvature and irregular rotations around the long axis. A second, prominent orientation had a fishbone-like appearance, with a central core filament and regularly protruding arms (Fig. 1D). We calculated a structure by subtomogram averaging, which resolved repeating-filament subunits arranged in a helix with a 180° twist and 6.5-nm rise. The filament core consisted of 8.5-nm-long modules zig-zagging at 95° angles. The 12.5-nm-long arm

segments were flexible and protruded at 45° angles (Fig. 1E, fig. S7, and movie S1).

To assign UMOD protein domains to densities in the subtomogram average, we studied an elastase-digested form of UMOD (eUMOD), wherein UMOD is cleaved between the D8C and EGF IV domains (18). We observed that eUMOD retained the zigzag core structure, but densities for the arms were absent (Fig. 1F; fig. S7; fig. S8, B to D; fig. S9; and movie S2). On the basis of the fitting of the previously published crystal structure of truncated UMOD (EGF IV–ZP module) (16) into our subtomogram averages, we propose a model in which the ZP module polymerizes into the filament backbone and the EGF I to III and D8C domains constitute the protruding arms (Fig. 1G and fig. S9, C and D). This alternating ZP-stacking model differs from previously suggested architectures (16, 19) of the UMOD filament (fig. S10).

Next, we investigated the interaction between UMOD filaments and the adhesin, FimH, of type 1-piliated UPEC strains. FimH at the pilus tip recognizes terminal mannosides in high-mannose N-glycans of the uroepithelial receptor uroplakin 1a (4, 20). Binding of type 1-piliated cells to UMOD filaments had been demonstrated, but the exact FimH binding site in UMOD remained unknown (6). We recorded the affinity of the isolated FimH lectin domain (FimH<sub>L</sub>) to UMOD filaments and obtained a single apparent dissociation constant ( $K_d$ ) of  $2.2 \times 10^{-8}$  M (Fig. 2A). Consistent with the high affinity of FimH<sub>L</sub> for UMOD, spontaneous dissociation of FimH<sub>L</sub> from UMOD filaments was very slow, with a half-life of 2.1 hours (Fig. 2B). Because FimH<sub>L</sub> binds mannosides with a 2000-fold higher affinity compared with full-length FimH—as a consequence of the ability of FimH to form catch bonds under tensile mechanical force (21, 22)—we calculated a  $K_d$  of  $\sim 4 \times 10^{-5}$  M for the UMOD-FimH complex in the absence of shear stress. Using analytical gel filtration and gel-band densitometry, we determined the stoichiometry of the UMOD-FimH<sub>L</sub> complex to be 1:2 (Fig. 2, C and D, and fig. S11).

To test which of the two high-mannose N-glycans of UMOD was recognized by FimH, we analyzed the UMOD-(FimH<sub>L</sub>)<sub>2</sub> complex using cryo-ET. Differences between UMOD-(FimH<sub>L</sub>)<sub>2</sub> and native UMOD were already visible in individual tomograms (fig. S12, A and B, and movie S3). The UMOD-(FimH<sub>L</sub>)<sub>2</sub> subtomogram average revealed a prominent additional density on the UMOD arms, which may be sufficient to accommodate two FimH<sub>L</sub> (Fig. 2, E and F; fig. S12, C to F; and movie S3). No notable additional density was seen at the core of UMOD-(FimH<sub>L</sub>)<sub>2</sub> filaments or on eUMOD (containing only the high-mannose glycan at Asn<sup>513</sup>) incubated with FimH<sub>L</sub> (fig. S12, G to I). Together, our data demonstrate that the

<sup>1</sup>Institute of Molecular Biology and Biophysics, ETH Zürich, Otto-Stern-Weg 5, CH-8093 Zürich, Switzerland. <sup>2</sup>Institute of Microbiology, ETH Zürich, Vladimir-Prelog-Weg 1-5/10, CH-8093 Zürich, Switzerland. <sup>3</sup>University Children's Hospital Zürich, Steinwiesstrasse 75, CH-8032 Zürich, Switzerland. <sup>4</sup>Institute of Physiology, Mechanisms of Inherited Kidney Disorders, University of Zürich, Winterthurerstrasse 190, CH-8057 Zürich, Switzerland. <sup>5</sup>Division of Nephrology, UCLouvain Medical School, Brussels, Belgium.

\*These authors contributed equally to this work.

†Present address: Department of Biochemistry, University of Washington, 1705 NE Pacific St., Seattle, WA 98195, USA.

‡Present address: Functional Genomics Center Zürich, Winterthurerstrasse 190, CH-8057 Zürich, Switzerland.

§Corresponding author. Email: pilhofer@biol.ethz.ch

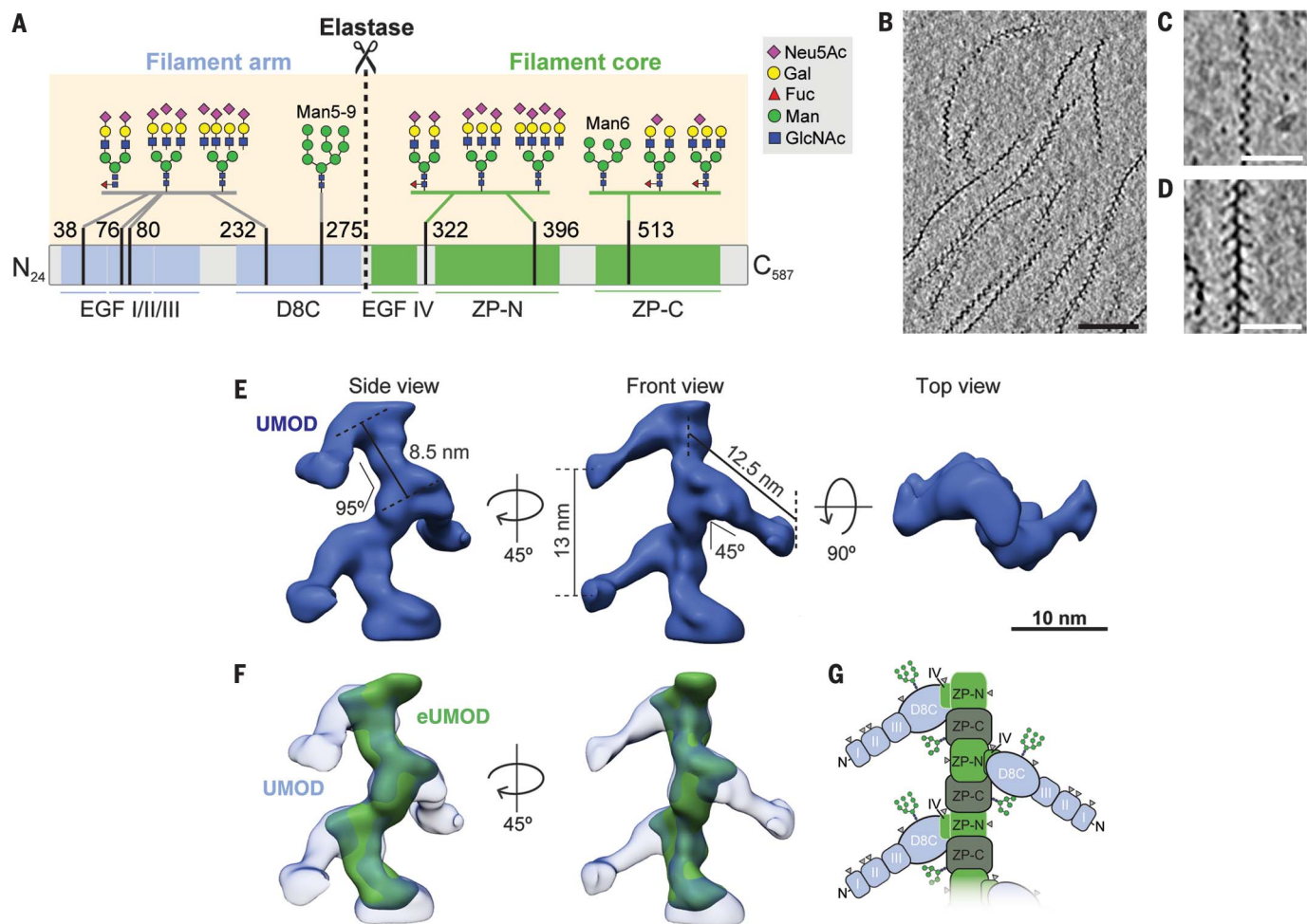


**Fig. 1. UMOD site-specific glycosylation pattern and filament architecture.**

(A) Domain organization of mature UMOD with four EGF-like domains (I to III, light blue; IV, green), the cysteine-rich D8C domain (light blue), and the bipartite ZP module (ZP-N and ZP-C, green) (1). The most abundant N-linked glycan forms identified at each N-glycosylation site are shown schematically (amino acid numbering according to UMOD with N-terminal signal peptide). Except for Asn<sup>275</sup> and Asn<sup>513</sup>, all N-glycans were confirmed to be di-, tri-, or tetra-antennary complex type that could be sialylated and/or fucosylated. We observed mixed N-glycan structures at Asn<sup>513</sup>, composed of Man6 and, as previously reported, complex-type N-glycans (8). The sum of the masses of all identified glycans corresponded well to the average mass difference (20.1 kDa) between glycosylated and deglycosylated UMOD. The elastase-digested form of UMOD (eUMOD = Ser<sup>292</sup> through C terminus Phe<sup>587</sup>) is marked in green, and scissors indicate the elastase cleavage site after Ser<sup>291</sup>. Neu5Ac, N-acetylneuraminic acid; Gal, galactose; Fuc, fucose; Man, mannose; GlcNAc, N-acetylglucosamine. (B to D) Cryo-ET of purified

UMOD filaments revealed irregular bending and helical parameters. (C) and (D) show magnified views of the two most common orientations, revealing the zigzag core (C) and the lateral arms causing a fishbone-like appearance (D). 13.8-nm slices through cryotomograms are shown. Scale bars, 100 nm in (B) and 50 nm in (C) and (D). (E) Different orientations of a UMOD subtomogram average (surface renderings). The subtomogram average was low-pass filtered to 27 Å to demonstrate the complete 3D architecture. (F) Different orientations (surface renderings, green) of the eUMOD subtomogram average. The superposition of eUMOD with native UMOD (transparent, light blue), low-pass filtered to the same resolution of 27 Å, demonstrates the absence of the lateral arms in eUMOD. The unfiltered averages can be seen in fig. S9. (G) Proposed alternating ZP-N- and ZP-C-stacking model of the UMOD filament architecture [same orientation as in (F), right]. The two high-mannose N-glycan structures in each UMOD monomer are indicated by green glycan trees, and complex-type N-glycans are shown as gray triangles.

high-mannose N-glycan at Asn<sup>275</sup> of the UMOD arm is the only accessible FimH<sub>2</sub>-recognition site.

We next analyzed binding of UMOD filaments to a mixture of type 1-piliated and nonpiliated *E. coli* cells by cryo-ET imaging. Each type 1-piliated cell exhibited a substantial increase in the local UMOD filament concentration around the cells ( $n = 6$  tomograms) (Fig. 3, A and B; fig. S13, A and B; and movie S4). Contact sites between pili and UMOD were mainly at the FimH-

containing pilus tips (Fig. 3A). In contrast, no UMOD filaments accumulated around nonpiliated cells ( $n = 7$  tomograms; fig. S13, C and D) or piliated cells incubated with eUMOD ( $n = 3$  tomograms; fig. S14). *E. coli*-UMOD association therefore requires both the presence of type 1 pili and the glycosylated UMOD arm.

Using light microscopy, we investigated bacteria-UMOD interactions on a larger scale. Incubation of type 1-piliated *E. coli* with

UMOD filaments resulted in the aggregation of bacteria and the formation of clumps that consisted of tens to hundreds of bacteria (Fig. 3C). Cell clumping occurred across a wide range of UMOD concentrations and was inhibited by an excess of D-mannose (Fig. 3C), which indicates that clumping was caused by FimH binding to UMOD glycans. However, preformed clumps proved to be resistant against dissociation by D-mannose (fig. S15). Total internal reflection fluorescence



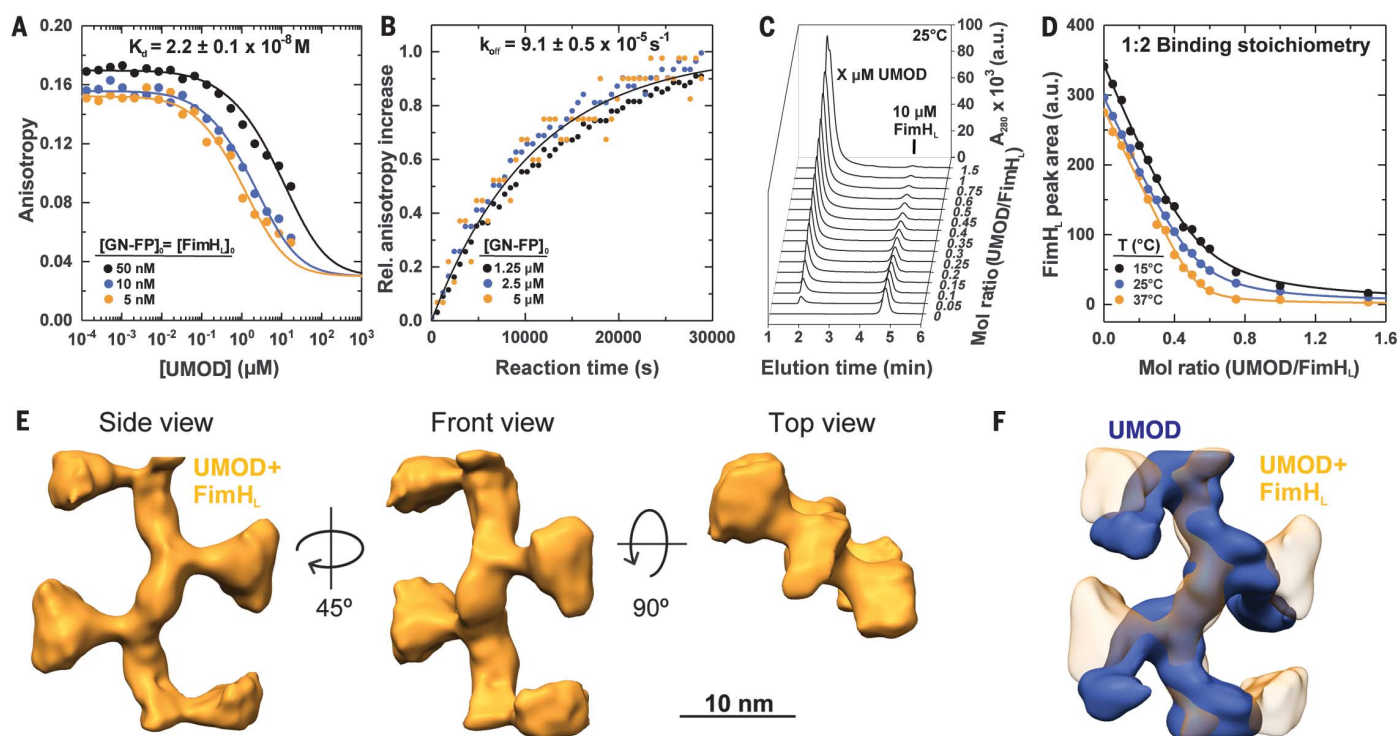


**Fig. 2. Two FimH<sub>L</sub> molecules bind to the high-mannose glycan on the UMOD arm.** (A and B) Thermodynamics and kinetics of UMOD binding and release by FimH<sub>L</sub> at pH 7.4 and 25°C. (A) Competitive equilibrium displacement of the fluorescent mannoside GN-FP (21, 22) from FimH<sub>L</sub> with increasing UMOD concentrations, recorded through the decrease in GN-FP fluorescence anisotropy. (B) Kinetics of spontaneous dissociation of FimH<sub>L</sub> from UMOD, recorded through the binding of excess GN-FP to released FimH<sub>L</sub>. The obtained first-order kinetics (solid lines) were independent of GN-FP concentration and thus directly monitored dissociation of FimH<sub>L</sub> from UMOD ( $k_{\text{off}} = 9.1 \times 10^{-5} \text{ s}^{-1}$ ). Direct determination of the affinity of full-length FimH for UMOD filaments proved to be impossible because of the limited solubility of UMOD filaments (~100-μM monomers). (C and D) Titration of FimH<sub>L</sub> with increasing amounts of UMOD filaments to determine the stoichiometry of complex formation at pH 7.4 and different temperatures (15°, 25°, and 37°C). (C) Size exclusion chromatography (SEC) elution profiles of 10 μM FimH<sub>L</sub> incubated with

different amounts of UMOD filaments (UMOD monomer concentrations between 0 and 20 μM), detected through protein absorbance at 280 nm. (D) Peak area of free FimH<sub>L</sub>, plotted against the UMOD monomer-to-FimH<sub>L</sub> ratio, revealing that, on average, two FimH<sub>L</sub> molecules can bind to a single UMOD monomer. a.u., arbitrary units. (E) Different orientations of the subtomogram average (shown as a surface rendering) of UMOD filaments that were incubated with a fourfold excess of FimH<sub>L</sub> over UMOD monomers. Notable additional densities are detectable on the filament arms, whereas no extra densities could be identified on the filament core. (F) Overlay of surface renderings of subtomogram averages of native UMOD (blue) and UMOD incubated with a fourfold excess of FimH<sub>L</sub> (transparent orange), both low-pass filtered to a resolution of 27 Å. The additional densities could accommodate two copies of FimH<sub>L</sub> (fig. S12, D to G). Together, the data indicate that up to two FimH<sub>L</sub> molecules bind to the high-mannose glycosylation site at Asn<sup>275</sup> in the D8C domain of the UMOD arm.

(TIRF) microscopy showed that cell aggregates colocalized with UMOD (Fig. 3D). UMOD-dependent cell aggregation also occurred with a UPEC strain (fig. S16) but was not detected with nonpiliated *E. coli* or with piliated *E. coli* incubated with eUMOD (figs. S17 and S18). To visualize the UMOD-induced cell aggregates by cryo-ET, we thinned the sample using cryo-focused ion beam (FIB) milling (23). The cryo-tomograms consistently revealed bacteria that were tightly surrounded by a dense mesh of UMOD filaments ( $n = 17$  tomograms; Fig. 3E, fig. S19, and movie S5).

In addition to type 1 pili, many UPEC strains express multiple pili with diverse glycan specificities. The UPEC strain CFT073 encodes type 1 pili (mannoside-specific lectin), F9 or Fml pili (lectin specific for galactosides), and S-pili (lectin specific for sialic acid) (24–26).

We therefore tested the inhibition of UMOD-mediated cell clumping of CFT073 by the addition of D-mannose, D-galactose, and sialic acid. Although D-mannose alone only slightly decreased cell aggregation (fig. S20, A and B), the addition of a cocktail of all three monosaccharides proved to be most effective in reducing UMOD-mediated cell clumping (fig. S20B). This indicates that the complex-type UMOD glycans might interact with different types of pilus adhesins presented by different uropathogens.

We verified these findings by analyzing unprocessed urine from patients with clinically diagnosed UTIs using light microscopy and cryo-ET. Urine from a patient with an *E. coli* UTI revealed bacterial clumps that were embedded into fibrous structures (Fig. 4A). Individual bacteria from the same sample

were heavily piliated and always surrounded by numerous UMOD filaments (Fig. 4B and movie S6;  $n = 27$  tomograms); several contact sites between pilus tips and UMOD were resolved (Fig. 4C and movie S6). Furthermore, we analyzed urine from UTI patients with other pathogens, including *Klebsiella pneumoniae*, *Pseudomonas aeruginosa*, and *Streptococcus mitis*. In all cases, we observed cell aggregates associated with fibrous structures using light microscopy, and 67 to 71% of cells imaged by cryo-ET confirmed the presence of UMOD filaments (fig. S21 and movie S7).

Our data provide a three-dimensional (3D) structure of native UMOD filaments and support the hypothesis that the polymerization of UMOD into a multivalent filament is required for its function as a FimH antagonist to effectively compete with the high concentration

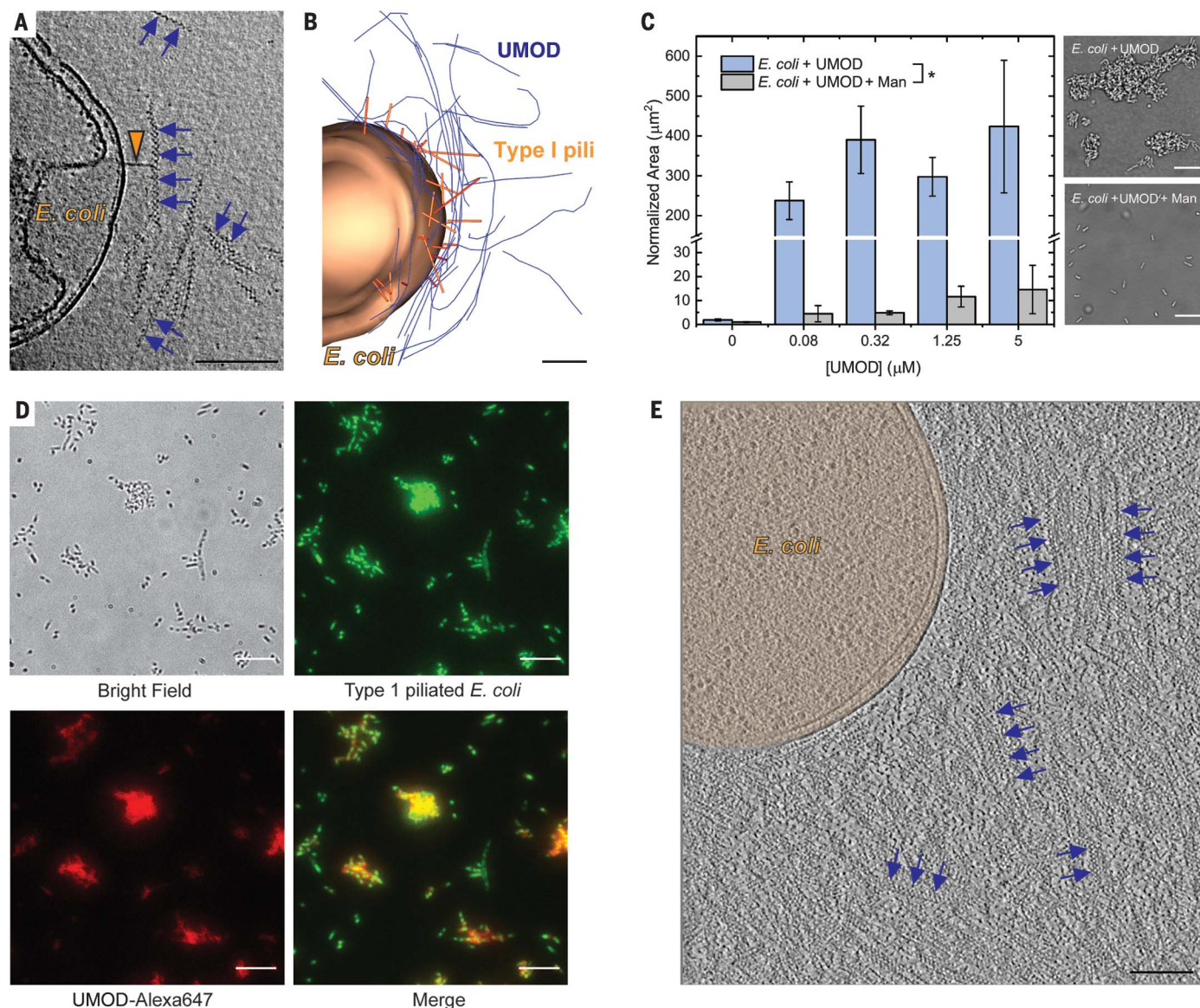


**Fig. 3. UMOD associates with piliated bacteria and can lead to cell aggregation.** (A and B) The type 1 pilus-deficient strain *E. coli* AAEC189 was transformed with the type 1 pilus expression plasmid pSH2, coincubated with UMOD filaments (1 μM UMOD monomers and  $\sim 1.6 \times 10^9$  *E. coli* cells/ml) and imaged with cryo-ET. A slice (8.6-nm thick) through a cryotomogram (A) and a segmentation of the same tomogram (B) are shown. Piliated bacteria (cell, brown; pili, orange) were always seen in close association with a loose mesh of UMOD filaments (blue lines or arrows). Note the contact site of the pilus tip with the UMOD filament. A partly lysed cell that resulted in higher image quality is shown. See fig. S13, A and B, for more examples. Scale bars, 100 nm. (C) Quantification of UMOD-mediated formation of cell aggregates with light microscopy. The bar graph shows the normalized clump area observed upon incubation (2 hours) at 37°C of a constant amount of type 1-piliated *E. coli* HB101 (FimAra) ( $\sim 10^8$  cells/mL), with different concentrations of UMOD

filaments (0.08 to 5.0 μM; concentrations refer to the UMOD monomer). The presence of 10 mM D-mannose inhibited aggregation across all UMOD concentrations tested. Representative light microscopy images are shown on the right (without and with 10 mM Man). Bars represent the means of biological triplicates  $\pm$  SEM. \* $P < 0.05$  difference between groups [two-way analysis of variance (ANOVA), post hoc Tukey test]. Scale bars, 10 μm. (D) Cell aggregates colocalized with UMOD filaments. Bright-field and TIRF microscopy images of type 1-piliated *E. coli* HB101 (FimAra) cells (excitation at 405 nm, green) that were incubated with fluorescent UMOD-Alexa647 filaments (red) are shown. Scale bars, 10 μm. (E) UMOD-induced *E. coli* aggregates were plunge-frozen, thinned by cryo-FIB milling, and imaged with cryo-ET (an 8.6-nm tomographic slice is shown). *E. coli* cells (brown) were always seen embedded in a highly dense meshwork of UMOD filaments (blue arrows). For further examples, see fig. S19. Scale bar, 100 nm.

of uroplakin 1a on the urinary epithelium (4, 14, 27). The intrinsic flexibility of UMOD filaments allows their adaptation to the bacterial surface, multivalent binding to pili from the same bacterium, and eventually encapsulation of entire cells. Analogous to the

mechanism by which antibody-cross-linked clumps of enchain *Salmonella* cells facilitate the removal of pathogens from the gut (28), UMOD-mediated cell aggregation may have a role in the efficient clearance of bacteria through micturition.

Our study also sheds light on interactions between UMOD and pathogens other than type 1-piliated UPEC. UPEC genomes, for example, encode up to 16 fimbrial gene clusters, and UPEC switch expression between pilus types with distinct receptor specificities (24, 29–31).



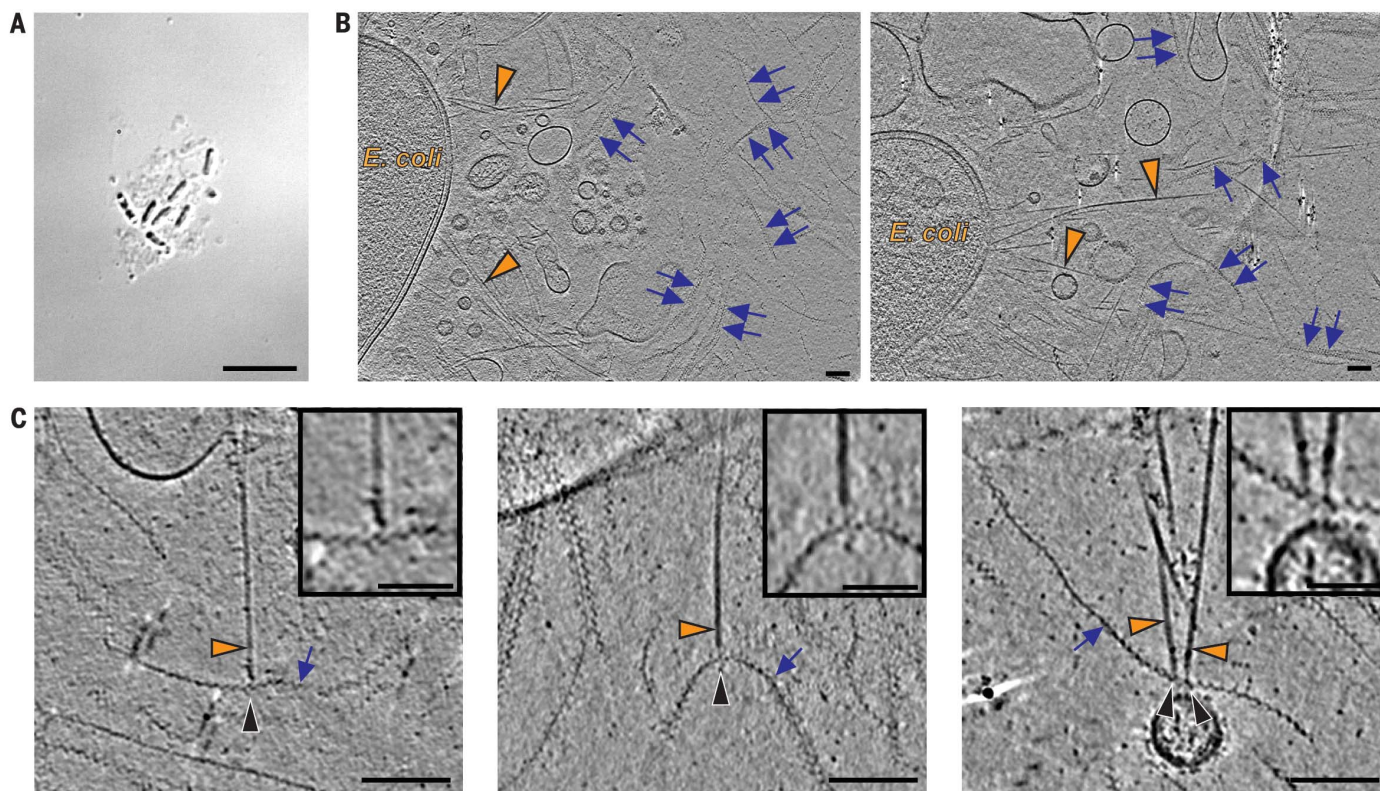


**Fig. 4. Urine from UTI patients shows cell aggregation and pilus-mediated UMOD association with bacterial cells.** (A) Differential interference contrast (DIC) light microscopy imaging of urine from a patient with acute *E. coli* UTI revealed clustered bacteria. Scale bar, 10  $\mu$ m. (B) Cryo-ET imaging of urine from the same patient showed piliated (orange arrowheads) bacterial cells (labeled *E. coli*). All analyzed cells

( $n = 27$  tomograms or cells; two representative examples are shown) were surrounded by filaments with the typical UMOD appearance (blue arrows). Scale bars, 100 nm. (C) The cryotomograms revealed multiple contact sites (black arrowheads) between pili (orange arrowheads) and UMOD (blue arrows). Scale bars, 100 nm. Magnified views are provided in the insets. Scale bars, 50 nm.

The seven different complex-type N-glycans on UMOD (Fig. 1A) may therefore competitively inhibit adhesion of other pathogens to other epithelial receptors. Finally, the resolved site-specific N-glycosylation pattern and architecture of UMOD filaments will serve as a framework for studying the mechanisms that underlie UMOD's roles in the regulation of salt transport, kidney diseases, and innate immunity (1, 19).

## REFERENCES AND NOTES

- O. Devuyst, E. Olinger, L. Rampoldi, *Nat. Rev. Nephrol.* **13**, 525–544 (2017).
- M. Trudu et al., *Nat. Med.* **19**, 1655–1660 (2013).
- S. Ghirotto et al., *J. Am. Soc. Nephrol.* **27**, 2983–2996 (2016).
- G. Zhou et al., *J. Cell Sci.* **114**, 4095–4103 (2001).
- J. Parkkinen, R. Virkola, T. K. Korhonen, *Infect. Immun.* **56**, 2623–2630 (1988).
- J. Pak, Y. Pu, Z. T. Zhang, D. L. Hasty, X. R. Wu, *J. Biol. Chem.* **276**, 9924–9930 (2001).
- M. S. Conover et al., *Cell Host Microbe* **20**, 482–492 (2016).
- F. Serafini-Cessi, A. Monti, D. Cavallone, *Glycoconj. J.* **22**, 383–394 (2005).
- D. Cavallone, N. Malagolini, A. Monti, X.-R. Wu, F. Serafini-Cessi, *J. Biol. Chem.* **279**, 216–222 (2004).
- J. M. Bates Jr. et al., *Kidney Int.* **65**, 791–797 (2004).
- L. Mo et al., *Am. J. Physiol. Renal Physiol.* **286**, F795–F802 (2004).
- M. Brunati et al., *eLife* **4**, e08887 (2015).
- K. R. Porter, I. Tamm, *J. Biol. Chem.* **212**, 135–140 (1955).
- B. Xie et al., *J. Biol. Chem.* **281**, 14644–14653 (2006).
- M. Beck, W. Baumeister, *Trends Cell Biol.* **26**, 825–837 (2016).
- M. Bokhove et al., *Proc. Natl. Acad. Sci. U.S.A.* **113**, 1552–1557 (2016).
- J. S. Hunt, P. R. MacDonald, W. A. Day, A. R. McGiven, *Pathology* **12**, 609–621 (1980).
- L. Jovine, H. Qi, Z. Williams, E. Litscher, P. M. Wassarman, *Nat. Cell Biol.* **4**, 457–461 (2002).
- L. Rampoldi, F. Scolari, A. Amoroso, G. Ghiggi, O. Devuyst, *Kidney Int.* **80**, 338–347 (2011).
- E. Hahn et al., *J. Mol. Biol.* **323**, 845–857 (2002).
- M. M. Sauer et al., *Nat. Commun.* **7**, 10738 (2016).
- M. M. Sauer et al., *J. Am. Chem. Soc.* **141**, 936–944 (2019).
- J. M. Medeiros, D. Böck, M. Pilhofer, *Curr. Opin. Microbiol.* **43**, 62–68 (2018).
- D. J. Wurpel, S. A. Beatson, M. Totsika, N. K. Petty, M. A. Schembri, *PLOS ONE* **8**, e52835 (2013).
- D. J. Wurpel et al., *PLOS ONE* **9**, e93177 (2014).
- T. J. Wiles, R. R. Kulesus, M. A. Mulvey, *Exp. Mol. Pathol.* **85**, 11–19 (2008).
- G. Min et al., *J. Mol. Biol.* **317**, 697–706 (2002).
- K. Moor et al., *Nature* **544**, 498–502 (2017).
- N. Holden, M. Totsika, L. Dixon, K. Catherwood, D. L. Gally, *Infect. Immun.* **75**, 3325–3334 (2007).
- S. Lindberg et al., *Infect. Immun.* **76**, 771–780 (2008).
- Y. Xia, D. Gally, K. Forsman-Semb, B. E. Uhlin, *EMBO J.* **19**, 1450–1457 (2000).
- P. Tittmann and M. Peterek for technical support during electron microscopy data collection; and ScopeM for instrument access at ETH Zürich. F. Eisenstein is acknowledged for help with subtomogram average processing and J. Xu for help with analyzing cryo-ET data. We thank G. Navarra and B. Ernst (University of Basel) for providing the fluorescent mannoside GN-FP. C. Giese is acknowledged for providing *E. coli* AAEC189 (pSH2) cells. T. Hennet is acknowledged for initial discussions about UMOD glycosylation. **Funding:** G.L.W. was supported by a Boehringer Ingelheim Fonds Ph.D. fellowship. M.P. was supported by the Swiss National Science Foundation (no. 31003A\_179255), the European Research Council (no. 679209), and the NOMIS foundation. R.G. was supported by the Swiss National Science Foundation (nos. 310030B\_176403/1 and 31003A\_156304). O.D. was supported by the Swiss National Centre of Competence in Research Kidney Control of Homeostasis (NCCR Kidney.CH) program, the Swiss National Science Foundation (no. 310030\_189044), and the Rare Disease Initiative Zürich (Radiz). J.T. was supported by the Swiss National Science Foundation (nos. PZ00P3\_161147 and PZ00P3\_183777). M.P. and R.G. were also supported by basic funding from ETH Zürich. **Author contributions:** G.L.W., J.J.S., M.M.S., O.D., M.P., and R.G. designed experiments. J.J.S., M.M.S., and J.E. purified and biophysically analyzed UMOD. C.-W.L. and M.A. performed and analyzed MS experiments. G.L.W. collected and processed cryo-ET data. D.S.Z. constructed the expression plasmid and performed TIRF microscopy. J.J.S. performed and analyzed light microscopy experiments. G.L.W. and J.T. collected patient urine. G.L.W., J.J.S., M.M.S., M.P., and R.G. wrote the manuscript with comments from all authors. **Competing interests:** The authors declare no competing interests. **Data and materials availability:** All subtomogram averages shown in this study were uploaded to the Electron Microscopy Databank (EMD) together with their respective half maps, masks for Fourier shell correlation (FSC) calculations, and an example tomogram. Accession numbers:

## ACKNOWLEDGMENTS

We thank the Functional Genomics Center Zürich, specifically S. Chesnov and P. Hunziker for performing the matrix-assisted laser desorption/ionization mass spectrometry (MALDI-MS) analysis and Edman sequencing, H. Debaix for the genotyping; E. Olinger and A. Yoshifuji for support in urinary UMOD analyses;

EMD-11128 and EMD-11129 (native UMOD), EMD-11130 and EMD11131 (eUMOD), EMD-1133 and EMD-11134 (UMOD incubated with FimH<sub>L</sub>), and EMD-11134 and EMD-11135 (eUMOD incubated with FimH<sub>L</sub>). Example tomograms of bacterial cells with UMOD were also uploaded to the EMD with accession numbers EMD-11136 to EMD-11143. All other data needed to evaluate the conclusions in the paper are present in the paper or the supplementary materials.

**SUPPLEMENTARY MATERIALS**

science.sciencemag.org/content/369/6506/1005/suppl/DC1  
Materials and Methods  
Figs. S1 to S21  
Tables S1 to S4  
References (32–63)  
MDAR Reproducibility Checklist

Movies S1 to S7

[View/request a protocol for this paper from Bio-protocol.](#)

25 October 2019; resubmitted 22 April 2020

Accepted 18 June 2020

Published online 2 July 2020

10.1126/science.aaz9866



## CORONAVIRUS

# Studies in humanized mice and convalescent humans yield a SARS-CoV-2 antibody cocktail

Johanna Hansen<sup>1\*</sup>, Alina Baum<sup>1\*</sup>, Kristen E. Pascal<sup>1</sup>, Vincenzo Russo<sup>1</sup>, Stephanie Giordano<sup>1</sup>, Elzbieta Wloga<sup>1</sup>, Benjamin O. Fulton<sup>1</sup>, Ying Yan<sup>1</sup>, Katrina Koon<sup>1</sup>, Krunal Patel<sup>1</sup>, Kyung Min Chung<sup>1</sup>, Aynur Hermann<sup>1</sup>, Erica Ullman<sup>1</sup>, Jonathan Cruz<sup>1</sup>, Ashique Rafique<sup>1</sup>, Tammy Huang<sup>1</sup>, Jeanette Fairhurst<sup>1</sup>, Christen Libertiny<sup>1</sup>, Marine Malbec<sup>1</sup>, Wen-yi Lee<sup>1</sup>, Richard Welsh<sup>1</sup>, Glen Farr<sup>1</sup>, Seth Pennington<sup>1</sup>, Dipali Deshpande<sup>1</sup>, Jemmie Cheng<sup>1</sup>, Anke Watty<sup>1</sup>, Pascal Bouffard<sup>1</sup>, Robert Babb<sup>1</sup>, Natasha Levenkova<sup>1</sup>, Calvin Chen<sup>1</sup>, Bojie Zhang<sup>1</sup>, Annabel Romero Hernandez<sup>1</sup>, Kei Saotome<sup>1</sup>, Yi Zhou<sup>1</sup>, Matthew Franklin<sup>1</sup>, Sumathi Sivapalasingam<sup>1</sup>, David Chien Lye<sup>2</sup>, Stuart Weston<sup>3</sup>, James Logue<sup>3</sup>, Robert Haupt<sup>3</sup>, Matthew Frieman<sup>3</sup>, Gang Chen<sup>1</sup>, William Olson<sup>1</sup>, Andrew J. Murphy<sup>1</sup>, Neil Stahl<sup>1</sup>, George D. Yancopoulos<sup>1</sup>, Christos A. Kyrtatsous<sup>1†</sup>

Neutralizing antibodies have become an important tool in treating infectious diseases. Recently, two separate approaches yielded successful antibody treatments for Ebola—one from genetically humanized mice and the other from a human survivor. Here, we describe parallel efforts using both humanized mice and convalescent patients to generate antibodies against the severe acute respiratory syndrome coronavirus 2 (SARS-CoV-2) spike protein, which yielded a large collection of fully human antibodies that were characterized for binding, neutralization, and three-dimensional structure. On the basis of these criteria, we selected pairs of highly potent individual antibodies that simultaneously bind the receptor binding domain of the spike protein, thereby providing ideal partners for a therapeutic antibody cocktail that aims to decrease the potential for virus escape mutants that might arise in response to selective pressure from a single-antibody treatment.

In the setting of the current coronavirus disease 2019 (COVID-19) pandemic, there has been urgency to develop potent antiviral treatments, and early efforts have hearkened back to the days of Emil von Behring, who won the Nobel prize for showing that antibodies can be transferred in serum. However, technological advances over the last century have allowed for the progression from using convalescent serum to the utilization of recombinant fully human antibodies. The proposal to genetically humanize the immune system of mice (1) has provided an efficient source of naturally selected, fully human antibodies. For example, such mice have been used to develop checkpoint inhibitors for immune oncology (2) as well as Food and Drug Administration (FDA)-approved antibodies for the treatment of rheumatoid arthritis, cardiovascular disease, cutaneous squamous cell carcinoma, and allergic diseases such as asthma and atopic dermatitis. More recently, the ability to sort individual B cells from previously infected human patients and molecularly clone the antibody genes from these B cells has led to an independent source of human antibodies, albeit limited to antibodies that target infectious agents. Recently,

these two fundamentally different approaches were independently exploited to develop fully human antibody treatments for the lethal infectious disease caused by the Ebola virus: Genetically humanized VelocImmune (VI) mice (3, 4) generated an Ebola antibody cocktail treatment (5), whereas sorting B cells from a recovered patient yielded a single-therapeutic antibody treatment (6).

In this work, we describe parallel high-throughput efforts using both mice and humans to generate antibodies against the spike protein of severe acute respiratory syndrome coronavirus 2 (SARS-CoV-2). The ability to derive antibodies using genetically humanized VI mice as well as B cells derived from convalescent patients enabled us to isolate a very large collection of fully human antibodies with diverse sequences, binding properties, and antiviral activities. The prospective goal of these parallel efforts was to generate a large and diverse collection so as to allow for the selection of pairs of highly potent individual antibodies that could simultaneously bind the critical receptor binding domain (RBD) of the spike protein, thereby providing ideal partners for a therapeutic antibody cocktail that would have the potential to decrease the likelihood of virus escape mutants that might arise in response to selective pressure from single-antibody treatments (7).

Anti-SARS-CoV-2 spike antibodies were generated with the following two methods. First, VI mice were immunized with a DNA plasmid that expresses SARS-CoV-2 spike protein and then were boosted with a recombinant

protein composed of the RBD of SARS-CoV-2 spike. Second, antibodies were isolated from peripheral blood mononuclear cells (PBMCs) of human donors previously infected with SARS-CoV-2. VI mice elicited a robust immune response against the SARS-CoV-2 spike protein after immunization. Titers of mice blood collected 7 days after the last boost were determined by enzyme-linked immunosorbent assay (ELISA) (fig. S1). Mice with the highest titers were used for antibody isolation. Spleens from these mice were subjected to biotin-labeled monomeric RBD antigen staining and fluorescence-activated single-cell sorting. In parallel, whole blood was collected from three patients 3 to 4 weeks after a laboratory-confirmed polymerase chain reaction (PCR) positive test for SARS-CoV-2 and after showing symptoms of COVID-19. PBMCs were isolated by ficoll gradient and RBD-specific B cells were fluorescence-activated single-cell sorted. The first sets of antibodies derived from these platforms are described here.

To assess antigen-specific responses, naturally paired heavy and light chain cDNAs were cloned from the mice and human-derived B cells (8) and transfected into Chinese hamster ovary (CHO) cells to produce recombinant fully human antibodies. Cultured supernatants containing secreted antibodies were subjected to high-throughput screening for RBD protein binding. Thousands of antibodies were isolated and subsequently screened for binding affinity to RBD monomer and dimer, epitope diversity, ability to block angiotensin-converting enzyme 2 (ACE2) receptor binding to RBD, and ability to neutralize vesicular stomatitis virus (VSV)-based SARS-CoV-2 spike pseudoparticles [pVSV-SARS-CoV-2-S(mNeon)]. Screening yielded >200 neutralizing monoclonal antibodies (mAbs) with broad potency ranges, dozens of which displayed neutralization potency in the picomolar range.

More than 200 of the VI mouse and human-derived antibodies isolated in the primary screen neutralized VSV-based SARS-CoV-2 spike pseudoparticles at >70% with ~2 µg/ml of expressed antibodies. The antibody variable regions were sequenced by next-generation sequencing, and the repertoire for heavy and light chain pairs was identified (Fig. 1). The predominant lineage of VI mouse antibodies utilized VH3-53 paired with VK1-9, VK1-33, or VK1-39, whereas our human-derived antibodies utilized VH3-66 paired with VK1-33 or VH2-70 paired with VK1-39. Notably, VH3-53 usage has recently been reported for another human-derived potent neutralizing antibody against SARS-CoV-2 spike protein (9–11), which indicates that combining the VI mouse approach with the human platforms allows the expanded capture of common rearrangements found in potent neutralizing SARS-CoV-2 mAbs seen in humans. Further analysis

<sup>1</sup>Regeneron Pharmaceuticals, Inc., Tarrytown, NY 10591, USA.

<sup>2</sup>National Centre for Infectious Diseases, Tan Tock Seng Hospital, Yong Loo Lin School of Medicine, Lee Kong Chian School of Medicine, 16 Jalan Tan Tock Seng, Singapore 308442, Singapore.

<sup>3</sup>Department of Microbiology and Immunology, University of Maryland School of Medicine, Baltimore, MD 21201, USA.

\*These authors contributed equally to this work.

†Corresponding author. Email: christos.kyrtatsous@regeneron.com

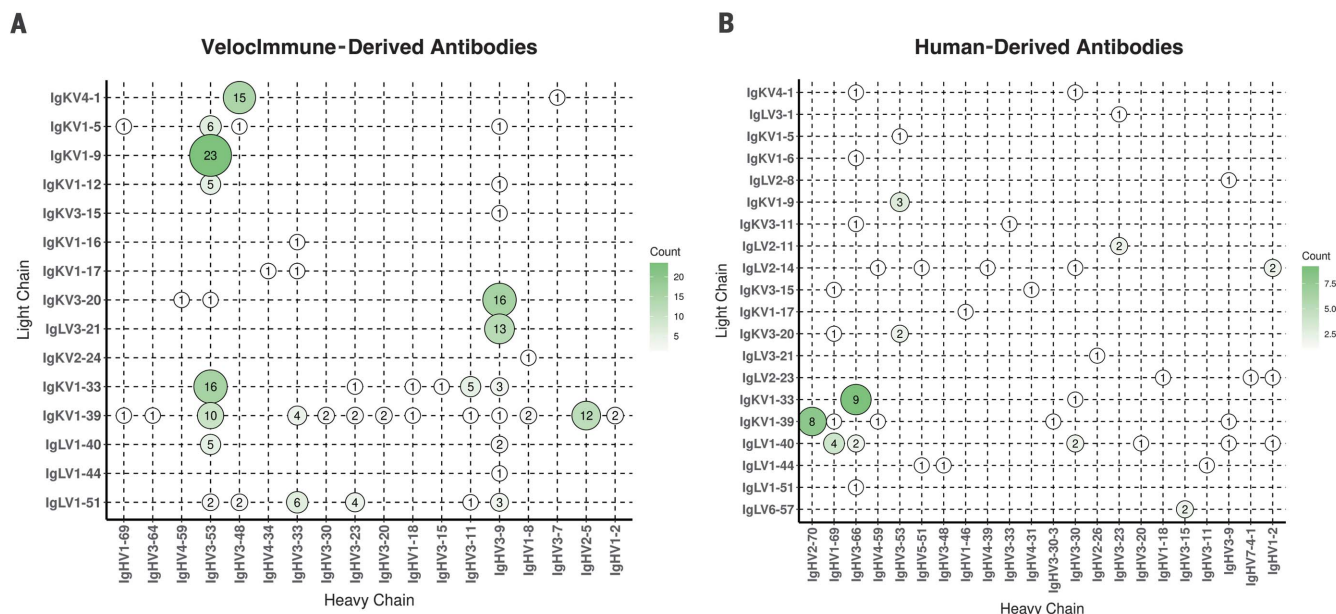


**Fig. 1. Paired antibody repertoire for human- and mouse-derived SARS-CoV-2 neutralizing antibodies.** (A and B) Variable (V) gene frequencies for paired heavy (x axes) and light (y axes) chains of isolated neutralizing antibodies to SARS-CoV-2 for VI mice (A) ( $N = 185$ ) and convalescent human donors (B) ( $N = 68$ ). The color and size of the circles correspond to the number of heavy and light chain pairs present in the repertoires of isolated neutralizing antibodies. Neutralization is defined as  $>70\%$  with 1:4 dilution of antibody ( $\sim 2 \mu\text{g/ml}$ ) in VSV-based pseudoparticle neutralization assay.

of overlaid sequences (fig. S2) showed strong overlap in the repertoire of isolated kappa chains between VI mouse and human-derived antibodies. Although the repertoire of lambda chains did not overlap well, that may be because only two lambda mice were included in this trial. The average complementarity-determining region (CDR) lengths (fig. S2D) for heavy chains was similar between VI mouse and human-derived antibodies, with average lengths of 13 and 14.5 amino acids, respectively. The average kappa CDR length (fig. S2E) was the same for VI mouse and human-derived antibodies at 9 amino acids, and the lengths were similar for lambda chains (fig. S2F), with an average length of 11.1 and 10.6 amino acids, respectively.

Approximately 40 antibodies with distinct sequences and potent neutralization activities were chosen for additional characterization, as described below. The neutralization potency of these mAbs spanned the single-digit to triple-digit picomolar range in the VSV-based pseudoparticle assay. Antibodies shown to cross-neutralize SARS-CoV-1 and SARS-CoV-2 spike proteins were weakly neutralizing (12). So instead of focusing on cross-neutralizers, we focused on nine of the most potent neutralizing mAbs, with neutralization potencies ranging from 7 to 99 pM (Fig. 2A and table S1). All of these neutralizing mAbs bound to the RBD of SARS-CoV-2 spike and blocked its ability to interact with ACE2 with double-digit picomolar median inhibitory concentrations ( $\text{IC}_{50}\text{s}$ ) (table S1), which supports ACE2 blockade as the primary mechanism for neutraliza-

tion. The antibodies bound specifically and with high affinity to monomeric SARS-CoV-2 RBD [dissociation constant ( $K_d$ ) = 0.56 to 45.2 nM] and dimeric SARS-CoV-2 RBD ( $K_d$  = 5.7 to 42.8 pM). Because recombinant ACE2 receptor is being considered as a COVID-19 therapeutic (13), we tested the potency of recombinant dimeric human ACE2-Fc (hACE2-hFc) in our neutralization assay. Although recombinant ACE2 was able to mediate neutralization of the VSV-based spike pseudoparticles as previously reported, its potency was reduced by more than a factor of 1000 compared with that of the best neutralizing mAbs (Fig. 2, A and B).

A smaller collection of four antibodies was chosen for further analyses to determine whether the above binding data to RBD reflected binding to trimeric spike protein, whether neutralization potencies noted in the above assays were consistent with those seen in other assays including with SARS-CoV-2, and whether these antibodies retained neutralization activity against pseudoparticles with mutations in the S1-S2 cleavage site. The binding affinity of these four antibodies against trimeric SARS-CoV-2 spike ( $K_d$  = 37.1 to 42.8 pM) largely paralleled the affinity against the RBD (table S3). Additionally, the potent neutralizing activity of these four antibodies was confirmed in the additional neutralization assays, including neutralization of pVSV-SARS-CoV-2-S (mNeon) in the human lung epithelial Calu-3 cell line, neutralization of replicating VSV-SARS-CoV-2-S in Vero cells, and neutraliza-

tion of SARS-CoV-2 in VeroE6 cells (Fig. 2, B to D). All neutralization assays generated similar potency across the four mAbs, and no combinations demonstrated synergistic neutralization activity (Fig. 2, C and D). As previous studies indicate pseudoparticles containing the SARS-CoV-2 spike are precleaved by furin-like proteases at the polybasic S1-S2 cleavage site during biogenesis in HEK293T cells, we assessed the impact of this cleavage on mAb neutralization potency. Spike-stabilized pseudoparticles (fig. S3A) with a monobasic cleavage site (FurMut) in the S1-S2 interface or deleted region (FurKO) were produced as previously described (14, 15). No differences were observed in neutralization of either FurMut- or FurKO-containing pseudoparticles relative to wild-type (WT) in Vero cells (fig. S3B). Notably, stabilized pseudoparticles had comparable or greater infectivity to those with WT cleavage sites in Vero cells, whereas substantial loss of infectivity was observed in Calu-3 cells (fig. S3C). Authentic SARS-CoV-2 with a natural deletion of the S1-S2 junction also had defects in infectivity in Calu-3 but not in Vero cells (16), which implicates differential protease usage between these two cell types. To investigate the mechanism of neutralization, we generated antigen-binding fragments (Fabs) for the four antibodies. We compared immunoglobulin G (IgG) with corresponding Fabs side by side for their ability to neutralize pseudotyped VSV (fig. S4). The  $\text{IC}_{50}\text{s}$  of all the Fabs were shifted compared with those of their parental IgGs, which indicates that bivalent



binding, cross-linking, and steric hindrance might all augment neutralization.

Although the role of antibody effector function in protection against SARS-CoV-2 is yet unknown, it has been well established that it plays an important role in mAb therapeutic efficacy against other viruses such as Ebola and influenza viruses (17–19). Effector cells including macrophages and monocytes have also been shown to be important for antibody-mediated protection from SARS-CoV-1 infection (20). To understand whether our lead antibodies are capable of mediating effector function, we assessed both antibody-dependent cellular cytotoxicity (ADCC) and antibody-dependent cellular phagocytosis (ADCP) activity in primary human cell bioassays utilizing natural killer (NK) cells and monocyte-derived phagocytes. All four lead antibodies demonstrated the ability to mediate ADCC and ADCP, albeit to slightly different degrees. REGN10987 displayed superior ability to mediate ADCC relative to the other three mAbs, whereas it performed similarly to REGN10989 and REGN10933

in the ADCP assay (fig. S5 and table S3). Although REGN10934 was able to mediate both ADCC and ADCP, it was not as strong of an inducer in those assays as the other three mAbs (fig. S6 and table S4). Further identification of mAb epitopes through high-resolution structural analysis may help illuminate the relationship between specific epitopes and effector function of anti-spike mAbs.

A prospective goal of our effort was to identify highly potent individual antibodies that could be paired in a therapeutic antibody cocktail, aiming to decrease the potential for decreased efficacy caused by variants arising as the pandemic spreads or by virus escape mutants that might be selected for in response to pressure from a single-antibody treatment (7). Thus, we examined our nine most-potent neutralizing antibodies in cross-competition binding assays (fig. S7) and identified several pairs of noncompeting mAbs with picomolar neutralization potency that could potentially be combined to form antibody cocktails. To further study the binding regions of our mAbs on

spike protein RBD, we performed hydrogen-deuterium exchange mass spectrometry (HDX-MS) with the same nine antibodies (Fig. 3), which revealed where each of the antibodies contacts the surface of the RBD and allowed comparison with the ACE2 binding site on the RBD (Fig. 3). As might be expected, most of our neutralizing antibodies contact the RBD in a manner that overlaps the RBD residues that comprise the ACE2 interface; furthermore, the antibodies can be grouped on the basis of their pattern of contacting the RBD surface. Comparing the cross-competition binding assays with the HDX-MS results provides structural insights into the mechanism by which noncompeting pairs of antibodies can simultaneously bind the RBD and can thus be ideal partners for a therapeutic antibody cocktail. REGN10987 and REGN10933 represent such a pair of antibodies: REGN10933 targets the spike-like loop region on one edge of the ACE2 interface. Within that region, the residues that show the most notable HDX protection by REGN10933 face upward, which suggests that

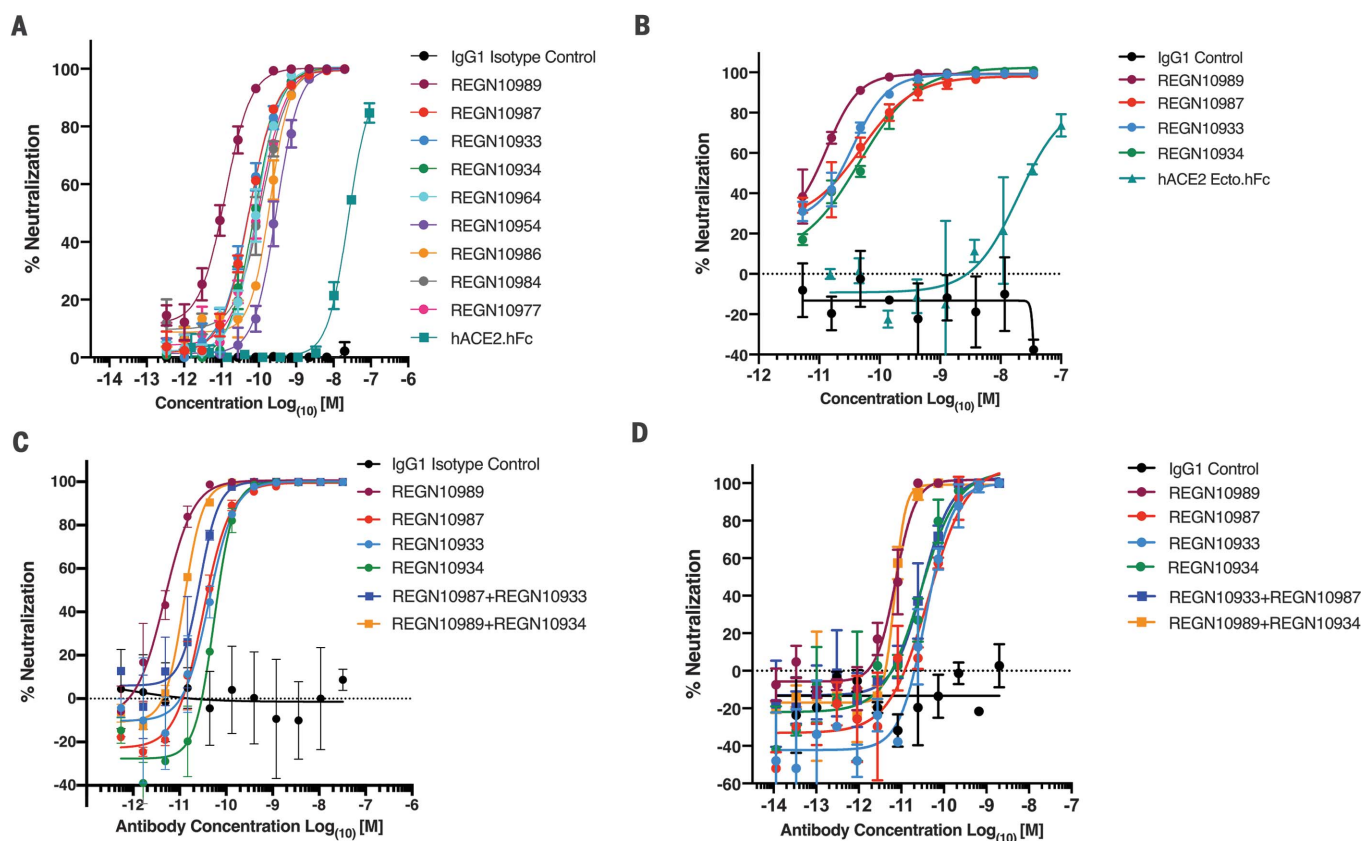


**Fig. 2. Neutralization potency of anti-SARS-CoV-2 spike mAbs.** (A) Serial dilutions of anti-spike mAbs, IgG1 isotype control, and recombinant dimeric ACE2 (hACE2.hFc) were added with pVSV-SARS-CoV-2-S(mNeon) to Vero cells, and mNeon expression was measured 24 hours after infection as a readout for virus infectivity. Data are graphed as percent neutralization relative to virus-only infection control. (B) Neutralization potency of anti-spike mAbs, recombinant dimeric ACE2, and IgG1 isotype control against nonreplicating

pVSV-SARS-CoV-2-S(mNeon) in Calu-3 cells. (C) Neutralization potency of individual anti-spike mAbs and combinations of mAbs against replicating VSV-SARS-CoV-2-S virus in Vero cells. Cells were infected with a multiplicity of infection (MOI) 1 of the virus and stained for viral protein 24 hours after infection to measure infectivity. (D) Neutralization potency of individual anti-spike mAbs and combinations of mAbs against SARS-CoV-2-S virus in VeroE6 cells.

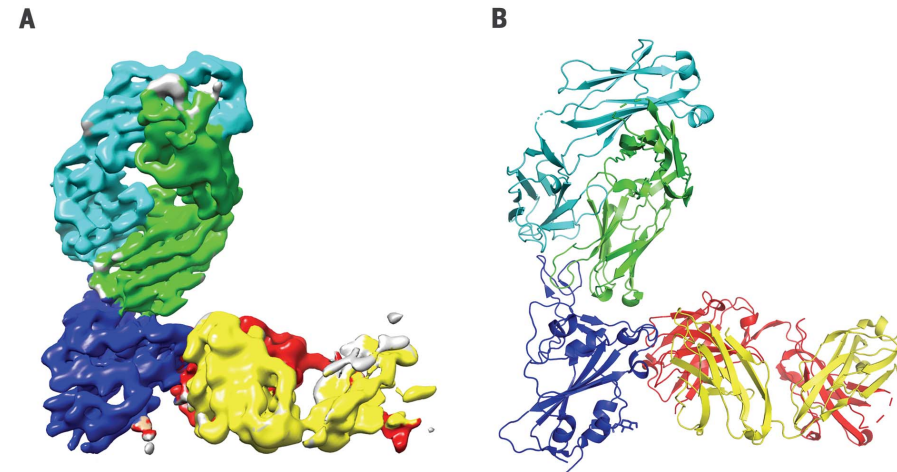
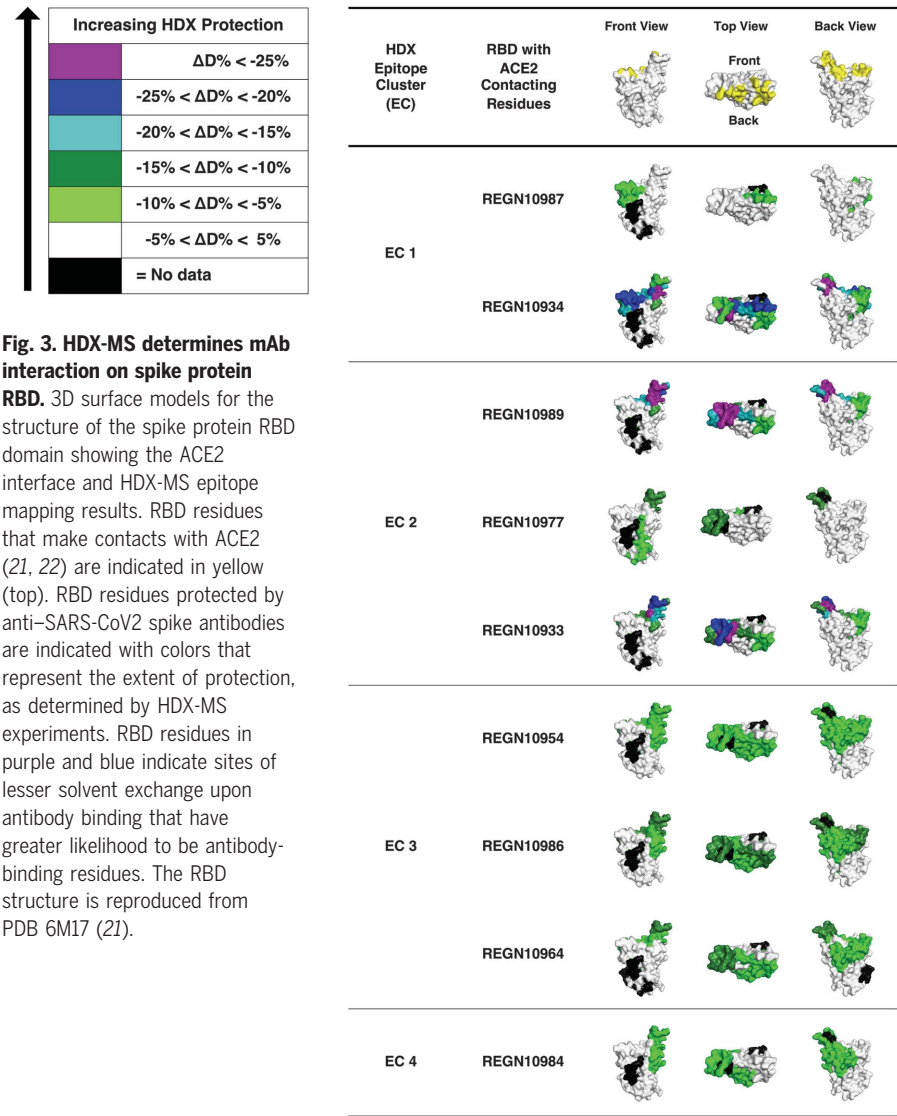


**Fig. 4. Complex of REGN10933 and REGN10987 with the SARS-CoV-2 RBD.** (A) 3.9-Å cryo-EM map of the REGN10933-RBD-REGN10987 complex, colored according to the chains in the refined model (B). RBD is colored dark blue; REGN10933 heavy and light chains are green and cyan, respectively; and REGN10987 heavy and light chains are yellow and red, respectively.

the Fab region of REGN10933 binds the RBD from the top direction, where REGN10933 will have collisions with ACE2. To avoid competition with REGN10933, REGN10987 can only bind to the HDX-defined protected regions from the front or the lower left side (in the front view of REGN10987 in Fig. 3). This would be consistent with the neutralization data, as REGN10987 would orient itself in a position that has high probability to interfere with ACE2. Confirming the above data, single-particle cryo-electron microscopy (cryo-EM) of the complex of SARS-CoV-2 spike RBD bound to Fab fragments of REGN10933 and REGN10987 shows that the two antibodies in this cocktail can simultaneously bind to distinct regions of the RBD (Fig. 4 and table S5). A three-dimensional (3D) reconstructed map of the complex with nominal resolution of 3.9 Å shows that the two Fab fragments bind at different epitopes on the RBD, which confirms that they are noncompeting antibodies. REGN10933 binds at the top of the RBD, extensively overlapping the binding site for ACE2. On the other hand, the epitope for REGN10987 is located on the side of the RBD, away from the REGN10933 epitope, and has little to no overlap with the ACE2 binding site.

We report notable similarities and consistencies in the antibodies generated from genetically humanized mice and from convalescent humans. The scale of the genetic-engineering approach used to create the VI mouse (involving genetic-humanization of more than 6 Mb of mouse immune genes) has resulted in the ability to effectively and indistinguishably mimic the antibody responses of normal humans. The genetically humanized-mouse approach has the advantages that it can potentially allow for further immunization optimization strategies and that it can be applied to noninfectious disease targets. By combining the efforts from two parallel and high-throughput approaches for generating antibodies to the RBD of the SARS-CoV-2 spike protein, we generated a sufficiently large collection of potent and diverse antibodies that we could meet our prospective goal of identifying highly potent individual antibodies that could be combined into a therapeutic antibody cocktail. Inclusion of such antibodies into an antibody cocktail may deliver optimal antiviral potency while minimizing the odds of virus escape (7)—two critical, desired features of an antibody-based therapeutic for treatment and prevention of COVID-19. Such an antibody cocktail is now being tested in human trials (clinicaltrials.gov NCT04426695 and NCT04425629).

REFERENCES AND NOTES

1. F. W. Alt, T. K. Blackwell, G. D. Yancopoulos, *Trends Genet.* **1**, 231–236 (1985).  
2. J. Larkin et al., *N. Engl. J. Med.* **373**, 23–34 (2015).  
3. A. J. Murphy et al., *Proc. Natl. Acad. Sci. U.S.A.* **111**, 5153–5158 (2014).



4. L. E. Macdonald *et al.*, *Proc. Natl. Acad. Sci. U.S.A.* **111**, 5147–5152 (2014).
5. K. E. Pascal *et al.*, *J. Infect. Dis.* **218**, S612–S626 (2018).
6. D. Corti *et al.*, *Science* **351**, 1339–1342 (2016).
7. A. Baum *et al.*, *Science* **369**, 1014–1018 (2020).
8. X. Wang, B. D. Stollar, *J. Immunol. Methods* **244**, 217–225 (2000).
9. Y. Cao *et al.*, *Cell* **182**, 73–84.E16 (2020).
10. Y. Wu *et al.*, *Science* **368**, 1274–1278 (2020).
11. T. F. Rogers *et al.*, *Science* **369**, 956–963 (2020).
12. M. Yuan *et al.*, *Science* **368**, 630–633 (2020).
13. C. Lei *et al.*, *Nat. Commun.* **11**, 2070 (2020).
14. A. C. Walls *et al.*, *Cell* **181**, 281–292.e6 (2020).
15. D. Wrapp *et al.*, *Science* **367**, 1260–1263 (2020).
16. S. Y. Lau *et al.*, *Emerg. Microbes Infect.* **9**, 837–842 (2020).
17. D. J. DiLillo, P. Palese, P. C. Wilson, J. V. Ravetch, *J. Clin. Invest.* **126**, 605–610 (2016).
18. E. O. Saphire, S. L. Schendel, B. M. Gunn, J. C. Milligan, G. Alter, *Nat. Immunol.* **19**, 1169–1178 (2018).
19. E. O. Saphire *et al.*, *Cell* **174**, 938–952.e13 (2018).
20. F. Yasui *et al.*, *Virology* **454–455**, 157–168 (2014).
21. R. Yan *et al.*, *Science* **367**, 1444–1448 (2020).
22. J. Lan *et al.*, *Nature* **581**, 215–220 (2020).

## ACKNOWLEDGMENTS

The authors thank K. Tramaglino for program management.  
**Funding:** A portion of this project has been funded in whole

or in part with federal funds from the U.S. Department of Health and Human Services, Office of the Assistant Secretary for Preparedness and Response, Biomedical Advanced Research and Development Authority, under OT number HHS0100201700020C.

**Author contributions:** J.H., A.B., B.O.F., A.H., E.U., A.R., T.H., J.F., P.B., R.B., B.Z., M.Fra., A.J.M., N.S., G.D.Y., and C.A.K. conceptualized and designed experiments. J.H., K.E.P., V.R., S.G., E.W., B.O.F., Y.Y., K.K., K.P., K.M.C., E.U., J.Ch., A.R., C.L., M.M., W.-y.L., R.W., S.P., J.Cr., B.Z., A.R.H., K.S., Y.Z., M.Fra., S.W., J.L., R.H., and M.Fri. performed research. J.H., K.E.P., V.R., S.G., E.W., B.O.F., Y.Y., K.K., K.P., K.M.C., E.U., J.Ch., A.R., J.F., C.L., M.M., W.-y.L., G.F., D.D., J.Cr., P.B., R.B., N.L., C.C., B.Z., A.R.H., K.S., Y.Z., M.Fra., S.W., J.L., R.H., M.Fri., G.C., W.O., N.S., G.D.Y., and C.A.K. analyzed data. S.S. and D.C.L. acquired reagents. J.H., A.B., A.R., B.Z., M.Fra., G.D.Y., and C.A.K. wrote the paper. C.A.K. acquired funding. **Competing interests:** Regeneron authors own options and/or stock of the company. This work has been described in one or more pending provisional patent applications. G.C., W.O., A.J.M., N.S., G.D.Y., and C.A.K. are officers of Regeneron. **Data and materials availability:** The structure of SARS-CoV-2 RBD in complex with REGN10933 and REGN10987 Fabs has been deposited in the Protein Data Bank, with PDB ID 6XDG. The corresponding cryo-EM map is available in the Electron Microscopy Data Bank, with ID EMD-22137. Sequences of the nine characterized antibodies have been deposited in GenBank and are available in the supplementary materials. Regeneron materials described in this manuscript may be made available to qualified, academic, noncommercial researchers

through a materials transfer agreement upon request at [https://regeneron.envisionpharma.com/vt\\_regeneron/](https://regeneron.envisionpharma.com/vt_regeneron/). For questions about how Regeneron shares materials, use the email address [preclinical.collaborations@regeneron.com](mailto:preclinical.collaborations@regeneron.com). This work is licensed under a Creative Commons Attribution 4.0 International (CC BY 4.0) license, which permits unrestricted use, distribution, and reproduction in any medium, provided the original work is properly cited. To view a copy of this license, visit <https://creativecommons.org/licenses/by/4.0/>. This license does not apply to figures/photos/artwork or other content included in the article that is credited to a third party; obtain authorization from the rights holder before using such material.

## SUPPLEMENTARY MATERIALS

[science.sciencemag.org/content/369/6506/1010/suppl/DC1](https://science.sciencemag.org/content/369/6506/1010/suppl/DC1)  
 Materials and Methods  
 Figs. S1 to S7  
 Tables S1 to S5  
 References (23–33)  
 MDAR Reproducibility Checklist  
 Data S1

[View/request a protocol for this paper from Bio-protocol.](#)

30 May 2020; accepted 11 June 2020  
 Published online 15 June 2020  
 10.1126/science.abd0827

## CORONAVIRUS

# Antibody cocktail to SARS-CoV-2 spike protein prevents rapid mutational escape seen with individual antibodies

Alina Baum, Benjamin O. Fulton, Elzbieta Wloga, Richard Copin, Kristen E. Pascal, Vincenzo Russo, Stephanie Giordano, Kathryn Lanza, Nicole Negron, Min Ni, Yi Wei, Gurinder S. Atwal, Andrew J. Murphy, Neil Stahl, George D. Yancopoulos, Christos A. Kyratsous\*

Antibodies targeting the spike protein of severe acute respiratory syndrome coronavirus 2 (SARS-CoV-2) present a promising approach to combat the coronavirus disease 2019 (COVID-19) pandemic; however, concerns remain that mutations can yield antibody resistance. We investigated the development of resistance against four antibodies to the spike protein that potently neutralize SARS-CoV-2, individually as well as when combined into cocktails. These antibodies remain effective against spike variants that have arisen in the human population. However, novel spike mutants rapidly appeared after *in vitro* passaging in the presence of individual antibodies, resulting in loss of neutralization; such escape also occurred with combinations of antibodies binding diverse but overlapping regions of the spike protein. Escape mutants were not generated after treatment with a noncompeting antibody cocktail.

**O**ne promising approach to combat the coronavirus disease 2019 (COVID-19) pandemic involves development of antiviral antibodies targeting the spike protein of severe acute respiratory syndrome coronavirus 2 (SARS-CoV-2). The spike protein is a key mediator of viral infectivity required for attachment and entry into target cells, which is achieved by binding the ACE2 receptor (1, 2). A concern for any antiviral therapeutic is the potential for acquiring drug resistance due to the rapid mutation of viral pathogens. Such resistance becomes more obvious when selective pressure is applied in the setting of drug treatment. For example, when HIV drugs were initially used individually, such drug-selected mutations resulted in widespread resistance. The subsequent success of combination therapy for HIV demonstrated that requiring the virus to simultaneously mutate at multiple genetic positions may be the most effective way to avoid drug resistance.

We recently described parallel efforts, using genetically humanized mice and B cells from convalescent humans, to generate a very large collection of highly potent, fully human neutralizing antibodies targeting the receptor-binding domain (RBD) of the spike protein of SARS-CoV-2 (3). The prospective goal of generating this very large collection was to select pairs of highly potent individual antibodies that could simultaneously bind the RBD spike, and thus might be ideal partners for a therapeutic antibody cocktail that not only could be an effective treatment, but might also protect against antibody resistance resulting from virus escape mutants that could arise

in response to selective pressure from single-antibody treatments.

To assess the efficacy of our recently described antiviral antibodies against the breadth of spike RBD variants represented in publicly available SARS-CoV-2 sequences identified through the end of March 2020 (representing more than 7000 unique genomes), we used the VSV pseudoparticle system expressing the SARS-CoV-2 spike variants. Our top eight neutralizing antibodies maintained their potency against all tested variants (Table 1), demonstrating broad coverage against circulating SARS-CoV-2.

Next, escape mutants were selected under pressure of single antibodies, as well as of antibody combinations, by using a replicating VSV-SARS-CoV-2-S virus (Fig. 1A). We rapidly identified multiple independent escape mutants for each of the four individual antibodies within the first passage (Fig. 1, B and C, and Fig. 2). Some of these mutants became readily fixed in the population by the second passage, representing 100% of sequencing reads, and are resistant to antibody concentrations of up to 50  $\mu\text{g/ml}$  [a factor of  $\sim 10,000$  to  $100,000$  greater concentration than half-maximal inhibitory concentration ( $\text{IC}_{50}$ ) against parental virus]. Sequencing of escape mutants (Fig. 2) revealed that single amino acid changes can ablate binding even to antibodies that were selected for breadth against all known RBD variants (Table 1) and that neutralize parental virus at  $\text{IC}_{50}$  values in the low picomolar range (3).

Analysis of 22,872 publicly available unique genome sequences (through the end of May 2020) demonstrated the presence of polymorphisms analogous to two of the escape amino acid residues identified in our study, albeit at an extremely low frequency of one each. Thus, although natural variants resist-

ant to individual antiviral antibodies were not widely observed in nature, these rare escape variants could easily be selected and amplified under the pressure of ongoing antibody treatment. These studies were conducted with a surrogate virus *in vitro*; one would expect that similar escape mutations may occur with SARS-CoV-2 virus *in vivo* under the selective pressure of single-antibody treatment. The differential propensity of VSV and SARS-CoV-2 viruses to acquire mutations may affect the speed at which these escape mutants may arise; however, the likelihood of eventual escape remains high.

Next, we evaluated escape after treatment with our previously described antibody cocktail (REGN10987+REGN10933), which was rationally designed to avoid escape through inclusion of two antibodies that bind distinct and non-overlapping regions of the RBD, and thus can simultaneously bind and block RBD function. Attempts to grow VSV-SARS-CoV-2-S virus in the presence of this antibody cocktail did not result in the outgrowth of escape mutants (Table 2, Fig. 1, B and C, and Fig. 2). Thus, this selected cocktail did not rapidly select for mutants, presumably because escape would require the unlikely occurrence of simultaneous viral mutation at two distinct genetic sites, so as to ablate binding and neutralization by both antibodies in the cocktail.

In addition to the above cocktail, we also evaluated escape after treatment with additional combinations (REGN10989+REGN10934 and REGN10989+REGN10987), this time consisting of antibodies that completely or partially compete for binding to the RBD—that is, two antibodies that bind to overlapping regions of the RBD. Under selective pressure of these combination treatments, we observed rapid generation of escape mutants resistant to one combination but not the other (Table 2, Fig. 1, B and C, and Fig. 2). For an antibody cocktail in which the components demonstrate complete competition (REGN10989+REGN10934), a single amino acid substitution was sufficient to ablate neutralization of the cocktail; hence, both of these antibodies require binding to the Glu<sup>484</sup> residue in order to neutralize SARS-CoV-2. Interestingly, such rapid escape did not occur for a different antibody cocktail in which the components exhibited only partial competition (REGN10989+REGN10987) (3); REGN10987 can weakly bind to RBD when REGN10989 is prebound. Thus, even a combination of antibodies that are not selected to simultaneously bind may occasionally resist escape because their epitopes only partially overlap, or because residues that would result in escape are not easily tolerated by the virus and are therefore not readily selected for.

To functionally confirm that the spike protein mutations detected by sequencing are responsible for the loss of SARS-CoV-2 neutralization by the antibodies, we generated



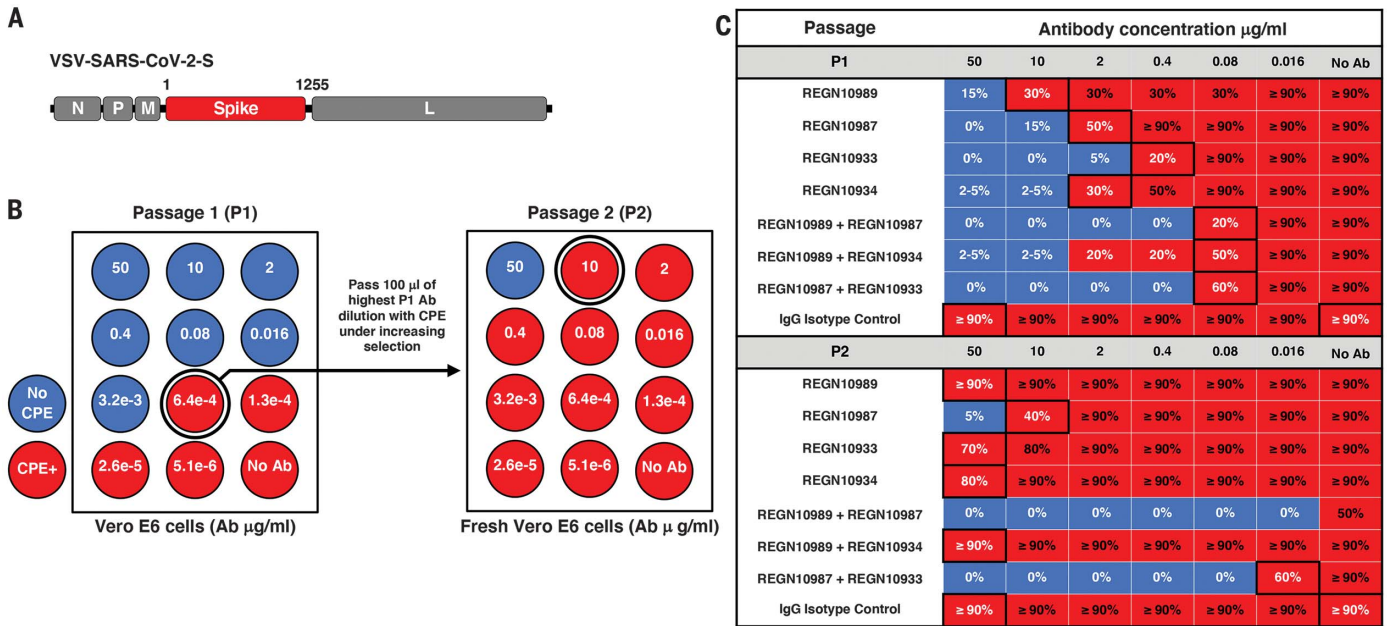


**Fig. 1. Escape mutant screening protocol.** (A) Schematic of the VSV-SARS-CoV-2-S virus genome encoding residues 1 to 1255 of the spike protein in place of the VSV glycoprotein. N, nucleoprotein; P, phosphoprotein; M, matrix; L, large polymerase. (B) A total of  $1.5 \times 10^6$  plaque-forming units (pfu) of the parental VSV-SARS-CoV-2-S virus was passed in the presence of antibody dilutions for 4 days on Vero E6 cells. Cells were screened for virus replication by monitoring for virally induced cytopathic effect (CPE). Supernatants and cellular RNAs were collected from wells under the greatest antibody selection with detectable viral replication (circled wells;  $\geq 20\%$  CPE). For a second round of selection,

100 µl of the P1 supernatant was expanded for 4 days under increasing antibody selection in fresh Vero E6 cells. RNA was collected from the well with the highest antibody concentration with detectable viral replication. The RNA was deep-sequenced from both passages to determine the selection of mutations resulting in antibody escape. (C) The passaging results of the escape study are shown with the qualitative percentage of CPE observed in each dilution (red,  $\geq 20\%$  CPE; blue,  $<20\%$  CPE). Black-bordered boxes indicate dilutions that were passaged and sequenced in P1 or sequenced in P2. A no-antibody control was sequenced from each passage to monitor for tissue culture adaptations.

Anti-SARS-CoV-2 spike mAbs demonstrate broad neutralization across SARS-CoV-2 spike RBD variants								
Eight anti-spike antibodies were tested against 16 SARS-CoV-2 spike protein RBD variants identified from viral sequences circulating through the end of March 2020. The listed variants were encoded into pVSV-SARS-CoV-2-S (mNeon) pseudoparticles, and neutralization assays were performed in Vero cells. IC <sub>50</sub> (M) values are shown for each variant. For all variants, no neutralization was observed with hlgG1 isotype control. Amino acid abbreviations: A, Ala; D, Asp; E, Glu; F, Phe; G, Gly; H, His; I, Ile; K, Lys; L, Leu; N, Asn; P, Pro; Q, Gln; R, Arg; S, Ser; T, Thr; V, Val; Y, Tyr.								
Variants	REGN10989	REGN10987	REGN10933	REGN10934	REGN10964	REGN10954	REGN10984	REGN10986
Wild-type	7.23 × 10 <sup>-12</sup>	4.06 × 10 <sup>-11</sup>	4.28 × 10 <sup>-11</sup>	5.44 × 10 <sup>-11</sup>	5.70 × 10 <sup>-11</sup>	9.22 × 10 <sup>-11</sup>	9.73 × 10 <sup>-11</sup>	9.91 × 10 <sup>-11</sup>
Q321L	1.46 × 10 <sup>-11</sup>	5.02 × 10 <sup>-11</sup>	6.85 × 10 <sup>-11</sup>	6.84 × 10 <sup>-11</sup>	5.65 × 10 <sup>-11</sup>	2.32 × 10 <sup>-10</sup>	2.75 × 10 <sup>-10</sup>	2.06 × 10 <sup>-10</sup>
V341I	1.61 × 10 <sup>-11</sup>	3.38 × 10 <sup>-11</sup>	3.37 × 10 <sup>-11</sup>	7.42 × 10 <sup>-11</sup>	1.13 × 10 <sup>-10</sup>	2.52 × 10 <sup>-10</sup>	2.49 × 10 <sup>-10</sup>	1.92 × 10 <sup>-10</sup>
A348T	7.33 × 10 <sup>-12</sup>	2.98 × 10 <sup>-11</sup>	4.13 × 10 <sup>-11</sup>	1.42 × 10 <sup>-10</sup>	3.52 × 10 <sup>-11</sup>	1.84 × 10 <sup>-10</sup>	2.01 × 10 <sup>-10</sup>	1.03 × 10 <sup>-10</sup>
N354D	1.14 × 10 <sup>-11</sup>	2.68 × 10 <sup>-11</sup>	5.89 × 10 <sup>-11</sup>	9.76 × 10 <sup>-11</sup>	1.93 × 10 <sup>-10</sup>	2.84 × 10 <sup>-10</sup>	2.64 × 10 <sup>-10</sup>	2.49 × 10 <sup>-10</sup>
S359N	4.30 × 10 <sup>-12</sup>	2.41 × 10 <sup>-11</sup>	2.12 × 10 <sup>-11</sup>	3.04 × 10 <sup>-11</sup>	6.83 × 10 <sup>-11</sup>	1.09 × 10 <sup>-10</sup>	1.23 × 10 <sup>-10</sup>	8.91 × 10 <sup>-11</sup>
V367F	1.33 × 10 <sup>-11</sup>	1.78 × 10 <sup>-11</sup>	2.40 × 10 <sup>-11</sup>	3.20 × 10 <sup>-11</sup>	8.92 × 10 <sup>-11</sup>	1.29 × 10 <sup>-10</sup>	1.53 × 10 <sup>-10</sup>	1.49 × 10 <sup>-10</sup>
K378R	1.21 × 10 <sup>-11</sup>	2.40 × 10 <sup>-11</sup>	3.52 × 10 <sup>-11</sup>	4.65 × 10 <sup>-11</sup>	6.19 × 10 <sup>-11</sup>	1.65 × 10 <sup>-10</sup>	1.88 × 10 <sup>-10</sup>	1.54 × 10 <sup>-10</sup>
R408I	1.09 × 10 <sup>-11</sup>	1.71 × 10 <sup>-11</sup>	1.98 × 10 <sup>-11</sup>	2.75 × 10 <sup>-11</sup>	4.96 × 10 <sup>-11</sup>	9.88 × 10 <sup>-11</sup>	1.35 × 10 <sup>-10</sup>	6.14 × 10 <sup>-11</sup>
Q409E	2.12 × 10 <sup>-11</sup>	4.06 × 10 <sup>-11</sup>	5.65 × 10 <sup>-11</sup>	5.94 × 10 <sup>-11</sup>	6.61 × 10 <sup>-11</sup>	2.64 × 10 <sup>-10</sup>	1.52 × 10 <sup>-10</sup>	1.95 × 10 <sup>-10</sup>
A435S	1.10 × 10 <sup>-11</sup>	3.88 × 10 <sup>-11</sup>	4.71 × 10 <sup>-11</sup>	8.07 × 10 <sup>-11</sup>	7.90 × 10 <sup>-11</sup>	2.11 × 10 <sup>-10</sup>	2.18 × 10 <sup>-10</sup>	1.51 × 10 <sup>-10</sup>
K458R	7.51 × 10 <sup>-12</sup>	1.68 × 10 <sup>-11</sup>	3.43 × 10 <sup>-11</sup>	3.46 × 10 <sup>-11</sup>	5.46 × 10 <sup>-11</sup>	1.45 × 10 <sup>-10</sup>	1.59 × 10 <sup>-10</sup>	1.00 × 10 <sup>-10</sup>
I472V	2.27 × 10 <sup>-11</sup>	4.18 × 10 <sup>-11</sup>	9.17 × 10 <sup>-11</sup>	9.40 × 10 <sup>-11</sup>	1.01 × 10 <sup>-10</sup>	3.44 × 10 <sup>-10</sup>	2.61 × 10 <sup>-10</sup>	2.24 × 10 <sup>-10</sup>
G476S	6.80 × 10 <sup>-12</sup>	1.86 × 10 <sup>-11</sup>	1.41 × 10 <sup>-10</sup>	3.51 × 10 <sup>-11</sup>	3.42 × 10 <sup>-11</sup>	1.83 × 10 <sup>-10</sup>	2.10 × 10 <sup>-10</sup>	1.13 × 10 <sup>-10</sup>
V483A	8.78 × 10 <sup>-12</sup>	2.60 × 10 <sup>-11</sup>	1.54 × 10 <sup>-11</sup>	4.43 × 10 <sup>-11</sup>	4.50 × 10 <sup>-11</sup>	1.12 × 10 <sup>-10</sup>	1.71 × 10 <sup>-10</sup>	9.70 × 10 <sup>-11</sup>
Y508H	1.71 × 10 <sup>-11</sup>	2.75 × 10 <sup>-11</sup>	4.77 × 10 <sup>-11</sup>	6.73 × 10 <sup>-11</sup>	1.02 × 10 <sup>-10</sup>	2.05 × 10 <sup>-10</sup>	2.83 × 10 <sup>-10</sup>	2.01 × 10 <sup>-10</sup>
H519P	4.51 × 10 <sup>-12</sup>	2.20 × 10 <sup>-11</sup>	3.03 × 10 <sup>-11</sup>	3.56 × 10 <sup>-11</sup>	4.45 × 10 <sup>-11</sup>	1.40 × 10 <sup>-10</sup>	1.08 × 10 <sup>-10</sup>	6.14 × 10 <sup>-11</sup>

Position in genome		3299	3312	3853	4326	4407	4411	4425	4435	4442	4527	4531	4533	4545	4546	4554	5040	5122	5130	5137	5383	5412	6460
Position in spike gene		222	235	776	1249	1330	1334	1348	1358	1365	1450	1454	1456	1468	1469	1477	1963	2045	2053	2060	2306	2335	3383
Reference nucleotide		T	T	C	A	A	T	A	A	G	G	G	T	T	T	C	C	G	C	T	G	C	T
Variant nucleotide		A	A	A	G	C	C	G	T	T	A	A	G	C	C	A	T	A	A	G	A	A	C
Position in protein		74	79	259	417	444	445	450	453	455	484	485	486	490	490	493	655	682	685	687	769	779	1128
Ref Residue		N	F	T	K	K	V	N	Y	L	E	G	F	F	F	Q	H	R	R	V	G	Q	V
Variant Residue		K	I	K	E	Q	A	D	F	F	K	D	V	L	S	K	Y	Q	S	G	E	K	A
P A S S A G E 1	Inoculum	0%	0%	0%	0%	0%	0%	0%	0%	0%	0%	0%	0%	0%	0%	0%	37%	16%	0%	1%	0%	0%	0%
	10933 0.4ug/ml	0%	0%	0%	12%	0%	0%	0%	29%	16%	0%	0%	11%	0%	0%	3%	51%	18%	0%	31%	11%	0%	0%
	10934 2ug/ml	0%	0%	0%	0%	3%	0%	34%	0%	0%	14%	0%	0%	0%	43%	0%	63%	43%	3%	0%	0%	0%	0%
	10987 2ug/ml	0%	0%	0%	0%	30%	36%	0%	0%	0%	0%	0%	0%	0%	0%	0%	54%	22%	29%	1%	0%	0%	0%
	10989 10ug/ml	0%	0%	0%	0%	0%	0%	0%	0%	0%	99%	0%	0%	0%	0%	0%	99%	2%	0%	0%	0%	15%	0%
	10989 0.08ug/ml	0%	0%	0%	0%	0%	0%	0%	0%	0%	25%	8%	0%	19%	14%	11%	67%	28%	0%	9%	0%	0%	0%
	10987/33 0.08ug/ml	0%	0%	0%	0%	0%	0%	0%	0%	0%	0%	0%	0%	0%	0%	0%	49%	26%	1%	3%	1%	0%	0%
	10989/34 0.08ug/ml	0%	0%	0%	0%	0%	0%	0%	0%	0%	51%	0%	0%	0%	22%	0%	76%	23%	0%	2%	0%	0%	0%
	10989/87 0.08ug/ml	0%	0%	0%	0%	0%	0%	0%	0%	0%	2%	0%	0%	0%	0%	0%	32%	27%	1%	3%	1%	0%	0%
	Isotype Control 50ug/ml	0%	0%	0%	0%	0%	0%	0%	0%	0%	0%	0%	0%	0%	0%	0%	61%	28%	0%	4%	0%	0%	0%
P A S S A G E 2	Virus Only	0%	0%	0%	0%	0%	0%	0%	0%	0%	0%	0%	0%	0%	0%	0%	64%	27%	0%	4%	0%	0%	0%
	10933 50ug/ml	0%	0%	0%	0%	0%	0%	0%	10%	0%	0%	0%	88%	0%	0%	0%	1%	90%	0%	15%	87%	0%	0%
	10934 50ug/ml	0%	0%	0%	0%	0%	0%	95%	0%	0%	6%	0%	0%	0%	1%	0%	10%	93%	0%	0%	0%	0%	0%
	10987 10ug/ml	0%	0%	0%	0%	45%	41%	0%	0%	0%	0%	0%	0%	0%	0%	0%	50%	6%	47%	0%	0%	0%	0%
	10989 50ug/ml	0%	0%	0%	0%	0%	0%	0%	0%	0%	100%	0%	0%	0%	0%	0%	100%	0%	0%	0%	0%	20%	0%
	10987/33 10ug/ml	ND	ND	ND	ND	ND	ND	ND	ND	ND	ND	ND	ND	ND	ND	ND	ND	ND	ND	ND	ND	ND	ND
	10989/34 50ug/ml	0%	0%	0%	0%	0%	0%	0%	0%	0%	100%	0%	0%	0%	0%	0%	93%	11%	0%	0%	0%	0%	0%
	10989/87 10ug/ml	ND	ND	ND	ND	ND	ND	ND	ND	ND	ND	ND	ND	ND	ND	ND	ND	ND	ND	ND	ND	ND	ND
	Isotype control 50ug/ml	16%	13%	10%	0%	0%	0%	0%	0%	0%	0%	0%	0%	0%	0%	0%	54%	50%	0%	8%	0%	0%	4%
Virus Only		8%	8%	22%	0%	0%	0%	0%	0%	0%	0%	0%	0%	0%	0%	0%	28%	83%	0%	7%	0%	0%	8%
		Frequency < 10%	Frequency 10% < x < 50%	Frequency > 50%																			

**Fig. 2. Deep sequencing of passaged virus identifies escape mutations.** VSV-SARS-CoV-2-S virus was mixed with anti-spike monoclonal antibodies (mAb), individually or in combination. Viral RNA from wells with the highest mAb concentration and detectable CPE on passage 1 or passage 2 (collected 4 days after infection) was isolated and RNA-seq analysis was performed to identify changes in spike protein sequence relative to input virus. For passage 2, viral RNA was isolated and sequenced from wells with high mAb concentrations (>10 µg/ml) with subsequently validated escape; if no validated escape was seen

at these high mAb concentrations and no virus was grown, ND indicates that no virus RNA was isolated. All mutated amino acid residues within the spike protein are shown. The specific condition (concentration in µg/ml) of the well that was selected for sequencing is shown in the left column (see Fig. 1 for outline of the experiment). Red boxes highlight residues that were mutated relative to input virus under each condition specified in the left column. Percentages of sequencing reads that contained the respective mutant sequence are identified. Residues mapping to the RBD are highlighted in blue.

VSV-SARS-CoV-2 spike pseudoparticles expressing the individual identified spike mutations. These pseudoparticles were used in neutralization assays with single- and multiple-antibody treatments, and IC<sub>50</sub> values were calculated (Table 2 and fig. S1). As expected, pseudoparticles with amino acid mutations that were selected by passaging the virus in the presence of the four single antibodies, as well as of the REGN10989 + REGN10934 competing antibody cocktail, were sufficient to completely eliminate or greatly decrease the ability of these treatments to neutralize in these assays. Single escape mutants that were detected at low frequency in early passages in virus populations generated by two antibodies [e.g., Lys<sup>444</sup> → Gln (K444Q) by both REGN10934 and REGN10987] but were fixed in the later passage by only one

of these antibodies (REGN10987) were able to ablate neutralization by both treatments. This suggests that antibodies can drive virus evolution and escape in different directions. However, if two antibodies have partially overlapping binding epitopes, then escape mutants fixed in the virus population by one can result in the loss of activity of the other; this highlights the risks of widespread use of single-antibody treatments. Notably, the REN10987 + REGN10933 antibody cocktail—which consists of two antibodies that can simultaneously bind to two independent epitopes on the RBD—retained its ability to neutralize all identified mutants, even those that were selected for by single treatment with one of its components. In our sequencing of passaged virus pools, we also identified multiple mutations outside of the RBD, most of which were present at

various abundances within control samples, including the original inoculum and virus-only passages (Fig. 2). The most abundant of these mutations [His<sup>655</sup> → Tyr (H655Y) and Arg<sup>682</sup> → Gln (R682Q)] are near the S1'/S2' cleavage site within the spike protein and contain residues within the multibasic furin-like cleavage site. Mutations and deletions in this region have been identified with tissue culture-passaged VSV-SARS-CoV-2-S as well as SARS-CoV-2 viruses and likely represent tissue culture adaptations (4, 5). Because RNA viruses are well known to accumulate mutations over time, a concern for any antiviral therapeutic is the potential for selection of treatment-induced escape mutants. A common strategy to safeguard against escape to antibody therapeutics involves selection of antibodies binding to conserved epitopes;



**Table 2. Neutralization potency of individual anti-spike antibodies and antibody combinations against pseudoparticles encoding individual escape mutants: IC<sub>50</sub> summary.** Escape mutations identified by RNA-seq analysis within the RDB domain were cloned and expressed on pseudoparticles to assess their impact on mAb neutralization potency. Boxes in boldface highlight conditions that resulted in a decrease in IC<sub>50</sub> of at least 1.5 log units relative to wild-type pseudoparticles or loss of neutralization. NC indicates that IC<sub>50</sub> could not be calculated because of poor neutralization ability. Reduction in IC<sub>50</sub> of less than 1 log unit can be seen in mAb combination conditions where one of the mAbs has no potency (e.g., K444Q and REGN10933/10987). See fig. S1 for full neutralization curves.

Anti-SARS-CoV-2 spike monoclonal antibodies							
Escape mutants	REGN10989	REGN10987	REGN10933	REGN10934	REGN10933/10987	REGN10989/10934	REGN10989/10987
Wild-type	7.27 × 10 <sup>-12</sup>	3.65 × 10 <sup>-11</sup>	5.57 × 10 <sup>-11</sup>	5.99 × 10 <sup>-11</sup>	3.28 × 10 <sup>-11</sup>	8.27 × 10 <sup>-12</sup>	1.22 × 10 <sup>-11</sup>
K417E	2.49 × 10 <sup>-11</sup>	3.10 × 10 <sup>-11</sup>	<b>8.33 × 10<sup>-9</sup></b>	2.70 × 10 <sup>-11</sup>	4.15 × 10 <sup>-11</sup>	2.64 × 10 <sup>-11</sup>	2.72 × 10 <sup>-11</sup>
K444Q	2.47 × 10 <sup>-11</sup>	NC	7.81 × 10 <sup>-11</sup>	<b>5.38 × 10<sup>-9</sup></b>	1.23 × 10 <sup>-10</sup>	4.19 × 10 <sup>-11</sup>	4.82 × 10 <sup>-11</sup>
V445A	2.65 × 10 <sup>-11</sup>	NC	8.82 × 10 <sup>-11</sup>	1.42 × 10 <sup>-10</sup>	1.54 × 10 <sup>-10</sup>	4.08 × 10 <sup>-11</sup>	5.74 × 10 <sup>-11</sup>
N450D	4.10 × 10 <sup>-11</sup>	<b>1.20 × 10<sup>-9</sup></b>	7.60 × 10 <sup>-11</sup>	NC	1.88 × 10 <sup>-10</sup>	6.04 × 10 <sup>-11</sup>	5.37 × 10 <sup>-11</sup>
Y453F	2.77 × 10 <sup>-11</sup>	1.04 × 10 <sup>-10</sup>	NC	2.17 × 10 <sup>-10</sup>	1.15 × 10 <sup>-10</sup>	3.52 × 10 <sup>-11</sup>	2.41 × 10 <sup>-11</sup>
L455F	1.77 × 10 <sup>-11</sup>	3.87 × 10 <sup>-11</sup>	NC	4.34 × 10 <sup>-11</sup>	5.87 × 10 <sup>-11</sup>	1.96 × 10 <sup>-11</sup>	1.70 × 10 <sup>-11</sup>
E484K	NC	6.25 × 10 <sup>-11</sup>	<b>1.13 × 10<sup>-9</sup></b>	NC	6.19 × 10 <sup>-11</sup>	NC	1.88 × 10 <sup>-10</sup>
G485D	NC	2.34 × 10 <sup>-11</sup>	2.05 × 10 <sup>-10</sup>	4.47 × 10 <sup>-11</sup>	4.71 × 10 <sup>-11</sup>	1.19 × 10 <sup>-10</sup>	4.58 × 10 <sup>-11</sup>
F486V	NC	3.16 × 10 <sup>-11</sup>	NC	3.50 × 10 <sup>-11</sup>	8.8 × 10 <sup>-11</sup>	1.29 × 10 <sup>-10</sup>	6.96 × 10 <sup>-11</sup>
F490L	<b>3.10 × 10<sup>-9</sup></b>	3.56 × 10 <sup>-11</sup>	4.53 × 10 <sup>-11</sup>	<b>1.94 × 10<sup>-9</sup></b>	3.64 × 10 <sup>-11</sup>	<b>2.50 × 10<sup>-9</sup></b>	8.37 × 10 <sup>-11</sup>
F490S	<b>2.23 × 10<sup>-10</sup></b>	4.42 × 10 <sup>-11</sup>	6.63 × 10 <sup>-11</sup>	<b>8.91 × 10<sup>-9</sup></b>	3.4 × 10 <sup>-11</sup>	<b>4.2 × 10<sup>-10</sup></b>	6.58 × 10 <sup>-11</sup>
Q493K	NC	4.19 × 10 <sup>-11</sup>	NC	3.45 × 10 <sup>-10</sup>	3.24 × 10 <sup>-11</sup>	<b>4.55 × 10<sup>-10</sup></b>	5.94 × 10 <sup>-11</sup>

however, this strategy may not suffice. Although some informed analysis can be made regarding epitope conservation based on sequence and structural analysis (6), the possibility of escape still exists under strong selection pressure. Indeed, escape studies performed with anti-influenza hemagglutinin stem binding antibodies have shown that escape mutants can arise despite high conservation of the stem epitope between diverse influenza subtypes, with some escape mutations arising outside of the antibody epitope region (7, 8). Antibodies that demonstrate broad neutralization across multiple species of coronaviruses, and thus may be targeting more conserved residues, have not been shown to be immune to escape upon selective pressure. In addition, their neutralization potency is orders of magnitude lower than that of the most potent neutralizing antibodies specific for SARS-CoV-2 (6, 9–11). Neutralization is thought to be the key mechanism of action of anti-coronavirus spike antibodies and has previously been shown to correlate with efficacy in animal models (12), and may therefore prove to be the most important driver of initial clinical efficacy. However, as demonstrated with our single-antibody escape studies, even highly potent neutralization does not protect against the rapid generation of viral escape mutants, and escape remains a major concern with individual antibody approaches.

Our data strongly support the notion that cocktail therapy may provide a powerful way to minimize mutational escape by SARS-CoV-2;

in particular, our studies point to the potential value of antibody cocktails in which two antibodies were chosen so as to bind to distinct and non-overlapping regions of the viral target (in this case, the RBD of the spike protein), and thus require the unlikely occurrence of simultaneous mutations at two distinct genetic sites for viral escape. A clinical candidate selection criterion for broad potency that includes functional assessment against naturally circulating sequence variants, as well as inclusion of multiple antibodies with non-overlapping epitopes, may provide enhanced protection against loss of efficacy. Future in vivo animal and human clinical studies will need to pay close attention to the possible emergence of escape mutants and potential subsequent loss of drug efficacy.

**REFERENCES AND NOTES**

1. R. Yan et al., *Science* **367**, 1444–1448 (2020).
2. Q. Wang et al., *Cell* **181**, 894–904.e9 (2020).
3. J. Hansen et al., Studies in humanized mice and convalescent humans yield a SARS-CoV-2 antibody cocktail. *Science* 10.1126/science.abd0827 (2020).
4. S.-Y. Lau et al., *Emerg. Microbes Infect.* **9**, 837–842 (2020).
5. M. E. Dieterle et al., A replication-competent vesicular stomatitis virus for studies of SARS-CoV-2 spike-mediated cell entry and its inhibition2020).
6. D. Pinto et al., *Nature* 10.1038/s41586-020-2349-y (2020).
7. K. Tharakaraman, V. Subramanian, D. Cain, V. Sasisekharan, R. Sasisekharan, *Cell Host Microbe* **15**, 644–651 (2014).
8. K. L. Prachanronarong et al., *J. Virol.* **93**, e01639-18 (2019).
9. S. J. Zost et al., Potently neutralizing human antibodies that block SARS-CoV-2 receptor binding and protect animals2020).
10. D. F. Robbiani et al., Convergent Antibody Responses to SARS-CoV-2 Infection in Convalescent Individuals2020).
11. Y. Cao et al., *Cell* 10.1016/j.cell.2020.05.025 (2020).
12. K. E. Pascal et al., *Proc. Natl. Acad. Sci. U.S.A.* **112**, 8738–8743 (2015).

**ACKNOWLEDGMENTS**

We thank K. Tramaglino for program management, J. Hansen for help with manuscript preparation, and E. Scolnick for useful discussions. **Funding:** A portion of this project has been funded in whole or in part with federal funds from the Department of Health and Human Services, Office of the Assistant Secretary for Preparedness and Response, Biomedical Advanced Research and Development Authority, under OT number HHSO100201700020C. **Author contributions:** A.B., B.O.F., E.W., and C.A.K. conceptualized and designed experiments; B.O.F., E.W., K.E.P., V.R., and S.G. performed research; A.B., B.O.F., E.W., K.E.P., V.R., S.G., G.S.A., A.J.M., N.S., G.D.Y., and C.A.K. analyzed data; R.C., K.L., N.N., M.N., and Y.W. prepared sequencing libraries and performed bioinformatics analysis; A.B., G.D.Y., and C.A.K. wrote the paper; and C.A.K. acquired funding. **Competing interests:** Regeneron authors own options and/or stock of the company. This work has been described in one or more pending provisional patent applications. A.J.M., N.S., G.D.Y., and C.A.K. are officers of Regeneron. **Data and materials availability:** Antibody sequences have been deposited to GenBank and are available in (3). Regeneron materials described in this manuscript may be made available to qualified, academic, noncommercial researchers through a material transfer agreement upon request at <https://regeneron.envisionpharma.com/vt/regeneron/>. For questions about how Regeneron shares materials, use the following email address: [preclinical.collaborations@regeneron.com](mailto:preclinical.collaborations@regeneron.com). This work is licensed under a Creative Commons Attribution 4.0 International (CC BY 4.0) license, which permits unrestricted use, distribution, and reproduction in any medium, provided the original work is properly cited. To view a copy of this license, visit <https://creativecommons.org/licenses/by/4.0/>. This license does not apply to figures/photos/artwork or other content included in the article that is credited to a third party; obtain authorization from the rights holder before using such material.

**SUPPLEMENTARY MATERIALS**

[science.sciencemag.org/content/369/6506/1014/suppl/DC1](https://science.sciencemag.org/content/369/6506/1014/suppl/DC1)  
Materials and Methods  
Fig. S1  
References (13–19)

30 May 2020; accepted 11 June 2020  
Published online 15 June 2020  
10.1126/science.abd0831



Postdocs need to prepare for many things during their job search, including a panel interview.

## Daunting but doable: Job searching after a postdoc

*How postdocs can compete in a historically tight academic job market*

By Kendall Powell

When neuroscientist **Nafisa Jadavji** entered the job market to search for an academic position in North America, she had already completed two successful postdoctoral stints in Berlin, Germany, and Ottawa, Canada; secured funding; and had 30 publications to her name. She applied to hundreds of positions, was invited for 10 onsite interviews, and eventually received one offer, for the assistant professor position she started in July 2019 at Midwestern University in Glendale, Arizona.

For better or worse, Jadavji's experiences are typical for academic job candidates. A survey of more than 300 applicants during the 2018–2019 academic job search season showed that the median number of onsite interviews was two and the median number of job offers was just one (1).

Recalling her own grueling, all-consuming search, Jadavji says postdocs need to develop a thick skin and persist in the process, especially women of color in science, technology, engineering, and mathematics (STEM) fields. Like many other candidates, she found the exercise hugely frustrating for its lack of transparency. When she asked for feedback from places that turned her down, she often got inactionable answers: "You don't smile enough. There were better candidates. You don't act like a PI [principal investigator]."

Searching for a permanent academic position after the postdoctoral term is not for the faint of heart. In some ways, postdocs have made a lot of progress—U.S.-based postdocs broke the USD 50,000 starting salary milestone this year as set by the U.S. National Institutes of Health (NIH) National Research Service Award pay scale (2). And nearly every university or institution that hires postdocs now has an office or program dedicated to their professional development.

### Upcoming features

■ Faculty—September 18 ■ Top Employers—October 30

Yet, those who want to continue on the academic track face steep hurdles. Only 14%–20% of U.S. biomedical Ph.D. holders will eventually move on to an assistant professor, group leader, or equivalent permanent position (3,4). Only one-quarter of postdocs graduating from prestigious posts at the University of California, San Francisco (UCSF) and the Massachusetts Institute of Technology advance to professorships (5).

For those who see this as their career path, however, it's possible to shed some light on this murky process. *Science* has interviewed postdocs who've recently succeeded with their job search. In addition, two recent studies collected data to characterize what makes a successful candidate and what criteria search committees are looking for (1, 6).

### Core characteristics

**Pearl Ryder**, a postdoc at Emory University and founder of the @FuturePI\_Slack group and Twitter account, says that candidates who stand out show they have a vision for the future lab they want to create.

That largely aligns with the most highly prioritized hiring characteristics revealed by in-depth interviews with faculty members on search committees from 20 life science departments (6). Researchers at UCSF and Northwestern University in Chicago developed a rubric broken down by type of university (teaching only, research and teaching, and research intensive). For research-intensive campuses, the highest priorities were candidates demonstrating the capability for feasible and independent research, the ability to communicate that research, a strong publication record, strong research vision and strategy, and a funding plan. All types of institutions also highly valued collegiality and fit, defined as research and teaching **cont.** >



postdocs

experience that matches the institution's mission, meets departmental needs, and brings the potential to collaborate. The research group has published a series of videos on how applicants can best use the rubric (<https://career.ucsf.edu/phds/academic/acra>).

Another study, led by cell biologist **Amanda Haage** at the University of North Dakota in Grand Forks and colleagues, surveyed a cohort of 317 job candidates who largely applied to academic positions in North America during the 2018–2019 cycle (7). These applicants submitted a median of 15 applications and spent a median of 4 years in their postdoctoral positions. The applicants had a median six first-author publications, with a median of 245 citations.

Fifty-eight percent of those surveyed got at least one offer at the end of their job search. Haage's group is also surveying candidates during the 2019–2020 academic job search season, and encourages postdoctoral researchers who applied for academic group leader positions in North America to participate ([https://und.qualtrics.com/jfe/form/SV\\_9nlisllMqqrYITL](https://und.qualtrics.com/jfe/form/SV_9nlisllMqqrYITL)).

Because research track records were similar among candidates who got interviews, many candidates feel their offers came down to their ability to showcase key soft skills, such as communication skills and problem-solving, on their applications and during interviews. Luckily, even a postdoc who finds herself in a less-than-ideal situation can find ways to hone those transferable skills that search committees crave.

## When to jump

Thinking about taking the plunge into the job market should start on day one of a postdoctoral position, says **Dara Wilson-Grant**, associate director of the Office of Postdoctoral Affairs at the University of North Carolina at Chapel Hill. "We push the idea at postdoc orientation that if you didn't come in with a career plan, you need to develop one now," she says.

In North America, the median time in all fields for a postdoc is 4 years before going on the market, and many universities have followed recommendations to limit the postdoc term to around 5 years (1). While the data are muddy as to whether postdocs are spending more total time as a postdoc (see sidebar), what is clear is that the minimum time needed is tightly tied to publishing successfully and developing a fundable research plan. Building such a portfolio usually takes a minimum of 3 years, applicants say.

## POSTDOCTORAL TIME WARP

Is the time spent as a postdoctoral researcher stretching out longer?

**Paula Stephan**, who studies the economics of science and has served on eight National Academy committees devoted to science workforce issues, says the answer is a resounding "yes." Stephan cites data showing that from 1973 until 1993, the percentage of biomedical doctorate holders serving in postdoctoral positions at 3–4 years post-Ph.D. and 5–6 years post-Ph.D. marched steadily upward.

"This is a story I've been hearing for a really long time," says Stephan. Around 2017, several reports called for a 5-year term limit on postdoctoral positions, and many universities adopted it. But, Stephan points out, that doesn't prevent a significant majority of postdoctoral researchers from doing multiple stints, nor does it prevent institutions from giving postdocs several different titles that mask their identity.

The Coalition for Next Generation Life Science database (<http://nglsccoalition.org/coalition-data>) was set up for institutions to report their post-Ph.D. and post-postdoctoral track records.

From the few that have posted data, the picture is sobering. At both the University of California, San Francisco and Massachusetts Institute of Technology, the median time spent in a postdoctoral position there is roughly 2.5–3 years.

However, only slightly more than 25% of their graduating postdocs go on to an academic tenure-track position. What's more, between 20%–50% of those graduating postdocs are moving on to another postdoctoral position (5).

One thing is crystal clear. Those who succeed at the very stiff odds of the academic job search gamble are those who have made the most of their 3–5 postdoctoral years, starting on day one.

**Alison Tebo**, a chemical biologist at the Laboratory of Biomolecules in Paris, France, started her job search in both the United States and Europe in her fourth postdoc year, before she felt quite ready. She

forced herself to begin writing drafts of her application materials and her first independent grant application, which gave her a slow-burn process to figure out her place in the research ecosystem.

"I just started throwing stuff onto paper, and that led me through the process of asking, 'What is my identity going to be as a scientist?'" Tebo will start as a group leader at the Howard Hughes Medical Institute's Janelia Research Campus in Ashburn, Virginia, in September.

**Alexandra Rutz**, a biomedical engineer postdoc at University of Cambridge, United Kingdom, followed a similar approach, going on the market before publishing the bulk of her postdoctoral work—against the advice of some peers. But she says it didn't seem to hurt her prospects, and she

will start her assistant professor position at Washington University in St. Louis in March 2021. "Nobody on the faculty search side once mentioned it, so maybe this is a false pressure postdocs are putting on ourselves," she says.

Applicants say that postdocs should plan for the search process to be very time-intensive, at some points all-consuming, and not to expect to produce research results at the same time. In addition, the process can be expensive when candidates must pay for interview travel and expenses up front. These factors may exclude or severely limit postdocs with caregiving responsibilities and those who come from groups underrepresented in STEM.

## Sharpening skills

Of course, most candidates say they planned well ahead to gain and hone the soft skills they would need to highlight in their applications.

**Juan Pablo Ruiz Villalobos**, postdoc at University of Wisconsin–Madison and president of the Future of Research advocacy group, recommends having a mentoring compact or formal agreement with your advisor. "Spend some time thinking about what your needs are" and how to get them met during your time as a postdoc, he advises.

In addition to advisors, postdocs can find other mentors within a department or institution or join the National Research Mentoring Network (<https://nrmnet.net>) or take online courses through the Postdoc Academy ([www.postdocacademy.org](http://www.postdocacademy.org)).

cont. >



### 3<sup>RD</sup> ANNUAL POSTDOCTORAL FELLOWSHIP AWARD IN NEUROSCIENCE

We are pleased to announce that the nomination period for the **3rd Annual Warren Alpert Distinguished Scholars Fellowship Award** is now open.

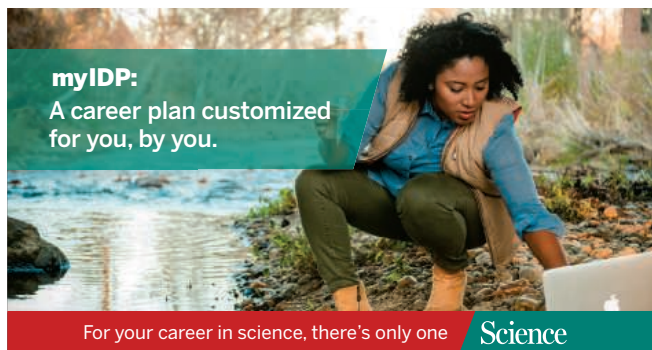
The Warren Alpert Distinguished Scholars program will support individual scientists of exceptional creativity who have an MD or PhD degree (or both) and who have completed a minimum of three years of a post-doctoral fellowship by **July 1, 2021** in the field of neurosciences and hold a post-doctoral research position at a United States medical school, research institute or academic hospital.

The dean or academic research officer of each medical school, academic hospital or research institute located in the United States is invited to nominate one candidate for research in basic or clinical neurosciences. Scholars will be chosen on the basis of the success in their prior post-doctoral work as well as in the importance and creativity of their continued work. The Foundation expects to make five awards in 2021.

These awards are given as a transitional post-doctoral award for recipients to enable their advance to a full-time faculty member at the Assistant Professor level or higher. The medical school, research institute or academic hospital appointing the scholar will be awarded \$200,000 annually for two years to cover their salary, lab costs, and related expenses. Under certain circumstances, the awardee may transfer funding in year 2 to support their faculty position. Indirect cost of up to 15% of direct costs, may be included in the \$200,000. All applicants are required to provide 75% effort.

Please visit our website for full details: [www.warrenalpertfoundation.org](http://www.warrenalpertfoundation.org)

**Applications are due by November 1, 2020**



**myIDP:**  
A career plan customized  
for you, by you.

For your career in science, there's only one **Science**

#### Features in myIDP include:

- Exercises to help you examine your skills, interests, and values.
- A list of 20 scientific career paths with a prediction of which ones best fit your skills and interests.



Visit the website and start planning today!  
[myIDP.sciencecareers.org](http://myIDP.sciencecareers.org)

Science Careers

AAAS

In partnership with:



The EGL Charitable Foundation  
invites you to apply to the

## Gruss Lipper Post-Doctoral Fellowship Program

### Eligibility

- Israeli citizenship
- Candidates must have completed PhD and/or MD/PhD degrees in the Biomedical Sciences at an accredited Israeli University/Medical School or be in their final year of study
- Candidates must have been awarded a postdoctoral position in the U.S. host research institution.

Details regarding the fellowship are available

at [www.eglc.org](http://www.eglc.org)

Application Deadline is October 4, 2020



## Featured participants

**Coalition for Next Generation Life Science Database**

<http://nglscoalition.org/coalition-data>

**Division of Biological Sciences Postdoctoral Association, University of Chicago**

<https://bsdpostdoc.uchicago.edu/contact-us>

**Future of Research**

[www.futureofresearch.org/about](http://www.futureofresearch.org/about)

**Future PI Slack @FuturePI\_Slack**

<https://futurepislack.wordpress.com>

**National Research Mentoring Network**

<https://nrmnet.net>

**Office of Postdoctoral Affairs, University of North Carolina at Chapel Hill**

<https://research.unc.edu/postdoctoral-affairs/postdocs>

**Postdoc Academy**

[www.postdocacademy.org](http://www.postdocacademy.org)

**University of North Dakota**

<https://und.edu>

Wilson-Grant, who spends much of her time doing one-on-one career counseling for postdocs, says they should decide on their target institutions and research recent hires at those places to see how many and what kinds of research publications they had. She also says that gaining the soft skills to be a good job candidate does not have to be extensive; she suggests taking a workshop to lay some groundwork in teaching, then teaching a summer or community college course to get hands-on experience.

To develop leadership skills, she recommends that postdocs join a committee of a professional association or scientific society to polish their communication, delegation, and conflict management skills. Some candidates joined departmental seminar-organizing committees, advisory councils of institutes or journals, and conference-organizing committees.

Nancy Schwartz, dean for postdoctoral affairs for the Division of Biological Sciences at the University of Chicago, advises postdocs to take advantage of all the resources on their campuses, including professional development seminars, alumni networks, and one-on-one sessions to practice for job interviews and negotiation.

"A lot of postdocs don't realize that they are doing many PI-like activities in the lab" and should explicitly include them on their CVs and applications, says Schwartz. Examples include "writing up protocols, mentoring graduate students, or maybe their PI went on sabbatical and left the postdoc in charge [of lab management]," she says.

**Adding sparkle to applications**

When all candidates have similar research productivity, how do successful applicants outshine the crowd? Recent job searchers say they've demonstrated other key characteristics: commitment to diversity, managing and mentoring others, and being savvy in securing funding.

Of the 46 engineering departments where Rutz applied, half asked for a diversity statement on the candidate's commitment to and experience with diversity, equity, and inclusion (DEI) efforts. Devang Mehta, a plant genomics researcher at the University of Alberta in Edmonton, Canada, highlighted an op-ed he'd published on racism in science, his participation in a DEI journal club, and his work on the *eLife* Early-Career Advisory Group that looks at DEI issues in publishing.

Even time that applicants spent working from home during the COVID-19 pandemic can be turned into a shining moment of management success. "If you were managing a team at home, with

school-aged coworkers at your side, you can talk about how you reworked schedules to come out of it successfully," says Tracy Costello, owner of Coach4Postdocs.com, a Tampa-based consulting business.

Rutz highlighted her mentoring of 18 students during her Ph.D. work and postdoc, publishing with many of them. This showcased her talents as an effective teacher and advisor.

Search committees also want to see how familiar an applicant is with the funding landscape in their field and region or country. If a postdoc doesn't already have their own funding from a career transition grant, such as the NIH Pathway to Independence Award (K99/R00), then they must find creative ways to show that their research is fundable and that they have grant-writing experience.

Mehta says he purposefully chose to join a relatively new group as a postdoc to learn from a mentor who was actively setting up his own group. "My PI was great about involving me in the grant-search and grant-writing process," he says, adding that postdocs should cowrite grants with their advisors, being listed as Co-PIs when possible.

As a postdoc abroad in Europe, Rutz wasn't eligible to apply for many U.S.-based career transition awards, so she listed all the grants she had cowritten or fully written in the past.

Jadavji went so far as to write out her first grant's aims and devised a plan for which grant mechanisms she would apply for in her first year. "Have that trajectory of how you will fund your research mapped out," she says.

**Cast a wide net**

Jadavji recommends that once a candidate has gotten an interview, they should "celebrate—and then get to work." After all, getting offered an interview by phone or video call is a huge success in this market—with a median of just one per candidate during the 2018–2019 cycle. But next comes the serious work of researching departments and their faculty members, and preparing for tough interview questions.

"The number of applications people put in was the most robust predictor of how well they did in terms of interviews, which then lead to offers," notes Haage (although that relationship tailed off sharply for respondents who filed more than 50 applications). Applicants should not be too rigid about the location, size, and focus of institutions they consider, and be willing to include undergraduate institutions, minority-serving institutions, and other settings. "Great science can happen outside of where you think it can."

**References**

1. J. D. Fernandes *et al.*, *eLife* (2019), available at <https://elifesciences.org/articles/54097>.
2. <https://grants.nih.gov/grants/guide/notice-files/NOT-OD-20-070.html>.
3. H. Sauermann, M. Roach, *PLOS One* **7**, e36307 (2012), available at <https://doi.org/10.1187/cbe.19-11-0235>.
4. S. Kahn, D. K. Ginther, *Nat. Biotechnol.* **35**, 90–94 (2017), available at <http://sites.bu.edu/shulamitkahn/files/2018/05/Nature-Value-of-Postdoc.pdf>.
5. Coalition for Next Generation Life Science, "Data for a Stronger Workforce," available at <http://nglscoalition.org/coalition-data>.
6. L. Clement, J.B. Dorman, R. McGee, *CBE Life Sci. Educ.* **19** (2019), available at <https://doi.org/10.1187/cbe.19-11-0235>.

Kendall Powell is a freelance science writer based in Lafayette, Colorado.

# Sloan Kettering Institute

Celebrating 75 years of breakthroughs

Join our faculty and help set the pace of biomedical science.

## JOIN US

Successful candidates will hold an appointment in one of SKI's research programs. Candidates may apply to up to two programs. MSK is an equal opportunity and affirmative action employer committed to diversity and inclusion in all aspects of recruiting and employment.

### Cancer Biology & Genetics

Chair: Scott Lowe, PhD

### Cell Biology

Chair: Kristian Helin, PhD

### Chemical Biology

Chair: Derek Tan, PhD

### Computational & Systems Biology

Chair: Dana Pe'er, PhD

### Developmental Biology

Chair: Anna-Katerina Hadjantonakis, PhD

### Immunology

Chair: Alexander Rudensky, PhD

### Molecular Biology

Chair: John Petrini, PhD

### Molecular Pharmacology

Chair: David Scheinberg, MD, PhD

### Structural Biology

Chair: Christopher Lima, PhD



Memorial Sloan Kettering  
Cancer Center

## AREAS OF BASIC AND TRANSLATIONAL RESEARCH

- Stem Cell Biology
- Developmental Oncology
- Regenerative Medicine
- Machine Learning
- 3D Single-Cell Analytics
- Biophysics & Imaging
- Organelle Biology
- Chromatin & Gene Regulation
- Genome Integrity and Functional Genomics
- Chemistry & Chemical Biology
- Metastasis & Tumor Microenvironment
- Immunity, Host-Microbial Interactions and Microbiomes
- Tumor Immunobiology
- Experimental Therapeutics, Imaging and Bioengineering

## RESEARCH AND TRAINING

- 100 research laboratories housed in state-of-the-art buildings
- 26 Core facilities offering cutting-edge scientific services
- More than 900 pre- and postdoctoral trainees
- Appointments in the Gerstner Sloan Kettering Graduate School of Biomedical Sciences and the Weill Cornell Graduate School of Medical Sciences

Visit [www.ski.edu](http://www.ski.edu) to learn more.



MSK is an equal opportunity and affirmative action employer committed to diversity and inclusion in all aspects of recruiting and employment. All qualified individuals are encouraged to apply and will receive consideration without regard to race, color, gender, gender identity or expression, sexual orientation, national origin, age, religion, creed, disability, veteran status or any other factor which cannot lawfully be used as a basis for an employment decision.



# 10 ways that Science Careers can help advance your career

1. Register for a free online account on **ScienceCareers.org**.
2. Search thousands of job postings and find your perfect job.
3. Sign up to receive e-mail alerts about job postings that match your criteria.
4. Upload your resume into our database and connect with employers.
5. Watch one of our many webinars on different career topics such as job searching, networking, and more.
6. Download our career booklets, including Career Basics, Careers Beyond the Bench, and Developing Your Skills.
7. Complete an interactive, personalized career plan at “my IDP.”
8. Visit our Employer Profiles to learn more about prospective employers.
9. Research graduate program information and find a program right for you.
10. Read relevant career advice articles from our library of thousands.

Visit **ScienceCareers.org**  
today — all resources are free



**Science Careers**

FROM THE JOURNAL SCIENCE  AAAS

SCIENCECAREERS.ORG

## FACULTY POSITION IN IMMUNOLOGY

Department of Microbiology,  
Boston University School of Medicine

The Department of Microbiology ([www.bumc.bu.edu/microbiology](http://www.bumc.bu.edu/microbiology)) invites applications for the position of **Assistant Professor in Immunology**. The successful applicant will join a collaborative, vibrant, and growing community of researchers in an environment that values creativity, collaboration and social and cultural diversity of our faculty, staff and students. The successful applicant will expand and complement existing departmental strengths in virology, host-pathogen interactions, innate immunity and inflammation. Applicants should have a demonstrated and ongoing record of research excellence with a focus that includes basic or translational studies on investigating immune responses to human pathogens. The Boston University Medical Campus includes a number of centers of excellence which offer rich collaborative opportunities, including the Immunology Training Program, Center for Regenerative Medicine, the Center for Network Systems Biology, and the National Emerging Infectious Diseases Laboratories, and supports state-of-the-art core facilities. The successful candidate is expected to oversee a vigorous, innovative, and extramurally funded research program, to participate in the teaching and training of graduate students and post-doctoral fellows, and support our institutional commitment to ensure BU is inclusive, equitable, diverse and a place where all constituents can thrive.

To be considered, please submit a curriculum vitae, a summary of research accomplishments, a description of future research plans, and the names of at least 3 references to Ms. Kathleen Marinelli ([kfurness@bu.edu](mailto:kfurness@bu.edu)). Applications will be considered as they are received, with the positions to be filled after **September 1, 2020**.

*Boston University School of Medicine is an equal opportunity/affirmative action employer, committed to building and maintaining robust diversity within all components of its community, and strongly welcomes applications from women, persons with disabilities, protected veterans, and under-represented minorities.*

## ScienceCareers

FROM THE JOURNAL SCIENCE 

Confused about your  
next career move?

 **Download Free Career  
Advice Booklets!**

[ScienceCareers.org/booklets](http://ScienceCareers.org/booklets)



## Faculty Positions in Cardiovascular Sciences

Virginia Tech (<https://vt.edu/>) is recruiting to fill up to three tenure track/tenured open rank faculty positions in cardiovascular sciences. The newly recruited faculty members will be part of a major initiative to expand the existing cardiovascular biomedical research team at the Fralin Biomedical Research Institute (FBRI) at Virginia Tech Carilion (<https://research.vtc.vt.edu/>) located on the Health Sciences and Technology campus in Roanoke, Virginia.

The research institute, led by Dr. Michael J. Friedlander and located in a 100,000 square foot purpose designed facility is entering its tenth year with 33 research teams, 350 employees and students with over \$125M in extramural research funding. A new 140,000 SF research building representing a \$90M investment from the state, Virginia Tech and Carilion Clinic and major additional investments from the university including a transformative \$50M gift to the research institute, opened in July, 2020. The new building houses state of the art labs and core facilities including those for in vitro, laboratory animal model, human subject and computational based research programs, a high field (9.4T) MRI, micro PET, surgical research suites, metabolic chambers, scanning block face EM, full molecular biology, cellular imaging, histology, data analytics and research participant monitoring core facilities. Recruitment of outstanding faculty in cardiovascular sciences will build on existing research strengths in cardiomyocyte coupling, drug development, sudden cardiac death, arrhythmogenesis and vascular remodeling and regulation. Faculty will be embedded in a transdisciplinary research environment that will include additional new teams of investigators focused on metabolism and obesity, infectious disease/immunology, neuroscience and body-device interfaces and comparative oncology.

Applicants for all positions should have an earned doctorate (PhD, MD, DVM or combined degrees), postdoctoral research experience in cardiovascular science, a demonstrated record of accomplishment of substantial research productivity through major publications and either active major extramural funding (preferably from NIH) or strong evidence of the likelihood of obtaining such funding in the near term. The new faculty will join the FBRI's highly successful and nationally regarded Center for Heart and Repenerative Medicine Research (CHRM) led by Dr. Robert Gourdie ([https://research.vtc.vt.edu/heart\\_center/](https://research.vtc.vt.edu/heart_center/)). Collaborations will be encouraged to collaborate within CHRM, with the other groups at the FBRI and across Virginia Tech and with clinical colleagues at the adjacent Carilion Clinic, including the division of cardiology under the direction of Dr. David Sane.

Successful candidates will be expected to establish and maintain a high quality, extramurally funded research program and participate in teaching and mentoring of graduate students as well as research project mentoring of undergraduate and medical students. Highly competitive salary, space, and startup packages will be provided.

Faculty members can draw from an outstanding and diverse pool of students to work with them in their research program. Specifically, Virginia Tech has over 6,000 graduate students with graduate programs in multiple biomedical disciplines including Translational Biology, Medicine, and Health (<http://www.tbmh.vt.edu>), Molecular and Cellular Biology (<https://www.mcb.vt.edu>), Biological Sciences (<https://www.biol.vt.edu/>), Biomedical Engineering and Mechanics (<https://beam.vt.edu/graduate.html>) and Biomedical Sciences and Pathobiology (<https://www.vetmed.vt.edu/academics/bmvs/>). In addition, the Virginia Tech Carilion School of Medicine (<https://medicine.vtc.vt.edu/>) is one of the nation's most research intensive allopathic medical schools where every medical student carries out a four year hypothesis driven research project under faculty mentorship.

The FBRI at VTC is located in Roanoke, Virginia and is a public private partnership between the Commonwealth of Virginia's leading research intensive university, Virginia Tech and a major health care system Carilion Clinic in Roanoke, VA. The research institute is located in the picturesque Roanoke Valley midway between Washington, DC and Charlotte, NC.

**Required qualifications:** Applicants for all positions should have an earned doctorate (PhD, MD, DVM or combined degrees), postdoctoral research experience in cardiovascular science, a demonstrated record of accomplishment of substantial research productivity through major publications and either active major extramural funding (preferably from NIH) or strong evidence of the likelihood of obtaining such funding in the near term.

To apply, please visit <http://careers.pageuppeople.com/968/cw/en-us/job/511099/cardiovascular-sciences-faculty>

*Virginia Tech is an Equal Opportunity Employer.*



By Akshata Naik

# Choose your adviser wisely

**T**he clock read 11 p.m. and I was still in the lab, staring at my poster abstract for what felt like the millionth time. I couldn't focus. But going home wasn't an option. My adviser had required me, and the rest of my labmates, to stay in the lab until she had time to read all of our abstracts. The submission deadline wasn't for a few days, but she had decided she wanted to meet early with each of us to discuss the single-paragraph descriptions of our work. We waited dutifully as each lab member took their turn. None of us dared to leave—or to challenge our boss. I didn't get home until 1:30 a.m.

It was one more reminder that I should have been more careful when selecting a graduate adviser. Unfortunately, I was foolish enough not to give mentoring style a second thought. I was simply happy to have received an offer.

Part of the problem was that I had limited options. I had moved to the United States with my husband, who had a good job in a particular city. It had only one university, with only one department that really interested me. So I started to volunteer in a research lab there.

I was a regular attendee at departmental seminars, and that's where I met my future adviser. After she presented a seminar, I approached her and we set up a time to chat. We had a productive discussion about her research. Later, I went to dinner with her lab group.

I didn't pick up any signs of trouble, although one person who worked in a lab that shared space with hers did tell me about coming across one of her lab members crying in the breakroom. Naïvely, I ignored that warning sign. Within a few weeks, the faculty member offered me a position in her lab as a master's student. The opportunity seemed too good to pass up. I hoped it would work out.

It wasn't long before reality set in. Group meetings were dreadful. Our adviser was often angry and verbally abusive. She persistently micromanaged her lab members and pitted us against one another. Once, she sent an irate email on a federal holiday, asking us why we weren't working. "The only lab that is empty is ours," she wrote. "How is this possible? Don't you have experiments or data to analyze?"

The situation wore me down, and I lost motivation to do my work. I wondered whether I should quit, but as an international student, I felt trapped. If I dropped out



**"The last thing you want is an adviser who brings you down."**

of my program, I'd not only be out of a job, but I'd also lose my student visa status. So I stuck it out and waited for the right moment to jump ship.

I applied to upgrade from the master's program to the Ph.D. program. That option wasn't available until I'd completed 1 year of graduate school, but it ultimately gave me a ticket out of her lab.

As I looked for a new adviser, I was careful not to repeat the mistakes I had made in the past. I approached another faculty member whose research interested me. But when I visited his lab, I paid attention to how he interacted with others, and I spoke with people who worked with him, specifically asking about his mentoring style. I

was amazed how friendly everyone was. His students had great regard for him, and I immediately sensed that his lab was an environment where I could thrive.

He took me on as a Ph.D. student, rescuing me from the misery I'd felt in graduate school up to that point. In my new lab, I arrived eager to work each day, and I didn't go home mentally exhausted by interpersonal disputes. That helped me be much more determined and efficient with my work.

Grad school is a tough, long road that requires patience and perseverance. Finding a lab that is a good match for you is critical. I encourage prospective students to learn from my mistakes and to do your due diligence before joining a lab. Ask a lot of questions and seek a lot of diverse opinions—because the last thing you want is an adviser who brings you down. ■

Akshata Naik is a postdoc at Wayne State University in Detroit, Michigan. Do you have an interesting career story to share? Send it to [SciCareerEditor@aaas.org](mailto:SciCareerEditor@aaas.org).